ISSN 0332-1649

Volume 23
Number 4
2004

COMPEL

The International Journal for Computation and Mathematics in Electrical and Electronic Engineering

Selected papers from the 6th International Symposium on Electric and Magnetic Fields (EMF) 2003, Aachen, Germany

Guest Editors
Patrick Dular, Kay Hameyer and Gerhard Henneberger

CONTENTS

Access this journal online 849

Editorial advisory board 850

Abstracts and keywords 851

Preface 858

SPECIAL ISSUE SECTION

Fast and efficient 3D boundary element method for closed domains
André Buchau, Wolfgang Hafla and Wolfgang M. Rucker 859

Formulation of mixed elements for the 2D-BEM
Klaus Schimmanz and Arnulf Kost 866

Coupled mechanical-electrostatic FE-BE analysis with FMM acceleration: application to a shunt capacitive MEMS switch
R.V. Sabariego, J. Gyselinck, P. Dular, J. De Coster, F. Henrotte and K. Hameyer 876

Access this journal electronically

The current and past volumes of this journal are available at:

www.emeraldinsight.com/0332-1649.htm

You can also search over 100 additional Emerald journals in Emerald Fulltext at:

www.emeraldinsight.com/ft

See page following contents for full details of what your access includes.

Emerald

CONTENTS
continued

Comparison of 3D magnetodynamic formulations in terms of potentials with imposed electric global quantities
T. Henneron, S. Clénet and F. Piriou 885

Modelisation of thin cracks with varying conductivity in eddy-current testing
Ph. Beltrame 894

Efficient modelling techniques for complicated boundary conditions applied to structured grids
Herbert De Gersem, Markus Wilke, Markus Clemens and Thomas Weiland 904

Non-nested geometric multigrid method using consistency error correction for discrete magnetic curl-curl formulations
M. Clemens, S. Feigh, M. Wilke and T. Weiland 913

Wavelet's application in electrostatic and their computing aspects
Aldo Artur Belardi, José Roberto Cardoso and Carlos Antonio França Sartori 923

Comparisons of finite element and Rayleigh methods for the study of conical Bloch waves in arrays of metallic cylinders
S. Guenneau, A. Nicolet, C. Geuzaine, F. Zolla and A.B. Movchan 932

The Newton-Raphson method for solving non-linear and anisotropic time-harmonic problems
H. Vande Sande, F. Henrotte and K. Hameyer 950

Complementary two-dimensional finite element formulations with inclusion of a vectorized Jiles-Atherton model
J. Gyselinck, L. Vandevelde, J. Melkebeek and P. Dular 959

Transient field-circuit coupled formulation based on the finite integration technique and a mixed circuit formulation
Galina Benderskaya, Herbert De Gersem, Thomas Weiland and Markus Clemens 968

Field-circuit model of the dynamics of electromechanical device supplied by electronic power converters
Lech Nowak and Jacek Mikołajewicz 977

Field-circuit transient analysis of a magnetorheological fluid brake
W. Szeląg, P. Sujka and R. Walendowski 986

CONTENTS
continued

The eggshell approach for the computation of electromagnetic forces in 2D and 3D
François Henrotte, Geoffrey Deliége and Kay Hameyer 996

Comparison of sliding-surface and moving-band techniques in frequency-domain finite-element models of rotating machines
Herbert De Gersem, Johan Gyselinck, Patrick Dular, Kay Hameyer and Thomas Weiland 1006

Orthogonal transformation of moving grid model into fixed grid model in the finite element analysis of induction machines
Andrzej Demenko and Dorota Stachowiak 1015

Axisymmetric transient electromagnetic finite-difference scheme including prescribed motion
M. Klocke 1023

Multi-domain topology optimization of electromagnetic systems
Semyung Wang, Seungkyu Park and Jenam Kang 1036

Optimal design of induction heating equipment for high-speed processing of a semiconductor
Yoshifumi Okamoto, Toshio Imai, Daisuke Miyagi, Norio Takahashi, Kazuhiro Ozaki, Hiroshi Ono and Naoki Uchida 1045

Optimal characterization of LF magnetic field using multipoles
R. Scorretti, R. Takahashi, L. Nicolas and N. Burais 1053

A new approach for shape optimization of resistors with complex geometry
M. Purcar, J. Deconinck, L. Bortels, C. Munteanu, E. Simion and V. Topa 1062

Comparison of static, dynamic, and static-dynamic eccentricity in induction machines with squirrel-cage rotors using 2D-transient FEM
Christoph Schlensok and Gerhard Henneberger 1070

Electrical machine analysis considering field – circuit – movement and skewing effects
A.M. de Oliveira, R. Antunes, P. Kuo-Peng, N. Sadowski and P. Dular 1080

FEM analysis of current limiting devices using superconducting thin film and AC losses of YBCO coated conductor
H. Ohsaki, Y. Ichiki and S. Sugita 1092

CONTENTS
continued

REGULAR PAPERS

Comparison of 3D and 2D field-circuit models of power transformer transients
Lech Nowak, Andrzej Demenko and Wojciech Szeląg 1100

Calculation of magnetization characteristic of a squirrel cage machine using edge element method
Andrzej Demenko, Lech Nowak and Wojciech Pietrowski 1110

Edge element analysis of brushless motors with inhomogeneously magnetized permanent magnets
Dorota Stachowiak 1119

Adaptive observer of rotor speed and position for PMSM sensorless control system
Konrad Urbański and Krzysztof Zawirski 1129

A shunt active power filter: development of properties
Andrzej Szromba 1146

Awards for Excellence 1163

Preface

The 6th International Symposium on Electric and Magnetic Fields (EMF) 2003, was held in Aachen, Germany, from 6 to 9 October 2003. Previous editions were held in Liège (September 1992), Leuven (May 1994), Liège (May 1996), Marseille (May 1998) and Ghent (May 2000).

The purpose of the EMF Symposium is to throw a bridge between the recent advances of research in numerical modelling of electromagnetic fields and the growing number of industrial problems requiring such techniques. Therefore, besides classical sessions on the progress of computational methods, special sessions were devoted to advanced industrial applications of electromagnetic modelling. The topics included numerical methods and techniques, coupled problems (mechanical, thermal, electric circuits), material modelling, optimisation and specific application oriented numerical problems.

More than 100 papers were presented by participants coming from 18 countries. A limited number of 25 papers were selected by the EMF'2003 Scientific Committee for publication in this special issue of the *COMPEL* Journal.

Special thanks are due to all the members of the Scientific Committee for their valuable reviewing work as well as to the AIM (Association of Engineers from the Montefiore Electrical Institute, University of Liège) secretariat for numerous organisational aspects.

We hope that this special issue will provide various interesting information to the readers.

Patrick Dular, Kay Hameyer and Gerhard Henneberger
Guest Editors

EMF'003 International Scientific Committee

J.P.A. BASTOS, Universidade Federal de Santa Catarina, Brazil
W.A. CRONJE, Rand Afrikaans University, South Africa
A. DEMENKO, Technical University of Poznan, Poland
P. DULAR, Université de Liège, Belgium
R.D. FINDLAY, McMaster University, Canada
J. GYSELINCK, Université de Liège, Belgium
K. HAMEYER, Katholieke Universiteit Leuven, Belgium
G. HENNEBERGER, RWTH Aachen, Germany
L. KETTUNEN, Tampere University of Technology, Finland
A. KOST, Universität Cottbus, Germany
J. MELKEBEEK, Universiteit Gent, Belgium
G. MEUNIER, Laboratoire d'Electrotechnique de Grenoble, France
G. MOLINARI, Universita Degli Studi di Genova, Italy
S.I. NABETA, Universidade de Sao Paulo, Brazil
A. NICOLAS, Centre de Génie Electrique de Lyon, France
A. NICOLET, Université d'Aix-Marseille III, France
F. PIRIOU, Université des Sciences et Technologies de Lille, France
A. RAZEK, Laboratoire de Génie Electrique de Paris, France
J.K. SYKULSKI, University of Southampton, United Kingdom
N. TAKAHASHI, Okayama University, Japan
M. TRLEP, University of Maribor, Slovenia
T. WEILAND, Universität Darmstadt, Germany

COMPEL: The International Journal for Computation and Mathematics in Electrical and Electronic Engineering
Vol. 23 No. 4, 2004
p. 858
© Emerald Group Publishing Limited
0332-1649

The Emerald Research Register for this journal is available at
www.emeraldinsight.com/researchregister

The current issue and full text archive of this journal is available at
www.emeraldinsight.com/0332-1649.htm

Fast and efficient 3D boundary element method for closed domains

André Buchau, Wolfgang Hafla and Wolfgang M. Rucker
Institute for Theory of Electrical Engineering, University of Stuttgart, Stuttgart, Germany

Keywords *Boundary-elements methods, Electrostatics, Galerkin method*

Abstract *An application of a boundary element method to the solution of static field problems in closed domains is presented in this paper. The fully populated system matrix of the boundary element method is compressed with the fast multipole method. Two approaches of modified transformation techniques are compared and discussed in the context of boundary element methods to further reduce the computational costs of the fast multipole method. The efficiency of the fast multipole method with modified transformations is shown in two numerical examples.*

Introduction

The solution of static field problems with a boundary element method (BEM) is very advantageous (Rao *et al.*, 1984). It suffices to discretize the surfaces of piecewise homogeneous, linear materials only. The surrounding free space is implicitly considered. BEMs can be divided into direct and indirect formulations. An indirect formulation is based on surface charges in the case of potential problems. The corresponding potential is a so-called single-layer potential. A direct formulation based on Green's theorem

$$c(\boldsymbol{r})u(\boldsymbol{r}) = \oint \frac{\partial u(\boldsymbol{r}')}{\partial n'} \frac{1}{|\boldsymbol{r}-\boldsymbol{r}'|}\,\mathrm{d}A' - \oint u(\boldsymbol{r}')\,\frac{\partial}{\partial n'}\frac{1}{|\boldsymbol{r}-\boldsymbol{r}'|}\,\mathrm{d}A' \tag{1}$$

is recommended for the solution of potential problems in closed domains.

Only the surface of a closed domain has been considered in equation (1), since the influence of the surrounding space is represented by equivalent Dirichlet and Neumann boundary conditions. The first integral in equation (1) corresponds to a single-layer potential and the second to a double-layer potential. The singular coefficient $c(\boldsymbol{r})$ depends on the position of the evaluation point in the domain.

The fully populated system matrix is compressed with the fast multipole method (FMM) (Greengard and Rokhlin, 1987). The FMM reduces the memory requirements from $O(N^2)$ to approximately $O(N)$. N is the number of unknowns. Additionally, the FMM accelerates post processing drastically. Nevertheless the FMM has a significant bottleneck, especially in combination with double-layer potentials. The computation of a single matrix-by-vector product is relatively expensive. Of course, it is proportional to CN, but the constant C is large (Buchau *et al.*, 2003b).

The computational costs of a matrix-by-vector product are mainly caused by the transformation of a multipole expansion into a local expansion (M2L-transformation). The costs of the M2L-transformation are of $O(L^4)$ (Greengard and Rokhlin, 1987). L is the order of the truncated series expansions. In the context of particle interactions a modified M2L-transformation reduces the computational cost to $O(L^3)$ or $O(L^2)$, respectively (Cheng *et al.*, 1998; Greengard and Rokhlin, 1997).

COMPEL: The International Journal for Computation and Mathematics in Electrical and Electronic Engineering
Vol. 23 No. 4, 2004
pp. 859-865
© Emerald Group Publishing Limited
0332-1649
DOI 10.1108/03321640410553283

A direct BEM formulation for the solution of potential problems is described in the following. An extension of the FMM is presented to treat the double-layer potential term in Green's theorem (equation (1)). Finally, the approaches presented in Cheng *et al.* (1998) and Greengard and Rokhlin (1997) are adapted to BEM computations with higher order elements and adaptive meshes. The efficiency of both approaches is analyzed in the framework of potential problems and a BEM.

Theoretical background

Direct BEM formulation

As aforementioned a direct BEM formulation based on Green's theorem (equation (1)) is especially suited to the solution of potential problems in closed domains. Several domains are coupled at their common boundaries. The Dirichlet boundary condition is the given potential at some parts of the surfaces of the domains. In the case of electrostatic problems the Neumann boundary condition is the continuity of the normal component of the electric displacement between two dielectric domains. The normal derivative of the potential vanishes at the remaining parts of the domain surfaces for steady current flow field problems.

All surfaces are discretized with eight-noded, quadrilateral, second-order elements. The system of linear equations is obtained by an application of the Galerkin method. It is solved iteratively with a generalized minimal residual method (GMRES) in combination with a Jacobi preconditioner (Axelsson, 1996; Barrett *et al.*, 1994).

Fast multipole method

The FMM was introduced for the fast and efficient simulation of particle interactions (Greengard and Rokhlin, 1987). An application of the FMM to an indirect BEM formulation with Dirichlet boundary conditions and constant elements was presented for example, in Nabors and White (1991). To deal with higher order elements and adaptive meshes the FMM algorithm must be extended. Then the real convergence radii of the cubes have to be considered to achieve numerical stability and a high accuracy (Buchau *et al.*, 2003a). All the above-mentioned approaches and applications have in common, the system matrix that is approximated accurately along with low memory requirements. The computational costs are in most cases satisfactory.

If the potential of charge distributions or single-layers are computed, the classical FMM approach (Greengard and Rokhlin, 1987) can be used. Here, potential problems shall be solved with a direct BEM formulation based on Green's theorem (equation (1)). That means the potential of a single- and a double-layer has to be evaluated.

FMM for double-layer potentials

There are two possibilities to include double-layer potentials

$$u(\boldsymbol{r}) = \frac{1}{4\pi\varepsilon_0}\int_A \tau(\boldsymbol{r}')\nabla_{r'}\frac{1}{|\boldsymbol{r}-\boldsymbol{r}'|}\cdot \boldsymbol{n}'\,\mathrm{d}A' \tag{2}$$

into the FMM. Either the local expansion or the multipole expansion can be modified.

The electric field strength can be computed by an analytical differentiation of the local expansion (Buchau *et al.*, 2000). Similarly a local expansion can be found to compute a double-layer potential (Buchau and Rucker, 2002)

$$u(\boldsymbol{r}) = -\frac{1}{4\pi\varepsilon_0} \sum_{n=1}^{L} \sum_{m=-n}^{n} \nabla\left(r^n Y_n^m(\theta, \varphi)\right) \cdot \boldsymbol{L}_n^m. \tag{3}$$

Y_n^m are spherical harmonics. To obtain the vector local coefficients $\boldsymbol{L}_n^m$ the double-layer τ is split into three Cartesian components. Each component of the vector local coefficients can be formally treated like a single-layer.

In the framework of the FMM the local coefficients are computed with a hierarchical scheme from the so-called multipole coefficients. Now a set of multipole coefficients is needed, which is obtained from the Cartesian components of the double-layer. Each set of multipole coefficients is converted with the classical FMM algorithm into a local expansion and then evaluated with equation (3). That means the FMM-algorithm has to be passed four times in each iteration step, thrice for the double-layer and once for the single-layer. The computational costs grow correspondingly.

Another approach is to modify the computation of the multipole coefficients (Of, 2001)

$$M_n^m = \int_A \tau(\boldsymbol{r}')\boldsymbol{n}(\boldsymbol{r}') \cdot \nabla_{r'}\left(r'^n Y_n^{-m}(\theta', \varphi')\right) \mathrm{d}A'. \tag{4}$$

In that case the multipole coefficients of single- and double-layers can be added. All remaining computations, transformations and local expansions are the same as in the original FMM algorithm. Only one set of multipole coefficient is obtained along with only one pass of the FMM algorithm in each iteration step. That means the total computational costs are approximately the same as in the classical FMM.

Modified multipole-to-local transformations

For a conversion of a multipole expansion M_n^m into a local expansion L_n^m a double sum has to be evaluated (Greengard and Rokhlin, 1987)

$$L_n^m = \sum_{k=0}^{L} \sum_{l=-k}^{k} \frac{M_k^l j^{|m-l|-|m|-|l|} A_k^l A_n^m Y_{k+n}^{l-m}(\mu, \nu)}{(-1)^k \rho^{k+n+1} A_{n+k}^{l-m}}. \tag{5}$$

The computational costs for equation (5) are of $O(L^4)$. If equation (5) is only applied to transformations in z-direction, it simplifies to

$$L_n^m = \sum_{k=m}^{L} M_k^m \frac{Y_{k+n}^0(0,0)(-1)^{k+m}(n+k)!}{\rho^{k+n+1}\sqrt{(k-m)!(k+m)!(n-m)!(n+m)!}}. \tag{6}$$

The double-sum reduces to a single-sum and the imaginary part of the transformation coefficients vanishes. Equation (6) is of $O(L^3)$. The coordinate system must be rotated in such a way that the transformation direction coincides with the z-axis, to use equation (6) in the FMM. The multipole coefficients are rotated about the z-axis by an angle β with the following transformation

$$M'^m_n = M_n^m \mathrm{e}^{\mathrm{j}m\beta}. \tag{7}$$

The rotation of the local coefficients is analogous to equation (7). The rotation of the multipole coefficients about the y-axis about an angle α is more expensive (Biedenharn and Louck, 1981)

$$M'^{m'}_n = \sum_{m=-n}^{-1} R(n, m, m', \alpha)(-1)^m \left(M_n^{-m}\right)^* + \sum_{m=0}^{n} R(n, m, m', \alpha) M_n^m. \tag{8}$$

The rotation matrices $R(n, m, m', \alpha)$ are discussed in detail in Biedenharn and Lauck (1981). Note that in Biedenharn and Lauck (1981) another normalization of the spherical harmonics was used. The other transformations, the multipole-to-multipole transformation and the local-to-local transformation, can be modified similarly

$$M_n^m = \sum_{k=0}^{n} \bar{M}_{n-k}^m \sqrt{\frac{(n-m)!(n+m)!}{k!k!(n-k-m)!(n-k+m)!}} \rho^k P_k(1) \tag{9}$$

and

$$L_n^m = \sum_{k=n}^{L} \bar{L}_k^m \sqrt{\frac{(k-m)!(k+m)!}{(k-n)!(k-n)!(n-m)!(n+m)!}} (-1)^{k+n} \rho^{k-n} P_{k-n}(1). \tag{10}$$

The size of the near-field and the order of the series expansions are determined heuristically (Buchau *et al.*, 2003a). For instance, $L = 9$ is a good choice, if the near-field is relatively small. Then the modified transformations in equations (6), (9), and (10) reduce the computational costs by approximately 60 percent.

Another approach is the use of "plane wave" expansions (Cheng *et al.*, 1998; Greengard and Rokhlin, 1997). All transformation directions are grouped in six main directions (up, down, north, south, east, and west). The main directions coincide with the axes of a Cartesian coordinate system. The multipole expansion is converted into an outgoing plane wave (Greengard and Rokhlin, 1997)

$$W(k,l) = \frac{w_k}{dM_k} \sum_{m=-L}^{L} \mathrm{j}^{|m|} \mathrm{e}^{\mathrm{j} m \alpha_{l,k}} \sum_{n=|m|}^{L} \frac{M_n^m}{\sqrt{(n-m)!(n+m)!}} \left(\frac{\lambda_k}{d} \right)^n . \tag{11}$$

After a rotation of the coordinate system. The outgoing plane wave is transformed into an incoming plane wave of another cube

$$V(k,l) = W(k,l) \mathrm{e}^{-\lambda_k z_0} \mathrm{e}^{\mathrm{j} \lambda_k (x_0 \cos(\alpha_{l,k}) + y_0 \sin(\alpha_{l,k}))} \tag{12}$$

and then converted back into a local expansion

$$L_n^m = \frac{\mathrm{j}^{|m|}}{\sqrt{(n-m)!(n+m)!}} \sum_{k=1}^{s(\varepsilon)} \left(-\frac{\lambda_k}{d} \right)^n \sum_{l=1}^{M_k} V(k,l) \mathrm{e}^{-\mathrm{j} m \alpha_{l,k}} . \tag{13}$$

Finally, the rotation of the coordinate system is reversed and the local expansion is evaluated. In total the computational costs are of $O(L^2)$.

The above described approach was applied very successfully to simulations of particle interactions. If this approach should be integrated into a FMM for a BEM, some modifications are necessary. In practice, elements can stick out of the cubes (Buchau *et al.*, 2003a). Then the near- and the far-field is defined based on the real convergence radii of the cubes. In Cheng *et al.* (1998) and Greengard and Rokhlin (1997) the cubes are assigned to the main directions based on their position in space, since all particles are lying always completely inside the cubes. In BEM computations it must be additionally checked, if two cubes are really separated in one coordinate direction. This direction is then the main direction. In some cases the convergence radii of two cubes are non-overlapping, but the cubes are not separated in at least one coordinate direction. Such configurations occur especially on the diagonals of the coordinate system. Then a plane wave expansion cannot be computed. Fortunately only a few transformations are concerned from this and are treated for example, with equation (6).

We tried this promising approach in the context of electrostatic problems. Unfortunately the computational costs are very large for $L = 9$. In our opinion the approach of equation (6) is more suitable for the solution of potential problems with a BEM.

Numerical examples

Two numerical examples are investigated, namely an electrostatic problem and a steady current flow field problem. In both cases a direct BEM formulation in combination with the FMM is applied. The surfaces of the domains are discretized with eight-noded, quadrilateral, second-order elements. The Galerkin method is used to obtain a system of linear equations. The system of linear equations is solved iteratively with GMRES and a Jacobi preconditioner. All examples were computed on a PC with an Intel Pentium III 1.0 GHz processor.

Electrostatic problem

The investigated electrostatic problem consists of two electrodes. One electrode is coated with a homogeneous, isotropic, linear dielectric (Figure 1). The potential of the electrodes is set between +1 and −1 V, respectively. At the outer surface of the dielectric the normal component of the electric displacement must be continuous.

All surfaces are discretized with 4,068 elements. The system of linear equations with 12,210 unknowns was solved in 179 iterations with a residuum smaller than 10^{-7}. When the FMM with classical transformations (equation (5)) is used, the solution of the whole problem took 5 h and 53 min. The memory requirements were 127 MB for

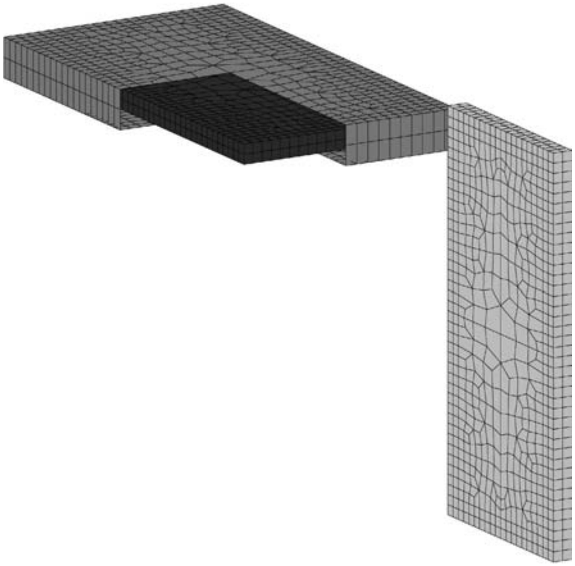

Figure 1.
Boundary element mesh of two electrodes, the left one is coated with a dielectric

the sparse near-field matrix, 102 MB for the far-field, and in total 243 MB. The application of multipole-to-local transformations only in the z-direction (equation (6)) reduces the total computational costs to 2 h and 47 min. This corresponds to a reduction of 53 percent. The assembly of the near- and far-field matrices and of the right hand side took approximately 36 min. The memory requirements were decreased to 176 MB. Especially the near-field matrix requirements were lowered by 37 percent.

Steady current flow field problem

A steady current flow field problem is examined to show further applicabilities of the proposed method. The electric currents inside a conductor are studied. Here we consider a model of a conducting path on a printed circuit board (Figure 2). The Dirichlet boundary condition is the given potential at the three ports of the conductor (1, 0.2, and −1 V). An electric current flows only inside a conductor. So the normal derivative of the potential must vanish at the remaining surfaces of the conductor (Neumann boundary condition). The mathematical description for this kind of problem is the same as for electrostatic problems. Hence the same numerical method can be used. Only different boundary conditions have to be considered.

After a discretization with 3720 elements, a system of linear equations with 11,244 unknowns are obtained. The problem was solved after 160 iteration steps in 1 h and 8 min. The compression rate of the system matrix was 88.3 percent. That means the memory requirements were reduced from 965 MB for a classical BEM to 113 MB. The potential in 17220 evaluation points inside the conducting path was computed in only 145 s and is shown in Figure 3.

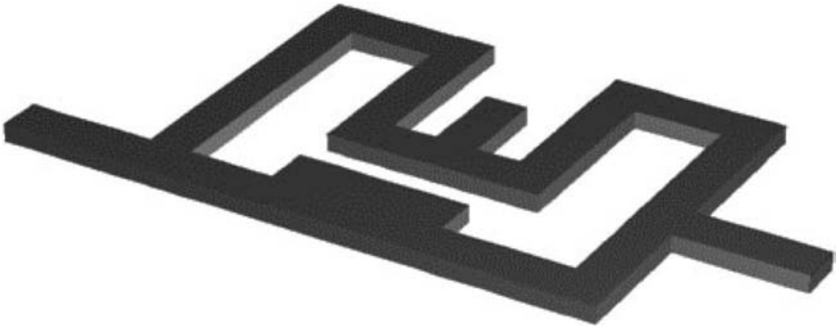

Figure 2.
Model of a conducting path on a printed circuit board

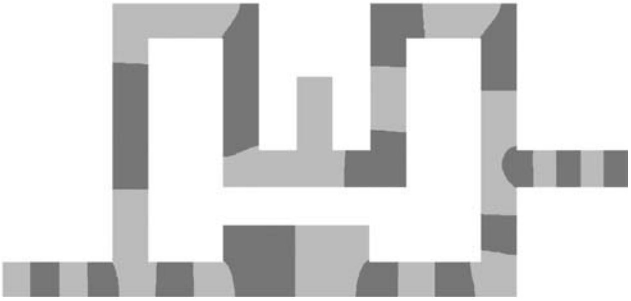

Figure 3.
Potential distribution inside the conducting path of Figure 2, the difference between two equipotential lines is 0.1 V

Conclusion

A direct BEM formulation in combination with the fast multipole method is very attractive for a fast and efficient solution of static field problems even in closed domains. Only the surfaces of the closed domains have to be modeled and discretized. The fast multipole method reduces the memory requirements and the computational costs. Modified transformation techniques for the series expansions were investigated and adapted to BEM computations with adaptive meshes. With the help of an electrostatic example the efficiency of the modified transformations were shown. The second example, a steady current flow field in a conducting path on a printed circuit board illustrates the possible fields of application of the presented method.

References

Axelsson, O. (1996), *Iterative Solution Methods*, Cambridge University Press, Cambridge.

Barrett, R., Berry, M., Chan, T.F., Demmel, J., Donato, J., Dongarra, J., Eijkhout, V., Pozo, R., Rominie, C. and Van der Horst, H. (1994), *Templates for the Solution of Linear Systems: Building Blocks for Iterative Methods*, SIAM, Philadelphia, PA.

Biedenharn, L.C. and Louck, J.D. (1981), *Angular Momentum in Quantum Physics: Theory and Application*, Addison-Wesley, London.

Buchau, A. and Rucker, W.M. (2002), "Efficient computation of double-layer potentials using the fast multipole method", paper presented at the Conference Digest of IEEE CEFC, p. 316.

Buchau, A., Huber, C.J., Rieger, W. and Rucker, W.M. (2000), "Fast BEM computations with the adaptive multilevel fast multipole method", *IEEE Transactions on Magnetics*, Vol. 36 No. 4, pp. 680-4.

Buchau, A., Hafla, W., Groh, F. and Rucker, W.M. (2003a), "Improved grouping scheme and meshing strategies for the fast multipole method", *COMPEL*, Vol. 22 No. 3, pp. 495-507.

Buchau, A., Rucker, W.M., Rain, O., Rischmüller, V., Kurz, S. and Rjasanow, S. (2003b), "Comparison between different approaches for fast and efficient 3D BEM computations", *IEEE Transactions on Magnetics*, Vol. 39 No. 3, pp. 1107-10.

Cheng, H., Greengard, L. and Rokhlin, V. (1998), "A fast adaptive multipole algorithm in three dimensions", Research Report YALEU/DCS/RR-1158, Department of Computer Science, Yale University.

Greengard, L. and Rokhlin, V. (1987), "The rapid evaluation of potential fields in three dimensions", in Anderson, C. and Greengard, C. (Eds), Lecture Notes in Mathematics 1360, Springer, Berlin, pp. 121-41.

Greengard, L. and Rokhlin, V. (1997), "A new version of the fast multipole method for the Laplace equation in three dimensions", *Acta Numerica*, pp. 229-69.

Nabors, K. and White, J. (1991), "Fastcap: a multipole accelerated 3D capacitance extraction program", *IEEE Transactions on Computer Aided Design*, Vol. 10 No. 11, pp. 1447-59.

Of, G. (2001), "Die Multipolmethode für Randintegralgleichungen", Diploma thesis at the Mathematical Department A, University of Stuttgart.

Rao, S.M., Sarkar, T.K. and Harrington, R.F. (1984), "The electrostatic field of conducting bodies in multiple dielectric media", *IEEE Transactions on Microwave Theory and Techniques*, Vol. 32 No. 11, pp. 1441-8.

The Emerald Research Register for this journal is available at
www.emeraldinsight.com/researchregister

The current issue and full text archive of this journal is available at
www.emeraldinsight.com/0332-1649.htm

Formulation of mixed elements for the 2D-BEM

Klaus Schimmanz and Arnulf Kost
Technical University of Cottbus, Cottbus, Germany

Keywords *Boundary-elements methods, Differential equations, Numerical analysis*

Abstract *Accuracy and time consumption in numerical computations are often in contradiction to each other. In modern industrial design processes flux field computation becomes more and more important. Thus, it is desirable to minimize any methodical error for better performance. This paper discusses a flaw of frequently used standard elements in boundary-element-method and shows a way to avoid it.*

1. Introduction

The boundary integral equation required by the boundary element method (BEM) can be deduced in a simple way based on considerations of weighted residuals. In the case of Laplacian differential equation ($\Delta\varphi = 0$), for instance, it leads to the following expression (Kost, 1994):

$$U_i = \oint_\Gamma \left(\omega_i \frac{\partial u}{\partial n} - u \frac{\partial \omega_i}{\partial n} \right) \mathrm{d}\Gamma \tag{1}$$

where Γ is the domains contour, u the boundaries potential function on Γ, and $\vec{n}$ the outward vector unit normal. ω and $\partial\omega/\partial n$ are the so-called fundamental solutions of the partial differential equation. The index i indicates an arbitrary location within the domain or on the contour. To determine a potential U_i somewhere in the domain by equation (1) it is necessary to know the whole potential function u along Γ and its directional derivative $\partial u/\partial n = \vec{n}\nabla u$. Some of them are given in sections by the necessary boundary conditions of the problem to be solved. But the missing ones need to be computed first. As is well known, this can be accomplished by dividing the boundary Γ into short segments, the elements, which leads to a finite set of equations and thus, to a linear algebraic equation system. For each element interpolation formulations of the potential functions and directional derivatives with some free parameters are used and the unknown values of the equation system will be these parameters.

2. Standard element flaw

Assume for simplicity that the body is two-dimensional and polygonal bounded. The points where unknown values are considered are called nodes and taken to be in the middle of the element for the so-called constant standard elements (Figure 1, left).

The values of u and $\partial u/\partial n = \vec{n}\nabla u$ are assumed to be constant over each constant standard element and equal to the mid-element node value. For standard elements the same interpolation function type is employed for both value approximations, that means in this case:

$$u_i = \text{const} \quad \text{and} \quad \frac{\partial u_i}{\partial n} = \text{const.} \tag{2}$$

COMPEL: The International Journal for Computation and Mathematics in Electrical and Electronic Engineering
Vol. 23 No. 4, 2004
pp. 866-875
© Emerald Group Publishing Limited
0332-1649
DOI 10.1108/03321640410553292

But exactly this is the reason for a "built in flaw" of the BEM which causes distortions of computed potential fields. Gradient calculations close to a standard element boundary, for instance, in the case of constant elements lead to (Kost, 1994; Schimmanz, 2002):

$$u_i = \text{const} \Rightarrow \frac{\partial u_i}{\partial t}\vec{t} \equiv 0$$

$$\Rightarrow \nabla u = \frac{\partial u_i}{\partial n}\vec{n} + \frac{\partial u_i}{\partial t}\vec{t} = \frac{\partial u_i}{\partial n}\vec{n} = \text{const}$$

where $\vec{t}$ is the tangential vector unit normal of the element. Thus, there is an additional error and this one is directionally dependent. The BEM minimizes the error on Γ and this approximation discrepancy shows also an impact on elements which have a sufficient order to solve the problem exactly. For example, for the two constant Dirichlet-borders in the left and right hand side in Figure 2 just one element for each edge would be enough to present the exact solution. But the value deviations along them depend strongly on the number of homogeneous Neumann-elements used. Thus, it proves that for standard elements an error locality on Γ is not present and cannot be expected. This effect here is also the result of the disappearing tangential component that is indicated by very high, but not realistic, flux densities across the corner Dirichlet-elements. It is obvious that the BEM error minimizing tries to compensate this contradiction of the homogeneous constant Neumann-elements with no tangential component by exciting an extreme flux along these elements. The potential value can jump from one Neumann-element to the next which suggests an existing tangential component in a more global sense, means in a wider distance to the border line. Thus, a higher number of constant Neumann-elements reduces the shown effect.

Similar effects like this are happening to all standard elements. To avoid such problems a different formulation for value interpolations is obligatory.

3. Mixed element formulation

The reason for disappearing tangential components in the case of constant standard elements is the higher polynomial approximation order of the normal component.

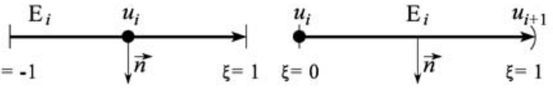

Note: *left*: Constant standard; *right*: Constant-linear mixed

Figure 1. Elements

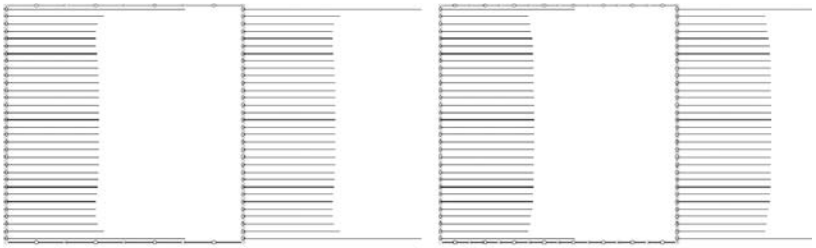

Note: 2 x 4 *left* image and 2 x 8 *right* hand side image

Figure 2. Flux density distributions across the same number of Dirichlet-elements (left and right hand side) of two equally quadratic shapes by constant standard formulation, but with a different number of homogeneous Neumann-elements

The order difference is exactly one. This will be the same for any other higher standard element type, too. Therefore, suppressing this disturbance means in the simplest case applying a constant-linear formulation in difference to equation (2) like:

$$u_i(\xi) = (1-\xi)\,u_i + \xi\, u_{i+1}, \quad \text{and} \quad \frac{\partial u_i(\xi)}{\partial n} = u_i' = \text{const} \tag{3}$$

where $\xi = [0;1)$ is the local coordinate of the element i. The node has to be located at one element bound for this mixed element type (for equation (3) see Figure 1, right). Consequentially, each element still owns exactly one node, i.e. node u_i, respectively, u_i' is allocated to only element E_i and node u_{i+1} belongs already to the following element E_{i+1} and is not a part of E_i anymore.

Adequate to the deduction of the BEM equation system in Schimmanz (2002) one can find the discrete expression for N elements:

$$\sum_{j=1}^{N} \begin{bmatrix} u_j & u_{j+1} \end{bmatrix} \begin{bmatrix} h_{ij}^a \\ h_{ij}^b \end{bmatrix} = \sum_{j=1}^{N} u_j' g_{ij}, \quad i = 1, \ldots, N, \quad u_{N+1} = u_1 \tag{4}$$

$$\Rightarrow \mathbf{H}\vec{u} = \mathbf{G}\vec{u}'$$

where

$$g_{ij} = \begin{cases} \frac{l_i}{2\pi}(1 - \ln l_i), & i = j \\ \int_{\Gamma_j} \omega_i \, \mathrm{d}\Gamma, & \text{otherwise} \end{cases}$$

$$h_{ij}^a = \begin{cases} \frac{\beta_i}{2\pi}, & i = j \\ \int_{\Gamma_j} (1-\xi)\, \frac{\partial \omega_i}{\partial n}\, \mathrm{d}\Gamma, & \text{otherwise} \end{cases} \tag{5}$$

$$h_{ij}^b = \begin{cases} 0, & i = j \\ \int_{\Gamma_j} \xi\, \frac{\partial \omega_i}{\partial n}\, \mathrm{d}\Gamma, & \text{otherwise} \end{cases}$$

where l_i is the length of the element i and β_i is the interior angle at node i. The angle β_i can be calculated implicitly by the assumption of a pure Dirichlet problem which has no flux through the domain as shown in Brebbia and Domingues (1992). Rearranging the above equation system by sorting unknowns to the left hand side and the knowns to the other will lead as usually to an ordinary linear equation system like $\mathbf{S}\vec{x} = \vec{b}$.

However, this linear equation system can be over-determined by some sorts of boundary condition transitions which will need a special but simple treatment of the equation set. This problem is shown in Figure 3, for instance. The example shows a closed domain with six constant-linear elements with all possible boundary condition transitions. Because of the Dirichlet-conditions the potential at $u_2 = u_3 = 1$ and

$u_1 = u_5 = u_6 = 0$ are known. The potential at u_4 is unknown. Further, the flux densities for the elements E_1, E_3 and E_4 are zero and thus, the homogeneous Neumann-conditions give $u'_1 = u'_3 = u'_4 = 0$, but u'_2, u'_5, u'_6 are unknown. Six elements will cause six equations. But there are only four unknowns which creates an over-determined equation system. The example shows that for the elements E_1 and E_3 all boundary node values are already known and hence, these equations contain no new information about the system. Thus, those equations can be left out of the set. This treatment is always applicable to any Dirichlet-to-Neumann-condition transition for this kind of mixed elements.

4. Exemplary comparison

Figure 4 shows the numerical solution of the same homogeneous potential field problem by using constant standard elements and constant-linear mixed elements. In all cases just four elements are employed. Left and right hand sides are constant, but different Dirichlet-conditions are applied and all other edges are homogeneous Neumann ones. The flux density view graphs are shown for an easier identification of field distortions, because the involved first potential derivation emphasizes such disorientations.

Theoretically constant-linear mixed elements are able to solve a homogeneous field problem exactly. The first two rows of Figure 4, however, seem to prove it wrong.

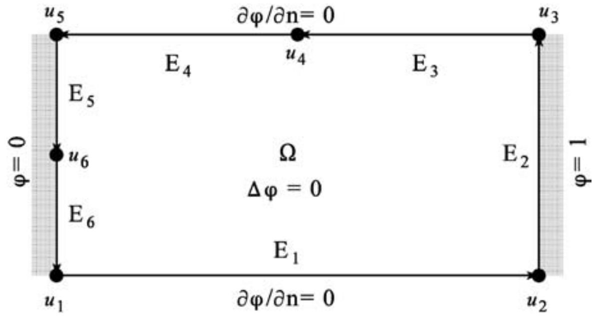

Figure 3.
Example for all possible boundary condition transitions of constant-linear mixed elements

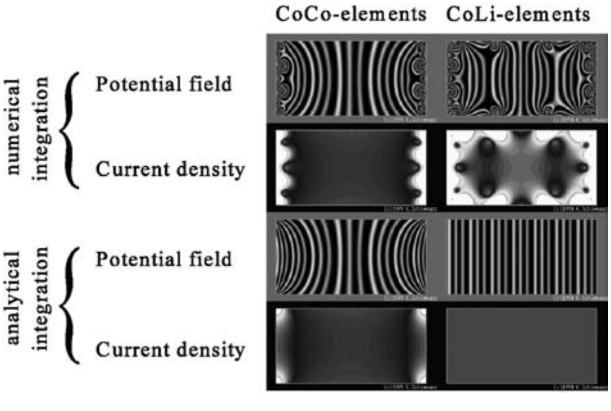

Figure 4.
Computed potential fields and flux density maps; left: constant standard elements; and right: constant-linear mixed elements

The reason for the much heavier field distortions was found in the numerical Gaussian quadrature algorithm (here with four collocation points). By using a mathematical software for symbolic computations the analytical expressions of the integrals in equation (5) and also for the similar integrals of constant standard elements have been found (Schimmanz, 2002). The effect is presented in the last two rows of Figure 4. Numerical experiments with 12 collocation points for the Gaussian quadrature had just a small improvement effect. Benchmark tests revealed that the analytical integral expressions can be calculated in about the same time as necessary for the Gaussian quadrature with six collocation points. Except the first two rows in Figure 4 all results presented in this paper are computed by analytical integral expressions, if not by other mentioned.

The analytical part of Figure 4 shows the correctness of the constant-linear mixed element formulation and shows again the reaction of the BEM to overcome the standard element flaw by a higher flux density at corner locations as already discussed in Section 2.

Results of the numerical integration in the boundary nodes are quite exact even if numerical quadrature algorithms produce distortions within domains potential field. Using Newton-Cotes quadrature with ten digits precision for constant-linear mixed elements showed a difference in the analytical solution of the Laplacian equation for the homogeneous case of less than 10^{-9}. This value is similar to that obtained by analytical integration formulas by using ten digits precision.

Figure 5 shows an impression of the differences between the constant standard and constant-linear mixed elements for a non-homogeneous potential problem. This again is a flux density map where the constant Dirichlet-conditions are applied to the lower left and right vertical edges. All other edges are homogeneous Neumann ones. In both cases the same number of 242 elements are employed and among them 16 are for Dirichlet edges.

Especially in the neighborhood of the small central re-entry cut the standard element solution still shows field confusions. This is not noticeable by the constant-linear mixed element computation, neither at the cut path way nor at any other edge region and also not at the geometry caused singularities.

5. Consequences of asymmetric elements

For the construction of standard elements of the BEM usually a symmetric node arrangement is used. But the element type introduced in Section 3 (Figure 1, right) is an asymmetric one. That is, however, a typical phenomenon of this kind of mixed element

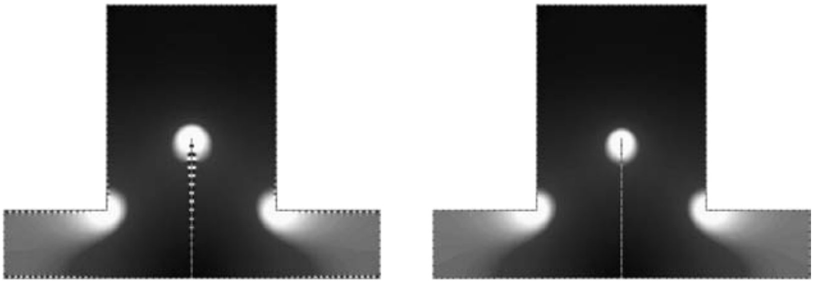

Figure 5.
Comparison of standard elements (left) and constant-linear mixed elements (right) for the same non-convex structure (flux density maps; the higher the density, the brighter the color)

formulations. It may be supposed that the asymmetry will have undesirable consequences in some applications.

Indeed, strange effects can be observed if a mixed element node is placed on a singularity. Figure 6 shows an example.

Next to the constant Dirichlet-conditions occupying the upper 2/3 of the edge lengths left and right hand side, this rectangular structure consists of homogeneous Neumann-conditions only. Mixed elements are directed because of their asymmetry. The shape shown in Figure 6 is described counterclockwise. Thus, at location A is a 180° Dirichlet-to-Neumann condition transition and the sequence is reversed at location B. Because of the disorientation of the flux vector at these points singularities will occur, of course. The structure itself is symmetric and therefore both singularities will have the same strength. The flux proportional flags at side A show an expectable behavior. On the other side, the flux across B is somewhat confused, which further confuses the field solution within the domain as well. Surprisingly, the integration along the whole boundary Γ of the domain reveals a very precise satisfaction of the Laplacian equation. It proves that this is a BEM solution – because the minimizing did not go wrong – and thus, it is not an implementation fault. The element-wise alternating flux density signs have been observed several times by pure constant-linear mixed element installations of certain singularity conditions.

The explanation of the differences at side A and B can be found by considering the element unknowns at the two singularities.

The potential along the whole boundary is continuous and therefore, the u_i values itself cannot convey any singularity, but the values of the first derivative u'_i can. The node placed in singularity A is one of the homogeneous Neumann-elements where the first derivative is a prescribed known finite condition. Furthermore, this element is one of the Dirichlet-to-Neumann transitions which will be let out of the linear equation system for the pure constant-linear mixed formulation as mentioned in Section 3. Thus, this singularity is completely hidden from the BEM algorithm and plays no role in solving the process. Hence, the solution behaves in the expected and, most important, in the correct manner.

The boundary side B has also such a transition, but because of the mixed element direction this one is at the upper right corner of the structure where no singularity occurs. The Neumann-to-Dirichlet transition at singularity B places the Dirichlet-node in it. That means the potential u_B is the known value prescribed here and u'_B has to be

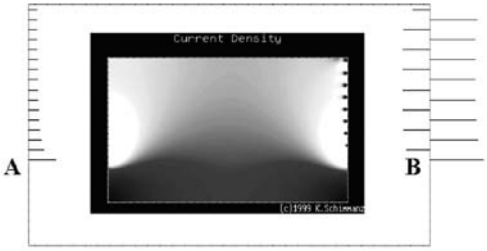

Note: All other edges are homogenous Neumann ones; center part: structures corresponding flux density map. The different behavior at **A**-side (flux source) and **B**-side (flux drain) singularity is caused by the node asymmetry of mixed elements only

Figure 6.
Unreal flux contra direction effect at B-sides Dirichlet-elements of a rectangular structure by using pure constant-linear elements (view graph of flux density proportional flags across constant Dirichlet-boundaries – upper 2/3 of the edge lengths left and right hand side)

computed and the equation of this element will stay to be a part of the linear equation system to be solved. The value of the singularity is infinite, theoretically. The numeric, however, can assign a finite value to this node only. Since the BEM is an integral equation method the node values express just the element average in some way by the interpolation function in equation (3), which is for this element also theoretically correct, a finite one. This may be the reason that in none of such cases the algorithm is stopped by a runtime error and further, the flag at B-singularity in Figure 6 has not the maximum possible value, respectively, length.

The BEM procedure will integrate along the whole contour related to this singular node as fixed point. But the interpolation functions in equation (3) are unable to return the infinity out of the node value u'_B. In fact, no polynomial interpolation formulation has this ability. Thus, the minimizing algorithm concludes having a too low node quantity and force it being higher. That is why the flag at B is longer than the equivalent one at A. The following Dirichlet-element unknown u'_{B+1}, tries to compensate the too high average of u'_B for satisfaction of the Laplacian equation in a small scale. This causes the contra direction of the flux in u'_{B+1}, what again produces a new – but unreal – singularity at the node of element B+1 and the process becomes repeated for the next element, and so on. Finally, the alternating flux directions arise along the entire Dirichlet-edge. This means, a higher number of Dirichlet-elements will not avoid nor essentially relax this effect as can be shown.

Splitting the node into two locations, means letting u_i at elements beginning location and moving u'_i more inward of the element, is mathematically impossible because ω_i and $\vec{n}\nabla\omega_i$ have to be taken from the same location i (equation (1)). But to resolve the singularity problem the whole node can be shifted inside the element. This can be done in a very similar way as for discontinuous linear standard elements (Brebbia and Domingues, 1992).

Constant-linear mixed elements have just one node per element. Displacing all these nodes to mid-element location in general would give back elements symmetry without having any singularity problem as for constant standard elements. The g_{ij} expression in equation (5) will become the same as for constant standard elements and the interior angle β_i will be always equivalent to π. Unfortunately, the necessary transformation matrix $\mathbf{T}$ has some restrictions and disadvantages, as shown in the following.

5.1 Global constant-linear mixed element transformation

The nodes of pure constant-linear elements are located at the start bounding of the elements. Thus, these elements are asymmetrical. The equation to be solved in this case is (equations (4) and (5)):

$$\left(\frac{1}{2\pi}\beta + \mathbf{H}\right)\vec{u} = \mathbf{G}\vec{u}',$$

where β is the diagonal matrix of interior angles β_i at nodes u_i. To avoid singularity problems it is desirable to shift the nodes onto mid-element location to gain back a symmetrical element description (Figure 7). To do so, the integrals within the matrices $\mathbf{H}$ and $\mathbf{G}$ have to be considered for the new locations, too. The result may be expressed as $\mathbf{H}_d$ and $\mathbf{G}_d$ matrix. If the mid-element nodes are called v_i, then the new equation to be solved should be:

$$\left(\frac{1}{2}\mathbf{I}+\mathbf{H}_d\right)\vec{v}=\mathbf{G}_d\vec{v}\,'.$$

β becomes the identity matrix **I**, because all interior angles β_i are equal to π now. But this equation is not correct, because the potentials at the element bounds are still needed for the integration (equation (4)). These potentials, however, are only constant multipliers for the integrals, as before. This finally leads to the equation system:

$$\left(\frac{1}{2}\mathbf{I}+\mathbf{H}_d\mathbf{T}\right)\vec{v}=\mathbf{G}_d\vec{v}\,'.$$

Therefore, **T** has to satisfy the expression: $\vec{u}=\mathbf{T}\vec{v}$. The diagonal matrix of the interior angles $(1/2)$**I** is adequate to the left side of equation (1) and thus, it is unaffected by the transformation (Brebbia and Domingues, 1992; Schimmanz, 2002).

The deduction of matrix **T** is easily approached in backward direction. The potential at mid-element node v_i is the arithmetical average of the potentials u_i and u_{i+1} because the linear formulation along the constant-linear mixed elements, i.e. $(u_{i+1}+u_i)/2=v_i$. For instance, the closed contour shown in Figure 7 (left) (called $\mathbf{T}_\mathrm{e}$) leads to the matrix equation:

$$\mathbf{T}_\mathrm{e}^{-1}\cdot u=2v\Rightarrow\begin{bmatrix}1&1&0&0\\0&1&1&0\\0&0&1&1\\1&0&0&1\end{bmatrix}\begin{bmatrix}u_1\\u_2\\u_3\\u_4\end{bmatrix}=2\begin{bmatrix}v_1\\v_2\\v_3\\v_4\end{bmatrix}$$

$$\Rightarrow\det\left(\mathbf{T}_\mathrm{e}^{-1}\right)=\begin{vmatrix}1&1&0&0\\0&1&1&0\\0&0&1&1\\1&0&0&1\end{vmatrix}=0\quad\Rightarrow\quad\mathbf{T}_\mathrm{e}\ \text{does not exist}$$

and for Figure 7 (right) (called $\mathbf{T}_\mathrm{o}$) to:

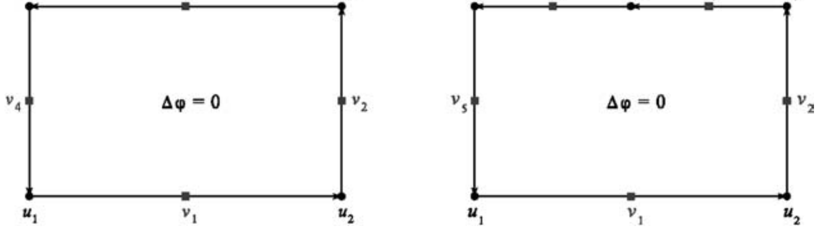

Figure 7.
Potential nodes u_i and mid-element nodes v_i at a rectangle structure with an even (left) and an odd (right) number of constant-linear elements

$$\mathbf{T}_{\mathrm{o}}^{-1} \cdot u = 2v \Rightarrow \begin{bmatrix} 1 & 1 & 0 & 0 & 0 \\ 0 & 1 & 1 & 0 & 0 \\ 0 & 0 & 1 & 1 & 0 \\ 0 & 0 & 0 & 1 & 1 \\ 1 & 0 & 0 & 0 & 1 \end{bmatrix} \begin{bmatrix} u_1 \\ u_2 \\ u_3 \\ u_4 \\ u_5 \end{bmatrix} = 2 \begin{bmatrix} v_1 \\ v_2 \\ v_3 \\ v_4 \\ v_5 \end{bmatrix}$$

$$\Rightarrow \det(\mathbf{T}_{\mathrm{o}}^{-1}) = 2 \Rightarrow \mathbf{T} = 2\mathbf{T}_{\mathrm{o}} = \begin{bmatrix} 1 & -1 & 1 & -1 & 1 \\ 1 & 1 & -1 & 1 & -1 \\ -1 & 1 & 1 & -1 & 1 \\ 1 & -1 & 1 & 1 & -1 \\ -1 & 1 & -1 & 1 & 1 \end{bmatrix}$$

It can be shown that this is a periodical problem, i.e. the transformation matrix **T** exists always for an odd number of constant-linear mixed elements per closed contour only. For an even number of elements $\mathbf{T}^{-1}$ will always result in a singular matrix. That means, for a global discontinuous constant-linear mixed element formulation the contour discretization must not have an even number of elements! The transformation matrix **T**, however, is fully populated and thus, the matrix multiplication $\mathbf{H} \cdot \mathbf{T}$ will cause a non-negligible additional effort for system matrix compilation and further, it will increase the time consumption for the field computation. The structure of **T** is quite simple – because cyclical – and therefore, an inversion of $\mathbf{T}^{-1}$ at runtime is not required. The effect is exemplary and is shown in Figure 8. But it has been found that the transformed constant-linear mixed elements usually consume less CPU-time than the constant standard element formulation for a similar precision in surface results of non-convex structures.

Such an effort is not necessary for problems with only constant Dirichlet-conditions and some constant Neumann-conditions. In that case constant standard elements can be employed at Dirichlet-boundaries, because the linear interpolation ability is not used here. But especially for inner edges, e.g. between two materials, the use of transformed elements is strongly recommended.

6. Conclusions

Mixed elements shown here provide a directionally independent approximation quality of the gradient and thus, a more homogeneous error distribution within the domain. For adaptive mesh refinement methods based on error estimations the property of error

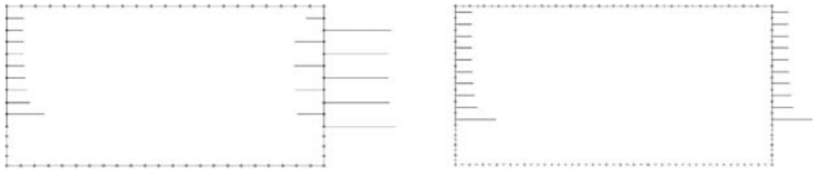

Figure 8.
Structure of Figure 6 computed with constant-linear mixed elements without (left) and with (right) global transformation

Note: View graph of flux density proportional flags across Dirichlet-boundaries

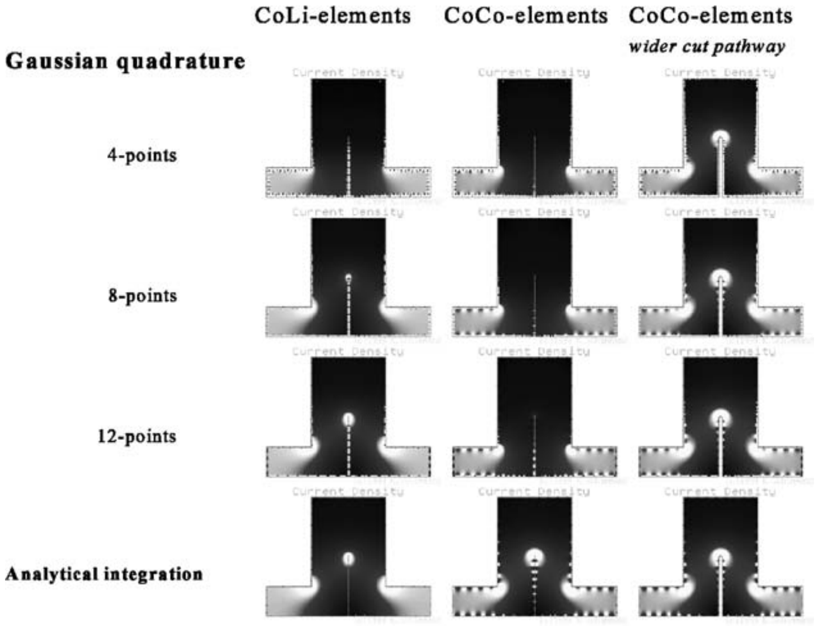

Note: The *left two columns* show exactly the same geometry, the *right column* shows the same shape like the left ones except the wider cut pathway diameter; all images are computed by the same number and distribution of elements (CoCo: constant standard type; CoLi: constant-linear mixed type)

Figure 9.
Flux density maps similar to Figure 5

locality is an indispensable precondition. Furthermore, such mixed elements can reduce the number of necessary elements for field computations and thus, speed up the method. The integration effort of constant-linear elements shown here is $3(N^2 - 2N)$. This is usually more than for constant standard elements $2(N^2 - N)$, but less than for linear standard elements $4(N^2 - 2N)$.

As well as for constant standard elements the integrals of constant-linear mixed elements can be carried out analytically. This further reduces field confusions at border adjacencies as it is happening by often using numerical Gaussian quadrature formulas. In standard BEM applications often observed inclination of numerical errors by structures with low distant edges (like the re-entry cut in Figure 5) vanishes almost completely by using the combination of analytical integration and mixed element formulation. Figure 9 shows an impression of the behavior.

References

Brebbia, C.A. and Domingues, J. (1992), *Boundary Element Method: An Introductory Course*, 2nd ed., Computational Mechanics Publications, Southampton, Boston, MA, pp. 76-7, 87-9.

Kost, A. (1994), *Numerische Methoden in der Berechnung elektromagnetischer Felder*, Springer, Berlin, pp. 222-3.

Schimmanz, K. (2002) “Konzipieren und Bewerten von Hochpräzisions-Hybridwiderständen durch Laser-Trimm-Simulation”, edocs TU-Berlin, Dr-Ing. thesis, Berlin, pp. 61-7, 155-8, available at: (TU-Berlin) http://edocs.tu-berlin.de/diss/2002/schimmanz_klaus.pdf

The Emerald Research Register for this journal is available at
www.emeraldinsight.com/researchregister

The current issue and full text archive of this journal is available at
www.emeraldinsight.com/0332-1649.htm

Coupled mechanical-electrostatic FE-BE analysis with FMM acceleration

Application to a shunt capacitive MEMS switch

R.V. Sabariego, J. Gyselinck and P. Dular
Department of Electrical Engineering and Computer Science (ELAP), University of Liège, Liège, Belgium
J. De Coster
Department of Electrical Engineering (ESAT-MICAS), Katholieke Universiteit Leuven, Leuven, Belgium
F. Henrotte and K. Hameyer
Department of Electrical Engineering (ESAT-ELECTA), Katholieke Universiteit Leuven, Leuven, Belgium

Keywords *Finite element analysis, Boundary-elements methods*

Abstract *This paper deals with the coupled mechanical-electrostatic analysis of a shunt capacitive MEMS switch. The mechanical and electrostatic parts of the problem are modelled by the FE and BE methods, respectively. The fast multipole method is applied to reduce the storage requirements and the computational cost of the BE electrostatic model. An adaptive truncation expansion of the 3D Laplace Green function is employed. The strong interaction between the mechanical and electrostatic systems is considered iteratively.*

1. Introduction

Electrostatic parallel-plate actuators are widely used in many types of microelectromechanical systems (MEMS). MEMS switches can be used in series or shunt mode and their contacts can be resistive or capacitive (Brown, 1998; Tilmans, 2002). A shunt capacitive MEMS switch consists of a metal armature (bridge) suspended over a bottom conductor, e.g. the center conductor of a coplanar waveguide, mechanically anchored and electrically connected to the ground. A thin dielectric film is deposited on the bottom conductor (Figure 1). When the bridge is up, the capacitance of the switch is very small and the RF signal passes through freely (the RF switch is on). By applying a bias voltage the switch is actuated: an electrostatic force occurs between the top and bottom conductors and the bridge is pulled down, the capacitance increases and causes an RF short to ground (the RF switch is off) (Brown, 1998; Tilmans, 2002).

These actuators can be treated, in first approximation, as lumped spring-mass systems with a single mechanical degree of freedom (Tilmans, 2002). This analysis is

COMPEL: The International Journal for Computation and Mathematics in Electrical and Electronic Engineering
Vol. 23 No. 4, 2004
pp. 876-884
© Emerald Group Publishing Limited
0332-1649
DOI 10.1108/03321640410553300

The research was carried out in the frame of the Inter-University Attraction Poles IAP P5/34 for fundamental research funded by the Belgian government. P. Dular is a Research Associate with the Belgian National Fund for Scientific Research (FNRS.).

helpful for physical insight, but disregards important effects such as the bending of the top plate and the stiction between the bridge and the bottom contact (Brown, 1998). The performance of RF MEMS switches strongly depends on the deformation of the top electrode. A detailed knowledge of the exact deformation for an accurate estimate of the capacitance is thus crucial.

A boundary element (BE) approach is particularly suited for the analysis of the real electrostatic problem (Farina and Rozzi, 2001). Indeed, the BE method provides a rigorous treatment for open problems and allows to consider the deformation without any remeshing. The elastic deformation of the top plate (and the suspension beams) can be handled by means of a finite element (FE) model. It depends directly on the electrostatic force exerted on the bridge and the material properties. The electrostatic field induces a force distribution, the value of which increases when the distance between the top and bottom plate diminishes. This interaction between the electrostatic and mechanical systems can be considered iteratively.

A significant disadvantage of the BE electrostatic model is that it leads to a fully populated system matrix limiting the size of the problems to be handled. The fast multipole method (FMM) (Rokhlin, 1983), combined with an iterative solver, e.g. GMRES (Saad and Schultz, 1986), can be employed to overcome this limitation by diminishing both storage requirements and the computational time. The FMM method has succesfully been applied to solve electrostatic problems in Buchau *et al.*, 2000; and Nabors and White, 1991.

In this paper, we discuss the coupled mechanical-electrostratic analysis of a capacitive MEMS shunt switch. Section 2 outlines the electrostatic BE model of the actuator. The FMM is briefly described in Section 3. An adaptive truncation scheme for the 3D Laplace Green function is employed. Section 4 deals with the elastic deformation FE model. In Section 5, the application example is considered. Simulated results obtained by means of different software packages are briefly compared.

2. Electrostatic BE model

We consider an electrostatic problem in $\mathbb{R}^3$. The conductors are embedded in multiple homogeneous isotropic dielectrics and set to fixed potentials.

The surfaces of conductors and dielectrics $\Gamma = \Gamma_C \cup \Gamma_D$ are discretised with plane triangles. The surface charge density q is assumed to be piecewise constant. The conductors can be replaced by their charge density on their surfaces q_c and

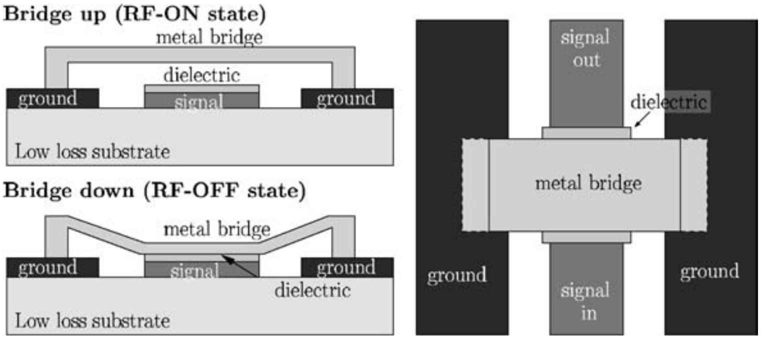

Figure 1. Electrostatically actuated capacitive shunt switch implemented on a CPW transmission line. Side and top views

the homogeneous dielectrics by the polarisation charge q_p. The total charge on the interface conductor-dielectric Γ_C is given by the sum of both types of charges. Analogously, on the surface between two dielectrics Γ_D the total charge is the sum of the polarisation charge due to both dielectrics (Rao *et al.*, 1984). The following system of n_q linear equations has to be solved

$$\mathbf{MQ} = \mathbf{B}, \tag{1}$$

where $\mathbf{Q} = [q_1 \ldots q_{n_q}]^\mathrm{T}$ contains the charge densities on the elements and $\mathbf{B} = [b_1 \ldots b_{n_q}]^\mathrm{T}$ depends on the boundary conditions. For an element on the surface of a conductor Γ_C, the entry in $\mathbf{B}$ is the imposed potential; for an element on the interface between two dielectrics Γ_D, the entry in $\mathbf{B}$ is zero. The elements of the dense nonsymmetric matrix $\mathbf{M}$ when k is an element on a conductor are given by

$$M_{k,l} = \frac{1}{\varepsilon_0} \oint_{\Gamma_l} G(\rho_k)\,\mathrm{d}\Gamma' \quad \text{with} \quad G(\rho_k) = \frac{1}{4\pi\rho_k}. \tag{2}$$

$G(\rho_k)$ is the 3D Laplace Green function, $\rho_k = |\underline{r}_k - \underline{r}'|$ being the distance between a source point $\underline{r}'$ (on $\Gamma_l \in \Gamma$) and an observation point $\underline{r}_k$ (on Γ_C). Considering the continuity of the normal component of the dielectric displacement $\underline{d} = \varepsilon \underline{e}$ at the dielectric-to-dielectric interface, Γ_D, the elements of $\mathbf{M}$ if k is an element on Γ_D read:

$$M_{k,l} = \begin{cases} \dfrac{\varepsilon_{k2} - \varepsilon_{k1}}{\varepsilon_0(\varepsilon_{k1} + \varepsilon_{k2})} \displaystyle\oint_{\Gamma_l} \operatorname{grad} G(\rho_k) \cdot \underline{n}_k \,\mathrm{d}\Gamma', & k \neq l, \\ \dfrac{1}{2\varepsilon_0}, & k = 1. \end{cases} \tag{3}$$

where $\underline{n}_k$ is the outward-normal unit vector pointing into the dielectric with permittivity ε_{k2}. The integrals in equations (2) and (3) can be evaluated analytically (Graglia, 1993).

The electrostatic force $\underline{F}_\mathrm{e}$ distribution can be calculated as

$$\underline{F}_\mathrm{e}(\underline{r}) = \frac{1}{2} q(\underline{r}) \underline{e}(\underline{r}). \tag{4}$$

The electric field $\underline{e}$ as $\underline{r}$ approaches the interface conductor-dielectric can be expressed as (Rao *et al.*, 1984):

$$\underline{e}^{\pm}(\underline{r}) = \pm \underline{n} \frac{q(\underline{r})}{2\varepsilon_0} + \frac{1}{4\pi\varepsilon_0} \langle \operatorname{grad} G(\rho), q(\underline{r}') \rangle_\Gamma, \tag{5}$$

where + indicates the outer face of the conducting surface and $-$ the inner one, $\underline{n}$ is the normal unit vector pointing outside the conductor and $\langle \cdot, \cdot \rangle_\Gamma$ denotes a surface integral on Γ of the product of its arguments. As inside the conductor $\underline{e}^- = 0$, considering equation (5), it follows that $\underline{e}^+$ on the surface of the conductor is given by

$$\underline{e}^+(\underline{r}) = \underline{n} \frac{q(\underline{r})}{\varepsilon_0}. \tag{6}$$

Substituting equation (6) in equation (4), the expression of $\underline{F}_\mathrm{e}$ as a function of the charge distribution is obtained as

$$\underline{F}_e(\underline{r}) = \frac{1}{2\varepsilon_0} q^2(\underline{r})\underline{n}. \tag{7}$$

3. Fast multipole method

The implementation of the FMM requires the grouping of the elements on the surface boundary

$$\Gamma = \cup_{g=1}^{\#g}\Gamma_g.$$

A good choice is a scheme based on cubes, i.e. un octree (Buchau *et al.*, 2000; Nabors and White, 1991). Note that in a single level FMM, as described in the present paper, only the finest level of the octree is. The interactions between the distant groups are then determined by means of the multipole expansion of the Laplace Green function.

3.1 Multipole expansion

Let Γ_s be a source group with center $\underline{r}_{\mathrm{sc}}$ and a source point $\underline{r}_{\mathrm{s}}$, and Γ_o an observation group with center $\underline{r}_{\mathrm{oc}}$ and an observation point $\underline{r}_{\mathrm{o}}$. We define the vectors $\underline{r} = \underline{r}_{\mathrm{o}} - \underline{r}_{\mathrm{oc}} = (r, \theta, \phi)$, $\underline{r}_{\mathrm{c}} = \underline{r}_{\mathrm{oc}} - \underline{r}_{\mathrm{sc}} = (r_{\mathrm{c}}, \theta_{\mathrm{c}}, \phi_{\mathrm{c}})$ and $\underline{r}' = \underline{r}_{\mathrm{sc}} - \underline{r}_{\mathrm{s}} = (r', \theta', \phi')$. Omitting the factor $1/4\pi$, the 3D Laplace Green function (2), with $\rho = |\underline{r}_{\mathrm{o}} - \underline{r}_{\mathrm{s}}|$, is expanded as (Rokhlin, 1983):

$$\frac{1}{\rho} = \Re\left(\sum_{m=0}^{\infty}\sum_{n=-m}^{m}\sum_{u=0}^{\infty}\sum_{v=-u}^{u} \mathcal{D}_{m,n}\,\mathcal{T}_{m+u,n+v}\,\mathcal{A}_{u,v}\right), \tag{8}$$

with

$$\mathcal{D}_{m,n}(\underline{r}) = \frac{r^m \mathcal{L}_m^n(\theta, -\phi)}{(m+n)!}, \tag{9}$$

$$\mathcal{T}_{m+u,n+v}(\underline{r}_{\mathrm{c}}) = \frac{(m+u-(n+v))!}{r_c^{m+u+1}} \mathcal{L}_{m+u}^{n+v}(\theta_{\mathrm{c}}, \phi_{\mathrm{c}}), \tag{10}$$

$$\mathcal{A}_{u,v}(\underline{r}') = \frac{r'^u \mathcal{L}_u^v(\theta', -\phi')}{(u+v)!}, \tag{11}$$

where $\mathcal{L}_m^n(\theta, \phi) = P_m^n(\cos\theta)e^{\imath n\phi}$, P_m^n being the Legendre function of degree m and order n. The imaginary number is denoted $\imath$ and $\Re$ indicates the real part.

In practice, the multipole expansion (8) must be truncated by taking $0 \leq m \leq p$ and $0 \leq u \leq p$, where the truncation number p must be sufficiently large to limit the error to a prescribed value ε. In most cases, the conventional choice $p = \log_2(1/\varepsilon)$ (Rokhlin, 1983) is too conservative. Indeed, if $r' \ll r_{\mathrm{c}}$ and $r \ll r_{\mathrm{c}}$, a smaller number of terms suffices. Let us consider the radii of the source and observation groups, $R_s = \max_{\Gamma_s}(r')$, $R_o = \max_{\Gamma_o}(r)$, and the distance between their centers d. A more economic law $p = p(R_s/d, R_o/d, \varepsilon)$, proposed by some of the authors in Sabariego *et al.* (2004), considers those distances.

The function grad G in equation (3) can be expanded in a similar way. It suffices to derive equation (9) with respect to the coordinates of the observation point.

3.2 Application to the BE model

Two groups Γ_s and Γ_o are said to be “far” groups if $R_s/d < \tau$ and $R_o/d < \tau$, where d is the distance between the group centers and τ is chosen smaller than 1/2.

For demonstrating the FMM, the BE dense matrix $\mathbf{M}$ equations (2) and (3) can be formally written as

$$\mathbf{M} \approx \mathbf{M}^{\text{near}} + \mathbf{M}^{\text{far}} = \mathbf{M}^{\text{near}} + \underbrace{\sum_{o=1}^{\#g}\sum_{s=1}^{\#g}}_{\Gamma_o,\,\Gamma_s\text{far}} \mathbf{M}^{\text{far}}_{o,s}. \tag{12}$$

Let us consider the degrees of freedom q_k and q_l of q in the respective far groups $\Gamma_o \in \Gamma_C$ and $\Gamma_s \in \Gamma$. Substituting equation (8) in equation (2), the contribution to the corresponding element $(M^{\text{far}}_{o,s})_{k,l}$ in M^{far} is given by

$$\Re\left(\sum_{m=0}^{p}\sum_{n=-m}^{m} M^{\mathscr{D}}_{o,k,m,n}\sum_{u=0}^{p}\sum_{v=-u}^{u} M^{\mathscr{T}}_{m+u,n+v}\, M^{\mathscr{A}}_{s,l,u,v}\right), \tag{13}$$

$$M^{\mathscr{D}}_{o,k,m,n} = \int_{\Gamma_{o,k}} \mathscr{D}_{m,n}\,\mathrm{d}\Gamma, \qquad M^{\mathscr{A}}_{s,l,u,v} = \int_{\Gamma_{s,l}} \mathscr{A}_{u,v}\,\mathrm{d}\Gamma, \tag{14}$$

$$M^{\mathscr{T}}_{m+u,n+v} = \frac{1}{4\pi\varepsilon_0}\mathscr{T}_{m+u,n+v}. \tag{15}$$

The iterative solution of the system of algebraic equations requires the multiplication of $\mathbf{M}^{\text{far}}$ by a trial vector $\mathbf{Q}$. Group by group, the field produced by the electric charge q in the considered group is aggregated into its center by equation (14). This aggregated field is then subsequently translated to the centers of all the far groups by equation (15), and finally, the aggregated and translated field are disaggregated into the degrees of freedom of the far groups, thanks to equation (14).

The multiplication of $\mathbf{M}^{\text{far}}\mathbf{Q}$ is further accelerated by means of the adaptive truncation scheme following the law $p = p(R_s/d, R_o/d, \varepsilon)$ (Sabariego *et al.*, 2004). In case of preconditioning of the iterative solver, the preconditioner is based on the sparse matrix comprising the BE near-field interactions.

The assembly stage of the FMM consists in calculating and storing the required complex numbers $M^{\mathscr{D}}_{o,k,m,n}, M^{\mathscr{T}}_{m+u,n+v}$ and $M^{\mathscr{A}}_{s,l,u,v}$. The matrix $\mathbf{M}^{\text{far}}$ itself is never built. The integrations in equation (14) are done numerically, but as we are dealing with far interactions a limited number of Gauss integration point suffices. The matrix $\mathbf{M}^{\text{near}}$ is calculated in the conventional way (see previous Section) and stored using a sparse storage scheme. For the $\mathbf{M}^{\mathscr{D}}$ and $\mathbf{M}^{\mathscr{A}}$ data of a given group, the truncation number p considered during the FMM assembly stage is determined by its closest far group, $p = p_{\max}$. For the $\mathbf{M}^{\mathscr{T}}$ data, the truncation number p is determined by the two groups Γ_s and Γ_o involved in the translation, $p = p_{\text{so}}$. During the iterative process, the aggregation step is carried out with $p = p_{\max}$, while $p = p_{\text{so}}$ suffices for the translation and disaggregation.

4. Elastic deformation-FE model

The upper electrode is deformed by the electrostatic force exerted on it. The elastic equation has to be considered alongside the electrostatic equations. For linear elastic isotropic materials, it reads:

$$\mathbf{D}^{\mathrm{T}}\underline{\underline{E}}\mathbf{D}\underline{u}+\underline{F}=0, \tag{16}$$

where $\mathbf{D}$ is the differential operator matrix with transpose $\mathbf{D}^{\mathrm{T}}$, $\underline{\underline{E}}$ is the elasticity tensor, $\underline{u}$ is the displacement vector and $\underline{F}$ is the total force exerted. The elasticity tensor $\underline{\underline{E}}$ relates the stress tensor with the strain tensor. It depends on the Young's modulus E and the Poisson's ratio ν (Pilkey, 2002).

5. Application example

The shunt capacitive MEMS switch shown in Figure 2 is chosen as the test case. It concerns a perforated top plate (thickness = $4\,\mu$m) suspended by a set of beams, and a bottom plate (thickness = $0.5\,\mu$m) coated with a thin dielectric layer (thickness = $0.2\,\mu$m, $\varepsilon_r = 7$). The beam suspension allows a vertical movement with respect to the fixed bottom plate. The top plate is perforated to facilitate the under-etching of the structure. The dimension of the holes is $25\,\mu\mathrm{m}\times 25\,\mu\mathrm{m}$, with a pitch of $50\,\mu$m. The mechanical material constants of the top plate are $E = 70$ Gpa and $\nu = 0.3$.

The BE method with FMM acceleration is applied for solving the electrostatic problem while the mechanical problem is handled by a FE model. All the above mentioned methods are implemented in GetDP (2003). The behaviour of the switch is simulated using a discretisation consisting of 6,544 triangles and 11,151 tetrahedra, which yields 6,544 degrees of freedom for the piecewise element constant charge q and 56,331 degrees of freedom for the second-order interpolation of the displacement $\underline{\mu}$.

The optimal number of FMM groups (for this particular mesh) is found to be 35. The maximum and average truncation number are $p_{\max} = 6$ and $p_{\mathrm{av}} = 4$ for $R_{\mathrm{far}} = 135\,\mu$m and $\varepsilon = 10^{-6}$.

The electrostatic and mechanical systems are solved iteratively by obtaining the new electrostatic force distribution and the new displacement. The number of

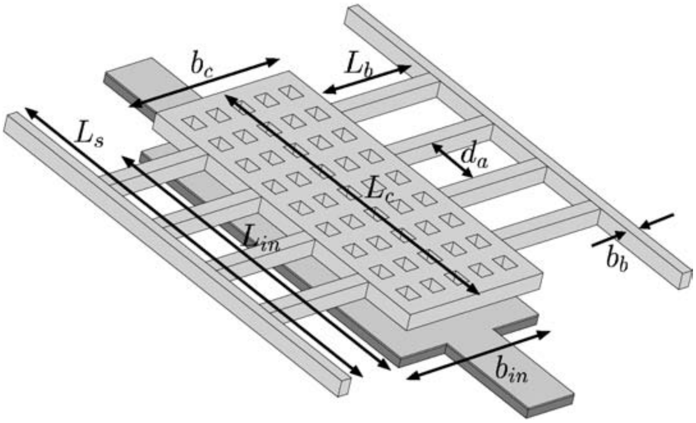

Figure 2.
Geometry of shunt capacitive MEMS switch: $L_c = 475\,\mu$m, $b_c = 275\,\mu$m, $L_{in} = 485\,\mu$m, $b_{in} = 285\,\mu$m, $L_s = 625\,\mu$m, $L_b = 205\,\mu$m, $b_b = 20\,\mu$m, and $d_a = 80\,\mu$m

iterations required for sufficient convergence of, e.g. the capacitance increases as the applied bias voltage approaches the pull-in voltage and the deformation of the top plate becomes bigger.

The calculated zero-voltage capacitance $C_{V=0}$ and pull-in voltage V_{IN} are 0.36 pF 14.2 V, respectively.

The deformation of the top electrode for a bias voltage of 11 V for the successive iterations is shown in Figure 3. Convergence is achieved after nine iterations.

The results obtained with GetDP (GetDP, 2003) are compared with those given by the commercial software packages Coventor (Coventor, Inc. 2003) and FemLab (FemLab, 1997-2004). In the simulations performed with the commercial programs, only a quarter of the geometry is considered. In the Coventor simulation, the electrostatic part is modelled by means of the BE method while the mechanical part is dealt with using the FE method and second-order elements. Only symmetry boundary conditions are considered for the mechanical problem. In the FemLab computation, the whole electromechanical problem is solved by the FE method. Symmetry conditions are imposed for the electrostatic problem. With regard to the mechanical part, the elastic behaviour of the suspension (beams) is approximated by a stiffness constant (Brown, 1998; Tilmans, 2002). For the face of the top electrode that is coupled with the suspension, the displacement is obtained by dividing the total electrostatic force by the stiffness constant.

The nominal capacitance $C_{V=0}$ obtained by Coventor and Femlab is 0.4 and 0.37 pF, respectively. The pull-in calculated voltage is 14.24 V for Coventor and 17.25 V.

The computed value of the capacitance as a function of the applied voltage is shown in Figure 4 for the three different solvers. The curves $C-V$ obtained with GetDP and FemLab agree well for low applied voltage, when the deformation is small. As the applied voltage increases, an accurate estimate of the displacement becomes critical, the approximation used for the suspension does not suffice. On the contrary, the agreement between the curves obtained with GetDP and Coventor is better as the voltage increases. The influence of three quarters of the device are disregarded for the electrostatic computation, but the mechanical part is solved accurately. Figure 5 shows

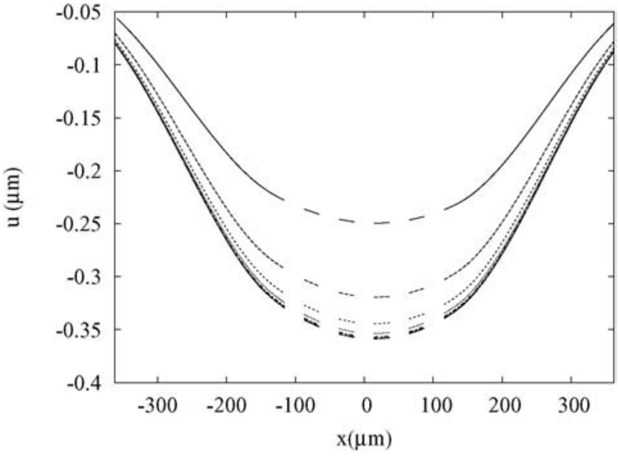

Figure 3.
Convergence of the vertical displacement along a line through the suspension beams and perforated plate for an applied bias voltage of 11 V

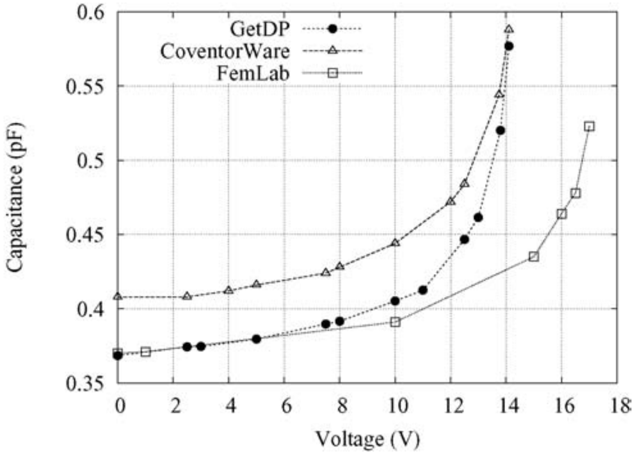

Figure 4. Calculated capacitance vs the applied bias voltage simulation explains the divergence of the curves

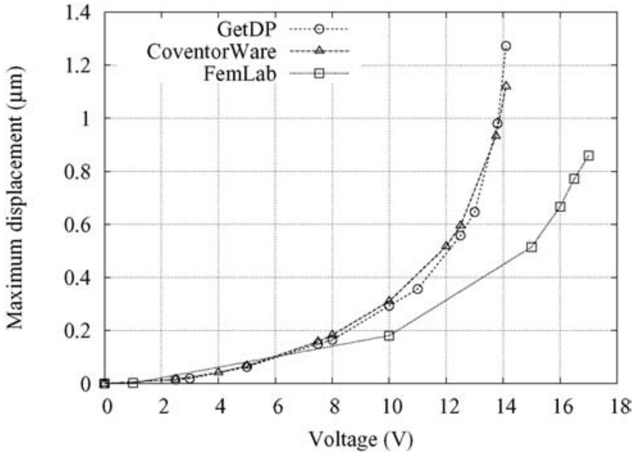

Figure 5. Maximum vertical displacement of the top electrode vs the applied bias voltage

the maximum vertical displacement of the top electrode as a function of the applied bias voltage. A good agreement between the values obtained by means of GetDP and Coventor is observed. Approximation is used for the mechanical problem with a stiffness constant for modelling the suspension in the FemLab.

6. Conclusion

A shunt capacitive MEMS switch has been modelled. The BE method, accelerated by the FMM, and the FE method have been applied to solve the electrostatic and mechanical problem, respectively. An adaptive truncation scheme for the 3D Laplace Green function has been employed. The results have been compared with those obtained with the commercial packages Coventor and FemLab.

References

Brown, E.R. (1998), “RF-MEMS switches for reconfigurable integrated circuits”, *IEEE Trans. on Microwave Theory and Techniques*, Vol. 46 No. 11, pp. 1868-80.

Buchau, A., Huber, C.J., Rieger, W. and Rucker, W.M. (2000), “Fast BEM computations with the adaptive multilevel fast multipole method”, *IEEE Transactions on Magnetics*, Vol. 36 No. 4, pp. 680-4.

Coventor, Inc. (2003), *Accelerating MEMS Innovations*, 4001 Weston Parkway, Cary, NC 27513, available at: www.coventor.com, USA

Farina, M. and Rozzi, T. (2001), “A 3D integral equation-based approach to the analysis of real-life MMICS-application to microelectromechanical systems”, *IEEE Trans. on Microwave Theory and Techniques*, Vol. 49 No. 12, pp. 2235-40.

Femlab (1997-2004), *Multiphysics modelling*, COMSOL, Inc., 1100 Glendon Avenue, 17th Floor Los Angeles, CA 90024, USA, available at: www.femlab.com

GetDP (2003), *A General Environment for the Treatment of Discrete Problems*, Department of Electrical Engineering (ELAP), Institut Montefiore, University of Liège, Sart Tilman Campus, available at: www.geuz.org/getdp, Belgium

Graglia, R.D. (1993), “On the numerical integration of the linear shape functions times the 3D Green’s Function of its gradient on a plane triangle”, *IEEE Trans. on Antennas and Propagation*, Vol. 41 No. 10, pp. 1448-55.

Nabors, K. and White, J. (1991), “Fastcap: a multipole accelerated 3D capacitance extraction program”, *IEEE Transactions on Computer-Aided Design*, Vol. 10 No. 11, pp. 1447-59.

Pilkey, W.D. (2002), *Analysis and Design of Elastic Beams: Computational Methods*, Wiley, New York, NY.

Rao, S.M., Sarkar, T.K. and Harrington, R.F. (1984), “The electrostatic field of conducting bodies in multiple dielectric media”, *IEEE Trans. on Microwave Theory and Techniques*, Vol. 32 No. 11, pp. 1441-8.

Rokhlin, V. (1983), “Rapid solution of integral equations of classical potential theory”, *Journal of Computational Physics*, Vol. 60, pp. 187-207.

Saad, Y. and Schultz, M.H. (1986), “GMRES: a generalized minimal residual algorithm for solving nonsymmetric linear systems”, *SIAM J. Sci. Comput.*, Vol. 7 No. 3, pp. 856-69.

Sabariego, R.V., Gyselinck, J., Dular, P., Geuzaine, C. and Legros, W. (2004), “Fast multipole acceleration of the hybrid finite element-boundary element analysis of 3D eddy current problems”, *IEEE Transactions on Magnetics*, Vol. 40 No. 2, pp. 1278-1281.

Tilmans, H.A.C. (2002), “MEMS components for wireless communications (invited paper)”, *Proc. EuroSensors XVI*, 15-18 September, Prague, Czech Republic, pp. 1-34 (CD-ROM only).

The Emerald Research Register for this journal is available at
www.emeraldinsight.com/researchregister

The current issue and full text archive of this journal is available at
www.emeraldinsight.com/0332-1649.htm

Comparison of 3D magnetodynamic formulations in terms of potentials with imposed electric global quantities

T. Henneron
USTL, Villeneuve d'ascq, France
S. Clénet
ENSAM CER Lille, Lille, France
F. Piriou
USTL, Villeneuve d'ascq, France

Keyword *Finite element analysis*

Abstract *Methods to impose a voltage or a current in massive conductors in dual magnetodynamic potential formulations (**A**-φ and **T**-**K**I-Ω) are presented. In the **A**-φ formulation, a supply voltage can be naturally imposed at the terminals of a conductor, but not a supply current. An equation must be added. This is the opposite for the **T**-**K**I-Ω formulation. In the paper all methods are described and compared on the basis of an example.*

1. Introduction

In the case of electromagnetic systems working at high frequencies, the distribution of the current cannot be considered as uniform in conductors. It is necessary to consider the eddy current effects. Two potential formulations can be used to solve such a problem: the **A**-φ formulation and the **T**-**K**I-Ω formulation. Either the current or the voltage is imposed to the conductor. Imposing such global quantities is not necessarily easy. Some methods have already been proposed (Dular, 2000) using special test functions.

In this communication, we propose to use functions already used in magnetostatics to impose currents and voltages in potential formulations (Le Menach, 2000) and to compare them.

First, we present the magnetodynamic problem. Second, the **A**-φ and **T**-**K**I-Ω formulations are described. Then, we develop methods to impose the current and the voltage at the terminals of a conductor in both formulations. Finally, an application example is studied to compare both formulations in terms of accuracy, memory resource requirements and computation times.

2. Magnetodynamic problem

We consider a simple system composed of a conducting part in a domain D_c with boundary Γ_c enclosed in a domain D. We denote Γ the boundary of D. The counterpart

---

The research was carried out in the frame of the Inter-University Attraction Pole IAP P5/34 for fundamental research funded by the Belgian Federal Government.

COMPEL: The International Journal for Computation and Mathematics in Electrical and Electronic Engineering
Vol. 23 No. 4, 2004
pp. 885-893
© Emerald Group Publishing Limited
0332-1649
DOI 10.1108/03321640410553319

of D_{c} in D is assumed to be a non-conducting domain (Figure 1). In magnetodynamics, Maxwell's equations are used to calculate the electric and magnetic field distributions:

$$\mathrm{curl}\,\mathbf{E} = -\partial_t\mathbf{B} \tag{1a}$$

$$\mathrm{curl}\,\mathbf{H} = \mathbf{J} \tag{1b}$$

with **E** the electric field, **B** the magnetic flux density, **H** the magnetic field and **J** the current density. The constitutive laws are:

$$\mathbf{B} = \mu(\mathbf{H})\mathbf{H} \;\text{ and }\; \mathbf{J} = \sigma\mathbf{E} \tag{2}$$

with σ the electric conductivity. The conductivity is equal to zero in the counterpart of $\mathrm{D_c}$ in D, and μ the magnetic permeability. Boundary conditions are added to ensure the uniqueness of the solution:

$$\mathbf{B}\cdot\mathbf{n} = 0 \;\text{ on }\; \Gamma_{\mathrm{B}} \;\text{ and }\; \mathbf{H}\times\mathbf{n} = 0 \;\text{ on }\; \Gamma_{\mathrm{H}} \tag{3}$$

with Γ_{B} and Γ_{H} two complementary parts of Γ such that $\Gamma = \Gamma_{\mathrm{B}} \cup \Gamma_{\mathrm{H}}$. In the following, we denote Γ_{c1} and Γ_{c2}, two surfaces of Γ_{c} which belong also to Γ (Figure 1). On these surfaces the supply voltage V applied at the conducting medium terminals or the current I flowing in it is imposed. To solve the previous equation system by the finite element method, two potential formulations can be used. In the following, the **A**-φ and **T**-**K**I-Ω formulations are presented, and in each formulation, methods are proposed to impose the current I or the voltage V.

3. A-φ Formulation

In the case of the **A**-φ formulation, two potentials are introduced: a magnetic vector potential **A** and an electric scalar potential φ. Since the magnetic flux density is divergence free, we have:

$$\mathbf{B} = \mathrm{curl}\,\mathbf{A} \;\text{ with }\; \mathbf{A}\times\mathbf{n} = 0 \;\text{ on }\; \Gamma_{\mathrm{B}} \tag{4}$$

Then, using equation (1a), the electric field can be defined in terms of **A** and φ:

$$\mathbf{E} = -\partial_t\mathbf{A} - \mathrm{grad}\,\varphi \tag{5}$$

Finally, the equation system becomes:

$$\mathrm{curl}\,(\mu^{-1}\,\mathrm{curl}\,\mathbf{A}) + \sigma(\partial_t\mathbf{A} + \mathrm{grad}\,\varphi) = 0 \tag{6}$$

$$\mathrm{div}\,\sigma(\partial_t\mathbf{A}^{+}\mathrm{grad}\,\varphi) = 0 \tag{7}$$

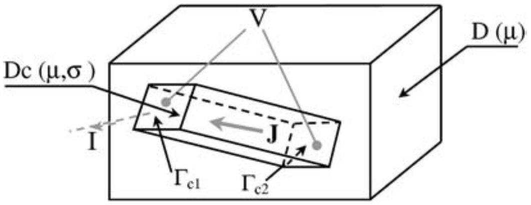

Figure 1.
Geometry of the application example

In the non-conducting part, equation (7) vanishes and the remaining system corresponds to the magnetostatic formulation (equation (6)). To numerically solve the equation system, Whitney's elements can be used (Bossavit, 1988). The potentials **A** and φ are discretised in the edge element space and in the nodal element space, respectively. Then, the discrete forms of **A** and φ are written:

$$\mathbf{A} = \sum_{a\in \mathrm{D}} \mathrm{A}_a \omega_a \quad \text{and} \quad \varphi = \sum_{n\in \mathrm{D_c}} \varphi_n \omega_n \tag{8}$$

with ω_a the interpolation function associated to the edge a, ω_n the nodal function associated to the node n, A_a the circulation of **A** along the edge a and φ_n the value of φ at the node n.

To impose a voltage V at the terminals of the conducting part (Γ_{c1} and Γ_{c2}), the values of φ are constant on Γ_{c1} and Γ_{c2} such that:

$$V = \varphi_i - \varphi_j \quad \forall i \in \Gamma_{c1} \quad \text{and} \quad \forall j \in \Gamma_{c2} \tag{9}$$

The value of φ on Γ_{c2} can be fixed arbitrarily. Fixing the value of φ equal to zero on Γ_{c2}, φ can be written under the following form:

$$\varphi = \sum_{n\in D_c - \Gamma_{c1} - \Gamma_{c2}} \varphi_n \omega_n + V \sum_{n\in \Gamma_{c1}} \omega_n \tag{10}$$

Moreover, on Γ_B-Γ_{c1}-Γ_{c2}, the nodal values of φ are also cancelled to satisfy the boundary condition (3). Consequently, in **A**-φ formulation, a voltage can be naturally imposed by fixing the values of V at the terminals of the conducting part. The second term of φ in equation (10) then becomes a source term in equation (6).

To impose a current I in D_c, an equation is added to the system, the voltage V is then an unknown. This approach has been already developed by Dular (2000). A scalar function α can be defined by the sum of nodal functions associated to the nodes on Γ_{c1}:

$$\alpha = \sum_{n\in \Gamma_{c1}} \omega_n \tag{11}$$

The expression of the current is obtained using the weak formulation of equation (7):

$$I = (\mathbf{J}, \operatorname{grad} \alpha)_D = (-\sigma(\partial_t \mathbf{A} + \operatorname{grad} \varphi), \operatorname{grad} \alpha)_{Dc1} \tag{12}$$

with $(\mathbf{a}, \mathbf{b})_c$ a volume integral onto c of the dot product of vectors **a** and **b**. The function α is non-zero only onto a domain D_{c1} of D_c gathering all elements having at least one node belonging to Γ_{c1}. Calculation of equation (12) must be carried out only on the small domain D_{c1}. Equation (12) can be also used to compute the current I by a post processing computation in the case of a voltage supply.

4. T-KI-Ω formulation

In the **T**-**K**I-Ω formulation, two potentials are introduced: an electric vector potential **T** and a magnetic scalar potential Ω. A vector **K** is also introduced such that curl $\mathbf{K} = \mathbf{N}$ to satisfy Ampere's law. In this relation, the vector **N** is divergence free outside of D_c. Moreover, it is defined such that its flux flowing between Γ_{c1} and Γ_{c2} is equal to 1 (Le Menach, 2000). Based on the previous conditions, the magnetic field can be written:

$$\mathbf{H} = \mathbf{T} + \mathbf{K}\mathrm{I} - \mathrm{grad}\,\Omega,\ \ \mathbf{T}\times\mathbf{n} = 0 \ \text{on}\ \Gamma_{\mathrm{C}},\ \ \mathbf{T} = 0 \ \text{in}\ D - D_{\mathrm{c}}$$
$$\text{and}\ \ \mathbf{K}\times\mathbf{n} = 0 \ \text{on}\ \Gamma_{\mathrm{H}},\ \ \Omega = 0 \ \text{on}\ \Gamma_{\mathrm{H}} \tag{13}$$

Finally, the equation system becomes:

$$\mathrm{curl}\ \ (\sigma^{-1}\mathrm{curl}\,(\mathbf{T} + \mathbf{K}\mathrm{I})) + \partial_t(\mu(\mathbf{T} + \mathbf{K}\mathrm{I} - \mathrm{grad}\,\Omega)) = 0 \tag{14}$$

$$\mathrm{div}\,\mu^{-1}(\mathbf{T} + \mathbf{K}\mathrm{I} - \mathrm{grad}\,\Omega) = 0 \tag{15}$$

Equation (14) is defined only in D_{c}. On the other hand, equation (15) is defined on the whole domain and corresponds to the equation to be solved in magnetostatics (with $\mathbf{T} = 0$). By using Whitney's elements, the potentials $\mathbf{T}$ and Ω are discretised in the edge element space of D_{c} and in the nodal element space of D, respectively. The field $\mathbf{K}$ is discretised in the edge element space by:

$$\mathbf{K} = \sum_{n\in D} K_{\mathrm{a}}\omega_{\mathrm{a}} \tag{16}$$

with K_{a} the circulation of $\mathbf{K}$ on the edge a. The distribution of $\mathbf{K}$ can be determined by an automatic procedure from a vector $\mathbf{N}$ already calculated in the facet element space (Le Menach, 2000). Other methods can be used to determine the vector $\mathbf{K}$ (Dular, 1997; Meunier, 1998). In the $\mathbf{T}$-$\mathbf{K}\mathrm{I}$-Ω formulation, the current can be naturally applied by fixing the value of I. The term $\mathbf{K}\mathrm{I}$ then becomes a source term in equations (14) and (15). To apply a voltage V, an equation is added to the system. The current I is then an unknown. This equation can be obtained with a similar approach than (Le Menach, 2000) by considering a weak form of equation (14) with the vector $\mathbf{K}$ as test function. Thus, we have:

$$\begin{aligned} V &= (\mathbf{E},\ \mathrm{curl}\,\mathbf{K})_D + \partial_{\mathrm{t}}(\mathbf{B},\mathbf{K})_D \\ &= (\sigma^{-1}\mathrm{curl}\,(\mathbf{T} + \mathbf{K}\mathrm{I}), \mathrm{curl}\,\mathbf{K})_D + \partial_{\mathrm{t}}(\mu(\mathbf{T} + \mathbf{K}\mathrm{I} - \mathrm{grad}\,\Omega),\ \mathbf{K})_D \end{aligned} \tag{17}$$

The current I is then an unknown of the system. Contrary to the $\mathbf{A}$-φ formulation, the previous equation has to be calculated on the whole domain because $\mathbf{K}$ is defined on D. Nevertheless, some conditions on vector $\mathbf{K}$ can be added to reduce its domain of definition. This domain must contain domain D_{c} and be simply connected. Equation (17) can be also used to compute the voltage by a post processing computation in the case of current supply.

5. Application

5.1 Presentation of application example

As an example of application, a coil enclosed in an air box is considered. Its geometry is shown in Figure 2. The mesh is made up of tetrahedral elements. Two meshes have been considered, the first (M1) has 3,612 nodes and 20,436 elements and the second (M2) has 20,179 nodes and 116,906 elements. For both formulations, both kinds of supply either a current I or a voltage V are compared. In the current supply, a sinusoidal current of magnitude equal to 3.14 A is applied to the conductor. We also

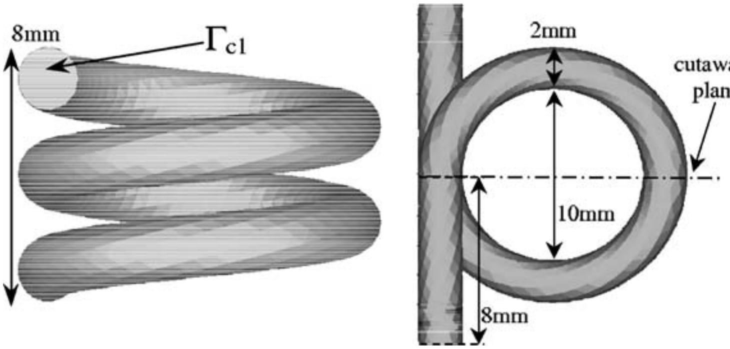

Figure 2.
Geometry of the application example

consider two supply frequencies ($f = 50\,\mathrm{Hz}$ and 1 kHz). Two periods have been simulated with 25 time steps per period.

In the case of $\mathbf{A}$-φ formulation the scalar potential φ on Γ_{c1} and Γ_{c2} are unknowns of the problem. Consequently, it is easy to calculate the voltage V corresponding to the applied current. As explained above (equation (17)) it is possible, in the case of **T**-**K**I-Ω formulation, to calculate in a post-processing step the voltage V with an imposed current. Consequently, to verify our models, we have calculated for both formulations the current when we applied the voltages V computed previously.

In these conditions, the calculated current magnitude should be equal to 3.14 whatever the formulation is (if errors introduced by quantification and iterative solver are neglected). The calculations have been carried on a 2 GHz INTEL XEON.

In Figure 3, the distribution of vector **K** is given on the cutaway plan shown in Figure 2. This one has no physical meaning and is not a physical field, but it verifies Ampere's law outside the massive conductor (all circulations of **K** along a closed path is equal to I if it encircles the conducting part and equal to zero on contrary).

In Figure 4, the distribution of **J** obtained from **T**-**K**I-Ω formulation is given for both frequencies on a section plane in the first time step. They are not the same on S1 and S2 for both frequencies. S1 and S2 are shown in Figure 3.

There is the skin depth effect and also the proximity effect (i.e. the influence of the other turns of the conductor). This phenomenon appears clearly on the current distribution at 1 kHz which is not axisymmetrical in a section S1. The current density is lower in an area close to the conductor (S2).

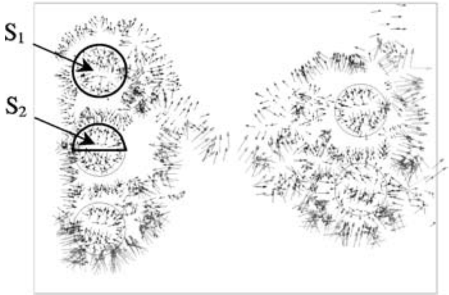

Figure 3.
Distribution of **K**

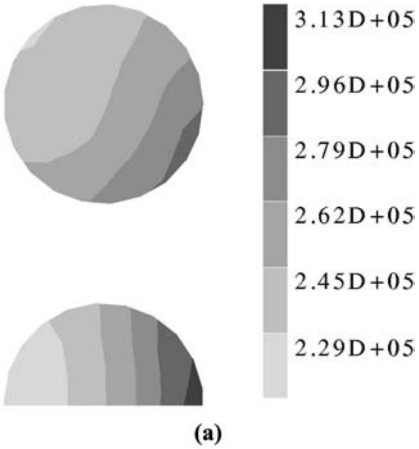

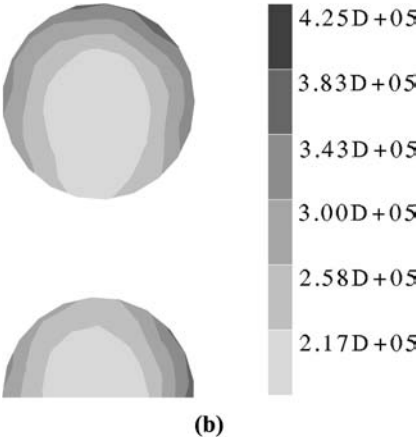

Figure 4.
Distribution of **J** (A/m^2) obtained with the **T**-**K**I-Ω formulation. (a) $f=50$ Hz; and (b) $f=1$ kHz

5.2 A-φ formulation

In Figures 5 and 6, the evolution of the voltage vs time is given for both meshes and both frequencies with the conductor supplied by a sinusoidal current. For a frequency of 50 Hz, the conductor behaves as a resistor, the phase difference between the current and the voltage is practically zero. For a frequency of 1 kHz, the phase difference is then practically equal to 35° and the magnitude of the voltage V increases. The impedance of the coil increases with the skin depth and proximity effects and also the self inductance effect.

In Table I, the magnitudes of the voltage and the current are given for a frequency of 50 Hz. In the case of current supply, equation (12) is added to the matrix system. The number of non-zero terms of the added line (corresponding to equation (12)) is small. As noticed earlier, only nodes located of Γ_{c1} are considered, therefore, only the unknowns associated to nodes of Γ_{c1} leads to non-zero terms (one of the two surfaces of the massive conductor belonging to the boundary of the studied system).

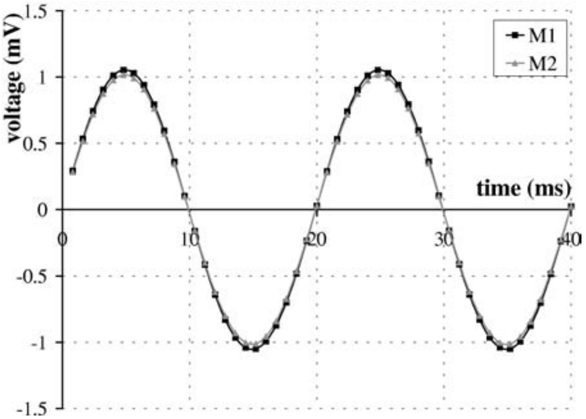

Figure 5.
Evolution of the voltage V versus time for $f = 50\,\text{Hz}$

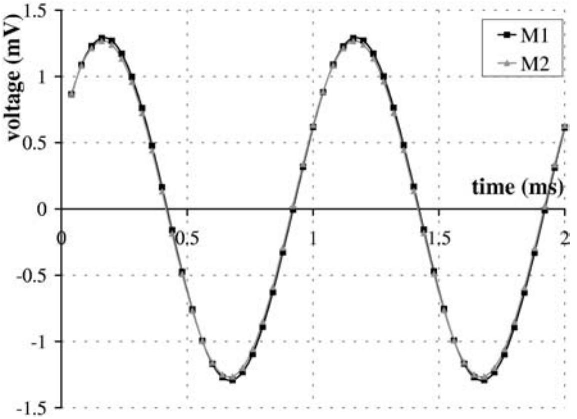

Figure 6.
Evolution of the voltage V versus time for $f = 1\,\text{kHz}$

	Mesh			
	M1		M2	
Supply	Current	Voltage	Current	Voltage
Unknowns	21,934	21,933	125,038	125,037
Non-null terms of the matrix	228,158	228,049	1,300,172	1,299,861
Average ICCG iteration	749	680	1,929	1,771
Computation time (min)	12	9	222	188
$V_{\max}$ (mV)	1.05		1.02	
$I_{\max}$ (A)		3.14		3.14

Table I.
Magnitudes of currents and voltages and features of the matrix system ($f = 50\,\text{Hz}$)

Consequently, computation time for both supply current and voltage are similar. The number of iterations increases slightly when an equation is added. By imposing the evolution of the voltage obtained by a current supply (for example, for M1 a voltage of magnitude of 0.105 V is applied), the magnitude of I is close to 3.14 A.

5.3 T-KI-Ω formulation

In Figures 7 and 8, the evolution of the voltages versus time are given for both meshes and both frequencies when a sinusoidal current is applied. The latter is very similar to the curves obtained in the case of the **A**-φ formulation.

In the case of voltage supply, equation (17) is added to the matrix system. Here, (Table II) the gap of calculation time between the models with two types of supply is

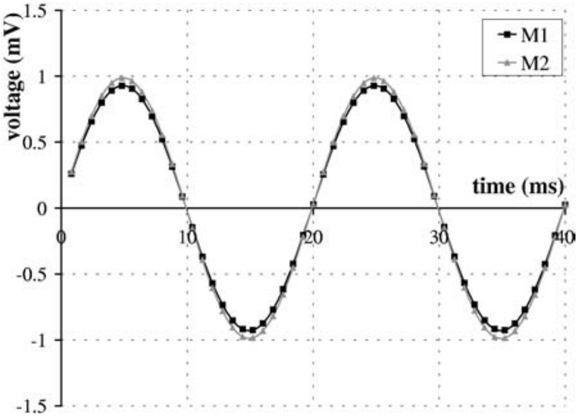

Figure 7.
Evolution of the voltage V vs time for $f = 50\,\text{Hz}$

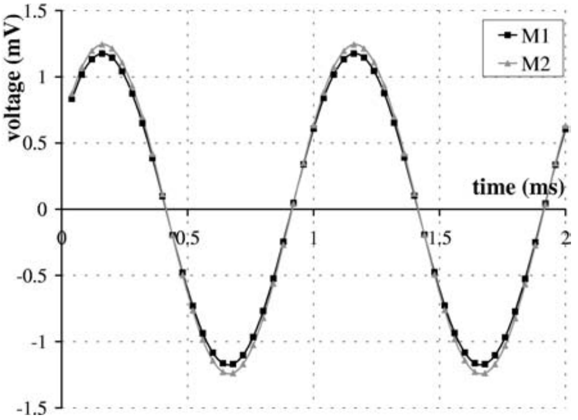

Figure 8.
Evolution of the voltage V vs time for $f = 1\,\text{kHz}$

Table II.
Magnitudes of currents and voltages and features of the matrix system ($f = 50\,\text{Hz}$)

	Mesh			
	M1		M2	
Supply	Current	Voltage	Current	Voltage
Unknowns	7,641	7,642	50,305	50,306
Non-null terms of the matrix	80,665	88,307	580,484	630,790
Average ICCG iteration	49	47	107	105
Computation time	2 min 23 s	5 min 3 s	17 min	112 min
$V_{\max}$ (mV)	0.928		0.987	
$I_{\max}$ (A)		3.125		3.13

more important. The number of non-zero terms in the matrix has increased much more than with the **A**-φ formulation. That is due to the added line which has a lot of non-zero terms. The vector **K** is defined in the whole domain. Consequently, the computation time is more important in the case of voltage supply.

5.4 Comparison of both formulations

For the considered example, both formulations give similar results in terms of global values (current, voltage, . . .) but the **T**-**K**I-Ω formulation is much faster. The difference is the greatest in the case of current supply (ratio of ten between both formulations). Moreover, improvements can be still done to speed up the solution when we impose voltage in the **T**-**K**I-Ω formulation. This improvement can be obtained by reducing the definition domain of **K** by adding boundary conditions inside the domain D.

6. Conclusion

Two magnetodynamic formulations have been presented. For each formulation, some methods have been given to impose a current or a voltage in a conductive medium using special test functions. An application example has been studied using both formulations and with two kinds of supply (current and voltage). For this example, the **T**-**K**I-Ω formulation seems to be well adapted because the global quantities obtained by both formulations are very similar, but its computation time is smaller.

References

Bossavit, A. (1988), "A rationale for 'edge-elements' in 3D fields computations", *IEEE Transactions on Magnetics*, Vol. 24 No. 1, pp. 74-9.

Dular, P. (1997), "A generalized source magnetic field calculation method for inductors of any shape", *IEEE Transactions on Magnetics*, Vol. 33 No. 2, pp. 1398-401.

Dular, P. (2000), "Dual magnetodynamic formulations and their source fields associated with massive and stranded inductor", *IEEE Transactions on Magnetics*, Vol. 36 No. 8, pp. 1293-9.

Le Menach, Y. (2000), "Numerical model to discretize source fields in the 3D finite element method", *IEEE Transactions on Magnetics*, Vol. 36 No. 4, pp. 676-9.

Meunier, G. (1998), "Computation of coupled problem of 3D eddy current and electric circuit by using T_0-T-ϕ formulation", *IEEE Transactions on Magnetics*, Vol. 34 No. 5, pp. 3074-7.

The Emerald Research Register for this journal is available at
www.emeraldinsight.com/researchregister

The current issue and full text archive of this journal is available at
www.emeraldinsight.com/0332-1649.htm

Modelisation of thin cracks with varying conductivity in eddy-current testing

Ph. Beltrame
University of Cottbus, Cottbus, Germany

Keywords *Simulation, Integral equations, Eddy currents*

Abstract *In the ideal crack model (negligible thickness and an impenetrable barrier to electric current) in eddy-current testing frame, the field-flaw is equivalent to a current dipole layer on its surface. This dipole density is the solution of an integral equation with a hyperstrong kernel. This model has shown its efficiency, as well the computing accuracy, as for the CPU time. Furthermore, the case of a current leakage across crack was considered by introducing an equivalent conductivity of the crack. This paper aims at simulating a local varying conductivity. In particular, we focus on a constant piecewise conductivity. In this last case, because of the presence of the hypersingular kernel in the equation, the numerical scheme using the ideal case has to be modified.*

1. Introduction

The thin crack problem in eddy-current testing (ECT) – i.e. the crack width e (Figure 1) is small compared to its other dimensions and skin depth δ – constitutes a major difficulty for the simulation. It is commonly assumed that a surface crack is “ideal”: being infinitesimally thin and allowing no current to flow across it. Then, Bowler (1994) showed that the crack is equivalent to a current dipole surface of density $\mathbf{p} = p\mathbf{n}$, where $\mathbf{n}$ is the normal of the crack (Figure 1). The density p is the solution of an integral equation with an hypersingular kernel on the crack surface related to the incident current. The resolution with a collocation method and second order shape functions is carried out by Beltrame and Burais (2002a) and the improvement with special elements at the crack edges is described by Beltrame (2002). The variation ΔZ of the coil impedance is obtained by a regular integration on the density p of the crack surface. The eddy-current perturbation is directly deduced from this density, but sets a problem of quasi-singular integrals. It is overcome with a regularization-like technique (Beltrame and Burais, 2002b).

The ideal crack model was improved by Harfield and Bowler (1998) and Villone and Harfield (2000) by introducing an uniform equivalent conductivity σ_{f} of the crack using two methods: finite elements and integral equations. This last formulation differs from our case and is applied for the thin skin depth approximation (frequency $f > 10\,\mathrm{MHz}$). Recently, Beltrame and Burais (2004), without this assumption of high frequency, have improved the ideal crack model by considering two small parameters: equivalent conductivity σ_{f} and a small thickness e of the crack. The last one is modelised by adding a correcting term in the impedance change. The conductivity modifies the integral equation by adding a term proportional to σ_{f}.

This work is supported by the Centre de Génie Electrique de Lyon (CeGeLy) at the Ecole Centrale Lyon (ECL). The author also thanks Noel Burais for his support.

COMPEL: The International Journal for Computation and Mathematics in Electrical and Electronic Engineering
Vol. 23 No. 4, 2004
pp. 894-903
© Emerald Group Publishing Limited
0332-1649
DOI 10.1108/03321640410553328

This paper aims to treat the case in which both parameters are no more constant. Because the thickness e takes place only in post-processing, its variations do not change basically the modelisation. It is not the case for the conductivity, first we give a criterion of the validity of the formulation presented by Beltrame and Burais (2004). Secondly, the convergence of the numerical scheme used in Beltrame and Burais (2002a, b, 2004) is discussed. We prove that it fails in the case of a discontinuity of the local conductivity. Such conductivity discontinuities can modelise, for example, a "material bridge": the crack is very thin at the surface and then a lot of contact between both crack surfaces crack induce a non-negligible conductivity, but the in-depth region is an electric insulation ($\sigma_{\mathrm{f}} = 0$) because of the large thickness no contact occurs (Figure 2).

2. Formulation

The lengths are divided by the standard skin depth δ, the conductivity by $\sigma_{\mathrm{m}} - \sigma_{\mathrm{f}}$, σ_{m} being the tested piece conductivity, and the electric current density is divided by a reference $J_{\max}$. Thus, we have the new variables:

$$\begin{aligned} \tilde{\sigma}_{\mathrm{f}} &= \frac{\sigma_{\mathrm{f}}}{\sigma_{\mathrm{m}} - \sigma_{\mathrm{f}}} \\ \tilde{e} &= \frac{e}{\delta} \\ \tilde{\mathbf{J}} &= \frac{\mathbf{J}}{J_{\max}} \\ \tilde{p} &= \frac{\delta}{J_0} p \end{aligned} \tag{1}$$

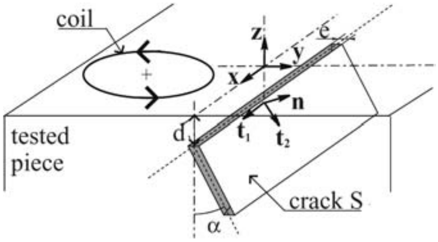

Figure 1.
Schematic configuration for the crack detection

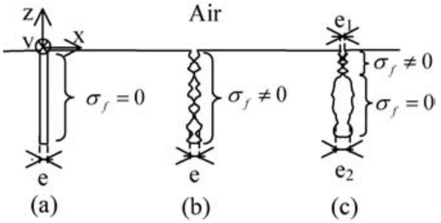

Figure 2.
Three model examples of the crack: zero conductivity (a), uniform conductivity (b), and variable conductivity (c)

Because the above equations are always in the adimensional form, the tildes will be omitted on the variables $\mathbf{J}, p\ldots$, but not when we are citing the physical parameters σ, e.

The tested piece is an amagnetic conductor, and the crack has a negligible thickness, more concretely, we suppose that:

$$\tilde{e} = \frac{e}{\delta} \ll 1 \tag{2}$$

2.1 Equation of p

In the previous assumptions frame, the **J** electric field in the presence of the crack is related to the $\mathbf{J}_0$ unperturbed one (without crack) by an integration of the dipole density p on the S crack surface (Beltrame, 2002; Bowler, 1994):

$$\mathbf{J}(\mathbf{r}') - \mathbf{J}_0(\mathbf{r}') = 2j \int_S \overline{\overline{\mathbf{G}}}(\mathbf{r}', \mathbf{r})\mathbf{p}(\mathbf{r})\,\mathrm{d}S_\mathrm{r} \tag{3}$$

where $\overline{\overline{\mathbf{G}}}$ is the electric-electric Green tensor and $\mathbf{r}'$ an "obsevation" point in the tested piece. If $\mathbf{r}'$ is on the crack then the integral has to be interpreted as the finite part of Hadamard, noted FP. The physical meaning and the computation methods of the finite part of the integral are explained in Beltrame and Burais (2002a). In order to obtain an equation on p the observation point $\mathbf{r}'$ tends to a point on the crack surface and equation (3) is projected on the crack normal **n**, then:

$$J_\mathrm{n}(\mathbf{r}') - J_{0\mathrm{n}}(\mathbf{r}') = 2j\,\mathbf{FP} \int_S \mathbf{n}\cdot\overline{\overline{\mathbf{G}}}(\mathbf{r}', \mathbf{r})\mathbf{p}(\mathbf{r})\,\mathrm{d}S_\mathrm{r} \tag{4}$$

If the crack is a perfect insulating $J_\mathrm{n} = 0$, but in the case of a local current leakage on the surface crack, the component J_n has to be expressed. In Appendix 1, we give its expression under the following assumption:

$$\tilde{e}\tilde{\sigma}_\mathrm{f} \ll 1, \tag{5}$$

if $\sigma_\mathrm{f} \approx \sigma_\mathrm{m}$, then the requirement in equation (5) is not satisfied and it will be very difficult to detect it, so we will assume that the requirement in equation (5) is satisfied. In this framework, let us introduce the local relative conductance on the crack:

$$\gamma = \frac{\tilde{\sigma}_\mathrm{f}}{\tilde{e}} = \frac{\sigma_\mathrm{f}}{\sigma_\mathrm{m} - \sigma_\mathrm{f}}\frac{\delta}{e}, \tag{6}$$

This last one is positive and the limit case $\gamma = 0$ corresponds to the ideal crack and $\gamma \rightarrow +\infty$ to the lack of crack (invisible for the eddy-current detection). The equation (4) of p becomes:

$$\mathbf{J}_0(\mathbf{r}_\mathrm{f})\cdot\mathbf{n} = -2j\mathbf{FP}\int_S \mathbf{n}\cdot\overline{\overline{\mathbf{G}}}(\mathbf{r}_\mathrm{f}, \mathbf{r})\mathbf{p}(\mathbf{r})\,\mathrm{d}S_\mathrm{r} - \gamma(\mathbf{r}_\mathrm{f})p(\mathbf{r}_\mathrm{f}) \tag{7}$$

We remark that this equation (7) differs from the ideal case one only by the term adding: $-\gamma p$. So, there does not appear an explicit requirement on the γ distribution, and the formulations between the constant and variable conductivity seem identical. Nevertheless, the regularity of γ could change the density p once, and thus, the evaluation formula of the singular integral presented in Beltrame and Burais (2002a) has to be changed. The necessary modifications are presented in Section 3. Before that we give the impedance change formula.

2.2 Impedance change

The expression of impedance change is similar to the case of constant conductivity:

$$I^2\Delta Z = \int_S \mathbf{J}_0(\mathbf{r})\mathbf{p}(\mathbf{r})\,\mathrm{d}S_\mathrm{r} + j\sum_i e_i \int_S \mathbf{J}_0(\mathbf{r})\mathbf{A}(\mathbf{r})\,\mathrm{d}S_\mathrm{r} \tag{8}$$

The first term is the classical expression of the ideal case. The second one is deduced from the thin thick model for an uniform thickness (Beltrame and Burais, 2004) when the crack thickness is piecewise constant in the direction $\boldsymbol{t}_1$. The expression of the potential $\mathbf{A}$ is given in these references.

3. Numerical implementation

3.1 The main difficulty

We adapt the numerical scheme used in Beltrame and Burais (2002a): it is a collocation method with a regular quadrangles mesh. The function p is evaluated by a second degree polynomial interpolation on nine nodes: eight at the boundary; the in-depth boundary elements special functions are used (Beltrame, 2002). The equation is evaluated at each center node. At the other boundary nodes the continuity of the gradient of p is imposed. In fact the solution is at least C^1 in the ideal crack case (Beltrame and Burais, 2002a).

In the case of local conductance, if the solution p is still regular, then we have to add only the relative conductance $\gamma(\mathbf{r}_\mathrm{c})$ in the self terms at each collocation point $\mathbf{r}_\mathrm{c}$. Yet, the question is to know the smoothness of p: continuity of p and of $\nabla_\mathrm{T}P$, where the operator ∇_T is the tangential gradient on the crack surface.

3.2 Continuity of p

The continuity of p is related to the assumption of thin crack (equation (2)) and not to the conductance. Let us suppose that the density is discontinuous at the "double point" AB, and let us denote C as a way around the crack between A and B (Figure 3). It is easy to see that the circulation of the electric field between A and B is the difference $p_A - p_B$ (Beltrame, 2002). Using the Maxwell-Faraday identity, this circulation is the flux of the induction through the surface Σ. Because the crack is thin, this surface vanishes, furthermore the induction is continuous and does not diverge through the crack (Beltrame, 2002), then this flux tends to zero. Finally, we have proved that the difference $p_A - p_B$ tends to zero, i.e. p is continuous.

3.3 Continuity of $\nabla_T p$

For the gradient the situation is more difficult. First, in Appendix 2, we prove that a discontinuity of the conductance induces in the same neighborhood a discontinuity of the gradient. The jump of the gradient is then evaluated in equation (A9).

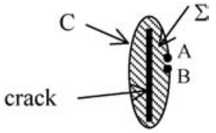

Figure 3.
Continuity of p: contour C around the crack

If the mesh is chosen such as the junction between the elements on the conductance discontinuity line, we have to put the jump requirement instead of the continuity as the one given in the previous numerical scheme. We note that these requirements are necessary if the nodes are free at this discontinuity line, i.e. if there is no condition on the gradient, then the system conditionment is very bad and the solution does not converge.

3.4 Conclusion

For a constant or continuous variation of the relative conductance γ, only the term operator proportional to identity is added. We remark that the conditionment decreases when the conductance increases. So the numerical scheme of Beltrame and Burais (2002a, b) can be applied.

If the relative conductance is discontinuous, we have in addition a jump term added at the discontinuity line. This new scheme still has a still a good conditionment.

4. Results and discussions

The physical parameters of the simulations are those used in the Team Workshop 15 (Bowler, 1994) and we will indicate, in the following, only the modifications. The conductance varies only in the z-direction. We will consider the following two cases.

(1) the conductance is uniform $\gamma(z) = \gamma_0$,

(2) "material bridge": $\gamma(z) = \gamma_0 > 0$ and $e_1 = 20\,\mu\text{m}$ if $0 > z > -1.2\,\text{mm}$ else $\gamma(z) = 0$ and $e_2 = 0.22\,\text{mm}$.

4.1 Density shape and eddy-current distribution

For an uniform conductance distribution the shape of the density p is not modified and in the eddy-current distribution the normal component appears at the crack surface (Beltrame, 2002). In the material bridge, the changes are more interesting. In the neighborhood of the conductance discontinuity, if $z < -1.2\,\text{mm}$ the density decreases rapidly like an in-depth crack edge, but it does not vanish (Figure 4). The phenomenon is local: a few incident current is deviated to the material bridge region $0 > z > -1.2\,\text{mm}$, the most part decreases under the crack (Figure 5). In "material bridge" region, the influence of the discontinuity is more global. The density p increases slowly with respect to the z-direction: almost all current crosses the crack with respect to the normal direction, but a small tangent component goes to the discontinuity line (Figure 5).

4.2 Impedance change vs the conductance

In the case 1 the variation of the impedance change vs the conductance are presented in Beltrame and Burais (2004) and Harfield and Bowler (1998). In this case, an interesting result is that the resistance R admits a maximum for $\gamma \neq 0$. In the case 2, the maximum for R and X is $\gamma = 0$ (electric insulation), but the resistance change admits an extremum for $\gamma \approx 6$ and vanishes for $\gamma \approx 0.6$ (Figure 6). For $\mathbf{r} < 0.01$ the impedance change is equivalent to the ideal crack case. For $0.1 < \gamma < 5$ the impedance change decreases a lot. For $\gamma > 100$ the crack is equivalent to the in-depth one.

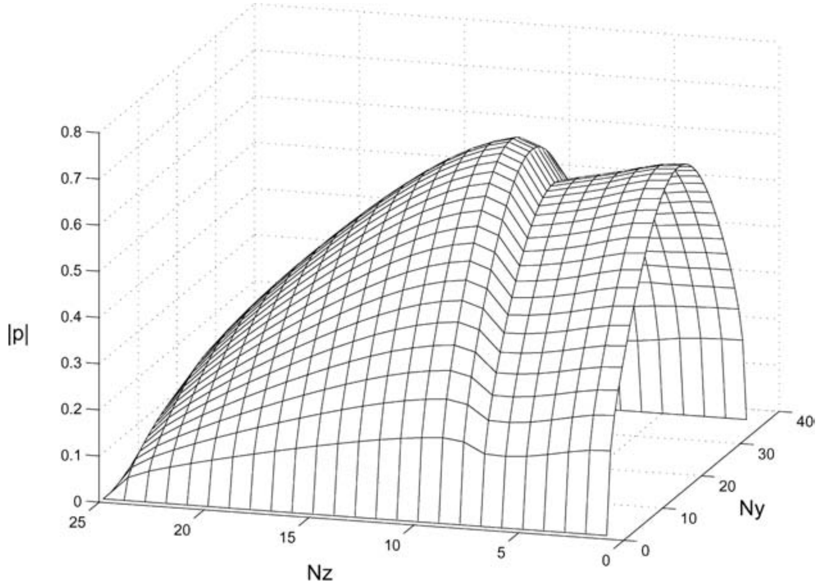

Figure 4.
Density p for the case 2 with $\gamma = 10$. The coordinates are the number of the nodes in the y and z directions

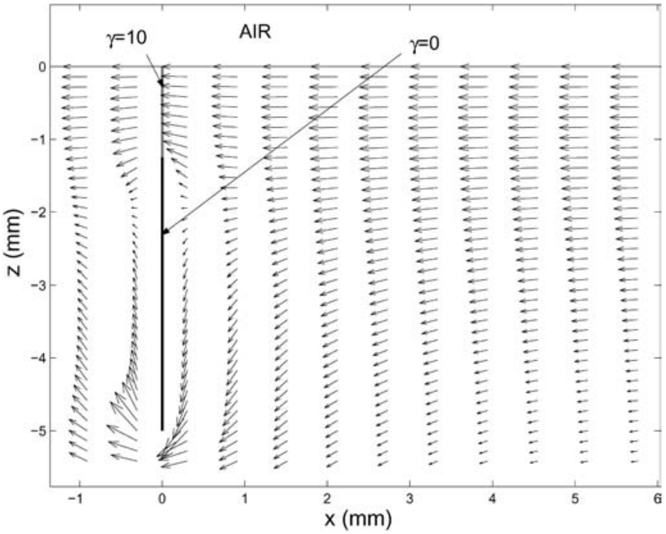

Figure 5.
Eddy current distribution for case 2 with $\gamma = 10$

4.3 Signatures

The coil is moving in the direction of x (Figure 1), and we have represented the signature for four cracks:

1. ideal crack;
2. uniform conductivity $\gamma = 5$;

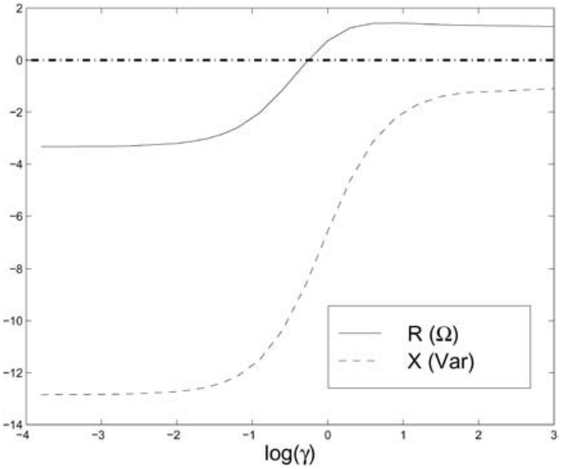

Figure 6.
Variation of the resistance *R* and the reactance *X* vs the conductance

(3) material bridge (case 2) with $\gamma_0 = 5$; and

(4) material bridge (case 2) with $\gamma = +\infty$ ($\approx$ in-depth crack).

The signature shapes are similar: the $|\Delta Z|$ amplitude increases when the coil draws close to the crack and reaches a maximum when a coil ring is on the crack and finally decreases rapidly when the coil center corresponds to crack center (Figure 7). Obviously, the amplitude of the impedance change is the greatest for the ideal crack and in the descending impedance amplitude place comes the 3rd, 4th and 2nd cases. The maximum of the amplitude decreases progressively between these different cases. But the phase change of case 2 is small. This particularity of case 2 can be explained by

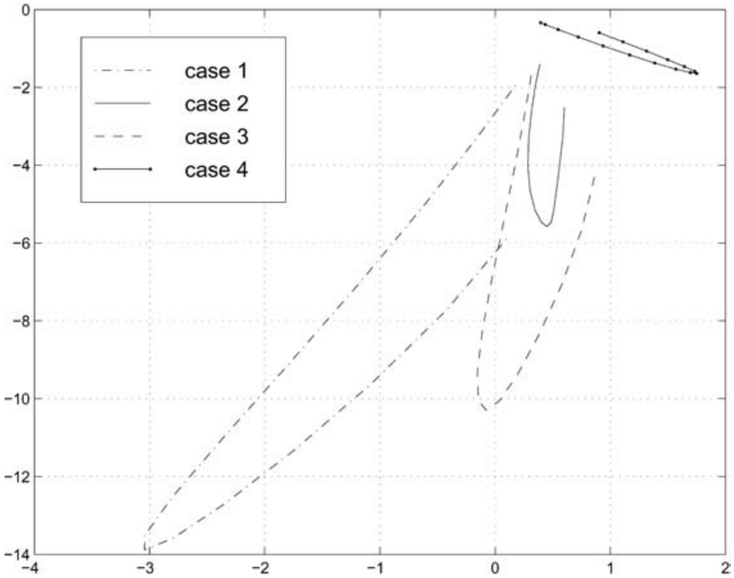

Figure 7.
Signatures in four cases

the fact that the electric current near the surface (i.e. the greatest amplitude) is slightly deviated by the crack contrary to the other cases.

5. Conclusion

The case of a varying conductance in the thin thickness frame was treated. In the case of a discontinuity of the conductance, we have proven and explicated the jump of the gradient of the dipole density. The necessary modifications are implemented in the numerical scheme. This formulation was applied for a planar surface crack with a material bridge to compute the impedance change and represent the eddy-current distribution near the crack.

The perspective is the confrontation with the experiment and in particular to precise the condition (5). The second one is to consider a non-planar surface: planar piecewise or curve surface.

References

Beltrame, Ph. (2002), “Modélisation 3D de la perturbation électromagnétique au voisinage d’une fissure mince. Application au Contrôle Non Destructif par courants de Foucault”, PhD Thesis, Ecole Centale Lyon, France.

Beltrame, Ph. and Burais, N. (2002a), “Computing methods of hypersingular intergal applied to eddy-current testing”, *IEEE Transactions on Magnetics*, Vol. 38, pp. 1269-72.

Beltrame, Ph. and Burais, N. (2002b), “Application of regularization method to compute eddy-current distribution near cracks”, *COMPEL*, Vol. 24 No. 4.

Beltrame, Ph. and Burais, N. (2004), “Generalization of the ideal crack model in eddy-current testing”, *IEEE Transactions on Magnetics*, Vol. 40 No. 2.

Bowler, J. (1994), “Eddy-current interaction with an ideal crack. The forward problem”, *J. Appl. Phys.*, Vol. 75 No. 12, pp. 8128-37.

Harfield, N. and Bowler, J. (1998), “A thin-skin theory of current leakage across surface cracks”, *Electromagnetic Nondestructive Evaluation (II)*, IOS Press, Amsterdam, pp. 1-8.

Villone, F. and Harfield, N. (2000), “Simulation of the effects of current leakage across thin cracks”, *Electromagnetic Nondestructive Evaluation (IV)*, IOS Press, Amsterdam, pp. 79-86.

Further reading

Badics, Z., *et al.* (1997), “An effective 3D finite element scheme for computing electromagnetic field distorsion due to defects in eddy-current nondestructive evaluation”, *IEEE Transactions on Magnetics*, Vol. 33 No. 2, pp. 1012-20.

Bowler, J., *et al.* (1991), “Eddy current probe impedance due to a volumetric flaw”, *J. Appl. Physics.*, Vol. 70 No. 3, pp. 1107-14.

Appendix 1. Expression of J_n

Let us consider the potential vector formulation $(\mathbf{A}, V)$ with the Coulomb gauge. The deviation of the electric current lines is the principal cause of the current dipole source. Then, the phenomenon is essentially electrostatic, more concretely in Beltrame (2002), we prove that the potential vector $\mathbf{A}$ is continuous through the crack and the adimensional jump $[V]$ of the scalar potential V is the opposite of the adimensional dipole density p: $p = -[V]$. The normal electric current density J_{n} is decomposed into two parts:

$$J_{\mathrm{n}} = \tilde{\sigma}_{\mathrm{f}}\left(-\frac{\partial V}{\partial n} + jA_{\mathrm{n}}\right).$$

Because the crack thickness is small:

$$\frac{\partial V}{\partial n} \approx -\frac{[V]}{\tilde{e}} = \frac{p}{\tilde{e}}.$$

Then, we have:

$$J_{\mathrm{n}} = \frac{1}{\tilde{e}}(\tilde{\sigma}_{\mathrm{f}} p + j\tilde{\sigma}_{\mathrm{f}}\tilde{e}A_{\mathrm{n}}) \tag{A1}$$

If we suppose that $\tilde{\sigma}_{\mathrm{f}}\tilde{e} \ll 1$, then the second term is negligible in equation (A1), and we obtain:

$$J_{\mathrm{n}} = \frac{\tilde{\sigma}_{\mathrm{f}}}{\tilde{e}} p \tag{A2}$$

Appendix 2. Jump of ∇p

The goal of this appendix is to determine the possible jump of the gradient of p when the conductance γ can be discontinuous. Let $\mathbf{r}_0$ be a point on the discontinuity line L of the conductance. This point is the center of the disc D, which is separated by the line L into two half discs D_1 and D_2 (Figure A1). In each disc D_i we consider the point $\mathbf{r}_i$ at the distance εL. In the region D_i the crack has the conductance γ_i and in general manner the index ${}_i(i = 1, 2)$ denotes the value at the point $\mathbf{r}_i$. If the quantity continues, the index 0 designates its value at $\mathbf{r}_0$. Finally, the possible jump of the gradient is noted as

$$[\nabla p_0] = \lim_{\varepsilon \to 0}(\nabla p_2 - \nabla p_1).$$

From equation (4) and from the continuities of the incident current and the current dipole density, we obtain the equality:

$$-2j\lim_{\varepsilon\to 0}\left(\mathbf{FP}\int_S \mathbf{n}\cdot\overline{\overline{\mathbf{G}}}(\mathbf{r}_2,\mathbf{r})\mathbf{p}(\mathbf{r})\,\mathrm{d}S_{\mathrm{r}} - \mathrm{FP}\int_S \mathbf{n}\cdot\overline{\overline{\mathbf{G}}}(\mathbf{r}_1,\mathbf{r})\mathbf{p}(\mathbf{r})\,\mathrm{d}S_{\mathrm{r}}\right) = (\gamma_2-\gamma_1)p_0 \tag{A3}$$

Because, we know that p is continuous, the possible difference between both limits in the integrals of equation (A3) are only due to the presence of hyperstrong singularities in the Green tensor $\overline{\overline{\mathbf{G}}}$, i.e. the electrostatic part $\overline{\overline{\mathbf{G}}}_0$ (Beltrame and Burais, 2002b). Thus, we can restrict the integrals of equation (A3) on the domain D with the $\overline{\overline{\mathbf{G}}}_0$ kernel. After their regularization, they take the form of Beltrame (2002) and Beltrame and Burais (2002a):

$$-2jFP\int_D \mathbf{n}\cdot\overline{\overline{\mathbf{G}}}_0(\mathbf{r}_i,\mathbf{r})\cdot\mathbf{p}\,\mathrm{d}S_{\mathrm{r}} = a_i p_i + b_i\cdot\nabla p_i + \int_D \frac{p_i^{(2)}(\mathbf{r})}{R_i}\,\mathrm{d}S_{\mathrm{r}} \tag{A4}$$

where

$$R_i = \|\mathbf{r}-\mathbf{r_i}\|,\quad p_i^{(2)}(\mathbf{r}) = \frac{p(\mathbf{r}) - p_i - \nabla p_i\cdot(\mathbf{r}-\mathbf{r}_i)}{R_i^2}$$

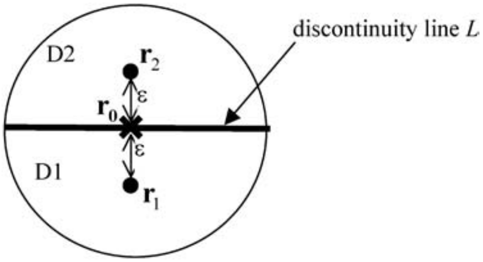

Figure A1. Scheme for the gradient jump

and the coefficients a_i and b_i depend on the geometry of the disc D and on the point $\mathbf{r}_i$. Then, these coefficients have the same limit when $\mathbf{r}_i \rightarrow \mathbf{r}_0$:

$$a_0 = -\int_0^{2\pi} \frac{1}{R_0(\theta)}\,\mathrm{d}\theta$$

$$b_0 = \int_0^{2\pi} \ln(R_0(\theta))\mathbf{u}_\mathbf{r}(\theta)\,\mathrm{d}\theta \tag{A5}$$

Furthermore, because D is a disc, $b_0 = 0$. Thus, the contribution of first terms in equation (A4) vanish in equation (A3):

$$\lim_{r\varepsilon\rightarrow 0}\left(\int_D \frac{p_2^{(2)}(\mathbf{r})}{R_2}\,\mathrm{d}S_\mathrm{r} - \int_D \frac{p_1^{(2)}(\mathbf{r})}{R_1}\,\mathrm{d}S_\mathrm{r}\right) = (\gamma_2 - \gamma_1)p_0 \tag{A6}$$

When the gradient of p is not continuous, the functions $p_i^{(2)}(\mathbf{r})$ diverges at $\mathbf{r}_0$ and the above integrals are not regular at this point. The inversion of the limit and the sign sum is not allowed. However, let us suppose that $p_i^{(2)}(\mathbf{r})$ admits a limit for $\mathbf{r} \in D_i$, i.e. p admits a second derivate in each region D_1 and D_2, then we can write:

$$\int_D \frac{p_2^{(2)}(\mathbf{r})}{R_2}\,\mathrm{d}S_\mathrm{r} = \int_{D_2} \frac{p_2^{(2)}(\mathbf{r})}{R_2}\,\mathrm{d}S_\mathrm{r} + \int_{D_1} \frac{p_2^{(2)}(\mathbf{r})}{R_2}\,\mathrm{d}S_\mathrm{r}$$

The integral on D_2 is weakly singular and we can take the limit $\mathbf{r}_2 \rightarrow \mathbf{r}_0$ without difficulty. Because the second member on equation (A6) is independent of D, we take the limit $D \rightarrow \{\mathbf{r}_0\}$. With this second limit, the first integral vanishes. For the second integral we write the Taylor series expansion of $p(\mathbf{r})$ near $\mathbf{r}_0$ in the domain D_1:

$$p_2^{(2)}(\mathbf{r}) = -\frac{[\nabla p_0]\cdot(\mathbf{r} - \mathbf{r}_0)}{R_2^2} + \frac{\nabla p_2 \cdot (\mathbf{r}_2 - \mathbf{r}_0)}{R_2^2} + O(1) \tag{A7}$$

Similarly, we show for $\mathbf{r} \in D_2$ that:

$$p_1^{(2)}(\mathbf{r}) = +\frac{[\nabla p_0]\cdot(\mathbf{r} - \mathbf{r}_O)}{R_1^2} + \frac{\nabla p_1 \cdot (\mathbf{r}_1 - \mathbf{r}_0)}{R_1^2} + O(1) \tag{A8}$$

Then, using the reflection symmetry between the regions 1 and 2, we deduce:

$$\int_D \frac{p_2^{(2)}(\mathbf{r})}{R_2}\,\mathrm{d}S_\mathrm{r} - \int_D \frac{p_1^{(2)}(\mathbf{r})}{R_1}\,\mathrm{d}S_\mathrm{r} = [\nabla p_0]\varepsilon \int_{D_1} \frac{1}{R_2^3}\,\mathrm{d}S_\mathrm{r} + \int_D O(1)\,\mathrm{d}S_\mathrm{r}$$

A classical calculus shows:

$$\lim_{\varepsilon\rightarrow 0}\left(\varepsilon \int_{D_2} \frac{1}{R_1^3}\,\mathrm{d}S_\mathrm{r}\right) = 2.$$

Finally, we deduce the jump of the gradient of p:

$$[\nabla p_0] = \frac{(\gamma_2 - \gamma_1)}{2} p_0 \tag{A9}$$

This relation shows that the gradient is discontinuous if and only if the conductance is discontinuous.

The Emerald Research Register for this journal is available at
www.emeraldinsight.com/researchregister

The current issue and full text archive of this journal is available at
www.emeraldinsight.com/0332-1649.htm

Efficient modelling techniques for complicated boundary conditions applied to structured grids

Herbert De Gersem, Markus Wilke, Markus Clemens and
Thomas Weiland
Institut für Theorie Elektromagnetischer Felder (TEMF),
Technische Universität Darmstadt, Darmstadt, Germany

Keywords *Boundary-elements methods, Modelling, Electrotechnology*

Abstract *Certain sophisticated boundary conditions offer powerful modelling features for many electrotechnical models. Their application, however, wipes out the particular structure of the system matrices which occurs when structured grids are applied. In this paper, this effect is prevented by considering the unconstrained system together with additional constraint equations or by projecting the algebraic system using an oblique or orthogonal projector. The numerical tests indicate that the efficiency of sparse iterative solvers can be preserved even in the presence of complicated boundary relations. The described projections are also advantageous for formulations derived for unstructured grids.*

1. Introduction

Structured grids have particular advantages over non-structured meshed. It has been shown that the discretisation error converges favourably in the case of structure grids (Monk and Süli, 1994). Models with structured discretisation result in banded system matrices for which highly optimised iterative solution techniques are developed (Saad, 1996). Recently, some typical disadvantages of structured grids have been alleviated. The geometrical error due to staircasing can be avoided by applying conformal discretisation techniques (Krietenstein *et al.*, 1998). The huge number of unknowns required to resolve local geometrical details by tensor grids can be reduced by local grid refinement (Podebrad *et al.*, 2003).

As an example of a structured-grid approach, a discretisation of an electrostatic formulation by the orthogonal finite integration technique (FIT) is considered here. The treatment of boundary conditions (BCs) as developed here, also carries over to other formulations and other discretisation techniques at structured grid as well as at unstructured meshes. The electrostatic partial differential equation

$$-\nabla\cdot(\varepsilon\nabla\phi) = \rho \tag{1}$$

with ε the permittivity, ϕ the electric scalar potential and ρ the charge density, is discretised using a staggered, dual-orthogonal grid pair, yielding

$$\underbrace{\tilde{\mathbf{S}}\mathbf{M}_{\varepsilon}\tilde{\mathbf{S}}^{T}}_{\mathbf{K}}\phi = \mathbf{q}, \tag{2}$$

COMPEL: The International Journal
for Computation and Mathematics in
Electrical and Electronic Engineering
Vol. 23 No. 4, 2004
pp. 904-912
© Emerald Group Publishing Limited
0332-1649
DOI 10.1108/03321640410553337

Herbert De Gersem is working in the cooperation project “DA-WE1 (TEMF/GSI)” with the “Gesellschaft für Schwerionenforschung (GSI)”, Darmstadt.

where $\tilde{\mathbf{S}}$ is the discrete divergence operator on the dual grid, $\mathbf{M}_\varepsilon$ is the diagonal permittivity material matrix, ϕ is the vector of nodal voltages and $\mathbf{q}$ is the vector of charges in the dual grid cells (Weiland, 1996). The sparsity pattern of equation (2) in the case of a cartesian 3D grid, is shown in Figure 1(a).

2. Boundary conditions

BCs for equations (1) and (2) are assigned to surfaces in the computational domain. The constrained surfaces are not necessarily located at the geometrical borders of the computational domain, as illustrated, e.g. by a capacitor model where voltages are applied at the electrodes inside the model. To the electrostatic example, commonly, Dirichlet BCs $\phi = \alpha(x, y, z)$ at Γ_d with $\alpha(x, y, z)$ a given potential distribution and homogeneous Neumann BCs

$$-\varepsilon \frac{\partial}{\partial n}\phi = 0 \quad \text{at}\, \Gamma_\mathrm{n}$$

with $\partial/\partial n$ the derivative normal to the boundary Γ_n are applied. BCs affect the primal unknowns (the voltage ϕ in equation (1)), the dual unknowns (the dielectric displacement $-\varepsilon(\partial/\partial n)\phi$ for equation (1)) or a combination of both. In this paper, only BCs applied to the primal unknowns are considered. BCs affecting the dual unknowns, e.g. non-homogeneous Neumann BCs or mixed BCs, however, can be treated similarly. No distinction is made between the BCs and interface conditions.

BCs may turn out to be powerful modelling features. Some examples of more sophisticated BCs are as follows.

(1) *Binary BCs*. When the geometry, the material distribution and the excitation of the electrotechnical device feature certain symmetries, only a part of the device has to be modelled. The potential at a slave boundary Γ_slv depends on the potential at a master boundary,

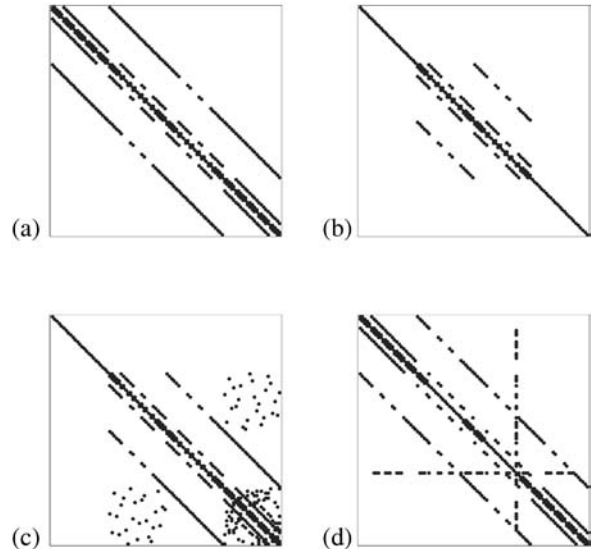

Figure 1.
Sparsity patterns of: (a) system (2) without constraints, (b) system (3) with Dirichlet BCs, (c) system (4) with binary BCs, and (d) system with floating-potential BCs

$$\phi_{\Gamma_{\mathrm{slv}}} = \gamma\phi_{\Gamma_{\mathrm{mst}}},$$

where the conversion factor γ is 1 for periodical BCs, -1 for anti-periodic BCs or $e^{j\psi}$ when a phase shift ψ is applied in the case of a time-harmonic model.

(2) *Floating-potential BCs*. A metallic surface in an electrostatic model can be modelled by a floating-potential BC $\phi = \beta$ at Γ_{fl} where β is an unknown constant.

(3) *External circuits*. For models, where some parts have to be discretised in order to resolve complicated geometries and local field effects whereas other parts can be represented by lumped parameters, a field-circuit coupled formulation is very effective. The coupling to the external circuit can be treated as a BC to the field model.

In practice, the configuration of a model may change in time. As a consequence, the type of BC may change during the time-stepping process. When, for example, a capacitor plate is disconnected from a voltage source, the Dirichlet BC changes into a floating-potential BC. The application of more complicated BCs and the treatment of BCs which change in time may be cumbersome and may result in a substantial increase of the computation time, especially in the case of structured-grid approaches. In this paper, techniques are offered for a convenient incorporation of such BCs.

3. Standard application of BCs

Commonly, the BCs are directly inserted in the system. Homogeneous Neumann BCs are natural BCs and do not require a special treatment. When the subscripts "f" and "d" distinguish between degrees of freedom and nodal voltages at which a Dirichlet BC $\phi_{\mathrm{d}} = \mathrm{g}_{\mathrm{d}}$ is applied, then system (2) with Dirichlet BCs reads:

$$\begin{bmatrix} \mathbf{K}_{\mathrm{ff}} & 0 \\ 0 & \mathbf{I} \end{bmatrix} \begin{bmatrix} \phi_{\mathrm{f}} \\ \phi_{\mathrm{d}} \end{bmatrix} = \begin{bmatrix} \mathbf{q}_{\mathrm{f}} - \mathbf{K}_{\mathrm{fd}}\mathbf{g}_{\mathrm{d}} \\ \mathbf{g}_{\mathrm{d}} \end{bmatrix}. \tag{3}$$

The block partitioning indicated in equation (3) is commonly not observed since, in practice, no reordering of the equations is carried out. The second diagonal block in equation (3) can be omitted, which is not done in practice in order to preserve the structure of the system matrix. When Dirichlet BCs are inserted by zeroing the appropriate rows and columns, the original structure of the system matrix is preserved (Figure 1(b)). This is no longer true when a binary BC $\phi_{\mathrm{b}} = \gamma\phi_{\mathrm{a}}$ is inserted:

$$\begin{bmatrix} \mathbf{K}_{\mathrm{ff}} & \mathbf{K}_{\mathrm{fa}} + \gamma\mathbf{K}_{\mathrm{fb}} \\ \mathbf{K}_{\mathrm{fa}} + \gamma\mathbf{K}_{\mathrm{fb}} & \mathbf{K}_{\mathrm{aa}} + \gamma^2\mathbf{K}_{\mathrm{bb}} \end{bmatrix} \begin{bmatrix} \phi_{\mathrm{f}} \\ \phi_{\mathrm{a}} \end{bmatrix} = \begin{bmatrix} \mathbf{q}_{\mathrm{f}} \\ \mathbf{q}_{\mathrm{a}} + \gamma\mathbf{q}_{\mathrm{b}} \end{bmatrix}. \tag{4}$$

Even without reordering and without omitting ϕ_{b}, the system (4) does not longer reflect the banded structure of the original structured-grid discretisation (Figure 1(c)). Hence, some of the beneficial numerical properties of structured grid models are lost. A more general, but also more expensive sparse matrix storage scheme (e.g. compressed row storage) has to be used. The canonical way of indexing, which is typical for structured grids, cannot be exploited further in fast matrix-vector products or parallellisation. For binary BCs, the banded matrix structure is lost whereas the bandwidth of the system still remains constant. The incorporation of a floating-potential BC, however, results in a single, but dense equation per floating potential (Figure 1(d)). Also when unstructured grids are applied, e.g. in combination with the finite element method, such a fill-in is undesirable since it diminishes the efficiency of the matrix-vector product. The loss of the system's sparsity, is even more pronounced when more sophisticated BCs such as, e.g. harmonic BCs (De Gersem *et al.*, 2002) and BCs at surfaces or lines which are not aligned with the grid are applied. The incorporation of the BCs in the system matrix requires every degree of freedom to be checked whether it is constrained or not during the matrix assembly. Moreover, the system matrix has to be recomputed when a change occurs in the model concerning the BCs. In the following, a general notation covering all mentioned BCs is set-up and three alternative approaches are proposed, each of them keeping the sparse and structured system matrix intact.

4. General primal boundary conditions

It is assumed that in the case of several BCs, each BC is applied to a disjunct slave boundary $\Gamma_{\mathrm{slv}}^{(p)}, \quad p = 1, \ldots, n_{\mathrm{bc}}$, of the domain. For each BC, a (possibly empty) master boundary $\Gamma_{\mathrm{mst}}^{(p)}$ and Dirichlet boundary values $g^{(p)}(x, y, z)$ are defined. It is further assumed that $\Gamma_{\mathrm{mst}}^{(p)} \cap \Gamma_{\mathrm{slv}}^{(p)} = \emptyset$, for all p. A general, discrete formulation of the BCs reads:

$$\mathbf{Bu} = \mathbf{C}_{\mathrm{slv}}\mathbf{Q}_{\mathrm{slv}} - \mathbf{D}_{\mathrm{mst}}\mathbf{Q}_{\mathrm{mst}} = \mathbf{g}_{\mathrm{cns}}. \tag{5}$$

The superscripts (p) are omitted in equation (5) and in all the following formulae when only one BC is considered. The matrix $\mathbf{C}_{\mathrm{slv}}$ is assumed to be square and invertible, $\mathbf{D}_{\mathrm{mst}}$ is a rectangular matrix, $\mathbf{Q}_{\mathrm{slv}}$ and $\mathbf{Q}_{\mathrm{mst}}$ are two selectors, i.e. sparse matrices consisting of entries 1, -1 and 0, and $\mathbf{g}_{\mathrm{cns}}$ is a vector containing the Dirichlet data. From the assumptions, it follows that

$$\begin{cases} \mathbf{Q}_{\mathrm{mst}}^{(p)}\mathbf{Q}_{\mathrm{slv}}^{(p)\mathbf{H}} = 0 \\ \mathbf{Q}_{\mathrm{slv}}^{(p)}\mathbf{Q}_{\mathrm{slv}}^{(q)\mathbf{H}} = 0 \end{cases} \quad \text{for all } p, q. \tag{6}$$

The BCs are discretised such that each degree of freedom at $\Gamma_{\mathrm{slv}}^{(p)}$ is selected only once and as a consequence, $\mathbf{Q}_{\mathrm{slv}}^{(p)}\mathbf{Q}_{\mathrm{slv}}^{(p)H} = \mathbf{I}$. Together with the assumption that $\mathbf{C}_{\mathrm{slv}}^{(p)}$ is invertible, this selection procedure leads to a rectangular matrix $\mathbf{B}$ which has maximal rank. The BCs described earlier can be formulated as in equation (5) (Table I).

Boundary condition	$\mathbf{C}_{\mathrm{slv}}$	$\mathbf{D}_{\mathrm{mst}}$	$\mathbf{g}_{\mathrm{cns}}$	$(\mathbf{BB}^H)^{-1}$
Dirichlet	$\mathbf{I}$	$\mathbf{0}$	$\mathbf{g}_{\mathrm{d}}$	I
Binary	$\mathbf{I}$	$\gamma\mathbf{I}$	$\mathbf{0}$	$\frac{\mathbf{1}}{\mathbf{1}+\gamma^2}\mathbf{I}$
Floating potential	$\mathbf{I}$	$\mathbf{E}_{n,1}$	$\mathbf{0}$	$\mathrm{I} - \frac{1}{n+1}\mathbf{E}$

Note: $\mathbf{I}_{ij} = \delta_{ij}$, $\mathbf{O}_{ij} = 0$, $\mathbf{E}_{ij} = 1$ and n is the number of constrained degrees of freedom

Table I. Matrices representing BCs are applied to the primal variables

5. Saddle-point formulation

The conditions (5) are added to the system with a vector of Lagrange multipliers *w*:

$$\begin{bmatrix} \mathbf{K} & \mathbf{B}^H \\ \mathbf{B} & \mathbf{0} \end{bmatrix} \begin{bmatrix} \mathbf{u} \\ \mathbf{w} \end{bmatrix} = \begin{bmatrix} \mathbf{f} \\ \mathbf{g}_{\mathrm{cns}} \end{bmatrix}. \tag{7}$$

This saddle-point formulation is indefinite even when the original system is definite. The augmented system has a unique solution because B has maximal rank (Saad, 1996). The system (7) can be solved by the minimal residual or the quasi-minimal residual method for symmetric indefinite systems with a diagonal block preconditioner:

$$\begin{bmatrix} \tilde{\mathbf{K}} & 0 \\ 0 & \tilde{\mathbf{S}} \end{bmatrix} \tag{8}$$

where $\tilde{\mathbf{K}}$ is a preconditioner for $\mathbf{K}$ and $\tilde{\mathbf{S}}$ is an approximation to the Schur complement system $\mathbf{S} = \mathbf{B}\mathbf{K}^{-1}\mathbf{B}^H$ (Fischer *et al.*, 1998; Saad, 1996). For $\tilde{\mathbf{K}}$, any available preconditioner for the unconstrained system matrix can be applied. The saddle-point formulation enables, e.g. the selection of a standard (algebraic) multigrid preconditioner for $\tilde{\mathbf{K}}$. The explicit computation of $\mathbf{S}$ is not possible in practice. The construction of an effective preconditioner for $\mathbf{S}$ is cumbersome and, in general, requires a spectral analysis of the type of BC in combination with the field problem. Here, an algebraic preconditioner $\tilde{\mathbf{S}} = \mathbf{B}\mathbf{M}^{-1}\mathbf{B}^H$, with $\mathbf{M}^{-1}$ a sparse approximation to $\mathbf{K}^{-1}$ is used. Typical choices for $\mathbf{M}$ are the diagonal part of $\mathbf{K}$ or the preconditioner $\tilde{\mathbf{K}}$.

6. Projected systems

The space $\mathscr{B}$ is defined as the space of vectors which obey the homogeneous BC, i.e. $\mathscr{B} = \{\mathbf{u} : \mathbf{B}\mathbf{u} = 0\}$. A vector $\mathbf{u}$ can be mapped onto $\mathscr{B}$ by the operator:

$$\mathbf{P}_{\mathscr{B}} = \mathbf{I} + \mathbf{Q}_{\mathrm{slv}}^H \mathbf{C}_{\mathrm{slv}}^{-1} \mathbf{D}_{\mathrm{mst}} \mathbf{Q}_{\mathrm{mst}} - \mathbf{Q}_{\mathrm{slv}}^H \mathbf{Q}_{\mathrm{slv}} \tag{9}$$

since all $\mathbf{u}$ satisfy $\mathbf{B}\mathbf{P}_{\mathscr{B}}\mathbf{u} = 0$. The operator $\mathbf{P}_{\mathscr{B}}$ is an *oblique projector* since $\mathbf{P}_{\mathscr{B}}\mathbf{P}_{\mathscr{B}} = \mathbf{P}_{\mathscr{B}}$ whereas $\mathbf{P}_{\mathscr{B}}^H \neq \mathrm{P}_{\mathscr{B}}$. The solution of the system with constraints (7) is decomposed into $\mathbf{u} = \mathbf{u}_{\mathrm{cns}} + \mathbf{u}_{\mathscr{B}}$ where $\mathbf{u}_{\mathrm{cns}}$ obeys the true BC $\mathbf{B}\mathbf{u}_{\mathrm{cns}} = \mathbf{g}_{\mathrm{cns}}$ and $\mathbf{u}_{\mathscr{B}} \in \mathscr{B}$. The first part $\mathbf{u}_{\mathrm{cns}}$ is chosen as

$$\mathbf{u}_{\mathrm{cns}} = \mathbf{Q}_{\mathrm{slv}}^H \mathbf{C}_{\mathrm{slv}}^{-1} \mathbf{g}_{\mathrm{cns}}, \tag{10}$$

whereas the remaining part $\mathbf{u}_{\mathscr{B}}$ is found from solving the projected system:

$$\mathbf{P}_{\mathscr{B}}^H \mathbf{K} \mathbf{P}_{\mathscr{B}} \mathbf{u}_{\mathscr{B}} = \mathbf{P}_{\mathscr{B}}^H (\mathrm{f} - \mathbf{K}\mathbf{u}_{\mathrm{cns}}). \tag{11}$$

It is easily shown that $\mathbf{u}_{\mathrm{cns}} + \mathbf{u}_{\mathscr{B}}$ solves the augmented system (7). The system (11) is singular but nevertheless consistent since the righthandside is in the range of the system matrix. For such systems, the preconditioned conjugate gradient algorithm is known to converge (Kaasschieter, 1988). When explicitly constructed, the singularity is removed when an identity matrix is inserted for the zero diagonal block, yielding the system $\mathbf{P}_{\mathscr{B}}^H \mathbf{K} \mathbf{P}_{\mathscr{B}} + \mathbf{Q}_{\mathrm{slv}}^H \mathbf{Q}_{\mathrm{slv}}$ which equals the system which is obtained when applying the BCs in the standard way.

Owing to the properties (equation (6)), two projectors are commutative ($\mathbf{P}_{\mathscr{B}}^{(p)}\mathbf{P}_{\mathscr{B}}^{(q)} = \mathbf{P}_{\mathscr{B}}^{(q)}\mathbf{P}_{\mathscr{B}}^{(p)}$, $\forall p, q$) and several BCs can be combined into a single projector

$$\mathbf{P}_{\mathscr{B}} = \cup_{p=1}^{n_{\mathrm{bc}}}\mathbf{P}_{\mathscr{B}}^{(p)}.$$

The definition of a projector mapping vectors onto $\mathscr{B}$ is not unique. It is possible to derive an orthogonal projector

$$\mathbf{P}_{\perp} = \mathbf{I} - \mathbf{B}^{H}(\mathbf{B}\mathbf{B}^{H})^{-1}\mathbf{B} \tag{12}$$

and solve the projected system

$$\mathbf{P}_{\perp}^{H}\mathbf{K}\mathbf{P}_{\perp}\mathbf{u}_{\perp} = \mathbf{P}_{\perp}^{H}(\mathbf{f} - \mathbf{K}\mathbf{u}_{\mathrm{cns}}) \tag{13}$$

instead of equation (11). The solution $\mathbf{u} = \mathbf{u}_{\mathrm{cns}} + \mathbf{u}_{\perp}$ equals the solution $\mathbf{u} = \mathbf{u}_{\mathrm{cns}} + \mathbf{u}_{\mathscr{B}}$ and therefore also solves the augmented system (7). Since $\mathbf{C}_{\mathrm{slv}}$ is invertible, the system

$$\mathbf{B}\mathbf{B}^{H} = \mathbf{C}_{\mathrm{slv}}\mathbf{C}_{\mathrm{slv}}^{H} + \mathbf{D}_{\mathrm{mst}}\mathbf{D}_{\mathrm{mst}}^{H} \tag{14}$$

is positive definite. Hence, the solution by equation (14) which is required at each application of $\mathbf{P}_{\perp}$, can be obtained by using a Cholesky factorisation of equation (14) or by applying a preconditioned conjugate gradient algorithm. For particular BCs, an analytical inverse of equation (14) is available (Table I).

Both projection approaches preserve the symmetry and semi-definiteness of the original system. The factorisations $\mathbf{P}_{\mathscr{B}}^{H}\mathbf{K}\mathbf{P}_{\mathscr{B}}$ or $\mathbf{P}_{\perp}^{H}\mathbf{K}\mathbf{P}_{\perp}$ are not calculated explicitly since this would lead to unacceptable dense matrices (Figure 2). For particular BCs, e.g. BCs incorporating fast Fourier transforms, even $\mathbf{P}_{\mathscr{B}}$ and $\mathbf{P}_{\perp}$ are commonly not represented by matrices (De Gersem *et al.*, 2002). Such treatment is only possible when used within a projected conjugate gradient algorithm as shown in Algorithm 1. The standard conjugate gradient algorithm only has to be changed at two places: $\mathbf{P}^{H}$ has to accompany the matrix-vector product whereas $\mathbf{P}$ has to be applied after

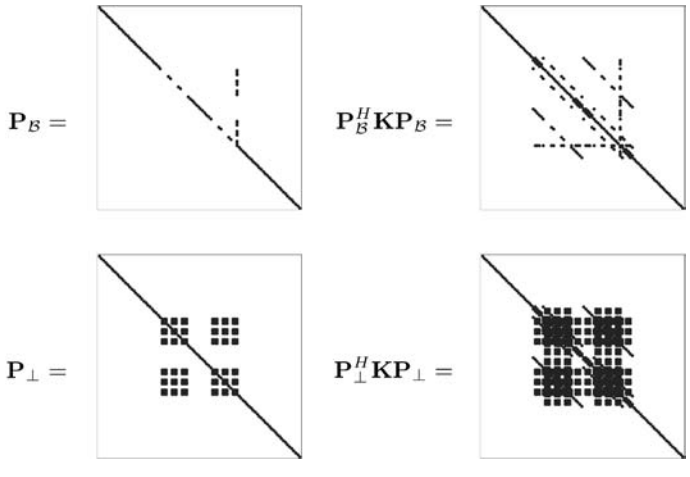
$\mathbf{P}_{\mathcal{B}} =$
$\mathbf{P}_{\mathcal{B}}^{H}\mathbf{K}\mathbf{P}_{\mathcal{B}} =$
$\mathbf{P}_{\perp} =$
$\mathbf{P}_{\perp}^{H}\mathbf{K}\mathbf{P}_{\perp} =$

Figure 2. Sparsity patterns of the oblique and orthogonal projectors and the corresponding projected systems

preconditioning. The unconstrained system matrix **K**, the corresponding preconditioner $\tilde{\mathbf{K}}$ and the selected projectors $\mathbf{P}_{\mathcal{B}}$ and $\mathbf{P}_{\mathcal{B}}^{H}$ or $\mathbf{P}_{\perp}$ and $\mathbf{P}_{\perp}^{H}$ are applied in each iteration step of the modified conjugate gradient algorithm. Both projectors are computationally inexpensive compared to **K** since they only adapt unknowns allocated at the constrained boundaries. Since, in the case of a linear model, the original system matrix **K** is left unchanged, the set-up phase of the preconditioner only has to be carried out once, even when the BCs change during the simulation.

7. Comparison and application

A capacitor model is used to test the numerical performance of the proposed techniques. A metallic brick, inserted in the dielectricum between the two electrodes, is modelled by a floating-potential BC. As a preconditioner for **K**, a standard algebraic Multigrid algorithm is used (Ruge and Stüben 1987). The convergence of the conjugate gradient algorithm applied to a positive semi-definite symmetric system is characterized by its spectral condition number, $k = \lambda_{\max}\lambda_{\min}$ with $\lambda_{\max}$ the largest and $\lambda_{\min}$ the smallest non-zero eigenvalue of the system matrix. In Table II, the spectral condition numbers of the system with oblique projection equation (11) and the system with orthogonal projection (equation (13)) are compared. The system with oblique projection has a single, large and isolated eigenvalue which is related to the floating-potential BC. It is observed that the condition number of orthogonally projected system is comparable to the virtual condition number obtained by discarding this eigenvalue for the system with oblique projection (Table II). The isolated

Algorithm 1. Modified conjugate gradient method for solving equations (11) and (13) with preconditioner $\tilde{\mathbf{K}}$ and projector **P**.

```
$\mathbf{r}_0 = \mathbf{P}^H(\mathbf{f} - \mathbf{K}\mathbf{u}_{\mathrm{cns}})$;   $\rho_{-1} = 1$;   $\mathbf{p}_0 = 0$;
For $k = 1, 2, \ldots$
    $z_{k-1} = \mathbf{P}\tilde{\mathbf{K}}^{-1}\mathbf{r}_{k-1}$
    $\rho_{k-1} = \mathbf{r}_{k-1}^{H}\mathbf{z}_{k-1}$
    $\beta_{k-1} = \rho_{k-1}/\rho_{k-2}$
    $\mathbf{p}_k = \mathbf{z}_{k-1} + \beta_{k-1}\mathbf{p}_{k-1}$
    $\mathbf{q}_k = \mathbf{P}^H\mathbf{K}\mathbf{p}_k$
    $\alpha_k = \frac{\rho_{k-1}}{\mathrm{p}_k^H \mathrm{q}_k}$
    $\mathbf{x}_k = \mathbf{x}_{k-1} + \alpha_k\mathbf{p}_k$
    $\mathbf{r}_k = \mathbf{r}_{k-1} - \alpha_k\mathbf{q}_k$
    stop if convergence
end
$\mathbf{u} = \mathbf{u} + \mathbf{u}_{\mathrm{cns}}$
```

Table II. Condition numbers of the systems projected by the oblique projector and orthogonal projectors

# nodes	$\mathbf{P}_{\mathcal{B}}^{H}\mathbf{K}\mathbf{P}_{\mathcal{B}}$	$\mathbf{P}_{\mathcal{B}}^{H}\mathbf{K}\mathbf{P}_{\mathcal{B}}$(a)	$\mathbf{P}_{\perp}^{H}\mathbf{K}\mathbf{P}_{\perp}$
100	52.7	11.8	28.4
384	225	37.9	40.4
968	587	63.3	75.8
3,610	4054	228	241

Note: [a] when the isolated eigenvalue related to the floating-potential BC is omitted eigenvalue is directly approximated by a eigenvalue of the Krylov approximation space underlying the conjugate gradient algorithm. The convergence of the conjugate gradient with oblique projection is adversely affected by this eigenmode as is observed in Table III. The augmented system exhibits a worse convergence behaviour compared to the projected systems which can partially be explained by the inefficient Schur complement preconditioner. In Table III, the computation times are given in both case when $\mathbf{P}_{\mathscr{B}}^{H}\mathbf{K}\mathbf{P}_{\mathscr{B}}$ and $\mathbf{P}_{\perp}^{H}\mathbf{K}\mathbf{P}_{\perp}$ are explicitly built, or in the case when they are used in factorised form together with the modified conjugate gradient algorithm (Algorithm 1). For this example, with a floating-potential BC, both computation times are comparable in case of oblique projection. For the larger problems, the explicit construction of $\mathbf{P}_{\perp}^{H}\mathbf{K}\mathbf{P}_{\perp}$ is not an option due to the excessive memory requirements. The standard treatment of BCs corresponds to the system with explicit oblique projection. From Table III, it can be concluded that for the numerical test model, the modified conjugate gradient algorithm solving the factorised system with orthogonal projection outperforms the standard approach significantly (897 s instead of 1,124 s). For BCs incorporating dense operators such as field-circuit coupling and harmonic BCs, the proposed approaches are particularly efficient.As a technical example, a surge arrester is simulated (Clemens *et al.*, 2003) (Figure 3). The Dirichlet BCs corresponding to the

# nodes	968	3,610	14,112	38,988
Saddle-point iterations	14	24	51	87
Time [s]	2.64	7.23	201	1653
Oblique iterations	8	14	35	62
Without time [s]	1.23	4.54	128	1143
With time [s]	1.26	4.34	132	1124
Orthogonal iterations	5	9	31	55
Without time [s]	0.86	2.74	92	897
With time [s]	8.78	36.43	[−]	[−]

Table III.
Iteration numbers and computation times for the solution of the saddle-point formulation and both projected formulation with or without the use of the explicitly constructed system matrix

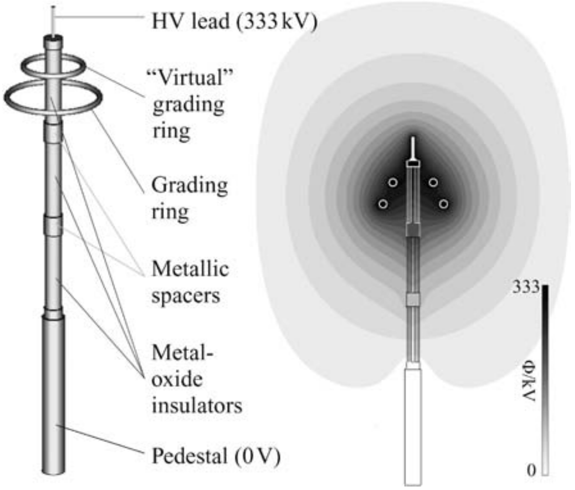

Figure 3.
Geometry and potential distribution of a surge arrester

applied voltages are inserted in the system whereas the floating potentials modelling the metallic spacers are considered by projecting the electrostatic system of equations.

8. Conclusions

The formulations described above prevent the introduction of non-trivial BCs in structured system matrices. Structured sparse matrix storage formats, optimal matrix-vector products and efficient preconditioning techniques originally developed for models with standard BCs can be maintained. It is shown that the application of an orthogonal projection onto the solution space satisfying the BCs, leads to the convergence of the conjugate gradient algorithm which is faster than when the BCs are considered by oblique projection or incorporated in the system matrix. The treatment of BCs, presented here, is especially efficient for sophisticated BCs incorporating dense operators and configurations when the BCs change during simulation.

References

Clemens, M., De Gersem, H., Koch, W., Wilke, M. and Weiland, T. (2003), "TEQSAS – transient electro-quasi-statics adaptive simulation – schemes", *Proc. COMPUMAG*, Vol. 1, Saratoga Springs, New York, NY, pp. 198-9.

De Gersem, H., Clemens, M. and Weiland, T. (2002), "Coupled finite-element, spectral-element discretisation for models with circular inclusions and far-field domains", *IEE Proc.-Sci. Meas. Technol.*, Vol. 149 No. 5, pp. 237-41.

Fischer, B., Ramage, A., Silvester, D. and Wathen, A. (1998), "Minimum residual methods for augmented systems", *BIT*, Vol. 38 No. 3, pp. 527-43.

Kaasschieter, E. (1988), "Preconditioned conjugate gradients for solving singular systems", *Journal of Computational and Applied Mathematics*, Vol. 24, pp. 265-75.

Krietenstein, B., Schuhmann, R., Thoma, P. and Weiland, T. (1998), "The perfect boundary approximation technique facing the big challenge of high precision field computation", *Proc. of the XIX Int. Linear Accelerator Conf., Chicago, USA*, pp. 860-2.

Monk, P. and Süli, E. (1994), "A convergence analysis of Yee's scheme on non-uniform grids", *SIAM J. Numer. Anal.*, Vol. 31, pp. 393-412.

Podebrad, O., Clemens, M. and Weiland, T. (2003), "New flexible subgridding scheme for the finite integration technique", *IEEE Trans. Magn.*, Vol. 39 No. 3, pp. 1662-5.

Ruge, J. and Stüben, K. (1987), "Algebraic multigrid", in McCormick, S. (Ed.), "Multigrid methods", *Frontiers in Applied Mathematics*, Vol. 3, SIAM, Philadelphia, PA, pp. 73-130.

Saad, Y. (1996), *Iterative Methods for Sparse Linear Systems*, PWS Publishing Company, Boston, MA.

Weiland, T. (1996), "Time domain electromagnetic field computation with finite difference methods", *International Journal of Numerical Modelling*, Vol. 9 No. 4, pp. 295-319.

The Emerald Research Register for this journal is available at
www.emeraldinsight.com/researchregister

The current issue and full text archive of this journal is available at
www.emeraldinsight.com/0332-1649.htm

Non-nested geometric multigrid method using consistency error correction for discrete magnetic curl-curl formulations

M. Clemens, S. Feigh, M. Wilke and T. Weiland
Institut für Theorie Elektromagnetischer Felder (TEMF), Technische Universität Darmstadt, Darmstadt, Germany

Keywords *Magnetic fields, Simulation, Numerical analysis*

Abstract *The simulation of magnetic fields with geometric discretization schemes using magnetic vector potentials involves the solution of very large discrete consistently singular curl-curl systems of equations. Geometric and algebraic multigrid schemes for their solution require intergrid transfer operators of restriction and prolongation that achieve the discrete conservation of integral quantities serving as state-variables of geometric discretization methods. For non-conservative restriction operations, a consistency error correction operator related to an algebraic filtering is proposed. Numerical results show the effects of the consistency correction for a non-nested geometric multigrid method.*

1. Introduction

Magnetic fields simulations using a modified magnetic vector potential $\mathbf{A}^*$-formulation

$$\nabla \times (\nu \nabla \times \mathbf{A}^*) = \mathbf{J}_s(t), \tag{1}$$

where the magnetic flux density is available by $\mathbf{B} = \nabla \times \mathbf{A}^*$ and the total current density $\mathbf{J} = \mathbf{J}_s + \mathbf{J}_{ec}$ contains the source current density $\mathbf{J}_s$ and the eddy current density

$$\mathbf{J}_{ec}(t) = \kappa \frac{\partial}{\partial t} \mathbf{A}^*(t)$$

if eddy current effects in conductive materials ($\kappa \neq 0$) are considered. For 3D magnetic field problems (1) geometric discretization schemes will result in large, sparse, positive semi-definite systems of equations. For their solution, geometric and algebraic multigrid schemes have been presented, e.g. in Cingoski *et al.* (2000), Hiptmair (1999), Reitzinger and Schöberl (2002), and Weiß and Bíro (2002) and were shown to yield faster methods than the established ICCG schemes. In a recent publication (Feigh *et al.*, 2003) a geometric multigrid approach has been introduced, in which the construction of intergrid transfer operators for restriction and prolongation takes into account the strict separation of metric and non-metric grid information which is the characteristic for conservative geometric discretization schemes. As will be shown, for the

COMPEL: The International Journal for Computation and Mathematics in Electrical and Electronic Engineering
Vol. 23 No. 4, 2004
pp. 913-922
© Emerald Group Publishing Limited
0332-1649
DOI 10.1108/03321640410553346

Work of S. Feigh is funded by the graduate student program "Physik und Technik von Teilchenbeschleunigern" of the Deutsche Forschungsgemeinschaft (DFG) GK GRK 410/1.

non-gauged, consistently singular discrete magnetic curl-curl formulations based on equation (1) the choice of suitable intergrid transfer operators is not unique and for non-conservative restriction operators a consistency correction based on the gauging techniques can be introduced.

2. Discrete magnetic formulations

Consistent geometric discretization schemes for Maxwell's equations are available with, e.g., the finite integration technique (FIT) pioneered by Weiland (1977), the lowest order Whitney-finite-element method (WFEM) by Nédélec (1980) in its interpretation of Bossavit and Kettunen (1999) and the more recently developed Cell Method (CM) by Tonti (2001). The matrix formulations, derived from the mapping of Maxwell's equations in their integral form onto a dual grid pair $\{G, \tilde{G}\}$, are dubbed Maxwell-grid-equations (MGE) following their first formulation in the FIT. In their context, the discretization of equation (1) with the WFEM in Kameari (1990), FIT in Clemens and Weiland (1999) and CM in Repetto and Trevisan (2003) yields linear algebraic systems of equations:

$$\tilde{\mathbf{C}}\mathbf{M}_\nu\mathbf{C}\hat{\mathbf{a}} = \hat{\hat{\mathbf{j}}}, \tag{2}$$

where

$$\hat{\mathbf{a}} = \left\{ \int_{L_i} \mathbf{A}^* \cdot \mathrm{d}\mathbf{s} \right\}_{i:L_i \in G}$$

is the vector of modified magnetic vector potentials integrated along the edges $L_i \in G$ and $\mathbf{A} = \tilde{\mathbf{C}}\mathbf{M}_\nu\mathbf{C}$ denotes the positive semi-definite curl-curl stiffness matrix. Without further gauge conditions for $\hat{\mathbf{a}}$ the magneto-quasistatic continuity equation

$$\tilde{\mathbf{S}}\hat{\hat{\mathbf{j}}} = \tilde{\mathbf{S}}\hat{\hat{\mathbf{j}}}_s + \tilde{\mathbf{S}}\hat{\hat{\mathbf{j}}}_{\mathrm{ec}} = 0$$

has to hold. In this case, the algebraic system equation (2) is consistently singular, i.e. the right-hand side vector lies in the range space of the system matrix, $\hat{\hat{\mathbf{j}}} \in \mathrm{Range}\{\mathbf{A}\}$.

The matrix operators $\mathbf{C}$ and $\tilde{\mathbf{C}}$ correspond to the curl-operators on the primary and on the dual grid and contain only grid topology information, i.e. they have entries in $\{-1, 0, +1\}$. The same holds for the discrete divergence-operators $\mathbf{S}$ and $\tilde{\mathbf{S}}$ and the discrete gradient-operators $\mathbf{G}$ and $\tilde{\mathbf{G}}$ (Tonti, 2001; Weiland, 1977). These matrix operators mimic the properties of the vector analytical identities:

$$\begin{aligned} \mathbf{CG} = 0, \quad \tilde{\mathbf{C}}\tilde{\mathbf{G}} = 0 \leftrightarrow \mathrm{curl}\,\mathrm{grad} \equiv 0 \\ \mathbf{SC} = 0, \quad \tilde{\mathbf{S}}\tilde{\mathbf{C}} = 0 \leftrightarrow \mathrm{div}\,\mathrm{curl} \equiv 0 \end{aligned} \tag{3}$$

which are essential for the conservation of energy and cell charges with the MGE. The assumed duality of the grid doublet $\{G, \tilde{G}\}$, where each edge of the primary grid is connected in a one-to-one relation to a dual cell facet and vice versa, results in the identities:

$$\tilde{\mathbf{G}} = -\mathbf{S}^{\mathrm{T}}, \quad \mathbf{C} = \tilde{\mathbf{C}}^{\mathrm{T}}, \quad \mathbf{G} = -\tilde{\mathbf{S}}^{\mathrm{T}}. \tag{4}$$

In the lowest order WFEM a dual grid $\tilde{G}$ only appears implicitly as barycentric grid and the dual grid operators just appear as the transposed matrices of the primal grid incidence operators following the equation (4) (Bossavit and Kettunen, 1999).

The approximation in this formulation of a discrete electromagnetism and the main difference between the FIT, the CM and the lowest order WFEM lies in the construction principles of the discrete constitutive material relations where the grid voltages on the edges of G are coupled with the flux degrees of freedom located on the facets of the dual grid $\tilde{G}$ and vice versa, i.e.,

$$\widehat{\mathbf{h}} = \mathbf{M}_{\nu}\widehat{\widehat{\mathbf{b}}}, \quad \widehat{\widehat{\mathbf{j}}} = \mathbf{M}_{\kappa}\widehat{\mathbf{e}}, \tag{5}$$

where $\mathbf{M}_{\nu}$ and $\mathbf{M}_{\kappa}$ are the material matrices for the magnetic reluctivities and conductivities, respectively.

2.1 Gauging

A regularization, i.e., a gauging of the formulation (2) is possible by adding a discrete grad-div term to $\mathbf{A}$ to yield the matrix:

$$\mathbf{A} = [\tilde{\mathbf{C}}\mathbf{M}_{\nu}\mathbf{C} - \mathbf{M}_{\hat{\kappa}}\mathbf{G}\mathbf{M}_{\mathrm{N}}\tilde{\mathbf{S}}\mathbf{M}_{\hat{\kappa}}] \tag{6}$$

where $\mathbf{M}_{\mathrm{N}}$ is a norm matrix and the artificial conductivity matrix, $\mathbf{M}_{\hat{\kappa}}$ of the regularizing term is constructed assuming a small non-physical conductivity κ_{air} in the non-conductive regions (Clemens and Weiland, 2002b). The enforced relation $\mathbf{S}\mathbf{M}_{\hat{\kappa}}\widehat{\mathbf{a}} = 0$ then corresponds to the coulomb gauge $(\kappa_{\mathrm{air}}(\nabla \cdot \mathbf{A}) = 0)$. For magnetodynamic formulations, the matrix $\mathbf{M}_{\hat{\kappa}}$ can also be adapted to take into account the original material matrix $\mathbf{M}_{\kappa}$ in the matrices

$$\mathbf{A} = \alpha\mathbf{M}_{\kappa} + \tilde{\mathbf{C}}\mathbf{M}_{\nu}\mathbf{C},$$

where the scalar $\alpha \neq 0$ depends on the chosen formulation (Clemens and Weiland, 1999). The gauge constraint $\tilde{\mathbf{S}}\mathbf{M}_{\hat{\kappa}}\widehat{\mathbf{a}} = 0$ can also be introduced with the operator

$$\mathbf{P}_{\mathrm{Div}} = \mathbf{I} - \mathbf{G}\mathbf{N}^{-1}\tilde{\mathbf{S}}\mathbf{M}_{\hat{\kappa}}, \tag{7}$$

for which $\mathbf{P}_{\mathrm{Div}}\mathbf{A} = \mathbf{A}\mathbf{P}_{\mathrm{Div}}^{\mathrm{T}}$ holds and which is a projector with $\mathbf{P}_{\mathrm{Div}}^{2} = \mathbf{P}_{\mathrm{Div}}$, if $\mathbf{N} = \tilde{\mathbf{S}}\mathbf{M}_{\hat{\kappa}}\mathbf{G}$. The projected system $\mathbf{P}_{\mathrm{Div}}^{\mathrm{T}}\mathbf{A}\mathbf{P}_{\mathrm{Div}}\widehat{\mathbf{a}} = \mathbf{P}_{\mathrm{Div}}^{\mathrm{T}}\widehat{\widehat{\mathbf{j}}}$ is regular.

3. Multigrid schemes

A multigrid scheme for the solution of the non-gauged linear schemes arising from equation (2) generally consists of the following building blocks: starting point is a set of suitably nested or non-nested grids

$$G_{h_i}, i = 0, \ldots, L_c,$$

where each grid resolution level L_{h_i} is coarser than the level $L_{h_{i-1}}$ with a stationary iteration scheme (smoother) on each grid level L_{h_i} that efficiently eliminates high frequency error components of the error vector (Trottenberg *et al.*, 2000).

For the intergrid transfer of integral quantities from two grids G_{h_i} and $G_{h_{i-1}}$ restriction operators $\mathbf{R}_{Y_{h_i}}^{\;h_{i+1}}$ and prolongation operators $\mathbf{P}_{Y_{h_{i+1}}}^{\;h_i}$ are required, where the generic parameter $Y \in \{N, \tilde{N}, L, \tilde{L}, A, \tilde{A}, V, \tilde{V}\}$ specifies whether the operator acts on vectors of integral electromagnetic quantities assigned to nodes $N, \tilde{N}$, edges $L, \tilde{L}$, facets $A, \tilde{A}$ or volumes $V, \tilde{V}$ of G or $\tilde{G}$.

For the discrete curl-curl equation (2) restriction operators $\mathbf{R}_{\tilde{A}h_i}^{h_{i+1}}$ for vectors of dual facet currents and prolongation operators $\mathbf{P}_{L_{h_{i+1}}}^{h_i}$ for vectors of primal edge degrees of freedom are required, whereas, e.g. for the discrete div-grad system of electrostatics $-\tilde{\mathbf{S}}\mathbf{M}_\varepsilon\mathbf{G}\Phi = \mathbf{q}$ the restriction operators $\mathbf{R}_{\tilde{V}h_i}^{h_{i+1}}$ for vectors of dual volume charges and prolongation operators $\mathbf{P}_{N_{h_{i+1}}}^{h_i}$ for primal nodal potential vectors Φ are required (Feigh *et al.*, 2003).

Accordingly, the defect (residual) vector corresponding to grid resolution level L_{h_i},

$$\hat{\hat{\mathbf{r}}}_{h_i} = \hat{\hat{\mathbf{j}}}_{h_i} - \tilde{\mathbf{C}}_{h_i}\mathbf{M}_{\nu,h_i}\mathbf{C}\hat{\mathbf{a}}_{h_i} \tag{8}$$

which represents a component vector of currents trough the dual facets $\tilde{A}_j \in \tilde{\mathbf{G}}$, is mapped to $L_{h_{i+1}}$ as

$$\hat{\hat{\mathbf{r}}}_{h_{i+1}} = \mathbf{R}_{\tilde{A}_{h_i,}}^{h_{i+1}}\hat{\hat{\mathbf{r}}}_{h_i}$$

using the restriction operator $\mathbf{R}_{\tilde{A}_{h_i,}}^{h_{i+1}}$. The restricted defect vector appears as right-hand side vector in the defect correction equations:

$$\mathbf{A}_{h_{i+1}}\hat{\mathbf{y}}_{h_{i+1}} = \hat{\hat{\mathbf{r}}}_{h_{i+1}} \tag{9}$$

featuring the restricted system matrix $\mathbf{A}_{h_{i+1}}$ and the error vector $\hat{\mathbf{y}}_{h_{i+1}}$ which corresponds to a component vector of line integrals on $\mathrm{G}_{h_{i+1}}$. A calculated error vector $\hat{\mathbf{y}}_{h_{i+1}}$ is then projected onto the finger grid level L_{h_i} using the prolongation operator $\mathbf{P}_{L_{h_{i+1}}}^{h_i}$ to add the correction

$$\hat{\mathbf{y}}_{h_i} = \hat{\mathbf{y}}_{h_i} + \mathbf{P}_{L_{h_{i+1}}}^{h_i}\hat{\mathbf{y}}_{h_{i+1}}.$$

The coarse grid system matrices are commonly achieved from a Galerkin projection with:

$$\mathbf{A}_{h_{i+1}} = \mathbf{R}_{\tilde{A}h_i}^{h_{i+1}}\mathbf{A}_{h_i}\mathbf{P}_{L_{h_{i+1}}}^{h_i}. \tag{10}$$

Symmetry can be maintained in equation (10) if the dual grid restriction operators for discrete curl-curl and grad-div systems, respectively, correspond to the equations:

$$\mathbf{R}_{\tilde{A}h_i}^{h_{i+1}} = \left(\mathbf{P}_{L_{h_{i+1}}}^{h_i}\right)^{\mathrm{T}}, \quad \mathbf{R}_{\tilde{V}h_i}^{h_{i+1}} = \left(\mathbf{P}_{N_{h_{i+1}}}^{h_i}\right)^{\mathrm{T}}. \tag{11}$$

For this reason, often only the construction of prolongation operators is considered and the restriction operation is derived according to equation (11).

Assuming that the defect vector in equation (8) fulfills the consistency condition $\tilde{\mathbf{S}}_{h_i}\hat{\hat{\mathbf{r}}}_{h_i} = 0$, from the relation of the restriction operators (Figure 1):

$$\tilde{\mathbf{S}}_{h_{i+1}}\mathbf{R}_{\tilde{A}h_i}^{h_{i+1}} = \mathbf{R}_{\tilde{V}h_i}^{h_{i+1}}\tilde{\mathbf{S}}_{h_i} \tag{12}$$

also $\tilde{\mathbf{S}}_{h_{i+1}}\hat{\hat{\mathbf{r}}}_{h_{i+1}} = 0$ follows. With the duality in equation (4) and the relations in equation (11) the condition (12) is identical to

$$\mathbf{G}_{h_i}\mathbf{P}_{N_{h_{i+1}}}^{h_i} = \mathbf{P}_{L_{h_{i+1}}}^{h_i}\mathbf{G}_{h_{i+1}} \tag{13}$$

for the vectors of nodal potentials $\Phi_{h_{i+1}}$ proposed (Reitzinger and Schöberl, 2002). This condition is related to the fact that the discrete gradients of the nodal potential vector

$\mathbf{G}\Phi$ form the nullspace of the discrete curl-operator on all grid resolution levels L_{h_i} according to the exactness relation (3) in simple topologies.

The operator $\mathbf{P}_{N_{h_{i+1}}}^{h_i}$ proposed by Reitzinger and Schöberl (2002) prolongates an L_{h_i}-coarse grid nodal potential value in a piecewise constant identity mapping to all adjacent fine grid nodes and fulfills conditions (12) and (13). In Bochev *et al.* (2003) for a prolongation $\mathbf{P}_{L_{h_{i+1}}}^{h_i}$ to commutate according to (13) a prolongation improved by a build-in smoothing step has been defined with:

$$\hat{\mathbf{P}}_{L_{h_{i+1}}}^{h_i} = \left[\mathbf{I}_{h_i} - \omega \mathbf{D}_{\mathrm{CC},h_i}^{-1} \tilde{\mathbf{C}}_{h_i} \mathbf{M}_{\nu,h_i} \mathbf{C}_{h_i}\right] \mathbf{P}_{L_{h_{i+1}}}^{h_i}, \tag{14}$$

where $\mathbf{I}_{h_i}$ is the unit matrix of grid level L_{h_i}, ω is a build-in relaxation factor and $\mathbf{D}_{\mathrm{CC},h_i}$ is the main diagonal of the curl-curl matrix. This refined prolongation is shown in Bochev *et al.* (2003) to exhibit better convergence properties than the one in Reitzinger and Schöberl (2002). By the identities in equation (3) this prolongation operator (14) also fulfils equation (12).

In the context of the MGE of the FIT, restriction and prolongation operators are formulated by Feigh *et al.* (2003) based on a linear interpolation of the integral state-variables assigned to the geometric objects, such that these intergrid operators commutate with all grid incidence operators as shown in Figure 2, whereas equation (14) is constructed to fulfill only the including conditions (12) and (13).

The commutative diagram in Figure 2 for the grid transfer operators and the grid incidence matrices allows, e.g. the following exchange of the operators in the discrete curl-curl matrix:

$$\begin{aligned} \mathbf{A}_{h_{i+1}} &= \mathbf{R}_{\tilde{A}h_i}^{h_{i+1}} \left[\tilde{\mathbf{C}}_{h_i} \mathbf{M}_{\nu,h_i} \mathbf{C}_{h_i}\right] \mathbf{P}_{L_{h_{i+1}}}^{h_i}, \\ &= \tilde{\mathbf{C}}_{h_{i+1}} \mathbf{R}_{\tilde{L}h_i}^{h_{i+1}} \mathbf{M}_{\nu,h_i} \mathbf{P}_{A_{h_{i+1}}}^{h_i} \mathbf{C}_{h_{i+1}}, \end{aligned} \tag{15}$$

where intrinsically a new coarse grid reluctivity matrix,

$$\mathbf{M}_{\nu,h_{i+1}}^{\mathrm{Galerkin}} = \mathbf{R}_{\tilde{L}h_i}^{h_{i+1}} \mathbf{M}_{\nu,h_i} \mathbf{P}_{A_{h_{i+1}}}^{h_i} \tag{16}$$

is defined algebraically. Thus, the intergrid operators with the commutative property restrict a Galerkin projection to the material matrices, such that the coarse grid system matrix again is a consistent representation of problem (1), where all the metric information and the material distribution of the coarse grid level is located in a discrete material matrix. The relations (15) and (16) immediately suggest to exchange the Galerkin projected material matrix with a material matrix originally constructed for the coarse grid, i.e.,

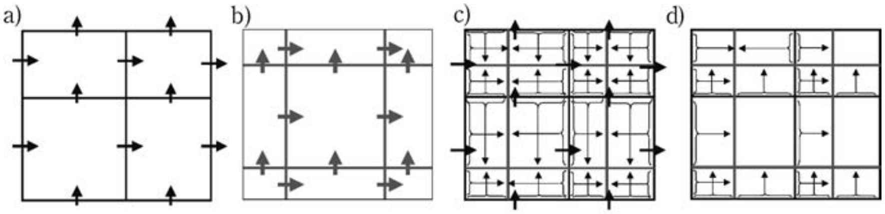

Notes: (a) Fine grid $\tilde{G}_{h_i}$. (b) Coarse grid $\tilde{G}_{h_{i+1}}$. (c) Conservative restriction scheme based on linear interpolation of currents through the facets corresponding to condition (12) for defect vector of currents $\hat{\mathbf{r}}_{h_i}$. (d) Non-conservative 'nearest-neighbor'-restriction scheme.

Figure 1.
Restriction operators $\mathbf{R}_{\tilde{A}h_i}^{h_{i+1}}$ on non-nested dual grids $\tilde{G}_{h_i}$ and $\tilde{G}_{h_{i+1}}$ (2D presentation)

a)

$$\begin{tikzcd}
\mathbf{\Phi}_{h_i} \arrow[r, "\mathbf{G}_{h_i}"] & \hat{\mathbf{a}}_{h_i} \arrow[r, "\mathbf{C}_{h_i}"] & \hat{\hat{\mathbf{b}}}_{h_i} \arrow[r, "\mathbf{S}_{h_i}"] & \mathbf{q}_{M,h_i} \\
\mathbf{\Phi}_{h_{i+1}} \arrow[u, "\mathbf{P}_{N}{}_{h_{i+1}}^{h_i}"'] \arrow[r, "\mathbf{G}_{h_{i+1}}"'] & \hat{\mathbf{a}}_{h_{i+1}} \arrow[u, "\mathbf{P}_{L}{}_{h_{i+1}}^{h_i}"'] \arrow[r, "\mathbf{C}_{h_{i+1}}"'] & \hat{\hat{\mathbf{b}}}_{h_{i+1}} \arrow[u, "\mathbf{P}_{A}{}_{h_{i+1}}^{h_i}"'] \arrow[r, "\mathbf{S}_{h_{i+1}}"'] & \mathbf{q}_{M,h_{i+1}} \arrow[u, "\mathbf{P}_{V}{}_{h_{i+1}}^{h_i}"']
\end{tikzcd}$$

b)

$$\begin{tikzcd}
\mathbf{\Phi}_{h_i} \arrow[d, "\mathbf{R}_{N}{}_{h_i}^{h_{i+1}}"] \arrow[r, "\mathbf{G}_{h_i}"] & \hat{\mathbf{a}}_{h_i} \arrow[d, "\mathbf{R}_{L}{}_{h_i}^{h_{i+1}}"] \arrow[r, "\mathbf{C}_{h_i}"] & \hat{\hat{\mathbf{b}}}_{h_i} \arrow[d, "\mathbf{R}_{A}{}_{h_i}^{h_{i+1}}"] \arrow[r, "\mathbf{S}_{h_i}"] & \mathbf{q}_{M,h_i} \arrow[d, "\mathbf{R}_{V}{}_{h_i}^{h_{i+1}}"] \\
\mathbf{\Phi}_{h_{i+1}} \arrow[r, "\mathbf{G}_{h_{i+1}}"'] & \hat{\mathbf{a}}_{h_{i+1}} \arrow[r, "\mathbf{C}_{h_{i+1}}"'] & \hat{\hat{\mathbf{b}}}_{h_{i+1}} \arrow[r, "\mathbf{S}_{h_{i+1}}"'] & \mathbf{q}_{M,h_{i+1}}
\end{tikzcd}$$

Source: Feigh *et al.* (2003)

Figure 2.
Commutative diagram for linear restriction and prolongation operators $\mathbf{R}_{Y}{}_{h_i}^{h_{i+1}}$ and $\mathbf{P}_{Y}{}_{h_{i+1}}^{h_i}$ in the discrete De Rham complex of the primal fine-/coarse-grid pair $\mathbf{G}_{h_i}$ and $\mathbf{G}_{h_{i+1}}$. Diagrams for dual grids $\tilde{\mathbf{G}}_{h_i}$ and $\tilde{\mathbf{G}}_{h_{i+1}}$ can be derived analogously

$$\mathbf{A}_{h_{i+1}} = \tilde{\mathbf{C}}_{h_{i+1}} \mathbf{M}_{\nu,h_{i+1}} \mathbf{C}_{h_{i+1}}. \tag{17}$$

In the WFEM and the CM this approach may result in a considerably less accurate coarse grid representation. In the recently proposed Conformal FIT multigrid scheme in Feigh *et al.* (2003), however, the CFIT material matrix $\mathbf{M}_{\nu,h_{i+1}}^{\mathrm{CFIT}}$ takes the curved material boundaries inside cell volumes of G exactly into account (Clemens and Weiland, 2002a). These material matrices are either reconstructed using the exact geometry of each grid level using a CAD-kernel or by using the metric information of $\mathbf{M}_{\nu,h_0}^{\mathrm{CFIT}}$ on the finest mesh level L_{h_0} to algebraically construct the material matrices for coarser grid resolutions $h_{i+1}, i \geq 0$, with, e.g.

$$\mathbf{M}_{\nu,h_{i+1}}^{\mathrm{ACFIT}} = \left(\prod_{j=0}^{i} \mathbf{R}_{D_{\tilde{L}}}{}_{h_j}^{h_{j+1}} \right) \mathbf{D}_{\tilde{L},h_0} \mathbf{D}_{\bar{\nu},h_0} \left(\prod_{j=0}^{i} \mathbf{R}_{D_A}{}_{h_j}^{h_{j+1}} \mathbf{D}_{L,h_0} \right)^{-1}, \tag{18}$$

where the left operators $\mathbf{R}_{D_{\tilde{L}}}{}_{h_j}^{h_{j+1}}$ and $\mathbf{R}_{D_A}{}_{h_j}^{h_{j+1}}$ correspond to the restriction matrices $\mathbf{R}_{\tilde{L}}{}_{h_j}^{h_{j+1}}$ and $\mathbf{R}_{\tilde{A}}{}_{h_j}^{h_{j+1}}$, acting on diagonal matrices. The original CFIT material matrices and the Algebraic CFIT matrices maintain their diagonal structure for dual-orthogonal grids, whereas the Galerkin projected material matrices in equation (15) become more condensed for coarser grids, which impedes efficient smoothing (Feigh *et al.*, 2003).

3.1 Restriction with consistency error correction

When using the CFIT-MG like construction of the system matrices in equation (17) on all coarser grids, the restriction operator $\mathbf{R}_{\tilde{A}}{}_{h_i}^{h_{i+1}}$ is required only for the restriction of the defect vectors of dual facet currents. Then, the restriction has to follow condition (12) to maintain that for consistent defect vectors with $\tilde{\mathbf{S}}_{h_i} \hat{\hat{\mathbf{r}}}_{h_i} = 0$ the relation $\tilde{\mathbf{S}}_{h_{i+1}} \mathbf{R}_{\tilde{A}}{}_{h_i}^{h_{i+1}} \hat{\hat{\mathbf{r}}}_{h_i} = 0$ holds, i.e., the coarsened grid system in equation (9) is consistently singular. If, e.g., a non-conservative restriction scheme based on a "nearest-neighbor" projection is used such that $\tilde{\mathbf{S}}_{h_{i+1}}\mathbf{R}_{\tilde{A}h_i}^{h_{i+1}}\widehat{\widehat{\mathbf{r}}}_{h_i} \neq 0$ holds, i.e., the restricted right-hand side vector is no longer in the range of the consistent curl-curl-matrix,

$$\mathbf{R}_{\tilde{A}h_i}^{h_{i+1}}\widehat{\widehat{\mathbf{r}}}_{h_i} \notin \mathrm{Range}\{\tilde{\mathbf{C}}_{h_i}\mathbf{M}_{\nu,h_i}\mathbf{C}\}.$$

As a consequence, system (9) has no exact solution and only least-square approximations are feasible (Kameari, 2003). The discrete consistency error of dual charges can then be eliminated by indirectly enforcing a discrete coulomb gauge $\mathbf{S}\mathbf{M}_{\hat{\kappa}}\widehat{\mathbf{a}} = 0$ for equation (9) with the definition of the projector $\mathbf{P}_{\mathrm{Div}}$ in equation (7) with the choice $\mathbf{N} = \tilde{\mathbf{S}}\mathbf{M}_{\hat{\kappa}}\mathbf{G}$. The system,

$$\tilde{\mathbf{C}}_{h_{i+1}}\mathbf{M}_{\nu,h_{i+1}}\mathbf{C}_{h_{i+1}}\widehat{\mathbf{y}} = \mathbf{P}_{\mathrm{Div}}^{\mathrm{T}}\mathbf{R}_{\tilde{A}h_i}^{h_{i+1}}\widehat{\widehat{\mathbf{r}}}_{h_i} \tag{19}$$

with the projected right-hand side vector is again consistently singular and can be solved again. The corrected restriction scheme is still non-conservative: the coarse grid problems no longer correspond physically to the original fine grid problem on the coarser grid levels. Thus, the convergence rates of the overall multigrid scheme are expected not to reach those of MG schemes with conservative intergrid operators.

4. Numerical results

Linear magnetostatic c-magnet problems are calculated using a non-nested geometric CFIT-MG scheme following equation (17) (Feigh *et al.*, 2003). In Figure 3 the CFIT-MG

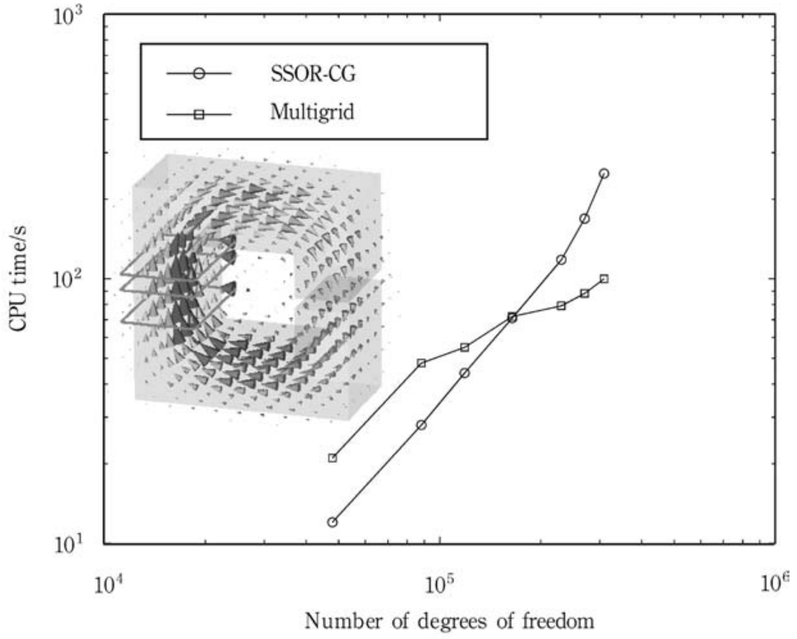

Source: Feigh *et al.* (2003)

Figure 3.
Comparison of the efficiency of SSOR-CG and the CFIT-MG scheme for the solution of the systems (2) from a CFIT-discretization of a c-magnet test problem

scheme using conservative intergrid operators shows an improved asymptotic complexity behavior when compared to a SSOR-preconditioned conjugate gradient solver.

The CFIT-MG method in Figure 4 shows the convergence for the scheme with non-conservative "nearest-neighbor" restrictions, although the internal systems are inconsistent and no convergence should be expected. The consistency correction operator in equation (19) eliminates erroneous charges due to the non-conservative restriction of the defect vectors as shown in Figure 5 and thus yields consistently singular systems at each grid level that are guaranteed to have solutions. The CFIT-MG method in Figure 4 with the consistency corrected non-conservative "nearest-neighbor" restrictions is still not as fast as the scheme with the conservative linear operators of Feigh *et al.* (2003).

5. Conclusion

The magnetic vector potential formulation discretized with geometric discretization methods as the FIT, the lowest order WFEM or the CM requires the solution of large linear algebraic systems of equations. A theoretical framework of multigrid methods amenable to this task was presented focusing on algebraic properties of the intergrid transfer operators. The relations of these operators to the metric-free incidence matrices were shown to be responsible for the conservation of discrete integral quantities such as fluxes and charges. For non-conservative schemes, possible sources of consistency errors were shown to occur and a correction scheme using a gauge projection operator was shown to restore the consistency of the singular formulation.

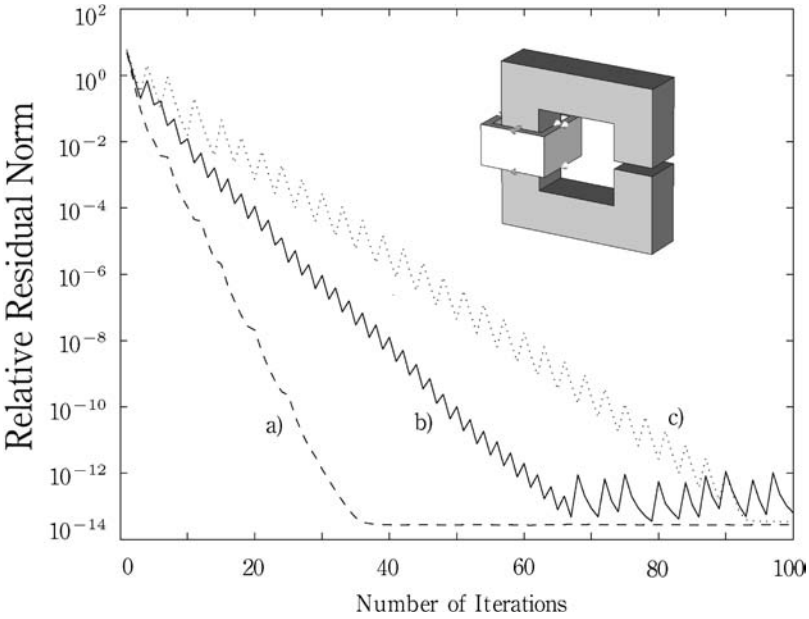

Figure 4.
Comparison of the convergence history of geometric CFIT-multigrid schemes using different defect restriction methods for a three-dimensional c-magnet test configuration: (a) the charge conservative restriction, (b) the "nearest-neighbor" restriction without consistency correction, and (c) the "nearest-neighbor" restriction with consistency correction

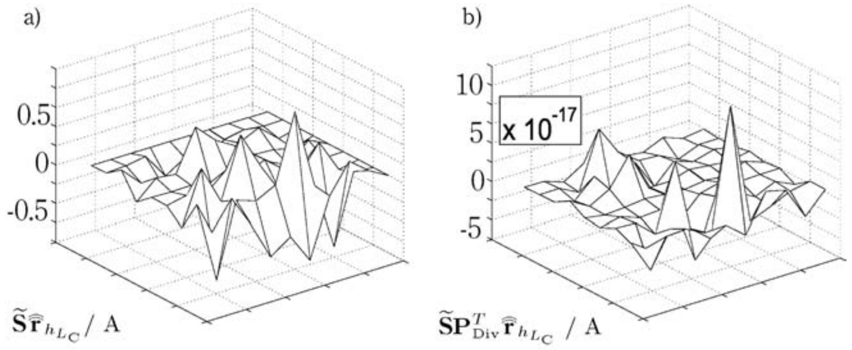

Notes: a) without consistency error correction b) with consistency error correction: the dual cell charge vector $\widetilde{\mathbf{S}}\widehat{\mathbf{r}}_{h_{L_C}}/\mathrm{A}$ is reduced to zero within machine accuracy

Figure 5. Righthand side consistency error $\widetilde{\mathbf{S}}\widehat{\mathbf{r}}_{h_{L_C}}/\mathrm{A}$ for nearest-neighbor-restriction: (cut through grid of c-magnet model on coarsest grid)

References

Bochev, P., Garasi, C., Hu, J., Robinson, A. and Tuminaro, R. (2003), "An improved algebraic multigrid method for solving Maxwell's equations", *SIAM J. Sci. Comput.*, Vol. 25 No. 2, pp. 623-42.

Bossavit, A. and Kettunen, L. (1999), "Yee-like schemes on a tetrahedral mesh with diagonal lumping", *Int. J. Numer. Model.*, Vol. 12 Nos 1/2, pp. 129-42.

Cingoski, V., Tokuda, R., Noguchi, S. and Yamashita, H. (2000), "Fast multigrid solution method for nested edge-based finite element meshes", *IEEE Trans. Magn.*, Vol. 36 No. 4, pp. 1539-42.

Clemens, M. and Weiland, T. (1999), "Transient eddy current calculation with the FI-method", *IEEE Trans. Magn.*, Vol. 35 No. 3, pp. 1163-6.

Clemens, M. and Weiland, T. (2002a), "Magnetic field simulation using conformal FIT formulations", *IEEE Trans. Magn.*, Vol. 38 No. 2, pp. 389-92.

Clemens, M. and Weiland, T. (2002b), "Regularization of eddy current formulations using discrete grad-div operators", *IEEE Trans. Magn.*, Vol. 38 No. 2, pp. 569-72.

Feigh, S., Clemens, M. and Weiland, T. (2003), "Geometric multigrid method for electro- and magnetostatic field simulations using the Conformal Finite Integration Technique", *Virtual Proc. 11th Copper Mountain Conf. on Multigrid Methods (CMCMM 2003), USA*, available at: www.mgnet.org

Hiptmair, R. (1999), "Multigrid method for Maxwell's equations", *SIAM Numer. Anal.*, Vol. 36 No. 1, pp. 204-25.

Kameari, A. (1990), "Calculation of transient 3d eddy current using edge elements", *IEEE Trans. Magn.*, Vol. 26 No. 5, pp. 466-9.

Kameari, A. (2003), "Regularization on ill-posed source terms in FEM computation using two magnetic vector potentials", *Proc. 14th Compumag*, Saratoga Springs, USA, Vol. 1, pp. 188-9.

Nédélec, J.C. (1980), "Mixed finite elements in R^3", *Numer. Math.*, Vol. 35, pp. 315-41.

Reitzinger, S. and Schöberl, J. (2002), "An algebraic multigrid method for finite element discretizations with edge elements", *Num. Lin. Alg. Appl.*, Vol. 9, pp. 223-38.

Repetto, M. and Trevisan, F. (2003), "3-d magnetostatic with the finite formulation", *IEEE Trans. Magn.*, Vol. 39 No. 3, pp. 1135-8.

Tonti, E. (2001), "A direct formulation of field laws: the cell method", *CMES-Comp. Mod. Eng.*, Vol. 2 No. 2, pp. 237-58.

Trottenberg, U., Schuller, A. and Oosterlee, C. (2000), *Multigrid*, Academic Press, London.

Weiland, T. (1977), "A discretization method for the solution of Maxwell's equations for six-component fields", *Int. J. Electron. Commun. (AEÜ)*, Vol. 31 No. 3, pp. 116-20.

Weiß, B. and Bíró, O. (2002), "Multigrid for transient 3d eddy current analysis", *Proc. 10th IGTE Symposium, Graz, Austria*, pp. 413-7.

The Emerald Research Register for this journal is available at
www.emeraldinsight.com/researchregister

The current issue and full text archive of this journal is available at
www.emeraldinsight.com/0332-1649.htm

Wavelet's application in electrostatic and their computing aspects

Aldo Artur Belardi
Department of Electrical Engineering, Centro Universitário da FEI,
São Paulo, Brazil

José Roberto Cardoso and Carlos Antonio França Sartori
Escola Politécnica da Universidade de São Paulo – Lmag/PEA/USP,
São Paulo, Brazil

Keywords *Waves, Optimization techniques, Numerical analysis*

Abstract *This paper presents the mathematical basis, and some results, concerning the application of the Haar's Wavelets as the expansion function in the method of moments. Some computational optimization techniques are used, and their main aspects are stressed in the paper. As an example, the surface charge density on a finite and thin plane plate calculation is presented, in which the main computational performance aspects are evaluated.*

1. Formulation

Regarding the formulation, in order to illustrate the proposed methodology, the main theoretical aspects of the method of moments and of the Haar's wavelets are presented here. For simplification, two-dimensional applications are considered.

1.1 Method of moments

Although the method of moments is a well-known numerical method, and the complete description and details of this method have already been presented in many papers, in order to guide the reader through the overall method explanation, a brief summary is shown here. In a simplified way, it can be mentioned that the basis of the method of moments is the application of approximation functions, like the following one (Harrington, 1968).

$$f(x) = \sum_n \alpha_n \boldsymbol{L} g_n \tag{1}$$

In the aforementioned expression, α_n is the unknown coefficients; g_n is the expansion function, e.g. the pulse or the Haar's wavelets, and "$\boldsymbol{L}$" a mathematical operator. When the inner product, using a weighed function "W_m", is carried out, it will result:

$$\sum_n \alpha_n \langle \boldsymbol{L} g_n, W_m \rangle = \langle f, W_m \rangle \ \text{para} \ m = 1, 2 \ldots N \tag{2}$$

The previous expression can be represented in a matrix form by $[\mathbf{A}][\alpha] = [\mathbf{B}]$, where $[\alpha]$ is the unknown approximated solution coefficients column vector, and the matrices $[\mathbf{A}]$ and $[\mathbf{B}]$ are given by:

COMPEL: The International Journal for Computation and Mathematics in Electrical and Electronic Engineering
Vol. 23 No. 4, 2004
pp. 923-931
© Emerald Group Publishing Limited
0332-1649
DOI 10.1108/03321640410553355

$$[\mathbf{A}] = \begin{bmatrix} \langle \boldsymbol{L}g_1, W_1\rangle & \ldots & \langle \boldsymbol{L}g_n, W_1\rangle \\ \langle \boldsymbol{L}g_1, W_2\rangle & \ldots & \langle \boldsymbol{L}g_n, W_2\rangle \\ \langle \boldsymbol{L}g_1, W_n\rangle & \ldots & \langle \boldsymbol{L}g_n, W_n\rangle \end{bmatrix}; \quad [\mathbf{B}] = \begin{bmatrix} \langle f, W_1\rangle \\ \langle f, W_2\rangle \\ \langle f, W_n\rangle \end{bmatrix} \tag{3}$$

If a square plane plate is considered as an example, we should remember that the potential in a finite and very thin plane plate can be evaluated by (Balanis, 1990):

$$V(x,y,z=0) = \frac{1}{4\pi\varepsilon}\int_{-a}^{a}\mathrm{d}x'\int_{-b}^{b}\mathrm{d}y'\frac{\rho(x',y')}{[(x-x')^2+(y-y')^2]^{1/2}} \tag{4}$$

Thus, after applying the method of the moments, knowing the function of the approximated solution $f(x, y)$, the expansion function $g(x, y)$ and the weighed function $W(x, y)$, the potential in a square plane plate will be estimated by the inner product of these functions:

$$V(x,y) = \langle g, W, f\rangle\frac{1}{R} = \int_{-a}^{a}\frac{g(x,y)W(x,y)f(x,y)}{R(x,y)}\,\mathrm{d}x \tag{5}$$

where

$$R(x,y) = \sqrt{(x-x')^2+(y-y')^2} \tag{6}$$

Dividing the plate in equal segments and applying the weighed function as being the Dirac delta function, we had that $W_m = \delta(x-x_m)\delta(y-y_m)$, being the inner product in the point given by:

$$\begin{aligned} V(x,y,z=0) &= \langle W_m, f, \boldsymbol{L}g\rangle \\ &= \delta(x-x_m)\,\delta(y-y_m)\frac{1}{4\pi\varepsilon}\int_{-a}^{a}\mathrm{d}x'\int_{-b}^{b}\mathrm{d}y'\frac{\sum_{n=1}^{N}\alpha_n g_n(x',y')}{[(x_m-x')^2+(y_m-y')^2]^{1/2}} \end{aligned} \tag{7}$$

Assuming the charges placed in the center of each sub division in relation to each axes, substituting the values of x and y by the distance of the charge position to the point $P(x_m, y_m)$, we will have an integral that is only function of x' and y'. For a fixed potential V, the equation can be represented, using the matrix notation, by $[V_m] = [Z_{mn}][\alpha_n]$, in which Z_{mn} is defined by:

$$Z_{mn} = \int_{-a}^{a}\mathrm{d}x'\int_{-b}^{b}\frac{g_n(x',y')}{4\pi\varepsilon\sqrt{(x_m-x')^2+(y_m-y')^2}}\,\mathrm{d}y' \tag{8}$$

1.2 The Haar's wavelets

It was earlier mentioned that many functions can be used as the expansion function. Among them, the pulse function, the truncate cosine function and the wavelets can be mentioned. Herein, the general aspects of the wavelets are shown. Thus, after applying the method of the moments, and considering the Haar's wavelets, a function $f(x, y)$ can be approximated by (Newland, 1993):

$$f(x,y) = \sum_{k=-\infty}^{\infty} c_k \phi(x,y) + \sum_{j=-\infty}^{\infty} \sum_{k=-\infty}^{\infty} d_{j,k} f_P(x,y) \psi_{j,k}(x,y) \tag{9}$$

In this equation "*j*" and "*k*" are the resolution and the translation levels, respectively.

Moreover, once the Haar's wavelets, and the so-called mother function (10) and scale function father (11) are applied, the formulation for two-dimensional applications will result in a product combination of equations (12) and (13), given by equation (14):

$$\psi_{j,k}^{(H)}(x) = 2^{j/2} \psi(2^j x - k) \quad j,k \in Z \tag{10}$$

$$\phi^{(H)}(x) = \begin{cases} 1 & 0 \leq x < 0.5 \\ 0 & \text{for other intervals} \end{cases} \tag{11}$$

$$\psi_{j,k}^{(H)}(x) = [\phi(x)\, \psi(x)\, \psi(2x)\, \psi(2x-1) \ldots \psi(2^j x - k)] \tag{12}$$

$$\psi_{j,k}^{(H)}(y) = \lfloor \phi(y)\, \psi(y)\, \psi(2y)\, \psi(2y-1) \ldots \psi(2^j y - k) \rfloor \tag{13}$$

$$\{\psi_{j,k}^{(H)}(x), (y)\} = \phi(x)\, \phi(y),\ \phi(x)\, \psi(y), \ldots,\ \psi(2x-1)\, \psi(2y-1) \tag{14}$$

As an illustration, Figure 1 shows the Haar's function regarding two dimensions and one level of resolution, for a point $P(x_m, y_m)$. On the other hand, if the potential in a finite and very thin plane plate is considered as an application, it can be evaluated by:

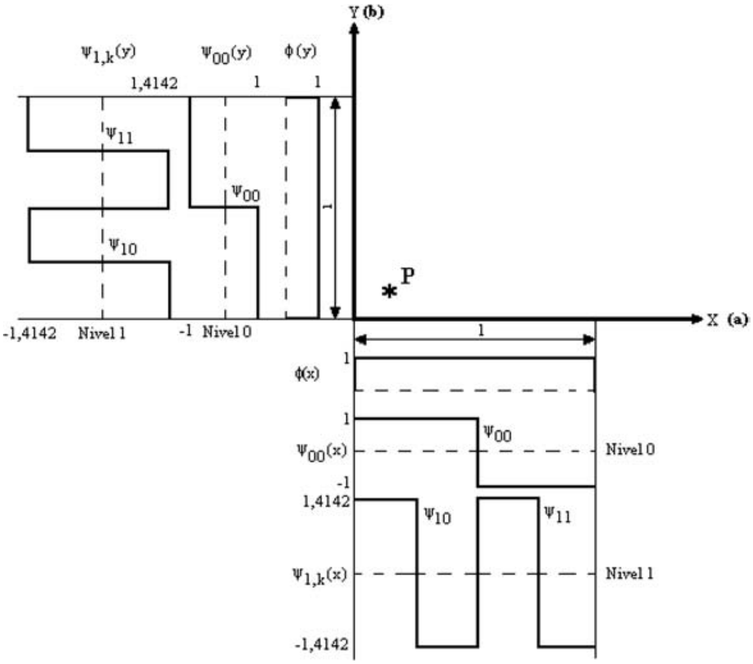
Y (b)
$\psi_{1,k}(y)$
$\psi_{00}(y)$
$\phi(y)$
1,4142
1
1
ψ_{11}
ψ_{00}
ψ_{10}
1
P
X (a)
-1,4142
Nivel 1
-1
Nivel 0
1
1
$\phi(x)$
1
ψ_{00}
$\psi_{00}(x)$
Nivel 0
-1
1,4142
ψ_{10}
ψ_{11}
$\psi_{1,k}(x)$
Nivel 1
-1,4142

Figure 1.
Representation of the Haar's function for two-dimensions and one level of resolution

$$
\begin{aligned}
V(x,y)4\pi\varepsilon = {} & a_j b_j \int_{-a}^{a}\int_{-b}^{b} \frac{\phi(x,y)}{\sqrt{(x_m - x')^2 + (y_m - y')^2}}\,\mathrm{d}x\,\mathrm{d}y \\
& + \sum_{j=-\infty}^{\infty}\sum_{k=-\infty}^{\infty} a_{j,k} b_{j,k} \int_{-a}^{a}\int_{-b}^{b} \frac{\psi_{j,k}^{(H)}(x,y)}{\sqrt{(x_m - x')^2 + (y_m - y')^2}}\,\mathrm{d}x\,\mathrm{d}y
\end{aligned}
\tag{15}
$$

Based on the previous formulation, it should be observed that they are indexed by two parameters, "*j*" and "*k*", allowing us to vary the precision of the results through these levels of resolution. Concerning the application of the Haar's wavelets, the main aspects are related to the resulting scattered matrices and null coefficients, an interesting property to be considered regarding the computational aspects (Aboufadel and Schlicker, 1999). Those can be mentioned as the main characteristic of this methodology.

In order to briefly illustrate those aspects, one can remember that the equation to determine the coefficients of the approximation function can be written as:

$$[Z_{mn}] \times [\rho] = [V] \tag{16}$$

where Z_{mn} is a square matrix that is not necessarily a scattered one, since it depends on the expansion function that was chosen.

Thus, taking advantages of the fact that the Haar's matrix is a scattered matrix, applying the matrix algebra, it will result (Wagner and Chew, 1995):

$$[Z'_{mn}] \times [\rho'] = [V'] \tag{17}$$

else,

$$
\begin{gathered}
[Z'_{mn}] = [H]\,[Z_{mn}]\,[H^{\mathrm{T}}] \\
[\rho'] = [H^{\mathrm{T}}]^{-1}\,[\rho] \quad [V'] = [H][V]
\end{gathered}
\tag{18}
$$

Consequently, we will obtain:

$$[H][Z_{mn}][H^{\mathrm{T}}][H^{\mathrm{T}}]^{-1}[\rho] = [H][V] \tag{19}$$

Thus, after applying such an approach, we got a symmetrical matrix. Moreover, due to the properties of Haar's function a number of "near" null matrix elements were obtained.

The used approach is based on the assumption of a threshold level. This level corresponds to a percentage of the difference between the maximum positive value and the minimum negative one. Once it is adopted, the matrix elements, inferior to this number, will be assumed as a null one. This approach will help to get an additional computing time reduction.

2. Applications and discussion

After applying the aforementioned formulation, some results were obtained. For example, Figure 2 shows the surface charge density in a square plate (1.0 m × 1.0 m), submitted to a potential of 1.0 V. In this case, it was adopted that 16 subdivisions for

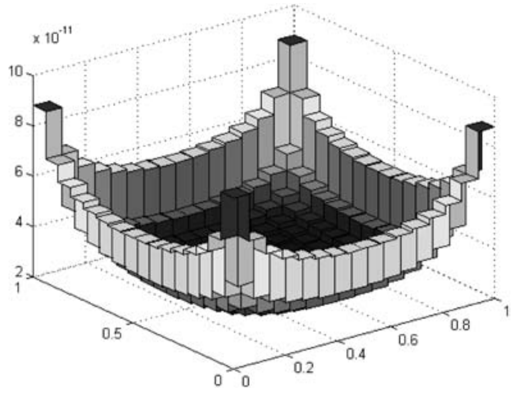

Figure 2.
The surface charge density on the plane plate

each of the axes, and the level 5 of resolution was applied to the Wavelets. Concerning the characteristic of the method, it should be emphasized that the application of the Haar's wavelets originates scattered matrices. Thus, we will have null coefficients that can result in a computing time reduction.

Table I shows the comparative results regarding the computing time values (Patterson and Hennessy, 2001; Stallings, 2002), function of the adopted axe division number, with or without applying the null value detection routine. A 800 MHz PC was used.

As estimated, when the null value detection routine is carried out, it will get an average 40 per cent computing time reduction. Figure 3 shows the comparative computing time (s), with and without using the null value detection routine.

Figures 4-6 show the Z'_{mn} matrix configuration for the threshold equal to 0.01, 0.02, and 0.05 per cent, respectively. The dark part is for the non-null values.

Table II shows the computing time, when the threshold level, and the axe subdivision numbers are considered.

Figure 7 shows the error variation for the surface charge density, considering a square plane plate, and 16-axe subdivisions, as a function of the selected threshold.

Moreover, it should be mentioned that the Cholesky's decomposition method was also implemented (Datta, 1995). Figure 8 shows the matrix configuration after applying it, assuming a threshold level equal to 0.01 per cent. In this case, an approximate increase of 64 per cent was obtained in the null value element of the matrix.

Regarding the computational performance, the average computing time decreased from 0.21 to 0.02 s, for 16-axe subdivision, and a reduction time from 11.49 to 0.351 s.

Table I.
Computing time (s) function of the axe subdivisions and of the null value detection use

Divisions	Computing time (s)		Difference
Plane plate	Without	With	(per cent)
4 × 4	0.321	0.25	22.12
8 × 8	7.931	5.488	30.80
16 × 16	451.960	222.60	50.75
32 × 32	27273.738	11994.487	56.02

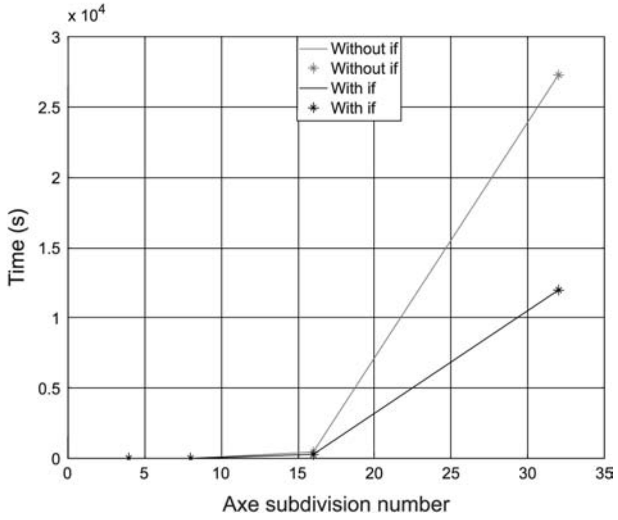

Figure 3.
The computing time (s) as a function of the subdivision axe number

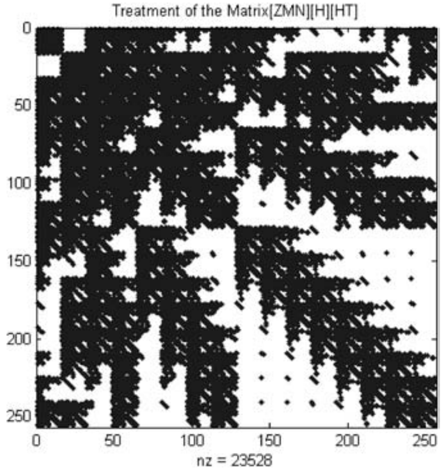

Figure 4.
Value of the threshold of 0.01 per cent (23,528 non-zero elements)

3. Conclusion

This paper features the theoretical aspects and applications concerning wavelets applied to the method of the moments. Although some simple applications on electrostatics were presented, the proposed methodology can be applied to more complex problems. Based on the results presented in the paper, we verified that the difference in the charge density value for a square plane plate is lower than 0.025 per cent, when the Haar's wavelets is used as an expansion function in the method of the moments, instead of the pulse function.

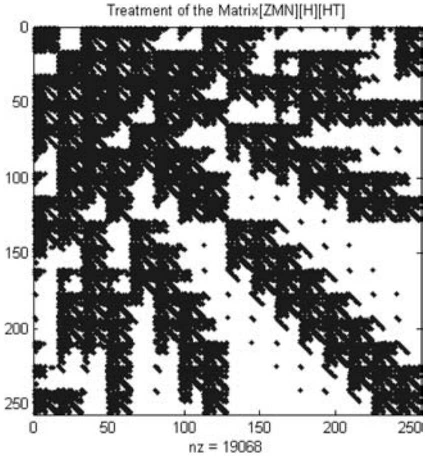

Figure 5.
Value of the threshold of 0.02 per cent (19,068 non-zero elements)

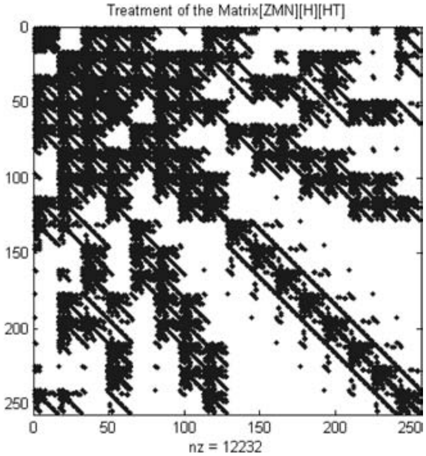

Figure 6.
Value of the threshold of 0.05 per cent (12,232 non-zero elements)

Table II.
Computing time (s) as a function of the axe subdivisions and of the adopted threshold level

	Threshold levels (per cent)			
Subdivision	0.00001	0.01	0.05	0.1
16 × 16	0.27	0.21	0.16	0.12
32 × 32	25.486	11.49	4.516	2.073

It should also be mentioned that the advantage of adopting the Haar's function to the reduction of the non-null matrix elements results in the improvement of its computational performance. After adopting the null-value detection routine, an average of 40 per cent computing time reduction was achieved. Moreover, the Cholesky's

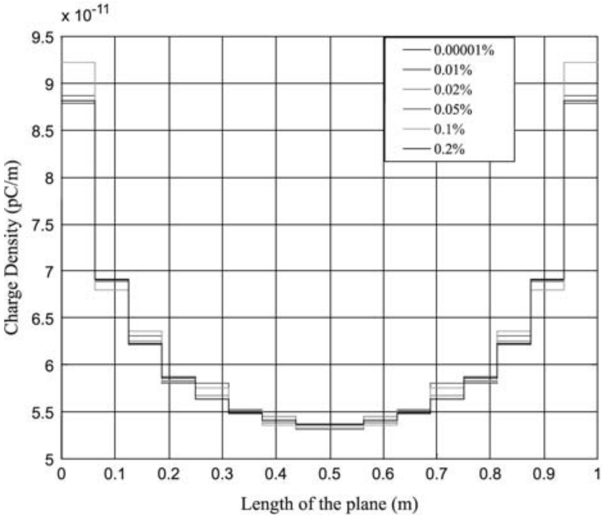

Figure 7.
Variation of the charge surface density as a function of a selected threshold

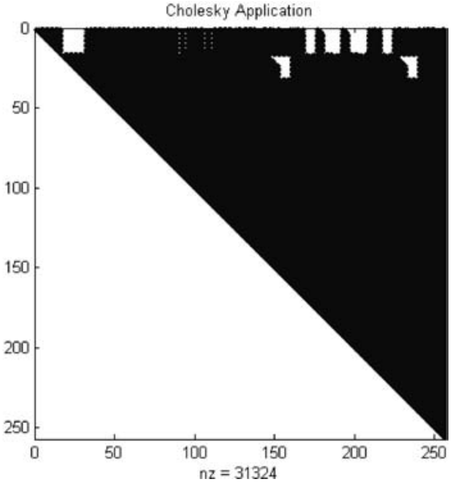

Figure 8.
Matrix configuration after applying the Cholesky's decomposition for the threshold equal to 0.01 per cent

decomposition method were implemented, getting an average of 64 per cent computing time reduction.

References

Aboufadel, E. and Schlicker, S. (1999), *Discovering Wavelets*, Wiley, New York, NY, pp. 1-42.

Balanis, C. (1990), *Advanced Engineering Electromagnetic*, Wiley, New York, NY, pp. 670-95.

Datta, B.N. (1995), *Numerical Linear Algebra and Applications*, 1st ed., Brooks/Cole Publishing Company, New York, NY.

Harrington, R. (1968), *Field Computation by Moment Methods*, Macmillan Series in Electrical Science, pp. 1-40.

Newland, D.E. (1993), *Random Vibrations Spectral and Wavelet Analysis*, Addison-Wesley Longman, Reading, MA, pp. 315-33.

Patterson, D.A. and Hennessy, J.L. (2001), *Computer Organization and Design the Hardware/Software Interface*, 1st ed., Morgan Kaufmann, Los Altos, CA, pp. 26-51.

Stallings, W. (2002), *Computer Organization and Architecture*, 5th ed., Prentice-Hall, Englewood Cliffs, NJ, pp. 42-6.

Wagner, R.L. and Chew, W.C. (1995), "A study of wavelets for the solution of electromagnetic integral equations", *IEEE Transactions on Antennas and Propagation*, Vol. 43 No. 8, pp. 802-10.

The Emerald Research Register for this journal is available at
www.emeraldinsight.com/researchregister

The current issue and full text archive of this journal is available at
www.emeraldinsight.com/0332-1649.htm

Comparisons of finite element and Rayleigh methods for the study of conical Bloch waves in arrays of metallic cylinders

S. Guenneau
Blackett Laboratory, Imperial College London, London, UK
A. Nicolet
Institut Fresnel, Université Aix-Marseille III, Marseille, France
C. Geuzaine
California Institute of Technology, Applied and Computational Mathematics, Pasadena, California, USA
F. Zolla
Institut Fresnel, Université Aix-Marseille I, Marseille, France
A.B. Movchan
Department of Mathematical Sciences, Liverpool, UK

Keywords *Communication technologies, Finite element analysis, Numerical analysis*

Abstract *This paper investigates new technological devices to be utilised in future optical communications, by means of variational method (FEM) and multipole scattering approach (Rayleigh method). This last one provides interesting asymptotic results in the long-wavelength limit. The so-called photonic crystal fibres (PCF) possess radically different guiding properties due to photonic band gap guidance: removing a hole within a macro-cell leads to a defect state within the gap. In the case of multi-core PCF, the localised modes start talking to each other which possibly leads to a new generation of multiplexer/demultiplexers.*

1. Introduction

Nanostructured materials containing ordered arrays of cylindrical holes pave the way of an optoelectronics revolution, doing for light what silicon did for electrons. The microelectronics revolution was based on the elaborate control of electric currents achieved with semiconductors as silicon. That control depends on a phenomenon called the band gap, i.e. a range of energies in which electrons are blocked from travelling through the semiconductor. By analogy with semiconductors, physicist have produced materials with a photonic band gap – a range of wavelengths of light that is blocked by the material – by structuring the material in carefully designed patterns at the nanoscopic-size scale. These so-called photonic crystals (PC) act as semiconductors for light and promise innumerable technological applications. Such structures can be stretched along the third dimension, forming a new kind of optical fibres, christened "photonic crystal fibres" (PCF). Conventional optical fibres have a high refractive index

COMPEL: The International Journal for Computation and Mathematics in Electrical and Electronic Engineering
Vol. 23 No. 4, 2004
pp. 932-949
© Emerald Group Publishing Limited
0332-1649
DOI 10.1108/03321640410553364

S. Guenneau acknowledges support from DoD/ONR MURI grant N00014-01-1-0803. C. Geuzaine is a Postdoctoral Researcher with the Belgian National Fund for Scientific Research.

at their core, which confines light by total internal reflection. Philip St J. Russell of the University of Bath in England demonstrated in 1999 how to make photonic band-gap fibres (Knight *et al.*, 1999). In one version, light travels along a central hole in the fibre, confined there by the two-dimensional band gap of a surrounding periodic cladding. More optical power can be sent through such a central void than through glass, enabling greater information-carrying capacity, perhaps 100 times that of conventional telecommunications fibres. Specialty fibres have advanced the most as commercial photonic band-gap products. Two companies, one of them being based in UK ("www.blazephotonics.com") and led by Philip St J. Russell, have already distributed sample quantities and will soon begin volume production of PCF. We present analysis of electromagnetic waves propagating through such doubly periodic array of cylindrical channels in oblique incidence. We use Floquet-Bloch quasi-periodicity conditions to take into account the periodicity of the problem (Nicolet *et al.*, 2004). Although one may argue that the PCF reportedly have a finite size in real world (Knight *et al.*, 1999), this model enables us to construct dispersion curves for the corresponding periodic structure. We exhibit band gaps in conical incidence and study localised modes associated with a defect in a macrocell.

2. Rayleigh method

2.1 Set up of the spectral problem

2.1.1 Maxwell's equations at work. We consider a periodic heterogeneous lossless medium. This micro-structure is characterised by its permittivity $\varepsilon = \varepsilon_{\mathrm{r}}\varepsilon_0$ (ε_0 is the permittivity of vacuum) and its permeability $\mu = \mu_{\mathrm{r}}\mu_0$ (μ_0 is the permeability of vacuum). We assume an implicit time dependence $\exp(-\mathrm{i}\omega t)$ of the electric field $\underline{\mathbf{E}}(x, y, z)$ and the magnetic field $\underline{\mathbf{H}}(x, y, z)$, which are therefore solutions of the time harmonic Maxwell's equations (in the sense of distributions in $\mathbb{R}^3$):

$$\begin{cases} \operatorname{curl} \underline{\mathbf{E}} = \mathrm{i}\omega\mu_0\mu_{\mathrm{r}}\underline{\mathbf{H}}, & \operatorname{div}(\varepsilon_{\mathrm{r}}\underline{\mathbf{E}}) = 0 \\ \operatorname{curl} \underline{\mathbf{H}} = -\mathrm{i}\omega\varepsilon_0\varepsilon_{\mathrm{r}}\underline{\mathbf{E}}, & \operatorname{div}(\mu_{\mathrm{r}}\underline{\mathbf{H}}) = 0 \end{cases} \tag{1}$$

Since we are studying propagation of modes in a periodic medium, the well posedness of this spectral problem is ensured by the Floquet-Bloch quasi-periodicity conditions which hold on the boundary of a basic cell (provided that ε_{r} and μ_{r} are real functions with strictly positive lower and upper bounds).

In the case of propagating waves in conical incidence in a medium invariant along the z-axis, $\underline{\mathbf{V}}$ ($\underline{\mathbf{V}}$ denoting either $\underline{\mathbf{E}}$ or $\underline{\mathbf{H}}$) is sought in the form:

$$\underline{\mathbf{V}} = \mathbf{V}(r, \Phi)\,\mathrm{e}^{\mathrm{i}\gamma z}, \tag{2}$$

where γ is the (strictly positive) propagation constant and r and Φ denote the radial and angular variables of $\mathbf{V}$ which is associated with one of the basic cells (Figure 1), which we denote as $Y = [0; d] \times [0; d]$ (d is the pitch of the square array).

From now on, we will study piecewise-constant permittivity and permeability: we restrict our analysis to the important case of a periodic assembly of infinite conducting cylindrical inclusions of circular cross-section C (Knight *et al.*, 1999). Using the vector Helmholtz decomposition

$$\operatorname{curl}(\operatorname{curl} \underline{\mathbf{V}}) = -\Delta\underline{\mathbf{V}} + \operatorname{grad}(\operatorname{div} \underline{\mathbf{V}}), \tag{3}$$

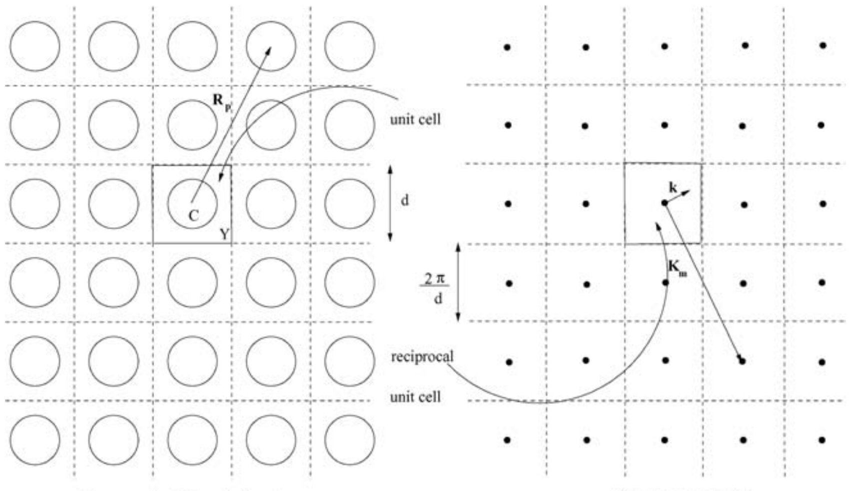

The array of cylinders in direct space.

The reciprocal lattice.

Figure 1.
Physical space and reciprocal space

we find that in the medium between the metallic inclusions, the electric and magnetic field satisfies the vector Helmholtz equation

$$(\Delta + k^2)\underline{\mathbf{V}} = 0, \tag{4}$$

where the spectral parameter k denotes $\sqrt{\omega^2 \varepsilon_0 \varepsilon_\mathrm{r} \mu_0 \mu_\mathrm{r}}$, ε_r and μ_r being, respectively, the relative permittivity and permeability in the matrix.

Because the rods are infinitely extended in the z-direction, the x and y components of the **E** and **H** fields can be reconstructed from their z-components, via the equations

$$\underline{\mathbf{E}}_t = \frac{1}{\varepsilon_0 \varepsilon_\mathrm{r} \mu_0 \mu_\mathrm{r} \omega^2 - \gamma^2} (\mathrm{i}\gamma \, \mathrm{grad}_t \underline{E}_z - \mathrm{i}\omega \mu_\mathrm{r} \mathbf{e}_z \times \mathrm{grad}_t \, \underline{H}_z), \tag{5}$$

$$\underline{\mathbf{H}}_t = \frac{1}{\varepsilon_0 \varepsilon_\mathrm{r} \mu_0 \mu_\mathrm{r} \omega^2 - \gamma^2} (\mathrm{i}\gamma \, \mathrm{grad}_t \underline{H}_z + \mathrm{i}\omega \varepsilon_\mathrm{r} \mathbf{e}_z \times \mathrm{grad}_t \, \underline{E}_z). \tag{6}$$

It should be noted that in the subsequent analysis we retain the z-dependence of the fields.

The mathematical model of infinite conducting inclusions amounts to assuming that the tangential part of the electric field $\mathbf{n} \times \mathbf{E}$ be vanishing on their boundary, unlike the tangential part of the magnetic field $\mathbf{n} \times \mathbf{H}$ which involves the (unknown) current. If we write the tangent vector at any given point on the inclusion surface ∂C as $\mathbf{e}_\tau$ and the normal vector as $\mathbf{n}$ then

$$\mathbf{n} \times \underline{\mathbf{E}}|_{\partial C} = \left\{ \underline{E}_z \mathbf{e}_\tau + \mathbf{e}_z \times \left(\frac{\mathrm{i}\gamma}{\varepsilon_\mathrm{r} \mu_\mathrm{r} \omega^2 - \gamma^2} \frac{\partial \underline{E}_z}{\partial \tau} - \frac{\mathrm{i}\omega \mu_\mathrm{r}}{\varepsilon_\mathrm{r} \mu_\mathrm{r} \omega^2 - \gamma^2} \frac{\partial \underline{H}_z}{\partial n} \right) \right\} \Bigg|_{\partial C} = 0. \tag{7}$$

2.1.2 Conical mounting for metallic cylinders: miracle making. Noting that $\mathbf{e}_\tau$ and $\mathbf{e}_z$ are perpendicular, we can express the boundary conditions as a set of restrictions on the z-components of the fields. These are

$$\underline{E}_z|_{\partial C} = 0, \tag{8}$$

$$\left(\frac{\mathrm{i}\gamma}{\varepsilon_{\mathrm{r}}\mu_{\mathrm{r}}\omega^2 - \gamma^2} \frac{\partial \underline{E}_z}{\partial \tau} - \frac{\mathrm{i}\omega\mu_{\mathrm{r}}}{\varepsilon_{\mathrm{r}}\mu_{\mathrm{r}}\omega^2 - \gamma^2} \frac{\partial \underline{H}_z}{\partial n} \right)\Bigg|_{\partial C} = 0. \tag{9}$$

When $\gamma = 0$, it follows straightforwardly from (9) that

$$\left.\frac{\partial \underline{H}_z}{\partial n}\right|_{\partial C} = 0. \tag{10}$$

So that we can split the problem into two fundamental polarisations in the sense that every field can be expressed as two decoupled fields, namely a T.E. field for which H_z is the solution of

$$(\Delta + k^2)H_z = 0, \quad \text{outside the metal,} \tag{11}$$

$$\left.\frac{\partial H_z}{\partial n}\right|_{\partial C} = 0, \quad \text{on the boundary of each cylinder,} \tag{12}$$

and a T.M. field for which E_z is the solution of

$$(\Delta + k^2)E_z = 0, \quad \text{outside the metal,} \tag{13}$$

$$E_z|_{\partial C} = 0, \quad \text{on the boundary of each cylinder.} \tag{14}$$

When $\gamma > 0$, the boundary conditions in equations (8) and (10) still hold, which is one of the peculiarities shared by the model of infinitely conducting metallic cylinders. The fact that the conical mounting does not mix the polarisations is certainly not trivial (and actually not true for dielectric cylinders). Hence, we thought that this remarkable fact deserves a little digression from the main stream of the paper.

If $0 < \gamma \ll 1$, we can assume that $\underline{E}_z$ and $\underline{H}_z$ are represented in the form

$$\underline{E}_z(\omega, \gamma) = \underline{E}_z^0(\omega) + \gamma\underline{E}_z^1(\omega) + \mathcal{O}(\gamma^2), \tag{15}$$

$$\underline{H}_z(\omega, \gamma) = \underline{H}_z^0(\omega) + \gamma\underline{H}_z^1(\omega) + \mathcal{O}(\gamma^2). \tag{16}$$

If we neglect all terms of order $\mathcal{O}(\gamma^2)$, the boundary condition in equation (9) implies that equation (10) is first order in γ.

Now, if $\gamma \gg 1$, $\underline{E}_z$ and $\underline{H}_z$ are represented in the form

$$\underline{E}_z(\omega, \gamma) = \gamma^{-1}\underline{E}_z^1(\omega) + \gamma^{-2}\underline{E}_z^2(\omega) + \mathcal{O}(\gamma^{-3}), \tag{17}$$

$$\underline{H}_z(\omega, \gamma) = \gamma^{-1}\underline{H}_z^1(\omega) + \gamma^{-2}\underline{H}_z^2(\omega) + \mathcal{O}(\gamma^{-3}). \tag{18}$$

If we neglect all terms of order $\mathcal{O}(\gamma^{-3})$, the boundary condition in equation (9) implies

$$\left.\frac{\partial \underline{E}_z}{\partial \tau}\right|_{\partial C} = 0$$

to order γ^{-2} which brings a trivial result. What saves us is the boundary condition in equation (8) which in any case (for every $\gamma > 0$) ensures us that equation (9) leads to equation (10)!

But that is not all, we should also note that equations (8) and (10) hold both for $(\underline{E}_z, \underline{H}_z)$ and (E_z, H_z) due to the definition (2) and the fact that $\mathbf{n}$ is perpendicular to the z-axis.

2.1.2 Recast of the problem into longitudinal components. Finally, the boundary value problem splits in two fundamental polarisations, namely T.E. polarisation

$$(\Delta + k_\perp^2)H_z = 0, \quad \text{outside the metal,} \tag{19}$$

$$\left.\frac{\partial H_z}{\partial n}\right|_{\partial C} = 0, \quad \text{on the boundary of each cylinder} \tag{20}$$

and T.M. polarisation

$$(\Delta + k_\perp^2)E_z = 0, \quad \text{outside the metal,} \tag{21}$$

$$E_z|_{\partial C} = 0, \quad \text{on the boundary of each cylinder} \tag{22}$$

with $k_\perp = \sqrt{\omega^2\varepsilon_0\varepsilon_{\mathrm{r}}\mu_0\mu_{\mathrm{r}} - \gamma^2}$. It should be noted that ω should be greater than the so-called cut-off frequency $\omega_c = \gamma/\sqrt{\varepsilon_0\varepsilon_{\mathrm{r}}\mu_0\mu_{\mathrm{r}}}$ to ensure a real (positive) transverse wave-number $k_\perp$.

2.1.3 The Bloch conditions: from boundary value to spectral problems. For the spectral problem to be completely specified, we further assume that the longitudinal part V_z of the vector field $\mathbf{V}$ satisfies an appropriate quasi-periodicity condition known as the Floquet-Bloch condition

$$\mathbf{V}(\mathbf{r} + \mathbf{R_p}) = \mathbf{V}(\mathbf{r})\mathrm{e}^{i\mathbf{k}\cdot\mathbf{R_p}}, \tag{23}$$

where $\mathbf{k}$ is known as the Bloch wave-vector and $\mathbf{R_p} = p_1\mathbf{a}^1 + p_2\mathbf{a}^2$ is the vector attached to the nodes $\mathbf{p} = (p_1, p_2) \in \mathbf{Z}^2$ of the lattice of translations vectors $\mathbf{a}^1$ and $\mathbf{a}^2$, which form the basis for the lattice as a whole (Figure 1).

2.1.4 An orphan: the TEM case. Most of the studies dealing with the infinite array of metallic cylinders light-heartedly skip the important issue of the most peculiar class of so-called transverse electric-magnetic waves, except in the noticeable work of McPhedran *et al.* (1997). These modes are of the form (2) but otherwise they should also fullfil the restrictive condition

$$E_z = 0, \quad H_z = 0, \tag{24}$$

within the PCF. Let us check whether or not such a constraint is achievable.

Firstly, it follows from either equation (5) or (6) together with equation (24) that the propagation constant γ has to be equal to the wavenumber $k = \omega\sqrt{\varepsilon_0\varepsilon_{\mathrm{r}}\mu_0\mu_{\mathrm{r}}}$ if we want non zero $\mathbf{E}_t$ or $\mathbf{H}_t$. Hence, in the transverse case ($\gamma = 0$) TEM modes would only stand a chance to exist in the static limit.

Secondly, plugging $\underline{\mathbf{E}} = \mathbf{E}_t\,\mathrm{e}^{\mathrm{i}\gamma z}$ and $\underline{\mathbf{H}} = \mathbf{H}_t\mathrm{e}^{\mathrm{i}\gamma z}$ in equation (1), we find

$$\operatorname{curl}\underline{\mathbf{E}} = (\operatorname{curl}\mathbf{E}_t + \mathrm{i}\gamma\mathbf{e}_z \times \mathbf{E}_t)\mathrm{e}^{\mathrm{i}\gamma z} = \mathrm{i}\omega\mu_0\mu_{\mathrm{r}}\underline{\mathbf{H}}_t \tag{25}$$

The second equality in equation (25) holds true if and only if $\operatorname{curl}\mathbf{E}_t = 0$ in the sense of distributions, since both $\mathbf{H}_t$ and $\mathbf{e}_z \times \mathbf{E}_t$ are orthogonal to $\mathbf{e}_z$ unlike $\operatorname{curl}\mathbf{E}_t$ which is colinear to $\mathbf{e}_z$. Owing to equation (20), (22) and (24) $\mathbf{E}_t|_{\partial C}$ is also null. Hence, $\mathbf{E}_t$ is irrotational in classical sense and it therefore derives from a potential W_{TE}:

$$\mathbf{E}_t = -\mathrm{grad}\, W_{\mathrm{TE}}, \quad \text{in } Y\backslash\bar{C} \tag{26}$$

A similar reasoning can be led for $\mathbf{H}_t$ but we notice that only its normal derivative will vanish of the boundary C and therefore it is only irrotational in distributional sense (due to the existence of a current $\mathbf{n} \times \mathbf{H}_t$ on ∂C). Now, from equations (1) and (26), we have

$$\Delta W_{\mathrm{TE}} = \mathrm{div}(\mathrm{grad}\, W_{\mathrm{TE}}) = -\mathrm{div}\, \mathbf{E}_t = 0, \quad \text{in } Y\backslash\bar{C}, \tag{27}$$

both in distributional and classical sense (due to Dirichlet boundary conditions on ∂C).

At this stage, we remark that $Y\backslash\bar{C}$ is a not simply connected set (it would be simply connected if we would consider an array of dielectric cylinders). Therefore, equation (27) does not imply that the (quasi-periodic) potential W_{TE} be constant over the basic cell (which would lead to $\mathbf{E}_t = 0$). It is important to note also that the potential W_{TE} is bound to take a value W^i_{TE} on the boundary ∂C in the ith basic cell within the array which is distinct from its value W^j_{TE} on the boundary ∂C in the jth basic cell if $i \neq j$. We are therefore in presence of a quasi-periodic potential solution of a problem of electrostatic type. The analysis of the quasi-static limit led by Poulton *et al.* (2001) reveals the following relationships between on the one hand, the dynamic field quantities H_z and our electrostatic potential W_{TE}:

$$H_z \sim 1 + k_{0,\perp} W_{\mathrm{TE}}, \tag{28}$$

where

$$k_{0,\perp} \sim \omega\left[\varepsilon_0\varepsilon_{\mathrm{r}}\mu_0\mu_{\mathrm{r}} - \frac{1}{2}\left(\frac{\gamma}{\omega}\right)^2\right]$$

is the quasi-static wavenumber.

On the other hand, in the T.M. case it is shown in Poulton *et al.* (2001) that

$$E_z \sim 1 + k_{0,\perp} W_{\mathrm{TM}}, \tag{29}$$

where

$$\Delta W_{\mathrm{TM}} = 0, \quad \text{in } Y\backslash\bar{C}, \tag{30}$$

which is supplied with Bloch conditions on opposite sides of Y and some Neumann boundary condition $\partial W_{\mathrm{TM}}/\partial n = 0$ on the boundary ∂C.

Remarkedly, the electrostatic solutions $W_{\mathrm{TE},x}$ and $W_{\mathrm{TM},y}$ (repectively corresponding to fields directed along the x- and y-axes) form a Cauchy-Riemann pair and are related by Keller's theorem (Keller, 1964) according to $\mathrm{grad}\, W_{\mathrm{TE},x} = -\mathbf{e}_z \times \mathrm{grad}[R(\pi/2) W_{\mathrm{TM},y}]$, where $R(\varphi)$ denotes a rotation by an angle φ. From this, it can be deduced that, in the quasi-static limit, the transverse field modes $\mathbf{E}_t$ and $\mathbf{H}_t$ (which are respectively proportional to $\mathbf{e}_z \times \mathrm{grad}\, W_{\mathrm{TE}}$ and $\mathrm{grad}\, W_{\mathrm{TM}}$) form a linearly independent (orthogonal) pair of TEM modes, identical up to a rotation through angle $\pi/2$.

Actually, for a square array of circular metallic inclusions, it can be shown that the potential W_{TE} solution of equation (27) can be expressed as

$$W_{\mathrm{TE}} = A \ln(r/r_{\mathrm{c}}) + B, \tag{31}$$

where A and B are some integration constants deduced from the boundary conditions (quasi-periodicity of W on opposite sides of the basic cell Y as well as vanishing normal derivative on the boundary $r = r_{\mathrm{c}}$).

2.2 Multipole expansions and boundary conditions

We expand the longitudinal fields E_z and H_z in terms of Bessel functions between the inclusions:

$$\xi_z = \sum_{m=-\infty}^{+\infty} \left[a_m^{\xi} J_m(k_{\perp} r) \mathrm{e}^{\mathrm{i}m\Phi} + b_m^{\xi} Y_m(k_{\perp} r) \right] \mathrm{e}^{\mathrm{i}m\Phi}, \quad \forall \xi \in \{E, H\}, \tag{32}$$

where r and Φ denote the radial and angular variables of E_z and H_z.

We derive from equations (20), (22) and (32) that the multipole coefficients a_m^{ξ} and b_m^{ξ} are linked by the boundary conditions

$$a_m^E = -\frac{Y_m(k_{\perp} r_{\mathrm{c}})}{J_m(k_{\perp} r_{\mathrm{c}})} b_m^E, \quad a_m^H = -\frac{Y'_m(k_{\perp} r_{\mathrm{c}})}{J'_m(k_{\perp} r_{\mathrm{c}})} b_m^H. \tag{33}$$

2.3 Quasi-periodic Green's function and Lattice sums

Another relation between the multipole coefficients can be gained by examining the structure of the lattice. This amounts to taking into account the quasi-periodicity of the transverse field (electric or magnetic), as stated by equation (23). Therefore, we introduce a two-dimensional quasi-periodic Green's function $G_{\mathbf{k}}$ which satisfies

$$(\Delta + k_{\perp}^2) G_{\mathbf{k}}(\mathbf{r}, \mathbf{r}') = \sum_{\mathbf{p} \in \mathbf{Z}^2} \delta(\mathbf{r} - \mathbf{r}' - \mathbf{R}_{\mathbf{p}}) \mathrm{e}^{\mathrm{i}\mathbf{k} \cdot \mathbf{R}_{\mathbf{p}}}, \tag{34}$$

where the sum stretches over the entire array of nodes $\mathbf{p}$ (locations of the centers of the cavities).

Using the Graf's addition theorem for Bessel functions, one can derive the representation of the Green's function $G_{\mathbf{k}}$ as a Neumann series within the central unit cell (Movchan *et al.*, 2002)

$$G_{\mathbf{k}}(\mathbf{r}, \mathbf{r}') = \frac{1}{4} Y_0(k_{\perp} |\mathbf{r} - \mathbf{r}'|) + \frac{1}{4} \sum_{l=-\infty}^{+\infty} S_l^Y(k_{\perp}, \mathbf{k}) J_l(k_{\perp} |\mathbf{r} - \mathbf{r}'|) \mathrm{e}^{-\mathrm{i}l\theta}, \tag{35}$$

where the dynamic lattice sums S_l^Y are defined by

$$S_l^Y(k_{\perp}, \mathbf{k}) = \sum_{\mathbf{p} \in \mathbf{Z}^2 \setminus (0,0)} Y_l(k_{\perp} |\mathbf{R}_{\mathbf{p}}|) \mathrm{e}^{\mathrm{i}\Phi_{\mathbf{p}} l + \mathrm{i}\mathbf{k} \cdot \mathbf{R}_{\mathbf{p}}}, \tag{36}$$

and $\Phi_{\mathbf{p}} = \arg(\mathbf{R}_{\mathbf{p}})$, $\theta = \arg(\mathbf{r} - \mathbf{r}')$. As this series is slowly convergent, we shall use the following formula, derived by McPhedran and Dawes (1992) to calculate the lattice sums

$$S_l^Y(k_\perp,\mathbf{k})J_{l+q}(k_\perp z) = -\delta_{l0}\left[Y_q(k_\perp z)+\frac{1}{\pi}\sum_{n=1}^{q}\frac{(q-n)!}{(n-1)!}\left(\frac{2}{k_\perp z}\right)^{q-2n+2}\right] - \frac{4i^l}{A}\sum_{\mathbf{p}\in\mathbf{Z}^2}\left(\frac{k_\perp}{|\mathbf{Q}_\mathbf{p}|}\right)^q\frac{J_{l+q}(|\mathbf{Q}_\mathbf{p}|z)\mathrm{e}^{\mathrm{i}l\theta_\mathbf{p}}}{|\mathbf{Q}_\mathbf{p}|^2-(k_\perp)^2}, \tag{37}$$

where $A = |\mathbf{a}_1 \times \mathbf{a}_2|$ denotes the area of the unit cell. For analytic purposes, it is convenient to use the values $\mathbf{p} = \mathbf{0}$, $z = \sqrt{A} = d$ (remember that d is the pitch of the direct array). The above formula is characterized by faster convergence via integration with respect to z. The integer parameter q gives the number of times the convergence of the lattice sums has been accelerated through integration and is thus called convergence acceleration index. The reciprocal unit cell is defined by the vectors[1]

$$\mathbf{a}^1 = 2\pi\frac{\mathbf{a}_2 \times \mathbf{e}_z}{A}, \quad \mathbf{a}^2 = 2\pi\frac{\mathbf{e}_z \times \mathbf{a}_1}{A}, \tag{38}$$

with the reciprocal lattice vectors

$$\mathbf{Q}_\mathbf{p} = p_1\mathbf{a}^1 + p_2\mathbf{a}^2 + \mathbf{k}, \quad \theta_\mathbf{p} = \arg(\mathbf{Q}_\mathbf{p}). \tag{39}$$

The lattice sums satisfy the identity

$$S_{-l}^Y(k_\perp,\mathbf{k}) = \overline{S_l^Y}(k_\perp,\mathbf{k}), \tag{40}$$

and hence it is sufficient to calculate them only for nonnegative values of l (here $\overline{\cdot}$ denotes the complex conjugate quantity).

2.4 Rayleigh identities and Rayleigh system

In equating the nonsingular field in the central unit cell with the superposed effect of all the other (singular) sources in the array, we obtain the following Rayleigh identities (Guenneau *et al.*, 2003) for every ξ in $\{E, K\}$,

$$a_l^\xi = \sum_{m=-\infty}^{+\infty}(-1)^{l+m}S_{m-l}^Y(k_\perp,\mathbf{k})b_m^\xi, \tag{41}$$

where the lattice sums $S_{m-l}^Y(k_\perp,\mathbf{k})$ provide the contribution of the lattice (Guenneau *et al.*, 2003). These two sets of equations are linked via boundary conditions equation (33) expressed in terms of multipoles and lead to the Rayleigh system (Guenneau *et al.*, 2003)

$$M_l^{\xi\xi}(k_\perp)b_l^\xi + \sum_{m=-\infty}^{+\infty}(-1)^{l+m}S_{m-l}^Y(k_\perp,\mathbf{k})b_m^\xi = 0, \quad \forall\xi\in\{E,H\}, \tag{42}$$

where $M_l^{EE} = Y_l(k_\perp r_\mathrm{c})/J_l(k_\perp r_\mathrm{c})$ and $M_l^{HH} = Y_l'(k_\perp r_\mathrm{c})/J_l'(k_\perp r_\mathrm{c})$.

This algebraic system can be written as $\mathbf{RB} = (\mathbf{M}+\mathbf{S})\mathbf{B}$ where $\mathbf{R}(k_\perp,\mathbf{k})$ is the so-called Rayleigh matrix. It possesses standard properties of the Rayleigh system: it neatly separates the effect of the boundary conditions (the $M_l^{\xi\xi}$) from that of the geometry of the lattice (the S_l^Y), so that quite wide-ranging results can be gained without specifying particular compositions of voids. It is also remarked that the coefficients $M_l^{\xi\xi}$ are real which makes $\mathbf{R}$ Hermitian due to equation (40). This is consistant with the fact that we consider lossless media.

2.5 Normalisation of the Rayleigh system

From the definition of the boundary terms $M_n^{\xi\xi}$, one can show that, as $n \to +\infty$,

$$M_n^{\xi\xi} = \mathcal{O}\left(\Gamma^2(n) n \left(\frac{1}{2} k_\perp r_{\mathrm{c}}\right)^{-2n}\right) \tag{43}$$

Similarly, one can show that, for the lattice sums,

$$S_l^Y(k_\perp, \mathbf{k}) = \mathcal{O}\left(\Gamma(l) \left(\frac{1}{2} k_\perp d\right)^{-l}\right), \quad \text{as } l \to +\infty. \tag{44}$$

This causes numerical difficulties when

$$\frac{k_\perp d}{2} \ll 1,$$

since the off-diagonal terms increase extremely rapidly with index l:

$$z_l^\xi + \sum_{m=-\infty}^{+\infty} D_{lm}^{\xi\xi} z_m^\xi = 0, \quad \forall \xi \in \{E, H\}, \tag{45}$$

where

$$z_l^\xi = b_l^\xi \sqrt{|M_l^{\xi\xi}|}$$

and

$$D_{lm}^{\xi\xi} = \frac{\operatorname{sign}\left(M_l^{\xi\xi}\right)}{\sqrt{\left|M_l^{\xi\xi}\right| |M_m|}} (-1)^{l+m} S_{m-l}^Y(k_\perp, \mathbf{k}) \text{ for } \xi \in \{E, H\}.$$

Using asymptotics of Bessel functions for large l and a fixed m, we get:

$$D_{lm}^{\xi\xi} = \mathcal{O}\left(\frac{(k_\perp r_{\mathrm{c}})^l}{\sqrt{\Gamma^2(l) l}} \frac{\Gamma(l-m)}{(k_\perp d)^l}\right) = \mathcal{O}\left(\frac{1}{\sqrt{l}} \left(\frac{r_{\mathrm{c}}}{d}\right)^l \frac{(l-m)!}{l!}\right). \tag{46}$$

Therefore, if m is fixed as $l \to +\infty$,

$$D_{lm}^{\xi\xi} = \mathcal{O}\left(\frac{l^{-m}}{\sqrt{l}} \left(\frac{r_{\mathrm{c}}}{\mathrm{d}}\right)^l\right). \tag{47}$$

With l and m playing a symmetric role, it is a straightforward matter to show that, if l is fixed as $m \to +\infty$,

$$D_{lm}^{\xi\xi} = \mathcal{O}\left(\frac{m^{-l}}{\sqrt{m}} \left(\frac{r_{\mathrm{c}}}{\mathrm{d}}\right)^m\right). \tag{48}$$

Owing to this normalisation, the elements in the Rayleigh system decay exponentially away from the main diagonal, giving rise to higher multipole coefficients that decay similarly quickly. The frequency of vibration ω can be calculated for any given value of the Bloch vector $\mathbf{k}$ by annulling the determinant of the system $\det(\mathbf{R}(k_\perp, \mathbf{k}))$ at fixed conical parameter γ. In this way one can specify the dispersion relation for high frequencies by taking some high-order truncations (Guenneau *et al.*, 2003). Also, in the dilute composite limit, one can truncate the system to the dipole order ($l, m \in \{-1, 0, 1\}$) to get some effective properties in the long-wavelength limit.

3. Finite element method

3.1 Operator formulation

The following operators are defined:

$$\begin{cases} \mathrm{grad}_\gamma\, \varphi(x,y) = \mathrm{grad}\,(\varphi(x,y)\mathrm{e}^{\mathrm{i}\gamma z})\mathrm{e}^{-\mathrm{i}\gamma z} \\ \mathrm{curl}_\gamma\, \mathbf{V}(x,y) = \mathrm{curl}\,(\mathbf{V}(x,y)\mathrm{e}^{\mathrm{i}\gamma z})\mathrm{e}^{-\mathrm{i}\gamma z} \\ \mathrm{div}_\gamma\, \mathbf{V}(x,y) = \mathrm{div}\,(\mathbf{V}(x,y)\mathrm{e}^{\mathrm{i}\gamma z})\mathrm{e}^{-\mathrm{i}\gamma z} \end{cases} \tag{49}$$

Their domains are classes of $(\mathbf{k}, Y)$-periodic (i.e. satisfying equation (23)) square integrable functions with values in $\mathbb{C}$ (for grad_γ) or $\mathbb{C}^3$ (for div_γ and curl_γ) which we denote as $L^2_\sharp(\mathbf{k}, Y)$ and $[L^2_\sharp(\mathbf{k}, Y)]^3$.

We say that the couple $(\mathbf{E_k}, \mathbf{H_k})$ associated with the Bloch vector $\mathbf{k}$ is an electromagnetic Bloch wave if $(\mathbf{E_k}, \mathbf{H_k})$ verifies equation (1) and is of the form specified by equation (2) with

$$\begin{cases} (\gamma, \omega, \mathbf{k}) \in \mathbb{R}_+ \times \mathbb{R}_+ \times \mathbb{R}^2 \\ (\mathbf{E_k}, \mathbf{H_k}) \neq (\mathbf{0}, \mathbf{0}) \\ \mathbf{E_k}, \mathbf{H_k} \in [L^2_\sharp(\mathbf{k}, Y)]^3. \end{cases} \tag{50}$$

The solutions $(\mathbf{E_k}, \mathbf{H_k})$ of the spectral problem defined by equations (1), (2) and (23) hence satisfy

$$\begin{cases} \mathrm{curl}_\gamma\, \mathbf{H_k} = -\mathrm{i}\omega\varepsilon_0\varepsilon_\mathrm{r}(x,y)\mathbf{E_k} \\ \mathrm{curl}_\gamma\, \mathbf{E_k} = \mathrm{i}\omega\mu_0\mu_\mathrm{r}(x,y)\mathbf{H_k} \end{cases} \tag{51}$$

with ε_r and μ_r defined as in equation (1). Note that $\mathrm{curl}_\gamma\,\mathrm{grad}_\gamma\varphi = 0$ for smooth scalar fields φ and $\mathrm{div}_\gamma\mathrm{curl}_\gamma\,\mathbf{U} = 0$ for smooth vector fields $\mathbf{U}$.

Since we consider a (perfectly conducting) metallic inclusion C in the basic cell Y, the presence of metallic walls introduces unknown currents equal to the tangential component of the magnetic field. Therefore, we choose an electric field formulation to deal with simple boundary conditions (the tangential component of the electric field is null on metallic walls). Eliminating the magnetic field from equation (51), one finds:

$$\frac{1}{\varepsilon_r}\,\mathrm{curl}_\gamma\,\frac{1}{\mu_\mathrm{r}}\mathrm{curl}_\gamma\,\mathbf{E_k} = k_0^2\mathbf{E_k} \tag{52}$$

where $k_0^2 = \varepsilon_o\mu_o\omega^2 = \omega^2/c^2$, c is the celerity of light in vacuum.

3.2 Weak formulation

The numerical formulation is given by the following residue (Guenneau *et al.*, 2002)

$$\begin{aligned}\mathscr{R}(\gamma;\mathbf{E}_{\mathbf{k}},\mathbf{E}'_{\mathbf{k}}) = \int_{Y\setminus\bar{C}} \mu_r^{-1}(&\mathrm{curl}_t\,\mathbf{E}_{t,\mathbf{k}}\cdot\mathrm{curl}_t\,\overline{\mathbf{E}}'_{t,\mathbf{k}} + \mathrm{grad}_t\,E_{l,\mathbf{k}}\cdot\mathrm{grad}_t\,\overline{E}'_{l,\mathbf{k}} \\ &- \mathrm{i}\,\gamma\mathbf{E}_{t,\mathbf{k}}\cdot\mathrm{grad}_t\,\overline{E}'_{l,\mathbf{k}} + i\gamma\,\mathrm{grad}_t\,E_{l,\mathbf{k}}\cdot\overline{\mathbf{E}}'_{t,\mathbf{k}} + \gamma^2\,\mathbf{E}_{t,\mathbf{k}}\cdot\overline{\mathbf{E}}'_{t,\mathbf{k}})\mathrm{d}x\,\mathrm{d}y \\ &- k_0^2\int_{Y\setminus\bar{C}} \varepsilon_{\mathrm{r}}(\mathbf{E}_{t,\mathbf{k}}\cdot\overline{\mathbf{E}}'_{t,\mathbf{k}} + E_{l,\mathbf{k}}\,\overline{E}'_{l,\mathbf{k}})\mathrm{d}x\,\mathrm{d}y.\end{aligned} \tag{53}$$

The weight vector field $\mathbf{E}'_{\mathbf{k}}$ is chosen in the same discrete Hilbert space as the unknown field $\mathbf{E}_{\mathbf{k}}$, i.e. a space with finite dimension equal to the number of numerical parameters to be determined. This formulation involves both a transverse field $\mathbf{E}_{t,\mathbf{k}}$ in the section of the guide and a longitudinal field $E_{l,\mathbf{k}}$ along its axis such that:

$$\mathbf{E}_{\mathbf{k}} = \mathbf{E}_{t,\mathbf{k}} + E_{l,\mathbf{k}}\mathbf{e}_z. \tag{54}$$

3.3 Discrete weak form

The section of the guide is meshed with triangles and Whitney finite elements (Bossavit, 1990) are used, i.e. edge elements for the transverse field and node elements for the longitudinal field:

$$\mathbf{E}_{\mathbf{k}} = \begin{cases} \mathbf{E}_{t,\mathbf{k}} = \sum\limits_{\text{edges}\,i} \alpha_i \mathbf{w}_i^{\mathbf{e}}(x,y) \\ E_{l,\mathbf{k}} = \sum\limits_{\text{nodes}\,j} \gamma_j w_j^n(x,y) \end{cases} \tag{55}$$

where α_i denotes the line integral of the transverse component $\mathbf{E}_{t,\mathbf{k}}$ on the edges, and γ_j denotes the line integral of the longitudinal component $E_{l,\mathbf{k}}$ along one unit of length of the axis of the guide (what is equivalent to a nodal value). Besides, $w_j^n(x,y) = \lambda_j(x,y)$ and $\mathbf{w}_i^{\mathbf{e}}(x,y) = \lambda_k(x,y)\mathrm{grad}\,\lambda_l(x,y) - \lambda_l(x,y)\mathrm{grad}\,\lambda_k(x,y)$ (where λ_j is the barycentric coordinate of node j and the edge i has nodes k and l as extremities) are, respectively, the basis functions of Whitney 1-forms (edge element discrete space W^1) and Whitney 0-forms (nodal element discrete space W^0).

Moreover, the use of the Whitney elements solves the spurious mode problem in a way similar to the one of the cavities (Bossavit, 1990).

As the eigenvalue problem involves, on the one side, k_0^2 only and, on the other side, both γ and γ^2, a more classical (though generalized) eigenvalue problem is obtained by fixing $\gamma \in \mathbb{R}_+$ (rather than k_0^2) for a given Bloch vector $\mathbf{k}$ and looking for $(k_0^2, \mathbf{E}_{\mathbf{k}})$ satisfying the discrete spectral problem.

3.4 Implementation of Bloch conditions

In order to find Bloch modes with the finite element method, some changes have to be performed with respect to classical boundary value problems that will be named Bloch conditions (Nicolet *et al.*, 2004). To avoid tedious notations, a simpler case is considered here: a scalar field $U_{\mathbf{k}}(x, y)$ (time and z dependence are irrelevant here and there is no particular problem to extend this method to vector quantities and edge elements) on the square cell Y with Bloch conditions relating the left and the right side. The set of nodes is separated in three subsets: the nodes on the left side, i.e. with $x = 0$, corresponding to the column array of unknowns $\mathbf{u_l}$, the nodes on the right side, i.e. with $x = 1$, corresponding to the column array of unknowns $\mathbf{u_r}$, and the internal nodes, i.e. with $x \in [0, 1]$, corresponding to the column array of unknowns $\mathbf{u}$. One has the following structure for the matrix problem (corresponding in fact to natural boundary conditions, i.e. Neumann homogeneous boundary conditions):

$$\mathbf{A}\begin{pmatrix}\mathbf{u}\\ \mathbf{u_l}\\ \mathbf{u_r}\end{pmatrix} = \mathbf{b} \tag{56}$$

where $\mathbf{A}$ is the (square Hermitian) matrix of the system and $\mathbf{b}$ the second member column array. The solution to be approximated by the numerical method is a Bloch function $U_{\mathbf{k}}(x,y) = U(x,y)\mathrm{e}^{\mathrm{i}(k_x x + k_y y)}$ with U Y-periodic and in particular $U(x+1,y) = U(x,y)$. Therefore, the relation between the left and the right side is:

$$U_{\mathbf{k}}(1,y) = U(1,y)\mathrm{e}^{\mathrm{i}(k_x + k_y y)} = U_{\mathbf{k}}(0,y)\mathrm{e}^{\mathrm{i}k_x} \Rightarrow \mathbf{u_r} = \mathbf{u_l}\mathrm{e}^{\mathrm{i}k_x} \tag{57}$$

Therefore, the set of unknowns can be expressed in function of the reduced set $\mathbf{u}$ and $\mathbf{u_l}$ due to:

$$\begin{pmatrix}\mathbf{u}\\ \mathbf{u_l}\\ \mathbf{u_r}\end{pmatrix} = \mathbf{P}\begin{pmatrix}\mathbf{u}\\ \mathbf{u_l}\end{pmatrix} \quad \text{with } \mathbf{P} = \begin{pmatrix}\mathbf{1} & \mathbf{0}\\ \mathbf{0} & \mathbf{1}\\ \mathbf{0} & \mathbf{1}\mathrm{e}^{\mathrm{i}k_x}\end{pmatrix} \tag{58}$$

where $\mathbf{1}$ and $\mathbf{0}$ are identity and null matrices, respectively, with suitable dimensions. The finite element equations related to the eliminated nodes have now to be taken into account. Owing to periodicity of the structure, the element on the left of the right side corresponds to elements on the left of the left side. Therefore their contributions (i.e. equations corresponding to $\mathbf{u_r}$) must be added to the equations corresponding to $\boldsymbol{u_l}$ with the correct phase factor, i.e. $\mathrm{e}^{-\mathrm{i}k_x}$ what amounts to multiplying the system matrix by $\mathbf{P}^*$, i.e. the Hermitian conjugate of $\mathbf{P}$. Finally, the linear system to be solved is:

$$\mathbf{P}^*\mathbf{A}\mathbf{P}\begin{pmatrix}\mathbf{u}\\ \mathbf{u_l}\end{pmatrix} = \mathbf{P}^*\mathbf{b} \tag{59}$$

where it is worth noting that the system matrix is still Hermitian what is important for numerical computation. Now a generalized eigenvalue problem (with natural boundary conditions) $\mathbf{Au} = \lambda\mathbf{Bu}$ is transformed to a Bloch mode problem according to $\mathbf{P}^*\mathbf{APu}' = \lambda\mathbf{P}^*\mathbf{BPu}'$. Such problems involving large sparse Hermitian matrices can be solved using Lanczos algorithm that gives the largest eigenvalues (Nicolet *et al.*, 2004). Physically we are in fact interested in the smallest eigenvalues and therefore $\mathbf{A}^{-1}$, the inverse of $\mathbf{A}$, instead of $\mathbf{A}$ itself must be used in the iterations. Of course, the inverse is never computed explicitly but the matrix-vector products are replaced by system solutions due to a GMRES method. It is therefore obvious that the numerical efficiency of the process relies strongly on Krylov subspace techniques and the Arnoldi iteration algorithm (Nicolet *et al.*, 2004). The practical implementation of the model has been performed thanks to the GetDP software (Dular *et al.*, 1998) (Figure 2).

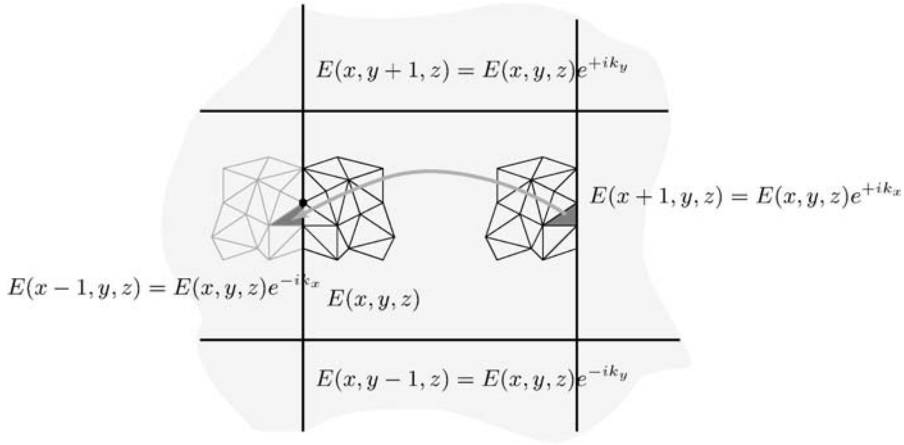
$E(x, y+1, z) = E(x, y, z)e^{+ik_y}$
$E(x+1, y, z) = E(x, y, z)e^{+ik_x}$
$E(x-1, y, z) = E(x, y, z)e^{-ik_x}$
$E(x, y, z)$
$E(x, y-1, z) = E(x, y, z)e^{-ik_y}$

Figure 2.
The Bloch theorem and virtual periodic meshing

4. Numerical results

In this section, we provide some numerical illustration for an array of channels filled with perfect metal (any metal in the microwave regime) which are drilled within a silica matrix in a densely packed configuration. We obtain some band diagrams exhibiting a nice photonic bandgap, i.e. a range of frequencies where no electromagnetic wave propagates (Figures 3 and 4). When we remove one channel, we observe some localised signal sitting right in the middle of the gap (its normalised frequency $\omega d/c = 7.95$ is independent of the Bloch vector $\mathbf{k}$). The practical application lies in futurist optical fibres (Knight *et al.*, 1999; Zolla *et al.*, 2004).

4.1 Effective properties and singular perturbation

On the dispersion diagrams of Figures 3 and 4, we can only see one acoustic band. The reason for this is that if we consider $k_\perp r_\mathrm{c} \ll 1$ in equation (42), the relationship between $k_\perp$ and $\mathbf{k}$ is supplied by

$$M_0^{\xi\xi}(k_\perp r_\mathrm{c}) + S_l^Y(k_\perp, \mathbf{k}) = 0, \quad \forall \xi \in \{E, H\}. \tag{60}$$

This equation provides the first perturbation away from the plane-wave state. It appears to hold true even for shorter wavelengths in comparison with the array spacing d, as long as $k_\perp r_\mathrm{c} \ll 1$. Now, for long-wavelengths, it is possible to obtain analytic expressions for the lattice sums S_l^Y in equation (37). We find that when $k_\perp \rightarrow |\mathbf{Q_m}|$, equation (60) can be approximated as (Guenneau *et al.*, 2003)

$$\begin{aligned} M_0^{\xi\xi}(|\mathbf{Q_m}| r_\mathrm{c}) - \frac{2}{\pi}\left[\ln\left(\frac{|\mathbf{k}|}{2}\right) + \chi_1\right] - 4\left(\chi_2 + \frac{\ln(2d)}{\pi}\right) \\ - \frac{4}{d^2}\frac{1}{|\mathbf{Q_m}|^2 - k_\perp^2}\sum_{|\mathbf{Q_n}|=|\mathbf{Q_m}|} 1 + O(||\mathbf{Q_m}| - k_\perp|) = 0, \end{aligned} \tag{61}$$

where $\chi_1 \simeq -0.318895593$, χ_2 is the Euler's constant 0.557215665 and $\mathbf{Q_m}$ is defined by equation (39). Hence, the boundary term M_0^{HH} in equation (61) becomes

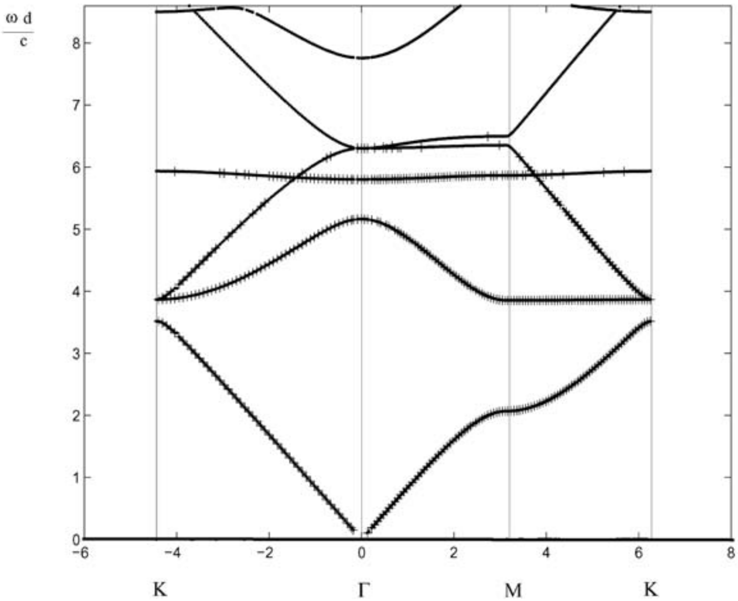

Figure 3.
The propagation constant is $\gamma = 0\mu\mathrm{m}^{-1}$ (transverse case). Band diagram for a periodic array of cavities arranged on a square lattice (radius 0.35 μm, center spacing $d = 1$ μm) in a matrix of silica ($\varepsilon_r = 1.5$)

Notes: The propagation constant is $\gamma = 0\mu\mathrm{m}^{-1}$ (transverse case). On the vertical axis we represent the normalised frequency *wd/c* and on the positive part of the horizontal axis the modulus *k* of the Bloch vector in $\mu\mathrm{m}^{-1}$ (respectively $-k$ on the negative part of the horizontal axis). Γ, *M*, *K* represent the nodes (0, 0), (0, π/*d*), (π/*d*, π/*d*) of the irreducible part of the Brillouin zone described by **k**. The crosses '+' correspond to finite element modeling whereas the dots '.' are given by the Rayleigh method

$$M_0^{HH} = \frac{Y_0'(|\mathbf{Q_m}|r_c)}{J_0'(|\mathbf{Q_m}|r_c)} = -\frac{1}{\pi}\left(\frac{2}{|\mathbf{Q_m}|r_c}\right)^2 + O((|\mathbf{Q_m}|r_c)^0), \tag{62}$$

and so this term (corresponding to TE polarised waves) dominates the perturbation in equation (61). It corresponds in fact to the first dispersion curve.

On the dispersion diagram, we can only see one acoustic band. The reason for this is that if we consider $k_\perp r_c \ll 1$ in equation (61), the boundary term M_0^{EE} becomes

$$M_0^{EE} = \frac{Y_0(|\mathbf{Q_m}|r_c)}{J_0(|\mathbf{Q_m}|r_c)} = -\frac{2}{\pi}(\ln(|\mathbf{Q_m}|r_c) + \chi_2) + O((|\mathbf{Q_m}|r_c)^2), \tag{63}$$

and so this term (corresponding to TM polarised waves) is of the same order as the contribution of lattice sums in equation (61). In this case, equation (61) becomes

$$k^2 - k_\perp^2 = \frac{2\pi}{d^2}\left(\ln\frac{r_c}{d} + C\right)^{-1}, \tag{64}$$

where $C = -2\pi\chi_1 - 2\ln 2 \simeq 1.31053292$. This corresponds in fact to the fourth dispersion curve. Also, we note that the acoustic curve $\omega(\mathbf{k})$ is quadratic in the neighbourhood of the origin in Figure 4 which is not the case in Figure 3. This can be also classified as a singular perturbation induced by the conical parameter γ. For small γ, the asymptotics of eigenfrequencies take the following form:

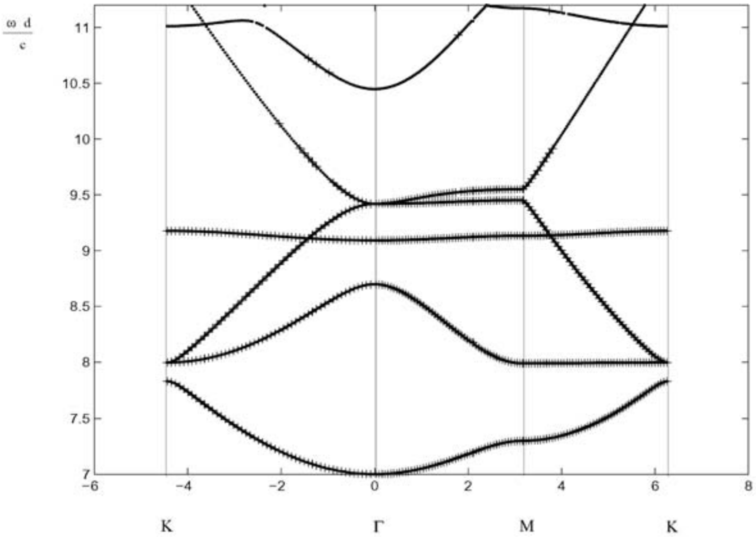

Figure 4.
The propagation constant is $\gamma = 7\mu\text{m}^{-1}$ (conical case). Band diagram for a periodic array of cavities arranged on a square lattice (radius 0.35 μm, center spacing $d=1$ μm) in a matrix of silica ($\varepsilon_r = 1.5$)

Notes: The propagation constant is $\gamma = 7\mu\text{m}^{-1}$ (conical case). On the vertical axis we represent the normalised frequency *wd/c* and on the positive part of the horizontal axis the modulus *k* of the Bloch vector in μm^{-1} (respectively $-k$ on the negative part of the horizontal axis). Γ, *M*, *K* represent the nodes (0, 0), (0, π/d), (π/d, π/d) of the irreducible part of the Brillouin zone described by **k**. The crosses '+' correspond to finite element modeling whereas the dots '.' are given by the Rayleigh method

$$\omega(\mathbf{k}, \gamma) \sim \omega_0(\mathbf{k}) + \gamma\omega_1(\mathbf{k}/\gamma), \tag{65}$$

so that the increment of the frequency may be small, whereas the (transverse) group velocity $\partial\omega/\partial k$ may change by a finite increment. This characterises the presence of noncommuting limit, namely between $\omega \rightarrow 0$ and $\gamma \rightarrow 0$, which is discussed in (Poulton *et al.*, 2004).

In transverse incidence ($\gamma = 0$) and for reasons of symmetry, it appears that in the neighbourhood of the origin $\mathbf{k} = (0, 0)$, the frequency ω is written as per:

$$\omega = v|\mathbf{k}| + \mathcal{O}(k_x, k_y), \tag{66}$$

and the effective index is given by $N^{\text{eff}} = c/v$ (see straight line going to the origin in Figure 3). But in oblique incidence ($\gamma > 0$), it is clear from Figure 4 that the effective refractive index N^{eff} is no longer given by the variation of group velocity at the origin. It is in fact connected to the notion of effective mass (second order derivatives) (Guenneau *et al.*, 2003).

4.2 Photonic band gaps for square periodic arrays

The complete gap occurs only for TE waves (since there is no acoustic band for TM waves). The second dispersion curve corresponds indeed to TE waves and it is called optical band. We observe that the group velocity can be negative in the neighbouhrood of Γ. This can be associated to a negative effective refractive index which possibly leads to newly discovered left-handed-materials (Smith *et al.*, 2004).

4.3 Localised modes associated with periodic multiple defects
As a simple illustration, we start with the removal of the central channel within a supercell containing 7×7 voids of the micro-structured fibre. We set some Bloch conditions on opposite sides of this supercell, thereby assuming some infinite extent of the PCF in the transverse plane $(x-y)$. We then observe in Figure 5 a new eigenstate

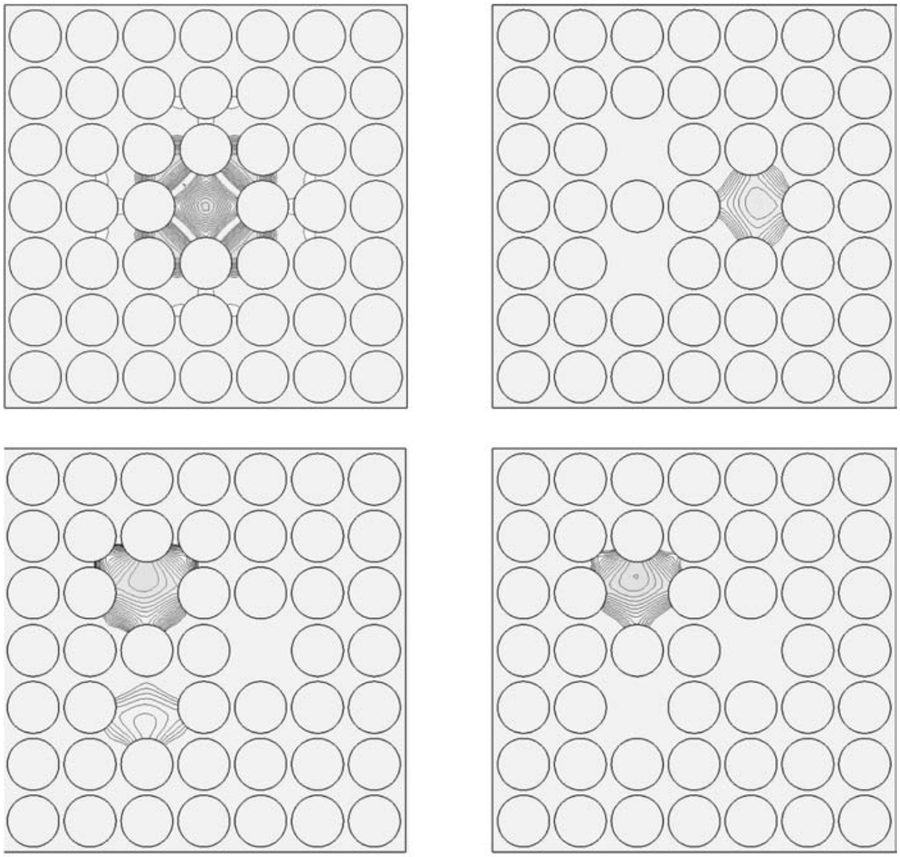

Notes: Upper-Left: Localised mode for the PCF corresponding to Figure 4, when we remove one cavity (real part of the longitudinal electric field for a null Bloch vector $E_{l,\mathbf{0}}$). The normalised frequency of this signal is $\omega d/c = 7.95$. Upper-right and lower-left (clockwise): real part of the longitudinal electric field $E_{l,\pi}$ (TM wave) for a Bloch vector $\mathbf{k} = (\pi, \pi)$ associated with the normalised eigenfrequencies $\omega d/c = 7.91$ (twofold degenerated modes) and $\omega d/c = 7.99$ for a given normalised propagation constant $\gamma d = 7.0$ and a square periodic array of pitch $d = 1\mu\text{m}$ consisting of circular cylindrical metallic cylinders of radius $r_c/d = 0.35 = 0.35$. Here, we have removed three cylinders (hence sculpting three 'high-index defects'). These frequencies remain unchanged when the normalised Bloch vector $\mathbf{k}d$ describes ΓMK, A linear combination of the aforementioned modes governs the phenomenon of 'cross-talk' between the upper-left, lower-left and right cores (Guenneau *et al.*, 2001 for detailed analysis of cross-talk between optical waveguides)

Figure 5.
Models for periodic
structures with defects

associated with an eigenfrequency sitting within the band gap of Figure 4. We note that this corresponds to a flat narrow pass-band on a corresponding dispersion diagram (not depicted since the number of dispersion curves increases dramatically with the size of the supercell) as checked numerically, this pass-band does not depend on the orientation of the Bloch vector within the first Brillouin zone ΓMK. The reader may argue that the Bloch conditions assumed on the opposite sides of the basic cell will influence the result. Even though our modelling does not contain within it all the physics at work (for instance, we cannot compute the leakage of the localised mode), we observe that removing any of the channels within the macrocell does not affect the eigenfrequency and associated eigenstate: this is a numerical evidence of the well-behaved convergence of the finite element algorithm for Bloch conditions.

We now move to the richer case of multiple defects within the macrocell. Provided that the cores are close enough, they start to talk to each other (Figure 5). This phenomenon is fairly well known in the field of optical waveguides (Guenneau *et al.*, 2001), but its extension to microstructured fibres is new and presents exciting applications in multiplexing/demultiplexing as was foreseen in the transverse case by Centeno *et al.* (1999).

5. Conclusion

In this paper, we have presented two algorithms by which one can construct some band diagrams associated with conical Bloch waves in arrays of metallic cylinders. The first one, the so-called Rayleigh method, is an analytic algorithm well suited for various asymptotic purposes such as the long-wavelength limit (homogenisation) and leads to an infinite algebraic system which is typically truncated as a 22×22 matrix. The second one, the so-called finite element method, leads to large sparse systems, but can tackle problems of more complex geometries (such as arrays of cylinders of arbitrary cross-section or models for periodic structures with defects as in Figure 5).

Note

1. We note that the dot product $\mathbf{k} \cdot \mathbf{R_p}$ in equations (23), (34) and (36) is nothing else but a duality product, hence we adopt covariant/contravariant notations for the lattice vectors in physical and reciprocal spaces.

References

Bossavit, A. (1990), "Solving Maxwell equations in a closed cavity, and the question of spurious modes", *IEEE Trans. Magn.*, Vol. 26 No. 2, p. 702.

Centeno, E., Guizal, B. and Felbacq, D. (1999), "Multiplexing and demultiplexing with photonic crystals", *J. Opt. A, Pure Appl. Opt.*, Vol. 1 No. 5, p. L10.

Dular, P., Geuzaine, C., Henrotte, F. and Legros, W. (1998), "A general environment for the treatment of discrete problems and its application to the finite element method", *IEEE Trans. Mag.*, Vol. 34 No. 5, pp. 3395, available at: www.geuz.org

Guenneau, S., Nicolet, A., Zolla, F., Geuzaine, C. and Meys, B. (2001), "A finite element formulation for spectral problems in optical fibers", *COMPEL, The International Journal For Computation and Mathematics in Electrical and Electronic Engineering*, Vol. 20 No. 1, p. 120.

Guenneau, S., Nicolet, A., Zolla, F. and Lasquellec, S. (2002), "Modeling of photonic crystal optical fibers with finite elements", *IEEE Trans. Mag.*, Vol. 38 No. 2, p. 1261.

Guenneau, S., Poulton, C.G. and Movchan, A.B. (2003), "Oblique propagation of electromagnetic and elastic waves for an array of cylindrical fibres", *Proc. Roy. Soc. Lond. A*, Vol. 459, p. 2215.

Keller, J.B. (1964), "On the conductivity of a composite medium", *J. Math. Phys.*, Vol. 5, p. 548.

Knight, J.C., Broeng, J., Birks, T.A. and Russell, P. St J. (1999), "Photonic band gap guidance in optical fibers", *Science*, Vol. 282, p. 1476.

McPhedran, R.C. and Dawes, D.H. (1992), "Lattices sums for a dynamic scattering problem", *J. Elect. Waves Appl.*, Vol. 6, p. 1327.

McPhedran, R.C., Nicorovici, N.A. and Botten, L.C. (1997), "The TEM mode and homogenization of doubly periodic structures", *J. Elect. Waves Appl.*, Vol. 11, p. 981.

Movchan, A.B., Movchan, N.V. and Poulton, C.G. (2002), *Asymptotic Models of Fields in Dilute and Densely Packed Composites*, Imperial College Press, London.

Nicolet, A., Guenneau, S., Geuzaine, C. and Zolla, F. (2004), "Modeling of electromagnetic waves in periodic media with finite elements", *Journal of Computational and Applied Mathematics*, Vol. 168 Nos 1/2, pp. 321-9.

Poulton, C.G., Guenneau, S. and Movchan, A.B. (2004), "Noncommuting limits and effective properties for oblique propagation of electromagnetic waves through an array of aligned fibres", *Phys. Rev. B*, Vol. 69 Nos 19, pp. 195112.

Poulton, C.G., Botten, L.C., McPhedran, R.C., Nicorovici, N.A. and Movchan, A.B. (2001), "Noncommuting limits in electromagnetic scattering: Asymptotic analysis for an array of highly conducting inclusions", *SIAM J. Appl. Math.*, Vol. 61, p. 1706.

Smith, D.R., Pendry, J.B., and Wiltshire, C.K. (2004), *Metamaterials and Negative Refractive Index Science*, Vol. 305, p. 788.

Zolla, F., Renversez, G., Nicolet, A., Kuhlmey, B., Guenneau, S. and Felbacq, D. (2004), *Foundations of Photonic Crystal Fibres*, Imperial College Press, London.

Further reading

Guenneau, S., Lasquellec, S., Nicolet, A. and Zolla, F. (2002), "Design of photonic band gap optical fibers using finite elements", *COMPEL, The International Journal For Computation and Mathematics in Electrical and Electronic Engineering*, Vol. 21 No. 4, p. 534.

White, T.P., Botten, L.C., McPhedran, R.C. and de Sterke, C.M. (2003), "Ultracompact resonant filters in photonic crystals", *Optics Letters*, Vol. 28, p. 2452.

The Emerald Research Register for this journal is available at
www.emeraldinsight.com/researchregister

The current issue and full text archive of this journal is available at
www.emeraldinsight.com/0332-1649.htm

The Newton-Raphson method for solving non-linear and anisotropic time-harmonic problems

H. Vande Sande
Flanders' Mechatronics Technology Centre, Heverlee, Belgium
F. Henrotte and K. Hameyer
Rheinisch-Westfälische Technische Hochschule, Aachen (RWTH Aachen)
Institut für Elektrische Maschinen (IEM), Aachen, Germany

Keywords *Modelling, Magnetic fields, Newton-Raphson method*

Abstract *This paper discusses the use of a complex-valued reluctivity tensor for modelling non-linear, anisotropic and hysteretic materials in a time-harmonic finite element context. It is shown how these problems can be solved by the Newton-Raphson method. The method is applied for the simulation of the magnetic field distribution in a three-phase transformer.*

1. Time-harmonic finite element method

The time-harmonic finite element method allows to simulate the steady-state behaviour of devices that are excited by sinusoidally varying currents. The governing equation of a two-dimensional time-harmonic problem is

$$\nabla\cdot(\nu'\nabla\tilde{A}) - j\sigma\omega\tilde{A} = -\tilde{J}, \tag{1}$$

where

$$\nu' = \begin{pmatrix} \nu_{yy} & -\nu_{yx} \\ -\nu_{xy} & \nu_{xx} \end{pmatrix} \tag{2}$$

is a matrix containing the entries of the reluctivity tensor $\underset{\sim}{\nu}$ [Am/Vs], σ the electric conductivity [A/Vm], ω the pulsation frequency [rad/s], $\tilde{A}$ the z-component of the magnetic vector potential [Vs/m] and $\tilde{J}$ the z-component of the applied current sources [A/m^2]. $\tilde{A}$ and $\tilde{J}$ are phasors and are represented by complex numbers. The instantaneous value of the vector potential in time-domain is determined by

$$\vec{A}(t) = \Re\{\tilde{A}e^{j\omega t}\}. \tag{3}$$

The piecewise continuous approximation of the magnetic vector potential over the finite element mesh writes

$$\tilde{A}(x,y) = \sum_{i=1}^{n}\tilde{A}_i\varphi_i(x,y), \tag{4}$$

COMPEL: The International Journal for Computation and Mathematics in Electrical and Electronic Engineering
Vol. 23 No. 4, 2004
pp. 950-958
© Emerald Group Publishing Limited
0332-1649
DOI 10.1108/03321640410553373

The authors are grateful to the Belgian "Fonds door Wetenschappelijk Onderzoek Vlaanderen" (project G.0427.98) and the Belgian Ministry of Scientific Research (IUAP No. P5/34).

where n is the number of nodes in the mesh and φ_i is the shape function in node i of the mesh. After applying the Galerkin approach, one finally ends up with a system of algebraic equations:

$$\tilde{\mathbf{r}}(\tilde{\mathbf{A}}) = (\mathbf{K}(\tilde{\mathbf{A}}) + j\mathbf{L})\tilde{\mathbf{A}} - \tilde{\mathbf{T}} = \mathbf{0}, \tag{5}$$

where $\tilde{\mathbf{A}}$ is the solution vector, $\tilde{\mathbf{T}}$ the source vector, $\tilde{\mathbf{r}}$ the residual vector, $\mathbf{K}$ the stiffness matrix and $\mathbf{L}$ the eddy-current matrix. The non-linearity of the problem is due to the dependency of $\mathbf{K}$ on $\tilde{\mathbf{A}}$, via the reluctivity tensor.

2. Reluctivity tensor

In a time-harmonic context, non-linear, anisotropic and hysteretic behaviour can be modelled by a complex-valued reluctivity tensor (Birkfeld, 1997, 1998). This complex-valued tensor representation is a generalisation of the complex-valued reluctivity scalar used in Lederer and Kost (1998) and Niemenmaa (1988). If ν is considered in its principal coordinate system (Nye, 1985), it is a diagonal tensor whose entries equal ν_{rd} and ν_{td}, respectively[1]. Hence:

$$\begin{pmatrix} \tilde{H}_{\mathrm{rd}} \\ \tilde{H}_{\mathrm{td}} \end{pmatrix} = \begin{pmatrix} \nu_{\mathrm{rd}} & 0 \\ 0 & \nu_{\mathrm{td}} \end{pmatrix} \begin{pmatrix} \tilde{B}_{\mathrm{rd}} \\ \tilde{B}_{\mathrm{td}} \end{pmatrix}, \tag{6}$$

with $\vec{\tilde{H}} = \tilde{H}_{\mathrm{rd}}\vec{e}_{\mathrm{rd}} + \tilde{H}_{\mathrm{td}}\vec{e}_{\mathrm{td}}$ the field strength [A/m] and $\vec{\tilde{B}} = \tilde{B}_{\mathrm{rd}}\vec{e}_{\mathrm{rd}} + \tilde{B}_{\mathrm{td}}\vec{e}_{\mathrm{td}}$ the flux density [Vs/m^2]. Since the x and y components of $\vec{\tilde{H}}$ and $\vec{\tilde{B}}$ are phasors, $\vec{H}(t)$ and $\vec{B}(t)$ describe an elliptical locus in space.

2.1 Polar tensor representation

By representing the tensor entries in a polar form, i.e.

$$\nu_{\mathrm{rd}} = |\nu_{\mathrm{rd}}|e^{j\alpha_{\mathrm{rd}}}, \tag{7}$$

$$\nu_{\mathrm{td}} = |\nu_{\mathrm{td}}|e^{j\alpha_{\mathrm{td}}}, \tag{8}$$

it follows that

$$\nu = \begin{pmatrix} |\nu_{\mathrm{rd}}| & 0 \\ 0 & |\nu_{\mathrm{td}}| \end{pmatrix} \begin{pmatrix} e^{j\alpha_{\mathrm{rd}}} & 0 \\ 0 & e^{j\alpha_{\mathrm{td}}} \end{pmatrix}. \tag{9}$$

The moduli $|\nu_{\mathrm{rd}}|$ and $|\nu_{\mathrm{td}}|$ basically determine the anisotropic behaviour, while the arguments α_{rd} and α_{td} yield a phase lag between the field and the flux density. To illustrate the meaning of this, a rotating flux density, e.g.

$$\tilde{B}_{\mathrm{rd}} = B, \tag{10}$$

$$\tilde{B}_{\mathrm{td}} = -jB, \tag{11}$$

is applied to a linear anisotropic material for which $|\nu_{\mathrm{td}}| = 4|\nu_{\mathrm{rd}}|$. The field strength locus,

$$\vec{H}(t) = \Re\{\nu\vec{\tilde{B}}e^{j\omega t}\}, \tag{12}$$

is shown in Figure 1. The instantaneous geometric angle δ(t) between $\vec{H}(t)$ and $\vec{B}(t)$ is shown in Figure 2. These figures reveal some important properties:

- if $\alpha_{\mathrm{rd}} = \alpha_{\mathrm{td}}$, the $\vec{H}$-locus is not oblique (Figure 1);
- in general, $\vec{B}$ and $\vec{H}$ are not parallel to each other, except when $\vec{B}$ aligns with one of the principal axes of the $\vec{H}$-locus (Figure 1);
- if $\alpha_{\mathrm{rd}} = \alpha_{\mathrm{td}} = \alpha$, the direction of $\vec{H}$ depends on the value of α (Figure 1); and
- if $\alpha_{\mathrm{rd}} = \alpha_{\mathrm{td}} = 0$, the average value of δ(t) is zero. The total loss

$$P_{\mathrm{h}} = \int_{\omega t=0}^{2\pi} \vec{H}\,\mathrm{d}\vec{B} = \int_{\omega t=0}^{2\pi} H_x\,\mathrm{d}B_x + \int_{\omega t=0}^{2\pi} H_y\,\mathrm{d}B_y \tag{13}$$

is zero as well (Figure 2).

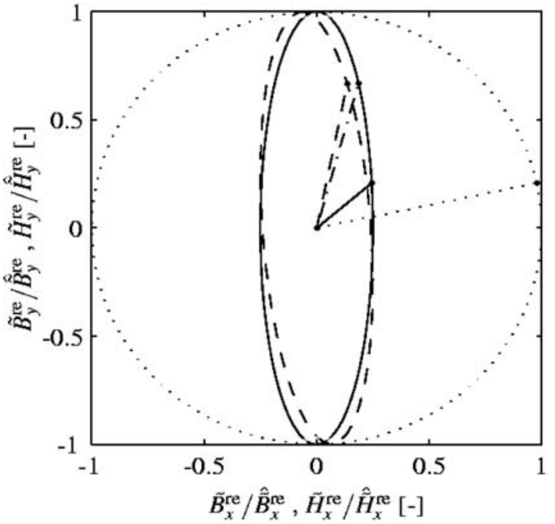

Figure 1.
Elliptical $\vec{H}$-loci obtained when applying a circular $\vec{B}$-locus to a linear anisotropic material, represented by a complex reluctivity tensor for which $|\nu_{\mathrm{td}}|=4\,|\nu_{\mathrm{rd}}|$, $\alpha_{\mathrm{rd}}=\alpha_{\mathrm{td}}=0°$ (solid), $\alpha_{\mathrm{rd}}=\alpha_{\mathrm{td}}=30°$ (dashdotted), $\alpha_{\mathrm{rd}}=45°$ and $\alpha_{\mathrm{td}}=30°$ (dashed)

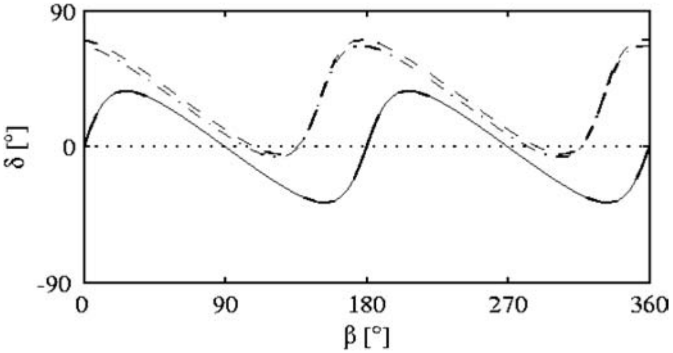

Figure 2.
Geometrical angle (δ(t) between $\vec{H}(t)$ and $\vec{B}(t)$, when applying a circular $\vec{B}$-locus to a linear anisotropic material, represented by a complex reluctivity tensor for which $|\nu_{\mathrm{td}}|=4|\nu_{\mathrm{rd}}|$, $\alpha_{\mathrm{rd}}=\alpha_{\mathrm{td}}=0°$ (solid), $\alpha_{\mathrm{rd}}=\alpha_{\mathrm{td}}=30°$ (dashdotted), $\alpha_{\mathrm{rd}}=45°$ and $\alpha_{\mathrm{td}}=30°$ (dashed)

- If $\alpha_{\mathrm{rd}} = \alpha_{\mathrm{td}} \in]0°, 180°[$ or $\alpha_{\mathrm{rd}} \neq \alpha_{\mathrm{td}} \in [0°, 180°]$, the average value of $\delta(t)$ is positive, resulting in a positive total loss (Figure 2).

As a consequence, a complex-valued reluctivity tensor allows to model the losses caused by simultaneously alternating and rotating fluxes, though in a simplified way (Birkfeld, 1998). If $|\nu_{\mathrm{rd}}| = |\nu_{\mathrm{td}}|$ and $\alpha_{\mathrm{rd}} = \alpha_{\mathrm{td}} \in [0°, 180°]$, the reluctivity tensor may be replaced by a complex-valued scalar reluctivity, which models a simplified form of alternating hysteresis (Lederer and Kost, 1998).

2.2 Cartesian tensor representation

By representing the reluctivity tensor components in cartesian form, i.e.

$$\nu_{\mathrm{rd}} = \nu_{\mathrm{rd}}^{\mathrm{re}} + j\nu_{\mathrm{rd}}^{\mathrm{im}}, \tag{14}$$

$$\nu_{\mathrm{td}} = \nu_{\mathrm{td}}^{\mathrm{re}} + j\nu_{\mathrm{td}}^{\mathrm{im}}, \tag{15}$$

it follows that:

$$\nu = \begin{pmatrix} \nu_{\mathrm{rd}}^{\mathrm{re}} & 0 \\ 0 & \nu_{\mathrm{td}}^{\mathrm{re}} \end{pmatrix} + j\begin{pmatrix} \nu_{\mathrm{rd}}^{\mathrm{im}} & 0 \\ 0 & \nu_{\mathrm{td}}^{\mathrm{im}} \end{pmatrix}. \tag{16}$$

Since $\mathbf{K}$ depends on ν, the entries of $\mathbf{K}$ may be complex-valued. By splitting up $\mathbf{K}$ in its real and imaginary part,

$$\mathbf{K} = \mathbf{K}^{\mathrm{re}} + j\mathbf{K}^{\mathrm{im}}, \tag{17}$$

the system of equation (5) becomes

$$\tilde{\mathbf{r}}(\tilde{\mathbf{A}}) = [\mathbf{K}^{\mathrm{re}}(\tilde{\mathbf{A}}) + j(\mathbf{L} + \mathbf{K}^{\mathrm{im}}(\tilde{\mathbf{A}}))]\tilde{\mathbf{A}} - \tilde{\mathbf{T}} = \mathbf{0}. \tag{18}$$

2.3 Material data

Birkfeld (1998), described how $\nu_{\mathrm{rd}}^{\mathrm{re}}$, $\nu_{\mathrm{rd}}^{\mathrm{im}}$, $\nu_{\mathrm{td}}^{\mathrm{re}}$ and $\nu_{\mathrm{td}}^{\mathrm{im}}$ can be determined from measurements in the rolling and transverse direction of grain-oriented silicon steels, by processing the measured signals in frequency domain. Obviously, the results depend on the shape of the exciting $\vec{B}$-locus.

For a circular $\vec{B}$-locus, these reluctivity tensor components are shown in Figure 3 as a function of the magnitude of $\vec{B}$. The measurements have been performed at 50 Hz on a square grain-oriented silicon steel sheet M111-35N of 80 mm length and 0.35 mm thickness (Beckley, 2000). For ease of notation, $\nu_{\mathrm{rd}}^{\mathrm{re,im}}$ denotes both $\nu_{\mathrm{rd}}^{\mathrm{re}}$ and $\nu_{\mathrm{rd}}^{\mathrm{im}}$. The solid and dashed lines correspond to the real and imaginary tensor component, respectively.

The polar equivalent of this figure, describing the dependency of $|\nu_{\mathrm{rd}}|$, $|\nu_{\mathrm{td}}|$, α_{rd} and α_{td} on $|\vec{B}|_{\max}$, is shown in Figure 4. Here, the solid and dashed lines correspond to the rolling and transverse direction, respectively. The moduli in this figure reveal the obvious result that the rolling direction is easier to magnetise than the transverse direction. Moreover, the elliptic $\vec{H}$-locus has its principal axes close to the rolling and transverse direction, because $\alpha_{\mathrm{rd}} \approx \alpha_{\mathrm{td}}$. The fact that they both differ from zero implies that the material is not lossless.

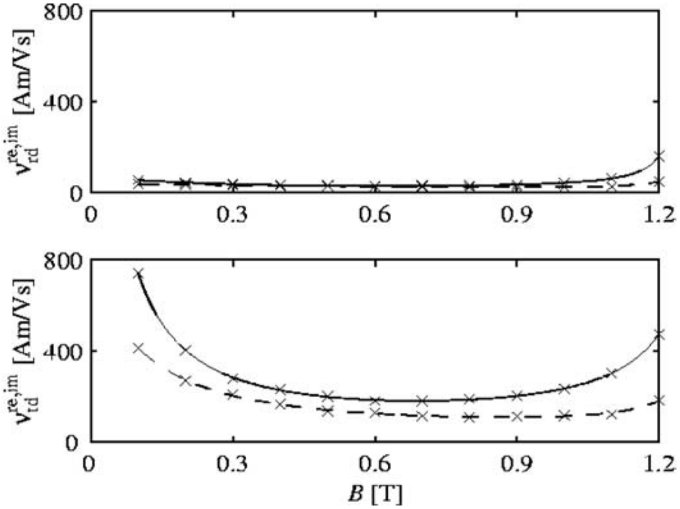

Figure 3.
Reluctivity tensor entries ν_{rd}^{re} (top, solid), ν_{rd}^{im} (top, dashed), ν_{td}^{re} (bottom, solid) and ν_{td}^{im} (bottom, dashed) as a function of the magnitude B of a circular flux density (Birkfeld, 1998)

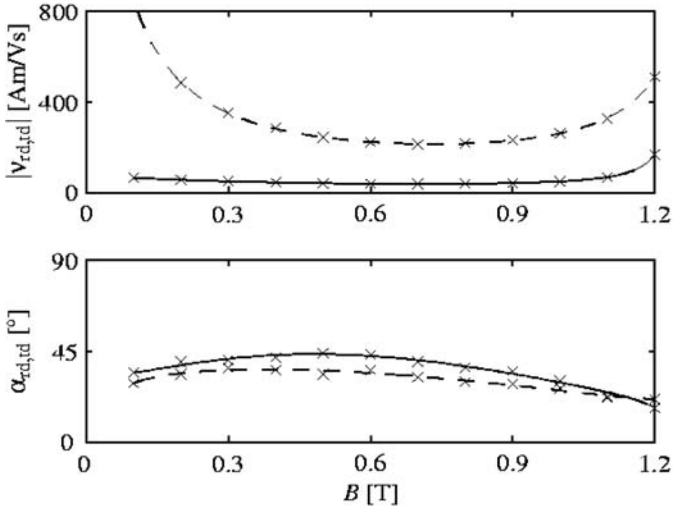

Figure 4.
Reluctivity tensor entries $|\nu_{rd}|$ (top, solid), $|\nu_{td}|$ (top, dashed), α_{rd} (bottom, solid) and α_{td} (bottom, dashed) as a function of the magnitude B of a circular flux density (Birkfeld, 1998)

3. Newton-Raphson method

It is possible to solve equation (18) numerically by successive substitution. The conjugate orthogonal conjugate gradient (COCG) method can be used for this purpose, since the complex-valued system is symmetric. Simulation time can be significantly decreased by considering derivative information of the reluctivity tensor entries as well, to yield the Newton-Raphson method. However, this requires a special treatment. The basic idea behind the Newton-Raphson algorithm is to set the first-order Taylor series expansion of the residual $\tilde{\mathbf{r}}(\tilde{\mathbf{A}})$ to zero. However, when working with complex variables, the Taylor series expansion is only defined if the residual is an analytic function of $\tilde{\mathbf{A}}$, i.e. the Cauchy-Riemann condition

$$\frac{\partial \tilde{\mathbf{r}}}{\partial \tilde{\mathbf{A}}_{\mathrm{k}}^{\mathrm{re}}} = \frac{1}{j} \frac{\partial \tilde{\mathbf{r}}}{\partial \tilde{\mathbf{A}}_{\mathrm{k}}^{\mathrm{im}}} \tag{19}$$

must be fulfilled. Unfortunately, in non-linear magnetodynamic problems, this is generally not the case (Lederer *et al.*, 1996).

Consequently, in order to obtain a Newton-Raphson scheme, one has to derive the Jacobian from the equivalent real representation of $\tilde{\mathbf{r}}$, defined by

$$\mathbf{r} = \begin{pmatrix} \tilde{\mathbf{r}}^{\mathrm{re}} \\ \tilde{\mathbf{r}}^{\mathrm{im}} \end{pmatrix}. \tag{20}$$

By setting

$$\mathbf{D} = \begin{pmatrix} \mathbf{K}^{\mathrm{re}} & -(\mathbf{L} + \mathbf{K}^{\mathrm{im}}) \\ \mathbf{L} + \mathbf{K}^{\mathrm{im}} & \mathbf{K}^{\mathrm{re}} \end{pmatrix}, \tag{21}$$

$$\mathbf{A} = \begin{pmatrix} \tilde{\mathbf{A}}^{\mathrm{re}} \\ \tilde{\mathbf{A}}^{\mathrm{im}} \end{pmatrix}, \tag{22}$$

$$\mathbf{T} = \begin{pmatrix} \tilde{\mathbf{T}}^{\mathrm{re}} \\ \tilde{\mathbf{T}}^{\mathrm{im}} \end{pmatrix}, \tag{23}$$

it follows that

$$\mathbf{r}(\mathbf{A}) = \mathbf{D}(\mathbf{A})\mathbf{A} - \mathbf{T}. \tag{24}$$

The $(2n \times 2n)$ matrix $\mathbf{D}$ has real-valued entries, but it is non-symmetric. The $(2n \times 1)$ vectors $\mathbf{r}$, $\mathbf{A}$ and $\mathbf{T}$ have real-valued entries. Setting the first-order Taylor expansion of $\mathbf{r}$ to zero,

$$\mathbf{r}(\mathbf{A} + \mathbf{d}) \approx \mathbf{r}(\mathbf{A}) + \mathbf{J}(\mathbf{A})\mathbf{d} = 0, \tag{25}$$

with $\mathbf{J}$ the Jacobian of $\mathbf{r}$, yields a direction $\mathbf{r}$ along which a line search is performed in order to determine a new approximation. Elaborating $\mathbf{J}$ on the level of a single linear finite element yields

$$\mathbf{J}^{(\mathrm{e})} = \mathbf{D}^{(\mathrm{e})} + \mathbf{M}^{(\mathrm{e})} + \mathbf{N}^{(\mathrm{e})}, \tag{26}$$

with

$$\mathbf{M}^{(\mathrm{e})} = \frac{2}{\Delta} \mathbf{Q}^{(\mathrm{e})} \begin{pmatrix} \tilde{\mathbf{A}}^{\mathrm{re,(e)}} \\ \tilde{\mathbf{A}}^{\mathrm{im,(e)}} \end{pmatrix} \begin{pmatrix} \tilde{\mathbf{A}}^{\mathrm{re,(e)}} \\ \tilde{\mathbf{A}}^{\mathrm{im,(e)}} \end{pmatrix}^{\mathrm{T}} \mathbf{P}^{(\mathrm{e})} \tag{27}$$

$$\mathbf{N}^{(e)} = \frac{2}{\Delta}\mathbf{R}^{(e)}\begin{pmatrix} -\tilde{\mathbf{A}}^{\mathrm{im},(e)} \\ \tilde{\mathbf{A}}^{\mathrm{re},(e)} \end{pmatrix}\begin{pmatrix} \tilde{\mathbf{A}}^{\mathrm{re},(e)} \\ \tilde{\mathbf{A}}^{\mathrm{im},(e)} \end{pmatrix}^{\mathrm{T}}\mathbf{P}^{(e)} \tag{28}$$

$$\mathbf{P}_{ij}^{(e)} = \frac{1}{4\Delta}\begin{pmatrix} b_i & c_i \end{pmatrix}\begin{pmatrix} b_j \\ c_j \end{pmatrix}, \tag{29}$$

$$\mathbf{Q}_{ij}^{(e)} = \frac{1}{4\Delta}\begin{pmatrix} b_i & c_i \end{pmatrix}\frac{\mathrm{d}\nu'\mathrm{re}}{\mathrm{d}B^2}\begin{pmatrix} b_j \\ c_j \end{pmatrix}, \tag{30}$$

$$\mathbf{R}_{ij}^{(e)} = \frac{1}{4\Delta}\begin{pmatrix} b_i & c_i \end{pmatrix}\frac{\mathrm{d}\nu'\mathrm{im}}{\mathrm{d}B^2}\begin{pmatrix} b_j \\ c_j \end{pmatrix}, \tag{31}$$

where Δ is the area of the element, $b_1 = y_2 - y_3, \ldots, c_1 = x_3 - x_2, \ldots$. Due to the non-symmetric structure of the Jacobian, the conjugate gradient (CG) method cannot be used to solve equation (25). The quasi minimal residual (QMR) method is appropriate here. Equating $\mathbf{M}^{(e)}$ and $\mathbf{N}^{(e)}$ in equation (26) to zero, i.e. omitting all non-linear contributions to the Jacobian, gives rise to the Picard or successive substitution method discussed earlier.

4. Simulation of a three-phase transformer

The 3-phase transformer shown in Figure 5 is now simulated using the complex-valued tensor data shown in Figure 3. The phase of the currents in the coils is $-85°$, 35° and 155°, respectively. For three different flux density levels, Figure 6 compares the convergence of the proposed Newton-Raphson method (solid) with the convergence of the Picard or successive substitution method (dashdotted). Obviously, the Newton-Raphson method converges much faster than the Picard method, except if the applied currents are small. This is caused by the negative derivatives of the reluctivity tensor entries at low flux densities shown in Figure 3 (Rayleigh region).

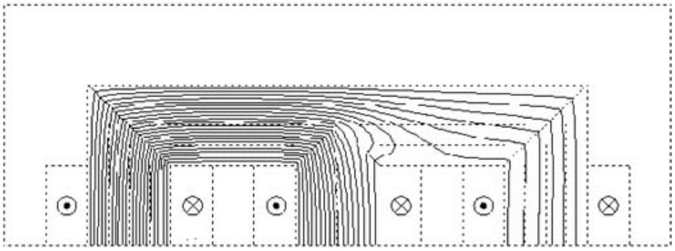

Notes: The phase of the currents in the coils is –85°, 35° and 155° respectively. The flux density in the middle limb is approximately alternating with an amplitude of 1.17 T

Figure 5.
Flux line distributions obtained with the complex-valued time-harmonic anisotropy model

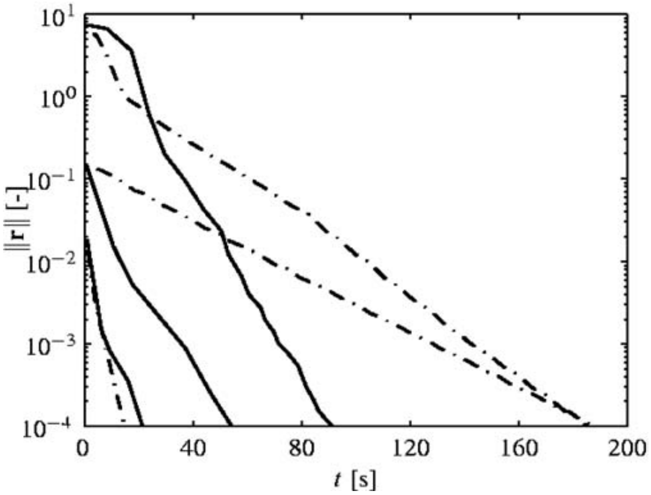

Figure 6.
Norm of the residual as a function of time, for three different flux density levels, when simulating with the Newton-Raphson method (solid) or the Picard method (dashdotted)

Figure 5 shows the flux line distribution. Since the material model used for this simulation assumes that all $\vec{B}$-loci are circular, it is expected that the obtained solution may differ significantly from reality. Data are required for elliptic $\vec{B}$-loci as well, in order to perform more accurate simulation. The use of a complex reluctivity tensor allows to visualise the loss density in each finite element. This is shown in Figure 7 for the region around the T-joint. This figure clearly indicates the increased losses due to rotational magnetisation at the top of the vertical limb.

5. Conclusions

The use of a complex-valued reluctivity tensor allows to model non-linear, anisotropic and hysteretic materials in a time-harmonic context. The equations for solving such type of problems with the Newton-Raphson method are elaborated. The convergence

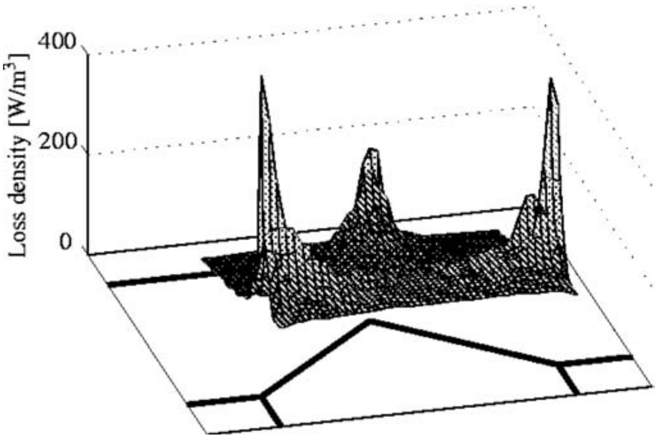

Figure 7.
Loss density distribution in the T-joint of the middle limb

rate for the Newton-Raphson method is significantly higher than for the successive substitution method, provided the simulation is performed outside the Rayleigh region of the material characteristics.

Note

1. "rd" and "td", respectively, stand for "rolling" and "transverse direction", since these directions generally coincide with the principal tensor axes.

References

Birkfeld, M. (1998), "Investigation of the permeability tensor of electrical steel sheet", *IEEE Transactions on Magnetics*, Vol. 34 No. 5, pp. 3667-73.

Birkfeld, M. and Hempel, K.A. (1997), "Calculation of the magnetic behaviour of electrical steel sheet under two-dimensional excitation by means of the reluctance tensor", *IEEE Transactions on Magnetics*, Vol. 33 No. 5, pp. 3757-9.

Beckley, P. (2000), *Electrical Steels*, European Electrical Steels, Newport.

Lederer, D. and Kost, A. (1998), "Modelling of non-linear magnetic material using a complex effective reluctivity", *IEEE Transactions on Magnetics*, Vol. 34 No. 5, pp. 3060-3.

Lederer, D., Igarashi, H. and Kost, A. (1996), "The Newton-Raphson method for complex equation systems", *Proceedings of the 7th International IGTE Symposium on Numerical Field Calculation in Electrical Engineering (IGTE'96), Graz, Austria*, pp. 391-4.

Niemenmaa, A. (1988), "Complex reluctivity modelling of iron losses in induction machines", *Proceedings of the International Conference on Electrical Machines (ICEM'88)*, pp. 633-6.

Nye, J.F. (1985), *Physical Properties of Crystals*, 2nd ed., Oxford Science Publications, Clarendon Press, Oxford.

The Emerald Research Register for this journal is available at
www.emeraldinsight.com/researchregister

The current issue and full text archive of this journal is available at
www.emeraldinsight.com/0332-1649.htm

Complementary two-dimensional finite element formulations with inclusion of a vectorized Jiles-Atherton model

J. Gyselinck
Department of Electrical Engineering (ELAP), Free University of Brussels (ULB), Belgium
L. Vandevelde and J. Melkebeek
Electrical Energy Lab (EELAB), Ghent University, Belgium
P. Dular
Department of Electrical Engineering (ELAP), University of Liège, Belgium

Keywords *Finite element analysis, Newton-Raphson method, Hysteresis*

Abstract *This paper deals with the magnetic vector and scalar potential formulation for two-dimensional (2D) finite element (FE) calculations including a vector hysteresis model, namely a vectorized Jiles-Atherton model. The particular case of a current-free FE model with imposed fluxes and magnetomotive forces is studied. The non-linear equations are solved by means of the Newton-Raphson method, which leads to the use of the differential reluctivity and permeability tensor. The proposed method is applied to a simple 2D model exhibiting rotational flux, viz the T-joint of a three-phase transformer.*

Introduction

In the domain of numerical electromagnetism, the inclusion of hysteresis models in finite element (FE) field computations remains a challenging task (Chiampi *et al.*, 1995; Dupré *et al.*, 1998; Sadowski *et al.*, 2002; Saitz, 1999). Mostly the scalar Preisach and Jiles-Atherton hysteresis models are used. They are applicable to 1D, 2D and 3D FE models displaying unidirectional flux (Chiampi, 1995; Sadowski *et al.*, 2002; Saitz, 1999). In applications having rotational flux in part of the computation domain, a vector hysteresis model should be used (Dupré *et al.*, 1998). The non-linear equations are iteratively solved by means of the fixed-point method (Chiampi *et al.*, 1995; Saitz, 1999) or the Newton-Raphson method (Dupré *et al.*, 1998; Sadowski *et al.*, 2002; Saitz, 1999). The latter method has the advantage of fast convergence (near the exact solution), but is somewhat more complicated to implement.

For 2D magnetic field computations, including those with hysteresis, the vector potential formulation is almost invariably adopted: the vector potential has only one non-zero component (along the third dimension) and the formulation is very easy to implement. The scalar potential formulation is rarely used as it requires the calculation

---

The research was carried out in the frame of the Inter-University Attraction Pole IAP P5/34 for fundamental research funded by the Belgian federal government. P. Dular is a Research Associate with the Belgian National Fund for Scientific Research (F.N.R.S.).

COMPEL: The International Journal for Computation and Mathematics in Electrical and Electronic Engineering
Vol. 23 No. 4, 2004
pp. 959-967
© Emerald Group Publishing Limited
0332-1649
DOI 10.1108/03321640410553382

of sources fields and the definition of cuts, unless the (2D or 3D) domain is current-free and simply-connected. However, the incorporation of a vector hysteresis model is very analogous in both formulations, as will be shown in this paper. Applying the Newton-Raphson method in a somewhat uncommon way, the differential reluctivity and permeability tensors, respectively, naturally emerge (Dupré *et al.*, 1998).

In this paper, we will consider a current-free 2D FE model with imposed fluxed and magnetomotive forces (Dupré *et al.*, 1998; Dular *et al.*, 1999) and a vector generalization of the Jiles-Atherton model (Bergqvist, 1996). The duality of the two formulations will be pointed out and some results for a simple model with rotational flux will be presented.

Complementary formulations

Governing equations

We consider a simply-connected and current-free domain Ω in the *xy*-plane. The magnetic field vector $\underline{h}(x,y)$ and the induction vector $\underline{b}(x,y)$ both have a zero z-component and are related by the magnetic constitute law $\underline{b}=\underline{b}(\underline{h})$ or $\underline{h}=\underline{h}(\underline{b})$.

For any continuous one-component vector potential $\underline{a}=a(x,y)\underline{1}_z$ and scalar potential $u(x,y)$, the induction $\underline{b}=\mathrm{curl}\;\;\underline{a}$ and the magnetic field $\underline{h}=-\mathrm{grad}\,u$ automatically satisfy $\mathrm{div}\,\underline{b}=0$ and $\mathrm{curl}\,\underline{h}=\underline{j}\equiv 0$, respectively. The FE discretisation of Ω leads to the definition of basis functions $\underline{\alpha}_l(x,y)=\alpha_l(x,y)\underline{1}_z$ and $\alpha_l(x,y)$ for the potentials $\underline{a}$ and u:

$$\underline{a}(x,y,t)=\sum_{l=1}^{n}a_l\underline{\alpha}_l(x,y) \tag{1}$$

$$u(x,y,t)=\sum_{l=1}^{n}u_l\alpha_l(x,y) \tag{2}$$

Commonly triangular elements and piecewise linear nodal basis functions are adopted.

The weak form of Ampère's law $\mathrm{curl}\,\underline{h}=\underline{j}\equiv 0$ and the flux conservation law $\mathrm{div}\,\underline{b}=0$ reads, before and after partial integration:

$$(\mathrm{curl}\,\underline{h},\underline{\alpha}'_k)_\Omega=0\Rightarrow(\underline{h},\mathrm{curl}\,\underline{\alpha}'_k)_\Omega+\langle\underline{h}\times\underline{n},\underline{\alpha}'_k\rangle_\Gamma=0, \tag{3}$$

$$(\mathrm{div}\,\underline{b},\alpha'_k)_\Omega=0\Rightarrow(\underline{b},\mathrm{grad}\,\alpha'_k)_\Omega+\langle\underline{b}\cdot\underline{n},\alpha'_k\rangle_\Gamma=0, \tag{4}$$

where $\underline{\alpha}'_k=\alpha'_k(x,y)\underline{1}_z$ and $\alpha'_k(x,y)$ are continuous test functions; $(\cdot,\cdot)_\Omega$ and $\langle\cdot,\cdot\rangle_\Gamma$ denote the integral of the (scalar) product of the two vector or scalar arguments over the domain Ω and on its contour Γ, respectively; $\underline{n}$ is the inward unit normal on Γ.

Considering the basis functions as test functions, a system of algebraic equations is obtained. For linear isotropic materials, having a constant scalar reluctivity ν and permeability $\mu=\nu^{-1}$, with $\underline{b}=\mu\underline{h}$, the elements of the system matrices (that are not affected by the boundary conditions) are given by the following expressions:

$$(\nu\,\mathrm{curl}\,\underline{\alpha}_l,\mathrm{curl}\,\underline{\alpha}_k)_\Omega=(\nu\,\mathrm{grad}\,\alpha_l,\mathrm{grad}\,\alpha_k)_\Omega, \tag{5}$$

$$(\mu\,\mathrm{grad}\,\alpha_l,\mathrm{grad}\,\alpha_k)_\Omega. \tag{6}$$

Boundary conditions with flux walls and flux gates

Let us consider the case where the boundary Γ is a sequence of the so-called flux walls Γ_{wi} and flux gates Γ_{gi} (Dupré *et al.*, 1998; Dular *et al.*, 1999). A flux wall Γ_{wi} is an interface with an impermeable medium ($\mu=0\Rightarrow\underline{b}=0$), on which thus holds $\underline{b}\cdot\underline{n}=0$; the associated magnetomotive force is $\mathscr{F}_i = \langle \underline{h} \times \underline{n}, \underline{1}_z \rangle_{\Gamma_{wi}}$. A flux gate Γ_{gi} is an interface with a perfectly permeable medium ($\mu = \infty \Rightarrow \underline{h} = 0$), on which thus holds $\underline{h} \times \underline{n} = 0$; the flux through the gate, inward Ω, is given by $\Phi_i = \langle \underline{b} \cdot \underline{n}, 1 \rangle_{\Gamma_{gi}}$. It follows that the sum of the magnetomotive forces $\mathscr{F}_i$ is zero, as well as the sum of the fluxes Φ_i.

An example with three flux walls and three flux gates is shown in Figure 1.

In the a-formulation, $a(x, y)$ has a constant value A_{wi} on each flux wall Γ_{wi}. Gate fluxes $\Phi_k = A_{wk} - A_{wl}$, or linear combinations of gate fluxes, can be strongly imposed by fixing two or more A_{wi} values. (At least one A_{wi} is to be set, e.g. to zero, in order to ensure the uniqueness of a.) An A_{wi} value can also constitute an unknown of the problem; this is a so-called floating potential. The corresponding magnetomotive force $\mathscr{F}_i$ is then given, and weakly imposed via the contour integral in equation (3). Hereto a dedicated basis function, denoted by $\underline{\alpha}_{wi}(x, y) = \alpha_{wi}(x, y)\underline{1}_z$, is defined. It has value 1 on Γ_{wi} and decreases linearly to 0 in the layer of elements surrounding Γ_{wi}; it is the sum of the classical nodal basis functions $\underline{\alpha}_i$ associated with the nodes situated on Γ_{wi}.

Analogously, in the u-formulation, flux gates have *a priori* known or floating potential $u(x, y) = U_{gi}$. In the latter case, the flux through the gate Φ_i is weakly imposed via the contour integral in equation (4).

Linear test case

By way of example, some results for a linear magnetostatic case (T-joint of Figure 1, $\Phi_1 = \Phi_2 = 1, \ \nu = \mu = 1$) are shown in Figures 2-4. The magnetomotive forces obtained with the two formulations (Figure 3) are observed to converge monotonously to each other, which is certainly not the case for the local induction value considered (Figure 4).

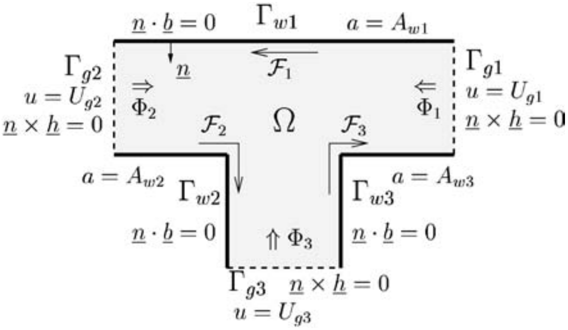
$\underline{n} \cdot \underline{b} = 0$
Γ_{w1}
$a = A_{w1}$
Γ_{g2}
$u = U_{g2}$
$\underline{n} \times \underline{h} = 0$
$\underline{n}$
$\mathcal{F}_1$
$\Rightarrow \Phi_2$
Ω
$\Leftarrow \Phi_1$
Γ_{g1}
$u = U_{g1}$
$\underline{n} \times \underline{h} = 0$
$\mathcal{F}_2$
$\mathcal{F}_3$
$a = A_{w2}$
Γ_{w2}
Γ_{w3}
$a = A_{w3}$
$\underline{n} \cdot \underline{b} = 0$
$\Uparrow \Phi_3$
$\underline{n} \cdot \underline{b} = 0$
Γ_{g3}
$\underline{n} \times \underline{h} = 0$
$u = U_{g3}$

Figure 1.
Two-dimensional model of T-joint of a three-phase transformer with three flux walls and three flux gates (width of limbs = 1 m)

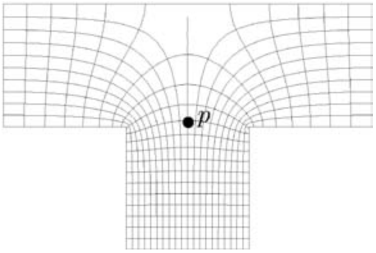

Figure 2.
Isolines of a and u (location of point p)

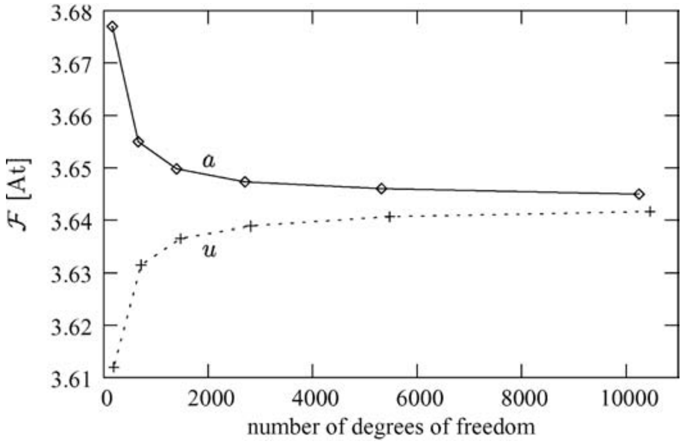

Figure 3.
Magnetomotive force $\mathscr{F}_2 = -\mathscr{F}_3$ as a function of number of degrees of freedom

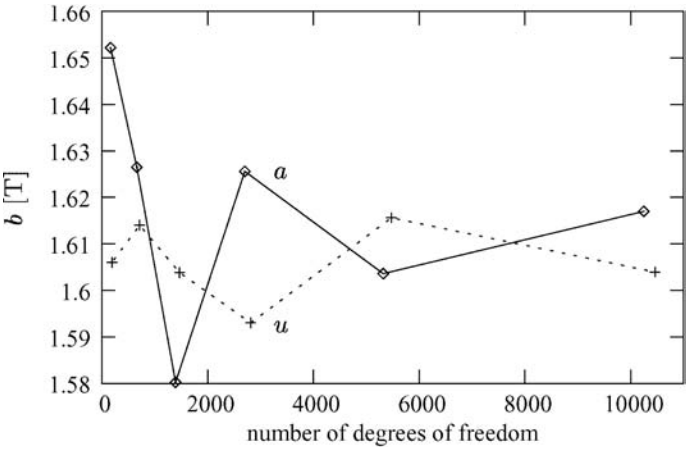

Figure 4.
Magnitude of $\underline{b}$ in point p as a function of number of degrees of freedom

Newton-Raphson method

Let us first consider a *reversible non-linear isotropic* material in Ω; hysteretic media will be dealt with in the next section. The scalar reluctivity and permeability can be written as a single-valued function of (the square of) the magnitude of $\underline{b}$ and $\underline{h}: \nu = \nu(b^2)$ and $\mu = \mu(h^2)$. The systems of algebraic equations are non-linear and have to be solved iteratively. The Newton-Raphson method is commonly used as it offers quadratic convergence near the exact solution. Starting from initial (zero) solutions $\underline{a}_{(0)}$ and $u_{(0)}$, subsequent approximations $\underline{a}_{(i)} = \underline{a}_{(i-1)} + \Delta\underline{a}_{(i)}$ and $u_{(i)} = u_{(i-1)} + \Delta u_{(i)}$, $i = 1, 2, \ldots$, are obtained by linearising the non-linear systems around the $(i-1)$th solutions $\underline{a}_{(i-1)}$ and $u_{(i-1)}$. The linearization of equations (3) and (4) requires the evaluation of their derivatives with respect to degrees of freedom a_l and u_l. Given that

$$\frac{\partial \underline{h}}{\partial a_l} = \frac{\partial \underline{h}}{\partial \underline{b}} \operatorname{curl} \underline{\alpha}_l \quad \text{and} \quad \frac{\partial \underline{b}}{\partial u_l} = -\frac{\partial \underline{b}}{\partial \underline{h}} \operatorname{grad} \alpha_l, \tag{7}$$

the elements of the matrix of the linearised systems can be concisely written in terms of the differential reluctivity and permeability tensors $\partial \underline{h}/\partial \underline{b}$ and $\partial \underline{b}/\partial \underline{h}$:

$$\left(\frac{\partial \underline{h}}{\partial \underline{b}} \operatorname{curl} \underline{\alpha}_l, \operatorname{curl} \underline{\alpha}_k\right)_\Omega \quad \text{and} \quad \left(\frac{\partial \underline{b}}{\partial \underline{h}} \operatorname{grad} \alpha_l, \operatorname{grad} \alpha_k\right)_\Omega . \tag{8}$$

For the isotropic materials considered, these tensors can be expressed in terms of the functions $\nu = \nu(h^2)$ and $\mu = \mu(b^2)$ and their derivatives:

$$\frac{\partial \underline{h}}{\partial \underline{b}} = \nu \underline{\underline{1}} + 2\,\frac{\mathrm{d}\nu}{\mathrm{d}b^2}\,\underline{bb} \quad \text{and} \quad \frac{\partial \underline{b}}{\partial \underline{h}} = \mu \underline{\underline{1}} + 2\,\frac{\mathrm{d}\mu}{\mathrm{d}h^2}\,\underline{bb}, \tag{9}$$

where $\underline{bb}$ and $\underline{hh}$ are the dyadic squares of $\underline{b}$ and $\underline{h}$, and $\underline{\underline{1}}$ is the unit tensor. In the xy coordinate system, the matrix representation of, e.g. the reluctivity tensor is

$$\left[\frac{\partial \underline{h}}{\partial \underline{b}}\right] = \begin{bmatrix} \dfrac{\partial h_x}{\partial b_x} & \dfrac{\partial h_x}{\partial b_y} \\[2ex] \dfrac{\partial h_y}{\partial b_x} & \dfrac{\partial h_y}{\partial b_y} \end{bmatrix} \tag{10}$$

$$= \nu \begin{bmatrix} 1 & 0 \\ 0 & 1 \end{bmatrix} + 2\,\frac{\mathrm{d}\nu}{\mathrm{d}b^2} \begin{bmatrix} b_x b_x & b_x b_y \\ b_y b_x & b_y b_y \end{bmatrix}. \tag{11}$$

It follows that the expression in equation (8) for the elements of the Jacobian matrices are equivalent with the more classical ones:

$$\begin{gathered} \nu \operatorname{curl} \underline{\alpha}_l \cdot \operatorname{curl} \underline{\alpha}_k + 2\,\frac{\mathrm{d}\nu}{\mathrm{d}b^2} (\operatorname{curl} \underline{\alpha}_l \cdot \underline{b})(\operatorname{curl} \underline{\alpha}_k \cdot \underline{b}) = \\ \nu \operatorname{grad} \alpha_l \cdot \operatorname{grad} \alpha_k + 2\,\frac{\mathrm{d}\nu}{\mathrm{d}b^2} (\operatorname{grad} \alpha_l \cdot \operatorname{grad} a)(\operatorname{grad} \alpha_k \cdot \operatorname{grad} a) \end{gathered} \tag{12}$$

and

$$\mu \operatorname{grad} \alpha_l \cdot \operatorname{grad} \alpha_k + 2\,\frac{\mathrm{d}\mu}{\mathrm{d}h^2} (\operatorname{grad} \alpha_l \cdot \operatorname{grad} u)(\operatorname{grad} \alpha_k \cdot \operatorname{grad} u), \tag{13}$$

which are obtained when deriving the non-linear equations on the basis of equations (5) and (6).

At the ith Newton-Raphson iteration, the Jacobian matrices and in particular the differential reluctivity and permeability tensors are evaluated for $\underline{b} = \underline{b}_{(i-1)}$ and $\underline{h} = \underline{h}_{(i-1)}$, respectively. The right hand side vector is composed of the residuals $(\underline{h}(\underline{b}_{(i-1)}), \operatorname{curl} \underline{\alpha}_k)_\Omega$ and $(\underline{b}(\underline{h}_{(i-1)}), \operatorname{grad} \alpha_k)_\Omega$, respectively, where for the sake of brevity the contour terms and associated boundary conditions have been omitted. Resolution of the linearised systems produces the increments $\Delta \underline{a}_{(i)}$ and $\Delta u_{(i)}$, and the ith solutions $\underline{a}_{(i)}$ and $u_{(i)}$.

Jiles-Atherton model

Scalar model

In the scalar Jiles-Atherton model (Bergqvist, 1996; Chiampi *et al.*, 1995; Sadowski *et al.*, 2002), the material is characterized by five (scalar) parameters (α, a, m_s, c and k).

The equations relevant to its vectorization (Bergqvist, 1996) and the FE implementation are briefly given hereafter.

The scalar magnetisation $m = b/\mu_0 - h$ is the sum of a reversible part m_r and an irreversible part m_i, with

$$m_\mathrm{i} = (m - cm_\mathrm{an})/(1 - c) \tag{14}$$

$$m_\mathrm{r} = c(m_\mathrm{an} - m_\mathrm{i}), \tag{15}$$

where the anhysteretic magnetization m_an is a single-valued function of the effective field $h_\mathrm{e} = h + \alpha m$:

$$m_\mathrm{an}(h_\mathrm{e}) = m_s\left(\coth\left(\frac{h_\mathrm{e}}{a}\right) - \frac{a}{h_\mathrm{e}}\right). \tag{16}$$

The irreversibility of the material is contained in

$$\frac{\mathrm{d}m_\mathrm{i}}{\mathrm{d}h_\mathrm{e}} = \frac{1}{\delta k}(m_\mathrm{an} - m_\mathrm{i}) \quad \text{with } \delta = \operatorname{sign}\left(\frac{\mathrm{d}h}{\mathrm{d}t}\right). \tag{17}$$

An alternative definition may be adopted in order to prevent $\mathrm{d}m_\mathrm{i}/\mathrm{d}h_\mathrm{e}$ and $\mathrm{d}b/\mathrm{d}h$ from becoming negative (Bergqvist, 1996):

$$\frac{\mathrm{d}m_\mathrm{i}}{\mathrm{d}h_\mathrm{e}} = \frac{|m_\mathrm{an} - m_\mathrm{i}|}{k} \quad \text{if } \mathrm{d}h\cdot(m_\mathrm{an} - m_\mathrm{i}) > 0, \quad \text{else } \frac{\mathrm{d}m_\mathrm{i}}{\mathrm{d}h_\mathrm{e}} = 0. \tag{18}$$

The differential susceptibility $\mathrm{d}m/\mathrm{d}h$ and the differential permeability $\mathrm{d}b/\mathrm{d}h$ can then be calculated for the given b, h and sign($\mathrm{d}h$):

$$\frac{\mathrm{d}b}{\mathrm{d}h} = \mu_0\left(1 + \frac{\mathrm{d}m}{\mathrm{d}h}\right) \quad \text{and} \quad \frac{\mathrm{d}m}{\mathrm{d}h} = \frac{c\frac{\mathrm{d}m_\mathrm{an}}{\mathrm{d}h_\mathrm{e}} + (1 - c)\frac{\mathrm{d}m_\mathrm{i}}{\mathrm{d}h_\mathrm{e}}}{1 - \alpha c\frac{\mathrm{d}m_\mathrm{an}}{\mathrm{d}h_\mathrm{e}} - \alpha(1 - c)\frac{\mathrm{d}m_\mathrm{i}}{\mathrm{d}h_\mathrm{e}}}. \tag{19}$$

For a given state (h_1, b_1) at an instant t_1, h_2 at a later instant t_2 can be calculated when given b_2, and vice versa:

$$b_2 = b_1 + \int_{h_1}^{h_2}\frac{\mathrm{d}b}{\mathrm{d}h}\mathrm{d}h \quad \text{and } h_2 = h_1 + \int_{b_1}^{b_2}\frac{\mathrm{d}h}{\mathrm{d}b}\mathrm{d}b, \tag{20}$$

where $\mathrm{d}h/\mathrm{d}b$ is the inverse of $\mathrm{d}b/\mathrm{d}h$. The integration has to be carried out numerically. Unfortunately, the integrand does not only depend on the integration variable, i.e. h and b, respectively, but also on b and h, respectively. Therefore, a Gauss integration cannot be applied (as such).

Vector extension

We now outline the vector extension as proposed by Bergqvist (1996), but limit the analysis to the isotropic case. In the vector generalization of equations (14-16) and (18-20), the scalar fields are replaced by vector fields, e.g. b becomes $\underline{b}$, while the scalar differential quantities are replaced by tensors, e.g. $\mathrm{d}b/\mathrm{d}h$ becomes $\partial\underline{b}/\partial\underline{h}$. The division in equation (19) is replaced by the multiplication of the nominator by the inverse of the denominator. The scalar 1 is replaced by the unit tensor $\underline{\underline{1}}$ where necessary. The vector extension of equations (16) and (18) needs special attention.

$\underline{m}_{\mathrm{an}}$ and $\partial\underline{m}_{\mathrm{an}}/\partial\underline{h}_{\mathrm{e}}$ are single-valued functions of $\underline{h}_{\mathrm{e}}$:

$$\underline{m}_{\mathrm{an}} = m_{\mathrm{an}}(|\underline{h}_{\mathrm{e}}|)\frac{\underline{h}_{\mathrm{e}}}{|\underline{h}_{\mathrm{e}}|}, \tag{21}$$

$$\frac{\partial\underline{m}_{\mathrm{an}}}{\partial\underline{h}_{\mathrm{e}}} = \frac{m_{\mathrm{an}}}{h_{\mathrm{e}}}\left(\underline{\underline{1}} - \frac{\underline{h}_{\mathrm{e}}\underline{h}_{\mathrm{e}}}{h_{\mathrm{e}}^2}\right) + \frac{\mathrm{d}m_{\mathrm{an}}}{\mathrm{d}h_{\mathrm{e}}}\frac{\underline{h}_{\mathrm{e}}\underline{h}_{\mathrm{e}}}{h_{\mathrm{e}}^2}. \tag{22}$$

According to Bergqvist (1996), the vector extension of equation (18) consists in assuming that the increment $d\underline{m}_{\mathrm{i}}$ is parallel to $\underline{m}_{\mathrm{an}} - \underline{m}_{\mathrm{i}}$, proportional to $|\underline{m}_{\mathrm{an}} - \underline{m}_{\mathrm{i}}|/k$ and non-zero only if $\mathrm{d}\underline{h}\cdot(\underline{m}_{\mathrm{an}} - \underline{m}_{\mathrm{i}}) > 0$. Considering a local coordinate system $x'y'$, with the x'-axis along the vector $\underline{m}_{\mathrm{an}} - \underline{m}_{\mathrm{i}}$ (Figure 5), we thus have

$$\left[\frac{\partial\underline{m}_{\mathrm{i}}}{\partial\underline{h}_{\mathrm{e}}}\right]_{x'y'} = \frac{|\underline{m}_{\mathrm{an}} - \underline{m}_{\mathrm{i}}|}{k}\begin{bmatrix}1 & 0\\ 0 & 0\end{bmatrix} \quad \text{if } \mathrm{d}\underline{h}\cdot(\underline{m}_{\mathrm{an}} - \underline{m}_{\mathrm{i}}) > 0, \quad \text{else } \frac{\partial\underline{m}_{\mathrm{i}}}{\partial\underline{h}_{\mathrm{e}}} = 0. \tag{23}$$

The matrix representation of $\partial\underline{m}_{\mathrm{i}}/\partial\underline{h}_{\mathrm{e}}$ in a coordinate system xy is then

$$\left[\frac{\partial\underline{m}_{\mathrm{i}}}{\partial\underline{h}_{\mathrm{e}}}\right]_{xy} = \mathbf{R}\left[\frac{\partial\underline{m}_{\mathrm{i}}}{\partial\underline{h}_{\mathrm{e}}}\right]_{x'y'}\boldsymbol{R}^{\mathrm{T}} \tag{24}$$

with

$$\boldsymbol{R} = \begin{bmatrix}\cos\theta & \sin\theta\\ -\sin\theta & \cos\theta\end{bmatrix}. \tag{25}$$

Using all the above equations (or their vector extension), $\partial\underline{b}/\partial\underline{h}$ can be calculated for the given $\underline{b}$ and $\underline{h}$, and given direction of $\mathrm{d}\underline{h}$. By inverting (the matrix representation of) $\partial\underline{b}/\partial\underline{h}$, $\partial\underline{h}/\partial\underline{b}$ is obtained.

Some calculated bh-loci (with $\mu_0 m_s = 2.1\,\mathrm{T}$, $a = 50\,\mathrm{A/m}$, $k = 82\,A/m$, $c = 0.1$ and $\alpha = k/m_s$ (Bergqvist, 1996)) are shown in Figure 6. Both alternating and rotational excitations are considered.

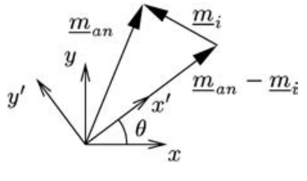

Figure 5.
Local coordinate system $x'y'$ with x'-axis along $\underline{m}_{\mathrm{an}} - \underline{m}_{\mathrm{i}}$

Incorporation in FE equations

For hysteretic material models, the differential reluctivity and permeability tensors depend on the present state $(\underline{b}, \underline{h})$ of the material as well as on the history of the material. For the vector Preisach model considered in (Dupré *et al.*, 1998), the history consists of extreme values of the magnetic field projected on a number of spatial directions. In the above outlined vectorized Jiles-Atherton model, the history is simply contained in the direction of $\mathrm{d}\underline{h}$.

For stepping from the instant t_1 to the next instant $t_2 = t_1 + \Delta t$, the ith Newton-Raphson iteration requires the evaluation of the differential tensors $\partial \underline{h}/\partial \underline{b}$ and $\partial \underline{b}/\partial \underline{h}$ for $\underline{b} = \underline{b}_{2(i-1)}$, $\underline{h} = \underline{h}_{2(i-1)}$ and $\mathrm{d}\underline{h} = \underline{h}_{2(i-1)} - \underline{h}_1$. After solving the systems of equations in terms of $\Delta a_{l(i)}$ and $\Delta u_{l(i)}$, $\underline{h}_{2(i)}$ and $\underline{b}_{2(i)}$ are obtained by integrating the differential tensors over $[\underline{b}_1, \underline{b}_{2(i)}]$ and $[\underline{h}_1, \underline{h}_{2(i)}]$, respectively.

Application example

The vector Jiles-Atherton model (with the parameter values given above) is applied to the T-joint model considered in the complementary formulations section. The fluxes $\Phi_1 = \cos(2\pi ft + 2\pi/3)$ and $\Phi_2 = \cos(2\pi ft)$, where the frequency f is arbitrarily chosen to be 1 Hz, are imposed strongly in the a-formulation and weakly in the u-formulation. Two periods are time-stepped with 200 time steps per period. During the first quarter of a period, the fluxes Φ_1 and Φ_2 are multiplied with the function $(1 - \cos(\pi t/t_{\mathrm{relax}}))/2$, with $t_{\mathrm{relax}} = 0.25$, in order to step smoothly through the first magnetization curve of the hysteretic material. The mesh with 661 spatial degrees for $a(x, y, t)$ and 715 for $u(x, y, t)$ is used.

The magnetomotive forces $\mathscr{F}_1(t)$ and $\mathscr{F}_2(t)$ obtained with a- and u-formulations are shown in Figure 7. A very good agreement is reached. The $\underline{b}$-locus and b_xh_x and b_xh_y-loops in the point p (shown in Figure 2) are shown in Figure 8. The agreement is somewhat less good, as could be expected for a local quantity.

Conclusions

The implementation of a vectorized Jiles-Atherton model in 2D FE magnetic field computations with complementary formulations has been studied. When solving the non-linear equations by means of the Newton-Raphson method, the differential reluctivity and differential tensors naturally emerge.

The proposed methods have been successfully applied to a simple 2D FE model with rotational flux. A good agreement has been achieved between the results obtained with the two formulations.

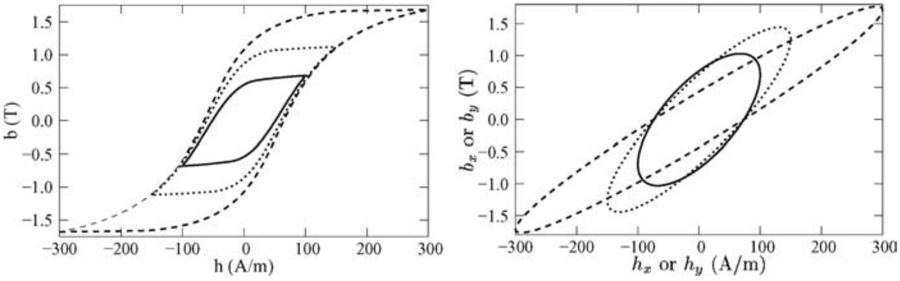

Figure 6.
bh-loci at alternating excitation (left) and b_xh_x-loci (or b_yh_y-loci) at rotational excitation (right), with $\hat{h} = 100$, 150 and 300 A/m

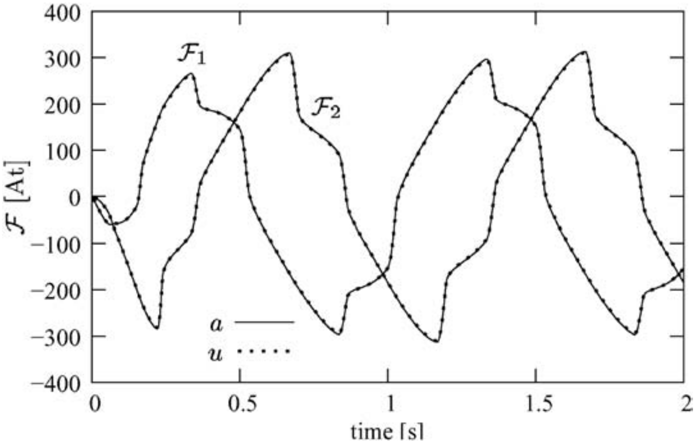

Figure 7.
Magnetomotive forces $\mathscr{F}_1(t)$ and $\mathscr{F}_2(t)$ obtained with *a* and *u* formulation

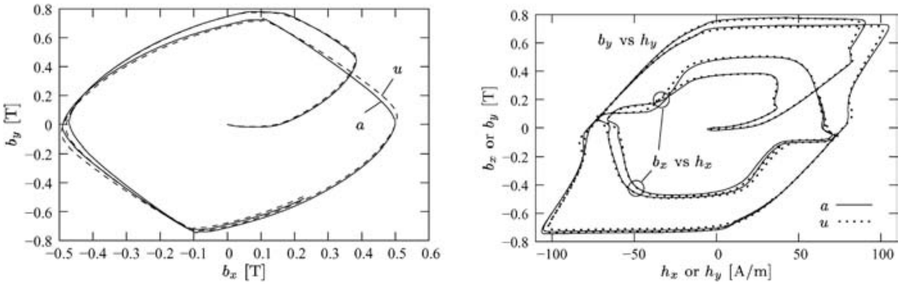

Figure 8.
$\underline{b}$-locus (up) and $b_x\ h_x$ and $b_y h_y$ loops (down) obtained with *a* and *u* formulations

References

Bergqvist, A. (1996), "A simple vector generalisation of the Jiles-Atherton model of hysteresis", *IEEE Trans. on Magn.*, Vol. 32 No. 5, pp. 4213-5.

Chiampi, M., Chiarabaglio, D. and Repetto, M. (1995), "A Jiles-Atherton and fixed-point combined technique for time periodic magnetic field problems with hysteresis", *IEEE Trans. on Magn.*, Vol. 31 No. 6, pp. 4306-11.

Dular, P., Gyselinck, J., Henrotte, F., Legros, W. and Melkebeek, J. (1999), "Complementary finite element magnetodynamic formulations with enforced magnetic fluxes", *COMPEL*, Vol. 18 No. 4, pp. 656-67.

Dupré, L., Gyselinck, J. and Melkebeek, J. (1998), "Complementary finite element methods in 2D magnetics taking into account a vector Preisach model", *IEEE Trans. on Magn.*, Vol. 34 No. 5, pp. 3048-51.

Sadowski, N., Batistela, N.J., Bastos, J.P.A. and Lajoie-Mazenc, M. (2002), "An inverse Jiles-Atherton model to take into account hysteresis in time-stepping finite-element calculations", *IEEE Trans. on Magn.*, Vol. 32 No. 2, pp. 797-800.

Saitz, J. (1999), "Newton-Raphson method and fixed-point technique in finite element computation of magnetic field problems in media with hysteresis", *IEEE Trans. on Magn.*, Vol. 35 No. 3, pp. 1398-401.

The Emerald Research Register for this journal is available at
www.emeraldinsight.com/researchregister

The current issue and full text archive of this journal is available at
www.emeraldinsight.com/0332-1649.htm

Transient field-circuit coupled formulation based on the finite integration technique and a mixed circuit formulation

Galina Benderskaya, Herbert De Gersem and Thomas Weiland
Institut für Theorie Elektromagnetischer Felder (TEMF), Technische Universität Darmstadt, Darmstadt, Germany

Markus Clemens
Helmut-Schmidt-Universität, Universität der Bundeswehr Hamburg, Hamburg, Germany

Keywords *Coupled systems, Circuit elements, Time integration*

Abstract *The coupling between a 3D modified magnetic vector potential formulation discretized by the finite integration technique and an electrical circuit that includes solid and stranded conductors is presented. This paper describes classical time integration methods and the implicit Runge-Kutta methods, the latter being an appropriate alternative to the first ones to solve effectively index 1 differential-algebraic equations arising from combined simulation of electromagnetic fields and electrical circuits.*

1. Introduction

The combined simulation of electromagnetic fields and electrical circuits is typical for quasistatic electromagnetic field calculations. In a field-circuit coupled model, a part of the model is discretized, e.g. by Whitney finite elements (Bedrosian, 1993; Bossavit, 1997; Tsukerman *et al.*, 1992) or by the finite integration technique (FIT) (Clemens *et al.*, 2001) which allows us to consider complicated geometries and local saturation or eddy current effects, whereas other parts, e.g. external sources and loads, are treated by lumped parameters within a circuit model (De Gersem *et al.*, 1998; Mertens *et al.*, 2000).

The point here is that the FIT discretization of the magnetodynamic part of the model and its following coupling with external circuits leads to large differential-algebraic systems of equations that cannot be treated numerically like regular ordinary differential equations (Nicolet and Delincé, 1996). Since they are index 1 problems they should be treated by implicit time integration schemes, e.g. by implicit Runge-Kutta-type methods. Their realization also makes possible to implement adaptive time-stepping within the integration process thus effectively optimizing the CPU time.

COMPEL: The International Journal for Computation and Mathematics in Electrical and Electronic Engineering
Vol. 23 No. 4, 2004
pp. 968-976
© Emerald Group Publishing Limited
0332-1649
DOI 10.1108/03321640410553391

Herbert De Gersem is working in the cooperation project “DA-WE1 (TEMF/GSI)” with the “Gesellschaft für Schwerionenforschung (GSI)”, Darmstadt.
Galina Benderskaya is supported by PhD research grant of the Technische Universität Darmstadt (TUD).

2. Finite integration technique

FIT (Weiland, 1977) is a generalized finite-difference discretization scheme mapping Maxwell's equations onto a dual grid doublet $\{G, \tilde{G}\}$ yielding the set of Maxwell-Grid-Equations (MGE),

$$\begin{aligned} \mathbf{C}\widehat{\mathbf{e}} = -\frac{\mathrm{d}}{\mathrm{d}t}\widehat{\widehat{\mathbf{b}}}; \quad \tilde{\mathbf{C}}\widehat{\mathbf{h}} = \frac{\mathrm{d}}{\mathrm{d}t}\widehat{\widehat{\mathbf{d}}} + \widehat{\widehat{\mathrm{j}}}, \\ \mathbf{S}\widehat{\widehat{\mathbf{b}}} = 0; \quad \tilde{\mathbf{S}}\widehat{\widehat{\mathbf{d}}} = \mathbf{q} \end{aligned} \tag{1}$$

where $\widehat{\mathbf{e}}$ and $\widehat{\mathbf{h}}$ denote component vectors of the electric and magnetic grid voltages, $\widehat{\widehat{\mathbf{d}}}$ and $\widehat{\widehat{\mathbf{b}}}$ are vectors of the electric and magnetic facet fluxes and $\widehat{\widehat{\mathbf{j}}}$ is a vector of dual facet currents. The matrix operators $\mathbf{C}$ and $\tilde{\mathbf{C}}$ correspond to the curl-operators on the primary and on the dual grid. They contain only grid topology information and repeat exact relations. The same holds for the discrete divergence-operators $\mathbf{S}$ and $\tilde{\mathbf{S}}$. The approximation in FIT is introduced only in the discrete constitutive material relations where the grid voltages on the edges of G are coupled with the flux degrees of freedom located on the facets of the dual grid $\tilde{G}$ and vice versa, i.e.

$$\widehat{\widehat{\mathbf{d}}} = \mathbf{M}_{\varepsilon}\widehat{\mathbf{e}}, \quad \widehat{\widehat{\mathbf{j}}} = \mathbf{M}_{\kappa}\widehat{\mathbf{e}}, \quad \widehat{\mathbf{h}} = \mathbf{M}_{\nu}\widehat{\widehat{\mathbf{b}}}, \tag{2}$$

where $\mathbf{M}_{\varepsilon}$, $\mathbf{M}_{\kappa}$ and $\mathbf{M}_{\nu}$ are the material matrices for the permittivities, conductivities and reluctivities, respectively.

The duality of the grid doublet $\{G, \tilde{G}\}$ results in the following topological property of the MGE

$$\mathbf{C} = \tilde{\mathbf{C}}^{\mathrm{T}}, \tag{3}$$

reflecting the analytical relations,

$$\begin{aligned} \mathbf{C}\tilde{\mathbf{S}}^{\mathrm{T}} = 0 \leftrightarrow \mathrm{curl\ \ grad} \equiv 0 \\ \mathbf{S}\mathbf{C} = 0 \leftrightarrow \mathrm{div\ \ curl} \equiv 0 \end{aligned} \tag{4}$$

which are essential for the stability and efficiency of the numerical schemes being used for time-integration (Clemens and Weiland, 1999).

3. Transient coupled formulation

The 3D transient field-circuit coupled formulation discretized by FIT reads:

$$\begin{aligned} \begin{bmatrix} \mathbf{M}_{\kappa} & 0 & 0 \\ -\mathbf{Q}^{\mathrm{T}}\mathbf{M}_{\kappa} & \mathbf{N}_{\mathrm{C}} & 0 \\ -\mathbf{P}^{\mathrm{T}} & 0 & -\mathbf{N}_{\mathrm{L}} \end{bmatrix} \frac{\mathrm{d}}{\mathrm{d}t} \begin{bmatrix} \widehat{\mathbf{a}} \\ \mathbf{v} \\ \mathbf{i} \end{bmatrix} + \begin{bmatrix} \tilde{\mathbf{C}}\mathbf{M}_{\nu}\mathbf{C} & -\mathbf{M}_{\kappa}\mathbf{Q} & -\mathbf{P} \\ 0 & \mathbf{N}_{\mathrm{G}} & \mathbf{D} \\ 0 & \mathbf{D}^{\mathrm{T}} & -\mathbf{N}_{\mathrm{R}} \end{bmatrix} \begin{bmatrix} \widehat{\mathbf{a}} \\ \mathbf{v} \\ \mathbf{i} \end{bmatrix} \\ = \begin{bmatrix} 0 \\ -\mathbf{D}_{\mathrm{S}}\mathbf{i}_{\mathrm{S}} \\ \mathbf{B}_{\mathrm{S}}\mathbf{v}_{\mathrm{S}} \end{bmatrix}, \end{aligned} \tag{5}$$

where $\widehat{\mathbf{a}}(t)$ is the vector of path integrated magnetic vector potentials, $\tilde{\mathbf{C}}\mathbf{M}_{\nu}\mathbf{C}$ stands for the positive-semidefinite curl-curl stiffness matrix and $\mathbf{M}_{\kappa}$ is the conductivity matrix, which is commonly singular (Clemens *et al.*, 2001). For the electrical network, a mixed formulation is preferred in order to avoid the introduction of additional nonzero entries in the large, but sparse matrices $\tilde{\mathbf{C}}\mathbf{M}_\nu\mathbf{C}$ and $\mathbf{M}_\kappa$ (De Gersem *et al.*, 1998) and to prevent zero entries at the diagonal of the circuit system matrix (Tsukerman *et al.*, 1992).

$\mathbf{D}$ is the fundamental cutset matrix part collecting the indices between the fundamental cutsets and the links for which circuit unknowns are defined. Construction of the fundamental cutset matrix itself is subjected to a priority rule that favours independent voltage sources, solid conductors and capacitors to be selected as tree branches. The voltage drops $\mathbf{v}$ and the currents $\mathbf{i}$ are assigned as degrees of freedom to the tree branches and the cotree branches, respectively. The Kirchhoff's current and voltage laws are expressed for the fundamental cutsets and loops. The circuit elements are represented by the conductance matrices $\mathbf{N}_\mathrm{G}$, resistance matrices $\mathbf{N}_\mathrm{R}$, capacitance matrices $\mathbf{N}_\mathrm{C}$, and inductance matrices $\mathbf{N}_\mathrm{L}$. The vectors $\mathbf{v}_\mathrm{s}$ and $\mathbf{i}_\mathrm{s}$ contain the voltage drops and the currents supplied to the system by independent voltage and current sources. $\mathbf{D}_\mathrm{s}$ is the fundamental cutset matrix part with the incidences between the considered fundamental cutsets and the independent current sources, where as $\mathbf{B}_\mathrm{s}$ is the fundamental loop matrix part with the incidences between fundamental loops and independent voltage sources.

A clear distinction between two possible types of conductors – stranded – and solid-type conductors is made. A stranded conductor is made of many thin strands. The cross-section of the individual strand of a stranded conductor is so small that for the expected frequencies the eddy currents are negligible. In formulation (5) this fact is taken into account by introducing zeros at the corresponding positions of the conductivity matrix $\mathbf{M}_\kappa$. Resolving the individual strands by the FIT grid is not required. In contrast, solid conductors are characterized by significant skin effects and carry non-negligible eddy currents. The corresponding models for the solid and stranded conductors are shown in Figure 1, where I_sol and I_str are the total currents through the solid and stranded conductors, respectively; S_sol and S_str are the cross-sections of the solid and stranded conductors, ΔV_sol and ΔV_str are the voltage drops along the solid and stranded conductors, S_w is the cross-section of a single strand, and Ω_FIT is the FIT domain.

Stationary current field simulations are carried out in advance in order to determine the source current distribution in the solid or stranded conductor and to derive the coupling blocks $\mathbf{M}_\kappa\mathbf{Q}$ and $\mathbf{P}$ (Dular *et al.*, 2000). For a solid conductor, coupling term between the field and the circuit model $\mathbf{Q} = \tilde{\mathbf{S}}\phi$ is solved from the stationary current field formulation $\tilde{\mathbf{S}}\mathbf{M}_\kappa\tilde{\mathbf{S}}^\mathrm{T}\phi = -\tilde{\mathbf{S}}\mathbf{M}_\kappa\widehat{\mathbf{e}}_{\mathbf{app}}$, where the voltage vector $\widehat{\mathbf{e}}_{\mathbf{app}}$ is constructed by assigning voltage drops of 1 V at a set of primary edges perpendicular to a cross-section of the solid conductor. For a stranded conductor, the current distribution due to the applied current of 1 A is determined in a geometrical way.

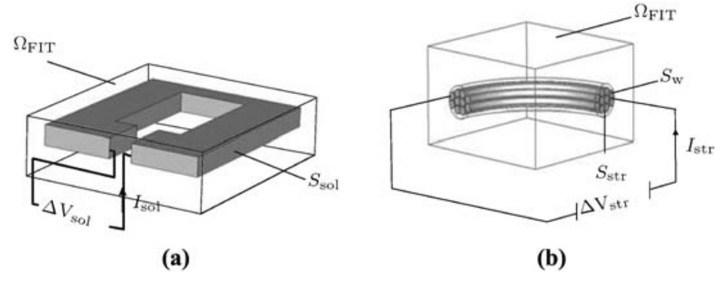

Figure 1.
(a) Solid conductor and (b) stranded conductor models

For a coil constructed by the extrusion of a profile along a curve, the current coupling term **P** equals the homogeneous distribution of a total current of 1 A multiplied by the number of turns over the successive cross-sections.

4. Adaptive time stepping

4.1 Classical integration methods

Formulation (5) represents an ill-conditioned index 1 differential-algebraic system of equations:

$$\mathbf{D}\frac{\mathrm{d}}{\mathrm{d}t}x + \mathbf{K}x = \mathbf{r}(t). \tag{6}$$

The θ-time discretization scheme applied to solve equation (6) is written in the form:

$$\frac{1}{\Delta t}\mathbf{D}(x_{n+1} - x_n) + \mathbf{K}(\theta x_{n+1} + (1-\theta)x_n) = \theta\mathbf{r}_{n+1} + (1-\theta)\mathbf{r}_n. \tag{7}$$

The lower indices n and $n+1$ correspond to the time instants t_n and $t_{n+1} = t_n + \Delta t$, respectively. Different choices of the parameter θ lead to the following classical methods of numerical integration: $\theta = 1$ yields the implicit Euler method, $\theta = 1/2$ corresponds to the Crank-Nicolson method, $\theta = 2/3$ yields the Galerkin method.

The symmetry of the matrix pencil $[(\theta/\Delta t)\mathbf{D} + \mathbf{K}]$ is restored by multiplying the circuit equation block by the scalar factor $\Delta t/\theta$. The resulting coupled system is indefinite due to the mixed nature of the circuit formulation. Therefore, for reasons of numerical stability, the transient formulation is turned into its positive semi-definite equivalent obtained by eliminating the circuit equations (in a Schur complement formulation). The θ-method is then applied only for the magnetic vector potential unknowns followed by the update of the circuit degrees of freedom with the corresponding Schur complement.

System (6) represents an index 1 differential-algebraic system and usually cannot be treated numerically as regular ordinary differential system of equations. Thus, some θ-methods may appear to be unstable for these types of problems hence implicit integration methods should be used instead.

4.2 Implicit Runge-Kutta methods

An s-stage implicit Runge-Kutta (RK) method is given by the Butcher table:

$$\begin{array}{c|c} \mathbf{c} & \mathbf{A} \\ \hline & \mathbf{b}^{\mathrm{T}} \end{array},$$

where $\mathbf{A}$ is a real matrix of dimension $s \times s$, $\mathbf{c}$ and $\mathbf{b}$ are real vectors of dimension s (Hairer *et al.*, 1993). Using the initial condition x_0 at t_0 the ith stage of an implicit RKM is defined as:

$$\mathbf{X}_i = x_0 + h\sum_{i=1}^{s} a_{ij}\mathbf{X}'_j. \tag{8}$$

After that, $\mathbf{X}_i$ should be substituted for x and $\mathbf{X}'_i$ for x' into system (6) and the resulting system of equations has to be solved. When all the stage values are calculated, the update for the solution in the next time point is followed by:

$$x_1 = x_0 + h\sum_{i=1}^{s} b_i \mathbf{X}'_j. \tag{9}$$

4.3 Adaptive time-stepping

Adaptive time-stepping can be implemented elegantly using embedded implicit RK methods, which for each time step deliver a solution of the given order p and an embedded solution of a lower order $\hat{p}$. Such embedded method uses the same matrix $\mathbf{A}$, but different update vectors $\mathbf{b}$ and $\hat{\mathbf{b}}$. Since the system is iterated only for the magnetic vector potential degrees of freedom, an error vector $\widehat{\mathbf{y}} = \widehat{\mathbf{a}}^{(p)} - \widehat{\mathbf{a}}^{(\hat{p})}$ with the solutions of the orders p and $\hat{p}$ is constructed similar as in Clemens *et al.* (2002).

The following step in the adaptive time-stepping procedure is to find a suitable norm for the error vector. A suitable norm is given in Wang *et al.* (2002):

$$\|\widehat{\mathbf{y}}\|_{\mathrm{err}} = \sqrt{\frac{\|\widehat{\mathbf{y}}\|_2^2}{\|\widehat{\mathbf{a}}_{n+1}^{(p)}\|_2^2 + \delta}} \tag{10}$$

where δ is an absolute error tolerance value. Following the idea presented by Clemens *et al.* (2002) the parameter δ in equation (10) is chosen as a proper fraction $\theta \in [10^{-3}, 10^{-2}]$ of the maximum norm of the magnetic fluxes that were calculated so far during the time marching process:

$$\delta = \theta \max_{t \in [t_0, t_i]} \left\{ \|\widehat{\mathbf{a}}(t)\|_2^2 \right\}. \tag{11}$$

Another suitable norm is given by:

$$\|\widehat{\mathbf{y}}\|_{\mathrm{err}} = \sqrt{\sum_{i=1}^{N} \left(\frac{\widehat{y}_i}{|\widehat{a}_i| + \breve{a}_i} \right)^2}, \tag{12}$$

where $\breve{a}_i$ is an absolute error tolerance for the component $\widehat{a}_i$ (Gustafsson, 1994). We will not choose different absolute tolerances for each specific solution component and according to Clemens *et al.* (2002), the proper choice for $\breve{a}$ is given by:

$$\breve{a} = \theta \times \max_{t \in [t_0, t_i]} \{ \|\widehat{\mathbf{a}}(t)\|_\infty \} \tag{13}$$

and $\theta \in [10^{-2}, 10^{-1}]$.

4.4 Time-step selection procedure

The choice whether the last integration step is to be repeated or a new simulation step can be performed, is determined by a step-size controller. Here, the solution is rejected if $\|\widehat{y}\|_{\mathrm{err}} > \mu \cdot \mathrm{tol}$ holds true; otherwise it is accepted. The variable μ denotes an accelerating factor usually set to 1.2 and *tol* is a user-specified tolerance.

As proposed by Gustafsson (1994), an I-controller-type time-step predictor is implemented by:

$$\Delta t_{n+1} = \rho \left(\frac{\mathrm{tol}}{\|\hat{\mathbf{y}}\|^{n}_{\mathrm{err}}} \right)^{1/p} \Delta t_n, \tag{14}$$

where ρ denotes a safety factor that is usually set to 0.9 (Lang, 1995).

5. Results

A test model consists of a conductive ring (Figure 2(a)) which is either treated as a current-driven solid conductor (Figure 2(b)) or a voltage-driven stranded conductor (Figure 2(c)). The excitation current and voltage functions of the independent sources are

$$I(t) = I_{\max} \sin(\omega t) \quad \text{and} \quad V(t) = V_{\max} \cos(\omega t),$$

respectively. For both models, the coupled formulations were derived and then treated with the implicit (backward) Euler method, the Galerkin method, and the Crank-Nicolson method (Nicolet and Delincé, 1996). The simulated currents and voltage drops are shown in Figures 3-5.

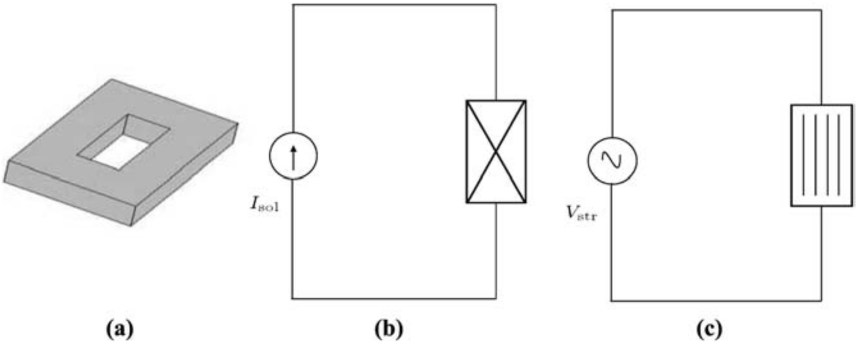

Figure 2.
(a) Conductive ring; electrical circuit models with: (b) solid conductor and (c) stranded conductor

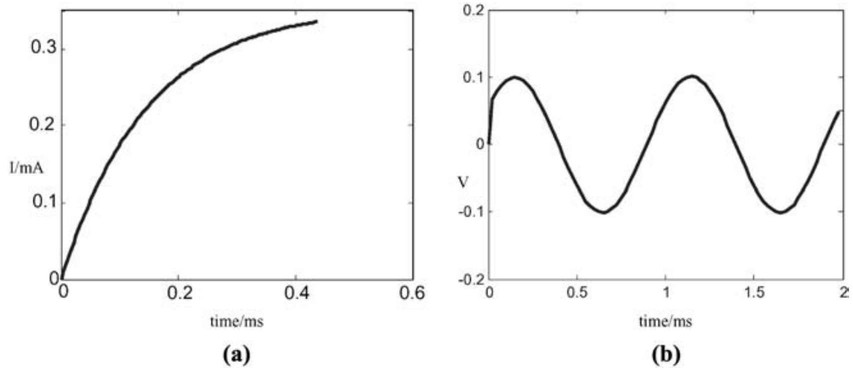

Figure 3.
Implicit Euler method: (a) calculated current for the stranded conductor and (b) calculated voltage for the solid conductor

In the stranded conductor test case, system (5) can be integrated in time in an analytical way. This allows for this test case the calculation of the absolute error of the different time integration schemes. For the solid conductor test case, only a complex-valued impedance reflecting the time-harmonic response of the system can be computed analytically. Hence, the time-integrated simulation results can only be compared to analytical data starting from that time instant when the transient phenomenon has vanished.

It is observed that only the stiffly accurate and L-stable implicit Euler method of first order is a suitable time integration method for field-circuit coupled problems (Hairer and Wanner, 1996). Some initial oscillations in the solution occur due to the lack of stiff accuracy of the Galerkin method. Since the Crank-Nicolson shows strong oscillations in the solution it is found to be unreliable for these simulations (Tsukerman, 1995).

The described model of the electrical network with the stranded conductor excited by the voltage source of the form $V(t) = V_{\max} \sin(\omega t)$ was also treated with the stiffly accurate singly diagonally implicit four stage Runge-Kutta method of order three with the embedded solution of order two (SDIRK3(2)), for which matrix $\mathbf{A}$ is (Cameron *et al.*, 1998):

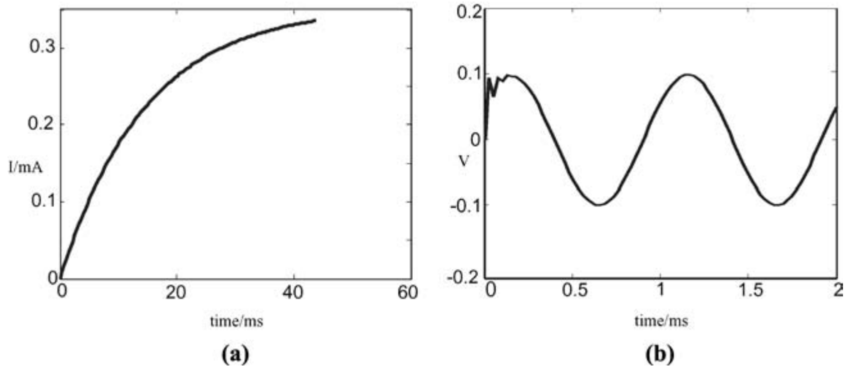

Figure 4.
Galerkin method:
(a) calculated current for the stranded conductor and (b) calculated voltage for the solid conductor

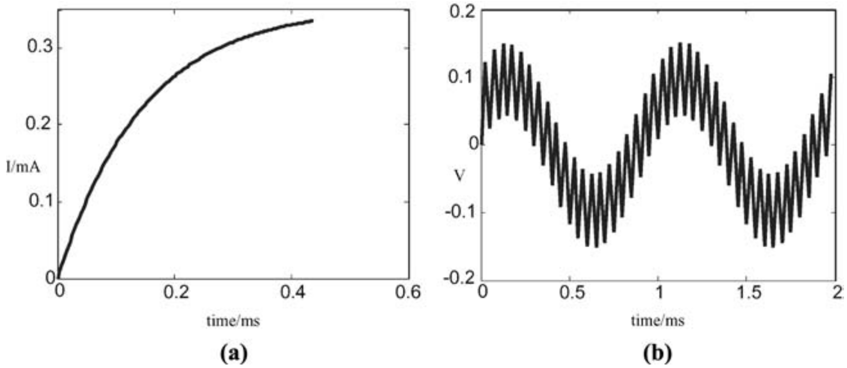

Figure 5.
Crank-Nicolson method:
(a) calculated current for the stranded conductor and (b) calculated voltage for the solid conductor

$$\begin{bmatrix} 1-\sqrt{2}/2 & 0 & 0 & 0 \\ \sqrt{2}/2 & 1-\sqrt{2}/2 & 0 & 0 \\ 5-3\sqrt{2} & 4\sqrt{2}-6 & 1-\sqrt{2}/2 & 0 \\ \sqrt{2}/3+1/6 & \sqrt{2}/6-1/3 & 1/6 & 1-\sqrt{2}/2 \end{bmatrix} \tag{15}$$

and the vectors $\mathbf{b}^{\mathrm{T}}$ and $\hat{\mathbf{b}}^{\mathrm{T}}$ are equal to the second and fourth rows of matrix $\mathbf{A}$, respectively, and $c_i = a_{ij},\ i,\ \ j = 1, \ldots, s$. Figure 6 shows the behavior of the higher order solutions for the current calculated with SDIRK3(2) for one and same values of *tol* and θ, namely $tol = 1.0 \times 10^{-2}$ and $\theta = 1.0 \times 10^{-2}$, but with different norms of the error vector applied. Table I contains the overall monitored data on the influence of the chosen error norm ((10) or (12)) and the absolute tolerance on the number of accepted and rejected time-steps and the observed maximum relative error.

6. Conclusion

Stiffly accurate and L-stable Implicit Runge-Kutta time-integration methods as the SDIRK3(2) with the embedded solutions of higher and lower order enable an error-controlled adaptive time-step selection which changes the time-step length depending on the behavior of the considered transient process. Therefore, they are the method of choice for simulating field-circuit coupled problems. The classical θ-methods do not feature such embedded solution and were shown to suffer from stability problems except for the lowest order implicit Euler scheme.

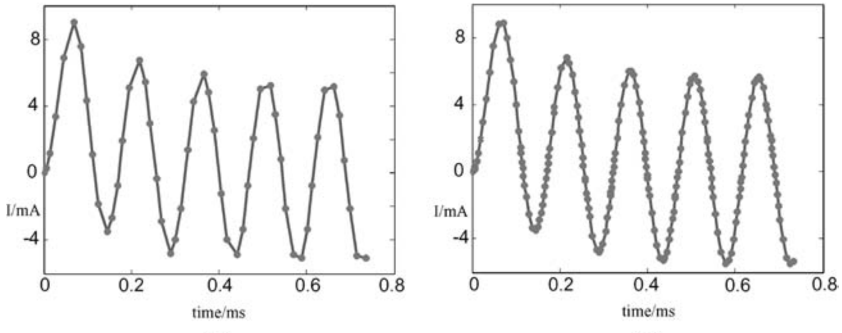

(a) **(b)**

Figure 6.
Stranded conductor: higher order currents calculated with: (a) norm (10) and (b) norm (12)

Table I.
The influence of the chosen error norm and the absolute tolerance on the number of accepted/rejected time-steps and the observed maximum relative error

		Tol					
		1.0×10^{-1}		1.0×10^{-2}		1.0×10^{-3}	
Norm		Steps	Error	Steps	Error	Steps	Error
10	$\theta = 1.0 \times 10^{-2}$	21/11	6.8×10^{-2}	50/24	3.8×10^{-2}	95/48	1.6×10^{-2}
	$\theta = 1.0 \times 10^{-3}$	22/16	6.2×10^{-2}	55/30	1.76×10^{-2}	104/57	1.3×10^{-1}
12	$\theta = 1.0 \times 10^{-1}$	76/42	7.6×10^{-2}	117/99	2.9×10^{-3}	369/217	3.8×10^{-4}
	$\theta = 1.0 \times 10^{-2}$	92/63	1.7×10^{-2}	177/106	1.3×10^{-2}	355/164	6.8×10^{-3}

References

Bedrosian, G. (1993), "A new method for coupling finite element field solution with external circuits and kinematics", *IEEE Trans. Magn.*, Vol. 29 No. 2, pp. 1664-7.

Bossavit, A. (1997), *Computational Electromagnetism: Variational Formulations, Complementary, Edge Elements*, Academic Press, San-Diego, CA.

Cameron, F., Piché, R. and Forsman, K. (1998), "Variable step size time integration methods for transient eddy current problems", *IEEE Trans. Magn.*, Vol. 34 No. 5, pp. 3319-23.

Clemens, M. and Weiland, T. (1999), "Transient eddy-current calculation with the FI-method", *IEEE Trans. Magn.*, Vol. 35 No. 3, pp. 1163-6.

Clemens, M., Wilke, W. and Weiland, T. (2001), "Advanced FI^2TD algorithms for transient eddy current problems", *COMPEL*, Vol. 20 No. 2, pp. 365-79.

Clemens, M., Wilke, W. and Weiland, T. (2002), "3-D transient eddy-current simulations using FI^2TD schemes with variable time-step selection", *IEEE Trans. Magn.*, Vol. 38 No. 2, pp. 605-8.

De Gersem, H., Mertens, R., Pahner, U., Belmans, R. and Hameyer, K. (1998), "A topological method used for field-circuit coupling", *IEEE Trans. Magn.*, Vol. 34 No. 5, pp. 3190-3.

Dular, P., Sadowski, N., Bastos, J. and Legros, W. (2000), "Dual complete procedures to take stranded inductors into account in magnetic vector potential formulations", *IEEE Trans. Magn.*, Vol. 36 No. 4, pp. 1600-5.

Gustafsson, K. (1994), "Control-theoretic techniques for stepsize selection in implicit Runge-Kutta methods", *ACM Trans. Math. Software*, Vol. 20 No. 4, p. 496.

Hairer, E. and Wanner, G. (1996), *Solving Ordinary Differential Equations II: Stiff and Differential-Algebraic Problems*, Springer, Berlin.

Hairer, E., Nørsett, S. and Wanner, G. (1993), *Solving Ordinary Differential Equations I: Nonstiff Problems*, Springer, Berlin.

Lang, J. (1995), "Two-dimensional fully-adaptive solutions of reaction-diffusion equations", *Appl. Numer. Math.*, Vol. 18, p. 223.

Mertens, R., De Gersem, H. and Hameyer, K. (2000), "Transient field-circuit coupling based on a topological approach", *COMPEL*, Vol. 19 No. 2, pp. 304-9.

Nicolet, A. and Delincé, F. (1996), "Implicit Runge-Kutta methods for transient magnetic field computation", *IEEE Trans. Magn.*, Vol. 32 No. 3, pp. 1405-8.

Tsukerman, I. (1995), "A stability paradox for time-stepping schemes in coupled field-circuit problems", *IEEE Trans. Magn.*, Vol. 31 No. 3, pp. 1857-60.

Tsukerman, I., Konrad, A. and Lavers, J. (1992), "A method for circuit connections in time-dependent eddy current problems", *IEEE Trans. Magn.*, Vol. 28 No. 2, pp. 1299-302.

Wang, H., Taylor, S., Simkin, J., Biddlecombe, C. and Trowbridge, B. (2002), "An adaptive-step time integration methods applied to transient magnetic field problems", *Proceedings of CEFC2000*, Milwaukee, WI.

Weiland, T. (1977), "A discretization method for the solution of Maxwell's equations for six-component fields", *Electronics and Communications AEÜ*, Vol. 31 No. 3, pp. 116-20.

The Emerald Research Register for this journal is available at
www.emeraldinsight.com/researchregister

The current issue and full text archive of this journal is available at
www.emeraldinsight.com/0332-1649.htm

Field-circuit model of the dynamics of electromechanical device supplied by electronic power converters

Lech Nowak and Jacek Mikołajewicz
Poznań University of Technology, Poznań, Poland

Keywords *Electromagnetism, Electric converters, Simulation*

Abstract *This paper presents a coupled field-circuit simulation of transients in a non-linear electromagnetic device supplied by electronic power converters (inverters, PWM systems). The eddy currents induced in solid cores are considered. The mathematical model of transients includes: equation of electromagnetic field, equations of the electric circuits and equation of motion. Numerical implementation of the algorithm is based on the finite element method. For time-stepping the Cranck-Nicholson scheme has been applied.*

1. Introduction

In modern electromechanical systems it is very convenient to control the supply voltage by the electronic power converters. In such case, we have an impact on the voltage value, frequency and the waveform shape.

In the paper, the dynamic operation of the electromagnetic actuators supplied with the inverters and PWM systems is analyzed. The coupled field-circuit model for simulation of transients has been elaborated. The model includes:

(1) equation of transient electromagnetic field,
(2) equations of the electric circuits of the converter and supply system, and
(3) equation of motion.

Numerical implementation is based on the finite element method. For time discretization the Cranck-Nicholson scheme has been applied. In order to include non-linearity the Newton-Raphson process has been adopted.

2. The finite element implementation

In the paper, converters with axial symmetry are considered. The two-dimensional cylindrical co-ordinate system r, z has been adopted. In such case the movement may be only in the z-direction and therefore, the equation describing transient field in a non-linear conducting and moving medium takes the form:

$$\frac{\partial}{\partial r}\left(\frac{\nu}{\rho}\frac{\partial \Phi}{\partial r}\right)+\frac{\partial}{\partial z}\left(\frac{\nu}{\rho}\frac{\partial \Phi}{\partial z}\right)=J_{\mathrm{w}}-\frac{\gamma}{\rho}\left(\frac{\partial \Phi}{\partial t}-v\frac{\partial \Phi}{\partial z}\right) \tag{1}$$

where J_{w} is the current density in the windings, $\rho = 2\pi r$; $\Phi(r,z,t) = \rho A_{\varphi}(r,z,t)$, ν, γ are the reluctivity and conductivity, respectively. As a result of FEM application, the following set of equations is obtained (Mikołajewicz, 2001; Nowak, 1999; Silvester and Ferrari, 1983):

COMPEL: The International Journal for Computation and Mathematics in Electrical and Electronic Engineering
Vol. 23 No. 4, 2004
pp. 977-985
© Emerald Group Publishing Limited
0332-1649
DOI 10.1108/03321640410553409

$$\mathbf{S\Phi} = \mathbf{Ni} - \mathbf{G}(\mathrm{d}\mathbf{\Phi}/\mathrm{d}t) - v\mathbf{\Gamma}_z\mathbf{\Phi} \tag{2}$$

where $\mathbf{S}$ is the stiffness matrix, $\mathbf{\Phi}$ is the vector of nodal potentials, $\mathbf{G}$ is the diagonal matrix of conductances of elementary rings formed by 2D mesh, $\mathbf{\Gamma}_z$ is the matrix representation of the operator "$\partial/\partial z$", $\mathbf{i}$ is the vector of currents in the windings, $\mathbf{N}$ is the matrix of turn numbers associated with the nodes within the winding regions (Mikołajewicz, 2001; Nowak, 1999).

The time-stepping Cranck-Nicholson scheme has been applied. At the nth time step the following set is obtained:

$$\mathbf{M}_n\mathbf{\Phi}_n = \mathbf{Ni}_n + \mathbf{GE}_{n-1} + v_n\mathbf{\Gamma}_z\mathbf{\Phi}_n \tag{3}$$

where

$$\mathbf{M}_n = \mathbf{S}_n + (0.5\Delta t)^{-1}\mathbf{G}; \quad \mathbf{E}_{n-1} = (0.5\Delta t)^{-1}\mathbf{\Phi}_{n-1} + \partial\Phi/\partial t|_{n-1}.$$

The last term in equation (3) is computed iteratively (Golub and Van Loan, 1983; Mikołajewicz, 2001).

If currents $\mathbf{i}(t)$ are enforced then at each time-step equation (3) may be solved directly. Otherwise, the currents in the device windings are not known in advance and therefore, the circuit equations must be considered (Nowak, 1999; Piriou and Razek, 1992; Ren and Razek, 1994).

3. Coupled discrete field-circuit model of transients

The separated branch of the electric circuit may contain: the exciting winding and external resistance, inductance and capacitance. The semiconductors are represented as non-linear, time-varying resistors.

Let n_b be the number of branches. Then, after branch connection into n_e independent loops, a system of n_e equations is obtained:

$$\mathbf{K}^\mathrm{T}\frac{\mathrm{d}\mathbf{\Psi}}{\mathrm{d}t} + \mathbf{K}^\mathrm{T}\left\{\mathbf{R}_\mathrm{w} + \mathbf{R} + \mathbf{L}\frac{\mathrm{d}}{\mathrm{d}t}\right\}\mathbf{Ki}' + \mathbf{K}^\mathrm{T}\mathbf{u}_\mathrm{c} = \mathbf{u}' \tag{4a}$$

$$\mathrm{d}(\mathbf{K}^\mathrm{T}\mathbf{u}_\mathrm{c})/\mathrm{d}t = \mathbf{K}^\mathrm{T}\mathbf{C}^{-1}\mathbf{Ki}' \tag{4b}$$

where $\mathbf{\Psi} = \mathbf{N}^\mathrm{T}\mathbf{\Phi}$ is the vector of flux linkages, $\mathbf{R}_\mathrm{w}$ is the matrix of winding resistances, $\mathbf{R}$, $\mathbf{L}$, $\mathbf{C}$ are the matrices of the external resistances, inductances and capacitances, $\mathbf{u}_\mathrm{c}$ is the vector of capacitance voltages, $\mathbf{i}'$ and $\mathbf{u}'$ are the loop currents and voltages, respectively, $\mathbf{K}$ is the incidence matrix describing the connections of branches, such that $\mathbf{i}=\mathbf{Ki}'$. After time discretization the discrete form of the Kirchhoff's equations is obtained. For the nth instant, after eliminating voltages $\mathbf{u}_{\mathrm{c}n}$, the following set of algebraic equations is obtained:

$$\begin{aligned}\mathbf{K}^\mathrm{T}\mathbf{N}^\mathrm{T}\mathbf{\Phi}_n + \Delta t\mathbf{K}^\mathrm{T}\{\mathbf{R}_\mathrm{w} + \mathbf{R} + \Delta t\mathbf{C}^{-1} + (\Delta t)^{-1}\mathbf{L}\}\mathbf{Ki}'_n \\ = \Delta t\mathbf{u}'_n + \mathbf{K}^\mathrm{T}\mathbf{N}^\mathrm{T}\mathbf{\Phi}_{n-1} + \mathbf{K}^\mathrm{T}\mathbf{LKi}'_{n-1} - \Delta t\mathbf{K}^\mathrm{T}\mathbf{u}_{\mathrm{c}n-1}\end{aligned} \tag{5}$$

Including field equations (equation (3)), the global system of coupled field-circuit equations contains $n_e + n_n$ unknowns, i.e. n_e independent currents $\mathbf{i}'_n$ and n_n nodal potentials $\mathbf{\Phi}_n$.

Because of the non-linearity of the ferromagnetic core, the stiffness matrix **S** in equation (2) and matrix **M** in equation (3) vary in successive time steps. At the *n*th instant, these matrices depend on the solution $\mathbf{\Phi}_n$ and therefore, they must be determined iteratively. In the elaborated algorithm the Newton-Raphson process has been adopted. At the *n*th instant and *k*th iteration, the vectors $\mathbf{\Phi}_n$ and $\mathbf{i}'_n$ in equations (3) and (5) are replaced with vectors $\boldsymbol{\delta}\mathbf{\Phi}_n^k = \mathbf{\Phi}_n^k - \mathbf{\Phi}_n^{k-1}$ and $\boldsymbol{\delta}\mathbf{i}'^k_n = \mathbf{i}'^k_n - \mathbf{i}'^{k-1}_n$, satisfying the sets of equations $\mathbf{P}_n^k\boldsymbol{\delta}\mathbf{\Phi}_n^k = \mathbf{R}^k_{\Phi n}$ and $\Delta t\mathbf{Z}'\boldsymbol{\delta}\mathbf{i}'^k_n = \mathbf{R}^k_{in}$ where $\mathbf{R}^k_{\Phi n}$, $\mathbf{R}^k_{in}$ are the residual vectors of the field and circuit equations (Mikołajewicz, 2001; Nowak, 1999; Piriou and Razek, 1992).

4. Discrete model of the dynamics

Under dynamic conditions, the electromagnetic force *F*(*t*) and consequently, the armature displacement *x*(*t*) are not known in advance. In such a case, the equation due to motion must also be included.

An equation of linear mechanical motion taking the friction into account can be written in the following form:

$$m(\mathrm{d}v/\mathrm{d}t) + k_\mathrm{f}v + F_\mathrm{l}(x) = F_\mathrm{e}(\mathbf{\Phi}, x) \tag{6}$$

where m is the moving mass; k_f is the coefficient of friction; $F_\mathrm{e}(\mathbf{\Phi}, x)$ and $F_\mathrm{l}(x)$ are the electromagnetic and loading forces, respectively; x and v are the displacement and velocity of moving parts, respectively.

According to the Cranck-Nicholson scheme the velocity and acceleration at $t = t_n$ are computed as follows (Mikołajewicz, 2001; Nowak, 1999):

$$v_n = 2(\Delta t)^{-1}(x_n - x_{n-1}) - v_{n-1} \tag{7}$$

$$\mathrm{d}v/\mathrm{d}t|_n = 2(\Delta t)^{-1}(v_n - v_{n-1}) - (\partial v/\partial t)|_{n-1} \tag{8}$$

Substituting equations (7) and (8) into the equation of motion the displacement x_n of the moving element can be obtained:

$$x_n = x_{n-1} + \frac{[m + 0.25\,k_\mathrm{f}\Delta t]v_{n-1}\Delta t}{m - 0.5\,k_\mathrm{f}\Delta t} + \frac{0.25[(F_{\mathrm{e}n} - F_{\mathrm{l}n}) + m(\partial v/\partial t)|_{n-1}](\Delta t)^2}{m + 0.5\,k_\mathrm{f}\Delta t} \tag{9}$$

Finally, using equation (7) the value of v_n is computed and then substituted into the set of FEM equation (3).

The electromagnetic force, $F_{\mathrm{e}n}$, and loading force, $F_{\mathrm{l}n}$, in equation (6) are not known in advance. Therefore, in order to determine the displacement x_n, the iterative calculations are required. In each iterations the non-linear field-circuits problem is solved. In a single time-step, the field distribution is calculated dozens or even hundreds of times, and therefore, it is very important to elaborate an effective procedure for determination x_n.

5. Algorithm of solving a motion equation

In the proposed algorithm, the displacement $\left(x_n^1\right)_{\mathrm{as}}$ in the first iteration of the *n*th time step is assumed on the basis of Newton's polynomial extrapolation $\tilde{x}(t)$ of function *x*(*t*). For example, assuming polynomial of order $r = 3$, we obtain:

$$\left(x_n^1\right)_{\mathrm{as}} = x_{n-4} + A_1(t_n - t_{n-4}) + B_2(t_n - t_{n-4})(t_n - t_{n-3}) \\ + C_3(t_n - t_{n-4})(t_n - t_{n-3})(t_n - t_{n-2}) \tag{10}$$

where A_1, B_2, C_3 are the coefficients of the polynomial constructed on the basis of four positions: $x_{n-4}, x_{n-3}, x_{n-2}, x_{n-1}$ of the moving element at four previous instants $t_{n-4}, t_{n-3}, t_{n-2}, t_{n-1}$ (Nowak, 1999). After assuming $(x_n^1)_{\mathrm{as}}$, the mesh is regenerated and then field distribution $\mathbf{\Phi}_n$, and electromagnetic force $F_{\mathrm{e}n}$ are computed. Next, on the basics of equation (9), the new value $(x_n^1)_{\mathrm{cal}}$ of the displacement is determined. If $|(x_n^1)_{\mathrm{as}} - (x_n^1)_{\mathrm{cal}}|/(x_n^1)_{\mathrm{cal}} > \varepsilon_x$ (ε_x – permissible incorrectness of the iterative process) then using the chord procedure, the next value of displacement is assumed.

If the moving part has an infinite length, then the structure of the system and the FEM mesh remain unchanged during the movement. In that case, calculation of the displacement is not necessary. Only the value v_n of the velocity in equation (3) has to be computed. After eliminating x_n in equations (7) and (8), the velocity can be expressed as follows:

$$v_n = \frac{(F_{\mathrm{e}n} - F_{\mathrm{l}n}) + (F_{\mathrm{e}n-1} - F_{\mathrm{l}n-1})}{2m/\Delta t + k_{\mathrm{f}}} + \frac{(m/\Delta t - 0.5k_{\mathrm{f}})v_{n-1}}{m/\Delta t + 0.5k_{\mathrm{f}}} \tag{11}$$

To test the elaborated algorithm, the dynamic state of the Tubular Linear Induction Motor (Figure 1) has been analyzed.

The number of iterations depends on the order of interpolation $\tilde{x}(t)$ or $\tilde{v}(t)$. Figure 2 shows the number of iterations versus the order of interpolation. Assuming permissible error $\varepsilon_v = 0.001$ in algorithm based on equation (11), the best results are obtained for approximation $v(t)$ of order $r = 2$ (Figure 2(a)). If the error ε_v is smaller, then the algorithms with higher approximation becomes more effective. For $\varepsilon_v = 0.00001$ the most effective is procedure with $r = 3$ (Figure 2(b)). When using algorithm concerning the displacement x_n, (based on equation (9)), the higher optimal order of approximation $x(t)$ is obtained. This is because

$$x(t) = \int v(t)\mathrm{d}t.$$

The results of dynamic simulation of the TLIM, after application of the supply three-phase voltage system are shown in Figure 3. The relative values of the electromagnetic force $F_{\mathrm{e}}(t)$, displacement $x(t)$ and velocity $v(t)$ the time have been

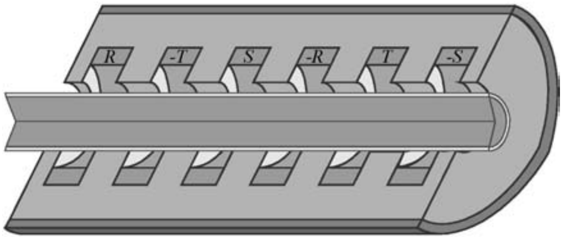

Figure 1.
Three-phase tubular linear induction motor (TLIM)

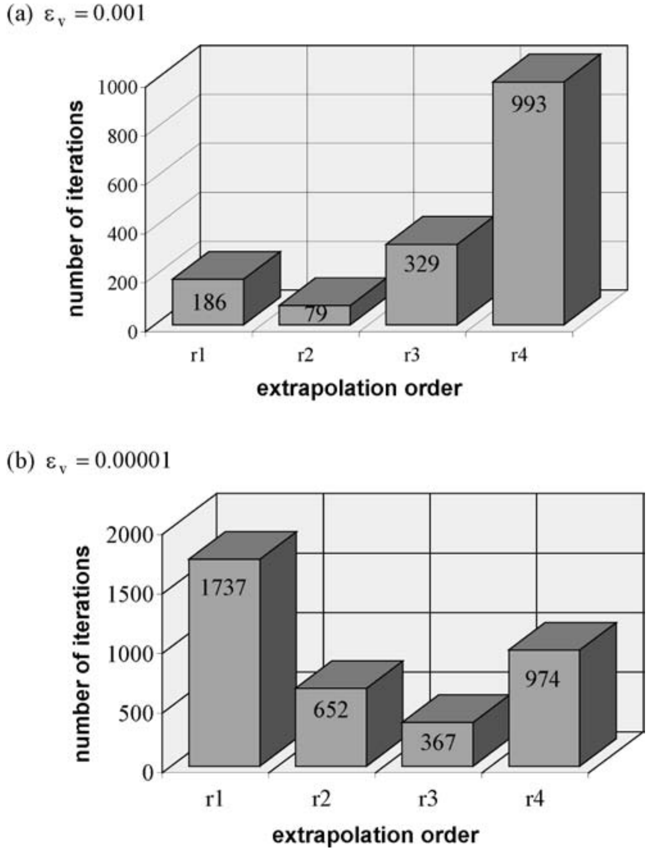

Figure 2.
Number of iteration vs order of approximation

shown. Calculations were performed for order $r = 2$ assuming permissible incorrectness $\varepsilon_v = 0.001$ (Figure 3(a)) and $\varepsilon_v = 0.01$ (Figure 3(b)).

In the second case the global number of iteration is about 30 percent less, but in the waveforms $F_e(t)$ some ripples (which does not exist in real object) occurred.

6. Inverter supplied linear motor

Three-phase TLIM supplied by three-phase voltage inverter (Figure 4) has been analyzed. Output voltage is controlled by d.c. voltage U_D and by the change of the conducting angle λ. Ideal characteristics of semiconductors has been assumed.

If the control angle $\beta = 0$, i.e. conducting angle $\lambda = \pi$, then we have six inverter steps. The circuits are characterized by two degrees of electric freedom. Assuming that in the first step the switches S1, S3 and S5 are on, the equivalent scheme corresponding to that step is shown in Figure 5.

Assuming loop currents i'_1, i'_2 as shown in Figure 5, the structure of the successive circuits can be described by six sequential incidence matrices:

(a) $\varepsilon_v = 0.001$

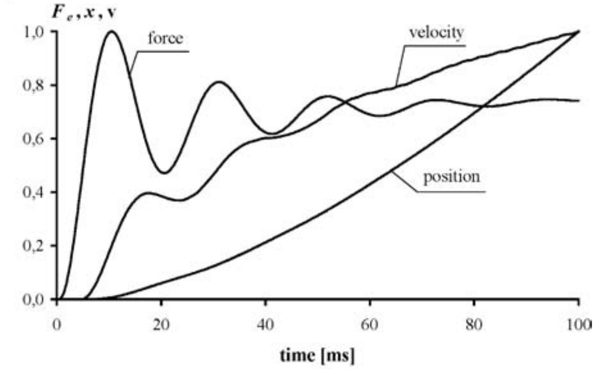

(b) $\varepsilon_v = 0.01$

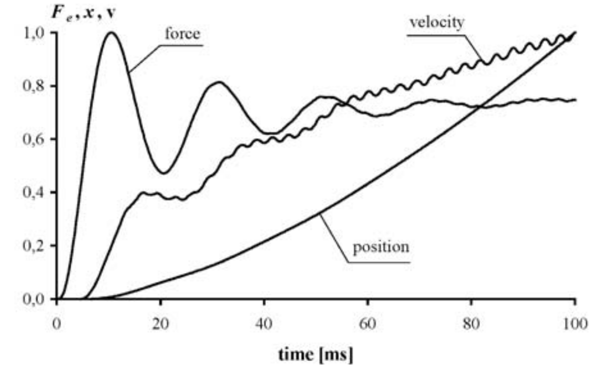

Figure 3.
Waveforms of: force $F_e(t)$, displacement $x(t)$, and velocity $v(t)$

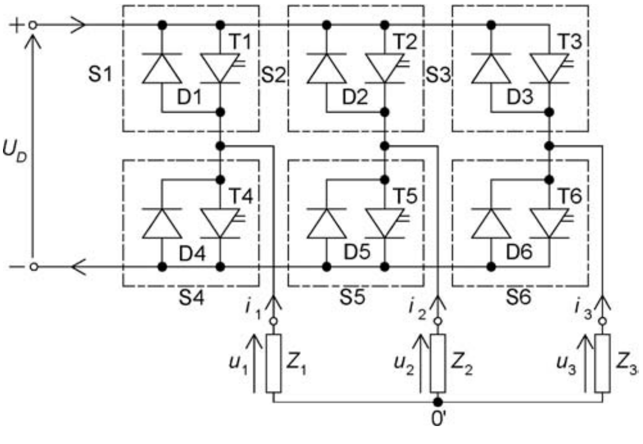
+
−
U_D
S1
S2
S3
S4
S5
S6
T1
T2
T3
T4
T5
T6
D1
D2
D3
D4
D5
D6
i_1
i_2
i_3
u_1
u_2
u_3
Z_1
Z_2
Z_3
0'

Figure 4.
Three-phase voltage inverter

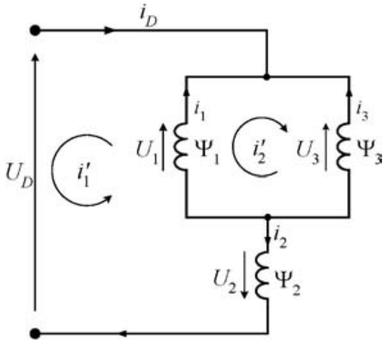

Figure 5.
Loop currents in inverter circuits

$$\mathbf{K}^{\mathrm{T}} = \begin{bmatrix} 1 & -1 & 0 \\ 1 & 0 & -1 \end{bmatrix}, \begin{bmatrix} 1 & -1 & 0 \\ 0 & -1 & 1 \end{bmatrix}, \begin{bmatrix} 1 & 0 & -1 \\ 1 & -1 & 0 \end{bmatrix}, \\ \begin{bmatrix} -1 & 1 & 0 \\ -1 & 0 & 1 \end{bmatrix}, \begin{bmatrix} -1 & 1 & 0 \\ 0 & 1 & -1 \end{bmatrix}, \begin{bmatrix} -1 & 0 & 1 \\ -1 & 1 & 0 \end{bmatrix} \tag{12}$$

If the angle $\beta > 0$, then we have 12 steps, so there are 12 incidence matrices. In additional steps one of the two parallel branches (Figure 5) is disconnected.

The transient simulation of the TLIM supplied by the voltage inverter has been performed. The field-circuits approach described in Section 3 has been applied. Figure 6 shows the currents $i_1(t), i_2(t)$ and $i_3(t)$ in the motor windings. The waveforms are non-sinusoidal and this means that additional power losses in the motor core are caused. The bold line shows the d.c. source current $i_{\mathrm{D}}(t)$.

7. Dynamic operation of PWM supplied electromagnetic actuator

To increase the initial electromagnetic force of an d.c. electromagnetic actuator and improve its dynamic characteristic, at the beginning of the operation the supply voltage is temporarily enhanced to the value $U_{\mathrm{E}} = k_{\mathrm{p}} U_{\mathrm{N}} > U_{\mathrm{N}}$ (Nowak *et al.*, 2000).

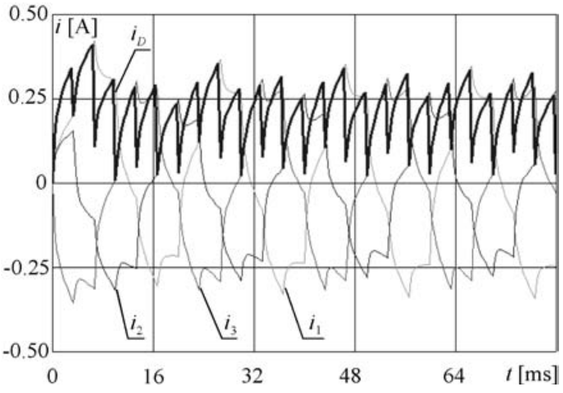

Figure 6.
Phase currents and the current absorb from the power source

On completion of the dynamic operation (at the time t_p) the voltage is decreased to the rated value U_N. The voltage control may be realized by the pulse width modulation. For $t < t_p$ the converter is supplied by the voltage $U_E = \text{const}$. For $t > t_p$ the pulsing process starts. In order to obtain the mean value of supply voltage equal to U_N the pulse width should be equal to $1/k_p f$, where f is the pulsing frequency.

The transient of an axisymmetrical plunger-type actuator with non-linear conducting core has been analyzed. Time-variations of winding current $i^*(t)$ and electromagnetic force $F^*(t)$ related to the steady-state values, for $t \geq t_p = 0.045\,\text{s}$, after the application of 2 and 24 kHz pulse voltage $U = 24\,\text{V}$ are shown in Figure 7(a) and (b).

8. Conclusion

The algorithm and software developed can be an effective tool for transient simulation of the electromechanical converters with non-linear conducting cores. The coupling of

(1) equations of electromagnetic field,

(2) equations of electric circuits, and

(a) 2 kHz

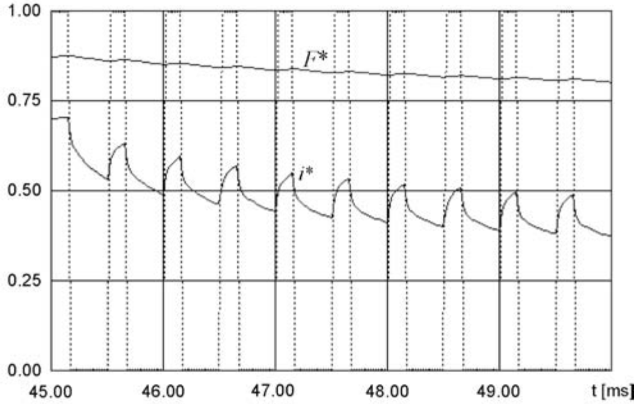

(b) 24 kHz

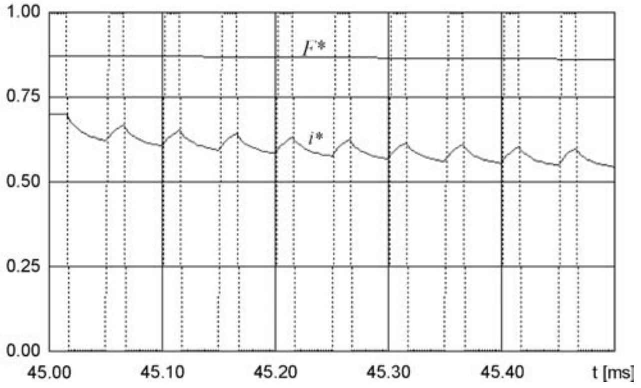

Figure 7.
Current pulsation for pulse frequency

(3) equation of the motion enables analysis of transient electromagnetic phenomena in cases of the device operation when the winding currents and the armature displacement are not known in advance.

The complicated supply systems may be considered.

References

Golub, G.H. and Van Loan, C.F. (1983), *Matrix Computations*, North Oxford Academic, Oxford.

Mikołajewicz, J. (2001), "Dynamics analysis of the linear induction motor taking the field model of the electromagnetic phenomena", Doctorate thesis (in polish), Poznań.

Nowak, L. (1999), *The Field Models of the Electromechanical Converter Transients*, (in polish), Poznań University of Technology Publishing House, Poznań.

Nowak, L., Mikołajewicz, J., Demenko, A. and Radziuk, K. (2000), "Pulse-excited transient electromagnetic field", *Proc. of XVI Symposium, Electromagnetic Phenomena in Nonlinear Circuits, 18-20 September, Kraków*, pp. 19-22.

Piriou, F. and Razek, A. (1992), "A non-linear coupled field and electric circuit equations", *Proc. of IEEE Transactions on Magnetics*, Vol. 28 No. 2, pp. 1295-8.

Ren, Z. and Razek, A. (1994), "A strong coupled model for analysing dynamic behaviours of non-linear electro-mechanical systems", *Proc. of IEEE Transactions on Magnetics*, Vol. 30 No. 5, pp. 3252-5.

Silvester, P.P. and Ferrari, K.L. (1983), *Finite Elements for Electrical Engineers*, Cambridge University Press, Cambridge.

The Emerald Research Register for this journal is available at
www.emeraldinsight.com/researchregister

The current issue and full text archive of this journal is available at
www.emeraldinsight.com/0332-1649.htm

Field-circuit transient analysis of a magnetorheological fluid brake

W. Szeląg, P. Sujka and R. Walendowski
Poznań University of Technology, Institute of Industrial Electrical Engineering, Poznań, Poland

Keywords *Magnetism, Rheology, Finite element analysis*

Abstract *This paper deals with coupled electromagnetic, hydrodynamic and mechanical motion phenomena in magnetorheological fluid brakes. The governing equations of these phenomena are presented. The numerical implementation of the mathematical model is based on the finite element method and a step-by-step algorithm. A computer program based on this algorithm was used to simulate the transients in a prototype of magnetorheological brake. The results of the calculations and measurements are presented.*

1. Introduction

The demand for electromechanical devices with upgraded functional parameters both in their steady and transient state has been growing in recent years. The research on how to improve these parameters has taken several directions. One of them involves, among others, the use of magnetorheological fluids with their physical properties changing under the influence of magnetic fields, for electromechanical converter applications.

Magnetorheological fluids (or simply MRF) were invented by Jacob Rabinow in the late 1930s (Rosensweig, 1985). Their characteristic features involve viscosity change upon the application of magnetic field. A change in viscosity is inseparably connected with a change of yield stress τ_0 in the fluid. The working principle of magnetorheological electromagnetic transducers is based on the fact that viscosity changes when the fluid is exposed to magnetic field. Naturally, the viscosity of the fluid and the stresses developed within it are related to the magnitude of the applied magnetic flux density B. The viscosity and the stresses increase with the growth of the field and so does the yield strength counteracting the motion of moveable parts in the transducers. Owing to their properties, magnetorheological fluids are useful for the efficient control of the transmission of torques and forces. They are used, among others, in rotary brakes, clutches, and rotary and linear dampers.

MR devices are studied in many renowned scientific centres throughout the world. The research focuses on the analyses of the operating states of existing devices and on the methods of improving their functional parameters but altogether new designs are also under constant development [1] (Carlson *et al.*, 1996, Verardi and Cardoso, 1998).

2. Properties of magnetorheological fluids

Magnetorheological fluid is a colloidal suspension of magnetically polarised particles with diameters ranging from 0.5 to 10 μm in a carrier fluid, mostly synthetic oil with a low evaporation rate or water [1] (Carlson *et al.*, 1996). A typical MRF contains ferromagnetic particles ranging from 20 to 80 per cent, by weight. The main feature of the fluid is dramatic change of viscosity and consequently, of shear stress upon the application of magnetic field. The relationship between the yield stress τ_0 and the

COMPEL: The International Journal for Computation and Mathematics in Electrical and Electronic Engineering
Vol. 23 No. 4, 2004
pp. 986-995
© Emerald Group Publishing Limited
0332-1649
DOI 10.1108/03321640410553418

magnetic flux density B for Lord MRF-132LD is shown in Figure 1. The stress changes during the increase and decrease of magnetic flux density occur in microseconds (Carlson *et al.*, 1996). The fluids retain their properties in the temperature range from -40 to 150°C. Relative magnetic permeability of the fluid is small, $\mu_r < 10$.

3. Magnetorheological brake

The magnetorheological fluid brake built at Poznań University of Technology is shown in Figure 2 (Szeląg, 2002). This is a cylindrical-rotor brake system. Magnetic field is excited by a ring coil in a stator. The 132LD MRF produced by Lord Corporation was used in the brake. The diameter and the length of the rotor are 26.8 and 27 mm, respectively. The maximum braking torque is c. 1.7 Nm. One of the advantages of the brake is low electric power consumption of the winding, not exceeding a couple of watts.

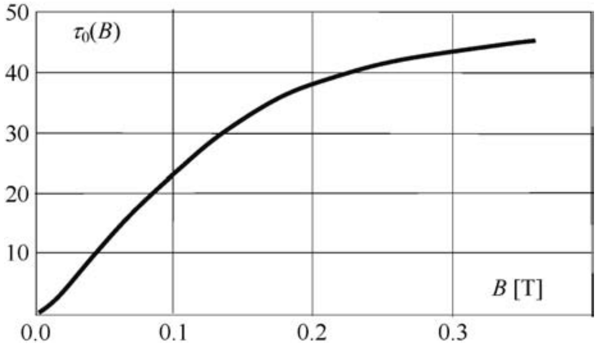

Figure 1.
The yield stress $\tau_0 = f(B)$ for MRF 132LD

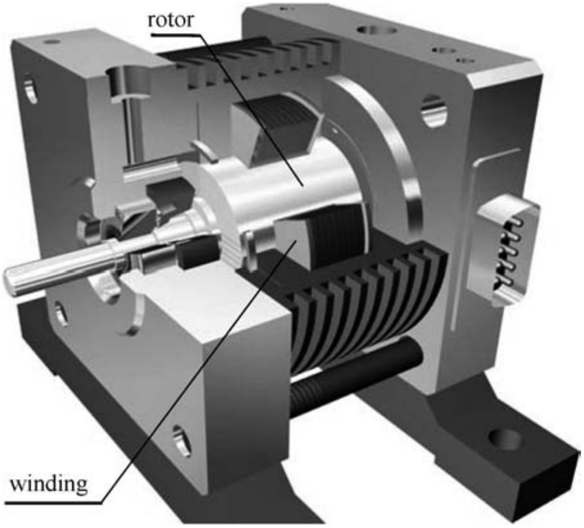

Figure 2.
The brake with MRF

The paper proposes a mathematical model of coupled electromagnetic, hydrodynamic and mechanical motion phenomena that can be applied to simulate steady and transient states of the magnetorheological fluid brake.

4. Coupled phenomena model

The phenomena observed in electromagnetic brakes with magnetorheological fluid needs to be analysed in terms of fields. In the brake the velocity field of the fluid depends on the angular velocity of the rotor and distribution of the yield stress in the fluid. These stresses are function of the magnetic field distribution. The yield strength counteracts the motion of the rotor in the brake. Therefore, the velocity field of the fluid and the mechanical stress field are coupled with the electromagnetic field. The field coupling makes the analysis of the transients in the brake highly complicated. What makes it even more intricate is the changing character of those fields and the non-linear character of the equations describing them. So far, there are no comprehensive approaches to elaborate the problem of solving the time dependent coupled field phenomena. Most papers concerning the subject usually deal with the field analysis of some selected phenomena observed in transducers (Besbes *et al.*, 1996; Chung, 1978; Demenko, 1994).

The paper is an attempt to build a model of coupled phenomena in magnetorheological transducers. It focuses on electromagnetic and hydrodynamic phenomena and also on the dynamics of movable elements in the brake. The problems pertaining to heat, ventilation and vibration have been disregarded.

A magnetorheological brake with axial symmetry is considered in the study. A cylindrical coordinate system r, z, ϑ was applied. In this case, the equation describing the transient electromagnetic field in the brake can be expressed as (Nowak, 1998; Szeląg, 2002)

$$\frac{\partial}{\partial r}\left(\frac{1}{\mu l}\frac{\partial \varphi}{\partial r}\right)+\frac{\partial}{\partial z}\left(\frac{1}{\mu l}\frac{\partial \varphi}{\partial z}\right)=J-\frac{\gamma}{l}\frac{\partial \varphi}{\partial t}. \tag{1}$$

Here $l = 2\pi r$, $\varphi = 2\pi r A_\vartheta$, where A_ϑ is the magnetic vector potential, $J = i/s$ is the current density in the winding, i is the winding current, s is the cross-sectional area of the conductor, μ is the magnetic permeability and γ is the conductivity of the region with eddy currents. For the MRF $\gamma = 0$.

In general, the transient electromagnetic field in MRF devices is voltage-excited. This means that the currents i in the windings are not known in advance, i.e. prior to the electromagnetic field calculation (Nowak, 1998; Szeląg, 2000). Therefore, it is necessary to consider the equations of the electric circuit of the device. The set of independent loop equations may be written as

$$\boldsymbol{u} = \boldsymbol{R}\boldsymbol{i} + \frac{\mathrm{d}}{\mathrm{d}t}\boldsymbol{\Psi}, \tag{2}$$

where $\boldsymbol{u}$ is the vector of supply voltages, $\boldsymbol{i}$ is the vector of loop currents, $\boldsymbol{R}$ is the matrix of loop resistances, and $\boldsymbol{\Psi}$ is the flux linkage vector. The vector $\boldsymbol{\Psi}$ is calculated by means of the field model.

The phenomenological approach was used to describe fluid dynamics. In this approach, the fluid is treated as a non-conducting continuum of properties determined by density ρ, dynamic viscosity υ and magnetic permeability μ (Bird *et al.*, 1960; Verardi and Cardoso, 1998). In the hydrodynamic model, the laminar flow of a non-compressible fluid with no mass sources is investigated. It is assumed that the gravitational forces acting on the fluid are negligible compared to the forces causing its motion in the transducer. The motion of the liquid in the ϑ-direction is caused by the motion of the rotor. It is also assumed that the internal energy and temperature of the fluid are constant. For such conditions, the differential equation of the motion of the fluid may by written as (Szeląg, 2002)

$$\frac{\partial}{\partial r}\left(\frac{\upsilon_z}{l}\frac{\partial \phi}{\partial r}\right)+\frac{\partial}{\partial z}\left(\frac{\upsilon_z}{l}\frac{\partial \phi}{\partial z}\right)=\frac{\rho}{l}\frac{\partial \phi}{\partial t}. \tag{3}$$

Here $\phi = 2\pi r v_\vartheta$, where v_ϑ is the component of velocity v in the ϑ-direction, ρ is the fluid density and υ_z is the equivalent dynamic viscosity of the fluid.

The description of the problem in equation (3) should be completed by non-slip boundary conditions $v_\vartheta = r\omega$ and $v_\vartheta = 0$ on the surface of the rotor and the frame, respectively, where ω is the angular velocity of the rotor.

In order to determine the equivalent dynamic viscosity of the fluid, physical properties of the fluid were considered. MRFs belong to the non-Newtonian group of fluids. The properties of such fluids can be described by the Bingham model (Bird *et al.*, 1960; Nouar and Frigaard, 2001). A typical characteristic family $\tau = \tau\ (D, B)$ for a one-dimensional fluid model is shown in Figure 3, where D is the velocity of deformation. The fluid behaves like a solid body for $\tau \leq \tau_0(B)$, and like a body of plastic viscosity η_p for $\tau > \tau_0(B)$, $\eta_\mathrm{p} = tg(\beta)$ (Figure 3). In the elaborated two-dimensional model of a magnetorheological fluid, the equivalent dynamic viscosity of the fluid is used (Szeląg, 2002)

$$\upsilon_z = \eta_\mathrm{p} + \tau_0(B)/\|\boldsymbol{D}\| \quad \text{for} \quad \|\boldsymbol{\tau}\| > \tau_0(B), \tag{4a}$$

$$\upsilon_z = \infty \quad \text{for} \quad \|\boldsymbol{\tau}\| \leq \tau_0(B). \tag{4b}$$

The yield stress $\tau_0(B)$ in equation (4) is determined on the basis of the distribution of the magnetic flux density B obtained from equations (1) and (2). The norms $\|\boldsymbol{D}\|$, $\|\boldsymbol{\tau}\|$ of the deformation tensor $\boldsymbol{D}$ and of the stress tensor $\boldsymbol{\tau}$ can be expressed as (Nouar and Frigaard, 2001; Szeląg, 2002)

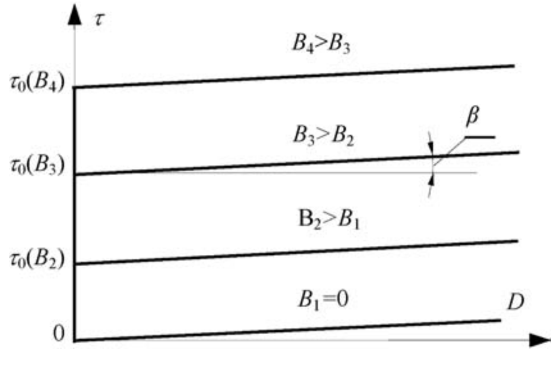

Figure 3.
The shear stress in MRF

$$\|\boldsymbol{D}\| = \left(\frac{1}{2}\sum_{i=1}^{2}\sum_{j=1}^{2} D_{i,j}^2\right)^{1/2}, \qquad \|\boldsymbol{\tau}\| = \left(\frac{1}{2}\sum_{i=1}^{2}\sum_{j=1}^{2} \boldsymbol{\tau}_{i,j}^2\right)^{1/2}, \tag{5a}$$

where

$$D_{i,j} = 0 \quad \text{for} \quad \|\boldsymbol{\tau}\| \le \tau_0(B), \tag{5b}$$

$$\boldsymbol{D} = 0.5\left[\nabla \boldsymbol{v} + (\nabla \boldsymbol{v})^T\right] \quad \text{for} \quad \|\boldsymbol{\tau}\| > \tau_0(B), \tag{5c}$$

$$\tau_{i,j} = (\eta_p + \tau_0(B)/\|\boldsymbol{D}\|)D_{i,j} \quad \text{for} \quad \|\boldsymbol{\tau}\| > \tau_0(B). \tag{5d}$$

When analysing the performance of a MRF electromechanical brake, equations (1)-(3) describing the electromagnetic and hydrodynamic phenomena must be solved together with the equation of dynamics of its movable elements. This equation has the following form

$$J_b \frac{\mathrm{d}\omega}{\mathrm{d}t} + T_b + T_0 = T_z \tag{6}$$

where J_b is the moment of inertia; T_b is the braking torque associated with the occurrence of magnetic field in the brake, T_0 is the braking torque produced in the brake when magnetic field is absent and T_z is the driving torque.

The braking torque T_b can be determined using the equation

$$T_b = \oint\!\!\!\oint_S r(\boldsymbol{\tau}_\vartheta + \boldsymbol{\tau}_{e\vartheta})\,\mathrm{d}\boldsymbol{s}. \tag{7}$$

The vectors $\boldsymbol{\tau}_\vartheta$, $\boldsymbol{\tau}_{e\vartheta}$ in this equation describe the stress in the fluid and the electromagnetic stress acting in the direction ϑ at a tangent to the external surface of the brake's rotor.

5. Finite element formulation

The equations (1)-(3) and (6) are coupled through the viscosity function $\boldsymbol{v}_z = \boldsymbol{v}_z(B, \|\boldsymbol{D}\|)$, the total braking torque $T_b = T_b(B, \|\boldsymbol{D}\|)$ and through the boundary condition $v_\vartheta = r\omega$. Therefore, these equations should be solved simultaneously.

In order to solve coupled equations the finite element method and a "step-by-step" procedure were used (Demenko, 1994; Szeląg, 2000). The backward difference scheme was also applied. The finite element and time discretisation lead to the following system of non-linear algebraic matrix equations

$$\begin{bmatrix} \boldsymbol{S}_n + (\Delta t)^{-1}\boldsymbol{G} & -\boldsymbol{w} \\ -\boldsymbol{w}^T & -\Delta t\boldsymbol{R} \end{bmatrix} \begin{bmatrix} \boldsymbol{\varphi}_n \\ \boldsymbol{i}_n \end{bmatrix} = \begin{bmatrix} (\Delta t)^{-1}\boldsymbol{G}\boldsymbol{\varphi}_{n-1} \\ -\Delta t\boldsymbol{u}_n - \boldsymbol{w}^{\mathrm{T}}\boldsymbol{\varphi}_{n-1} \end{bmatrix}, \tag{8}$$

$$\left[\boldsymbol{S}_n' + (\Delta t)^{-1}\boldsymbol{G}'\right]\boldsymbol{\phi}_n = (\Delta t)^{-1}\boldsymbol{G}'\boldsymbol{\phi}_{n-1}, \tag{9}$$

where n denotes the number of time-steps, Δt is the time-step, $\boldsymbol{S}$, $\boldsymbol{S}'$ are the magnetic and hydrodynamic stiffness matrices, $\boldsymbol{\varphi}$, $\boldsymbol{\phi}$ are the vectors of the nodal potentials

φ and ϕ, respectively, $\boldsymbol{w}^{\mathrm{T}}$ is the matrix that transforms the potentials φ into the flux linkages with the windings, $\boldsymbol{G}$ is the matrix of conductances of elementary rings formed by the mesh and $\boldsymbol{G}'$ is the matrix whose elements depend on the dimensions of the elementary rings and fluid density $\boldsymbol{\rho}$.

Motion equation (6) is approximated by the explicit difference formula (Szeląg, 2000).

$$J_b(\alpha_{n+1} - 2\alpha_n + \alpha_{n-1})/(\Delta t)^2 = T_{z,n} - T_{b,n} - T_0, \tag{10}$$

where α is the position of the rotor, $T_{z,n} = T_z(t_n)$, and $T_{b,n} = T_b(t_n)$.

The angular velocity ω of the rotor may be calculated according to the formula

$$\omega(t_n + 0.5\Delta t) = (\alpha_{n+1} - \alpha_n)/\Delta t. \tag{11}$$

The braking torque $T_{b,n}$ is described by formula (7). In the considered brake the component B_ϑ of the magnetic flux density $\boldsymbol{B}$ is equal to zero. Therefore, in equation (7) the component $\boldsymbol{\tau}_{e\vartheta}$ of Maxwell stress tensor is equal to zero.

In the presented model of coupled phenomena in the MR brake the distribution of the magnetic field does not depend on the fluid velocity. Therefore, the algorithm for solving equations (8)-(10) can be simplified. Instead of solving the equations (8) and (9) simultaneously for each time step, one may first calculate the distribution of the magnetic flux density B from equation (8) and next obtain fluid velocity distribution from equation (9). Finally, the braking torque T_b, the angular position α and the velocity ω of the rotor can be calculated from equations (7), (10) and (11), respectively.

The primary difficulty in obtaining a numerical solution of MRF flow problem, given by equation (9), is the existence of a surface separating the regions of sheared and non-sheared fluid (Bird *et al.*, 1960). The position of this surface is not known in advance, i.e. prior to the velocity field calculation (Hammand, 2000). Utilizing the previously described equivalent dynamic viscosity formulations eliminates the need to track the surface separating these two flow regions and simplifies the solution. It leads, however, to singularities since the equivalent dynamic viscosity υ_z attains an infinite value in the regions where $\|\boldsymbol{D}\| = 0$, i.e. in the regions where the fluid behaves like a solid body. In order to avoid such a problem, equations (4a) and (4b) are replaced by following equation proposed by Hammand (2000)

$$\upsilon_z = \eta + \frac{\tau_0}{\|\boldsymbol{D}\|}\left(1 - e^{-m\|\boldsymbol{D}\|}\right) \tag{12}$$

where m is an exponential growth parameter.

This approach has been utilized to provide a good approximation of the Bingham fluid properties for both low and high shear stresses τ. Extensive numerical experimentation led to the establishment of $m = 1,000$ as high enough to obtain accurate solutions (Hammand, 2000).

Equations (8) and (9) are non-linear. This results from the non-linear relationships $\mu(B)$, $\upsilon_z = \upsilon_z(B, \|\boldsymbol{D}\|)$. In order to solve these equations the Newton iterative method was used (Besbes *et al.*, 1996; Szeląg, 2000).

6. Results

The algorithm presented for solving the equations within the field model of phenomena was implemented in a computer program that simulates coupled phenomena in a magnetorheological brake. The transients in the prototype of the electromagnetic brake shown in Figure 1 were analysed.

The magnetic field was calculated in the whole cross-section of the brake shown in Figure 4 while the velocity field was analysed only in the region with the magnetorheological fluid. In the consideration it was assumed that the magnetic and velocity fields in the region with the magnetorheological fluid were calculated using the same mesh. The influence of the density of this mesh on the results of the calculations was analysed. The density was increased until the difference between the two consecutively calculated values of current or torque were observed. Finally, the region was divided into about 23,000 triangular elements. The stopping criterion for the Newton process was set at 10^{-4}. For one time step a few iterative Newton steps were sufficient to solve the equation (8) describing the electromagnetic field. In order to calculate the velocity field from equation (9) 2-15 Newton steps were required. The length of the time step was chosen as equal to 0.00005 s.

First, the elaborated program was used to determine the electromagnetic field and the velocity field of the fluid when constant voltage is applied to the winding of the brake. It was assumed that the rotor's angular velocity ω equals 150 rad/s and that the delay values for which the fluid reacts to the changes in the magnetic field are neglected. Selected examples of the distributions of magnetic field lines and the respective distributions of lines connecting the points with identical velocity values are shown in Figures 4-6.

Next, transient states in a brake driven by an induction motor were analysed. The motor was supplied from an inverter. The characteristic $T_z = f(\omega)$ of the motor and the braking torque $T_0(\omega)$ from equation (10) associated with friction were measured. The test stand is shown in Figure 7.

A transient state associated with the supply of voltage on the field-exciting coil in the brake was considered. It was assumed that prior to the voltage supply the angular velocity ω of the motor had been equal to 50 rad/s. The calculated torque-time $T(t) = J_b\,\mathrm{d}\omega/\mathrm{d}t + T_b + T_0$, current-time $i(t)$ and the velocity-time $\omega(t)$ characteristics are shown in Figure 8. The torque T_b has been calculated from equation (7).

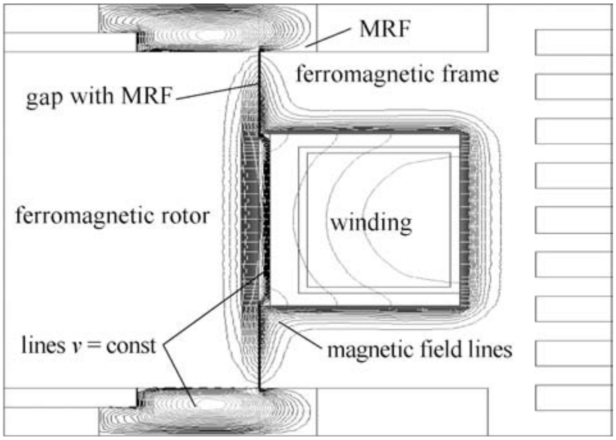

Figure 4.
Distribution of the magnetic field lines and the lines $\nu = \text{const}$, for $t = 0.004$ s

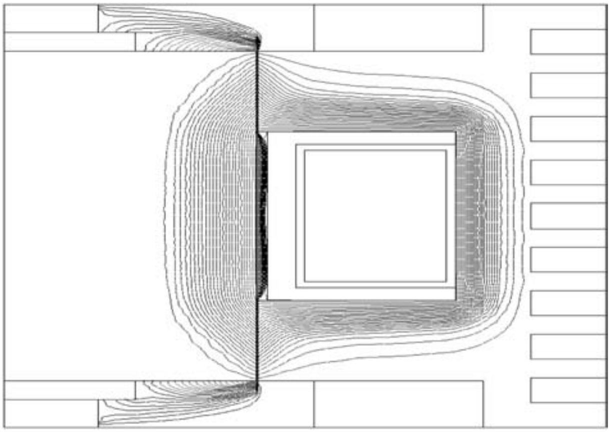

Figure 5.
Distribution of the magnetic field lines and the lines $\nu = \text{const}$, for $t = 0.05\,\text{s}$

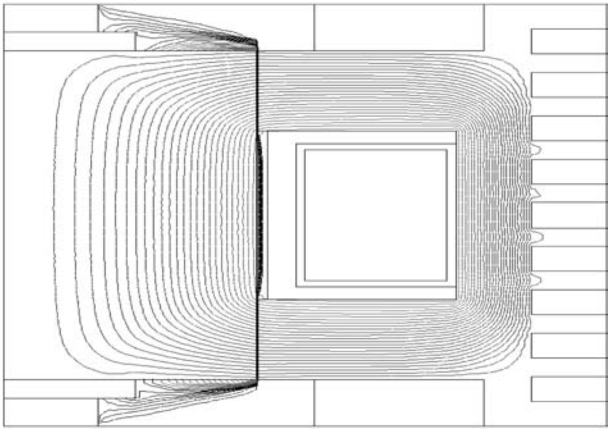

Figure 6.
Distribution of the magnetic field lines and the lines $\nu = \text{const}$ for steady state

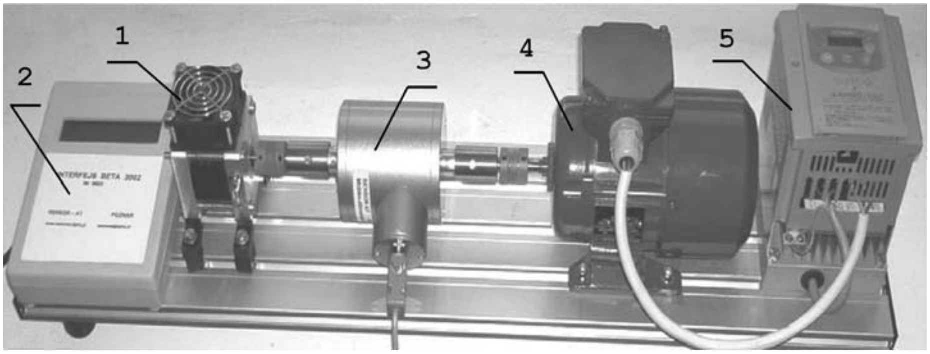

Figure 7.
Torque measuring test stand of the MRF brake: brake (1), interface BETA (2), measuring head Mt5Nm (3), induction motor (4) and converter (5)

In order to verify the calculations, the driving torque $T_z(t)$, the current $i(t)$ and the angular velocity $\omega(t)$ were measured on the prototype of the brake. The results are shown in Figure 9. Good concordance between the calculations and measurements was achieved.

The results of the calculations and measurements indicate the relevance of this simulation method in the designing process of magnetorheological brakes.

7. Conclusions

In the paper, a field model of coupled phenomena in an electromechanical brake with MR fluid was presented. The algorithm for solving the equations of the model was suggested. On the basis of this algorithm a computer program was written. The program proved to be useful in simulating the transient magnetic field and the velocity field of the fluid in magnetorheological brakes. In the analysis the non-linear properties of materials, the eddy currents induced in solid elements and the rotor movement were considered.

The model of coupled phenomena shown above and the calculation software enable a more detailed analysis of the phenomena in magnetorheological brakes than analytical models. The approach presented in the paper is very useful in devices design process when magnetorheological fluids are used as a working medium.

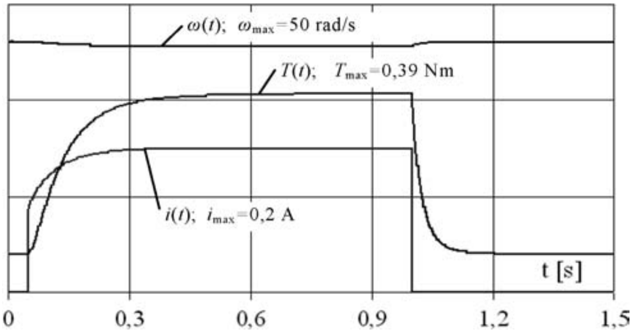

Figure 8.
Calculated torque-time $T(t)$, current-time $i(t)$ and the velocity-time $\omega(t)$ characteristics

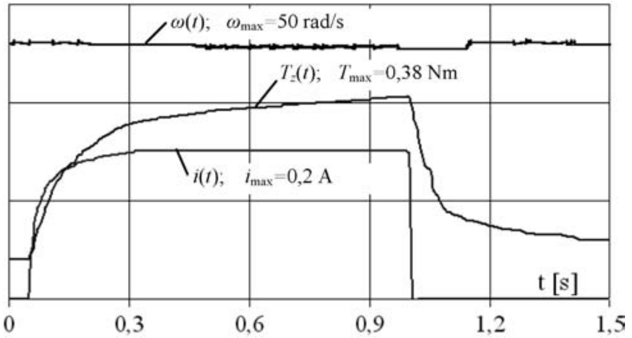

Figure 9.
Measured torque-time T_z (t), current-time $i(t)$ and the velocity-time $\omega(t)$ characteristics

Note

1. www.rheonetic.com

References

Besbes, M., Ren, Z. and Razek, A. (1996), "Finite element analysis of magneto-mechanical coupled phenomena in magnetostrictive materials", *IEEE Trans. Magn.*, Vol. 32 No. 3, pp. 1058-61.

Bird, R.B., Stewart, W.E. and Lightfoot, E.N. (1960), *Transport phenomena*, Wiley, New York, NY.

Carlson, J.D., Catanizarite, D.M. and Clair, K.A. (1996), "Commercial magnetorheological fluid device", *Proceedings of 5th International Conference on ER Fluids, MR Suspensions and Associated Technology*, *Singapore*, pp. 20-8.

Chung, T.J. (1978), *Finite Element Analysis in Fluid Dynamics*, McGraw-Hill, New York, NY.

Demenko, A. (1994), "Time stepping FE analysis of electric motor drives with semiconductor converter", *IEEE Trans. Magn.*, Vol. 30 No. 5, pp. 3264-7.

Hammand, K.J. (2000), "The effect of hydrodynamic conditions on heat transfer in a complex viscoplastic flow field", *International Journal of Heat and Mass Transfer*, No. 43, pp. 945-62.

Nouar, C. and Frigaard, I.A. (2001), "Nonlinear stability of Poiseuilla flow of Bingham fluid: theoretical results and comparison with phenomenological criteria", *Journal Non-Newtonian Fluid Mechanic*, No. 100, pp. 127-49.

Nowak, L. (1998), "Simulation of the dynamics of electromagnetic driving device for comet ground penetrator", *IEEE Trans. Magn.*, Vol. 34 No. 5, pp. 3146-9.

Rosensweig, R.E. (1985), *Ferrohydrodynamics*, Cambridge University Press, Cambridge.

Szeląg, W. (2000), "Demagnetization effects due to armature transient currents in the permanent magnet self starting synchronous motor", *EMF*, Gent, pp. 93-4.

Szeląg, W. (2002), "Finite element analysis of coupled magnetorheological fluid devices", *Proceedings of XVI Symposium Electromagnetic Phenomena in Non-linear Circuits*, Leuven, pp. 5-10.

Verardi, S.L. and Cardoso, J.R (1998), "A solution of two-dimensional magnetohydrodynamic flow using the finite element method", *IEEE Trans. Magn.*, Vol. 34 No. 5, pp. 3134-7.

The Emerald Research Register for this journal is available at
www.emeraldinsight.com/researchregister

The current issue and full text archive of this journal is available at
www.emeraldinsight.com/0332-1649.htm

The eggshell approach for the computation of electromagnetic forces in 2D and 3D

François Henrotte
Institut für Elektrische Maschinen, IEM RWTH-Aachen, Aachen, Germany
Geoffrey Deliége
Department of Computerwetenschappen, Katholieke Universiteit Leuven, Heverlee, Belgium
Kay Hameyer
Institut für Elektrische Maschinen, IEM RWTH-Aachen, Aachen, Germany

Keywords *Electromagnetism, Energy, Numerical analysis*

Abstract *The expressions of the material derivative of differential forms in the language of vector analysis are introduced. These formulae allow us to describe naturally the electromechanical coupling, and the coupling term appears to be a volume integral. A general approach to compute forces is then proposed, which takes that fact into consideration. The method is applicable in 2D and 3D with dual formulations. Numerical evidences of its efficiency are given.*

1. Introduction

The existence of such a long controversy about the computation of electromagnetic (EM) forces undoubtedly ascribes to the fact that the problem cannot be solved with the tools of vector analysis. The mathematical analysis of this problem requires indeed to consider a deforming body, and to apply adequately energy conservation rules to it. The correct background to perform such operations is differential geometry (Schutz, 1980), and one needs in particular the Lie derivative. Fortunately, the final results of the analysis can be expressed in the language of vector analysis. This gives in Section II, a set of formulae, which must be considered as axioms, and are used in Section III to solve the problem of the electromechanical coupling in a continuous medium. It turns out that the fundamental representation of the electromechanical coupling term has the form of a stress-strain product, where the Maxwell stress tensor plays by definition the role of the stress. This leads, in Section IV, to a new approach for the computation of EM forces, which is more clearly backed by the theory.

2. Lie derivative and material derivative

Let M be a continuous set of points and $u_t(X)$, $X \in M$, $t \in [a,b]$ be the trajectory of point X in an Euclidean space E. The set of trajectories of all points in M defines a flow. We call placement the map

COMPEL: The International Journal for Computation and Mathematics in Electrical and Electronic Engineering
Vol. 23 No. 4, 2004
pp. 996-1005
© Emerald Group Publishing Limited
0332-1649
DOI 10.1108/03321640410553427

This text presents research results of the Belgian programme on Interuniversity Poles of Attraction initiated by the Belgian State, Prime Minister's Office, Science Policy Programming.

$$p_t : X \in M \mapsto u_t(X) \in E, t \in [a, b]. \tag{1}$$

The flow, which is entirely defined by the placement map, is assumed to be smooth and regular enough to be differentiable and invertible when required.

The *velocity* $\mathbf{v}$ at point $x = u_t(X)$ is the vector tangent to the curve $u_t(X)$. It is defined by

$$\mathbf{v} = \frac{\partial}{\partial t} u_t(X)$$

and belongs to $T_x E$, the set of all vectors anchored at point x. The velocity field is the set of tangent vectors to all trajectories of the flow at a given instant of time.

The notions of length and angle are defined in E by means of the metric

$$g : \mathbf{v}, \mathbf{w} \in T_x E \mapsto g(\mathbf{v}, \mathbf{w}) = g_{ij} v^i w^j \in \mathbb{R} \tag{2}$$

which, at each point x, associates a number to any pair of anchored vectors. An Euclidean space is characterised by $g_{ij} = \delta_{ij}$.

Let us now consider a small piece of curve in E. As each point of the curve follows its own trajectory, the curve deforms, i.e. it changes in length, orientation, curvature, etc. But the so-called vectors, which are by definition the vectors tangent to all curves in E, are also transformed by the flow, and so is it as well in general for all tensors. All required information to describe that transformation, called convection, is actually contained in the placement map p_t. So a tensor field T becomes $p_{t+\mathrm{d}t}(p_t^{-1} T)$ at time $t + \mathrm{d}t$ by the only effect of flow convection. If now $T \neq p_{t+\mathrm{d}t}(p_t^{-1} T)$, the tensor field has got a non-zero derivative along the flow. The *Lie derivative* of the tensor field $\mathcal{L}_\mathbf{v} T$ (Schutz, 1980) is precisely that derivative along the flow. It is defined by

$$\mathcal{L}_\mathbf{v} T = \lim_{\mathrm{d}t \to 0} \frac{p_t(p_{t+\mathrm{d}t}^{-1} T) - T}{\mathrm{d}t}. \tag{3}$$

Finally, if the tensor field T depends also on time, the material derivative is defined by:

$$\mathscr{L}_\mathbf{v} T = \frac{\partial T}{\partial t} + \mathcal{L}_\mathbf{v} T, \tag{4}$$

where a notation with the velocity field explicitly mentioned has been prefered in order to remind that the material derivative depends on the flow.

Differential geometry provides the rules to compute the material derivative and the material derivative of any tensor field, and in particular of the differential forms (Bossavit, 1988; Schutz, 1980), which are the particular tensor fields we need in this paper. In a three dimensional space, there exist four kinds of differential forms called p-forms, $p = 0, 1, 2, 3$, which all have a specific expression of the material derivative, i.e.

$$\mathscr{L}_\mathbf{v} f = \frac{\partial f}{\partial t} + v^k \frac{\partial f}{\partial x^k} \tag{5}$$

$$(\mathscr{L}_{\mathbf{v}}\mathbf{h})_i = \frac{\partial h_i}{\partial t} + v^k \frac{\partial h_i}{\partial x^k} + \frac{\partial v^k}{\partial x^i} h_k \tag{6}$$

$$(\mathscr{L}_{\mathbf{v}}\mathbf{b})^i = \frac{\partial b^i}{\partial t} + v^k \frac{\partial b^i}{\partial x^k} - b_k \frac{\partial v^i}{\partial x^k} + b^i \frac{\partial v^k}{\partial x^k} \tag{7}$$

$$\mathscr{L}_{\mathbf{v}}\rho = \frac{\partial \rho}{\partial t} + v^k \frac{\partial \rho}{\partial x^k} + \rho \frac{\partial v^k}{\partial x^k} \tag{8}$$

respectively, for the 0-forms (e.g. a scalar function), the 1-forms (e.g. the magnetic field), the 2-forms (e.g. the induction field) and the 3-forms (e.g. the energy density). With obvious definitions, this can be written with more concise notations

$$\mathscr{L}_{\mathbf{v}} f = \dot{f} \tag{9}$$

$$\mathscr{L}_{\mathbf{v}}\mathbf{h} = \dot{\mathbf{h}} + (\nabla\mathbf{v}) \cdot \mathbf{h} \tag{10}$$

$$\mathscr{L}_{\mathbf{v}}\mathbf{b} = \dot{\boldsymbol{b}} - \mathbf{b} \cdot (\nabla\mathbf{v}) + \mathbf{b}\,\mathrm{tr}(\nabla\mathbf{v}) \tag{11}$$

$$\mathscr{L}_{\mathbf{v}}\rho = \dot{\rho} + \mathrm{tr}(\nabla\mathbf{v})\rho \tag{12}$$

where $\dot{z}$ denotes the total derivative of $z(t, x^k)$, obtained by applying the chain rule, component by component if z is a vector field. Finally, the material derivative allows us to compute the time derivative of integrals over moving domains:

$$\frac{\mathrm{d}}{\mathrm{d}t} \int_\Omega \rho \,\mathrm{d}\Omega = \int_\Omega \mathscr{L}_{\mathbf{v}}\rho \,\mathrm{d}\Omega. \tag{13}$$

3. Maxwell stress tensor

In an electromechanical problem, the variation of the EM energy functional is not equal to the variation (in the sense of change) of the EM energy stored in the system. One misses indeed the work W_{EM} done by the EM forces. Let the EM energy density ρ^Ψ of an electromechanical system Ω be a known function of the induction field $\mathbf{b}$. By means of the formulae (9)-(13) and the classical chain rule of derivatives, the time derivative of the EM energy Ψ writes

$$\begin{aligned} \dot{\Psi} &= \int_\Omega \mathscr{L}_{\mathbf{v}}\rho^\Psi = \int_\Omega (\dot{\rho}^\Psi + \mathrm{tr}(\nabla\mathbf{v})\rho^\Psi) = \int_\Omega \left(\frac{\partial \rho^\Psi}{\partial \mathbf{b}} \cdot \dot{\mathbf{b}} + \mathrm{tr}(\nabla\mathbf{v})\rho^\Psi \right) \\ &= \int_\Omega \left(\frac{\partial \rho^\Psi}{\partial \mathbf{b}} \cdot \mathscr{L}_{\mathbf{v}}\mathbf{b} \right) + \int_\Omega \left(\mathbf{b} \cdot \nabla\mathbf{v} \cdot \frac{\partial \rho^\Psi}{\partial \mathbf{b}} - \mathrm{tr}(\nabla\mathbf{v}) \left(\frac{\partial \rho^\Psi}{\partial \mathbf{b}} \cdot \mathbf{b} - \rho^\Psi \right) \right). \end{aligned} \tag{14}$$

The first term at the equation (14) is the definition of the change in stored EM energy and the second term is the mechanical power $\dot{W}_{\mathrm{EM}}$ received by the EM system.

A similar calculation for the EM coenergy Φ gives

$$\dot{\Phi} = \int_\Omega \left(\frac{\partial \rho^\Phi}{\partial \mathbf{h}} \cdot \mathscr{L}_{\mathbf{v}}\mathbf{h} \right) - \int_\Omega \left(\frac{\partial \rho^\Phi}{\partial \mathbf{h}} \cdot \nabla\mathbf{v} \cdot \mathbf{h} - \mathrm{tr}(\nabla\mathbf{v})\rho^\Phi \right) \tag{15}$$

where the first term at the rhs is the change in stored EM coenergy and the second term is $-\dot{W}_{\mathrm{EM}}$.

One can now notice that $\dot{W}_{\mathrm{EM}}$ does not involve the velocity field $\mathbf{v}$ itself but only its gradient $\nabla\mathbf{v}$. The Maxwell stress tensor is by definition the dual of the latter:

$$\dot{W}_{\mathrm{EM}} = \int_{\Omega} \sigma_{\mathrm{EM}} : \nabla\mathbf{v}. \tag{16}$$

Simple calculations give

$$\sigma_{\mathrm{EM}} = \mathbf{b}\frac{\partial\rho^{\Psi}}{\partial\mathbf{b}} - \left(\frac{\partial\rho^{\Psi}}{\partial\mathbf{b}}\cdot\mathbf{b} - \rho^{\Psi}\right)\mathbb{I} \tag{17}$$

$$\sigma_{\mathrm{EM}} = \frac{\partial\rho^{\Phi}}{\partial\mathbf{h}}\mathbf{h} - \rho^{\Phi}\mathbb{I} \tag{18}$$

where $\mathbb{I}$ is the identity matrix, respectively, for the formulations in $\mathbf{b}$ and in $\mathbf{h}$. Note the use of the dyadic (undotted) vector product $(\mathbf{vw})_{ij} = v^i w^j$ and the tensor product $a : b = a_{ij}b_{ij}$.

It should be carefully noted that the Maxwell stress tensor σ_{EM} is defined as a true mechanical stress, i.e. its work is delivered by the mechanical system and received by the electromagnetic system. On the other hand, the EM forces defined by $\rho^{\mathbf{f}} = \operatorname{div}\sigma_{\mathrm{EM}}$ are magnetic forces. Their work is delivered by the electromagnetic system and received by the mechanical system. This should be clearer after integrating equation (16) by part:

$$\int_{\Omega} \sigma_{\mathrm{EM}} : \nabla\mathbf{v} = -\int_{\Omega} \rho^{\mathbf{f}}_{\mathrm{EM}}\cdot\mathbf{v} + \int_{\partial\Omega} \mathbf{n}\cdot\sigma_{\mathrm{EM}}\cdot\mathbf{v} \tag{19}$$

with $\partial\Omega$ the boundary of Ω and $\mathbf{n}$ the exterior normal to $\partial\Omega$. Moreover, being defined as the EM energy dual of $\nabla\mathbf{v}$ at the local level, the Maxwell stress tensor can, as such, directly play the role of an applied stress in the structural equations of the system

$$\operatorname{div}(\sigma + \sigma_{\mathrm{EM}}) + \rho^{\mathbf{f}} = 0, \tag{20}$$

which is easier than coupling through the EM forces ρ_{EM}, since the latter are singular at material interfaces.

4. The eggshell approach

Let us consider a system Ω with a piece Y that can move in the aperture of a C-core X, not completely represented here. An eggshell shaped region S is defined, that encloses the moving piece (Figure 1) and whose thickness need not be constant. The region Z is defined such that $X \cup Y \cup S \cup Z = \Omega$; Z and S only contain air. The problem is now how to compute the EM forces on Y. The natural mechanical unknowns of this problem are the velocities $\mathbf{v}$ (or equivalently the displacements) at all nodes of the region Y. We have seen however that the coupling term equation (16) involves a velocity field, virtual or not, defined on the whole study domain Ω. We must thus first understand the role played by the velocity field $\mathbf{v}$ in $\Omega - Y$. For the sake of simplicity, X and $\partial\Omega$ are assumed rigid and fixed, i.e. we are only interested in the forces on Y. We have then from (19)

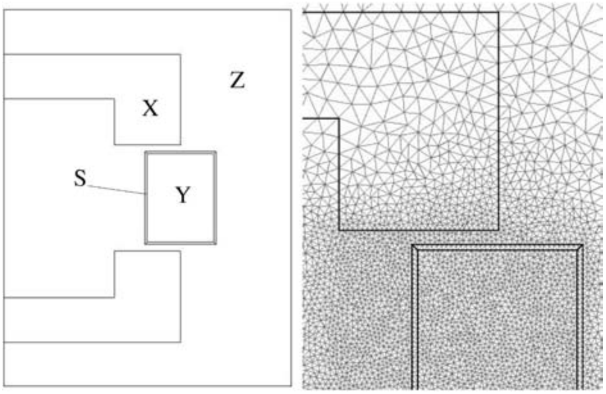

Figure 1.
Geometry of the c-core and detail of the mesh in the airgap

$$\int_{\Omega-Y} \sigma_{\mathrm{EM}} : \nabla \mathbf{v} = -\int_{\partial Y} \mathbf{n} \cdot \sigma_{\mathrm{EM}} \cdot \mathbf{v}, \tag{21}$$

because $\mathbf{v} = 0$ on $X \cup \partial\Omega$ (clamped rigid parts) and $\rho^{\mathrm{f}}_{\mathrm{EM}} = 0$ in $Z \cup S$ (air). This means that the contribution of the exterior of Y to the coupling term is completely determined by the value of the velocity field on its boundary ∂Y. Consequently, the velocity field $\mathbf{v}$ is arbitrary in the interior of $Z \cup S$, but it must connect continuously with $\mathbf{v}$ on ∂Y, which is not zero. The velocity field blurs thus necessarily out of the moving region. The idea of the eggshell approach is to set the velocity field to zero in Z, confining the non-zero velocity field in the shell S, and of course in Y.

Let us now state that the moving piece Y is rigid and shifted by an infinitesimal displacement $\delta\mathbf{u}$. The only region that deforms is S. The (virtual) velocity field associated with that deformation, and its gradient are

$$\mathbf{v} = \gamma\,\delta\dot{\mathbf{u}}, \quad \nabla\mathbf{v} = \nabla\gamma\,\delta\dot{\mathbf{u}}, \tag{22}$$

where γ is any smooth function whose value is 1 on the inner surface of the shell and 0 on the outer surface. Using (16), one can write

$$\dot{W}_{\mathrm{EM}} = -\mathbf{F} \cdot \delta\dot{\mathbf{u}} = \int_S \sigma_{\mathrm{EM}} : \nabla\mathbf{v}\, \mathrm{d}S, \tag{23}$$

where $\mathbf{F}$ is the resultant force on Y, and finally, using equation (22), one gets

$$\mathbf{F} = -\int_S \sigma_{\mathrm{EM}} \cdot \nabla\gamma\, \mathrm{d}S, \tag{24}$$

which is the eggshell formula for the EM resultant force on a rigid body. Only the Maxwell stress tensor of empty space is required here. The formula applies in 2D and in 3D. It applies also directly to dual formulations, provided one uses equation (17) for the **b**-formulation and equation (18) for the **h**-formulation. The eggshell formula can be seen as a generalized variant of Arkkio's formula for torque in electrical machines (Arkkio, 1987). The Coulomb's technique to compute nodal EM forces (local derivative of the Jacobian, Coulomb, 1983) can also be considered as the independent application of the eggshell method to the different nodes of a mesh, the support of a node-based shape function being the eggshell around that node. At the limit for an infinitely thin shell, one finds back the classical result that the resultant EM force on a rigid body is given by the flux of the Maxwell stress tensor through an enclosing surface.

The eggshell formula for rigid body movement is tested in 2D on the C-core problem (Figure 1). The moving piece Y ($3 \times 4\,\mathrm{mm}$) is inserted in the magnetic core X, leaving an airgap of 0.4 mm on both sides. The magnetic horizontal force tends to bring the moving piece back in alignment with the C-core. The problem is solved with dual finite element formulations, so as to check the accuracy of the computed fields and forces, (Figure 2). The constitutive law $\mathbf{b} = \mu(|\mathbf{h}|)\mathbf{h}$ with

$$\mu(h) = \begin{cases} a + \mu_{\mathrm{fix}} & \text{if } h \leq h_{\mathrm{fix}} \\ a + \frac{1}{d\,h + c} & \text{if } h > h_{\mathrm{fix}} \end{cases} \tag{25}$$

with $c = 1/\mu_{\mathrm{fix}} - dh_{\mathrm{fix}}$, is representative of a saturable material and has the technical advantage that it can be inverted, i.e. $\mathbf{h}$ can be expressed as a function of $\mathbf{b}$, and the (co)energy functionals can be integrated analytically. The parameters were set to $\mu_{\mathrm{fix}} = 7.55 \times 10^{-3}$, $h_{fix} = 103.35$, $a = 1.5 \times 10^{-5}$ and $d = 0.625$ (all quantities in SI units).

In Figure 3, the global forces computed with the eggshell formula (24) are compared with the forces computed by a direct differentiation of the EM (co)energy, using a second order finite difference scheme for the derivative. A perfect match is observed, which shows the validity of the eggshell approach. The eggshell formula however, requires only one solution of the system whereas direct differentiation requires several solutions, with slightly changed positions of the moving body. The difference between the values computed with the **b**-formulations and with the **h**-formulation are due to the discretisation error. For variational consistency, it is better not to mix fields from

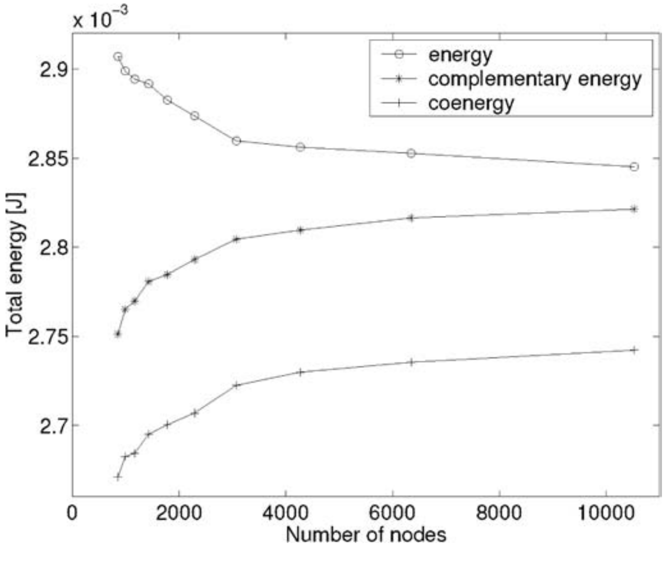

Figure 2.
Energy Ψ, coenergy Φ and complementary energy $\int_{\Omega} \mathbf{b} \cdot \mathbf{h}\, d\Omega - \Phi$ as a function of the number of nodes. The difference between energy and complementary energy is a measure of the global discretisation error

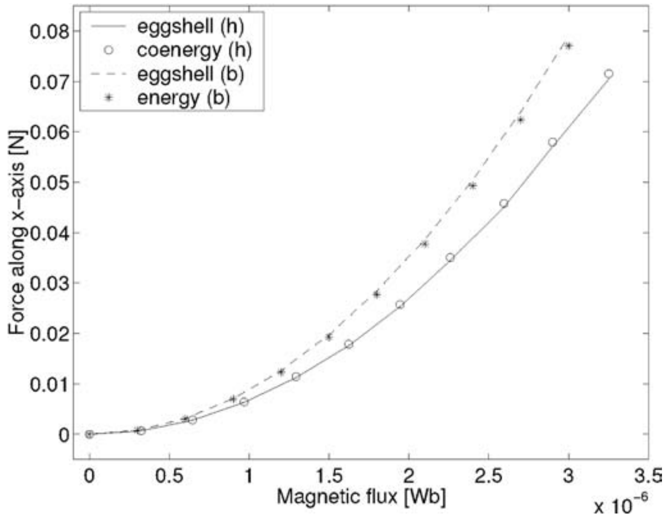

Figure 3.
Comparison of the horizontal forces computed with the eggshell method and the direct derivation of energy (**b**-formulation) or of coenergy (**h**-formulation)

different formulations when evaluating the Maxwell stress tensor, i.e. for instance, not to mix the **h** field from a **h**-formulations with the **b** field from a **b**-formulations, although this may seem a good idea from the point of view of the individual accuracy of the different fields. Figure 4 shows indeed that the forces computed with the mixed expression

$$\sigma_{\mathrm{EM}} = \mathbf{b}\,\mathbf{h} - \frac{\mathbf{b}\cdot\mathbf{h}}{2}\mathbb{I}$$

are less accurate.

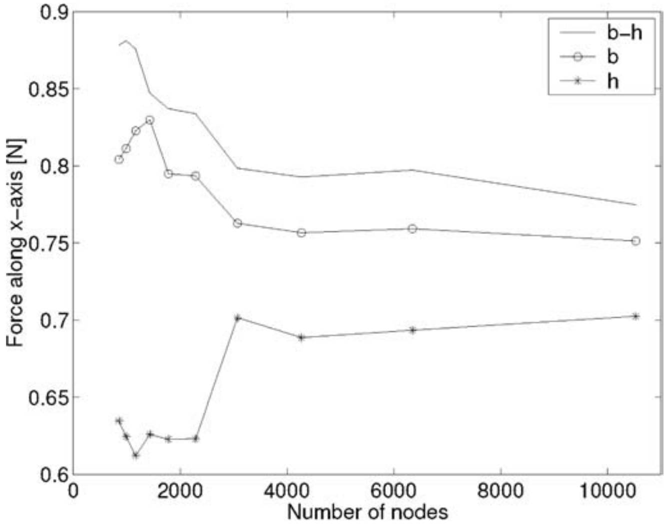

Figure 4.
Effect of a variational inconsistency

The eggshell approach gives a certain freedom in the definition of the shell. This is one of its advantages. The shape is actually free and the shell needs not be in contact with the moving piece. The effect of the thickness of the shell and of the distance between the moving piece and the shell are shown at Figures 5 and 6, respectively. One sees that a better accuracy is obtained if the shell is not placed directly in contact with the magnetic moving piece, because of the singularity of EM fields at material corners. Another way to define the eggshell is to select all finite elements in $\Omega - Y$ that have at least one node on ∂Y. The γ function is then the sum of the shape functions of the nodes of ∂Y.

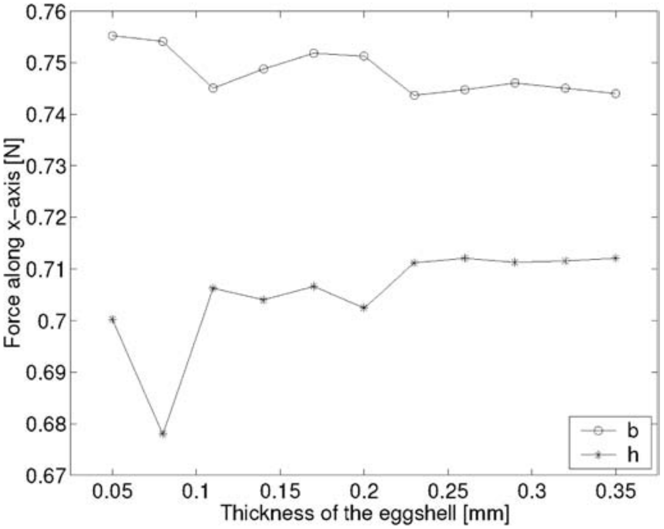

Figure 5.
Effect of the thickness of the shell

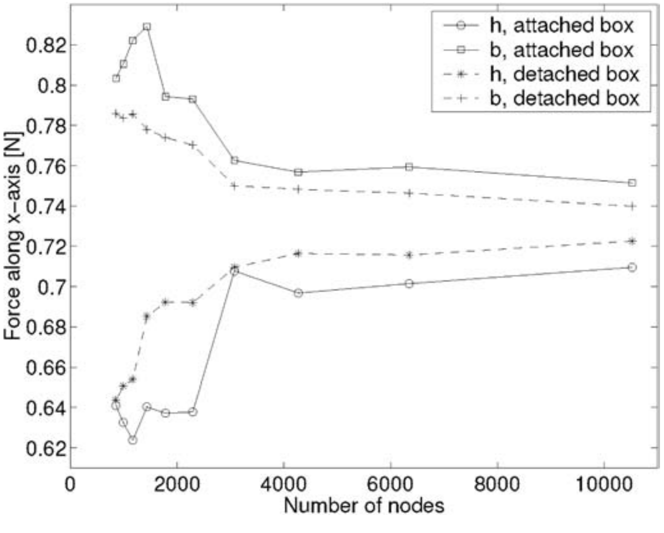

Figure 6.
Effect of not placing the shell in contact with the ferromagnetic moving piece

This way of defining the eggshell has been used in 3D to compute the deformation of a rectangular magnetic frame, of which by symmetry only one quarter was modelled (Figure 7).

Let Y be the deforming piece. The weak form of equation (20) can be written

$$\int_Y \sigma : \nabla \mathbf{v}' + \int_\Omega \sigma_{\mathrm{EM}} : \nabla \mathbf{v}' + \int_Y \rho^{\mathbf{f}} \cdot \mathbf{v}' = 0 \quad \forall\, \mathbf{v}' \tag{26}$$

so as to make explicit use of the coupling term equation (16). As the trial functions $\mathbf{v}'$ are the shape functions of the nodes of Y, the integration of the coupling term can be limited to $Y \cup S$, where the egsshell S is the set of all finite elements in $\Omega - Y$ that have at least one node on ∂Y. In this case, the eggshell approach allows a very straightforward implementation of an electromechanical problem. It avoids to compute the trace of σ_{EM} on ∂Y, making benefit of the existing magnetic mesh outside the deforming piece

5. Conclusion

The Lie derivative and the material derivative of differential forms have been introduced, in the language of vector analysis. They allow us to determine the fundamental form of the electromechanical coupling term in continuous media. The eggshell approach is based on that particular form and the classical methods to compute EM forces (Arkkio's method, Coulomb's method, integration of Maxwell stress tensor on an enclosing surface, …) are particular cases of it. However, the eggshell approach is more directly and more clearly linked with the underlying energy considerations at the continuous and at the discrete level, for rigid and non-rigid

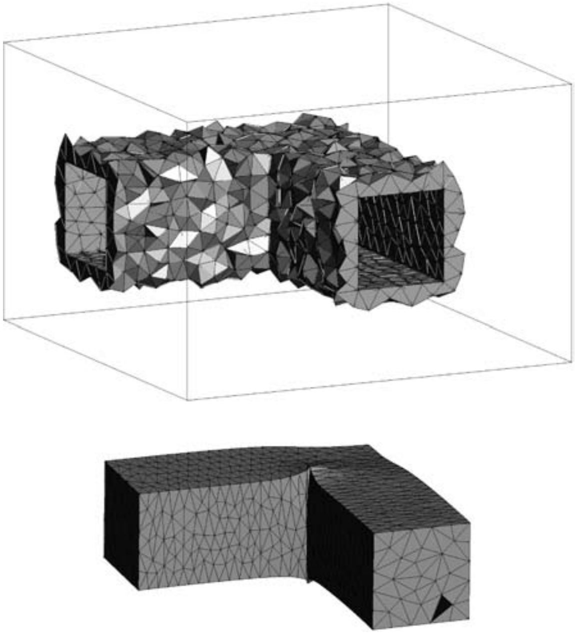

Figure 7.
Eggshell around a quarter of the rectangular magnetic frame, and deformed state

movements. This makes this approach easier to understand and to implement in a finite element program.

References

Arkkio, A. (1987), “Analysis of induction motors based on the numerical solution of the magnetic field and circuit equations”, *Acta Polytechnica Scandinavica*, p. 56.

Bossavit, A. (1988), “Whitney forms: a class of finite elements for 3D computations in electromagnetism”, *IEE Proceedings*, Part A, Vol. 135 No. 8, pp. 493-500.

Coulomb, J.L. (1983), “A methodology for the determination of global electromechanical quantities from a finite element analysis and its application to the evaluation of magnetic forces, torques and stiffness”, *IEEE Transactions on Magnetics*, Vol. 19 No. 6, pp. 2514-19.

Schutz, B. (1980), *Geometrical Methods of Mathematical Physics*, Cambridge University Press, Cambridge.

Further reading

Henrotte, F. and Hameyer, K. (2004), “Computation of electro-magnetic force densities: Maxwell stress tensor vs virtual work principle”, *Journal of Computational and Applied Mathematics*, forthcoming.

The Emerald Research Register for this journal is available at
www.emeraldinsight.com/researchregister

The current issue and full text archive of this journal is available at
www.emeraldinsight.com/0332-1649.htm

Comparison of sliding-surface and moving-band techniques in frequency-domain finite-element models of rotating machines

Herbert De Gersem
Institut für Theorie Elektromagnetischer Felder (TEMF), Technische Universität Darmstadt, Darmstadt, Germany
Johan Gyselinck and Patrick Dular
Department of Electrical Engineering and Computer Science (ELAP), University of Liège, Liège, Belgium
Kay Hameyer
RWTH Aachen, Institut für Elektrische Maschinen, Aachen, Germany
Thomas Weiland
Institut für Theorie Elektromagnetischer Felder (TEMF), Technische Universität Darmstadt, Darmstadt, Germany

Keywords *Finite element analysis, Electric machines, Electrotechnology*

Abstract *The sliding-surface and moving-band techniques are introduced in frequency-domain finite element formulations to model the solid-body motion of the rotors in an cylindrical machine. Both techniques are compared concerning their feasibility and computational efficiency. A frequency-domain model of a capacitor motor is equipped with a sliding surface and compared to a transient model with moving band. This example illustrates the advantages of frequency-domain simulation over transient simulation for the simulation of steady-state working conditions of electrical machines.*

1. Introduction

One of the most important design criteria for electrotechnical devices is given by their characteristics for steady-state operation. Properties such as, efficiency, produced torque, magnitude of the effective current, harmonic contents of currents and voltages, temperature rise at nominal operation are examined prior to fine tuning the design towards characteristics of secondary importance. The nominal operation mode of almost all electrical energy transducers is an operation at steady-state, i.e. periodically changing currents, voltages, speed and torque. For the numerical simulation of such conditions, frequency-domain formulations may be advantageous over transient formulations, especially when only a small number of *a priori* known significant time-harmonic components are expected. Standard static and time-harmonic approaches are commonly

---

The research was carried out in the frame of the Inter-University Attraction Pole IAP P5/34 for fundamental research funded by the Belgian federal government. Herbert De Gersem is working in the cooperation project "DA-WE1 (TEMF/GSI)" with the "Gesellschaft für Schwerionenforschung (GSI)", Darmstadt.

COMPEL: The International Journal for Computation and Mathematics in Electrical and Electronic Engineering
Vol. 23 No. 4, 2004
pp. 1006-1014
© Emerald Group Publishing Limited
0332-1649
DOI 10.1108/03321640410553436

applied to particular transformer and motor models. Neglecting the influence of higher harmonics, introduced by e.g. ferromagnetic saturation, non-linear loads, power electronic equipment and moving parts, is however, only acceptable in specific cases. The increasing machine performance and the application of inverters necessitates to account for higher harmonic effects in the simulations. A multi-harmonic approach meets this requirement by considering a set of harmonic components at predefined frequencies (Yamada *et al.*, 1989). The higher harmonics introduced by saturation and switching devices can be considered as illustrated by transformer examples. The application of the frequency-domain approach to models with moving parts, e.g. electrical machines, is not straightforward (Vandevelde *et al.*, 1994; Vinsard and Laporte, 1994). The Lagrangian approach which is commonly applied for transient, motional eddy current simulation, ties different coordinate systems to each of the solid, moving or non-moving bodies. The continuity of the magnetic field is enforced by e.g. a moving-band approach (Davat *et al.*, 1985) or a sliding-surface technique (Rodger *et al.*, 1990). Although these techniques are well-established in transient simulation schemes, their application in frequency-domain formulations still causes numerical inconveniences. In this paper, the moving-band and sliding-surface techniques are introduced in frequency-domain finite element (FE) models and compared for their efficiency.

2. Multi-harmonic simulation

A comparison is set-up for a 2D frequency-domain FE model of a rotating machine, using the magnetodynamic formulation:

$$-\frac{\partial}{\partial x}\left(\nu\frac{\partial A_z}{\partial x}\right)-\frac{\partial}{\partial y}\left(\nu\frac{\partial A_z}{\partial y}\right)+\sigma\frac{\partial A_z}{\partial t}=J_{\mathrm{s}} \qquad (1)$$

in terms of the z-component A_z of the magnetic vector potential with ν the reluctivity, σ the conductivity and J_{s} the source current density. The coordinate system at the stator is denoted by (x, y) or in polar coordinates (r, θ). The coordinate systems at the rotor, i.e. (x', y') and (r, θ'), are related to those at the stator by $\theta' = \theta - \omega_m t$ with ω_m the constant angular mechanical velocity.

The frequency-domain FE technique applies a twofold weighted residual approach together with a twofold discretisation, i.e. a spatial discretisation of a domain Ω by a linear independent set of n_{fe} FE shape functions $\alpha_j(x, y)$ and a time discretisation at a temporal domain Υ over the time period T by an orthonormal set of n_{hm} harmonic functions $H_q(t)$ (Gyselinck *et al.*, 2002). The harmonic functions are chosen from the set $\{1, \sqrt{2}\cos(\omega_q t), -\sqrt{2}\sin(\omega_q t)\}$, where 1 represents the DC components and ω_q belongs to a set of *a priori* chosen electrical pulsations which are multiples of the fundamental pulsation $\omega_{\mathrm{fund}} = 2\pi/T$. The combined shape functions $\alpha_j(x,y)H_q(t)$ are basis functions for the product space combining both approximation spaces. The discretisation of the magnetic vector potential reads:

$$A_z(x,y,t)=\sum_{j=1}^{n_{\mathrm{fe}}}\sum_{q=1}^{n_{\mathrm{hm}}}u_{j,q}\alpha_j(x,y)H_q(t). \qquad (2)$$

The application of the Ritz-Galerkin technique, i.e. the weighing of the partial differential equation (1) with A_z discretised by equation (2) results in the system of equations:

$$\mathbf{K}\mathbf{u} = \mathbf{f} \tag{3}$$

where

$$\begin{aligned}\mathbf{K}_{i,p,j,q} &= \int_{\Omega}\int_{\Upsilon}\left(\nu H_p H_q \nabla\alpha_i \cdot \nabla\alpha_j + \sigma H_p \frac{\mathrm{d}H_q}{\mathrm{d}t}\alpha_i\alpha_j\right)\mathrm{d}t\,\mathrm{d}x\,\mathrm{d}y;\\ \mathbf{f}_{i,p} &= \int_{\Omega}\int_{\Upsilon} J_s \alpha_i H_q\,\mathrm{d}t\,\mathrm{d}x\,\mathrm{d}y.\end{aligned} \tag{4}$$

The particular choice of harmonic functions H_q as the temporal shape functions characterises the frequency-domain approach. Because of the fact that temporal shape functions are orthonormal in Υ, the system matrix **K** has a block diagonal structure when the equations are ordered according to the spatial shape functions first.

3. Machine model

The stator and rotor domains Ω_{st} and Ω_{rt} are treated independently. Different sets of temporal harmonics are allowed for both domains. The frequency-domain FE discretisation reads:

$$\mathbf{K}_{\mathrm{st}}\mathbf{u}_{\mathrm{st}} = \mathbf{f}_{\mathrm{st}}; \tag{5}$$

$$\mathbf{K}_{\mathrm{rt}}\mathbf{u}_{\mathrm{rt}} = \mathbf{f}_{\mathrm{rt}}. \tag{6}$$

When a sliding-surface technique is applied, the stator domain Ω_{st} and the rotor domain Ω_{rt} share the common circular interface $\Gamma = \Omega_{\mathrm{st}} \cap \Omega_{\mathrm{rt}}$ in the air gap of the rotating device (Figure 1). When constructing equations (5) and (6), independent degrees of freedom are considered at the stator and rotor sides of Γ. In case of the moving-band approach, a single layer of finite elements is constructed in a small circular domain Ω_{mb}, situated in the air gap of the machine between Ω_{st} and Ω_{rt} (Davat *et al.*, 1985). The connection between the inner boundary of the stator and the outer boundary of the rotor is discussed in the following sections.

The distribution of the magnetic vector potential at a circle in the air gap can be decomposed in a sum of rotating waves:

$$u(\theta, t) = \sum_{p}\sum_{k} u_{p,k}\cos(\omega_p t - \lambda_k\theta - \phi_{p,k}) \tag{7}$$

where ω_p, λ_k and $\phi_{p,k}$ denote the pulsation, the pole-pair number and the phase of the wave and $u_{p,k}$ are unknown coefficients. An observer attached to the rotor experiences the air-gap field:

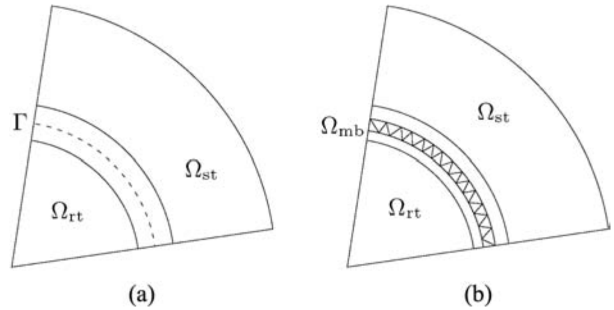

Figure 1.
(a) Sliding-surface, and (b) moving-band techniques, for an electrical machine model

$$u'(\theta', t) = \sum_p \sum_k u_{p,k} \cos(\tilde{\omega}_{p,k} t - \lambda_k \theta' - \phi_{p,k}), \tag{8}$$

i.e. a linear combination of waves with the same pole-pair numbers and phases, but at the slip pulsations $\tilde{\omega}_{p,k} = \omega_p - \lambda_k \omega_m$. Hence, the selection of the set of harmonics to be considered at the rotor, not only depends on the harmonics present in the stator but also on the spatial-harmonic contents expected for the air-gap field, e.g. the higher harmonics introduced by the winding scheme and those due to the slotting of stator and rotor.

4. Sliding-surface technique

Several sliding-surface techniques can be distinguished based on the choice of method for enforcing the continuity at the common interface. In general, the stator and rotor meshes at Γ do not match for all positions attained during the time integration. Hence, the field at one of the both sides has to be interpolated (Perrin-Bit and Coulomb, 1995) or mortar-projected (Rodger *et al.*, 1990) on the mesh of the other side. A third non-matching mesh treatment which is particularly efficient for rotating devices, is a mortar-element method with harmonic test functions as proposed in De Gersem and Weiland (2003). This approach is particularly suited in case of a frequency-domain FE formulation and is favoured here.

The continuity of the magnetic vector potential at the sliding surface is enforced by weighing the difference between the magnetic vector potential at Γ with the spatial harmonic test functions $\xi_{k,p}(\theta, t) = G_k(\theta) H_p(t)$

where

$$G_k(\theta) \in \{1, \sqrt{2}\cos(\lambda_k \theta), -\sqrt{2}\sin(\lambda_k \theta)\} \tag{9}$$

and $\lambda_k \in \mathbb{N}$. The resulting constraint equation is:

$$\mathbf{B}_{\mathrm{st}} \mathbf{u}_{\mathrm{st}} - \mathbf{B}_{\mathrm{rt}} \mathbf{u}_{\mathrm{rt}} = 0 \tag{10}$$

where

$$\mathbf{B}_{\mathrm{st},k,p,j,q} = \int_\Gamma \int_\Upsilon \alpha_j(\theta) H_q(t) G_k(\theta) H_p(t)\, \mathrm{d}\theta\, \mathrm{d}t;$$

$$\mathbf{B}_{\mathrm{rt},k,p,j,q} = \int_\Gamma \int_\Upsilon \alpha_j(\theta') H_q(t) G_k(\theta' + \omega_m t) H_p(t)\, \mathrm{d}\theta' \mathrm{d}t.$$

The constraints are added to the formulation using a set of Lagrange multipliers $\mathbf{z}$, resulting in the saddle-point model:

$$\begin{bmatrix} \mathbf{K}_{\mathrm{st}} & 0 & \mathbf{B}_{\mathrm{st}}^H \\ 0 & \mathbf{K}_{\mathrm{rt}} & -\mathbf{B}_{\mathrm{rt}}^H \\ \mathbf{B}_{\mathrm{st}} & -\mathbf{B}_{\mathrm{rt}} & 0 \end{bmatrix} \begin{bmatrix} \mathbf{u}_{\mathrm{st}} \\ \mathbf{u}_{\mathrm{rt}} \\ \mathbf{z} \end{bmatrix} = \begin{bmatrix} \mathbf{f}_{\mathrm{st}} \\ \mathbf{f}_{\mathrm{rt}} \\ 0 \end{bmatrix}. \tag{11}$$

If a sliding surface is applied at a circular interface with an equidistant grid, the computational cost of the operators $\mathbf{B}_{\mathrm{st}}$ and $\mathbf{B}_{\mathrm{rt}}$ can be reduced considerably by weighing the magnetic vector potential at a discrete set of points, e.g. at the FE vertices at Γ (De Gersem and Hameyer, 2002). Then, the discretisation is no longer conforming, but the integrations in equation (11) can be rearranged such that the fast Fourier transform (FFT) can be applied $\mathbf{F}$ instead of the dense matrices $\mathbf{B}_{\mathrm{st}}$ and $\mathbf{B}_{\mathrm{rt}}$, for each temporal harmonic separately:

$$\mathbf{B}_{\mathrm{st},p,q} = \delta_{pq}\mathbf{F} \tag{12}$$

$$\mathbf{B}_{\mathrm{rt},p,q} = \mathbf{R}_{pq}\mathbf{F} \tag{13}$$

where $\mathbf{R}_{k,p,k,q} = 1$ if $\omega_p = \omega_q - \lambda_k\omega_m$, i.e. if the pulsation ω_p at the rotor side matches the slip pulsation introduced by the air-gap wave with pulsation ω_q and pole pair number λ_k. The approach with the FFT does not account for the curvature of Γ and the exact distribution of the magnetic vector potential between the FE vertices at Γ. This approximation is, however, acceptable for many machine models as long as a sufficient fine discretisation is constructed at Γ.

5. Moving-band technique

A moving-band Ω_{mb} is a small circular domain, situated in the air gap of the machine in which a single layer of FEs is constructed (Davat *et al.*, 1985 and Demenko, 1996) (Figure 1). The moving band is remeshed for every angular position. Hence, the supports of the spatial FE shape functions in the moving band change depending on the position. The contributions of the elements of Ω_{mb} read, e.g. for $i \in \Omega_{\mathrm{st}}$ and $j \in \Omega_{\mathrm{rt}}$,

$$\mathbf{K}_{\mathrm{mb,st,rt},i,p,j,q} = \int_{\Omega_{\mathrm{mb}}} \int_{\Upsilon} \nu H_p(t) H_q(t) \nabla\alpha_i(x,y) \cdot \nabla\alpha_j(x',y')\, \mathrm{d}t\, \mathrm{d}x\, \mathrm{d}y. \tag{14}$$

Since the relation between the coordinate systems (x,y) and (x',y') and the overlap of the supports of two spatial FE shape functions $\alpha_i(x,y)$ and $\alpha_j(x',y')$ depend on the velocity and time, the contributions of elements of Ω_{mb} to the stiffness matrix result in a full coupling between all harmonics (Gyselinck *et al.*, 2003). The combined system of equations is:

$$\begin{bmatrix} \mathbf{K}_{\mathrm{st}} + \mathbf{K}_{\mathrm{mb,st,st}} & \mathbf{K}_{\mathrm{mb,st,rt}} \\ \mathbf{K}_{\mathrm{mb,rt,st}} & \mathbf{K}_{\mathrm{rt}} + \mathbf{K}_{\mathrm{mb,rt,rt}} \end{bmatrix} \begin{bmatrix} \mathbf{u}_{\mathrm{st}} \\ \mathbf{u}_{\mathrm{rt}} \end{bmatrix} = \begin{bmatrix} \mathbf{f}_{\mathrm{st}} \\ \mathbf{f}_{\mathrm{rt}} \end{bmatrix}. \tag{15}$$

6. Comparison between moving-band and sliding-surface approaches

6.1 Computational complexity

In case of a multi-harmonic formulation, the stator-rotor coupling gives rise to additional dense matrix parts or to dense constraint equations, both when using the moving-band technique or the sliding-surface approach. This is the main drawback for multi-harmonic formulations compared to transient formulations. The number of FE vertices at Γ scales as $\sqrt{n_{\mathrm{fe}}}$. The computational complexities of the individual components of the system matrix components are gathered in Table I. The dense matrix pats $\mathbf{K}_{\mathrm{mb}}$, $\mathbf{B}_{\mathrm{st}}$ and $\mathbf{B}_{\mathrm{rt}}$ have the same complexity as the multi-harmonic FE system matrices $\mathbf{K}_{\mathrm{st}}$ and $\mathbf{K}_{\mathrm{rt}}$ themselves and, hence, may lead to a substantial increase of the computational cost of the algorithm. When the FFT-variant of the sliding-surface technique is applied, the asymptotical complexity of $\mathbf{B}_{\mathrm{st}}$ and $\mathbf{B}_{\mathrm{rt}}$ remains below the one of $\mathbf{K}_{\mathrm{st}}$ and $\mathbf{K}_{\mathrm{rt}}$. Hence, the stator-rotor coupling does not kill the numerical efficiency of multi-harmonic simulation.

6.2 Applicability

The moving-band technique also applies to models with more sophisticated motion patterns. The sliding-surface technique with harmonic test functions is restricted to circular interfaces or to integer parts of them. An efficient implementation of the sliding-surface technique moreover requires an equidistant mesh at the interface in the air gap. The construction of generally applicable preconditioners for the systems augmented with sliding-surface constraints is cumbersome (De Gersem *et al.*, 2003).

6.3 Discretisation error

The moving-band technique yields conforming, variational formulations, i.e. the FE meshes match in the air gap and a constrained FE test and trial space is used for the magnetic vector potential. For the sliding-surface technique with FFTs, the discretisation is not matching at Γ and a saddle-point system is attained. The additional discretisation error introduced at Γ is acceptable for the models considered here.

6.4 Non-propagated harmonic components

A wave component at pulsation ω_p and pole-pair number λ_k induced by the stator in the air gap, corresponds to a wave at pulsation $\omega_q = \omega_p - \lambda_k \omega_m$ and pole-pair number λ_k observed by the rotor. A non-propagated harmonic components arises when either the component at pulsation ω_p is not considered at the stator or the component at pulsation ω_q is not considered at the rotor. The question arises which boundary conditions are inherently applied for these components in the air gap. Here, an important difference between the sliding-surface and the moving-band techniques is observed. In case of the moving-band approach, a wave component which is considered at the stator but not at the rotor vanishes at the boundary between the rotor and the moving band. Similarly, a component introduced by the rotor vanishes at the boundary between the stator and the moving band. Hence, non-propagated components experience homogeneous Dirichlet conditions at one of the boundaries of the moving band. As a consequence, the moving-band technique as presented here is flux-conservative in the air gap. In case of the sliding-surface technique presented, a stator harmonic component which is not propagated to the rotor does not vanish at the stator side of Γ. The non-propagated components experience a homogeneous Neumann constraint at the stator and rotor sides of Γ. This results in a discontinuous magnetic flux at Γ, even if an exact integration as in equation (10) is applied. The application of

Table I.
Asymptotic order of the computational complexity of the individual system matrix components

Matrix	Order
$\mathbf{K}_{\mathrm{st}}$, $\mathbf{K}_{\mathrm{rt}}$	$n_{\mathrm{hm}} n_{\mathrm{fe}}$
$\mathbf{K}_{\mathrm{mb}}$	$n_{\mathrm{hm}} n_{\mathrm{fe}}$
$\mathbf{B}_{\mathrm{st}}$, $\mathbf{B}_{\mathrm{rt}}$	$n_{\mathrm{hm}} n_{\mathrm{fe}}$
$\mathbf{B}_{\mathrm{st}}$(FFT), $\mathbf{B}_{\mathrm{rt}}$(FFT)	$n_{\mathrm{hm}} \sqrt{n_{\mathrm{fe}}} \log \sqrt{n_{\mathrm{fe}}}$

homogeneous Dirichlet constraints to non-propagated flux components requires the addition of additional constraints of the form $\mathbf{S}_{\mathrm{st}}\mathbf{F}\mathbf{u}_{\mathrm{st}} = 0$ and $\mathbf{S}_{\mathrm{rt}}\mathbf{F}\mathbf{u}_{\mathrm{rt}} = 0$ where $\mathbf{S}_{\mathrm{st}}$ selects all components with wave numbers (ω_p, λ_k) for which the corresponding slip pulsations $\omega_q = \omega_p - \lambda_k\omega_m$ are not considered at Ω_{rt} and $\mathbf{S}_{\mathrm{rt}}$ selects all components with wave numbers (ω_q,λ_l) for which the corresponding excitation pulsations $\omega_p = \omega_q + \lambda_l\omega_m$ are not considered at Ω_{st}.

7. Capacitor motor example

Both techniques are compared for a capacitor motor induction machine. The motor has a nominal power of 0.75 kW, a nominal speed of 2,760 rpm, a voltage of 230 V, a nominal current of 5.2 A and a $\cos\phi$ of 0.96. The main winding of the motor is connected directly to a single-phase alternating current supply whereas the auxiliary winding is connected through a capacitor of 19.7 μF. The stator has 24 slots whereas the rotor has 16 slots. Here, as an example, the no-load behaviour of the capacitor motor is simulated. The power supply is assumed to be a perfect sine at 50 Hz. Because of ferromagnetic saturation, additional harmonic components are introduced at the stator of which only the 150 and 250 Hz are considered in the frequency-domain approach. The air-gap field of a single-phase motor is elliptical. Hence, at no-load, there is besides the 0 Hz component, rotating synchronously to the forward rotating air-gap field, a significant component at 100 Hz introduced by the backward rotating air-gap field. Substantial components at 750 and 850 Hz are detected due to the slotting of the stator and rotor. The magnetic flux distributions for the different time-harmonic components are shown in Figure 2. The spectrum of the current through the main winding indicates that the slot harmonics at 750 and 850 Hz are substantially more important than the harmonics introduced by saturation (Figure 3). A transient simulation of the start-up of the capacitor motor shows that a large number of periods have to be stepped through before reaching a steady state, which is not necessary when using a multi-harmonic

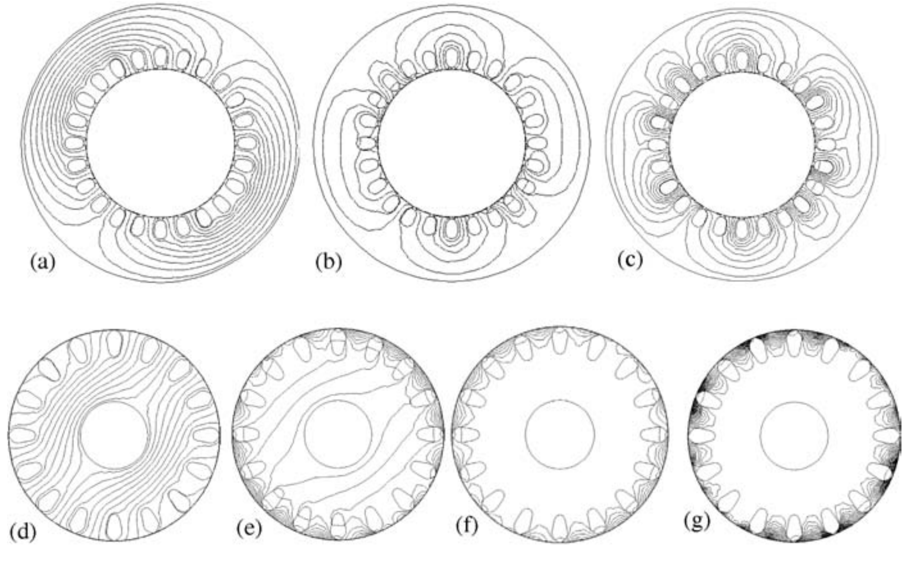

Figure 2.
Magnetic flux plot in the stator at: (a) 50 Hz, (b) 750 Hz, and (c) 850 Hz; magnetic flux plot in the rotor at: (d) 0 Hz, (e) 100 Hz, (f) 800 Hz, and (g) 900 Hz

approach as is proposed in this paper. For the capacitor motor model with 24832 FE nodes, the multi-harmonic simulation takes 16 min whereas the transient simulation requires 5 h (Figure 4).

8. Conclusions

Multi-harmonic FE machine models require the solution of large systems of equations, but may be advantageous over transient schemes which need to step through a start-up process before reaching a steady state.

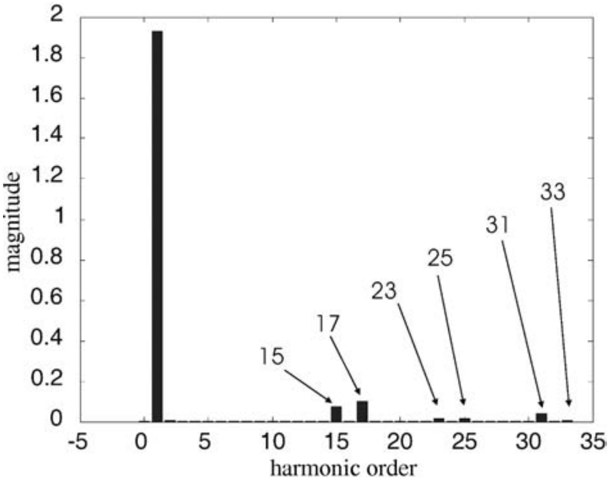

Figure 3.
Spectrum of the current through the main stator winding at no-load

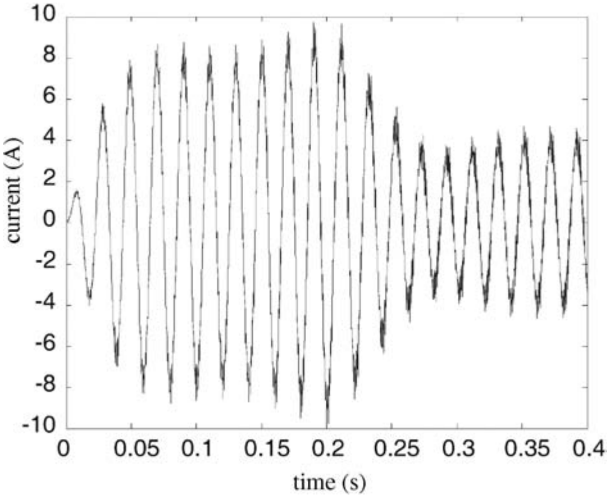

Figure 4.
Current through the main stator winding at start-up

References

Davat, B., Ren, Z. and Lajoie-Mazenc, M. (1985), "The movement in field modeling", *IEEE Trans. Magn.*, Vol. 21 No. 6, pp. 2296-8.

De Gersem, H. and Hameyer, K. (2002), "Air-gap flux splitting for the time-harmonic finite-element simulation of single-phase induction machines", *IEEE Trans. Magn.*, Vol. 38 No. 2, pp. 1221-4.

De Gersem, H. and Weiland, T. (2004), "Harmonic weighting functions at the sliding interface of a finite element machine model incorporating angular displacement", *IEEE Trans. Magn.,*, Vol. 40 No. 2, pp. 545-8.

De Gersem, H., Vandewalle, S., Clemens, M. and Weiland, T. (2003), "Interface preconditioners for non-trivial interface conditions in air gaps of rotating electrical machines", in Herrera, I, Keyes, D., Widlund, O. and Yates, R. (Eds), *Proceedings of the Fourteenth International Conference on Domain Decomposition Methods, Cocoyoc, Mexico*, Domain Decomposition Methods in Science and Engineering, National Autonomous University of Mexico (UNAM), Mexico City, pp. 381-8.

Demenko, A. (1996), "Movement simulation in finite element analysis of electric machine dynamics", *IEEE Trans. Magn.*, Vol. 32 No. 3, pp. 1553-6.

Gyselinck, J., Dular, P., Geuzaine, C. and Legros, W. (2002), "Harmonic-balance finite-element modeling of electromagnetic devices: a novel approach", *IEEE Trans. Magn.*, Vol. 38 No. 2, pp. 521-4.

Gyselinck, J., Vandevelde, L., Dular, P. and Geuzaine, C. (2003), "A general method for the frequency domain FE modeling of rotating electromagnetic devices", *IEEE Trans. Magn.*, Vol. 39 No. 3, pp. 1147-50.

Perrin-Bit, R. and Coulomb, J. (1995), "A three-dimensional finite element mesh connection for problems involving movement", *IEEE Trans. Magn*, Vol. 31 No. 3.

Rodger, D., Lai, H. and Leonard, P. (1990), "Coupled elements for problems involving movement", *IEEE Trans. Magn.*, Vol. 26 No. 2, pp. 548-50.

Vandevelde, L., Gyselinck, J. and Melkebeek, J. (1994), "Steady-state finite element analysis in the frequency domain of inverter-fed squirrel cage induction motors", *Proc. SPEEDAM*, Taormina, Italy, pp. 29-34.

Vinsard, G. and Laporte, B. (1994), "A new formulation for induction machine computation", *IEEE Trans. Magn.*, Vol. 30 No. 5, pp. 3693-6.

Yamada, S., Bessho, K. and Lu, J. (1989), "Harmonic balance finite element method applied to nonlinear AC magnetic analysis", *IEEE Trans. Magn.*, Vol. 25 No. 4, pp. 2971-3.

The Emerald Research Register for this journal is available at
www.emeraldinsight.com/researchregister

The current issue and full text archive of this journal is available at
www.emeraldinsight.com/0332-1649.htm

Orthogonal transformation of moving grid model into fixed grid model in the finite element analysis of induction machines

Andrzej Demenko and Dorota Stachowiak
Institute of Industrial Electrical Engineering, Poznań University of Technology, Poznań, Poland

Keywords *Finite element analysis, Motion, Electromagnetism, Induction machines*

Abstract *The equivalent fixed grid and moving grid models for the finite element (FE) analysis of an induction machine are presented. The discussed transformation is the FE representation of the classical commutator transformation. The obtained fixed grid model takes into account the higher space harmonics of the flux density wave and can be used in the FE analysis of the machines with solid rotor, drug-cap rotor, and squirrel cage winding. The models have been applied in the calculations of TEAM Workshop problem No. 30. The test problem has been solved analytically. The FE results and analytical results are very close.*

1. Introduction

The finite element (FE) methods that consider the movement can be divided into two categories:

1. the techniques with the fixed grid (FG) independent of the rotor position; and
2. the techniques with the moving grid (MG) in the rotor region (Williamson, 1994).

The MG techniques are more universal. In these techniques, the grid is divided into two parts: the fixed part associated with the stator and the moving part associated with the rotor. Between these parts, the slip surface or the interconnecting band is created.

In the classical circuit analysis of electrical machines we have also two types of techniques of movement representation. We can describe the voltage equations of rotor windings in the moving coordinates "α,β" (α,β-model) or in the fixed coordinates "d,q" (d,q-model) (Jones, 1967). The equations of d,q-model have been obtained by the application of the so-called commutator transformation. This transformation is orthogonal and linearizes the impedance matrix, i.e. eliminates functions of the rotor angle α from the impedance matrix (Jones, 1967).

The authors of this paper propose to apply the idea of commutator transformation in the FE analysis of an induction machine. It has been shown that the MG model discussed by Demenko (1996) can be transformed into equivalent FG model. The FG and MG models have been applied for the analysis of TEAM Workshop problem No. 30 (Davey, 1998). The analytical results presented by the author of the problem have been compared with the FE results.

COMPEL: The International Journal for Computation and Mathematics in Electrical and Electronic Engineering
Vol. 23 No. 4, 2004
pp. 1015-1022
© Emerald Group Publishing Limited
0332-1649
DOI 10.1108/03321640410553445

2. Moving grid model

The problem is simplified by assuming the field to be 2D, independent of the coordinate parallel to the shaft of the machine. In order to describe the field distribution the modified magnetic potential φ has been used. This potential represents the edge value of vector magnetic potential $\mathbf{A}$ and is defined as the product of core length l and A_z component of $\mathbf{A}$. The MG model has been formed by the application of band interpolation technique (Demenko, 1996). The circular band is placed inside the air gap. The band is subdivided into FEs with a given number m of equidistant nodes or equidistant groups of nodes (Figure 1). The trigonometric interpolating polynomial has been applied to form the reluctance (stiffness) matrix for the band. The interpolation is based on the discrete positions of the rotor ($\alpha_i = \alpha_0 + i\beta$; $i = 0, 1, 2, \ldots, m-1$; $\beta = 2\pi/m$). The FE equations for the band can be expressed as:

$$\begin{bmatrix} \mathbf{S}_\mathrm{s} & \mathbf{S}_\mathrm{b}\mathbf{k}(\alpha) \\ (\mathbf{S}_\mathrm{b}\mathbf{k}(\alpha))^\mathrm{T} & \mathbf{S}_\mathrm{r} \end{bmatrix} \begin{bmatrix} \varphi_1 \\ \varphi_2 \end{bmatrix} = \begin{bmatrix} \theta_1 \\ \theta_2 \end{bmatrix}. \tag{1}$$

Here $\mathbf{S}_\mathrm{r}$, $\mathbf{S}_\mathrm{s}$, $\mathbf{S}_\mathrm{b}$ are the submatrices of band reluctance matrix for initial rotor position, $\mathbf{k}(\alpha)$ is the conversion matrix which project the rotor displacement, φ_i ($i = 1, 2$) are the vectors of nodal values of φ for $r = r_i$. The vectors θ_1 and θ_2 consist of the components related to FEs in the stator and rotor region. The conversion matrix $\mathbf{k}(\alpha)$ may be written as:

$$\mathbf{k}(\alpha) = \begin{bmatrix} \mathbf{1}k_{1,1} & \mathbf{1}k_{2,1} & \ldots & \mathbf{1}k_{u,1} & \ldots & \mathbf{1}k_{m,1} \\ \mathbf{1}k_{1,2} & \mathbf{1}k_{2,2} & \ldots & \mathbf{1}k_{u,2} & \ldots & \mathbf{1}k_{m,2} \\ \ldots & \ldots & \ldots & \ldots & \ldots & \ldots \\ \mathbf{1}k_{1,v} & \mathbf{1}k_{2,v} & \ldots & \mathbf{1}k_{u,v} & \ldots & \mathbf{1}k_{m,v} \\ \ldots & \ldots & \ldots & \ldots & \ldots & \ldots \\ \mathbf{1}k_{1,m} & \mathbf{1}k_{2,m} & \ldots & \mathbf{1}k_{u,m} & \ldots & \mathbf{1}k_{m,m} \end{bmatrix}, \tag{2}$$

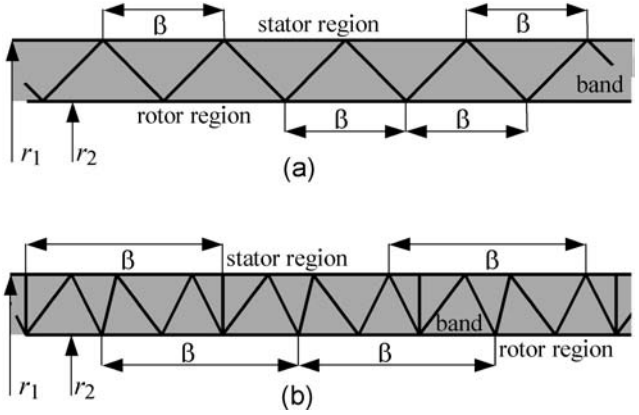

Figure 1.
Moving bands: (a) with equidistant nodes, (b) with equidistant groups of nodes for initial rotor position α_0

where **1** is the unit matrix of rank w, where w is the number of nodes in the group on the boundary $r = r_2$ ($w = 1$ for the band in Figure 1(a), and $w = 3$ for the band in Figure 1(b), and

$$k_{u,v} = k_{u,v}(\alpha) = \frac{1}{m}\sum_{j=0}^{n} c_j \cos j(\alpha - \alpha_0 + (v - u)\beta). \tag{3}$$

Here,

$$n = (m + \delta)/2, \;\; c_0 = 1, \;\; c_j = 2 \;\; (j = 1, 2, 3, \ldots, n - 1), \;\; c_n = 1 - \delta, \;\; \delta = 1$$

if m is an odd number, $\delta = 0$ if m is an even number. It can be seen that as a result of displacement of angle $i\beta$ the non-zero elements of matrix $\mathbf{S}_\mathrm{b}\mathbf{k}(\alpha)$ change their position in relation to matrix $\mathbf{S}_\mathrm{b}$.

In the FE analysis of induction motors with solid rotor or with a drug-cap rotor it is advantage to subdivide the rotor region into the bands similar to the band shown in Figure 1(a). For the obtained grid in the rotor region the nodal values of φ can be expressed by the subvectors $\varphi_2, \varphi_3, \ldots, \varphi_q$ related to the nodes on the concentric circles of radius $r_2, r_3, \ldots, r_q$ ($r_2 > r_3 > r_q$). Then the FE equations for the rotor region can be written as:

$$\begin{bmatrix} \mathbf{S}_{2,2} + \mathbf{G}_{2,2}p & \mathbf{S}_{2,3} + \mathbf{G}_{2,3}p & \ldots & 0 \\ \mathbf{S}_{2,3}^\mathrm{T} + \mathbf{G}_{2,3}^\mathrm{T}p & \mathbf{S}_{3,3} + \mathbf{G}_{3,3}p & \ldots & 0 \\ \ldots & \ldots & \ldots & \ldots \\ 0 & 0 & \ldots & \mathbf{S}_{q,q} + \mathbf{G}_{q,q}p \end{bmatrix} \begin{bmatrix} \varphi_2 \\ \varphi_3 \\ \ldots \\ \varphi_q \end{bmatrix} = \begin{bmatrix} -\mathbf{S}_{b\alpha}^\mathrm{T}\varphi_1 \\ 0 \\ \ldots \\ 0 \end{bmatrix}. \tag{4}$$

Here, $\mathbf{S}_{i,j}$ are the submatrices of reluctance matrix, $p = \mathrm{d}/\mathrm{d}t$, $\mathbf{S}_{\mathrm{b}\alpha} = \mathbf{S}_\mathrm{b}\mathbf{k}(\alpha)$, and $\mathbf{G}_{i,j}$ are the matrices of conductances associated with the nodes in the region with conducting material.

3. Fixed grid model

Matrix $\mathbf{k}(\alpha)$ is orthogonal and

$$\mathbf{k}(\alpha)\mathbf{S}_\mathrm{r}(\mathbf{k}(\alpha))^\mathrm{T} = \mathbf{S}_\mathrm{r}. \tag{5}$$

Therefore equation (1) can be transformed into the equations of FG model:

$$\begin{bmatrix} \mathbf{S}_\mathrm{s} & \mathbf{S}_\mathrm{b} \\ \mathbf{S}_\mathrm{b}^\mathrm{T} & \mathbf{S}_\mathrm{r} \end{bmatrix} \begin{bmatrix} \varphi_1 \\ \varphi_{2f} \end{bmatrix} = \begin{bmatrix} \theta_1 \\ \theta_{2f} \end{bmatrix}, \tag{6}$$

where $\varphi_{2f} = \mathbf{k}(\alpha)\varphi_2$; $\theta_{2f} = \mathbf{k}(\alpha)\theta_2$ are the vectors related to the rotor part of the band in the FG model.

In order to transform equation (4) into the equations of FG model vectors φ_i ($i = 2, 3, \ldots, q$) should be expressed by vectors φ_{if},

$$\varphi_i = (\mathbf{k}(\alpha))^\mathrm{T}\varphi_{if}. \tag{7}$$

It can be evidenced that

$$\begin{aligned} p(\mathbf{k}(\alpha))^{\mathrm{T}}\varphi_{if} &= \Omega\{\mathrm{d}(\mathbf{k}(\alpha))^{\mathrm{T}}/\mathrm{d}\alpha\}\varphi_{if} + (\mathbf{k}(\alpha))^{\mathrm{T}}p\varphi_{if} \\ &= (\mathbf{k}(\alpha))^{\mathrm{T}}\{\Omega(\mathrm{d}(\mathbf{k}(\alpha))^{\mathrm{T}}/\mathrm{d}\alpha)_{\alpha=\alpha_{\mathrm{o}}} + \mathbf{1}p\}\varphi_{if}, \end{aligned} \tag{8}$$

where Ω is the rotor speed. Moreover, if the moving region is subdivided into the bands similar to the band shown in Figure 1(a) and in each band medium is homogeneous, then

$$\mathbf{k}(\alpha)\mathbf{G}_{i,j}(\mathbf{k}(\alpha))^{\mathrm{T}} = \mathbf{G}_{i,j}, \tag{9a}$$

$$\mathbf{k}(\alpha)\mathbf{S}_{i,j}(\mathbf{k}(\alpha))^{\mathrm{T}} = \mathbf{S}_{i,j}. \tag{9b}$$

Therefore, as a result of transformation, we obtain:

$$\begin{bmatrix} \mathbf{S}_{2,2}+\mathbf{G}_{2,2}\mathbf{Y} & \mathbf{S}_{2,3}+\mathbf{G}_{2,3}\mathbf{Y} & \dots & 0 \\ \mathbf{S}_{2,3}^{\mathrm{T}}+\mathbf{G}_{2,3}^{\mathrm{T}}\mathbf{Y} & \mathbf{S}_{3,3}+\mathbf{G}_{3,3}\mathbf{Y} & \dots & 0 \\ \dots & \dots & \dots & \dots \\ 0 & 0 & \dots & \mathbf{S}_{q,q}+\mathbf{G}_{q,q}\mathbf{Y} \end{bmatrix} \begin{bmatrix} \varphi_{2f} \\ \varphi_{3f} \\ \dots \\ \varphi_{qf} \end{bmatrix} = \begin{bmatrix} -\mathbf{S}_{\mathrm{b}}^{\mathrm{T}}\varphi_{1} \\ 0 \\ \dots \\ 0 \end{bmatrix}, \tag{10}$$

where

$$\mathbf{Y} = \Omega(\mathrm{d}(\mathbf{k}(\alpha))^{\mathrm{T}}/\mathrm{d}\alpha)_{\alpha=\alpha_{\mathrm{o}}} + \mathbf{1}p. \tag{11}$$

In the case of the complex variable application, the transformation gives:

$$\mathbf{Y}\varphi_{if} \Rightarrow \Omega(\mathrm{d}(\mathbf{k}(\alpha))^{\mathrm{T}}/\mathrm{d}\alpha)_{\alpha=\alpha_{\mathrm{o}}}\bar{\varphi}_{if} + j\omega\bar{\varphi}_{if}, \tag{12}$$

where ω is the supply angular frequency.

However, for the time-stepping method and Crank-Nicholson procedure we obtain:

$$(\mathbf{Y}\varphi_{if})_{t_n} = \frac{2}{\Delta t}\{(\varphi_{if})_{t_n} - \mathbf{k}(\Delta\alpha_n)(\varphi_{if})_{t_{n-1}}\} - \mathbf{k}(\Delta\alpha_n)(\mathbf{Y}\varphi_{if})_{t_{n-1}}, \tag{13}$$

where

$$\mathbf{k}(\Delta\alpha_n) = \mathbf{k}(\alpha = \alpha_0 + \alpha(t_n) - \alpha(t_{n-1})), \quad \Delta t = t_n - t_{n-1}.$$

The presented transformation can be applied in the FE analysis of a squirrel cage motor. In order to obtain the FG model of the motor, the rotor region should be subdivided into the bands similar to the band in Figure 1(b). The angle β shown in Figure 1(b) should be equal to the rotor slot pitch angle. As a result, we obtain the FE model with the N identical groups of elements, where N is the number of rotor slots. The groups are related to the slot pitch regions. The FE equations of this model may be written in the form similar to equation (4) for MG method and in the form similar to equation (10) for FG method. Unfortunately, the obtained MG model is equivalent to the FG model in the case of linear problems only, i.e. when, for each band, the reluctivity of the equidistant elements is identical.

It is interesting to notice that the presented transformation gives the FG model (for time-steeping method) similar to the model proposed by Demenko and Nowak (1996).

The model proposed by Demenko and Nowak (1996) has been obtained by the trigonometric interpolation of the field distribution for the successive time steps.

4. Examples

TEAM Workshop problem No. 30 has been considered, refer Figure 2 (Davey, 1998). The reluctance matrix of MG model is a function of α. Therefore, the equations of MG model have been solved using time-stepping method (MGDT). In the case of FG model the complex variables are used (FGCO). The calculations have been performed for three-phase motor and for single-phase motor. In the analysis of three-phase motor, the well-known classical fixed grid model (FGCS) has also been applied (Williamson, 1994). In this model all rotor quantities are assumed to vary at slip-frequency, and

$$\mathbf{Y}\varphi_{if} \Rightarrow js\omega\bar{\varphi}_{if}, \tag{14}$$

where s is the per-unit slip.

The electromagnetic torque T has been calculated from the formula presented by Demenko (1998). For the models with complex variables, this formula gives:

$$T = 0.25\beta^{-1}\mathscr{R}\left\{\bar{\varphi}_1^{*\mathrm{T}}\mathbf{S}_{\mathrm{b}}(\mathbf{k}(\alpha = \alpha_0 - \beta) - \mathbf{k}(\alpha = \alpha_0 + \beta))\bar{\varphi}_{2f}\right\}. \tag{15}$$

First, the influence of the position of the boundary surface on the calculated values of torque has been investigated. It has been assumed that on the cylindrical surface of $r = r_5 + \Delta r$ the radial component of flux density is equal to zero (Figure 2). The calculations have been performed for different values of Δr. The three-phase motor has been considered. As a result of calculation the distance Δr is assumed to be $5r_5$.

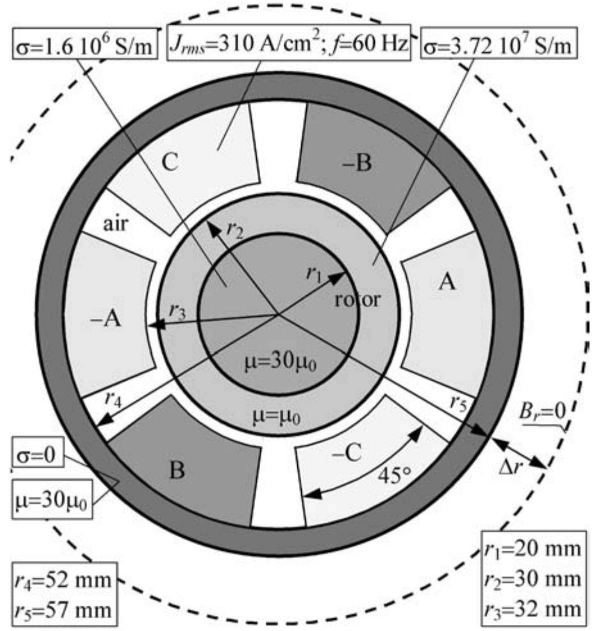

Source: Davey (1998)

Figure 2.
Induction motor problem

The considered region has been subdivided into 41 bands (16 bands in the rotor). The bands have been subdivided into the curvilinear rectangles of $\beta = \pi/120$. In the time-stepping method $\Delta t = 1/(480f)$, where $f = 60\,\text{Hz}$.

The obtained results and analytical results (AN) for three- phase motor are shown in Table I.

The results of FGCO and MGDT are practically the same. Moreover, these results and analytical results (AN) are very close. The relative error of torque calculation using FGCO and MGDT is equal to 1.27 per cent for $\Omega = 400\,\text{rad/s}$ and is less than 0.44 per cent for the other values of speed. The error of torque calculation using classical FG method (FGCS) is greater and is equal to 3.12 per cent for $\Omega = 400\,\text{rad/s}$ and 4.86 per cent for $\Omega = 1200\,\text{rad/s}$. The authors of the paper have considered the application of the classical FG method in the analysis of single-phase motor. The electromagnetic torque of single-phase motor has been calculated as a difference of the positive-sequence torque and negative-sequence torque (Jones, 1967). For the analysed test problem this method gives:

$$T(\Omega) = (T_{\text{three phase}}(\Omega) - T_{\text{three phase}}(-\Omega))/9. \tag{16}$$

Unfortunately, the results show that the method is inaccurate. Therefore, the results of the classical FG method application are not shown in Table II. For example, the method

Table I.
Calculated values of torque, voltage, and loss for three-phase induction motor, problem No. 30

Speed (rad/s)	Method	Torque (Nm/m)	Voltage (V/m/turn)	Rotor loss (W/m) Aluminium	Rotor loss (W/m) Steel
0	AN	3.825857	0.637157	1455.644	17.40541
	FGCO	3.820808	0.633566	1436.245	17.40598
	MGDT	3.820765	0.633563	1436.250	17.40592
	FGCS	3.820808	0.633566	1436.245	17.40598
200	AN	6.505013	0.845368	1179.541	16.98615
	FGCO	6.476808	0.841447	1158.734	16.90509
	MGDT	6.476793	0.841446	1158.740	16.90511
	FGCS	6.527325	0.841700	1141.566	16.89164
400	AN	−3.89264	1.477981	120.0092	1.383889
	FGCO	−3.84329	1.466824	118.8809	1.365781
	MGDT	−3.84329	1.466824	118.8299	1.365794
	FGCS	−3.77079	1.467936	85.47208	1.351745
600	AN	−5.75939	0.761760	1314.613	17.87566
	FGCO	−5.74527	0.758027	1295.322	17.81303
	MGDT	−5.74525	0.758024	1295.381	17.81303
	FGCS	−5.65684	0.759562	1248.657	17.80368
800	AN	−3.59076	0.617891	1548.240	16.88702
	FGCO	−3.59026	0.614147	1533.020	16.90873
	MGDT	−3.59020	0.614143	1533.141	16.90862
	FGCS	−3.48954	0.615763	1475.547	16.90503
1000	AN	−2.70051	0.575699	1710.686	14.32059
	FGCO	−2.70427	0.571828	1700.701	14.42507
	MGDT	−2.70417	0.571823	1700.920	14.42474
	FGCS	−2.59470	0.573440	1634.315	14.42665
1200	AN	−2.24996	0.556196	1878.926	12.01166
	FGCO	−2.25611	0.552233	1874.181	12.17822
	MGDT	−2.25598	0.552226	1874.444	12.17861
	FGCS	−2.14071	0.553808	1800.045	12.18523

Table II. Calculated values of torque, voltage, and loss for one-phase induction motor, problem No. 30

				Rotor loss (W/m)	
Speed (rad/s)	Method	Torque (Nm/m)	Voltage (V/m/turn)	Aluminium	Steel
0	AN	0	0.536071	341.7676	3.944175
	FGCO	0	0.533353	337.5397	3.948291
	MGDT	0	0.533351	337.5411	3.948281
39.79351	AN	0.052766	0.537466	341.2464	3.933111
	FGCO	0.048395	0.534792	337.1410	3.937207
	MGDT	0.048396	0.534671	337.1425	3.937196
79.58701	AN	0.096143	0.541495	340.4618	3.900878
	FGCO	0.094419	0.538708	336.3499	3.905010
	MGDT	0.094416	0.538707	336.3518	3.904998
119.3805	AN	0.143050	0.548603	340.0396	3.848117
	FGCO	0.140634	0.545803	336.0284	3.852558
	MGDT	0.140638	0.545802	336.0309	3.852543
159.1740	AN	0.199570	0.560074	340.2250	3.767681
	FGCO	0.196318	0.557254	336.3465	3.772825
	MGDT	0.196323	0.557252	336.3498	3.772806
198.9675	AN	0.275400	0.578808	339.2994	3.635357
	FGCO	0.270935	0.575934	335.6122	3.641514
	MGDT	0.270942	0.575932	356.6166	3.641489
238.7610	AN	0.367972	0.609649	333.6163	3.404092
	FGCO	0.361721	0.606625	330.2321	3.411467
	MGDT	0.361728	0.606623	330.2379	3.411436
278.5545	AN	0.442137	0.658967	317.9933	2.999715
	FGCO	0.433338	0.655544	315.1379	3.009069
	MGDT	0.433347	0.655542	315.1456	3.009031
318.3481	AN	0.375496	0.728552	288.0790	2.355622
	FGCO	0.364385	0.724226	286.1841	2.370061
	MGDT	0.364395	0.724224	286.1941	2.370015
358.1416	AN	− 0.0707	0.790068	256.6437	1.674353
	FGCO	− 0.07835	0.784542	256.0160	1.698020
	MGDT	− 0.07834	0.784540	256.0288	1.697965

gives $T = 0.5202\,\mathrm{N}$ for $\Omega = 238.761\,\mathrm{rad/s}$ and $T = 0.0876\,\mathrm{N}$ for $\Omega = 358.1416\,\mathrm{rad/s}$. However, the results of FGCO and MGDT are satisfactorily accurate, refer Table II.

The calculations show that the zero-sequence torque T_0 should be taken into account in the analysis of the test problem. This torque is caused by the pulsating field that has $3k$ $(k = 1, 2, 3\ldots)$ as many poles as the fundamental space harmonic of the wave produced by three-phase system. For $\Omega = 238.761\,\mathrm{rad/s}$, the FGCO method gives $T_0 = -0.1457\,\mathrm{N}$. When we add this value of T_0 to the result of equation (16) we obtain $T = 0.3745\,\mathrm{N}$. This result and the result of analytic analysis are close, refer result of AN in Table II.

The method can be used in the calculations of torque produced by the fundamental space harmonic only. In the models for the fundamental space harmonic (FGCO-1h, MGDT-1h) the band consists of three equidistant groups of nodes and $\beta = 2\pi/3$. For one-phase motor, these models and equation (16) give the same results of torque calculation. In the analysis of three-phase motor using FGCO-1h or MGDT-1h the results of torque calculation from equation (15) and from the rotor loss P_{r}, $T = P_{\mathrm{r}}/(\omega s)$, are very close.

The FG time-stepping method has been successfully used in the analysis of saturation effects in a squirrel cage motor. The results are presented in the work of Demenko and Nowak (1996). The authors applied also the equivalent MG time-stepping model. The difference between the obtained results and the results presented by Demenko and Nowak (1996) is very small.

5. Conclusion

The presented transformation leads to the equivalent FG and MG FE models of unsaturated induction machines. The MG model can be considered to be the FE representation of the classical α,β-model. However, the FG model is the FE representation of d,q-model. For unsaturated machine, the reluctance (stiffness) matrix of FG model is constant. Therefore, the set of FE equations with sinusoidal forcing functions in the time domain can be transformed into the set of FE equations with complex coefficients (FGCO method).

The proposed FGCO method takes into account the higher space harmonics of the wave in the air gap. Whereas well-known FG method (FGCS) ignores these harmonics. For the considered TEAM Workshop problem the FG and MG models give the satisfactory accurate results. The results presented by Demenko and Nowak (1996) show that the FG time-stepping method can be successfully applied in the analysis of saturation effects in a squirrel cage motor.

References

Davey, K.R. (1998), “Analytic analysis of single and three phase induction motors”, *IEEE Trans. Magn.*, Vol. 34 No. 5, pp. 3721-7, available at: http://ics.ec-lyon.fr/team.html

Demenko, A. (1996), “Movement simulation in finite element analysis of electric machine dynamics”, *IEEE Trans. Magn.*, Vol. 32 No. 3, pp. 1553-6.

Demenko, A. (1998), “3D edge element analysis of permanent magnet motor dynamics”, *IEEE Trans. Magn.*, Vol. 34 No. 5, pp. 3620-3.

Demenko, A. and Nowak, L. (1996), “Finite element analysis of saturation effects in a squirrel cage electrical machine”, *COMPEL*, Vol. 15 No. 4, pp. 88-95.

Jones, V.Ch. (1967), *The Unified Theory of Electrical Machines*, Butterworth, London.

Williamson, S. (1994), “Induction motor modelling using finite elements”, *Proceedings of ICEM 1994*, Paris, Vol. 1, pp. 1-8.

The Emerald Research Register for this journal is available at
www.emeraldinsight.com/researchregister

The current issue and full text archive of this journal is available at
www.emeraldinsight.com/0332-1649.htm

Axisymmetric transient electromagnetic finite-difference scheme including prescribed motion

M. Klocke

Institute of Electrical Machines, University of Dortmund, Dortmund, Germany

Keywords *Numerical analysis, Electromagnetism, Inductance, Simulation*

Abstract *A finite-difference-scheme for axisymmetric transient electromagnetic fields is presented, which also takes into account an arbitrary prescribed motion of a substructure and motion inductive effects arising therefrom. For the arrangement at rest transient effects governed by the consequences of electromagnetic induction, e.g. the skin effect, are also taken into account. The behaviour of lumped external network elements is modelled by additional equations. A remeshing procedure is avoided by a special modelling technique. The method is tested for simple arrangements with axial and radial, i.e. expansive motion of a rectangular ring cross-section. Comparisons with lumped parameter analysis are carried out.*

The finite-difference scheme in cylindrical coordinates

Basic considerations

The finite-difference scheme for electromagnetic fields can easily be derived from a discretisation of integrally expressed Maxwell equations. Organisational effort in the implementation is low due to the use of orthogonal grids.

Axisymmetric problems can usually be described in cylindrical coordinates. Owing to symmetry all field quantities spatially depend only on the radial coordinate r and the axial coordinate z. Current densities and vector potentials are directed only circumferentially:

$$\vec{J}(r,z) = J_\varphi(r,z)\cdot\vec{e}_\varphi, \quad \vec{A}(r,z) = A_\varphi(r,z)\cdot\vec{e}_\varphi \tag{1}$$

The magnetic field is advantageously described by a modified vector potential denoted as Φ' here, since it can be considered a flux function:

$$\Phi' = r\cdot A_\varphi \tag{2}$$

The value $2\pi\cdot\Phi'(r,z)$ at a point (r,z) is the flux through a circular loop positioned concentrically and perpendicularly to the z-axis and passing through the given point. Flux lines are represented by lines with $\Phi'(r,z) = \text{const}$.

In the finite-difference scheme the modified vector potentials on the nodes of an orthogonal grid are calculated. A linear equation for the value Φ'_0 of the central node and its immediate neighbours $\Phi'_{1\ldots4}$ can be derived by applying Ampere's law on a rectangular integration path through the middle of the grid cells as shown by the dashed line in Figure 1. Differential quotients are replaced by quotients of differences.

COMPEL: The International Journal for Computation and Mathematics in Electrical and Electronic Engineering
Vol. 23 No. 4, 2004
pp. 1023-1035
© Emerald Group Publishing Limited
0332-1649
DOI 10.1108/03321640410553454

The work presented here is partially supported by the German Research Foundation (DFG) within the research group For 443 at the University of Dortmund.

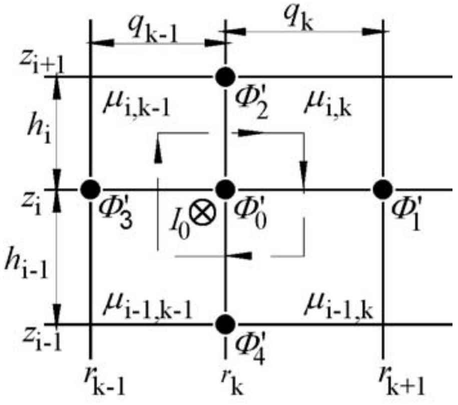

Note: Node-assigned total current I_0

Figure 1.
Detail from orthogonal FD-grid, five-point-star operator defined thereon and integrational path for deriving coefficients

$$-\sum_{l=1}^{4} \alpha_l \cdot \Phi'_l + \Phi'_0 \sum_{l=1}^{4} \alpha_l - I_0 = 0 \tag{3}$$

For the coefficients α_1 and α_2 the following is obtained:

$$\alpha_1 = \frac{1}{2q_k(r_k + q_k/2)} \left(\frac{h_i}{\mu_{i,k}} + \frac{h_{i-1}}{\mu_{i-1,k}} \right) \tag{4a}$$

$$\alpha_2 = \frac{1}{h_i} \left[\frac{1}{\mu_{i,k}} \ln\left(1 + \frac{q_k}{2r_k}\right) - \frac{1}{\mu_{i,k-1}} \ln\left(1 - \frac{q_{k-1}}{2r_k}\right) \right] \tag{4b}$$

The coefficients α_3 and α_4 are calculated accordingly with index $k-1$ in equation (4a) and index $i-1$ in equation (4b). Unlike Cartesian coordinates but similar to polar coordinates like in Gottkehaskamp (1993) logarithmic expressions occur in equation (4b) by integrating the $1/r$-dependence of the source-free field strength.

Current excitation by stranded conductor windings

The nodal current I_0 in equation (3) may be of different origin. In a stranded conductor winding the total amperage $N_{\text{turn}} \cdot i$ through a given cross-section with area a_{cs} will be distributed uniformly. So the relation between the winding current i and the nodal current I_0 for a node lying inside the cross-section is:

$$I_0 = J \cdot a_0 = \frac{N_{\text{turn}} \cdot i}{a_{\text{cs}}} \frac{1}{4} \sum_{\Delta i=-1}^{0} \sum_{\Delta k=-1}^{0} h_{i+\Delta i} q_{k+\Delta k} \tag{5}$$

For nodes on the boundary of a winding cross-section the area a_0 affected by the current density is given only by parts of the sum occurring in equation (5). If a node under consideration is adjacent to more than one different winding cross-sections, the nodal current I_0 is related to more than one winding current and can be expressed by a sum, e.g. for a radial boundary as follows:

$$I_0 = \sum_{w=1}^{2} J_w \cdot a_{0,w} = \sum_{w=1}^{2} \frac{N_{\mathrm{turn},w} \cdot i_w}{a_{\mathrm{cs},w}} \frac{1}{4} h_{i-2+w}(q_{k-1} + q_k) \\ = F_{\mathrm{N},0,w=1} \cdot i_{w=1} + F_{\mathrm{N},0,w=2} \cdot i_{w=2} \tag{6}$$

The coefficients related to the winding currents result from the areal winding density and the partial cross-sectional area of the winding adjacent to the node under consideration. These factors are denoted by $F_{\mathrm{N},0,w}$ here, similar to the notation in Gottkehaskamp (1993).

Voltage equations of stranded conductor windings

If not the current but the terminal voltage of the windings is prescribed, the ohmic-inductive voltage equation implying also Faraday's law of induction has to be taken into account and discretised, too. The flux linkage Ψ_w is given by the average value of the flux function Φ' on the winding cross-section. A leakage flux represented by the inductance $L_{\sigma,w}$, e.g. for supply lines, can be taken into account additionally:

$$u_w = R_w \cdot i_w + \frac{\mathrm{d}}{\mathrm{d}t}\Psi_w \quad = R_w \cdot i_w + \frac{\mathrm{d}}{\mathrm{d}t}\left(L_{\sigma,w} i_w + N_{\mathrm{turn},w} \frac{2\pi}{a_{\mathrm{cs},w}} \iint_{\mathrm{CS},w} \Phi' \, \mathrm{d}r \, \mathrm{d}z \right) \tag{7}$$

The spatial discretisation converts the areal integral into a sum, where again the factors $F_{\mathrm{N},j,w}$ occur.

$$u_w = R_w \cdot i_w + \frac{\mathrm{d}}{\mathrm{d}t}\left(L_{\sigma,w} i_w + 2\pi \sum_{j(\mathrm{CS},w)} F_{\mathrm{N},j,w} \Phi'_j \right) \tag{8}$$

Time discretisation with a time step h is carried out by using the θ-method (Krawczyk and Tegopoulos, 1993), which finally leads to:

$$-\sum_{j(\mathrm{CS},w)} F_{\mathrm{N},j,w} \Phi'_j \Bigg|_{t+h} + \frac{1-\theta}{2\pi} h \cdot u_w \Bigg|_{t+h} - \frac{L_{\sigma,w} + (1-\theta) h R_w}{2\pi} i_w \Bigg|_{t+h} \\ = -\sum_{j(\mathrm{CS},w)} F_{\mathrm{N},j,w} \Phi'_j \Bigg|_{t} - \frac{\theta h}{2\pi} u_w \Bigg|_{t} - \frac{L_{\sigma,w} - \theta h R_w}{2\pi} i_w \Bigg|_{t} \tag{9}$$

θ is a parameter to be chosen between 0 and 0.5, which influences the numerical stability (Krawczyk and Tegopoulos, 1993).

Massive conductors and eddy-current phenomena

In massive conductors the current density distribution in general cannot be expected to be uniform not depending on whether the conductor is a short-circuited ring or a voltage supplied coil. The current driving electric field can be considered a sum of a circumferential gradient field E_{ex} and the induced electric field E_{i}. The former vanishes for a short-circuited conductor. In the case of an externally supplied conductor it is just the external feeding voltage u_{ex} divided by the circumferential path length $2\pi r$. The induced electric field results from the change rate of the flux through the loop with radius r. For the current density these considerations lead to:

$$J_{\varphi} = \gamma\cdot(E_{\mathrm{ex}} + E_{\mathrm{i}}) = \frac{\gamma}{r}\cdot\left(\frac{u_{\mathrm{ex}}}{2\pi} - \frac{\mathrm{d}}{\mathrm{d}t}\Phi'\right) \tag{10}$$

For the nodal current in equation (3) the change rate of Φ' in equation (10) is considered constant on the adjacent area and depending only on Φ'_0 in the central node. Combining equation (3) with equation (10) under this assumption one obtains:

$$-\sum_{l=1}^{4}\alpha_l\cdot\Phi'_l + \Phi'_0\cdot\sum_{l=1}^{4}\alpha_l - \iint_{a_0}\frac{\gamma}{r}\cdot\left(\frac{u_{\mathrm{ex}}}{2\pi} - \frac{\mathrm{d}}{\mathrm{d}t}\Phi'_0\right)\mathrm{d}r\,\mathrm{d}z = 0 \tag{11}$$

The integration over the adjacent area a_0 results in a node assigned conductivity coefficient $F_{\gamma,0}$, which can be calculated as follows:

$$F_{\gamma,0} = \sum_{\Delta k=0}^{1}\left[(-1)^{\Delta k}\ln\left(1 + (-1)^{\Delta k}\frac{q_{k-\Delta k}}{2r_k}\right)\sum_{\Delta i=0}^{1}\frac{\gamma_{i-\Delta i,k-\Delta k}\cdot h_{i-\Delta i}}{2}\right] \tag{12}$$

Applying the θ-method on equation (11) with equation (12) inserted and reordering the expressions one obtains:

$$\begin{aligned} &-\sum_{l=1}^{4}\alpha_l\Phi'_l\bigg|_{t+h} + \left(\frac{F_{\gamma,0}}{(1-\theta)h} + \sum_{l=1}^{4}\alpha_l\right)\Phi'_0\bigg|_{t+h} - \frac{F_{\gamma,0}}{2\pi}u_{\mathrm{ex}}\bigg|_{t+h} \\ &= \frac{\theta}{1-\theta}\sum_{l=1}^{4}\alpha_l\Phi'_l\bigg|_{t} + \left(\frac{F_{\gamma,0}}{(1-\theta)h} - \frac{\theta}{1-\theta}\sum_{l=1}^{4}\alpha_l\right)\Phi'_0\bigg|_{t} + \frac{\theta}{1-\theta}\frac{F_{\gamma,0}}{2\pi}u_{\mathrm{ex}}\bigg|_{t} \end{aligned} \tag{13}$$

In contrast to stranded conductors cases with massive conductors in immediate neighbourhood are not considered here.

Current equations of massive conducting regions

If the total current through a massive conductor i_m is of interest, e.g. as prescribed course of time or in order to couple to external lumped network elements, an additional equation for that current occurs by discretising the areal integral of the current density from equation (10) over the conducting cross-section.

$$i_m = \iint_{\mathrm{CS},m}\frac{\gamma}{r}\cdot\left(\frac{u_{\mathrm{ex}}}{2\pi} - \frac{\mathrm{d}}{\mathrm{d}t}\Phi'\right)\mathrm{d}r\,\mathrm{d}z \tag{14}$$

The spatial discretisation results in:

$$i_m = \sum_{j(\mathrm{CS},m)}F_{\gamma,j}\left(\frac{u_{\mathrm{ex}}}{2\pi} - \frac{\mathrm{d}}{\mathrm{d}t}\Phi'_j\right) = \frac{u_{\mathrm{ex}}}{2\pi}\sum_{j(\mathrm{CS},m)}F_{\gamma,j} - \sum_{j(\mathrm{CS},m)}F_{\gamma,j}\frac{\mathrm{d}}{\mathrm{d}t}\Phi'_j \tag{15}$$

The sum over all conductivity coefficients of a massive conductive cross-section equals the dc-conductance times 2π and is denoted as $G'_{\mathrm{CS},m}$ in the following.

Time discretisation according to the θ-method finally leads to:

$$\begin{aligned}&-\sum_{j(\text{CS},m)} F_{\gamma,j}\Phi'_j\Big|_{t+h} + (1-\theta)h\frac{G'_{\text{CS},m}}{2\pi}u_{\text{ex}}\Big|_{t+h} - (1-\theta)hi_m\Big|_{t+h} \\ &= -\sum_{j(\text{CS},m)} F_{\gamma,j}\Phi'_j\Big|_{t} - \theta h\frac{G'_{\text{CS},m}}{2\pi}u_{\text{ex}}\Big|_{t} + \theta h i_m\Big|_{t}\end{aligned} \qquad (16)$$

With this method described above arrangements at rest can be treated. As an example for the application of the overall computation program Figure 2 shows a field map taken 12.5 μs, i.e. 50 time steps here, after turning on a dc-voltage source at the terminals of a spiral coil made of a massive, rectangularly shaped copper wire. The coil is covered by an aluminium plate. Field and current density distribution in the coil cross-section are obviously strongly affected by the skin effect. The shielding effect of the plate can also be observed.

Extension of the scheme for moving structures

For many technical purposes it is desirable to take into account moving structures like in Bendjima *et al.* (1997) and Nowak (1989). However, in some special cases like, e.g. electromagnetic sheet metal forming these conductive regions also change their shape.

The method of embedding the moving structure in the system and deriving adequate equations for considering eddy-currents and motion inductive effects used here is based on independent meshes for a complete base domain and an additional moving structure layed over the base grid as shown in Figure 3.

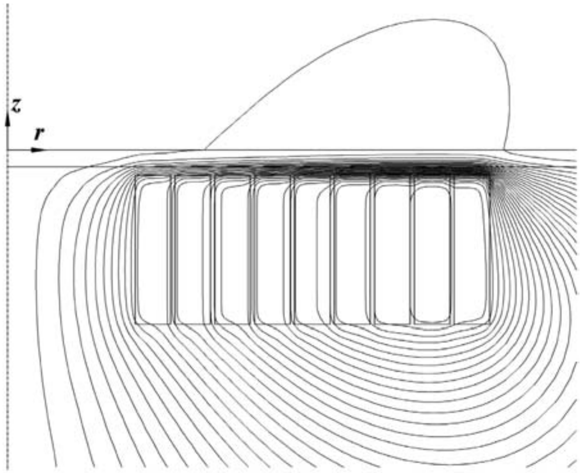

Note: Instant of time 12.5 µs after switching a dc-voltage source on a pancake coil with 9 turns of massive copper wire. Conductor height 10.5 mm. Coil covered by Aluminium sheet of 1.2 mm thickness

Figure 2.
Extract from field map computed by transient finite-difference scheme

The flux-function values in the nodes of the moving overlay-grid Φ'_{M} are described by linear interpolation formulae over the values in the base grid $\Phi'_{\mathrm{b},1\ldots4}$ of those four nodes adjacent to the grid cell, the overlay node under consideration lies in:

$$\Phi'_{\mathrm{M},0} = \sum_{n=1}^{4} \beta_{0,n} \cdot \Phi'_{\mathrm{b},n} \tag{17}$$

The interpolation coefficients depend on the position of the overlaid node ($r_{\mathrm{M},0}$, $z_{\mathrm{M},0}$) under consideration and the adjacent base grid nodes $(r_{k\ldots k+1}, z_{i\ldots i+1})$ as follows:

$$\beta_{0,n} = \frac{1}{V'} |r_{k+\Delta k} - r_{\mathrm{M},0}|(r_{k+\Delta k} + r_{\mathrm{M},0})(z_{i+\Delta i} - z_{\mathrm{M},0})$$

with

$$V' = (r_{k+1} - r_k)(r_{k+1} + r_k)|z_{i+1} - z_i| \tag{18}$$

and

$$\Delta k = \begin{cases} 1 & \text{for } n = 1 \text{ or } 4 \\ 0 & \text{for } n = 2 \text{ or } 3 \end{cases}, \quad \Delta i = \begin{cases} 1 & \text{for } n \leq 2 \\ 0 & \text{for } n \geq 3 \end{cases}$$

Since only short-circuited structures at motion are considered, no external voltage has to be accounted for. The induced current densities therefore only depend on the change rate of the modified vector potential in the overlay-grid. For each node of that grid a current $I_{\mathrm{M},0}$ can be calculated by approximating the areal integral, where $\tilde{a}_{\mathrm{M},0}$ denotes an effective conducting cross-sectional area adjacent to the node. For a sufficiently fine discretisation this effective area may be equated with the geometric area. However, an exact integration of the nodal conductance would be possible.

$$\begin{aligned} i_{\mathrm{M},0} &= -\iint_{a_{\mathrm{M},0}} \frac{\gamma}{r} \cdot \frac{\mathrm{d}}{\mathrm{d}t} \Phi'_{\mathrm{M}} \mathrm{d}r\,\mathrm{d}z \approx -\frac{\mathrm{d}}{\mathrm{d}t} \Phi'_{\mathrm{M},0} \iint_{a_{\mathrm{M},0}} \frac{\gamma}{r} \mathrm{d}r\,\mathrm{d}z \\ &= -\frac{\gamma}{r_{\mathrm{M},0}} \tilde{a}_{\mathrm{M},0} \frac{\mathrm{d}}{\mathrm{d}t} \Phi'_{\mathrm{M},0} = -\frac{\gamma}{r_{\mathrm{M},0}} \tilde{a}_{\mathrm{M},0} \frac{\mathrm{d}}{\mathrm{d}t} \sum_{n=1}^{4} \beta_{0,n} \cdot \Phi'_{\mathrm{b},n} \end{aligned} \tag{19}$$

Since the total derivative of the flux function with respect to time is evaluated, motion inductive effects are also included here as well as those contributions resulting from the mere time variation of the modified vector potential.

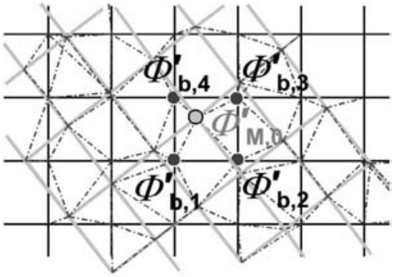

Note: The dashed lines indicate interpolation relations

Figure 3.
Detail from orthogonal basic FD-grid in black and overlaid grid of a moving structure in light gray

In the case of motion the radial coordinate of the node as well as the effective area are functions of time, too. Time discretisation and reordering the equation yields:

$$\begin{aligned} &-\sum_{n=1}^{4}\beta_{0,n}\Big|_{t+h}\Phi'_{\mathrm{b},n}\Big|_{t+h}-(1-\theta)h\frac{r_{\mathrm{M},0}|_{t+h}}{\gamma\tilde{a}_{\mathrm{M},0}|_{t+h}}i_{\mathrm{M},0}|_{t+h} \\ &=-\sum_{n=1}^{4}\beta_{0,n}\Big|_{t}\Phi'_{\mathrm{b},n}\Big|_{t}+\frac{\theta h r_{\mathrm{M},0}|_{t}}{\gamma\tilde{a}_{\mathrm{M},0}|_{t}}i_{\mathrm{M},0}|_{t}=-\Phi'_{\mathrm{M},0}|_{t}+\frac{\theta h r_{\mathrm{M},0}|_{t}}{\gamma\tilde{a}_{\mathrm{M},0}|_{t}}i_{\mathrm{M},0}|_{t} \end{aligned} \qquad (20)$$

Vice versa these currents induced in the overlay-grid have to be redistributed onto the nodes of the base grid, i.e. the original right hand side of equation (2) for the simultaneous overall solution of the system of equations. The partial contributions of $i_{\mathrm{M},0}$ to the nodal currents of the underlying base-grid nodes are considered dependent on the interpolation coefficients in a reciprocal manner:

$$\Delta I_{\mathrm{b},n}=\beta_{0,n}\cdot i_{\mathrm{M},0} \qquad (21)$$

If in other words a matrix (β) with the coefficients β is set up and the modified overlay-grid vector potentials collected in a vector (Φ'_{M}) are calculated by $(\Phi'_{\mathrm{M}})=(\beta)(\Phi'_{\mathrm{b}})$ with (Φ'_{b}) being the vector of the base-grid vector potentials, then the redistributed nodal currents in the base grid are given by a multiplication with the transposed matrix:

$$(I_{\mathrm{b}})=(\beta)^{\mathrm{T}}\cdot(i_{\mathrm{M}}) \qquad (22)$$

External lumped elements, their branch voltages and currents can be included in the system of equations, too. Each element contributes an equation obtained as an algebraic equation or by time discretisation of the first order differential equation describing the behaviour of the branch element. The topology of the whole network including stranded winding coils and massive conductors of the field model is described by Kirchhoff's well-known laws. Neither loop current nor node potential methods are applied. The reducing effects are considered negligible compared to the number of field equations.

The overlay node current equations (20) are appended as the last block in the system of equations, the solution of which for the time step $t+h$ is carried out directly. On the one hand, the bandwidth of the system matrix is undesirably high for these equations despite sparsity. On the other hand, only one overlay-grid nodal current in such an equation occurs. Therefore unlike the usual algorithm during the elimination process the base-grid nodal current contributions from equation (22) in equation (3) are eliminated by equations of type (20) first. The bandwidth of the mere field coefficient matrix (α) is only affected negligibly by adding the linear combinations of the β-coefficients.

Test examples

Axial motion

A simple test arrangement consisting of a closed cylindrical slot with excitation coils at top and bottom and a short-circuit ring inside the slot moving axially from the central position towards the bottom excitation coil is investigated (Figure 4).

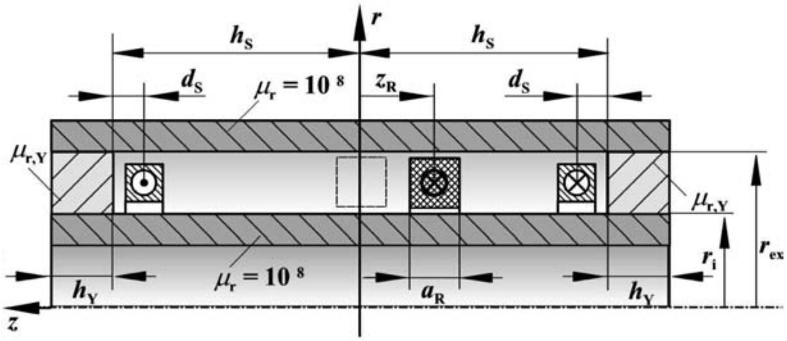

Note: Measures: $h_S = 40$ mm, $d_S = 5$ mm, $h_Y = 10$ mm, $a_R = 8$ mm, $r_i = 25$ mm, $r_{ex} = 35$ mm. Relative yoke permeability: $\mu_{r,Y} = 20$, ring conductivity: $\gamma = 115 \cdot 10^3\ 1/(\Omega m)$

Figure 4.
Test arrangement for axial motion of short-circuit ring

From analytical reasoning the mutual inductance of the short-circuited ring to the excitation winding M_R and the self-inductance of the ring L_R as well as the resistance R_R can be calculated as lumped parameters of the arrangement, which depend on the axial position z_R of the ring. Eddy-current effects are neglected in this test-example, which can be achieved by a sufficiently but of course unpractically low conductivity.

$$M_R = -\frac{2\pi\mu_0}{\ln\frac{r_{ex}}{r_i}} \cdot \frac{(d_S + \mu_{r,Y} h_Y) \cdot z_R(t)}{\mu_{r,Y} h_Y + h_S} \tag{23a}$$

$$L_R = \frac{\pi\mu_0}{\ln\frac{r_{ex}}{r_i}} \cdot \left[\frac{(\mu_{r,Y} h_Y + h_S)^2 - z_R(t)^2}{\mu_{r,Y} h_Y + h_S} - \frac{a_R}{3}\right] \tag{23b}$$

$$R_R = \frac{2\pi}{\gamma a_R \cdot \ln\frac{r_{ex}+r_i+a_R}{r_{ex}+r_i-a_R}} \tag{23c}$$

Assuming a constant imprinted exciting current I_{exc} one can reduce the system of two coupled circuit equations to:

$$R_R i_R + \frac{d}{dt}(L_R i_R) = -I_{exc} \frac{d}{dt} M_R \tag{24}$$

The function $z_R(t)$ prescribed here is continuous and so is their derivative. It is given by a period at rest of 20 μs, a 10 μs acceleration interval, 20 μs of uniform motion, a 10 μs deceleration interval and at the end again 20 μs of rest.

After the process a displacement of 24 mm of the ring is achieved. With this course the parameters as functions of time are calculated and equation (24) is solved numerically for the ring current i_R by applying the θ-method on equation (24).

The problem is also treated using the finite-difference scheme. The current courses calculated by the two methods are congruent as shown in Figure 5. Owing to the symmetry of the arrangement at start no current in the ring is induced when turning on

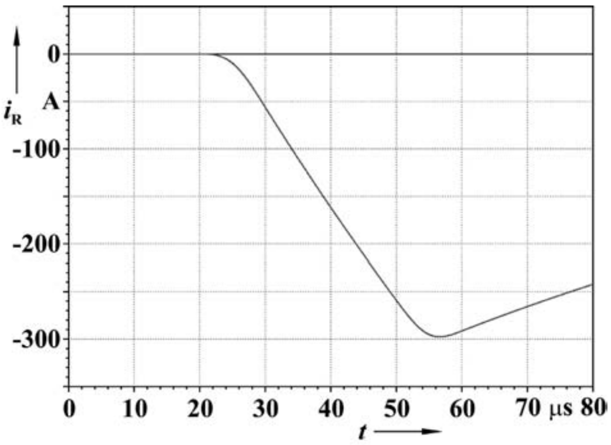

Note: Exciting current $I_{exc} = 2$ kA

Figure 5.
Motion induced ring current as function of time from finite-difference time stepping and lumped parameter analysis

the excitation. When the ring moves with constant speed the induced voltage is nearly time independent and starts loading an *RL*-circuit represented by the short circuited ring. The induced voltage becomes zero again at rest and the induced current starts decreasing according to the time constant of the ring.

The field map in Figure 6 taken at 80 μs shows the asymmetric flux distribution in the core caused by the ring current field.

Radial expansive motion

The test arrangement for the radial motion shown in Figure 7 is similar to that for the axial motion. However, it has only one exciting coil and no symmetry in the starting position. Therefore inductive effects by the increasing magnetic field when turning on the exciting current have to be taken into account.

A further difference is the velocity field, which is nonuniform due to the invariance of the moving volume. Since the radial thickness a_R and the circumferential length vary with time, the ring resistance R_R is also a function of time. For the inner ring contour the same displacement characteristic as above is prescribed, but in positive radial direction.

Analytical considerations based on a stationary current density distribution with $1/r$-characteristic in the ring lead to lumped parameters of the system according to equation (25a)-(c).

The self-inductance of the excitation winding can be calculated by replacing a_R by a_{Exc} and r_R by r_{Exc} in equation (25a).

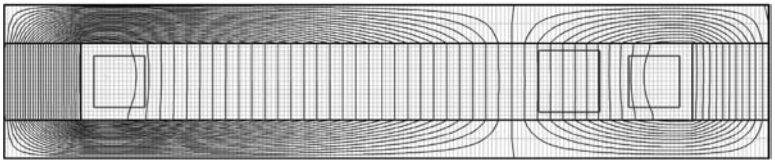

Figure 6.
Field map after 80 μs from FD-computation with time step $h = 0.1\ \mu$s and $\theta = 0.333$ and base-grid (light grey)

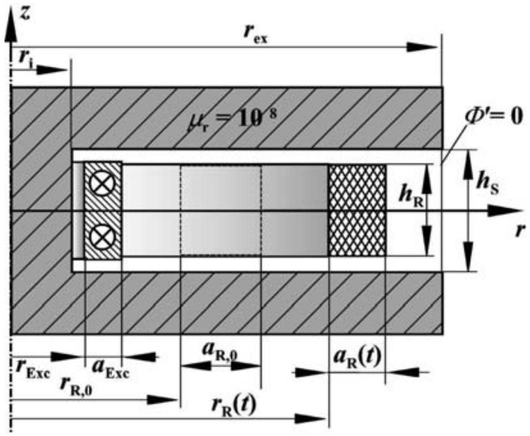

Note: Measures: $h_S = 20$ mm, $h_R = 15$ mm, $r_{Exc} = 12$ mm, $a_{Exc} = 6$ mm, $h_{Exc} = 16$ mm, $r_{R,0} = 27.5$ mm, $a_{R,0} = 15$ mm, $r_i = 10$ mm, $r_{ex} = 70$ mm. Ring conductivity: $\gamma = 115 \cdot 10^3$ 1/(Ωm)

Figure 7.
Test arrangement for radial expansion of short-circuit ring

$$L_R = \frac{\pi\mu_0}{h_S}\left(r_{ex}^2 - \frac{r_R^2}{\ln\left(1+\frac{a_R}{r_R}\right)}\left(\left(1+\frac{a_R}{r_R}\right)^2 - \frac{\frac{a_R}{r_R}\left(1+\frac{a_R}{2r_R}\right)}{\ln\left(1+\frac{a_R}{r_R}\right)}\right)\right) \tag{25a}$$

$$M_R = \frac{\pi\mu_0}{h_S}\left(r_{ex}^2 - a_R\frac{r_R + \frac{a_R}{2}}{\ln\left(1+\frac{a_R}{r_R}\right)}\right) \tag{25b}$$

$$R_R = \frac{2\pi}{\gamma h_R \ln\left(1+\frac{a_R}{r_R}\right)} \tag{25c}$$

A system of equations for two inductively coupled circuits can be set up and solved numerically.

$$\begin{aligned} U_{Exc} &= R_{Exc} i_{Exc} + \frac{d}{dt}(L_{Exc} i_{Exc}) + \frac{d}{dt}(M_R i_R) \\ 0 &= R_R i_R + \frac{d}{dt}(M_R i_{Exc}) + \frac{d}{dt}(L_R i_R) \end{aligned} \tag{26}$$

Here, U_{Exc} is a dc-voltage source switched to the exciting winding at $t = 0$, in the present case 2,000 V. The resistance of the exciting winding is set to $R_{Exc} = 1\,\Omega$.

Unlike the former case without transformer induction at the beginning the courses of the ring current computed by the finite-difference scheme and the lumped parameter model slightly differ from each other as shown in Figure 8. In the lumped parameter model a higher current at the start is calculated, which even exceeds the exciting

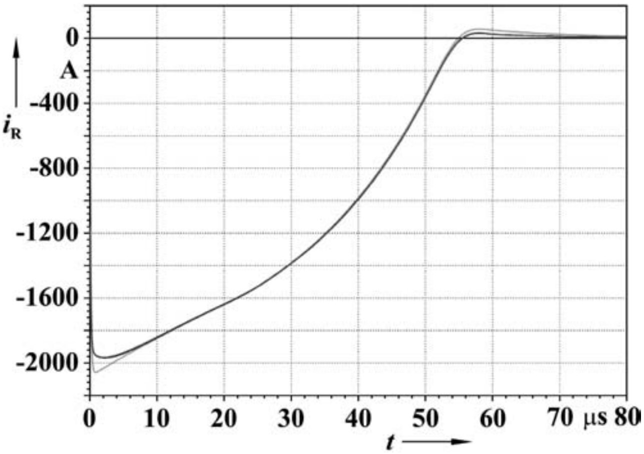

Figure 8.
Induced ring current as function of time from finite-difference time stepping (black) and lumped parameter analysis (grey)

current during a short period of time. When the ring stops again, the remaining current is also higher than in the FD-computation. This is due to the neglection of current-density nonuniformities.

For a better comparison a more sophisticated network model can be applied. The short-circuited ring is subdivided into several, e.g. $N_R = 10$, cylindrical layers. Each partial ring can then be represented by a branch of its own carrying a part of the total ring current. From evaluating Faraday's law of induction between partial rings in immediate neighbourhood mesh equations are derived. In these the sum of all inner partial ring currents and the exciting current occurs multiplied by a factor interpretable as a leakage inductance between the rings. The sum of currents can be considered a result of Kirchhoff's node law. From these considerations the network scheme in Figure 9 is derived.

Depending on the central average radii $r_{c,1\ldots Nr}$ of the N_R layers the resistances can be calculated in analogy to equation (25c). For the inductances simply the differences of the squared radii occur.

$$
\begin{aligned}
L_k &= \frac{\pi\mu_0}{h_S} \cdot \left(r^2_{c,k+1} - r^2_{c,k}\right), \quad k = 1, \ldots, N_R \quad \text{with } r_{c,Nr} = r_{ex} \\
L_0 &= L_{Exc} - \sum_{k=1}^{N_R} L_k
\end{aligned}
\tag{27}
$$

Calculating all time functions of inductances and resistances with respect to the nonuniform velocity and the resulting radial positions of the layers and inserting them into the network simulation according to Figure 9 one obtains a current course, which again is congruent to the one determined by the finite-difference scheme in Figure 8.

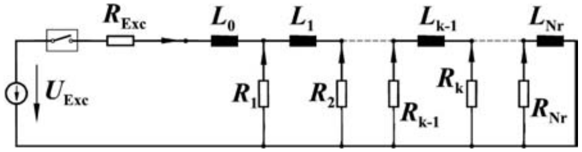

Figure 9.
Network scheme for partial conductor analysis of short circuited ring

The field map in Figure 10 taken at the instant of maximum radial velocity $t = 40\ \mu\text{s}$ is slightly disturbed in the region of the moving conductor but mostly uniform in front of and behind the ring. The field outside the ring is weakened due to the opposite induced current in the ring, which can be seen from the field map. Since every pair of adjacent flux lines leads the same flux, the distance of flux lines should decrease towards the outer radius in a uniform field. But in Figure 8 the density of flux lines does not increase in the outer region thus indicating a weaker field than in the inner region.

Relatively good agreement is also achieved for the time course of the exciting current, which slightly varies during the expansion process (Figure 11). Again the finite-difference computation is confirmed by the result of the partial conductor model.

However, the graph also shows possible stability problems of the FD-scheme presented here, as can be seen from the spurious oscillations in the computed current courses.

Therefore further research including also remeshing strategies instead of overlay-interpolation will be needed in order to check whether the scheme is applicable for practical cases like electromagnetic forming, whether improvements are necessary and possible or other methods have to be preferred.

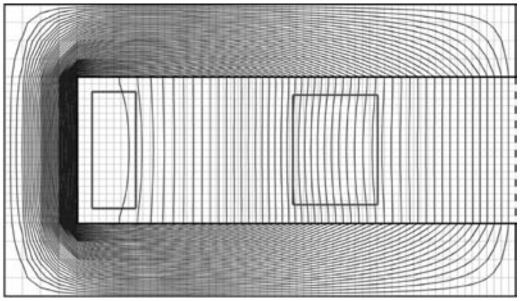

Figure 10.
Field map after 40 μs from FD-computation with time step $h = 0.1\ \mu\text{s}$ and $\theta = 0.333$ and base-grid (light grey)

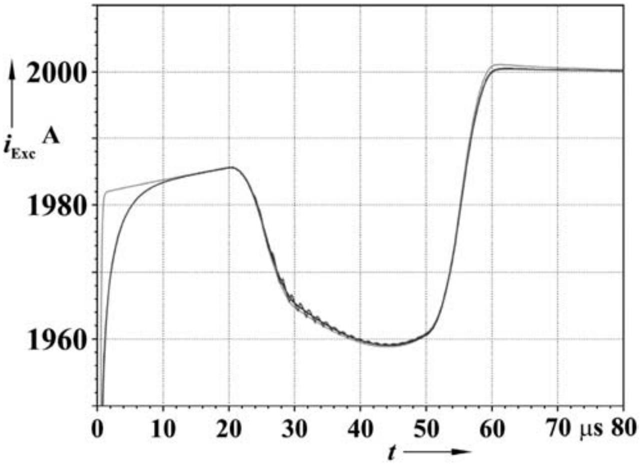

Figure 11.
Exciting current as function of time from finite-difference time stepping (black with oscillations), lumped parameter two circuit analysis (grey) and partial conductor model (almost congruent to FD-result but without oscillation)

Conclusion

A finite-difference scheme for axisymmetric problems including prescribed motion of a substructure has been presented. Remeshing is avoided by independent grids and an overlay-interpolation technique. The method is applied onto elementary test arrangements with axial and radial expansive motion, which can be described by lumped parameter analysis as a comparison. The results achieved by using these different methods are in good agreement. However, further research concerning the practical applicability is needed.

References

Bendjima, B., Srairi, K. and Feliachi, M. (1997), "A coupling model for analysing dynamical behaviours of an electromagnetic forming system", *IEEE Transactions on Magnetics*, Vol. 33, pp. 1638-41.

Gottkehaskamp, R. (1993), *Nichtlineare Berechnung von Asynchronmaschinen mit massiveisernem Rotor und zusätzlichem Käfig im transienten Zustand mittels finiter Differenzen und Zeitschrittrechnung*, PhD Thesis at chair TEM, University of Dortmund, 1992, VDI-Verlag, Düsseldorf.

Krawczyk, A. and Tegopoulos, J.A. (1993), *Numerical Modelling of Eddy Currents*, Clarendon Press, Oxford.

Nowak, L. (1989), "Field diffusion in magnetic circuits containing moving conducting parts", *Archiv für Elektrotechnik AfE*, Vol. 72, pp. 11-18.

The Emerald Research Register for this journal is available at
www.emeraldinsight.com/researchregister

The current issue and full text archive of this journal is available at
www.emeraldinsight.com/0332-1649.htm

Multi-domain topology optimization of electromagnetic systems

Semyung Wang
Department of Mechatronics, Gwangju Institute of Science and Technology (GIST), Gwangju, Korea
Seungkyu Park
R&D Center, YG-1 Co. Ltd, Korea
Jenam Kang
DA Research Center, LG Electronics, Seoul, Korea

Keywords *Electromagnetism, Optimization techniques, Actuators*

Abstract *The design of multi-domain that considers all components of electromagnetic systems such as air, iron, magnet, and coil is investigated using topology optimization, interpolation method, and FEM. The design sensitivity equation for topology optimization is derived using the adjoint variable method and the continuum approach. The proposed method is applied to topology optimization of C-core actuator and shows significant improvement.*

Introduction

Topology optimization is very useful for a conceptual design. The principle of topology optimization of electromagnetic systems is the same as that of the structural system (Bendsoe and Kikuchi, 1988). The topology optimization for the electromagnetic systems using the density method has already been studied (Dyck and Lowther, 1996; Wang and Kang, 2002a).

The topology optimization with two materials using the interpolation method in micro-electro-mechanical-systems (MEMS) was studied (Sigmund, 2001). However, the electrostatic fields were only considered as a driving force.

The topology optimization of electromagnetic systems with two materials was studied by introducing two-step optimization (Wang and Kang, 2002b). In previous work, the design of coil was neglected. And also, the final topologies of air and two materials could not be obtained at the same time.

In this paper, the previous work (Wang and Kang, 2002b) is extended to the design of multi-domain that considers all components of electromagnetic systems such as air, iron, magnet, and coil.

To find the final topology of three phases (air, iron, and magnet) at the same time, the interpolation method is used. But the topology optimization of coil is achieved independently unlike other components because coil is located separately as the source of the electromagnetic system.

This work was supported by the RRC-HECS, CNU under grant 01-gi-02 and by Center of Innovative Design Optimization Technology (iDOT), Korea Science and Engineering Foundation.

COMPEL: The International Journal for Computation and Mathematics in Electrical and Electronic Engineering
Vol. 23 No. 4, 2004
pp. 1036-1044
© Emerald Group Publishing Limited
0332-1649
DOI 10.1108/03321640410553463

Finally, topology optimizations of coil part and other parts (air, iron, and magnet) are carried out sequentially.

The design sensitivity expressions are analytically derived using the continuum approach and the adjoint variable method (AVM) (Edward *et al.*, 1986; Sigmund, 2001; Wang and Kang, 2002a, b). The sensitivity is calculated using a commercial FEM tool, ANSYS. The optimization routine is implemented using sequential linear programming (SLP) in design optimization tool (DOT), which is one of the commercial optimization codes. Then, to show the efficiency of the proposed method, the topology optimization of the C-core actuator is solved to reduce the volume while maximizing the energy.

Theory of multi-domain topology optimization

The magnetostatic field can be described by using the set of Maxwell's equations.

$$\nabla \times H = J_{\mathrm{s}}, \quad H = \frac{1}{\mu}(B - \mu_0 M), \quad \nabla \cdot B = 0 \tag{1}$$

where $H, J_{\mathrm{s}}, B, \mu, \mu_0$, are the magnetic field intensity vector, the current density vector (A/m^2), the magnetic flux density vector, the permeability of material, and the permeability of free space ($4\pi \times 10^{-7}$), respectively.

The vector M represents the magnetization vector (A/m) in the permanent magnet. The magnetization vector is related to the coercive force and the residual flux density.

$$H_{\mathrm{c}} = \frac{\mu_0}{\mu} M = \frac{1}{\mu} B_{\mathrm{r}} \tag{2}$$

where H_{c} and B_{r} are the coercive force and the residual magnetic flux density, respectively.

By introducing a vector potential $B = \nabla \times A$ and eliminating H in equation (1), we have a single governing equation

$$\nabla \times \left(\frac{1}{\mu} \nabla \times A \right) = J_{\mathrm{s}} + \nabla \times H_{\mathrm{c}} \tag{3}$$

There are two forms of governing equation. One is an integral form using continuum approach (Wang and Kang, 2002a, b).

$$a_{\mathrm{u}}(A, \bar{A}) = l_{\mathrm{u}}(\bar{A}) \quad \text{for all} \quad \bar{A} \in A \tag{4}$$

$$\begin{cases} a_{\mathrm{u}}(A, \bar{A}) = \iiint_{\Omega} (\nabla \times A) \cdot \left(\frac{1}{\mu} \nabla \times \bar{A} \right) \mathrm{d}\Omega \\ l_{\mathrm{u}}(\bar{A}) = \iiint_{\Omega} [J_{\mathrm{s}} \cdot \bar{A} + H_c \cdot (\nabla \times \bar{A})] \, \mathrm{d}\Omega \end{cases} \tag{5}$$

where $\bar{A}$ is virtual vector potential.

The other is a matrix form using a discrete approach.

$$\mathbf{KA} = \mathbf{Q} \tag{6}$$

where **K** is the stiffness matrix which is a function of permeability, **Q** is the force matrix which is a function of current density and coercive force.

$$K(\mu)A = Q_1(J_{\mathrm{s}}) + Q_2(H_{\mathrm{c}}) \tag{7}$$

Design variables are permeability, current density, and coercive force of each element as shown in equation (8).

$$b = f(\mu, J_{\mathrm{s}}, H_{\mathrm{c}}) \tag{8}$$

Those variables must be converted to density variables by the density method for using topology optimization. Figure 1 shows the general roles of density equations about permeability, current density, and coercive force.

To represent the porous material, suppose a fictitious material whose properties, like the current density J_s, can be represented as a P-powered function of ρ_1, material interpolations for the coil part are shown in equations (9) and (10).

$$J_{\mathrm{s}} = J_{\mathrm{s}_0}\rho_1^{P_1} \tag{9}$$

$$\mu = \rho_1^{P_1}(\mu_{\mathrm{c}}\mu_0 - \mu_0) + \mu_0 \tag{10}$$

where J_{s_0}, P_1, μ_{c} are initial current density, power factor, and relative permeability of coil, respectively. And ρ_1 is a compactness variable of coil. If ρ_1 becomes 1, the element becomes coil; otherwise it becomes air.

And in topology optimization for the core part, material interpolations can be shown in equations (11) and (12)

$$H_{\mathrm{c}} = \mathrm{H}_{\mathrm{c}_0}\rho_2^{P_2}\rho_3^{P_3} \tag{11}$$

$$\frac{\mu}{\mu_0} = \rho_2^{P_2}\left(\rho_3^{P_3}(\mu_{\mathrm{m}} - \mu_{\mathrm{s}}) + \mu_{\mathrm{s}} - 1\right) + 1 \tag{12}$$

where a compactness variable ρ_2 determines whether there is material (magnet and iron) or air in each element, and ρ_3 determines whether each element becomes iron or magnet.

Design sensitivity analysis

Consider a measure of electromagnetic performance that may be written in integral form as (Edward *et al.*, 1986)

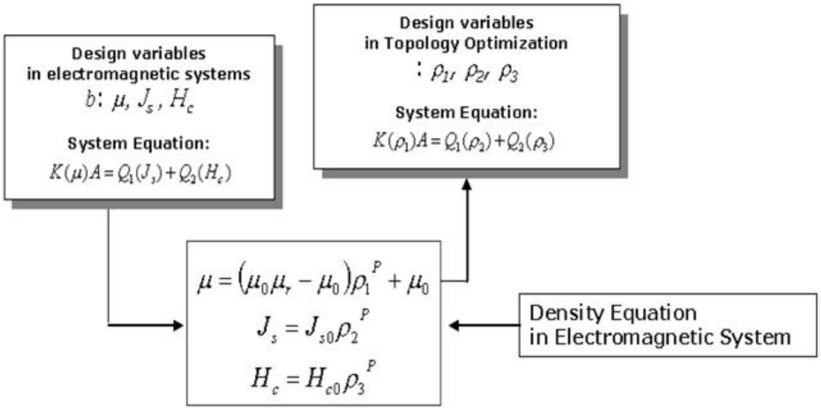
Design variables
in electromagnetic systems
b: μ, J_s, H_c
System Equation:
$K(\mu)A = Q_1(J_s) + Q_2(H_c)$
Design variables
in Topology Optimization
: ρ_1, ρ_2, ρ_3
System Equation:
$K(\rho_1)A = Q_1(\rho_2) + Q_2(\rho_3)$
$\mu = (\mu_0\mu_r - \mu_0)\rho_1^P + \mu_0$
$J_s = J_{s0}\rho_2^P$
$H_c = H_{c0}\rho_3^P$
Density Equation
in Electromagnetic System

Figure 1.
Density equation

$$\psi = \iiint_{\Omega} g(A, \nabla A, b)\, \mathrm{d}\Omega \tag{13}$$

The adjoint equation for the adjoint variable λ is (Edward *et al.*, 1986)

$$a_{\mathrm{u}}(\lambda, \bar{\lambda}) = \iiint_{\Omega} [g_A \bar{\lambda} + g_{\nabla A} \nabla \bar{\lambda}]\, \mathrm{d}\Omega \tag{14}$$

which must hold for all admissible virtual vector potential $\bar{\lambda} \in \tilde{A}$.

where $\bar{\lambda}$ is the virtual adjoint vector potential, $\tilde{A}$ is the space of virtual vector potential.

Using the variational form of objective function of equation (13) and direct differentiation result (Edward *et al.*, 1986), the sizing design sensitivity equation is

$$\begin{aligned} \psi' &= \iiint_{\Omega} [g_A A' + g_{\nabla A} \nabla A' + g_b \delta b]\, \mathrm{d}\Omega \\ &= \iiint_{\Omega} g_b \delta b\, \mathrm{d}\Omega + \iiint_{\Omega} [g_A A' + g_{\nabla A} \nabla A']\, \mathrm{d}\Omega \\ &= \iiint_{\Omega} g_b \delta b\, \mathrm{d}\Omega + l'_{\delta b}(\lambda) - a'_{\delta b}(A, \lambda) \end{aligned} \tag{15}$$

In the matrix form, general design sensitivity of an objective function is

$$\begin{aligned} \frac{\mathrm{d}\psi}{\mathrm{d}\rho} &= \frac{\partial \psi}{\partial \rho} + \lambda^{\mathrm{T}} \left(\frac{\partial Q_1}{\partial \rho} + \frac{\partial Q_2}{\partial \rho} - \frac{\partial K}{\partial \rho} A \right) \\ &= \frac{\partial \psi}{\partial \rho} + \lambda^{\mathrm{T}} \left(\frac{\partial Q_1}{\partial J_{\mathrm{s}}} \frac{\partial J_{\mathrm{s}}}{\partial \rho} + \frac{\partial Q_2}{\partial H_{\mathrm{c}}} \frac{\partial H_{\mathrm{c}}}{\partial \rho} - \frac{\partial K}{\partial \mu} \frac{\partial \mu}{\partial \rho} A \right) \end{aligned} \tag{16}$$

Numerical example

The objective of a C-core actuator is to control a blade's movement as shown in Figure 2 by using the attraction force. So it is important to design the magnet's shape to maximize the force. This design can be an optimization problem in which the force is

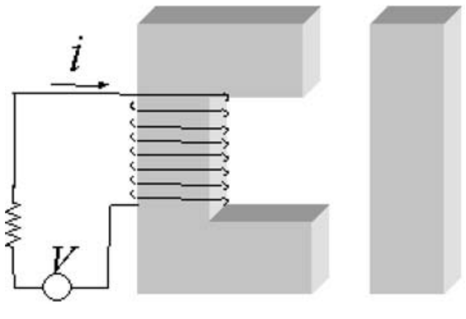

Figure 2.
C-core actuator

maximized in a specific volume. Because the energy variation is equal to the force, we can define the objective function as the magnetic energy (Wang and Kang, 2002a).

Figure 3 shows a 2D finite element model in ANSYS. There are two examples. One is a C-core actuator with small current density of the coil, i.e. 2.0 A/mm^2 (Case A). The other is a C-core actuator with large current density, i.e. 10.0 A/mm^2 (Case B). The width of both the blade and the core is 20 mm. The length of the core and the blade are 60 and 50 mm, respectively.

The geometry and material properties of two examples are the same except input current density as shown in Table I. In this paper, in topology optimization, linear material properties are used for reducing computation time as shown in Table I, but, in reanalysis of optimized models, non-linear material properties are used for considering the saturation of core and blade (Wang and Kang, 2002a).

The objective function of optimization is the magnetic energy in airgap and constraints are the volume of coil and core, and a gray level indicator (Wang and Kang, 2002a).

$$\text{Objective:}\quad \text{Max}\,\Psi = \sum\left(\frac{1}{2}A^{\mathrm{T}}KA\right) \tag{17}$$

$$\text{Constraint:}\quad g_1 = \frac{\sum_{k}^{\mathrm{NDV}} \rho_k V}{V_r} - 1 \leq 0 \quad (0 \leq \rho_e \leq 1) \tag{18}$$

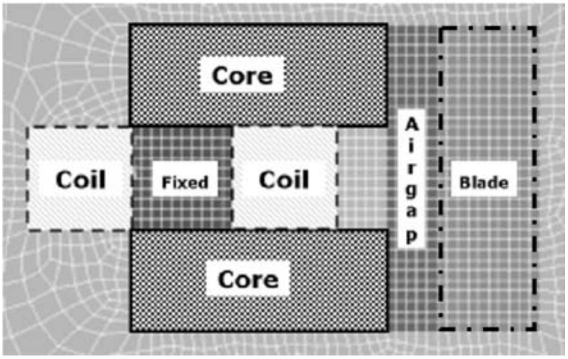

Figure 3.
2-D finite element model

Table I.
Material properties

	Relative permeability	Current density (J_s) (A/mm^2)	Coercive force (H_c) (A/m)
Core	3,000	–	–
Blade	3,000	–	–
Coil	0.95	(Case A) 2 (Case B) 10	–
Magnet	1.05	–	951,808
Air	1	–	–

$$g_2 = 1 - \frac{\sum_{k}^{\text{NDV}} (\rho_\kappa - 0.5)^2}{\text{NDV} \cdot GI_d} \leq 0 \quad (0 < GI_d \leq 0.25) \tag{19}$$

where V_r is the total volume to remain after the topology optimization, V is the volume of each element.

Figure 4 shows the design domain for topology optimization. In the three-domain (air, iron, magnet) optimization, the design domain of core parts is only considered while the design domain for coil is neglected. However, in the four-domain optimization, the design domain for coil is considered as total area of design domain for coil is increased about 20 percent as shown in Figure 4.

Figure 5 shows results of Case A. Three-domain means that air, steel and magnet are considered as design domain. And four-domain means that air, steel, magnet and coil are considered as design domain. From topology optimization, finally, the core part consists of 50 percent air, 40 percent iron, and 10 percent magnet. Those results show the topology optimization can give significantly improved design.

The initial magnetic energy is 0.33 J/m, and the final magnetic energy is 4.8 J/m. Therefore, the magnetic system energy is significantly increased by adding optimized magnet as shown in Figure 5. The magnetic force generated in blade is obtained by reanalysis of the optimized model with non-linear material property.

Figure 6 shows results of Case B. The initial magnetic energy is 8.02 J/m, and the final magnetic energy is 10.42 J/m. The difference of energy or force between original and optimized model is less than that of Case A because the core is saturated due to large current density in Case B.

Therefore, from the proposed multi-domain topology optimization, we can get the optimized model that has suitable material ratio while saving the material cost.

Conclusion

In this paper, the topology optimization of the electromagnetic systems in multi-domain that considers air, iron, magnet, and coil is studied. The topology sensitivity equation is derived using the continuum approach. The multi-domain of C-core actuator is optimized to produce maximum magnetic force under a given source

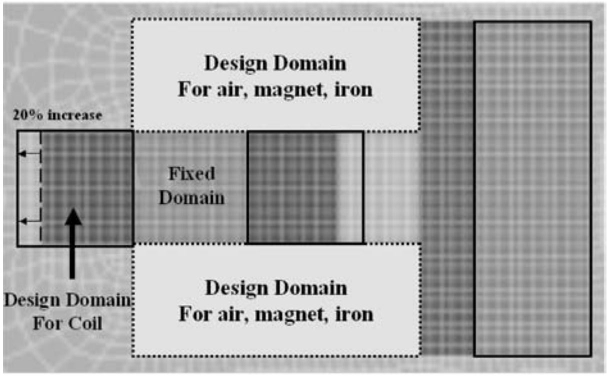

Figure 4.
Design domain

	Original model	Three-domain Optimization	Four-domain Optimization
C-core shape	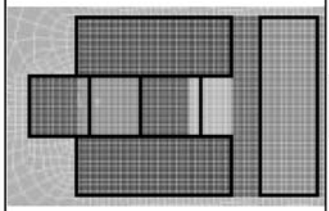	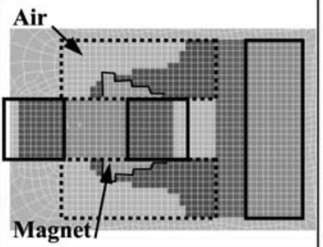	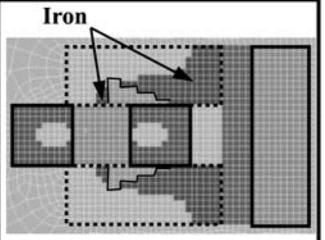
Air : Steel : Magnet *in core*	**0 : 10 :0**	**5 : 4: 1**	**5 : 4 : 1**
Air : Coil *in coil*	**2 : 8**	**2 : 8**	**2 : 8**
Energy [J/m]	**0.33**	**4.7**	**4.8**
Reanalysis Force [N/m]	**29.4**	**424.8**	**430.1**

Figure 5.
The final results of multi-domain topology optimization (Case A)

	Original Model	Three-domain Optimization
C-core shape	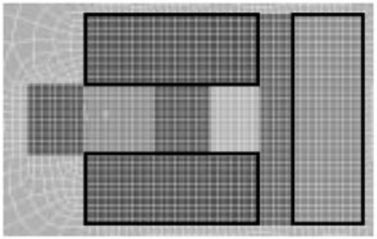	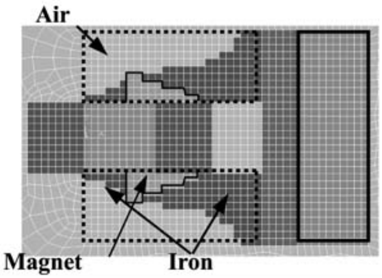
Air : Steel : Magnet *in core*	**0 : 10 : 0**	**5 : 4 : 1**
Energy [J/m]	**8.02**	**10.42**
Reanalysis Force [N/m]	**731.05**	**943.3**

Figure 6.
The final results of multi-domain topology optimization (Case B)

current. Numerical examples show that multi-domain topology optimization can give significantly improved design.

References

Bendsoe, M.P. and Kikuchi, N. (1988), “Generating optimal topologies in structural design using a homogenization method”, *Computer Method in Applied Mechanics and Engineering*, Vol. 71, pp. 197-224.

Dyck, D.N. and Lowther, D.A. (1996), “Automated design of magnetic devices by optimizing material distribution”, *IEEE Transactions on Magnetics*, Vol. 32 No. 3.

Edward, J.H., Choi, K. and Vadim, K. (1986), *Design Sensitivity Analysis of Structural Systems*, Academic Press, London.

Sigmund, O. (2001), “Design of multiphysics actuators using topology optimization – part II: two-material structures”, *Comput. Methods Appl. Mech. Eng.*, Vol. 190, pp. 6605-27.

Wang, S. and Kang, J. (2002a), “Topology optimization of nonlinear magnetostatics”, *IEEE Transactions on Magnetics*, Vol. 38 No. 2, pp. 1029-32.

Wang, S. and Kang, J. (2002b), “Topology optimization of electromagnetic systems with two materials”, *CEFC’ 2002*, p. 47.

The Emerald Research Register for this journal is available at
www.emeraldinsight.com/researchregister

The current issue and full text archive of this journal is available at
www.emeraldinsight.com/0332-1649.htm

Optimal design of induction heating equipment for high-speed processing of a semiconductor

Yoshifumi Okamoto, Toshio Imai, Daisuke Miyagi and Norio Takahashi
Department of Electrical and Electronic Engineering, Okayama University, Okayama, Japan
Kazuhiro Ozaki, Hiroshi Ono and Naoki Uchida
Mitsui Engineering & Shipbuilding Co., Ltd

Keywords *Heating, Optimization techniques, Finite element analysis*

Abstract *Induction heating is widely used in the industry due to high efficiency, precise control, rapid heating and low pollution properties. To process a semiconductor of high quality, uniform heating is necessary, but it is not easy to heat uniformly by using the conventional induction heating equipment. For this purpose, the zone control induction heating equipment is jointly developed with Mitsui Engineering Shipbuilding Co., Ltd. In this paper, the optimization of current in each coil is carried out using the finite element method and the optimization method in order to obtain a uniform eddy current loss distribution on graphite.*

1. Introduction

From the viewpoint of heating efficiency, temperature control and realization of clean work environment, the induction heating is widely used (Mai and Henneberger, 1999). If the induction heating technology can be improved by using the finite element method (FEM), it will contribute to the development of the industry in this field.

For example, features such as quickness, high precision and uniform heating is needed for semiconductor wafer used for a photovoltaic cell. In order to realize uniform heating, it is necessary to supply the electric energy uniformly to the graphite. When only one exciting coil is used in the induction heating, the temperature in the graphite cannot be controlled. Then, a new technique called zone control (Figure 1) is introduced. In this technique, the exciting coil is divided into several small coils and each coil is connected to an independent power supply of high frequency, and the current in each coil is controlled to realize uniform heating. However, there may be no report about the optimization of the current and the shape of graphite for uniform heating.

In this research, the optimal design for uniform heating is performed using FEM and the optimization method (Evolution Strategy (ES)) (Bäck, 1996; Horii *et al.*, 2000). The optimal shape of graphite to realize uniform heating is investigated, and about uniform eddy current loss distribution is obtained by controlling the current in each coil.

2. Analyzed model and optimal design method

2.1 Analyzed model

The analyzed model is shown in Figure 2. The heating coil is divided into eight zones where the high frequency inverters are connected. The graphite is set just under the

COMPEL: The International Journal for Computation and Mathematics in Electrical and Electronic Engineering
Vol. 23 No. 4, 2004
pp. 1045-1052
© Emerald Group Publishing Limited
0332-1649
DOI 10.1108/03321640410553472

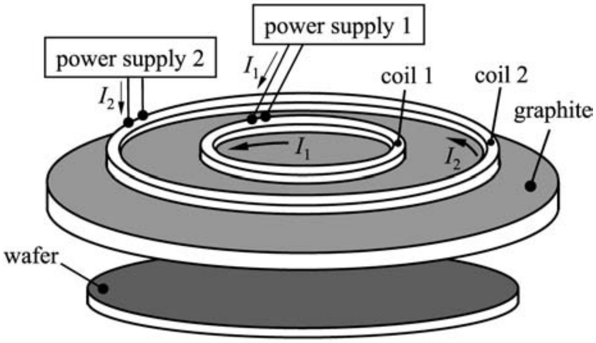
power supply 1
power supply 2
I_1
I_2
coil 1
coil 2
graphite
I_1
I_2
wafer

Figure 1.
Induction heating equipment with zone control

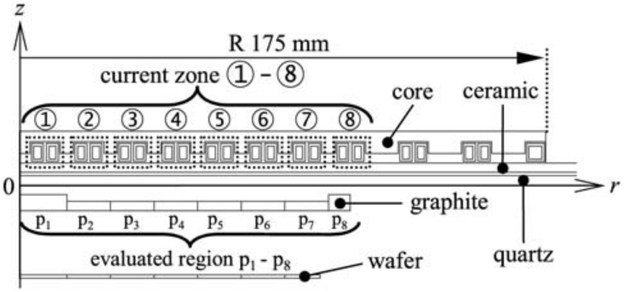
z
R 175 mm
current zone ① - ⑧
①
②
③
④
⑤
⑥
⑦
⑧
core
ceramic
0
r
graphite
p_1
p_2
p_3
p_4
p_5
p_6
p_7
p_8
evaluated region p_1 - p_8
wafer
quartz

Figure 2.
Analyzed model

excitation coils and is heated by eddy losses produced by the exciting coils. The graphite is divided into eight regions (p_1-p_8) as shown in Figure 2. The shape of graphite and the currents in the eight exciting coils are changed in order to obtain the uniform distribution of the eddy current loss in graphite. The frequency of exciting current is 40 kHz. The eddy current is considered in the graphite, wafer, core and exciting coils. Each material constant is shown in Table I.

2.2 Governing equation

Governing equation of eddy current problem can be described using the Maxwell's equation as follows:

$$\mathrm{rot}\left(\frac{1}{\mu}\mathrm{rot}\,\dot{\boldsymbol{A}}\right) = \dot{\boldsymbol{J}}_0 - j\omega\sigma\dot{\boldsymbol{A}} - \sigma\,\mathrm{grad}\,\phi \tag{1}$$

where μ is the permeability $\dot{\boldsymbol{A}}$ the magnetic vector potential, $\dot{\boldsymbol{J}}_0$ the given current density, σ the conductivity and ϕ the electric scalar potential. The dot (·) denotes a

Table I.
Material constant

	Graphite	Water	Core	Exciting coil
Relative permeability	1	1	32	1
Conductivity (S/m)	1.1236×10^5	9.09×10^3	2.5×10^{-2}	5.0×10^7

complex variable. As the core is not saturated, the phasor method (the so-called $j\omega$ method) is applied in axissymmetric eddy current analysis by assuming that the magnetic characteristic is linear.

2.3 Optimal design method

To achieve the uniform heating on the graphite, the optimal design is performed using the axissymmetric FEM combined with the (1+1)-ES for searching the global optimal solution. In this optimization problem, the amount of current supplied to each zone ((1)-(8)) is set as design variables (I_i, i=1-8). The constraint range of I_i is given by

$$0 \text{ per cent} \leq I_i \leq 200 \text{ per cent} \quad (i = 1\text{-}8) \tag{2}$$

Each zone consists of two coils. The amount of current I_i is optimized so that the distribution of eddy current loss in graphite becomes uniform. Therefore, the objective function F is defined by

$$F = \frac{W_{\max}}{W_{\min}} \tag{3}$$

where $W_{\max}$ is the maximum eddy current loss, and $W_{\min}$ is the minimum eddy current loss of W_i (i=1-8) in each region p_1-p_8 in Figure 2.

The flow chart of optimal design method of induction-heating equipment is shown in Figure 3. This optimization procedure of every step is explained as follows.

Step 1: decision of initial current value. The initial current value (I_1-I_8) of each zone ((1)-(8)) is determined. The initial value was set-up with 100 per cent in all zones.

Step 2: Step 5: calculation of objective function. The eddy current loss produced in the regions p_1-p_8 of graphite is calculated by using FEM. The eddy current loss density in the region p_8 of the basic model shown in Figure 2 is normalized to unity. The objective function F is calculated using equation (3).

Step 3: mutation. The driving force of ES is the mutation. The updating formula of the design variable is given by:

$$\boldsymbol{I}_{\mathrm{o}}^{(k)} = \boldsymbol{I}_{\mathrm{p}}^{(k)} + \boldsymbol{N}_8(0, \sigma^2) \tag{4}$$

where $\boldsymbol{I}_{\mathrm{o}}^{(k)}$ is the offspring vector, $\boldsymbol{I}_{\mathrm{p}}^{(k)}$ is the parent vector in the kth generation and $N_8(0, \boldsymbol{\sigma}^2)$ is the normalized random vector consisting of eight different normalized random numbers based on standard deviation $\boldsymbol{\sigma}$. The initial value of σ is set to 50.

Step 4: judgment of constraint condition. The offspring vector is judged whether equation (2) is satisfied or not. If the offspring vector obtained at Step 3 does not satisfy equation (2), the operation returns to Step 3.

Step 6: natural selection. The objective function of the offspring vector and the parent vector is compared, and a smaller objective function is chosen as a parent vector of the next generation as shown in the following equation:

$$\boldsymbol{I}_{\mathrm{p}}^{(k+1)} = \begin{cases} \boldsymbol{I}_{\mathrm{p}}^{(k)} & (F_{\mathrm{p}} \leq F_{\mathrm{o}}) \\ \boldsymbol{I}_{\mathrm{o}}^{(k)} & (F_{\mathrm{o}} \leq F_{\mathrm{p}}) \end{cases} \tag{5}$$

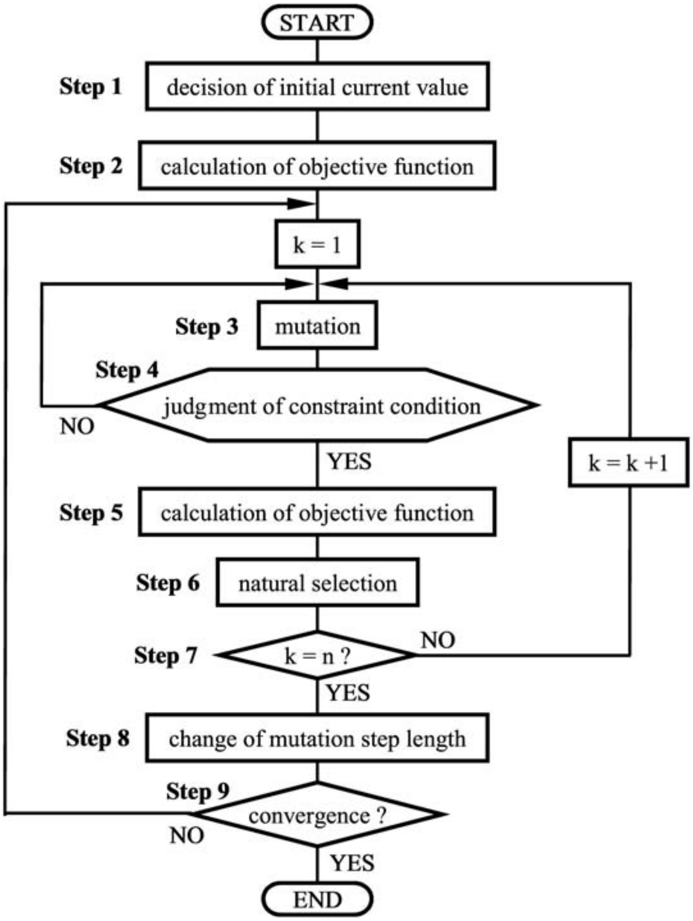
START
Step 1
decision of initial current value
Step 2
calculation of objective function
k = 1
Step 3
mutation
Step 4
judgment of constraint condition
NO
YES
k = k +1
Step 5
calculation of objective function
Step 6
natural selection
Step 7
k = n ?
NO
YES
Step 8
change of mutation step length
Step 9
convergence ?
NO
YES
END

Figure 3.
Optimization process using (1 + 1)-ES and FEM

where F_p is the objective function of the parent vector and F_o the objective function of the offspring vector.

Step 7: $k = n$?. The number of iterations n of mutation is set as 80, that is ten times the design variable. If k is equal to n, the operation progresses to Step 8, otherwise, return to Step 3.

Step 8: change of mutation step length. The standard deviation σ is changed at every n calculations as shown in the following equation:

$$\sigma = \begin{cases} \sigma \times 0.85 & (\psi < 0.2) \\ \sigma & (\psi = 0.2) \\ \sigma/0.85 & (\psi > 0.2) \end{cases} \tag{6}$$

where ψ shows the probability of success during n searches.

Step 9: convergence ?. If the standard deviation σ is smaller than 0.5, the optimal design is ended. Otherwise, the operation returns to Step 3 and the same calculation is performed.

3. Optimal design of induction heating equipment

3.1 Optimization of basic model

The current in each zone of the basic model shown in Figure 2 is optimized. While the eddy current losses of p_1 and p_2 are smaller than those of other regions in the initial state (the current I_1-I_8 are all the same), the loss in each region of graphite was mostly made uniform after optimal design as shown in Figure 4. The current of each zone and the objective function are shown in Table II. I_1 and I_2 are increased because the eddy current losses of regions p_1 and p_2 are lower in the initial state. In order to make the eddy current losses of regions p_1 and p_2 almost equal to the losses of p_3-p_8, the currents of I_3-I_8 should be reduced. By using the optimization technique, the objective function F is decreased from 7.3 to 1.2 as shown in Table II. The optimization of basic model took

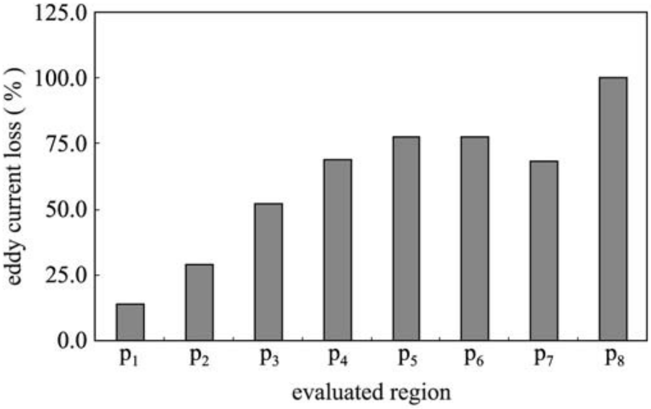

(a) initial

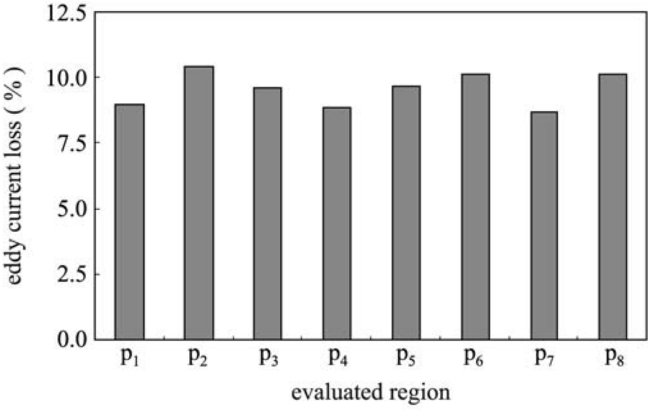

(b) optimal

Figure 4.
Eddy current distributions (basic model)

24.4 h during 2,320 iterations using PC (CPU: Intel Pentium 4 Processor 2.8 GHz, Memory: 1.5 GB).

3.2 Optimization of modified model

By the optimization of the basic model, the eddy current loss in each region could not be made almost uniform. Then, to make the loss distribution of the graphite more uniform, the shape of graphite was changed based on some forward analyses. The modified model obtained is shown in Figure 5(b). In order to make the eddy current losses of the graphite region p_1, p_4 and p_7 larger, the thickness of these regions are increased compared with those of other regions. The thickness of regions p_2 and p_6 are reduced compared with those of other regions in order to reduce the eddy current loss. The thickness of regions p_3 and p_5 are also changed as shown in Figure 5(b) to adjust the eddy current loss distribution. The thickness of region p_8 is made larger than those of other regions so that the leakage flux to wafer is prevented.

The optimal current of each coil is obtained by using ES. The flux distributions at the initial and optimal states are shown in Figure 6. Since the flux density generated at the end of the graphite region p_8 is high as shown in Figure 6(a), the eddy current loss in the region p_8 becomes large. The flux distribution becomes more uniform in the graphite at the optimal state as shown in Figure 6(b).

Figure 7 shows the eddy loss distributions. The eddy current loss of the basic model is more uniform than that of the basic model at initial state. By changing the shape of the graphite, the eddy current losses of regions p_4 and p_7 at initial state are increased. A considerably uniform eddy current loss distribution is obtained after optimization in the case of the modified model as shown in

Table II.
Optimal result

Model	State	Objective function F	Current (per cent) I_1	I_2	I_3	I_4	I_5	I_6	I_7	I_8
Basic model	Initial	7.3	100.0	100.0	100.0	100.0	100.0	100.0	100.0	100.0
	Optimal	1.2	179.8	128.9	28.7	9.9	45.9	21.8	78.7	03
Modified model	Initial	6.9	100.0	100.0	100.0	100.0	100.0	100.0	100.0	100.0
	Optimal	1.0	186.8	105.9	19.7	19.6	10.2	69.3	12.5	27.4

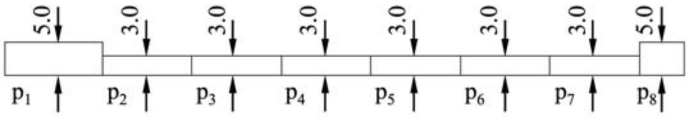

(a) basic model

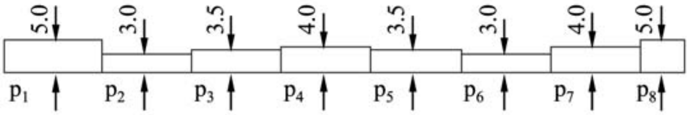

(b) modified model unit: mm

Figure 5.
Graphite form

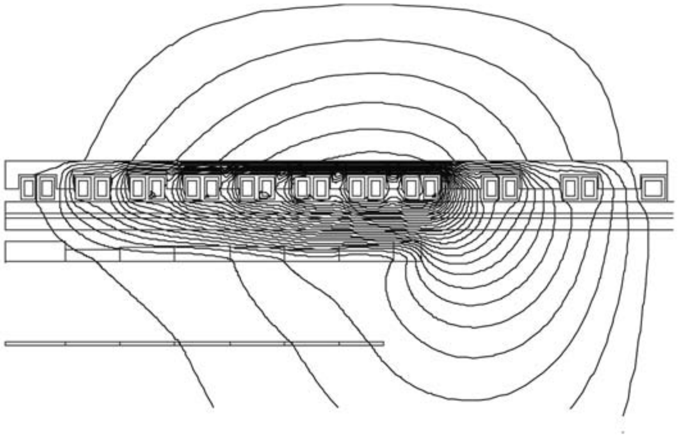

(a) initial state

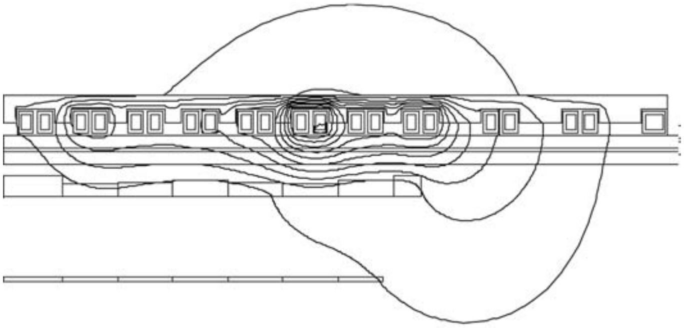

(b) optimal state

Figure 6. Flux distributions (modified model)

Figure 7(b). As shown in Table II, the objective function F of the modified model after optimization is smaller than that of the basic model. The total amount of current is decreased like the case of optimization of the basic model because the eddy current loss in each region of the initial state is considerably different from each other. The optimization of the modified model took 27.4 h during 2,320 iterations.

4. Conclusion

It is shown that the nearby uniform distribution of eddy current loss in graphite can be obtained by changing the shape of graphite and controlling the exciting current in each zone.

The optimization of both shape of graphite and amplitude of exciting current of each zone coil is a future research subject.

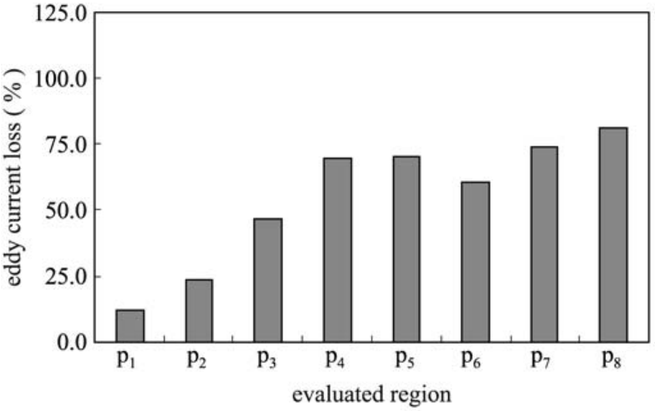

(a) initial

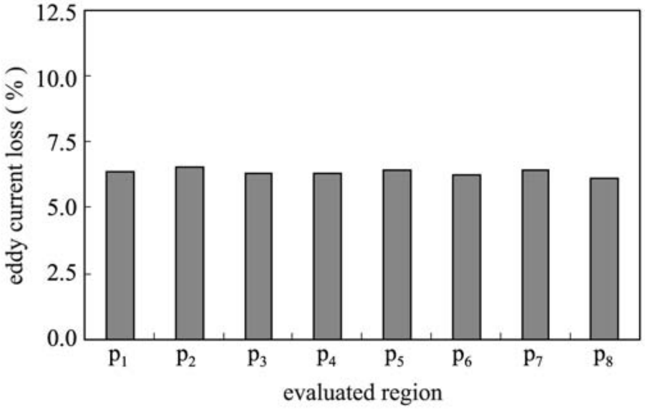

(b) optimal

Figure 7.
Eddy current distributions (modified model)

References

Bäck, T. (1996), *Evolutionary Algorithms in Theory and Practice*, Oxford University Press, New York, NY, pp. 66-91.

Horii, M., Takahashi, N. and Narita, T. (2000), "Investigation of evolution strategy and optimization of induction heating model", *IEEE Trans. Magn.*, Vol. 36 No. 4, pp. 1085-8.

Mai, W. and Henneberger, G. (1999), "Field and temperature calculations in transverse flux inductive heating devices heating non-paramagnetic materials using surface impedance formulations for non-linear eddy-current problems", *IEEE Trans. Magn.*, Vol. 35 No. 3, pp. 1590-3.

The Emerald Research Register for this journal is available at
www.emeraldinsight.com/researchregister

The current issue and full text archive of this journal is available at
www.emeraldinsight.com/0332-1649.htm

Optimal characterization of LF magnetic field using multipoles

R. Scorretti
CEGELY UMR 5005 – Ecole Centrale de Lyon, Ecully, France
R. Takahashi
Universidade Federal de Minas Gerais (UFMG), Belo Horizonte, Brazil
L. Nicolas and N. Burais
CEGELY UMR 5005 – Ecole Centrale de Lyon, Ecully, France

Keywords *Magnetic Fields, Electrical equipment, Environmental health and safety*

Abstract *The LF magnetic field (50 Hz-100 kHz) generated in the air by electrical appliances is characterised using multipoles. The maximum likelihood estimation of an equivalent multipolar source is computed using a genetic algorithm. The choice of the position and the number of measurement points are discussed.*

1. Introduction

The increasing number of electrical appliances in the daily life, rises the question of the interaction of these fields with the living systems. The effects on the human health of occasional (unwanted) exposure to the electromagnetic fields are still not well known. For this reason, the governments have imposed some restrictions on the fields generated in the air by electrical appliances. In the case of low frequency (50 Hz-100 kHz) magnetic fields, these limits are defined on the basis of the currents induced into the human body. Unfortunately, these currents are extremely weak, and a direct measurement is impossible. The simplest model to compute these current is a 1D model (ICNIRP, 1998), where the magnetic field is supposed to be uniform. Clearly, this is not a realistic situation in proximity of the appliance, and by consequence the reference levels on the field which derive from this model are too restrictive (Burais *et al.*, 1998; Gaspard *et al.*, 2000). Thus, it is important to be able to characterize the fields generated in the air by electrical appliances using experimental data. The main idea is to perform some measurements of the magnetic field in the air, and use them to fit the parameters of an equivalent source. This source can replace the real appliance, in the computation of the induced currents in the human body. The simplest model of equivalent source which has been proposed is a magnetic dipole (Yamazaki and Kawamoto, 2001; Zaffanella *et al.*, 1997). However, a simple dipole may be not representative enough of the field distribution, depending upon the kind of the appliance (Salomon and O-Mun, 2001), and on the distance from it. In this case, a multipolar source can be used. Compared to the magnetostatic case, the main difficulty with this technique in the harmonic regime is the need to measure both amplitude and phase (Lyon, 1994) of the magnetic field. However, the measurement of the phase is really necessary only when dealing with rotating fields. This paper presents an approach based on the maximum likelihood estimation (MLE) of a multipolar source, using a genetic algorithm (GA). First, the formulation of the problem is presented. Then, the method is tested on a simple source (a coil) using

COMPEL: The International Journal for Computation and Mathematics in Electrical and Electronic Engineering
Vol. 23 No. 4, 2004
pp. 1053-1061
© Emerald Group Publishing Limited
0332-1649
DOI 10.1108/03321640410553481

computer-generated data. The choice of the measurement points is discussed. Finally, the application to a real device is presented.

2. Formulation of the problem

The simplified Maxwell equations for the harmonic, quasi-magnetostatic case (Durand, 1968) are:

$$\vec{\nabla}\cdot\vec{B}=0 \tag{1}$$

$$\vec{\nabla}\times\vec{H}=\vec{J} \tag{2}$$

The air surrounding the electrical appliance is supposed to be free from currents ($\vec{J}=0$), so that the magnetic field $\vec{H}$ can be described using either a scalar potential ψ, or a vector potential $\vec{A}$:

$$\vec{H}=-\vec{\nabla}\psi=\frac{1}{\mu_o}\vec{\nabla}\times\vec{A} \tag{3}$$

Both these potentials obeys the Laplace's equation, and thus can be described by a multipolar development (Lorange, 2001):

$$\psi=\sum_{n=1}^{\infty}\left(\frac{R}{r}\right)^{n+1}\sum_{m=-n}^{n}\underline{A}_{n,m}Y_n^m(\vartheta,\varphi) \tag{4}$$

$$\vec{A}=-\sum_{n=1}^{\infty}\frac{1}{n}\left(\frac{R}{r}\right)^{n+1}\underline{A}_{n,m}\vec{r}\times\vec{\nabla}Y_n^m(\vartheta,\varphi) \tag{5}$$

where $\underline{A}_{n,m}$ is the coefficient of the development, R is an arbitrary distance, and $Y_n^m(\vartheta,\varphi)$ is the spherical harmonics (available at: www.mathworld.wolfram.com/SphericalHarmonic.html). The coefficients $\underline{A}_{n,m}$ depend upon the choice of R and the coordinate system (i.e. the position and the orientation of the equivalent source).

2.1 Choice of R

Equations (4) and (5) hold outside the sphere of radius R. Thus, R must be large enough, such that the appliance is contained inside this sphere. On the other hand, to achieve an accurate characterization of the field in the air, R should be chosen as small as possible. However, the choice of R is not crucial, in that a different choice $R' \neq R$ leads to a simple scaling of the coefficients.

2.2 Choice of the coordinate system

The choice of the coordinate system (i.e. the centre and the orientation of the multipole) turns out to be very important for the quality of the characterization. First, it should be observed that the number P of the coefficients grows quickly with the order N of the development (Table I):

From the mathematical point of view, the problem is definitely solved by the equations (4) or (5). However, in practical applications the infinite sums in equations (4) and (5) have to be bounded to a certain order (i.e. $n \leq N$). It turns out that a smart

Table I.
Number of coefficients of the development

Order	$N=1$	$N=2$	$N=3$
Coefficients	$P=3$	$P=8$	$P=15$

choice of the coordinate system improves the accuracy of the fit, and avoids the unnecessary complications dues to high-order harmonics. An explication of this fact is that the symmetries of the system may be (implicitly) considered in the choice of the coordinate system.

2.3 MLE of the coefficient

Assume currently that R and the coordinate system have been chosen, and that the magnetic field $\vec{H}$ is measured onto a set of M points. For the sake of simplicity, assume that the field is periodic with time, and that only the fundamental component[1] is considered: thus, a 3D complex vector $\underline{\vec{H}}$ is associated to each measurement point. It can be observed that the field depends linearly upon the coefficients:

$$[\underline{\mathbf{H}}] = [\mathbf{C}] \cdot [\underline{\mathbf{A}}] + \sigma^2[\mathbf{I}] \tag{6}$$

where the term $\sigma^2[\mathbf{I}]$ models a white Gaussian measurement noise, and the coefficients and the measured values of the field are arranged into the vectors $[\underline{\mathbf{A}}]$ and $[\underline{\mathbf{H}}]$, respectively. The MLE (Strang, 1986) of the coefficients $[\hat{\underline{\mathbf{A}}}]$ and its covariance matrix can be computed using the well-known formulas:

$$[\underline{\mathbf{A}}] = ([\mathbf{C}]^H[\mathbf{C}])^{-1}[\mathbf{C}]^H \cdot [\underline{\mathbf{H}}] \tag{7}$$

$$\operatorname{cov}[\underline{\mathbf{A}}] = \frac{1}{3M - P}([\mathbf{C}]^H[\mathbf{C}])^{-1} \cdot [\underline{\mathbf{H}}]^H([\mathbf{I}] - [\mathbf{C}]([\mathbf{C}]^H[\mathbf{C}])^{-1}[\mathbf{C}]^H)[\underline{\mathbf{H}}] \tag{8}$$

The number of measurement points M must be large enough for the system in equation (7) to be over determined: $3M > P$.

2.4 The optimization problem

The "core" of the method (Figure 1) consists in choosing the coordinate system in a somehow optimal way. To this purpose, a GA (Goldberg, 1989; Takahashi *et al.*, 2003) is

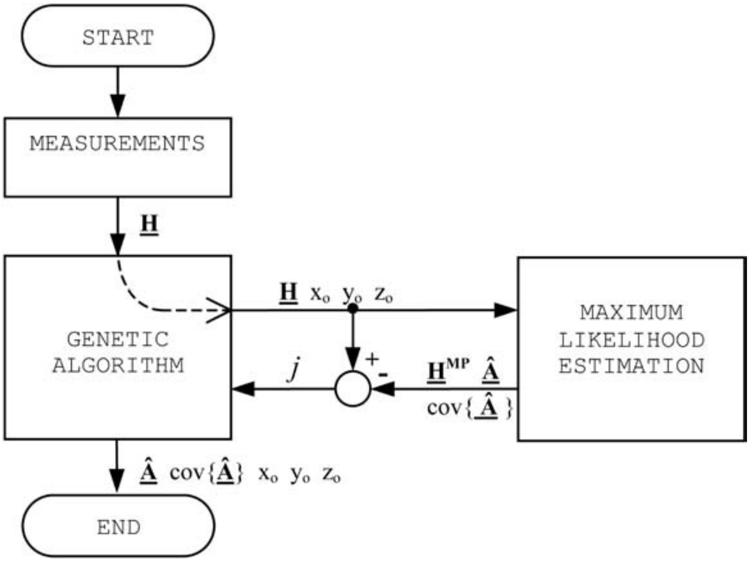
START
MEASUREMENTS
$\underline{\mathbf{H}}$
GENETIC ALGORITHM
$\underline{\mathbf{H}}$ x_o y_o z_o
MAXIMUM LIKELIHOOD ESTIMATION
j
+
-
$\underline{\mathbf{H}}^{MP}$ $\hat{\underline{\mathbf{A}}}$
cov{$\hat{\underline{\mathbf{A}}}$}
$\hat{\underline{\mathbf{A}}}$ cov{$\hat{\underline{\mathbf{A}}}$} x_o y_o z_o
END

Figure 1.
Sketch of the method

used. The parameters to be optimised are the coordinates of the centre of the source: x_o, y_o, z_o. The cost function j, to be minimized, is the mean square reconstruction error:

$$j = \frac{1}{M}\sum_{k=1}^{M}\left\| \vec{\underline{H}}_k - \vec{\underline{H}}_k^{(\mathrm{MP})} \right\|^2 \tag{9}$$

where $\vec{\underline{H}}_k^{(\mathrm{MP})}$ is the magnetic field computed in the kth measurement point, using the equivalent multipole.

3. Results

First, the effectiveness of the method has been tested with a simple source (a coil). In this case, the "measurement" data have been computed using analytical formulas (Durand, 1968). Then, the method has been applied on real measurements from a test device.

3.1 Application to a circular coil

The coil (radius $a = 40\,\mathrm{cm}$, current $I = 1\,\mathrm{A}$) is placed at the origin, the axis oriented along the z-direction, and modelled with a third-order multipole. First, 36 measurement points (Figure 2) have been taken on a sphere of radius 1 m. The coefficients has been

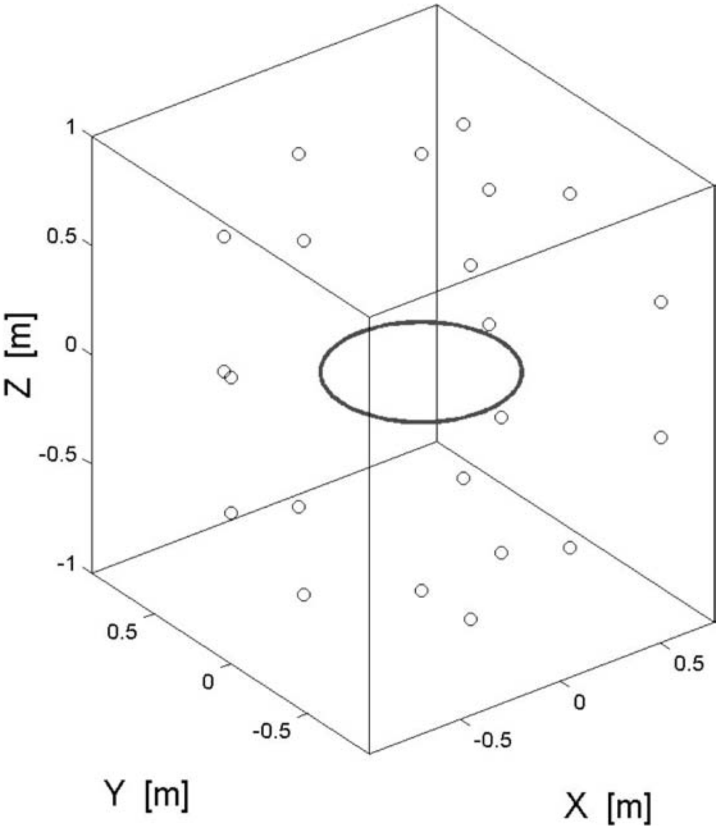

Figure 2.
The coil with the measurement points

first estimated when the multipole is placed at the origin (real position), at two other arbitrary positions (case a, b – Table II), and at the position obtained with the GA. Only the position of the coordinate system has been optimised.

First of all, one sees that the optimised location computed by the GA is very close to the real position.

In Figure 3, the absolute values of the coefficients have been plotted. One observe that when the location of the multipole is chosen arbitrarily (case a, b), some high-order harmonic terms appear. These terms have no physical meaning, and are introduced only to fit the data. Thus, the solution obtained by the GA is, in some way, the simplest one.

In order to quantify the effectiveness of the solution, we define in each point the error criterion:

$$\varepsilon = \left\| \underline{\vec{H}} - \underline{\vec{H}}^{(\mathrm{MP})} \right\| \Big/ \max \left\| \underline{\vec{H}} \right\| \cdot 100 \,\text{per cent} \tag{10}$$

This criterion has been computed over a sphere of radius 2 m, centred into the origin. The maximum values of ε obtained are: 3.3 per cent in the case (a), 44 per cent in the

Real position	Case (a)	Case (b)	GA
$x_o = 0$	$x_o = 0.1$	$x_o = 0.3$	$x_o = -0.0217$
$y_o = 0$	$y_o = -0.05$	$y_o = -0.3$	$y_o = -0.0090$
$z_o = 0$	$z_o = -0.030$	$z_o = 0.4$	$z_o = 0.0014$

Table II.
Center of the equivalent multipole

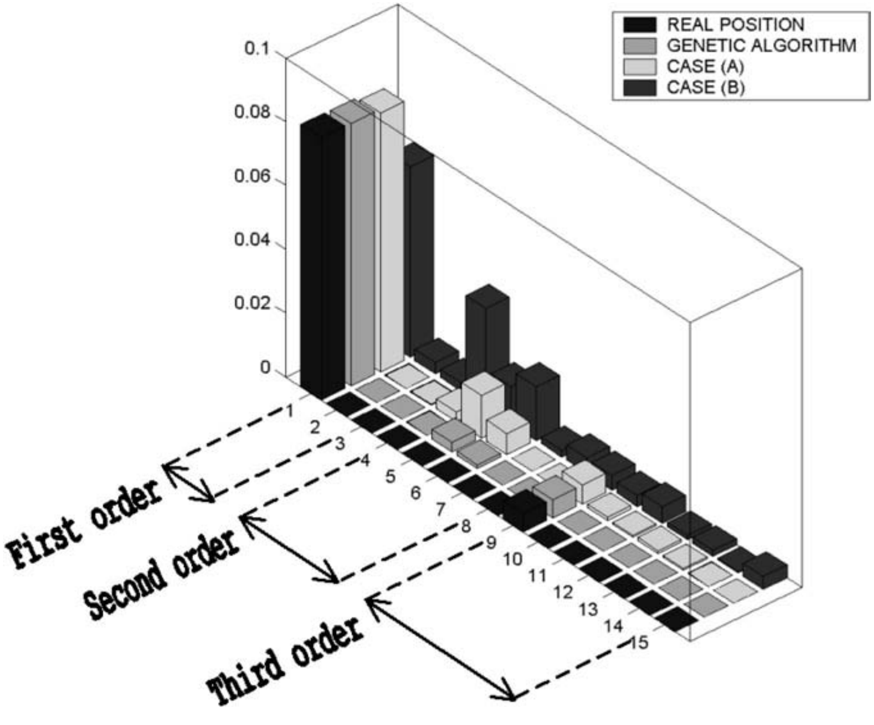

Figure 3.
Coefficients of the multipole

case (b), and 0.87 per cent when the centre is optimised. Thus, when the position of the multipole is optimised, a better agreement is arrived with the data.

3.2 The choice of the measurement points

An important question which arises when dealing with a real appliance is where to perform the measurements of the field. In the previous section, the measurement points have been placed onto a sphere which surround the source of the field. This is seldom a realistic situation, in that one may actually not be able to locate the field sensors all around the appliance. Moreover, the effectiveness of the method has been validated a posteriori, using a second set of data. Even if this is an unavoidable step, it is important to have an *a priori* criterion about the goodness of the choice of the measurement points. To this purpose, some other configurations of the measurement points have been simulated. Among them, a case which has a high practical interest (Zaffanella *et al.*, 1997) is when the points are placed onto a straight line (Figure 4). In this case the method fails. This result merits to be investigated more carefully.

First of all, it can be observed that the estimated values of the coefficients (Figure 5) are meaningless: not only the order of magnitude is wrong (10^5 compared to 10^{-1}) but also the dipolar character of the coil cannot be argued in any way.

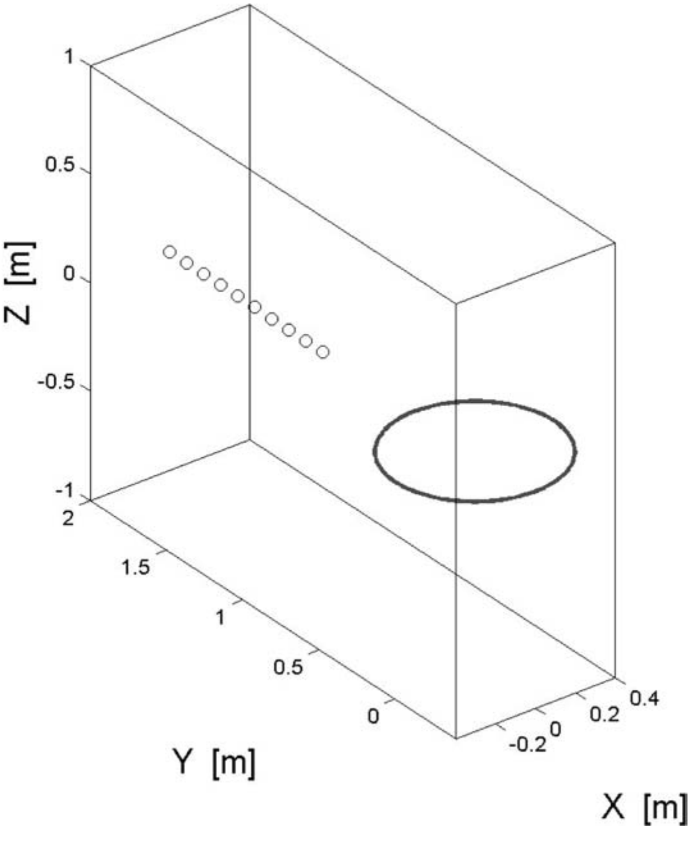

Figure 4.
The measurement points placed onto a straight line

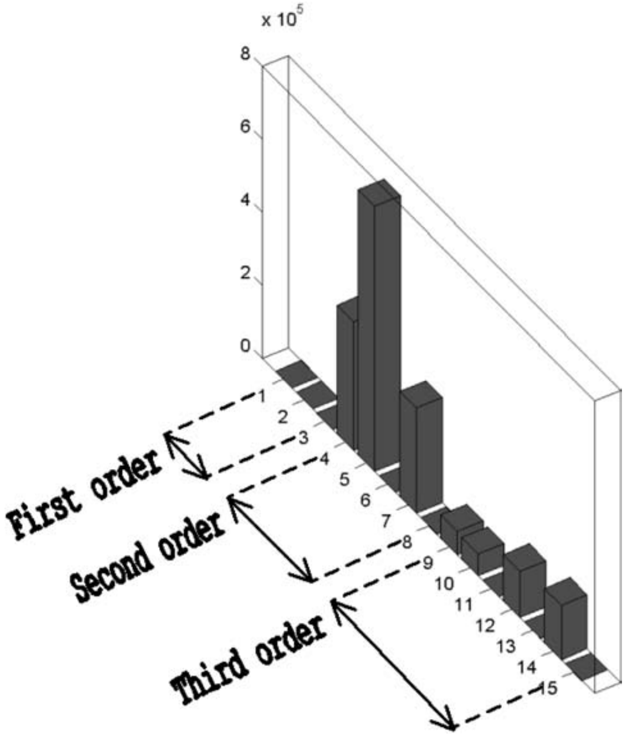

Figure 5.
Estimated coefficients for the points placed onto a straight line

Most importantly, we find that the multipole fits perfectly the field in the points used for the estimation ($\varepsilon < 10^{-5}$ percent), but fails utterly elsewhere ($\varepsilon = 10^{8}$ percent). We have checked that the problem is not the GA: even if one imposes that the multipole is located in the origin, the result is not improved. Indeed, one sees that the problem is intrinsic to the choice of the measurement points. This is confirmed by the fact that the condition number of the matrix [**C**] in equation (7) has been estimated to 3×10^{32}. On the other hand, one may think to make use of the condition number of [**C**] to find out some useful *a priori* informations about the goodness of the choice of the measurement points.

3.3 Application to a real test-appliance

The method has been tested on the device shown in Figure 6, which is composed of a magnetic core with two air-gap, excited by a coil. Two set of measurements have been taken:

(1) on a plane above the device (64 points); and

(2) on a straight line (15 points).

The set (1) has been used to identify a multipole of the first- and third-order. The set (2) is used to validate these models. In both cases, a good localization of the device is found. Moreover, the two models are compatibles: in fact the first-order terms of the two models are close, and dominate the high-order terms. The error criterion are shown in Table III.

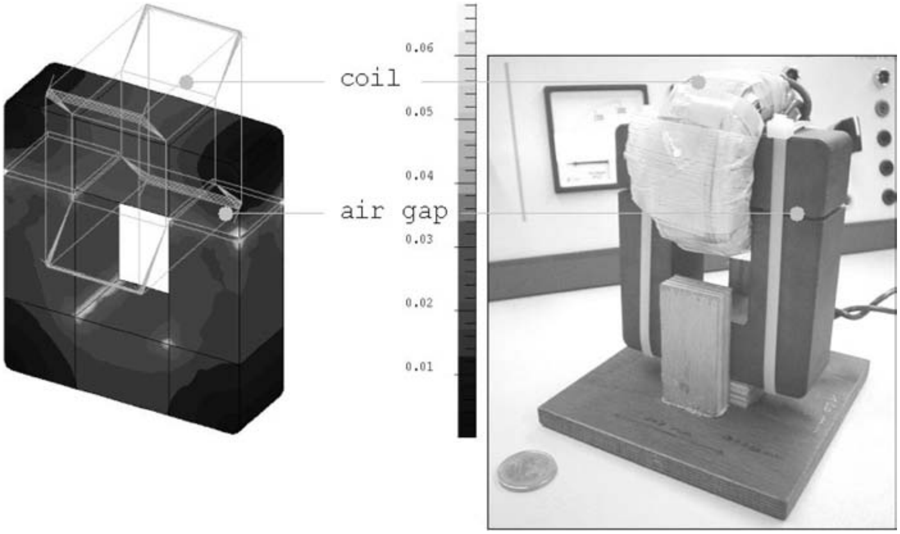

Figure 6.
The test-device (right) and the flux density computed using the finite elements software Flux 3D (left)

Table III.
Error criterion

First-order model	Set (a): $\varepsilon < 16$ per cent	Set (b): $\varepsilon < 22$ per cent
Third-order model	Set (a): $\varepsilon < 3$ per cent	Set (b): $\varepsilon < 64$ per cent

The first-order model is more representative than the third-order one. One observes that for the third-order model, the condition number of [**C**] is about 10^3: thus, a better choice of the measurement points is likely to improve the results.

4. Conclusions

A method to model the LF magnetic field generated by electrical appliances by an equivalent multipole is studied. The choice of the measurement points appears to be crucial: it would be interesting to explore the possibility of improving the estimation using multi-objective formulations.

Note

1. Actually, this can be assumed without loss of generality. In fact, the Laplace's equation is linear: thus, each component can be considered independently from others by the superposition principle.

References

Burais, N., Baraton, P. and Gaspard, J.Y. (1998), "Modélisation numérique des courants induits dans le corps humain par des dispositifs électromagnétiques dans la gamme des fréquences intermédiaires", *Proceedings 9èmè Colloque International sur la Compatibilité Electromagnétique*.

Durand, E. (1968), *Magnétistatique*, Masson, Paris.

Gaspard, J.Y., Burais, N. and Deschamps, F. (2000), "Exposition des personnes aux champs électromagnétiques: des nouvelles contraintes pour l'industrie électrique", *Proceedings 10èmè Colloque International sur la Compatibilité Electromagnétique*.

Goldberg, D.E. (1989), *Genetic Algorithms in Search, Optimization and Machine Learning*, Addison-Wesley, Reading, MA.

ICNIRP (1998), "Guidelines for limiting exposure to time-varying electric, magnetic, and electromagnetic fields (up to 300 GHz)", *Health Phys.*, Vol. 74 No. 4.

Lorange, J. (2001), "Couplage des inductances par rayonnement magnétique. Etude théorique et expérimentale", PhD thesis, Laboratoire d'Electrotechnique de Grenoble (LEG), Grenoble, pp. 11-30.

Lyon, C.E. (1994), "Modelling of magnetic fields generated by low frequency sources using multipole techniques", PhD thesis, Washington State University, Pullman, WA.

Salomon, S. and O-Mun, K. (2001), "External fields of permanent magnet motors", *Proceeding 13th Compumag*, Vol. 3, pp. 58-9.

Strang, G. (1986), *Introduction to Applied Mathematics*, Wellesley, Cambridge, MA, p. 398.

Takahashi, R., Vasconcelos, J.A., Ramirez, J.A. and Krahenbuhl, L. (2003), "A multiobjective methodology for evaluating genetic operators", *IEEE Trans. Mag.*, Vol. 39 No. 3.

Yamazaki, K. and Kawamoto, T. (2001), "Simple estimation of equivalent magnetic dipole moment to characterize ELF magnetic fields generated by electric appliances incorporating harmonics", *IEEE Trans. EMC*, Vol. 43 No. 2.

Zaffanella, L., Sullivan, T. and Visintainer, I. (1997), "Magnetic field characterization of electrical appliances as point source through *in situ* measurements", *IEEE Trans. Pow. Del.*, Vol. 12 No. 1.

The Emerald Research Register for this journal is available at
www.emeraldinsight.com/researchregister

The current issue and full text archive of this journal is available at
www.emeraldinsight.com/0332-1649.htm

A new approach for shape optimization of resistors with complex geometry

M. Purcar, J. Deconinck and L. Bortels
TW-ETEC Department, Vrije Universiteit Brussel, Brussels, Belgium
C. Munteanu, E. Simion and V. Topa
Technical University of Cluj-Napoca, Cluj-Napoca, Romania

Keywords *Optimization techniques, Electrical resistivity*

Abstract *This paper presents a new numerical approach for shape optimization of resistors with complex geometry. The aim of this method is to develop a systematic modification of resistor design in combination with the computation of the electric field, in order to optimize some chosen properties like homogenization of the power dissipation on the resistor surface.*

1. Introduction

The design of the electrical resistance has a large impact on the performance of the electric circuits. Often, the designed pattern contains corners, which play an important role in the final resistance and increase the power consumption and heat dissipation.

Munteanu *et al.* (1998) used a genetic algorithm coupled with the boundary element method in order to optimize the shape of resistors with complex geometry. This paper uses a new algorithm that is based on a combination of the finite element method (FEM) and the level set method (LSM) (Adalsteinnson and Sethian, 1995). The basic LSM has shown its quality in the design optimization of elastic structures in the work of Sethian and Weigmann (2000).

Given the resistor's design pattern the FEM is used to compute the current density distribution and dissipated power on the given shape (electric field problem). Then the LSM that represents the design structure through an embedded implicit function is used to perturb the shape and progress towards an improved design with the rates depending on the dissipated power on the actual design (optimization problem). Such an application falls into the category of constrained minimization problems. This technique allows improving the homogenization of the power dissipation on the resistor surface, but cannot guarantee that it will find a global minimum.

2. Numerical model description

2.1 The electric field problem

Consider the geometry from Figure 1 where a 2D cross-section of a resistor pattern with thickness th is presented.

COMPEL: The International Journal for Computation and Mathematics in Electrical and Electronic Engineering
Vol. 23 No. 4, 2004
pp. 1062-1069
© Emerald Group Publishing Limited
0332-1649
DOI 10.1108/03321640410553490

The authors are grateful to the Flemish Government and to the Romanian Minister of Scientific Research and Technology for the financial support in the frame of the Flemish-Romanian Joint Project BW 502/05.

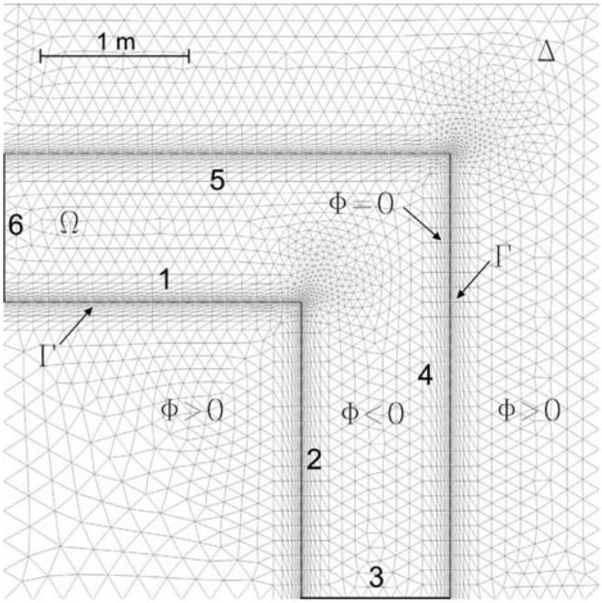

Note: Γ represents the zero level set contour and Φ the level set function; Δ is the computation domain for LSM (Ω ⊂ Δ)

Figure 1.
The resistor's geometry (domain Ω) with the fixed boundaries 6, 3 as terminal electrodes and changing boundaries 1, 2, 4 and 5 as insulators

The resistor is modeled as an electric field problem without charge distributions inside a domain Ω and is governed by Laplace's equation:

$$\overline{\nabla}\cdot(-\sigma\cdot\nabla U)=0, \tag{1}$$

where U represents the electric field potential distribution and σ the electric conductivity.

The boundary conditions attached to equation (1) are:

$$\frac{\partial U}{\partial n}=0, \tag{2}$$

on the insulating boundaries (1, 2, 4 and 5), and:

$$U=ct, \tag{3}$$

on the electrodes (3 and 6). $\partial U/\partial n$ is the electric field normal to boundary surface (the normal vector $\bar{n}$ is outward directed).

In order to reduce the continuum problem described by equation (1) to a discrete system of algebraic equations, the standard FEM is used. The domain Ω having the electric conductivity σ, is discretized into elements (triangles) as shown in Figure 1. The FEM formulation for Laplace equation (4) on the domain can be written as in the work of Fagan (1992).

$$\sum_j \left[\int_{\Gamma_{\mathrm{el}}} N_i \left(\frac{\partial N_j}{\partial x} n_x + \frac{\partial N_j}{\partial y} n_y \right) \mathrm{d}\Gamma_{\mathrm{el}} - \int_{\Omega_{\mathrm{el}}} \left(\frac{\partial N_j}{\partial x} \cdot \frac{\partial N_i}{\partial x} + \frac{\partial N_i}{\partial y} \cdot \frac{\partial N_j}{\partial y} \right) \mathrm{d}\Omega_{\mathrm{el}} \right] \cdot U_j = 0. \quad (4)$$

where N_i and N_j are the weighting and shape functions, respectively, $i,j = 1\ldots 3\times 3$ (the vertices of the triangles), U_j is the potential in vertex j ($j = 1\ldots 3$), Γ_{el} is the boundary of the element.

Equation (4) can be rearranged for all nodes j of Ω in the following system of equations:

$$[K]\{U\} = \{F\}. \quad (5)$$

with $[K]$ the source term matrix, $[U]$ the potential vector and $[F]$ the first term of equation (4).

When the conductivity is constant over the domain this system of equations can be solved directly. Otherwise an iterative, Newton-Raphson, process is used.

2.2 The level set problem

The LSM is a numerical technique especially developed to model the shape evolution. It was introduced by Osher and Sethian (1988) and has the strong feature that the interfaces can evolve in such a way that, for example, it can break and further merge naturally.

This technique has a wide range of applications, including problems in fluid mechanics, combustion, manufacturing of computer chips, image processing, electrochemical deposition and etching.

Principle behind the LSM is to track the front, which propagates with a speed normal to every point on the interface. This supposes the embedding of the interface as the zero level set of a higher dimension function. Given a moving closed hyper surface $\Gamma(t)$, propagating the front with a speed $\bar{v}$ in its normal direction, an Eulerian formulation for the motion of the hyper surface is produced.

At each moment the location of the interface $\Gamma(t)$ is given by a zero level set function $\Phi(x,y,t)$. At time $t = 0$, $\Phi(x,y,t) = \pm d$ is initialized on the whole domain Δ ($\Omega \subset \Delta$). "*d*" is the distance from the interface $\Gamma(t)$ to every point (x, y) of triangulated domain and is called the signed distance function and ensure the interface is represented by the 0 level set. The sign convention is chosen as indicated below (Hirch, 1992) (Figure 1):

$$\begin{cases} \Phi(x,y,t) < 0, & \text{in } \Omega(t) \\ \Phi(x,y,t) = 0, & \text{on } \Gamma(t) \\ \Phi(x,y,t) > 0, & \text{in } \Delta - \Omega \end{cases} \quad (6)$$

Therefore, by differentiating the level set $\Phi(x,y,t)$ with respect to time t, the equation of the level set motion is obtained:

$$\frac{\partial \Phi}{\partial t} + \bar{v} \cdot \overline{\nabla} \Phi = 0, \quad (7)$$

with $\Phi(x,y,t=0)$ given.

The equation describes the motion of fronts and it is a typical first order hyperbolic equation in (x, y, t). The LSM tracks the whole boundary, with a rate $\bar{v}$ (speed) normal to every point, function of the dissipated power, p and current density, $\bar{J}$, which are provided by the field problem (1).

Equation (7) is discretized using the residual distribution formulation (Hirch, 1992) with the standardd Galerkin finite element shape functions. The residuals to the triangles vertices are distributed using a multidimensional upwind method (Fagan, 1992) such as *N* or Low Diffusion A scheme (LDA). The time integration is approached using the second order accurate Petrov-Galerkin formulation.

The system of equations derived from equation (7) can be written as:

$$\overline{\overline{M}}\left\{\frac{\partial \Phi}{\partial t}\right\} + \overline{\overline{C}} \cdot \{\Phi\} = 0 \tag{8}$$

where $\partial\Phi/\partial t$ is the time variation vector of Φ in every node [N × 1], $\{\Phi\}$ the vector of the unknown Φ at time step [N × 1], $\overline{\overline{M}}$ the global mass matrix [N × N], and $\overline{\overline{C}}$ the global convection matrix [N × N].

Solving equation (7) for $\Phi = 0$ on the boundary Γ and $\Phi = \pm d$ on $\Delta - \Omega$, respectively, Ω, the new resistor's boundaries are found through interpolation of the LSM solution on the FEM mesh.

2.3 Domain discretization

To solve the problem, two meshes are used. A local mesh (on Ω) is used to compute the electric field problem and a global mesh (on Δ) is used by the LSM.

In order to capture with accuracy the level set solution, a fine mesh is necessary in the neighborhood of the zero level set. For that purpose a hybrid grid generator (AMEGOS) (Athanasiadis and Deconinck, 2003) is used to create a thin structured layer of triangles along the moving boundary Γ (Figure 1). The remaining part of the domain is filled with unstructured grid of triangles. The number of elements used for the first optimization step (Figure 1) is 2,564 on Ω and 5,820 on Δ.

3. Optimization algorithm

The principal idea is to remove material in the regions of low power dissipation and to add material in region of high power dissipation.

In many situations, this kind of solution is not unique because situations with many local minima could arise. For these minima any small perturbation that satisfies the constraints requires more material such that the new given shape will not represent the global minimum.

The optimization algorithm structure is shown in Figure 2.

3.1 Speed law and objective function definition

A distribution of the current density field on the computational domain Ω is found from equations (1)-(5). The speed $\bar{v}$ in every point of the mesh is then defined using equation (9) which describes the balance between the maximal initial dissipated power below which the material may be eliminated and above which material should be added:

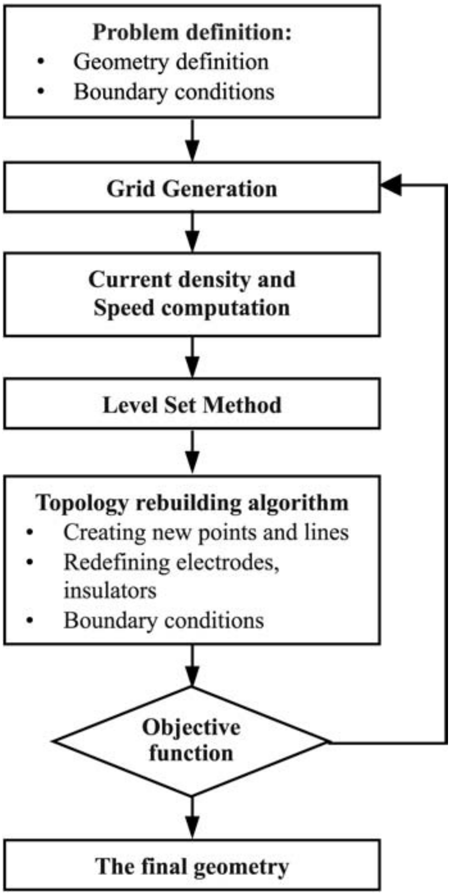
Problem definition:
Geometry definition
Boundary conditions
Grid Generation
Current density and Speed computation
Level Set Method
Topology rebuilding algorithm
Creating new points and lines
Redefining electrodes, insulators
Boundary conditions
Objective function
The final geometry

Figure 2.
Structure of the electrode growth algorithm

$$\left.\begin{aligned} v_x &= -\frac{(p_\mathrm{c} - p_\mathrm{imp})}{p_\mathrm{c}}\frac{J_y}{|J|}, \\ v_y &= \frac{(p_\mathrm{c} - p_\mathrm{imp})}{p_\mathrm{c}}\frac{J_x}{|J|}, \end{aligned}\right. \quad \text{if} \quad p_\mathrm{c} - p_\mathrm{imp} > 10^{-3}, \tag{9}$$

and

$$v_x = 0, v_y = 0, \quad \text{if } p_\mathrm{c} - p_\mathrm{imp} < 10^{-3}. \tag{10}$$

v_x, v_y are the components of the speed vector (m/s), J_x, J_y are the components of the current density vector (A/m^2),

$$|J| = \sqrt{J_x^2 + J_y^2}$$

is the absolute value of the current density (A/m^2), $p_\mathrm{c} = |J|^2/\sigma$ is the computed dissipated power (W/m^3) and p_imp is the imposed power for which the resistor should be optimally designed and is computed from the mean current density on the electrode six represented by boundary of the initial geometry (Figure 1).

Equation (7) supposes that $\bar{v}$ for all level sets is defined. This implies the definition of $\bar{v}$ in all the points of Δ. The distribution of speed from the moving boundary Γ to the whole computation domain is called speed extension. Several methods are known in literature. The method described by Adalsteinnson and Sethian, (1995) uses for the velocity extension the fast marching method (Sethian and Wiegmann, 2000).

In this paper an original technique is used. It supposes the extension of the current density from the interface Γ in $\Delta - \Omega$ by solving a Laplace equation with boundary conditions $|J|$ on Γ and $U = 0$ elsewhere on the boundaries of $\Delta - \Omega$. Then using equations (9) and (10) the adding or removing material's rates $\bar{v}$ in every mesh point is defined.

As can be seen from Figure 3, the evolution of the boundary profile decreases in the neighborhood of the optimal profile and level set march less than one layer of triangles. In order to stop the algorithm a condition $p_{\mathrm{c}} \cong p_{\mathrm{imp}}$ as objective function is far more too stringent.

It is realistic to state for the objective function, equation (11), that the mean between the maximum and minimum dissipated power on the optimized geometry is less than 20 per cent than imposed power at the beginning of the optimization. This represents also the stop criteria of the optimization process.

$$(p_{\mathrm{mean}} - p_{\mathrm{imp}})/p_{\mathrm{imp}} \times 100 < 20 \text{ per cent} \tag{11}$$

Besides the objective function (11) two constraints have been imposed. Since the resistor's topology and the computation domain are reconstructed during the optimization process, the electrodes (3 and 6) are constrained to not move or change in size.

3.2 Level set time-step definition

The time-step is chosen in such a way that maximum ten layers of triangle are overcome within one level set iteration (7 and 8). The time step is calculated from the speed $\bar{v}$ of the boundary Γ and the average size of the triangles from boundary layer. All of these provide a maximum time-step of 0.1 s for a boundary layer of 10^{-2} (m).

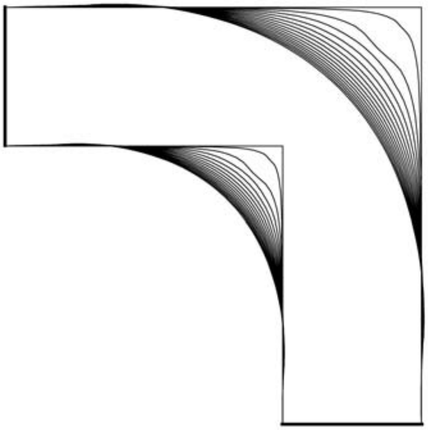

Figure 3.
Boundary evolution profiles during the optimization

4. Results

Consider the geometry from Figure 1 with the dimension in meters, th = 0.001 m and $\sigma = 5.72 \times 10^6$ (Ω/m). On the boundaries 3 and 6 are applied $U = 0$ V, respectively, $U = 100$ V.

The corners of the resistor play a negative role in the power dissipation in the original design. The maximum and minimum dissipated power for the initial geometry and for some of the optimisation steps can be seen in Table I. The imposed power in the equations (9), (10) and (11) is $p_{\mathrm{imp}} = 2.77 \times 10^8$ (W/m^3).

At the end of the optimisation process, the geometry is changed in such way (Figures 3 and 4) that the dissipated power is almost constant in the entire resistor if it refers to the initial geometry.

The computation time needed for the optimization process was around 912 s for 17 iterations on a PC PIII 560 MHz and 256 MB RAM. In average 50 s per iteration.

5. Conclusions

A new algorithm based on LSM for the optimal design of resistors has been presented. This supposes the solution of two problems: an electric field problem, in order to find a suitable law for adding or removing material on the optimized geometry, and a level set problem, which uses the quantities founded before, in order to alter the shape towards the final geometry. The example presented here proves that the LSM is a sharp and efficient tool for optimization applications. Thought not shown here, the LSM handles more complex geometries and objective functions.

Table I.

Iteration	1	2	3	10	17
$p_{\max}$ (W/m^3)	4.21×10^9	1.29×10^9	6.74×10^8	5.72×10^8	5.23×10^8
$p_{\min}$ (W/m^3)	1.92×10^4	7.79×10^6	3.47×10^7	1.19×10^8	1.42×10^8

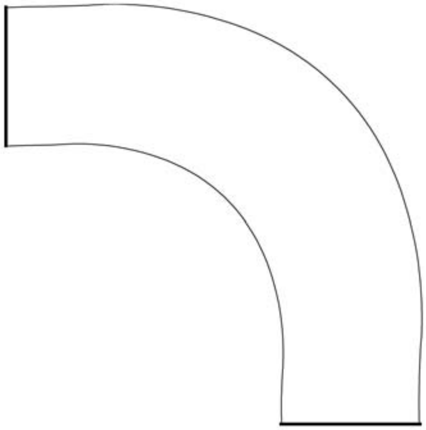

Figure 4.
Optimized resistor

References

Adalsteinnson, D. and Sethian, J.A. (1995), "A fast level set for propagating interfaces", *Journal of Computational Physics*, Vol. 120, p. 128.

Athanasiadis, A.N. and Deconinck, H. (2003), "Object-oriented three-dimensional hybrid grid generation", *International Journal for Numerical Methods in Engineering*, Vol. 58, pp. 301-18.

Fagan, M.J. (1992), *Finite Element Analysis Theory and Practice*, Longman Scientific and Technical, Harlow.

Hirch, C. (1992), *Numerical Computation of Internal and External Flows*, Wiley, Chichester.

Munteanu, C., Topa, V., Simion, E., De Mey, G. and Dobbelaere, M. (1998), "Shape optimization of the resistors with complex geometry using spline boundary elements and genetic algorithms", *Proceedings of JSAEM*, Vol. 8, p. 177.

Osher, S.J. and Sethian, J.A. (1988), "Fronts propagating with curvature dependent speed: algorithms based on Hamilton-Jacobi formulation", *Journal of Computational Physics*, Vol. 79, p. 12.

Sethian, J.A. and Wiegmann, A. (2000), "Structural boundary design via level set and immersed interface methods", *Journal of Computational Physics*, Vol. 163, p. 489.

The Emerald Research Register for this journal is available at
www.emeraldinsight.com/researchregister

The current issue and full text archive of this journal is available at
www.emeraldinsight.com/0332-1649.htm

Comparison of static, dynamic, and static-dynamic eccentricity in induction machines with squirrel-cage rotors using 2D-transient FEM

Christoph Schlensok and Gerhard Henneberger
Institute of Electrical Machines (IEM), RWTH, Aachen University, Aachen, Germany

Keywords *Finite element analysis, Simulation, Inductance, Electric machines*

Abstract *Finite-element simulations of induction machines with squirrel-cage rotor require transient solution algorithms. For this reason a transient 2D solver is utilized which takes rotational movement of the rotor into account. Its formulation and the time-step algorithm are given. Two different kinds of eccentricity of the rotor and their combination are defined and studied. The three motor variants are computed and the torque, the net force, and the surface-force density are compared in time and frequency domain.*

1. Introduction

Owing to fabrication tolerances the rotors of electrical machines are usually not positioned centrically. In the case of an induction machine with squirrel-cage rotor used as a power-steering drive this has strong effect on the acoustic behavior. Eccentricity can cause extra force excitation of the stator teeth which then produces extra noise radiation. In order to estimate the effects of eccentricity the induction machine with squirrel-cage rotor is modeled and simulated using the finite-element method (FEM).

In this paper the two types of eccentricity – static and dynamic eccentricity – and their combination are simulated. Therefore, three different two-dimensional FE-models of the entire machine have to be generated. The FE-models are simulated with a 2D-transient solver which applies a node-based $\vec{A}$-approach and the first order time-step algorithm. The results provided by the solver for each time step are next to the flux-density distribution the torque and the net force acting on the rotor. Using the flux-density distribution the surface-force density is derived for each time step. Finally torque, net force and the surface-force density on the stator teeth are analyzed in time and frequency domain.

2. Definition of the different types of eccentricity

Figure 1 shows the three "pure" types of rotational movement of a rotor of an electrical machine. The centric case is the optimal case (Figure 1(a)). The rotor axis is fixed to the stator and the rotational axis. The air gap δ is equidistant along the entire circumference. Therefore, forces arising on the one side of the machine are

COMPEL: The International Journal for Computation and Mathematics in Electrical and Electronic Engineering
Vol. 23 No. 4, 2004
pp. 1070-1079
© Emerald Group Publishing Limited
0332-1649
DOI 10.1108/03321640410553508

This article is dedicated to Prof. Gerhard Henneberger, who is released into his well deserved retirement with gratitude and appreciation for his meritorious scientific work.

compensated on the opposite in case the number of rotor slots is even. The studied machine has $N_R = 26$ rotor slots. In the case of static eccentricity which is depicted in Figure 1(b) the rotor and rotational axis are now shifted to one side of the machine. The air gap is no longer symmetrical. Owing to the fixed rotor axis the maximum and minimum force excitation are spatially fixed as well. The machine is excited very asymmetrical. If the rotational axis is then shifted back into the position of the stator axis the rotor shows dynamical eccentricity behavior (Figure 1(c)). The minimum air gap is no longer spatially fixed but rotates with the rotor as well as the maximum and minimum force excitation. Since these are "pure" types of eccentricity the most probable case is a combination of these, which is the static-dynamic case. The rotational axis lies between the rotor and the stator axis. The force excitation is a mix of both the fixed and the rotating excitation.

3. Formulations

3.1 Transient solver

The applied solver is part of the object-oriented solver package *i*MOOSE (Arians *et al.*, n.d.). The transient FEM formulation takes the rotational movement into account and two finite-element meshes have to be handled once at a time. The two-dimensional $\vec{A}$-approach is node-based. The magnetic vector potential is used in all regions. The equation

$$\int_\Gamma \left(\nabla \cdot \alpha_i \cdot \nu \cdot \nabla \cdot A_z(t) + \alpha_i \cdot \sigma \cdot \frac{\partial}{\partial t} A_z(t) \right) \mathrm{d}\Gamma = \int_\Gamma (\alpha_i \cdot J_{z0}(t)) \mathrm{d}\Gamma \qquad (1)$$

has to be solved in the complete model Γ and is presented in Galerkin formulation (Arians and Henneberger, 2000). The material parameters ν and σ represent the non-linear reluctivity and the linear conductivity. The shape function of an element is defined by α_i. Triangular shaped elements are used. $J_{z0}(t)$ describes the z-component of the given coil-current density as the only excitation.

For linear interpolation of the time-dependent variables the first order time-step algorithm is applied and $A(t)$ is written as function of time:

$$A(t) = (1 - \Theta)A_n + \Theta A_{n+1} \qquad (2)$$

$$\Theta = \frac{t - t_n}{t_{n+1} - t_n} = \frac{t - t_n}{\Delta t}; \quad 0 \leq \Theta \leq 1. \qquad (3)$$

Θ is the weighting parameter and is set to $\Theta = 2/3$ according to the Galerkin scheme (Zienkiewicz and Taylor, 1989). Δt is the time step.

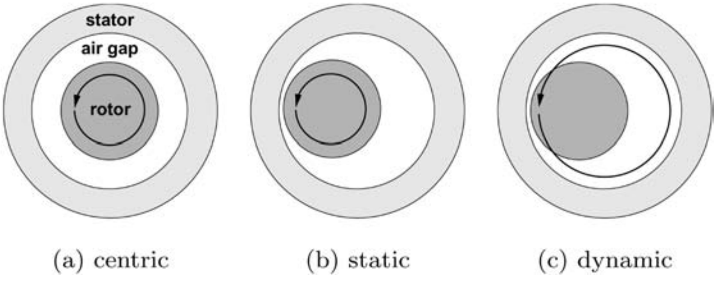

(a) centric (b) static (c) dynamic

Figure 1.
Different types of eccentricity

3.2 Formulation of the surface-force density

With the Maxwell stress tensor

$$\vec{\sigma} = \frac{1}{2}\vec{n}_{12}[B_n\,(H_{1n} - H_{2n}) - (w'_1 - w'_2)] \tag{4}$$

an expression for the normal component of the local surface-force density is given (Ramesohl *et al.* (1996). The index n represents the normal components of $\vec{B}$ and $\vec{H}$. $\vec{n}_{12}$ is the normal vector of the boundary surface from region 2 to 1. w'_1 and w'_2 are the magnetic-coenergy densities of these regions. The surface-force density vector is perpendicular to the line element. Lorentz forces and forces stemming from magnetostriction can be neglected because they are much smaller than the electro-magnetic forces.

4. Finite-element models

For the regarded application investigations have shown that an induction machine with $N_S = 36$ stator slots and $N_R = 26$ rotor bars is a very good variant. The lamination is shown in Figure 2. The machine consists of a two-layer wave-winding with three phases which is not chorded. The spread factor is $q = 3$ (Nürnberg, 1979). This results in a more sinusoidal air gap flux-density behavior. For easier modeling the two layers are not on top of each other but next to each other. This has no effect to the electromagnetic simulation because the magneto-motive force depends only on the current coverage of the slot. Since there is no symmetry in the models because of the eccentricity full 360°-models have to be generated. Figure 2 shows only the half of the model. The FE-model for the dynamic eccentric case depicted consists of $E = 13,600$ first-order triangular elements with $N = 6,874$ nodes.

In Figure 3 closeups of the maximum and minimum air gap in the initial position of the same model are depicted. The rotor is shifted $v = 0.1$ mm to the right (positive x-direction). The air gap of $\delta_{\mathrm{nominal}} = 0.3$ mm now varies between $\delta_{\min} = 0.2$ and 0.4 mm.

5. Transient 2D simulation

The three eccentric FE-models are simulated with the 2D-transient solver which calculates the torque and the net force on the rotor. The torque behavior of all three cases is shown in Figure 4.

In all three cases the torque pulsates because of the different reluctivities in each time step stemming from the rotor and stator slots. Although the average torque of

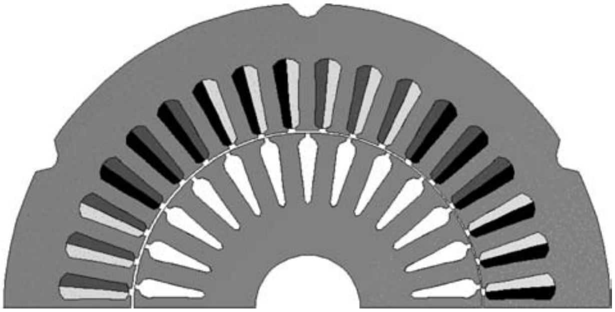

Figure 2.
Lamination of the induction machine, two pole pitches

$\overline{T} = 4.337\,\mathrm{N\,m}$ is the same for all variants the instantaneous values do not match exactly. All graphs appear to reach the maximum value at some time so it is not significant which kind of eccentricity is given.

Figure 5 shows the net-force behavior. Again the graphs of all three variants pulsate now showing a very different behavior. If the rotor is positioned statically eccentric the net force pulsates with rotor frequency:

$$f_\mathrm{R} = 20\,\mathrm{Hz}, \quad T_\mathrm{R} = 1/f_\mathrm{R} = 0.05\,\mathrm{s}. \tag{5}$$

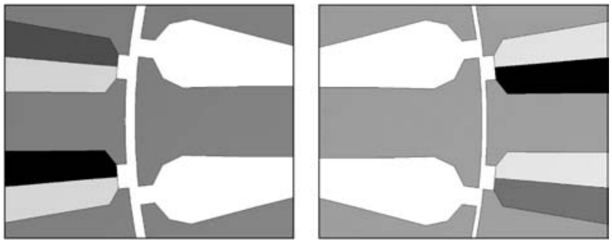

Figure 3.
Closeups of the maximum and the minimum air gap

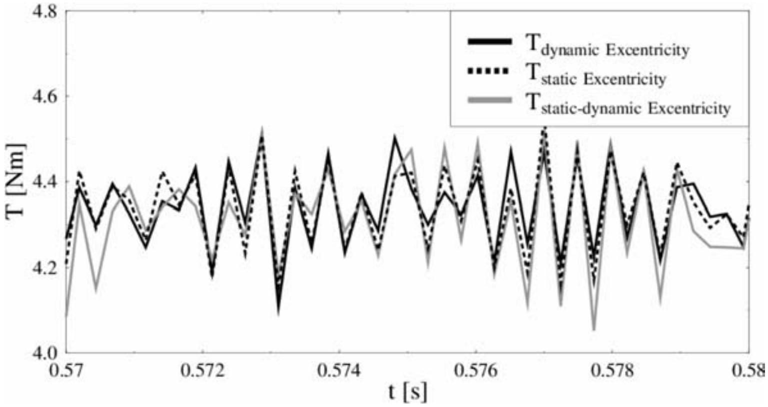

Figure 4.
Torque behavior of the three eccentric FE-models

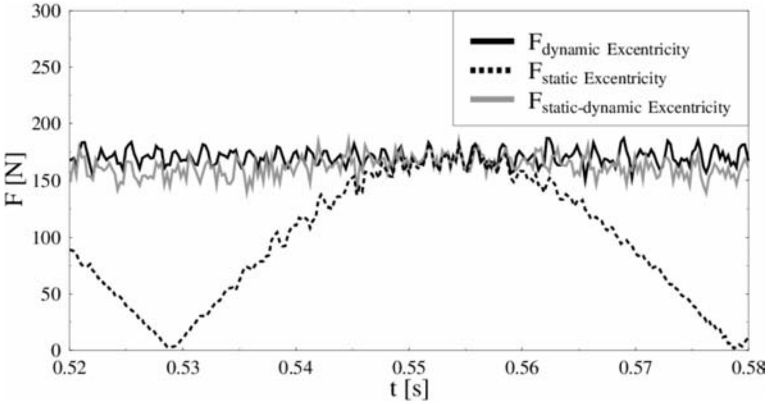

Figure 5.
Force behavior of the three eccentric FE-models

The average value in the case of static eccentricity is $\overline{F}_{\mathrm{stat}} = 107.4\,\mathrm{N}$. In comparison the net force in the case of dynamic eccentricity oscillates weakly. The average value is $\overline{F}_{\mathrm{dyn}} = 170.2\,\mathrm{N}$. When the maximum net force in the case of static eccentricity is reached the two graphs match each other. This configuration is reached for the initial position of the rotor. If both eccentricities are combined the average value is $\overline{F}_{\mathrm{stat-dyn}} = 163.9\,\mathrm{N}$. The net force has a main harmonic with $f_{\mathrm{R}} = 20\,\mathrm{Hz}$ because the statical portion of the signal behaves strongly like in the case of dynamic eccentricity. At the point when the maximum net force in the case of static eccentricity is reached all three graphs reach the same value. In that moment the direction of the three net forces are all the same as Figure 6 shows.

6. Computation of the excitation of the stator-teeth

The computation of the normal component, i.e. radial component, of the electromagnetic stator-teeth force-density is performed as described by Schlensok *et al.* (2003). The three computations have the same initial rotor position. The rotor is shifted in positive x-direction (to the right) with $v = 0.1\,\mathrm{mm}$.

Figure 7 depicts the force-density distribution of the stator teeth for all three types of eccentricity for the same time step using the same scaling. In the chosen time step the rotor is positioned at $v = -0.1\,\mathrm{mm}$ (to the left) in the case of dynamic eccentricity. The major electromagnetic force excitation is in horizontal direction. Figure 7(a) shows the distribution for dynamic eccentricity. On the left as well as on the right side the stator is assigned with about the same force values. In the case of static eccentricity which is shown in Figure 7(b) the force density has the largest values on the right side of the stator. For the combination of both types of eccentricities (Figure 7(c)) the dynamic portion outweighs the static. The maximum force density is again found on the left side although in the case of static-dynamic eccentricity the rotor is positioned in the center of the stator for this time-step. On each stator tooth itself the maximum force-density appears at the up-running edge as the zoom in Figure 7(d) depicts.

In a next step the time-dependent force-density behavior is analyzed for the up-running edge element of each stator tooth applying the Fast Fourier Transformation (FFT) (Bronstein and Semendjajew, 1991).

Figure 8 shows the spectrum that results of a FFT. The orders occurring in the spectrum are the double ($f = 96.4\,\mathrm{Hz}$) and four times ($f = 195.7\,\mathrm{Hz}$) the stator

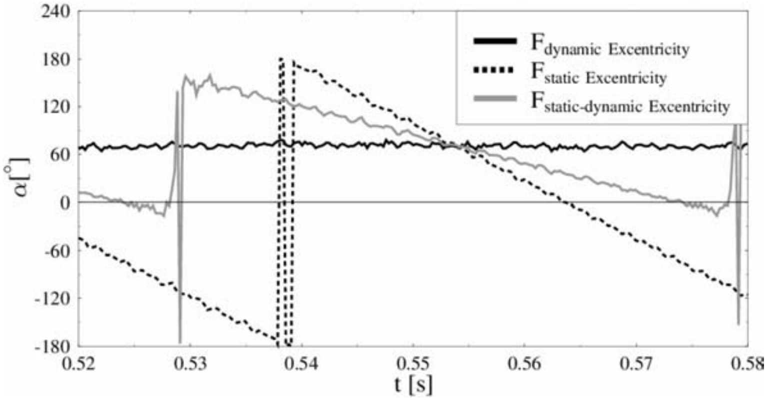

Figure 6.
Direction α of the force for all three types of eccentricity

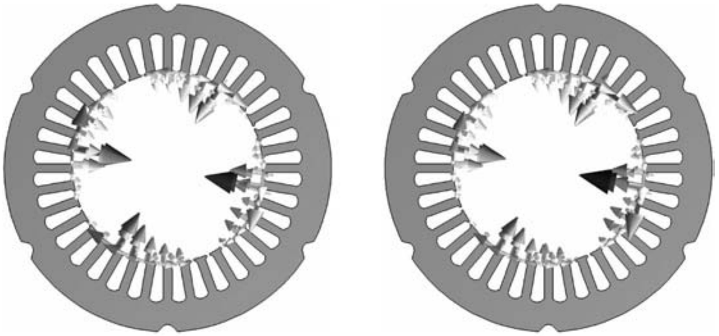

(a) dynamic case (b) static case

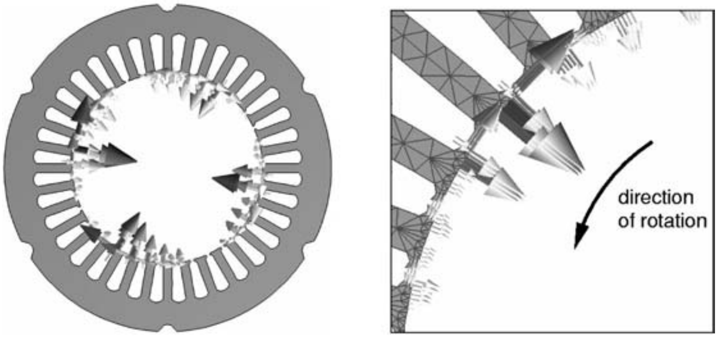

(c) static-dynamic case (d) close-up

Figure 7.
Surface-force density-distribution of the stator teeth at one time step

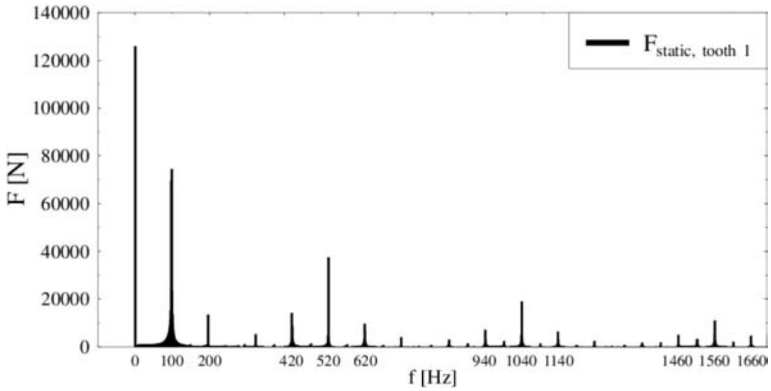

Figure 8.
Result of FFT of the force-density excitation of the element at up-running edge of stator tooth 1 for static eccentricity

frequency, the 26th ($f = 520\,\mathrm{Hz}$), 52nd ($f = 1.040\,\mathrm{Hz}$) and 78th ($f = 1.560\,\mathrm{Hz}$) order of the rotor frequency ($f_{\mathrm{R}} = 20\,\mathrm{Hz}$) and their modulations with twice the stator frequency, 26th, 52nd, and 78th are the first, second, and third rotor-slot harmonics (Nau, 2000; Seinsch, 1992).

Figure 9 shows the amplitudes of the force-density of all 36 stator teeth for the first order of the rotor frequency $f_{\mathrm{R}} = 20\,\mathrm{Hz}$. The highest amplitudes are reached in the case of dynamic eccentricity. Because of the eccentric revolution of the rotor all teeth are stressed with rotor frequency in this case. For static eccentricity the effect is always stationary. So there is no interrelationship between this spectral order and the rotor frequency. If both eccentricities are combined the effects of both are mixed. So the amplitudes reach the average height of both.

For the second order of the stator frequency $f = 96.4\,\mathrm{Hz}$ the results of the FFT are shown in Figure 10. The excitation differs depending on which tooth is regarded but is independent of the type of eccentricity. The average force density for all three calculations lies between $\sigma_{96.4\,\mathrm{min}} = 13.4\,\mathrm{N/m^2}$ and $\sigma_{100\,\mathrm{max}} = 13.6\,\mathrm{N/m^2}$. Measurements and acoustic simulations have shown that this order does not generate any significant acoustic noise although compared to the other studied orders where the highest amplitudes are reached.

Figure 11 shows that there is a strong correlation of the orders with the rotation of the rotor. The shown orders are the 26th ($f = 520\,\mathrm{Hz}$), the 52nd ($f = 1,040\,\mathrm{Hz}$), and the 78th ($f = 1,560\,\mathrm{Hz}$) order of the rotor frequency ($f_{\mathrm{R}} = 20\,\mathrm{Hz}$). These are the first,

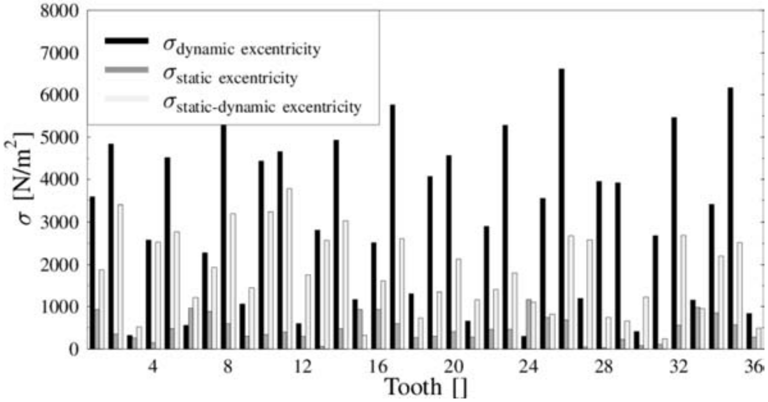

Figure 9.
Amplitudes of the force-density of all 36 stator teeth for first order of rotor frequency: $f_{\mathrm{R}} = 20\,\mathrm{Hz}$

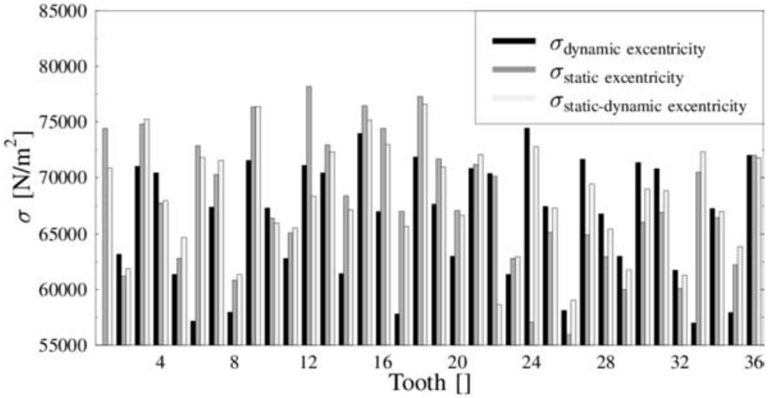

Figure 10.
Amplitudes of the force-density of all 36 stator teeth for second order of stator frequency: $f = 96.4\,\mathrm{Hz}$

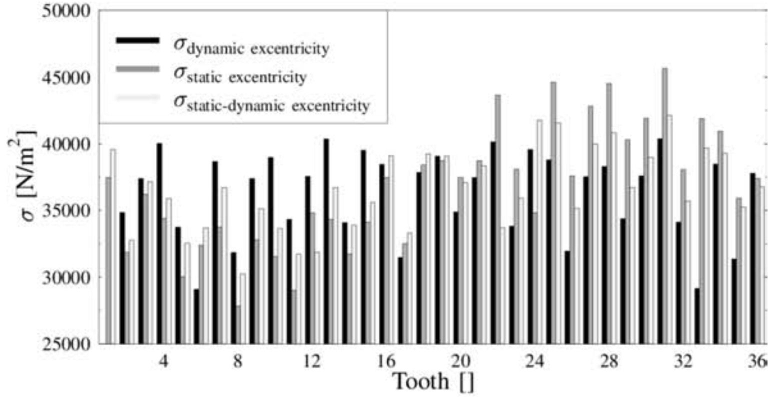

(a) $f = 520\,\text{Hz}$: 26th order of rotor frequency

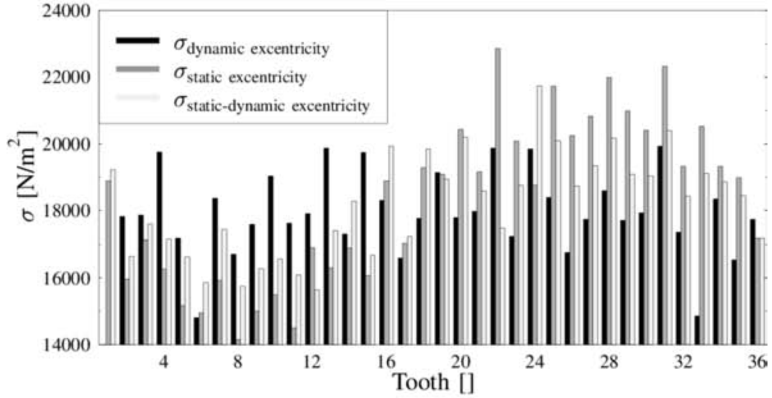

(b) $f = 1040\,\text{Hz}$: 52nd order of rotor frequency

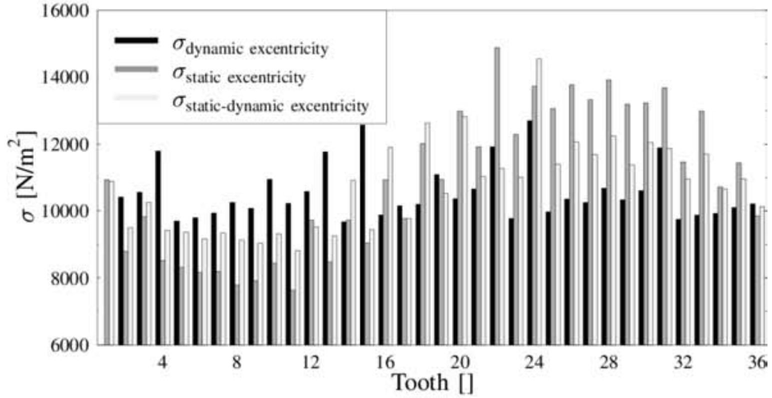

(c) $f = 1560\,\text{Hz}$: 78th order of rotor frequency

Figure 11.
Amplitudes of the force density of all 36 stator teeth

second, and third rotor-slot harmonic. For all three orders the highest amplitudes for the case of static eccentricity are reached at the teeth where the air gap is smallest (near tooth 27). The lowest excitations are reached on the opposite side of the stator near tooth 9. For dynamic eccentricity all teeth are excited nearly in the same way. The amplitudes do not differ strongly. The reason is the same as in the case of $f_{\mathrm{R}} = 20\,\mathrm{Hz}$. Owing to the revolving narrowest air gap the excitation revolves as well. If both cases are combined the stator teeth at the position of the smaller air gap are stressed more than those on the opposite side. Nevertheless, the effect is not as strong as in the case of static eccentricity. For all three orders shown in Figure 11 the average force density does not differ significantly depending on the type of eccentricity.

7. Conclusion

For an induction machine with squirrel-cage rotor as power-steering drive the acoustic behavior is of high significance. The subjective safety sensation of the passenger is strongly affected by the noise radiation of such important devices like the steering. Owing to the manufacturing process it is not possible to build 100 percent perfect electrical machines. This will always result in some kind of eccentricity. If the type of eccentricity which arises primarily can be detected it is possible to make predictions if there will be a strong effect on the acoustics or not.

The three types of eccentricity regarded here behave in very different ways. Dynamic eccentricity causes revolving force excitations, whereas static eccentricity produces fixed force excitations depending on the direction of the displacement of the rotor. The combination of both, the static-dynamic eccentricity, brings up both effects. Therefore, FE-models of the three variants are built and simulated with a 2D-transient solver in order to compare the effects. The formulations of the transient solver and the surface-force density are given and the time-stepping algorithm explained.

Torque and the net force acting on the rotor are computed and compared for all three models. In all three cases the torque acts in the same way and is not significantly affected by the type of eccentricity. In contrast the net-force behavior depends strongly on the case of eccentricity. For any point in time all variants are excited asymmetrically. But in the case of dynamic eccentricity the asymmetrical force excitation revolves. Static eccentricity results in fixed spatial to the direction of the minimal air gap. For the combination of both the effects are combined. The net force excitation revolves and has a stationary part as well.

In a second step the time dependent surface-force density on the stator teeth is derived from the flux-density distribution of each time step. Main orders excited are the double stator frequency and its multiples and multiples of the rotor-slot harmonics and their modulation with the double stator frequency. These orders are regarded explicitly for all 36 stator teeth and the three cases of eccentricity. Depending on the origin of the order the force density has the same amplitudes for all teeth or is fixed to the location of certain teeth. The order at double stator frequency is the same for all three variants, the order at rotor frequency is highest for the dynamic eccentricity. The other three orders (multiples of the rotor-slot harmonic) depend on the type of eccentricity and are the highest for static eccentricity and fixed to the teeth in direction of the smallest air gap. Measurements of the manufactured machines must now detect which is the most possible type of eccentricity in reality. This way the origin of the generated noise of these machines can be detected as a result of eccentricity or another source.

References

Arians, G., Bauer, T., Kaehler, C., Mai, W., Monzel, C., van Riesen, D. and Schlensok, C. (n.d.), “Innovative modern object-oriented solving environment – iMOOSE”, available at: www.imoose.de

Arians, G. and Henneberger, G. (2000), “Object oriented analysis and design of transient finite element solvers applied to coupled problems”, paper presented at the 9th Conference on Electromagnetic Field Computation, CEFC, Milwaukee, WI.

Bronstein, I.N. and Semendjajew, K.A. (1991) in Teubner, B.G. (Ed.), *Taschenbuch der Mathematik, 25. Auflage*, Verlagsgesellschaft, Stuttgart, Leipzig.

Nau, S.L. (2000), “Acoustic noise of induction electric motor: causes and solutions”, paper presented at the Second International Seminar on Vibrations and Acoustic Noise of Electric Machinery, Lódź, September, VANEM.

Nürnberg, W. (1979), *Die Asynchronmaschine*, Springer, Berlin, Göttingen, Heidelberg.

Ramesohl, I., Küppers, S., Hadrys, W. and Henneberger, G. (1996), “Three dimensional calculation of magnetic forces and displacements of a claw-pole generator”, *IEEE Transactions on Magnetics*, Vol. 32 No. 3, pp. 1685-8.

Schlensok, C., Schneeloch, G. and Henneberger, G. (2003), “Analysis of stator-teeth forces in induction machines with squirrel cages using 2D-FEM”, paper presented at the 6th International Symposium on Electric and Magnetic Fields, EMF, Aachen.

Seinsch, H.O. (1992), in Teubner, B.G. (Ed.), *Oberfelderscheinungen in Drehfeldmaschinen*, Stuttgart.

Zienkiewicz, O.C. and Taylor, R.L. (1989), *The Finite Element Method*, McGraw-Hill Book Company, London, pp. 346-61.

The Emerald Research Register for this journal is available at
www.emeraldinsight.com/researchregister

The current issue and full text archive of this journal is available at
www.emeraldinsight.com/0332-1649.htm

Electrical machine analysis considering field – circuit – movement and skewing effects

A.M. de Oliveira, R. Antunes, P. Kuo-Peng and N. Sadowski
University of Santa Catarina, Florianópolis SC, Brazil
P. Dular
University of Liège, Liège, Belgium

Keywords *Electric machines, Simulation, Numerical analysis*

Abstract *This paper presents a method to analyse electrical machines considering simultaneously the electromagnetic field, electric circuit, control loop, movement and skewing effects. The major contribution of this work leans on its generality, i.e. it can be applied to electrical machines connected to static converters submitted to any control laws, avoiding an a priori analysis. Simulation results of a three-phase Brushless AC (BLAC) motor fed by a PWM converter is presented as well as a comparison of simulation and experimental results obtained using a two-phase-on converter were also presented.*

1. Introduction

Electrical machines are complex structures and in their design, various aspects such as magnetic fields, feeding electronic circuits, control strategies, movement, heat transfer, acoustic noise, etc., must be considered. Their performances are not defined only by their electromagnetic or mechanical characteristics, but mainly by the interaction between the following quantities: mechanical characteristics, magnetic field distribution, feeding electronic circuit, etc. A few years back, the analysis of such complete system considering multiple aspects in a same set of equations was prohibitive, due to the unavailability of enough computational resources for data processing. Therefore, many simplified considerations were assumed and indirect coupling methods were developed to solve this kind of problem.

Nowadays, thanks to the improvements in the computation area, the analysis of such complex systems is more affordable. This enables the development of more realistic models which can include in their formulations a major part of the phenomena described above. In this way, many researchers have proposed numerical procedures to investigate the coupling effects of electromagnetic fields and mechanical structures, electronic circuits, etc.

Jang *et al.* (2002) present an analysis of a brushless DC (BLDC) motor considering a coupled system of magnetic and mechanic finite element equations. An *a priori* analysis of the operation sequences of a PWM converter and its speed control loop is considered in the simulation. Ho *et al.* (2001) also studied a BLDC motor. They use the multi-slice technique to evaluate the eddy-current losses in the permanent magnets. In a separate block, the control strategy defines the terminal voltage to be applied to the motor windings. Consequently, the circuit and field equations are indirectly coupled. A general method to perform a direct coupling of static converters and

COMPEL: The International Journal for Computation and Mathematics in Electrical and Electronic Engineering
Vol. 23 No. 4, 2004
pp. 1080-1091
© Emerald Group Publishing Limited
0332-1649
DOI 10.1108/03321640410553517

electromagnetic devices considering closed loop control strategies is described by Roel Ortiz *et al.* (2001). The switching control signals are generated automatically according to the value of the variable to be controlled and the control law. Nevertheless, in this study, the movement of the electromagnetic device is not considered. Thus, to improve the previous work and to make possible the analysis of electrical machines, the motion is now considered by means of the moving band technique (sadowski *et al.*, 1992). The Maxwell stress tensor and the mechanical oscillation equation are used to consider the dynamic aspects of the mechanical transient. To consider the skewed slots effect in the electrical machine, the multi-slice technique is used (Dziwniel *et al.*, 2000).

2. The direct coupling method

The electrical machine is modelled in a 2D domain, using the Maxwell equations to formulate the field behaviour and the FEM to discretize the domain. The formulation uses the magnetic vector potential as unknown, the Galerkin method to obtain the set of equations to be solved numerically, the Euler recurrence method to discretize the temporal derivatives and the Newton-Raphson method to consider the non-linear characteristic of magnetic materials (Oliveira *et al.*, 2002). The multi-slice technique is used to consider the skewing of stator slots. In this technique, the motor is divided into M slices uniformly distributed along its axis (Dziwniel *et al.*, 2000). In each slice the magnetic potential and the electric currents have only an axial component. The strong coupling between all slices is imposed by the continuity of the currents circulating through them. Equation (1) shows the matrix system of the field equations:

$$\begin{gathered}\mathbf{M}(\mu)\cdot\mathbf{A}(t)+\mathbf{N}\cdot\frac{\mathrm{d}}{\mathrm{d}t}\mathbf{A}(t)-\mathbf{P}\cdot\mathbf{I}(t)=\mathbf{D}\\ \mathbf{Q}\cdot\frac{\mathrm{d}}{\mathrm{d}t}\mathbf{A}(t)-\mathbf{R}\cdot\mathbf{I}(t)-\mathbf{L}\cdot\frac{\mathrm{d}}{\mathrm{d}t}\mathbf{I}(t)=\mathbf{U}(t)\end{gathered}\tag{1}$$

where $\mathbf{A}$ is a set of M vectors of magnetic vector potentials in the finite element mesh nodes; $\mathbf{I}$ the vector of electric currents in the windings of the electromagnetic structure; $\mathbf{M}$ a set of M matrices related to permeability; $\mathbf{N}$ a set of M matrices related to electric conductivity; $\mathbf{D}$ a set of M vectors related to permanent magnet contributions; $\mathbf{P}$ a set of M matrices that relates the element current and its nodes; $\mathbf{Q}$ a set of M matrices associated with flux linkage; $\mathbf{R}$ a diagonal matrix representing windings resistances; $\mathbf{L}$ a diagonal end-winding inductances matrix. $\mathbf{U}$ is the vector corresponding to the voltage across the electromagnetic device windings.

To define the vector $\mathbf{U}$, the external electric circuit is modelled using the state variable approach in association with the graph theory. This technique gives the necessary support to fully automate the construction process of the electric equation system (Kuo-Peng *et al.*, 1997). According to these theories, we can write the equations that describe the electric circuit behaviour as follows:

$$\begin{gathered}\frac{\mathrm{d}}{\mathrm{d}t}\mathbf{X}(t)=\mathbf{G}_1(t)\cdot\mathbf{X}(t)+\mathbf{G}_2(t)\cdot\mathbf{E}(t)+\mathbf{G}_3(t)\cdot\mathbf{I}(t)\\ \mathbf{U}(t)=\mathbf{G}_4(t)\cdot\mathbf{X}(t)+\mathbf{G}_5(t)\cdot\mathbf{E}(t)+\mathbf{G}_6(t)\cdot\mathbf{I}(t)\end{gathered}\tag{2}$$

where $\mathbf{X}$ is the circuit state variables vector. The state variables are the capacitor tree branch voltages and the inductor link currents. $\mathbf{E}$ is the independent voltage and current sources vector and $\mathbf{G}_1$-$\mathbf{G}_6$ are matrices that depend on the converter topology and change at each switch commutation, and so they have to be determined at each calculation time step. This is made in an entirely automatic way, according to the switch type and its commutation characteristics (Kuo-Peng *et al.*, 1997).

The equation systems (1) and (2) have two common variables (**U** and **I**), and so the field and the circuit equations can be coupled together in a single system in equation (3), using **U** as a direct linking variable. System (3) is the complete system that includes the field equations for a domain divided into M slices coupled to the circuit ones.

$$\begin{bmatrix} \mathbf{M}_1+\dfrac{\mathbf{N}_1}{\Delta t} & \dots & 0 & \dots & 0 & \mathbf{P}_1 & 0 \\ \vdots & & \vdots & & \vdots & \vdots & \vdots \\ 0 & \dots & \mathbf{M}_m+\dfrac{\mathbf{N}_m}{\Delta t} & \dots & 0 & \mathbf{P}_m & 0 \\ \vdots & & \vdots & & \vdots & \vdots & \vdots \\ 0 & \dots & 0 & \dots & \mathbf{M}_M+\dfrac{\mathbf{N}_M}{\Delta t} & \mathbf{P}_M & 0 \\ \dfrac{\mathbf{Q}_1}{\Delta t} & \dots & \dfrac{\mathbf{Q}_m}{\Delta t} & \dots & \dfrac{\mathbf{Q}_M}{\Delta t} & \mathbf{R}+\dfrac{\mathbf{L}}{\Delta t}-\mathbf{G}_6 & -\mathbf{G}_4 \\ 0 & \dots & 0 & \dots & 0 & -\mathbf{G}_3 & \dfrac{1}{\Delta t}-\mathbf{G}_1 \end{bmatrix} \begin{bmatrix} \mathbf{A}_1(t) \\ \vdots \\ \mathbf{A}_m(t) \\ \vdots \\ \mathbf{A}_M(t) \\ \mathbf{I}(t) \\ \mathbf{X}(t) \end{bmatrix}$$

$$= \begin{bmatrix} \dfrac{\mathbf{N}_1}{\Delta t} & \dots & 0 & \dots & 0 & 0 & 0 \\ \vdots & & \vdots & & \vdots & \vdots & \vdots \\ 0 & \dots & \dfrac{\mathbf{N}_m}{\Delta t} & \dots & 0 & 0 & 0 \\ \vdots & & \vdots & & \vdots & \vdots & \vdots \\ 0 & \dots & 0 & \dots & \dfrac{\mathbf{N}_M}{\Delta t} & 0 & 0 \\ \dfrac{\mathbf{Q}_1}{\Delta t} & \dots & \dfrac{\mathbf{Q}_m}{\Delta t} & \dots & \dfrac{\mathbf{Q}_M}{\Delta t} & \dfrac{\mathbf{L}}{\Delta t} & 0 \\ 0 & \dots & 0 & \dots & 0 & 0 & \dfrac{1}{\Delta t} \end{bmatrix} \begin{bmatrix} \mathbf{A}_1(t-\Delta t) \\ \vdots \\ \mathbf{A}_m(t-\Delta t) \\ \vdots \\ \mathbf{A}_M(t-\Delta t) \\ \mathbf{I}(t-\Delta t) \\ \mathbf{X}(t-\Delta t) \end{bmatrix} + \begin{bmatrix} \mathbf{D}_1(t-\Delta t) \\ \vdots \\ \mathbf{D}_m(t-\Delta t) \\ \vdots \\ \mathbf{D}_M(t-\Delta t) \\ \mathbf{G}_5(t-\Delta t) \\ \mathbf{G}_2(t-\Delta t) \end{bmatrix} \tag{3}$$

The moving band technique is chosen to consider the movement during the field calculation (Sadowski *et al.*, 1992). At each time step, the electromagnetic torque is calculated via the maxwell stress tensor. The force is evaluated along a line placed in the airgap and the electromagnetic torque T_{e} is calculated by the following relationship:

$$T_{\mathrm{e}} = L \int_{\Gamma} \left\{ \mathbf{r} \times \left[\frac{1}{\mu_0}(Bn)B - \frac{1}{2\mu_0} B^2 n \right] \right\} \mathrm{d}\Gamma \tag{4}$$

where L is the length, B the induction in the elements and $\mathbf{r}$ the vector that connects the origin to the midpoint of segment $\mathrm{d}\Gamma$.

The new angular speed and rotor displacement are evaluated by the mechanical oscillation equation:

$$\omega_{\mathrm{r}}(t) = \omega_{\mathrm{r}}(t - \Delta t) + \frac{(T_{\mathrm{e}} - T_{\mathrm{L}} - B_{\mathrm{m}} \cdot \omega_r(t - \Delta t))}{J} \cdot \Delta t \tag{5}$$

$$\theta(t) = \theta(t - \Delta t) + \omega_{\mathrm{r}} \cdot \Delta t \tag{6}$$

where T_{L} is the load torque, J the moment of inertia, B_{m} the friction coefficient, ω_{r} the rotor speed and θ the rotor position.

When a commutation of the switches occurs, the time step has to be refined to well represent the converter/machine operation. This must be accomplished by a refinement of the rotor movement which implies in turning backward and then forward the rotor.

The control loop implementation is detailed in Roel Ortiz *et al.* (2001). It consists of two blocks. The first block represents the coupled system and the second one, the control loop system. Data exchange between these two blocks occurs at each time step.

To illustrate how the proposed methodology is implemented, Figures 1-3 show the flowcharts with its main parts.

3. Application examples

To demonstrate the effectiveness of the presented method, a three-phase BLAC motor fed by a converter (Figure 4) driven by two types of control strategies is tested.

The motor characteristics are presented in Table I. The motor has skewed stator slots and to consider the skewing effects, five slices equally distributed along its axis are used in the simulation.

The study domain consists of one machine pole, i.e. a 45° domain (Figure 5). Anti-periodic conditions are used to represent the whole machine.

3.1 Three-phase BLAC motor fed by PWM converter

The converter operates in a three-phase-on configuration. The PWM triangular frequency is 8 kHZ. The three sinusoidal reference frequencies are determined by a closed loop speed control. In this manner, the reference frequency varies according to the instantaneous rotor speed, starting the movement softly until the speed reaches the imposed reference one. The DC voltage source is constant and is equal to 230 V. Figures 6-8 show the three sinusoidal references, the winding voltage W1 and the speed and torque waveforms, respectively.

3.2 Three-phase BLAC motor fed by a two-phase-on excitation converter

The tested structure is the same as the one shown in Figure 4, but the control strategy is different. The control generates a sequence of six pulses with the same width and the rotor speed is monitored and provides a feedback signal to control the pulse frequency. If the rotor speed is smaller than the imposed reference, the pulse frequency is

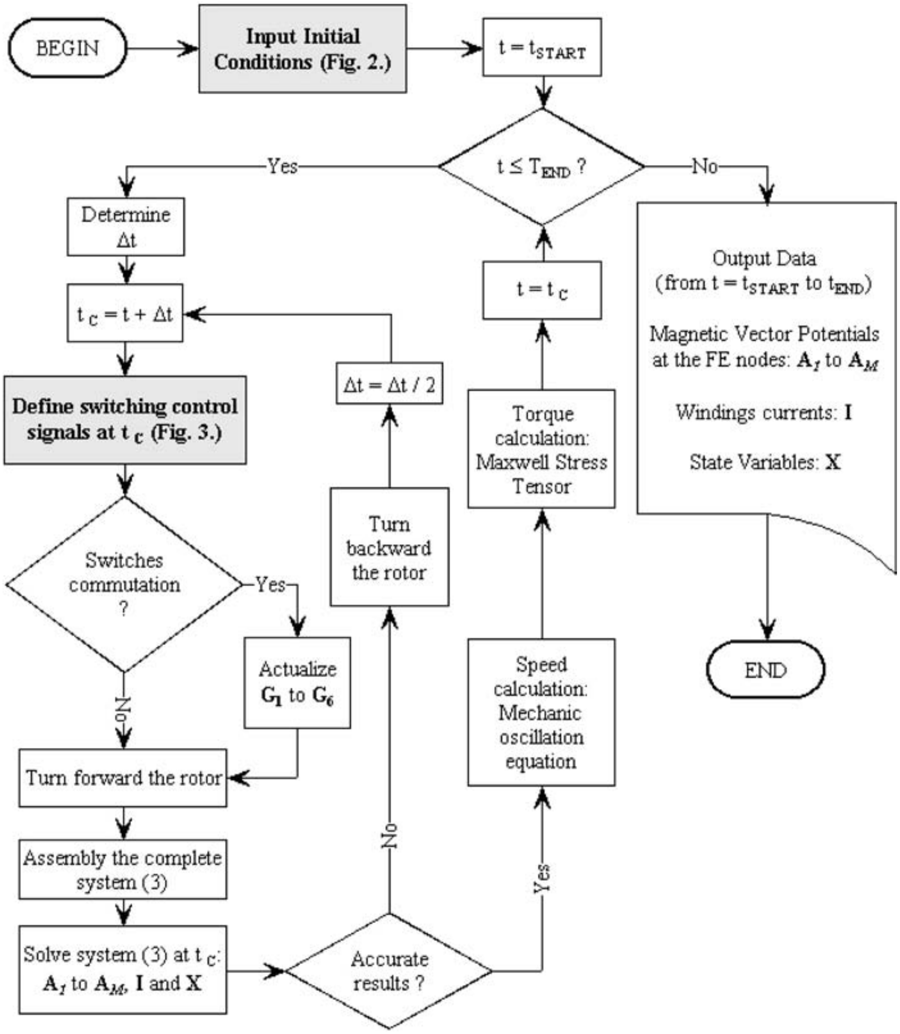
BEGIN
Input Initial Conditions (Fig. 2.)
$t = t_{START}$
$t \leq T_{END}$?
Yes
No
Output Data (from $t = t_{START}$ to t_{END})
Magnetic Vector Potentials at the FE nodes: $\mathbf{A}_1$ to $\mathbf{A}_M$
Windings currents: $\mathbf{I}$
State Variables: $\mathbf{X}$
END
Determine Δt
$t_C = t + \Delta t$
Define switching control signals at t_C (Fig. 3.)
Switches commutation ?
Yes
No
Actualize $\mathbf{G}_1$ to $\mathbf{G}_6$
Turn forward the rotor
Assembly the complete system (3)
Solve system (3) at t_C: $\mathbf{A}_1$ to $\mathbf{A}_M$, $\mathbf{I}$ and $\mathbf{X}$
Accurate results ?
No
Yes
Turn backward the rotor
$\Delta t = \Delta t / 2$
Speed calculation: Mechanic oscillation equation
Torque calculation: Maxwell Stress Tensor
$t = t_C$

Figure 1.
Implemented method flowchart

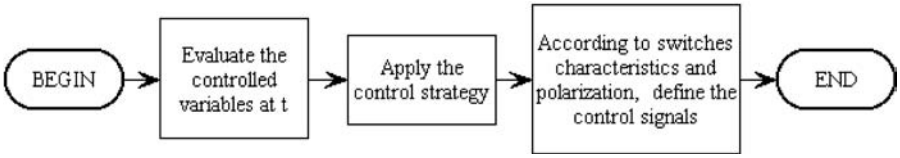
BEGIN
Evaluate the controlled variables at t
Apply the control strategy
According to switches characteristics and polarization, define the control signals
END

Figure 2.
Control action

increased, inversely it is decreased if the reference is exceeded. The DC voltage source is maintained constant and is equal to 30 V.

This control strategy acts only on the frequency since the pulse width is kept constant. Consequently, the average voltage does not change. This characteristic

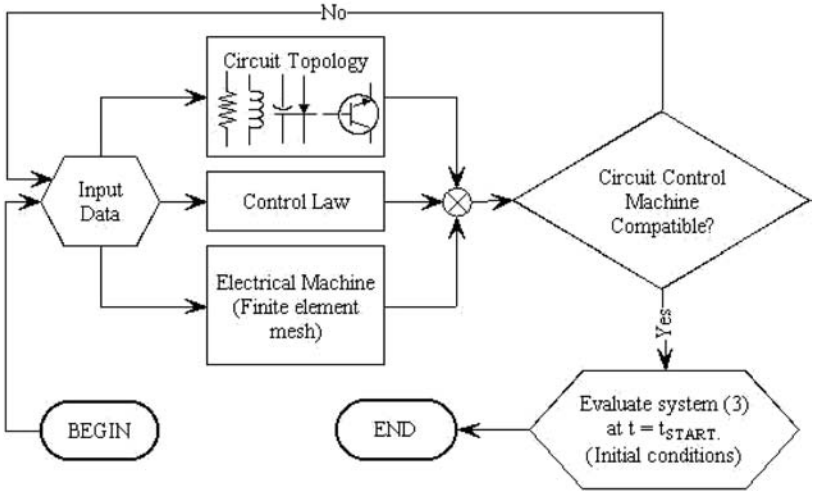
No
Circuit Topology
Input Data
Control Law
Electrical Machine (Finite element mesh)
Circuit Control Machine Compatible?
Yes
BEGIN
END
Evaluate system (3) at t = t$_{START}$. (Initial conditions)

Figure 3.
Input data definition

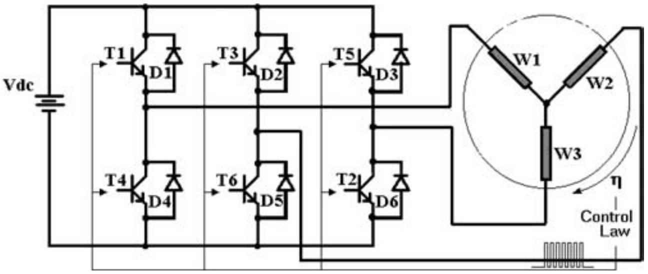
Vdc
T1
D1
T3
D2
T5
D3
T4
D4
T6
D5
T2
D6
W1
W2
W3
η
Control Law

Figure 4.
The simulated and experimented structure

V_0	200 V	Length	40 mm
Phases	3	# PM	16 (8/pole)
Poles	8	PM dim.	14.1×20.3 mm
Turns/pole	33	Magn. airgap	0.7 mm
Slots	24	Mech. airgap	0.45 mm
R25°C/phase	2.14713 Ω	J	0.21894 kgm^2
Volt. constant	47.1 V/Krpm	PM induction	1.03 T
Stator radius	26-47 mm	Rotor radius	10.5-25.4 mm
Skew angle	15°(1 slot)	Double layer-series connection	

Table I.
Blac motor characteristics

produces ripples in the transitory and in the steady-state operation. Thus, the starting process is not as soft as in the previous example (three-phase BLAC motor fed by a PWM converter). Figure 9 shows the transient speed and torque waveforms.

Figure 10 shows the transient current and line voltage waveforms.

Figures 11 and 12 show the comparison of experimental and simulated waveforms at steady-state operation.

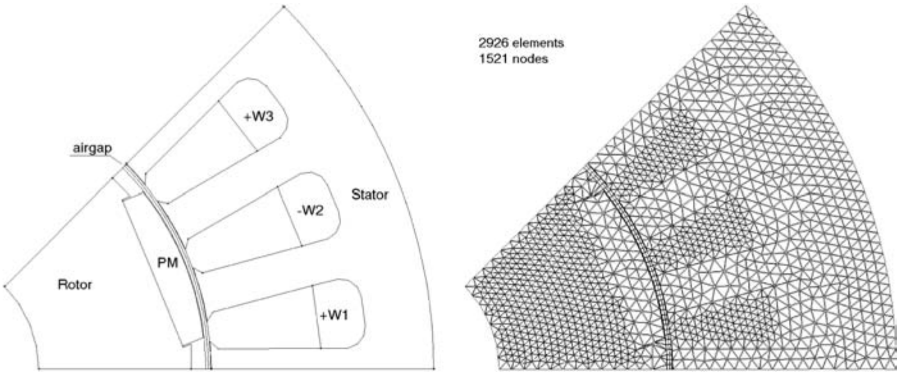
airgap
+W3
-W2
Stator
PM
Rotor
+W1
2926 elements
1521 nodes

Figure 5.
BLAC motor: finite element domain

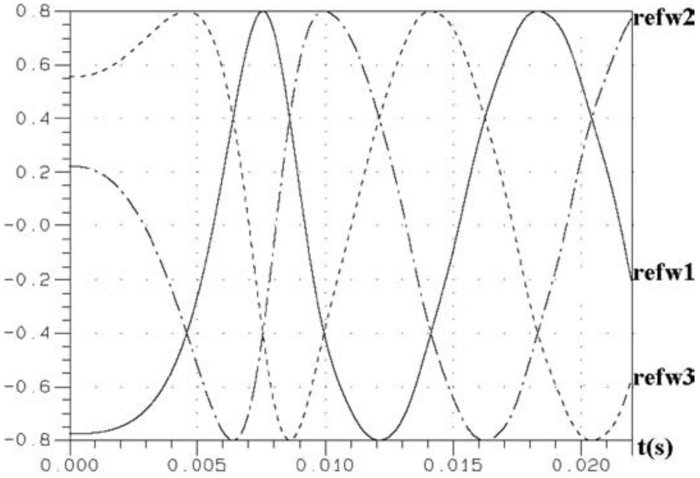

Figure 6.
Sinusoidal references: phases 1, 2 and 3

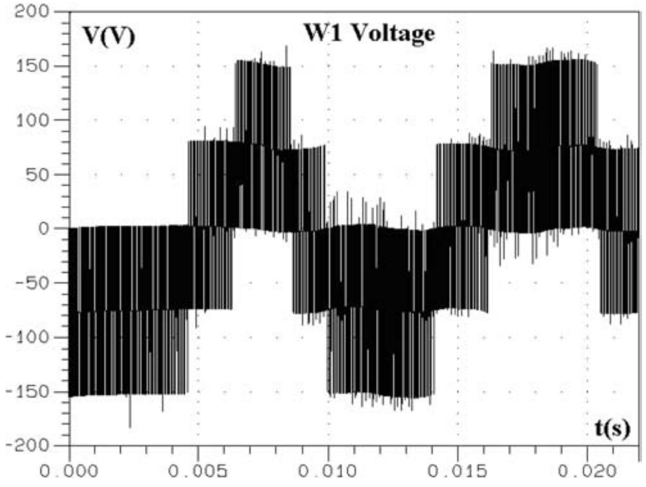

Figure 7.
W_1 voltage waveform

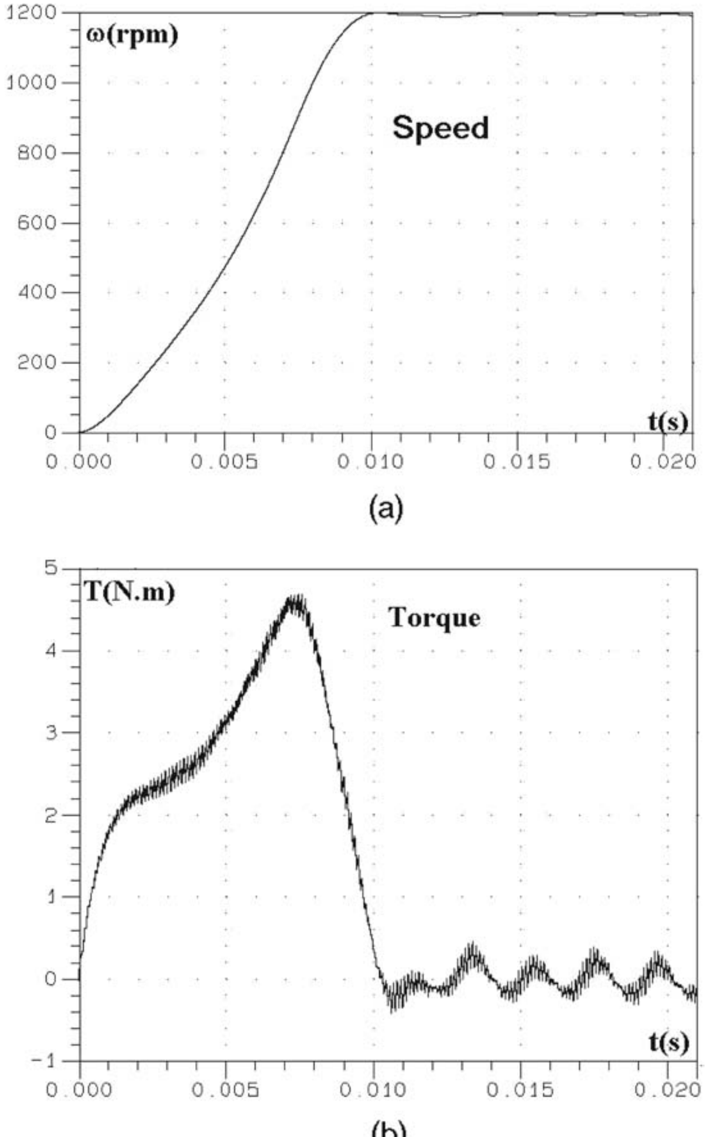

(a)

(b)

Figure 8.
(a) Speed; and
(b) electromagnetic torque

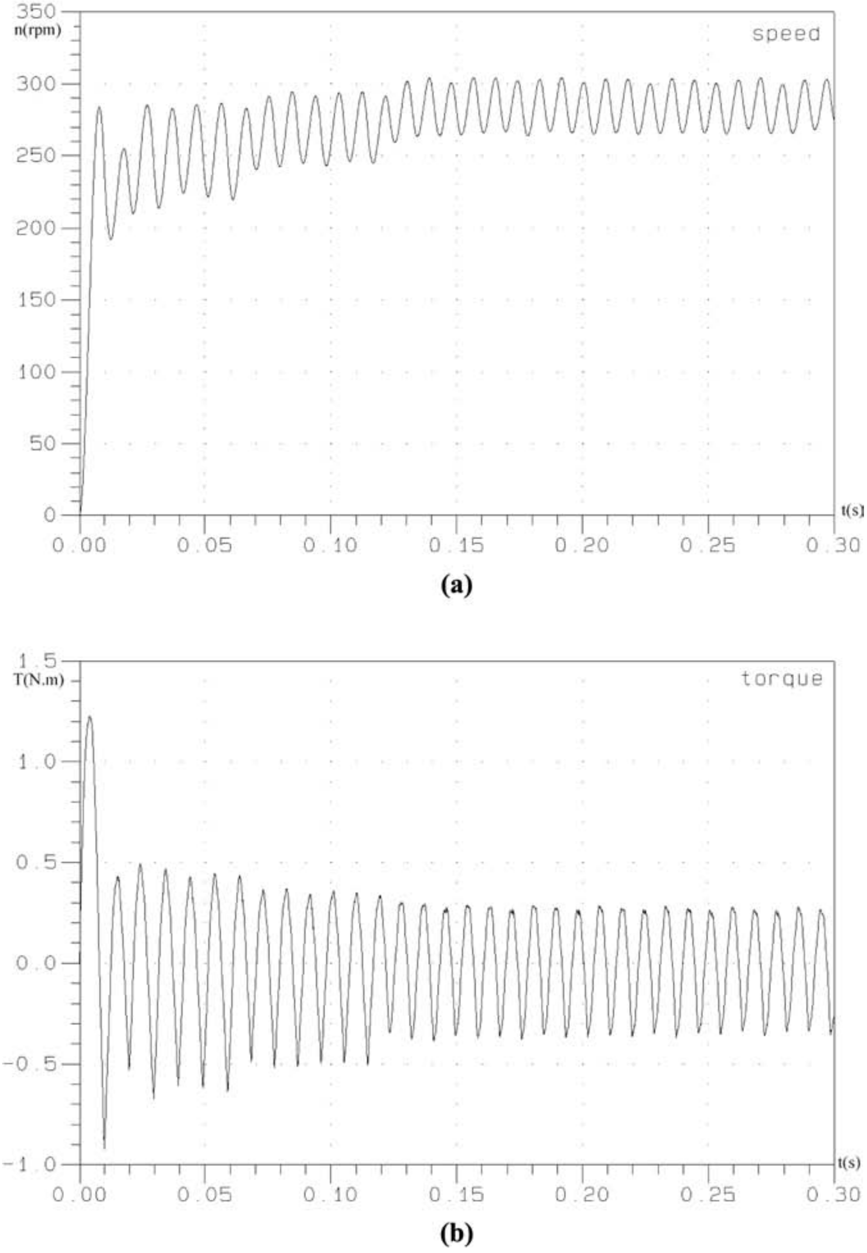

Figure 9.
(a) Speed; and
(b) electromagnetic torque

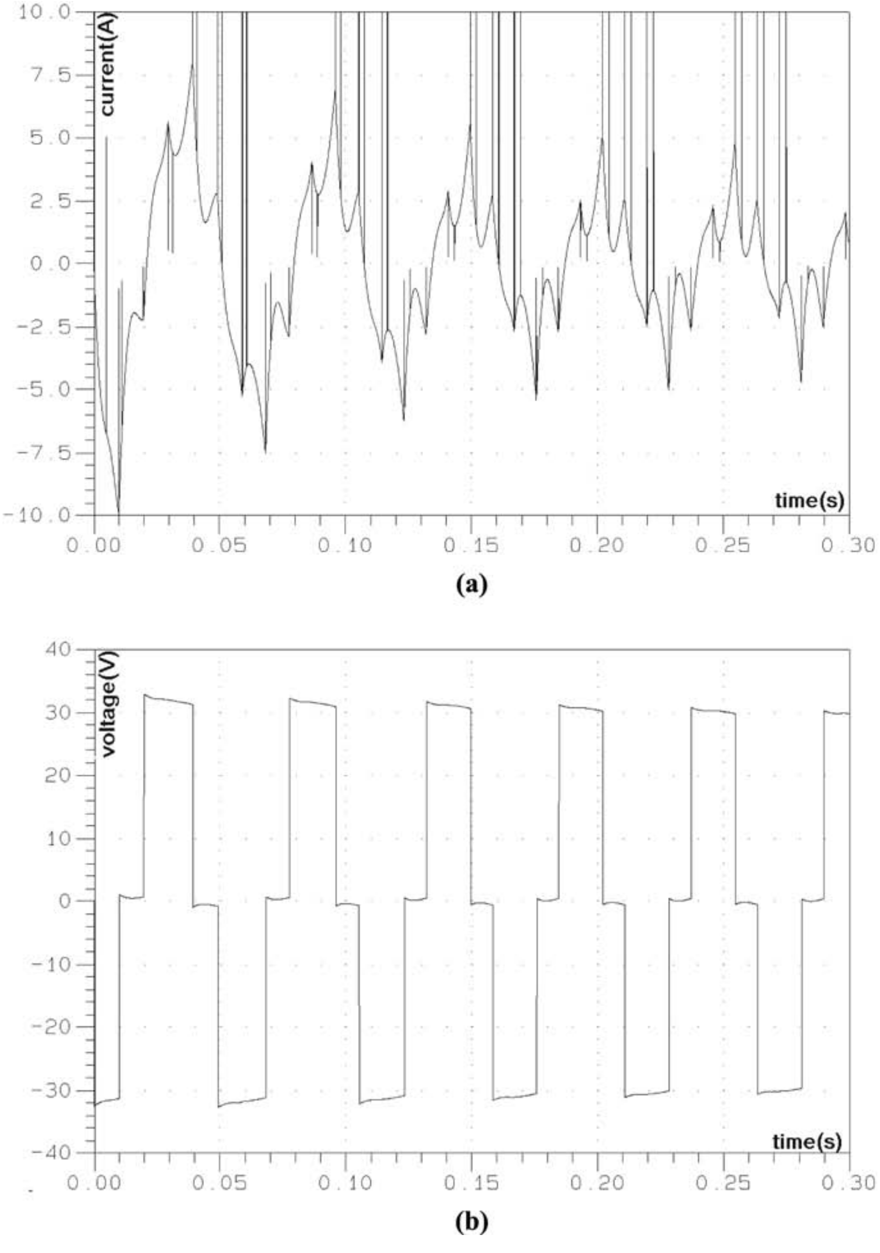

Figure 10.
(a) Transient current waveform; and (b) transient line voltage waveform

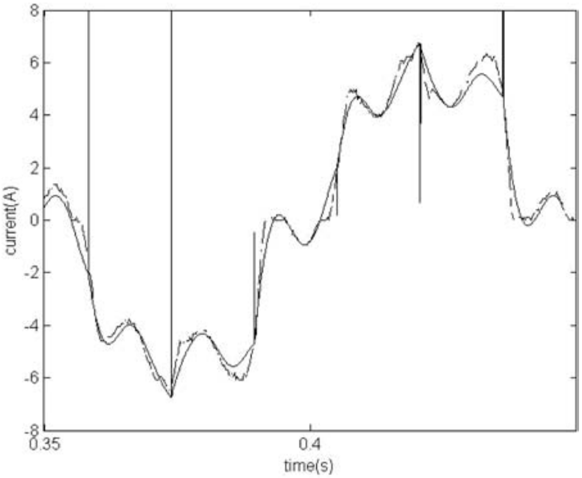

Figure 11.
Steady-state current waveform – dashed line: experimental result; and solid line: simulation result

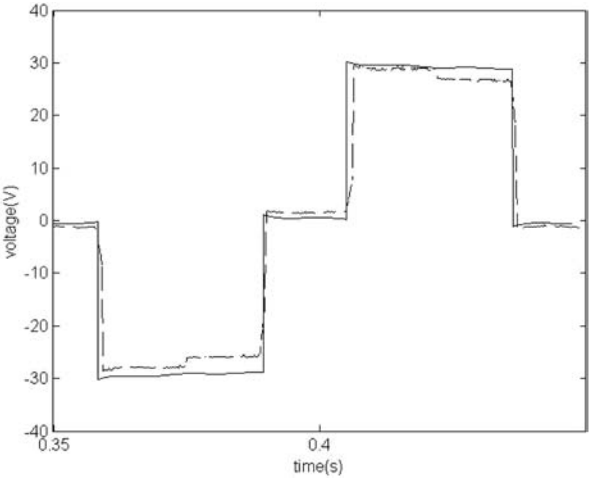

Figure 12.
Steady-state line voltage waveform – dashed line: experimental result; and solid line: simulation result

4. Conclusion

A general method coupling directly the electromagnetic field including the machine skewing slots effect, the closed loop controlled converters and the movement equations is presented. This method is implemented in an easy-to-use way, thanks to its flexibility, allowing the analysis of electrical machines coupled to different circuit topologies, controlled by several control laws. The comparison of simulated and experimental results shows a good agreement.

References

Dziwniel, P., Boualem, B., Piriou, F., Ducreux, J.-P. and Thomas, P. (2000), "Comparison between two approaches to model induction machines with skewed slots", *IEEE Trans. on Magn.*, Vol. 36 No. 4, pp. 1453-7.

Ho, S.L., Fu, W.N., Li, H.L., Wong, H.C. and Tan, H. (2001), "Performance analysis of brushless DC motors including features of the control loop in the finite element modelling", *IEEE Trans. on Magn.*, Vol. 37 No. 5, pp. 3370-4.

Jang, G.H., Chang, J.H., Hong, D.P. and Kim, K.S. (2002), "Finite-element analysis of an electromechanical field of a BLDC motor considering speed control and mechanical flexibility", *IEEE Trans. on Magn.*, Vol. 38 No. 2, pp. 945-8.

Kuo-Peng, P., Sadowski, N., Bastos, J.P.A., Carlson, R. and Batistela, N.J. (1997), "A general method for coupling static converters with electromagnetic structures", *IEEE Trans. on Magn.*, Vol. 33 No. 2, pp. 2004-9.

Oliveira, A.M., Kuo-Peng, P., Sadowski, N., de Andrade, M.S. and Bastos, J.P.A. (2002), "A non *a priori* approach to analyze electrical machines modelled by FEM connected to static converters", *IEEE Trans. on Magn.*, Vol. 38 No. 2, pp. 933-6.

Roel Ortiz, J.L., Sadowski, N., Kuo-Peng, P., Batistela, N.J. and Bastos, J.P.A. (2001), "Coupling static converter with control loop and non-linear electromagnetic devices", *IEEE Trans. on Magn.*, Vol. 37 No. 5, pp. 3514-7.

Sadowski, N., Lefevre, Y., Lajoie-Mazenc, M. and Cros, J. (1992), "Finite element torque calculation in electrical machines while considering the movement", *IEEE Trans. on Magn.*, Vol. 28 No. 2, pp. 1410-3.

The Emerald Research Register for this journal is available at
www.emeraldinsight.com/researchregister

The current issue and full text archive of this journal is available at
www.emeraldinsight.com/0332-1649.htm

FEM analysis of current limiting devices using superconducting thin film and AC losses of YBCO coated conductor

H. Ohsaki and Y. Ichiki
Department of Advanced Energy, Graduate School of Frontier Sciences, The University of Tokyo, Japan
S. Sugita
Tokyo Electric Power Company, Japan

Keywords *Electrical conductivity, Thin films, Finite element analysis*

Abstract *A numerical analysis tool has been developed to study electromagnetic characteristics of high-temperature superconducting thin film used for a resistive-type fault current limiter (FCL) and coated conductor. It adopts the finite element method based on current vector potentials with thin-plate approximation. Transport current, temperature dependence and strong non-linearity of electromagnetic properties, and state transition of superconductor are taken into account by solving a three-dimensional coupled problem of electromagnetic field, an electric circuit and thermal field. Then using this numerical analysis tool the current imbalance and current limiting characteristics of a FCL device, the influence of inhomogeneity of superconducting properties on them, and AC losses in YBCO coated conductor are studied.*

1. Introduction

YBCO ($YBa_2Cu_3O_x$) thin film possesses good superconducting characteristics: high critical current density even at a high magnetic field at a temperature of 20-50 K. Therefore, a YBCO superconducting wire is strongly expected as a second-generation high-temperature superconducting wire after Bi-Sr-Ca-Cu-O wires, and has been intensively developed in the world (Tokunaga *et al.*, 2002). In addition, YBCO superconducting film can be used in a resistive-type fault current limiter (FCL), which is highly expected to be developed for electric power networks (Kubota *et al.*, 1999; Shimohata *et al.*, 2002).

When electromagnetic characteristics are theoretically investigated, the finite element method (FEM) is a general and powerful tool. In YBCO superconducting wires and FCLs the film structure is a specific condition for FEM analysis. So a numerical analysis tool has been developed to calculate electromagnetic characteristics of coated conductors and resistive-type FCLs using YBCO superconducting film (Sugita and Ohsaki, 2003a). The analysis tool uses FEM based on current vector potentials with thin-plate approximation (Tsuboi and Kunisue, 1991) with transport current, temperature dependence and strong non-linearity of electromagnetic properties, and state transition of superconductor taken into account. It can deal with a three-dimensional coupled problem of electromagnetic field, an electric circuit and thermal field. Current imbalance phenomenon and current limiting characteristics of a fault current limiting device, and AC losses in the thin-film superconductor were calculated with this software tool (Sugita and Ohsaki, 2003b).

COMPEL: The International Journal for Computation and Mathematics in Electrical and Electronic Engineering
Vol. 23 No. 4, 2004
pp. 1092-1099
© Emerald Group Publishing Limited
0332-1649
DOI 10.1108/03321640410553526

In this paper, the analysis model and method are first described and then some calculation results of current limiting performance of a superconducting fault current limiting device and AC losses of coated conductor are shown.

2. Analysis model

2.1 Fault current limiting device

A fault current limiting device has a three-layered structure consisting of a sapphire substrate, a YBCO superconducting film, and a metal layer for protection against hot spot generation. Figure 1 shows the electric circuit of the numerical analysis model. Table I lists the parameters of the FCL device and the electric circuit. Without the FCL device the circuit current reaches its maximum value of 210 A, which is three times larger than the critical current of the superconductor.

To investigate the influence of inhomogeneity of superconducting properties on current imbalance and current limiting characteristics, the analysis model of YBCO superconducting film shown in Figure 2 was used. Transport current flows in the superconductor from the left to the right. Inhomogeneous superconducting properties were given to the areas "a" and "b" shown in Figure 2.

2.2 Coated conductor

To study fundamental characteristics of AC losses in the YBCO coated conductor, a one-dimensional model of superconducting film can be used with the two-dimensional magnetic field considered. Table II lists the specifications of YBCO coated conductor model.

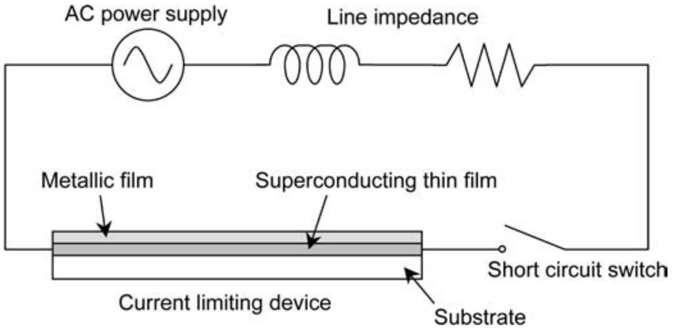

Figure 1.
Electric circuit of FCL for numerical analysis

Thickness	0.35 μm
Width	10 mm
Length	42 mm
Critical current	70 A
Critical current density	2.0×10^{10} A/m^2
Reference electric field	1.0×10^{-4} V/m
n-value	20
Metal layer thickness (gold)	50 nm
Substrate thickness (sapphire)	0.55 mm
AC voltage	200 V, 60 Hz
External resistance	1.349 Ω

Table I.
Specifications of FCL device

3. FEM analysis method

3.1 Current vector potential method

For computation of current distribution in the superconducting thin film, the finite element method based on current vector potentials with thin-plate approximation was used (Sugita and Ohsaki, 2003a; Tsuboi and Kunisue, 1991). The current flow in the superconductor is limited in the tangential direction, and so the current density $\boldsymbol{J}$ is defined by $\boldsymbol{J} = \nabla \times (\boldsymbol{n}T)$, where $\boldsymbol{n}$ is the unit vector normal to the computation surface and T is the normal component of the current vector potential. Therefore, it becomes a two-dimensional problem of the scalar variable T. The governing equation of T is given by

$$\rho\nabla^2 T = \frac{\mu h}{4\pi}\frac{\partial}{\partial t}\iint_S \frac{\{\nabla\times(\boldsymbol{n}T)\}\times\boldsymbol{r}\cdot\boldsymbol{n}}{r^3}\,\mathrm{d}S + \frac{\partial \boldsymbol{B}_0\cdot\boldsymbol{n}}{\partial t} \tag{1}$$

where ρ is the electric resistivity, μ is the magnetic permeability, h is the thickness of the superconducting thin film, t is the time, $\boldsymbol{r}$ is the vector from the source point to the field point and $\boldsymbol{B}_0$ is the flux density of externally applied magnetic field.

3.2 Modeling of superconducting characteristics

A non-linear *E-J* relation (*E*: electric field, *J*: current density) based on the power law was used for modeling electromagnetic property of the superconductor. It is described by the following equation:

$$E = E_C\left(\frac{J}{J_C}\right)^n \tag{2}$$

where J_C is the critical current density that is defined by the reference electric field E_C, and n is known as the index number, n-value. Figure 3 shows an *E-J* curve of the superconductor. The equivalent resistivity of the superconductor ρ_{SC} is given by

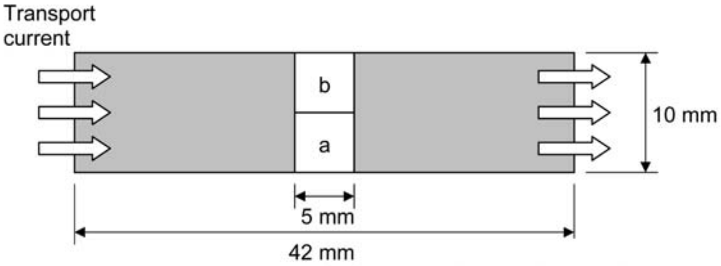

Note: Inhomogeneous superconducting properties are given to the areas "a" and "b"

Figure 2. Numerical analysis model of YBCO superconducting film for a fault current limiting device.

Table II. Specifications of YBCO coated conductor

Thickness	$0.3\,\mu$m
Width	10 mm
Critical current	87.4 A
Critical current density	2.9×10^6 A/cm
Reference electric field	$1.0\,\mu$V/cm
n-value	36.6

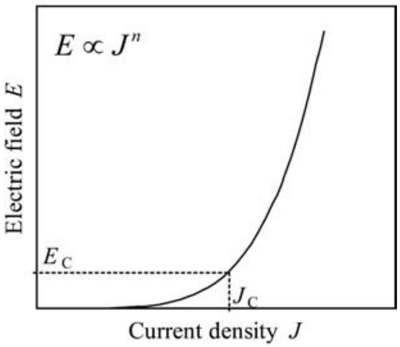

Figure 3.
E-J characteristics of superconductor

$$\rho_{SC} = \frac{E}{J} = \frac{E_C}{J_C}\left(\frac{J}{J_C}\right)^{n-1} \tag{3}$$

The critical current density J_C depends on the temperature T_{SC} and the magnetic flux density B, which is described by the following equation in general:

$$J_C(B, T_{SC}) = A\left[1 - \left(\frac{T_{SC}}{T_C}\right)^2\right]^m B^{\gamma-1}\left(1 - \frac{B}{B_{C2}}\right)^\delta \tag{4}$$

where T_C is the critical temperature and B_{C2} is the upper critical flux density, A, m, γ, and δ are constants.

There is a metal protection layer on the superconducting film. The effective resistivity of the conductor ρ_e is as follows:

$$\rho_e = \frac{\rho_{metal}\rho_{SC}(t_{metal} + t_{SC})}{\rho_{metal}t_{SC} + \rho_{SC}t_{metal}} \tag{5}$$

where ρ_{SC} is the resistivity of the superconductor, ρ_{metal} the resistivity of the metal layer, t_{SC} the thickness of the superconducting layer, and t_{metal} the thickness of the metal layer. When the YBCO thin film layer is in the superconducting state, equation (5) becomes $\rho_e \approx \rho_{SC}$. When the superconducting layer is getting normal, the current sharing between two layers starts.

3.3 Boundary condition

The transport current and the coupling with the electric circuit are taken into account through the boundary conditions of the electromagnetic field analysis. The total transport current I_0 can be given by the boundary condition.

$$I_0 = \iint_S \boldsymbol{J} \cdot \boldsymbol{n}\,\mathrm{d}S = \iint_S (\nabla \times \boldsymbol{T}) \cdot \boldsymbol{n}\,\mathrm{d}S = \int_C \boldsymbol{T} \cdot \mathrm{d}\boldsymbol{s} \tag{6}$$

If the normal components of $\boldsymbol{T}$ on both side boundaries are assumed to be uniform with values of 0 and T_0, respectively, then the following equation can be derived from equation (6).

$$T_0 = \frac{I_0}{h} \tag{7}$$

The electromagnetic field and the electric circuit are combined through equation (7).

3.4 Electric circuit equation

The equation of electric circuit is as follows:

$$V_1 = R_S I + R_1 I + L_1 \frac{\mathrm{d}I}{\mathrm{d}t} \tag{8}$$

where V_1 is the AC voltage source, R_S is the resistance of FCL, R_1 is the external resistance and L_1 is the external inductance

3.5 Non-linear calculation

The FEM equations with the backward differential approximation applied become the following form:

$$\left[[R] + \frac{1}{\Delta t}[M]\right]\{T\}_k - \frac{1}{\Delta t}[M]\{T\}_{k-1} + \left\{\frac{\partial B_0}{\partial t}\right\}_k = 0 \tag{9}$$

where $[R]$ is the symmetric sparse matrix depending on the node locations and electric resistivity of the elements, $[M]$ is the asymmetric dense matrix depending on the node locations and obtained by Biot-Savart's law and Gauss-Legendre integration formula, Δt is the interval time, and k is the time step number. For strong non-linearity of resistivity ρ_SC, Newton-Raphson method was adopted.

$$\left[\frac{\partial\{\varphi\}}{\partial\{T\}}\right]\{\delta T\} = -\{\phi\} \tag{10}$$

$$\{\phi\} = \left[[R] + \frac{1}{\Delta t}[M]\right]\{T\} - \frac{1}{\Delta t}[M]\{T^*\} + \left\{\frac{\partial B_0}{\partial t}\right\} \tag{11}$$

where $\{T\}$ is the potential vector at time t and $\{T^*\}$ is the value at time $t - \Delta t$.

3.6 Thermal field calculation

For FCL analysis, three-dimensional thermal field analysis is necessary because temperature distribution strongly affects the operating characteristics of superconductor. The governing equation of thermal field analysis is given by

$$\kappa\nabla^2 T_\mathrm{SC} - \rho_\mathrm{m} c \frac{\partial T_\mathrm{SC}}{\partial t} = 0 \tag{12}$$

where κ is the thermal conductivity of the substrate, T_SC is the temperature of the superconductor and substrate, ρ_m is the mass density, c is the specific heat, and t is the time. Temperature dependence of κ and c as well as cooling characteristics of liquid nitrogen are considered.

4. FEM analysis results

4.1 Current imbalance

The current imbalance and current limiting characteristics of the YBCO current limiting device were analyzed by the developed tool. Current distribution in the superconducting film affects AC losses and the uniformity of S-N transition. Figure 4 shows the current distribution across the homogeneous superconducting film when the transport current changes from 14.6 to 98.6 A before S-N transition. At first the current density at the edges increases up to $2.2 \times 10^{10}\,\mathrm{A/m^2}$. As the transport current increases, more current gradually penetrates towards the center. When the transport current becomes about 90 A, the current density is almost uniform in the superconductor. The current distribution can be considered uniform in homogeneous superconducting thin film when the film works as a fault current limiter.

Inhomogeneous superconducting properties, namely, the critical current density of $1.6 \times 10^{10}\,\mathrm{A/m^2}$, which is 20 per cent smaller than that of the other part, was given to the area "a" shown in Figure 2. Figure 5 shows the current distribution under this condition. The transport current bypasses the area "a" because the resistivity of the area "a" is larger than that of the other part. Figure 6 shows the current density vectors when the transport current is 85.4 A.

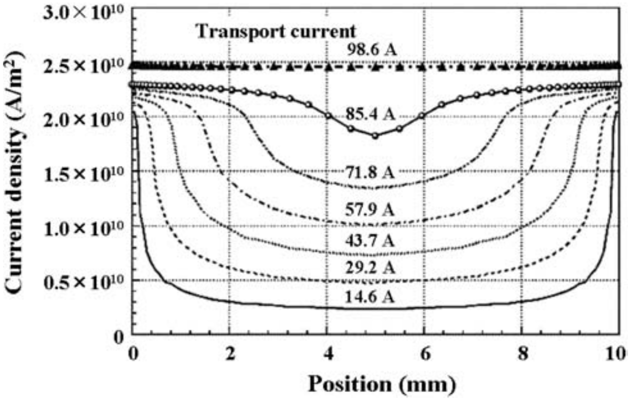

Figure 4.
Distribution of current density when the transport current changes from 14.6 to 98.6 A in the homogeneous superconductor

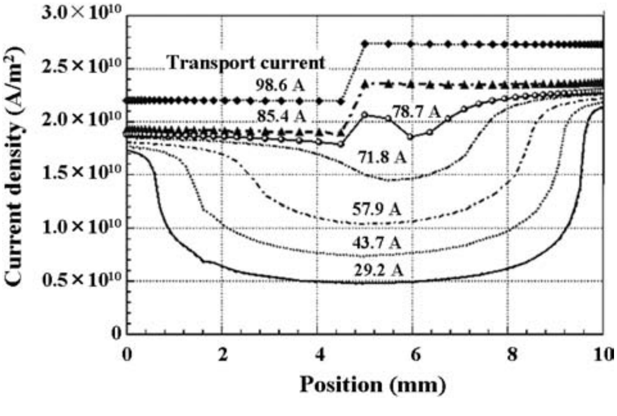

Figure 5.
Distribution of current density when the transport current changes from 29.2 to 98.6 A in the inhomogeneous superconductor

4.2 Current limiting characteristics

The influence of inhomogeneity of the superconducting properties on current limiting characteristics has been also investigated. Figure 7 shows calculated results of current limiting characteristics when lower critical current densities were given to the area “a” shown in Figure 2. A smaller critical current density of the weak part decreases the starting current of current limiting process and lengthens current limiting transient period.

4.3 AC losses of YBCO coated conductor

Figure 8 shows AC losses per cycle of the YBCO coated conductor shown in Table II. The losses were normalized by the square of the critical current, I_C^2. The value of I_C was

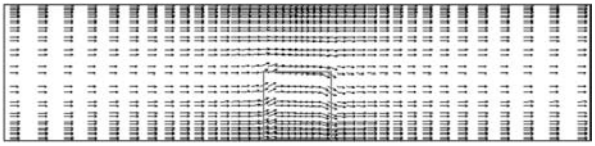

Figure 6.
Current density vectors for the transport current of 85.4 A

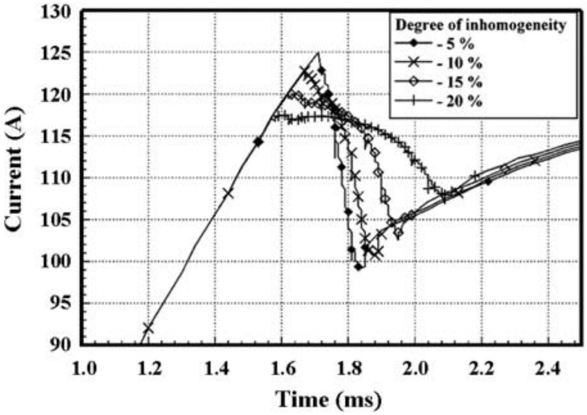

Figure 7.
Dependence of current limiting characteristics on inhomogeneity of the area “a”

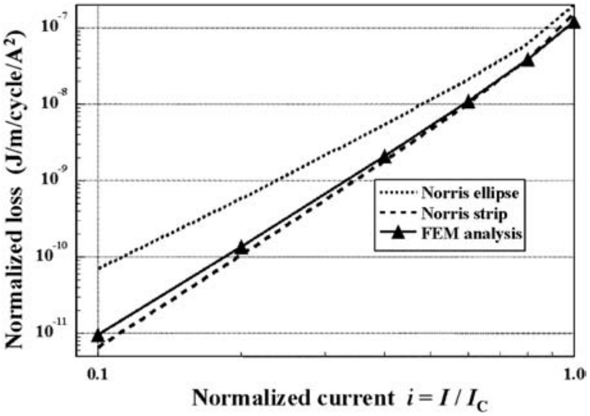

Figure 8.
AC loss characteristics calculated by FEM

210 A, which was not the critical current defined by the criteria 1×10^{-4} V/m but determined by the analysis. The obtained curve of AC losses characteristics was between the curves obtained by the Norris's formula for an ellipse and formula for a strip (Norris, 1970).

5. Conclusions

The FEM analysis tool was developed for study on electromagnetic characteristics of YBCO superconducting film that could be applied to resistive-type fault current limiters and coated conductor. With this analysis tool, fundamental characteristics, such as current imbalance, AC losses, switching behaviors, etc. were successfully calculated. It is expected that this tool can be used for further analysis and design of superconducting apparatuses.

References

Kubota, H., Arai, Y.K., Yamazaki, M. and Yoshino, H. (1999), "A new model of fault current limiter using YBCO thin film", *IEEE Transactions on Applied Superconductivity*, Vol. 9 No. 2, pp. 1365-8.

Norris, W.T. (1970), "Calculation of hysteresis losses in hard superconductors carrying ac: isolated conductors and edges of thin sheets", *Journal of Physics D*, Vol. 3 No. 4, pp. 489-507.

Shimohata, K., Yokoyama, S., Inaguchi, T., Nakamura, S. and Ozawa, Y. (2002), "Design of a large current-type fault current limiter with YBCO films", *Physica C*, Vol. 372-376, pp. 1643-8.

Sugita, S. and Ohsaki, H. (2003a), "FEM analysis of current limiting characteristics of a superconducting thin film current limiting device by the current vector potential method", *IEEE Transactions on Applied Superconductivity*, Vol. 13 No. 2, pp. 2020-3.

Sugita, S. and Ohsaki, H. (2003b), "Numerical analysis of AC losses in REBCO thin film for tape wire and fault current limiter", *Physica C*, Vol. 392-396, pp. 1150-5.

Tokunaga, Y., Izumi, T. and Shiohara, Y. (2002), "All Japan efforts on fundamental materials technology developments for HTS applications focusing on R&D of coated conductors", *Cryogenics*, Vol. 42 Nos 6-7, pp. 393-8.

Tsuboi, H. and Kunisue, K. (1991), "Eddy current analysis of thin plates taking account of the source current distributions and its experimental verifications", *IEEE Transactions on Magnetics*, Vol. 27 No. 5, pp. 4020-3.

The Emerald Research Register for this journal is available at
www.emeraldinsight.com/researchregister

The current issue and full text archive of this journal is available at
www.emeraldinsight.com/0332-1649.htm

Received September 2002
Revised March 2003
Accepted March 2003

Comparison of 3D and 2D field-circuit models of power transformer transients

Lech Nowak, Andrzej Demenko and Wojciech Szeląg
Institute of Industrial Electrical Engineering, Poznań University of Technology, Poznań, Poland

Keywords *Power transistors, Field testing, Transient voltages, Magnetic fields, Transformers*

Abstract *This paper deals with a coupled field-circuit simulation of transients in a three-phase, three-limb power transformer taking non-linearity into consideration. A comparative analysis of the results obtained from the application of 3D and 2D field models has been carried out. Owing to core saturation and the non-periodic components of the magnetic fluxes, the magnetic field exists also within the space surrounding the core. Hence, three-dimensional description is necessary. It has been proved that assuming the 2D model significantly overstated peak values of currents are obtained.*

1. Introduction

Computer simulation is a helpful tool for the designer of electromagnetic devices. However, it requires a very precise and credible model of electromagnetic phenomena.

Analyses of three-phase transformers are very often performed on the basis of the model with lumped parameters (the circuit model). However, such a model does not provide sufficient accuracy in the case of non-symmetrical or transient operations, especially in transformers with a non-linear magnetic core. During transients the non-periodic components of magnetic fluxes cause very strong saturation of some core parts (limbs, yokes) while other parts remain non-saturated. The reluctances of core parts may differ hundred times; their relations vary in time. This disrupts the symmetry of the magnetic field. Furthermore, in the case of a three-limb transformer the magnetic field also penetrates the space surrounding the core due to the core saturation and the non-periodic components of fluxes. Hence, three-dimensional description is necessary.

In transients, after the application of supply voltages, the currents in the transformer windings are not known in advance, i.e. prior to the field calculation (Nowak, 1995; Nowak and Kowalski, 1996). Therefore, the equations describing the transient three-dimensional field must be coupled with the equations of the electric circuits of the transformer.

In this paper, an algorithm for coupled field-circuit simulation of transients in a three-phase, three-limb power transformer is presented. The non-linearity and

COMPEL: The International Journal for Computation and Mathematics in Electrical and Electronic Engineering
Vol. 23 No. 4, 2004
pp. 1100-1109
© Emerald Group Publishing Limited
0332-1649
DOI 10.1108/03321640410510811

This is a revised and enhanced version of a paper which was originally presented as a conference contribution at the *XVII Symposium on Electromagnetic Phenomena in Nonlinear Circuits (EPNC)*, held in Leuven, Belgium, on 1-3 July 2002. This is one of a small selection of papers from the Symposium to appear in the current and future issues of *COMPEL.*

anisotropy of the transformer core have been considered. A comparative analysis of the results obtained from the application of the 3D or 2D field models has been carried out. It has been shown that assuming the simplified 2D field-circuit model, one obtains significantly overstated peak values of currents.

The effectiveness of the algorithm of 3D magnetic field computations is especially important in the case of transient simulation. In such simulation, step by step computations are performed hundreds of times. At each time-step, the computation are iteratively repeated dozens or more times (due to strong core saturation). Thus, the 3D magnetic field has to be computed many thousands of times. For that reason, a special iterative procedure based on the decomposition of the 3D task has been adopted. The proposed method is much faster (even up to five times) than the standard codes based on the ICCG algorithm.

2. Iterative procedure for 3D magnetic field calculation

The magnetic vector potential (MVP) for 3D magnetic field description has been employed (Demerdash *et al.*, 1981; Preis *et al.*, 1990). In a non-homogeneous environment, the MVP distribution is described by the following equation:

$$\operatorname{curl} \nu \operatorname{curl} \boldsymbol{A} = \boldsymbol{J} \tag{1}$$

where $\boldsymbol{J}$ is the current density vector, ν is the reluctivity.

After imposing the Coulomb's gauge $\operatorname{div} \boldsymbol{A} = 0$, the components of vector equation (1) can be written as:

$$\operatorname{div}(\nu \operatorname{grad} A_u) = -J_u + \operatorname{grad} \nu \cdot \frac{\partial \boldsymbol{A}}{\partial u} \tag{2}$$

where $u = x, y, z$. In spite of the Coulomb's gauge, in non-homogeneous areas the magnetic vector potential components are associated with one another. Therefore, the formulation without gauging has been applied (Biro *et al.*, 1996).

The problem becomes more complicated in the case of anisotropic material. Assuming orthogonal anisotropy, the x-component of equation (1) takes the following form:

$$\frac{\partial}{\partial y}\left(\nu_z \frac{\partial A_x}{\partial y}\right) + \frac{\partial}{\partial z}\left(\nu_y \frac{\partial A_x}{\partial z}\right) = -J_x + \frac{\partial}{\partial y}\left(\nu_z \frac{\partial A_y}{\partial x}\right) + \frac{\partial}{\partial z}\left(\nu_y \frac{\partial A_z}{\partial x}\right) \tag{3}$$

where ν_y and ν_z are the reluctivities in y and z directions.

Numerical implementation of the algorithm is based on the spatial finite element method. A special block-relaxation algorithm has been proposed. In the algorithm, the 3D task has been decomposed and substituted with a sequence of "quasi-2D" problems (Nowak, 1995). Decomposition consists of apparent separation of the vector potential components and space division into layers. Mutual connections between vector potential components are considered iteratively. The division into layers is performed using n_{s} surfaces. On each surface discretization is two-dimensional, with triangle elements constituting the bases of the prism located between two adjoining surfaces (Figure 1).

The elements of the stiffness matrix of the FEM equations $\mathbf{SA} = \mathbf{VJ}$ concerning the MVP can be arranged into $3n_{\mathrm{s}} \times 3n_{\mathrm{s}}$ sub-matrices $\mathbf{S}_{uw}^{pq}$, which describe connections

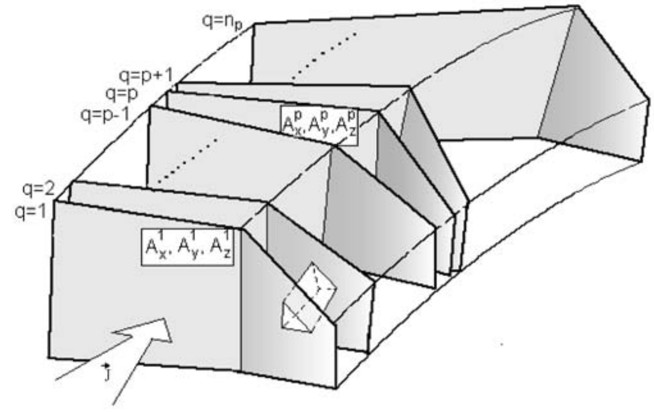

Figure 1.
Space division

between the uth and wth MVP components in pth and qth surfaces ($q = p-1, p, p+1$) (Nowak, 1995). The *basic* iterative block relaxation formula can be written in the following form:

$$\mathbf{S}_{uu}^{pp}\left(\mathbf{A}_u^p\right)_{m_A} = \mathbf{V}_u^p\mathbf{J}_u^p - \sum_{q=p-1}^{q=p+1}\sum_{w=x,y,z}\mathbf{S}_{uw}^{pq}\left\{\omega\left(\mathbf{A}_w^q\right)_l + (1-\omega)\left(\mathbf{A}_w^q\right)_{l-1}\right\} \tag{4}$$

where $\omega \in \langle 1, 2\rangle$ is the convergence coefficient, m is the iteration number, $l = m$ or $l = m-1$. Equation (4) makes it possible to calculate $\left(\mathbf{A}_u^p\right)_m$, i.e. the uth MVP component in the pth surface in the mth *basic* iteration. There are $3n_s$ such equations. To solve equation (4) for each component and each surface, Cholesky's non-iterative method has been applied.

The structure of system (4) corresponds to the structure of differential equations (2) and (3). The first term on the right-hand side of equation (4) represents the field sources. The remaining terms are known from the current or previous iteration (Nowak, 1995).

In order to improve the convergence of the iterative process, the division into layers should be carried out by surfaces possibly perpendicular to the direction of the predominant component of the potential A. Owing to core lamination, the magnetic field in the region of core length in the transformer is nearly two-dimensional with the domination of component A_z perpendicular to the sheets plane (Figure 2). The division into layers should be performed by planes $z =$ const.

3. Non-linearity

The algorithm consists of two iterative procedures: the *basic* procedure for the solution of the sequence of 2D problems, and the *superior* procedure taking *non-linearity* into consideration. The "chord" iterative process has been adopted. In the case of transient states, an additional time-stepping process has been applied.

In the non-linear case, sub-matrices $\mathbf{S}_{uw}^{pq}$ must be computed at each *non-linear* iteration. In such a case, computer time consumption depends, to a high extent, on the procedures of stiffness matrix formation. Therefore, each of sub-matrices $\mathbf{S}_{uw}^{pq}$ is

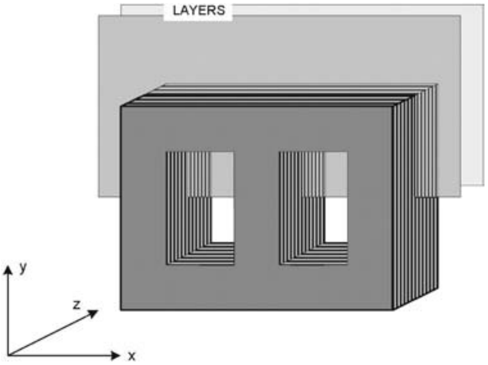

Figure 2.
The transformer core division into layers

represented as a sum of several contributory sub-matrices. The elements of the *i*th row of these constituents represent contributions from all prisms with common node Q_i. The contributory sub-matrices are computed only once at the beginning of iterative calculations, assuming reluctivity $\nu_x = \nu_y = \nu_z = \nu_0$, and they are stored in this form in computer memory. Consequently, the time-consuming process of sub-matrices $\mathbf{S}_{uw}^{pq}$ formation is, with each iteration, replaced with the simple operation of summing the contributions. This reduces the computation time considerably (Nowak, 1995).

4. Electric circuit equations

After the application of the Cranck-Nicolson scheme, Kirchhoff's equation describing the *i*th winding at the *n*th instant can be written in the following discrete form (Nowak and Kowalski, 1996):

$$\psi_{i,n} - \psi_{i,n-1} + 0.5\Delta t R_i i_i = 0.5\Delta t\left(u_i + \left.\frac{\mathrm{d}\psi}{\mathrm{d}t}\right|_{n-1}\right); \quad i = 1, 2, 3 \tag{5}$$

where R_i is the resistance and ψ_i is the flux linkage.

Since the problem is linearized at separate *non-linear* iterations, the principle of superposition can be adopted. Let vector $\mathbf{A}_{j0}$ denotes the MVP distribution generated from the provisionally assumed sample current i_0 in the *j*th winding, while the currents in the remaining windings are equal to zero, and let ψ_{ij0} denotes the magnetic flux linked with *i*th winding coming from current i_0 in the *j*th winding. Then, the total *i*th magnetic linkage can be expressed as follows:

$$\psi_i = \sum_{j=1}^{3} \lambda_j \psi_{ij0} \tag{6}$$

where λ_j is the ratio of real (unknown) current i_j in the *j*th winding to the sample current i_0. Finally, the system of Kirchhoff's equation can be written in the following form:

$$\sum_{j=1}^{3} \lambda_j \psi_{ij0} + \lambda_i 0.5\Delta t R_i i_0 = \psi_{i,n-1} + 0.5\Delta t\left(u_i + \left.\frac{\mathrm{d}\psi}{\mathrm{d}t}\right|_{n-1}\right) \tag{7}$$

After solving equation (7) with respect to λ_j, the MVP global distribution at the nth time step and kth iteration can be found

$$\mathbf{A}_n = \sum_{j=1}^{3} \lambda_j \mathbf{A}_{j0} \tag{8}$$

In the linear case, three contributory distributions $\mathbf{A}_{j0}$ and nine contributory fluxes ψ_{ij0} have to be found but only at the first time-step. At the next time-steps the field calculations are not necessary. The procedure corresponds to the equivalent circuit method with self-inductances and mutual inductances.

The task becomes more intricate in the non-linear case. During the transient state the reluctances of the individual parts of the transformer core vary at successive time-steps and, as a result, the set of stiffness sub-matrices $\mathbf{S}^{pq}_{uw}$ also changes. The contributory distributions $\mathbf{A}^k_{i0,n}$ must be computed at each time-step and even at each *non-linear* iteration. In the algorithm, the real values of currents are also calculated iteratively. After computing contributory distributions $\mathbf{A}^k_{i0,n}$, the set of Kirchhoff's equations is solved and coefficients λ^k_{jn}, i.e. currents $i^k_{jn} = \lambda^k_{jn} i_0$ are determined. Next, using equations (6) and (8), the fluxes ψ^k_{in} and the field distribution $\mathbf{A}^k_n$, are computed. Finally, the distribution of the magnetic flux density and reluctivities of individual spatial finite elements are calculated.

At successive *non-linear* iterative steps, the field sources are constant corresponding to sample currents i_0 in separate windings. Therefore, the field distributions $\mathbf{A}^k_{i0,n}$ at successive time steps, and especially at successive *non-linear* iterations, are very close to one another. Thus, it is very convenient to assume the field distributions from the previous *non-linear* iteration to be the initial approximation of the *basic* iterative procedure, i.e.:

$$\left(\mathbf{A}^k_{j0,n}\right)_{m=0} = \mathbf{A}^{k-1}_{j0,n} \tag{9}$$

where m is the number of block iterations. This significantly decreases the number of *basic* iterations (Nowak and Kowalski, 1996).

5. Transformer transients

A transformer of power $S_n = 160\,\mathrm{kV\,A}$ and voltage $U_n = 20/0.525\,\mathrm{kV}$ on no-load operation has been investigated. The transient state after the application of the supply symmetric voltage system:

$$u_j(t) = \sqrt{2/3}U \sin(100\pi t + 2\pi/3(j-2) + \varphi_u)$$

has been considered. Here, j denotes the number of windings and at the same time – the number of transformer limbs (the central limb is the second one). This case corresponds to delta connected or zero-star connected windings.

Zero-boundary conditions: $A_{xB} = A_{yB} = A_{yB} = 0$ have been assumed. The boundary surfaces in the proper distance from the transformer have been chosen. Owing to symmetry, only the half of the transformer has been considered. The origin of the coordinate system is situated on the symmetry plane $z = \text{const.}$, which overlap the central sheet of the core. The conditions on this initial plane ($z = 0$) are:

$$A_x = A_y = 0; \quad \partial A_z/\partial n = \partial A_z/\partial z = 0.$$

Figure 3(a) and (b) shows the current waveforms after the application of the voltage $U = 0.3U_n$ (the phase angle $\varphi_u = 0$), where $U_n = 20\,\mathrm{kV}$ is the rated value. The computations have been carried out using the 3D model (case "a") and next using the 2D description (case "b"). In both 3D and 2D models, the discretization remains unchanged. In the case of the two-dimensional model, the computation has been performed using formula (4), but only for $u = z$ and only for one chosen surface $z = \text{const.}$ which includes a ferromagnetic core. The second term on the right-hand side of equation (4) has been disregarded. The equivalent length of the 2D model is therefore equal to the core thickness.

The corresponding current waveforms for higher voltage $U = 0.8U_n$, are shown in Figure 4(a) and (b).

The peak values of transient currents depend strongly on the supply voltage. For $U = 0.3U_n$, the peak value of current $i_{2\max}$ is equal to 0.10 A for the 3D model and 0.12 A for the 2D model. Assuming $U = 0.8U_n$, one obtains $i_{2\max} = 40.7$ A for the 3D model and $i_{2\max} = 69.2$ A for the 2D description.

Owing to the core saturation, in the case of voltage $0.8U_n$ the currents are hundred times greater. It goes without saying that the peak value depends on the voltage phase

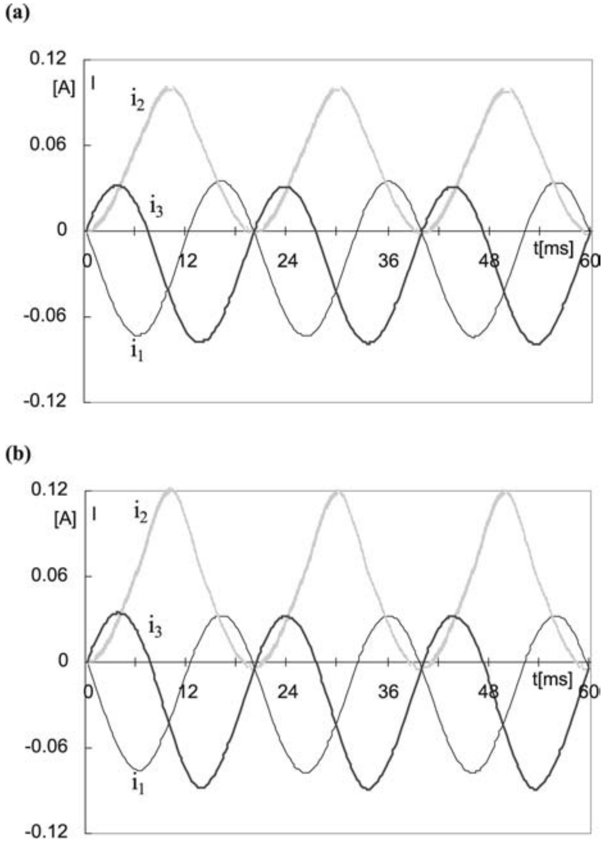

Figure 3.
Current waveform after the application of supply voltage $U = 0.3U_n$, $\varphi_u = 0$, for: (a) 3D and (b) 2D models

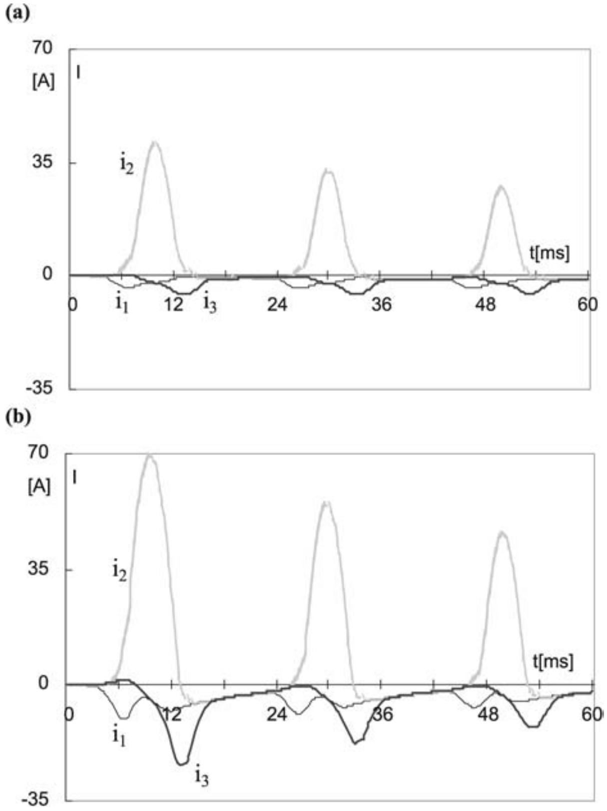

Figure 4.
Current waveform after the application of supply voltage $U = 0.8U_n$, $\varphi_u=0$, for: (a) 3D and (b) 2D models

angle. For $\varphi_u = \pi/2$ ($U = 0.8U_n$, 3D model) the current $i_{2\max}$ decreases to a small value of 2.29 A. The greatest peak value of current occurs in the first winding: $i_{1\max} = -30.7$ A (Figure 5).

The most unfavourable condition occurs for $\varphi_u = 2\pi/3$ (Figure 6). In this case, $u_3(0) = 0$, while in the case presented in Figure 4(a), the voltage $u_2(0) = 0$. The peak

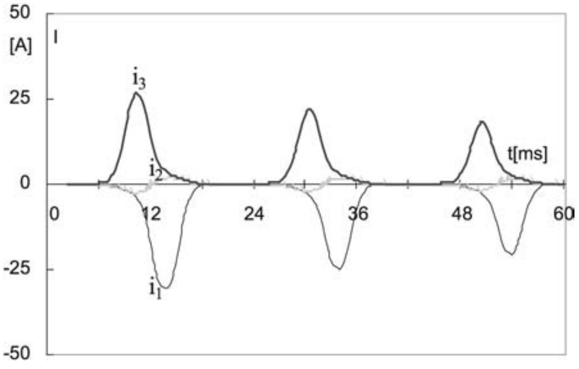

Figure 5.
Current waveform after the application of supply voltage $U = 0.8U_n$, for $\varphi_u = \pi/2$ (3D model)

value is greater and equal to $i_{3\max} = 43.4$ A. The difference stems from the asymmetry of the transformer core; the central winding is linked to a greater flux than the side ones.

In order to validate the proposed algorithm, the measured waveform of the current $i_3(t)$ has been shown in Figure 6. Both waveforms, the calculated and the measured, nearly overlap.

As noticed, the peak values of transient currents depend strongly on the supply voltage. Figure 7 shows the peak value $i_{2\max}$ versus the voltage U/U_n, for 2D and 3D models, assuming the angle $\varphi_u = 0$. The difference $\Delta i_{2\max}$ between the results obtained in 2D and 3D models also depends on the supply voltage (Figure 8). This difference is slight for small values of voltage. In this case, the transformer core is not saturated and, therefore, the magnetic field outside the core is negligible. With the growth of voltage, the difference $\Delta i_{2\max}$ also increases. The core becomes saturated and a considerable magnetic field occurs in the space outside the core. The field becomes three-dimensional (Figure 9). The two-dimensional model does not ensure sufficient accuracy. The incorrectness reaches (for $U = 0.6U_n$) a value of up to 242 per cent.

For $U > 0.6U_n$, the difference between the peak values obtained in 2D and 3D models decreases as shown in Figure 8. For greater values of supply voltage, the transformer core becomes temporarily and strongly saturated during the transients.

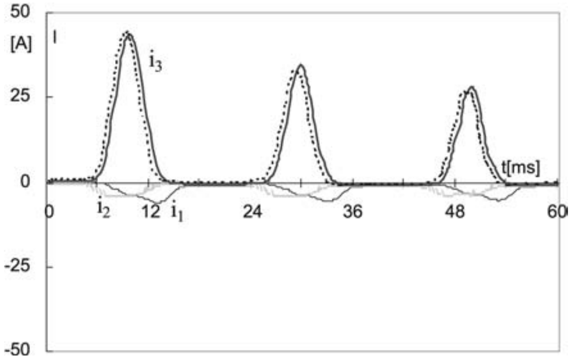

Figure 6.
Current waveform after the application of supply voltage $U = 0.8U_n$, for $\varphi_u = 2\pi/3$ (3D model)

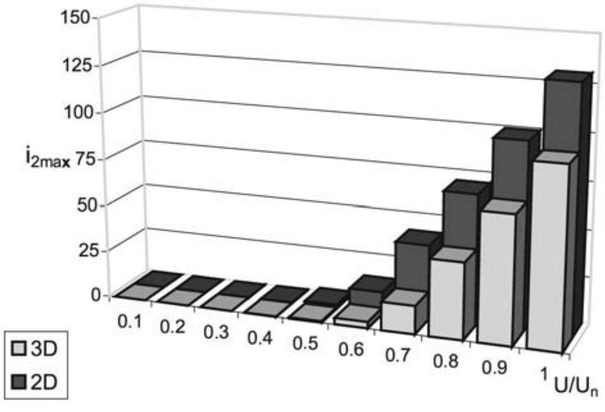

Figure 7.
Peak value $i_{2\max}$ obtained in 2D and 3D models

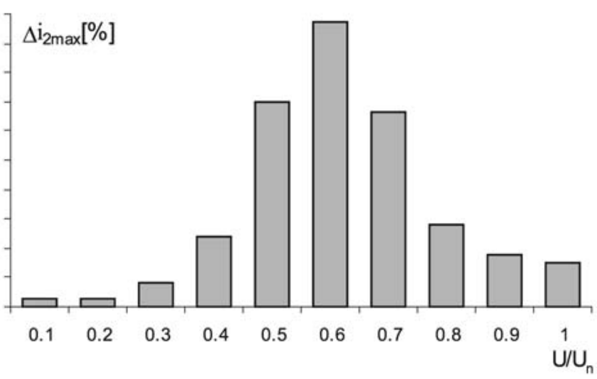

Figure 8.
The difference between 2D and 3D results

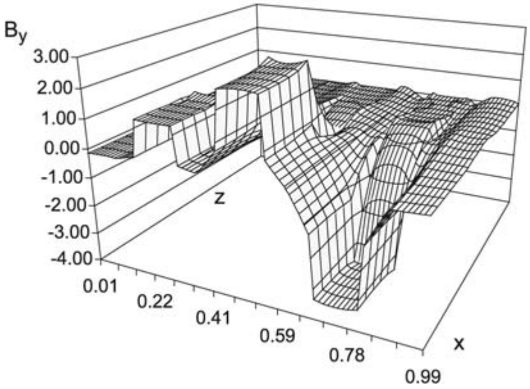

Figure 9.
Magnetic flux distribution in the transformer

The instantaneous inductances reach very small values and the winding resistances dominate. The inaccuracy of the field computation is of less importance.

Figure 9 shows the distribution $B_y(x,z)$ of the y-component of the magnetic flux density (component parallel to the limb axes) in the plane $y = \text{const.}$ crossing the limbs perpendicularly in the middle. Three-dimensionality of the magnetic field can be observed.

6. Conclusions

The elaborated algorithm and computer code can be an effective tool for transient analyses of electromagnetic devices. It enables analyses of the voltage-excited, three-dimensional magnetic field taking the non-linearity and anisotropy of ferromagnetic cores into consideration. The proposed algorithm, after introducing the electric potential, may be successfully extended to include currents in massive parts of the device.

It has been shown that a two-dimensional model of the transient electromagnetic phenomena in a power transformer does not ensure sufficient accuracy. The difference between peak values of transient winding currents obtained by using 2D and 3D models can reach hundreds of percents.

References

Biro, O., Preis, K. and Richter, K.R. (1996), "On the use the magnetic vector potential in the nodal and edge finite element analysis of 3D magnetostatic problem", *IEEE Transactions on Magnetics*, Vol. 32 No. 3, pp. 651-4.

Demerdash, N.A., Nehl, T., Fouad, F.A. and Mohammed, O.A. (1981), "Three dimensional finite element vector potential formulation of magnetic fields in electrical apparatus", *IEEE Transactions on Power Apparatus and Systems*, Vol. 100 No. 8, pp. 4104-22.

Nowak, L. (1995), "Iterative procedure for 3D modelling of electromagnetic actuators", *IEEE Transactions on Magnetics*, Vol. 31 No. 3, pp. 1428-31.

Nowak, L. and Kowalski, K. (1996), "The 3D coupled field-circuit simulation of transients in non-linear systems", *IEEE Transactions on Magnetics*, Vol. 32 No. 3, pp. 1078-81.

Preis, K., Biro, O., Magele, C., Renhart, K.R. and Vrisk (1990), "FEM analysis of 3D magnetostatic fields", *Proc. of 4-th International IGTE Symposium*, *Graz, Austria*, pp. 195-204.

The Emerald Research Register for this journal is available at
www.emeraldinsight.com/researchregister

The current issue and full text archive of this journal is available at
www.emeraldinsight.com/0332-1649.htm

Received September 2002
Revised June 2003
Accepted June 2003

Calculation of magnetization characteristic of a squirrel cage machine using edge element method

Andrzej Demenko, Lech Nowak and Wojciech Pietrowski
Institute of Industrial Electrical Engineering,
Poznań University of Technology, Poznań, Poland

Keywords *Finite element methods, Inductance, Electromotive force, Nonlinear magnetic circuit*

Abstract *This paper presents the finite element method for the calculation of open-circuit characteristic of a squirrel cage machine with saturated core. The flux linkage with the stator winding and the winding inductances have been calculated using the edge element method. The calculations show that the equivalent inductance of a balanced three-phase no-loaded induction machine with saturated core may be defined like a quadrature-axis inductance in synchronous machine. The algorithm of this inductance calculation has been proposed. The equivalent inductances have been used in the calculation of electromotive force. The results obtained from numerical calculations have been compared with the measured results.*

1. Introduction

The development of numerical techniques and growth of computer capacities make it possible to apply the method of 3D field simulation to the analysis of induction motor performance. Recently, the coupled field-circuit formulations are developed (Matsubara *et al.*, 1995; Piriou and Razek, 1990; Williamson, 1994). The coupled field-circuit model includes the field and circuit equations which describe the windings connections and the supply system. Moreover, in the analysis of electromechanical transients, these equations are coupled through the electromagnetic torque to the equation of motion (Demenko, 1999; Demenko and Nowak, 1996).

The coupled field-circuit formulation can be successfully applied in the calculation of open-circuits characteristics. In the open-circuit test, the magnetic field is voltage-excited, and this means that in the machine with saturated core, the winding currents are not known in advance, i.e. prior to the calculation of field distribution. Therefore, the Kirchhoff's equations for stator winding should be included and the time-stepping method should be applied.

A significant disadvantage of the field-circuit formulation is that it takes two or more orders of magnitude more CPU time than the algorithm for solving the finite element equations only. In order to reduce the computation time, the authors propose to

---

This is a revised and enhanced version of a paper which was originally presented as a conference contribution at the *XVII Symposium on Electromagnetic Phenomena in Nonlinear Circuits (EPNC)*, held in Leuven, Belgium, on 1-3 July 2002. This is one of a small selection of papers from the Symposium to appear in the current and future issues of *COMPEL*.

COMPEL: The International Journal for Computation and Mathematics in Electrical and Electronic Engineering
Vol. 23 No. 4, 2004
pp. 1110-1118
© Emerald Group Publishing Limited
0332-1649
DOI 10.1108/03321640410510820

apply the simplified method of magnetization characteristic calculation. The characteristic is formed on the basis of the solution of finite element equations for the given values of stator winding currents.

2. Edge element model

The applied edge element model of a squirrel cage machine is similar to that presented in Demenko (1999).

The rotor of the considered machine has skewed slots. Therefore, the machine is cut into m disks (sections) along the z axis parallel to the shaft. Each of the section shows the rotor in a different position with respect to the stator. The sections are divided into nine-edge prisms and 12-edge curved rectangular parallelepipeds. The trace of the elements in the x, y-plane is a grid with triangles and curved rectangles.

The edge element equations have been written as follows

$$\boldsymbol{k}_e^{\mathrm{T}} \boldsymbol{S} \boldsymbol{k}_e \boldsymbol{\varphi} = \boldsymbol{\theta}, \tag{1}$$

where $\boldsymbol{S}$ is the reluctance matrix for facet elements, $\boldsymbol{\varphi}$ is the vector of edge values of $\boldsymbol{A}$, and the matrix $\boldsymbol{k}_e$ transforms the edge values of $\boldsymbol{A}$ into the facet values of flux density $\boldsymbol{B}$. The entries of $\boldsymbol{k}_e$ are equal to 1, 0 or -1, and depend on the position of the edges in relation to the facet. The matrix $\boldsymbol{k}_e$ is the discrete form of *curl* operator (Bossavit, 1988). For the three-phase system of phase currents i_1, i_2, i_3 the right side vector $\boldsymbol{\theta}$ may be defined as follows

$$\boldsymbol{\theta} = [\boldsymbol{N}_1 \quad \boldsymbol{N}_2 \quad \boldsymbol{N}_3] \begin{bmatrix} i_1 \\ i_2 \\ i_3 \end{bmatrix}, \tag{2}$$

where the vector $\boldsymbol{N}_u$ $(u = 1, 2, 3)$ transforms the phase current i_u into the ampere-turns associated with the edges (Bouissou and Piriou, 1994).

The formulation of the vector $\boldsymbol{N}_u$ has strong effect on the convergence of the iteration procedure of solving equation (1) for the ungauged edge element approach. In order to obtain good convergence, the discrete form of the current continuity equation should be exactly satisfied, i.e. the entries of the product $\boldsymbol{G}^{\mathrm{T}}\boldsymbol{N}_u$ should be exactly equal to zero, where $\boldsymbol{G}^{\mathrm{T}}$ is the discrete form of *div* operator in relation to the nodes of the conjoint set of elements (Ren, 1996). To satisfy this condition the source terms are usually expressed by the edge values of current vector potential $\boldsymbol{T}$. These edge values represent the loop currents that flow in the closed paths around the edges. Here, the source terms are also calculated on the basis of the loop currents. The method presented in Demenko *et al.* (2001) has been applied. The vector $\boldsymbol{N}_u$ can be used in the calculations of flux linkage with the phase winding. The flux linkage with the uth phase may be found from the expression

$$\psi_u = \boldsymbol{N}_u^{\mathrm{T}} \boldsymbol{\varphi}, \tag{3}$$

which is the numerical representation of line integral $\int \boldsymbol{A}\, \mathrm{d}\boldsymbol{l}$ along the loop which defines the phase winding.

3. Calculation of stator winding inductances

The stator winding inductance $L_{u,v}$ has been defined as follows

$$L_{u,v} = \frac{\psi_v}{i_u}. \tag{4}$$

Here, ψ_v is the flux linkage with the vth phase winding for the system which is excited by the uth phase current i_u,

$$\psi_v = \boldsymbol{N}_v^{\mathrm{T}} \boldsymbol{\varphi}_u, \tag{5}$$

where $\boldsymbol{\varphi}_u$ is the solution of equation (1) for $\boldsymbol{\theta} = \boldsymbol{\theta}_u = \boldsymbol{N}_u i_u$. If the inductances are affected by saturation then $L_{u,v} = L_{u,v}(i_1, i_2, i_3)$, and we must solve equation (1) twice. First, we solve non-linear edge element equations,

$$\boldsymbol{k}_e^{\mathrm{T}} [\boldsymbol{S}(\boldsymbol{\varphi})] \boldsymbol{k}_e \boldsymbol{\varphi} = \boldsymbol{N}_1 i_1 + \boldsymbol{N}_2 i_2 + \boldsymbol{N}_3 i_3, \tag{6}$$

and we determine reluctance matrix $\boldsymbol{S}(\boldsymbol{\varphi})$. Then the linear edge element equations of $\boldsymbol{S} = \boldsymbol{S}(\boldsymbol{\varphi})$ are solved,

$$\boldsymbol{k}_e^{\mathrm{T}} [\boldsymbol{S}(\boldsymbol{\varphi})] \boldsymbol{k}_e \boldsymbol{\varphi}_u = \boldsymbol{N}_u i_u. \tag{7}$$

It has been assumed that the phase currents i_u are sinusoidal, i.e.

$$i_u = I_s \sqrt{2} \sin\left(\omega t - (u-1)\frac{2}{3}\pi\right), \quad (u = 1, 2, 3), \tag{8}$$

where I_s is the rms value of phase current. As a result, the inductance $L_{u,v}$ has been expressed as a function of ωt and I_s, i.e. $L_{u,v} = L_{u,v}(I_s, \omega t)$.

The calculations have been performed for $\omega t = k\pi/252$ ($k = 1, 2, 3, \ldots, 504$) and for different values of I_s. Figure 1 shows the calculated waveforms of self inductance $L_{1,1}$, however Figure 2 shows the calculated waveforms of mutual inductance $L_{2,3}$, for all considered values of the amplitude of current.

The results presented in these figures show that the considered functions can be approximated by Fourier series of the following form

$$L_{u,u} = \sum_{k=0,1,2,\ldots} L_{2k}(I_s) \cos 2k\left(\omega t - (u-1)\frac{2}{3}\pi\right) \quad (u = 1, 2, 3), \tag{9a}$$

$$L_{2,3} = \sum_{k=0,1,2,\ldots} M_{2k}(I_s) \cos 2k(\omega t), \tag{9b}$$

$$L_{1,3} = \sum_{k=0,1,2,\ldots} M_{2k}(I_s) \cos 2k\left(\omega t - \frac{2}{3}\pi\right), \tag{9c}$$

$$L_{1,2} = \sum_{k=0,1,2,\ldots} M_{2k}(I_s) \cos 2k\left(\omega t - \frac{4}{3}\pi\right). \tag{9d}$$

Here, L_{2k} and M_{2k}, are the amplitudes of the kth harmonic. The values of the amplitudes depend on the value of I_s, i.e. $L_{2k} = L_{2k}(I_s)$ and $M_{2k} = M_{2k}(I_s)$ (Figure 3).

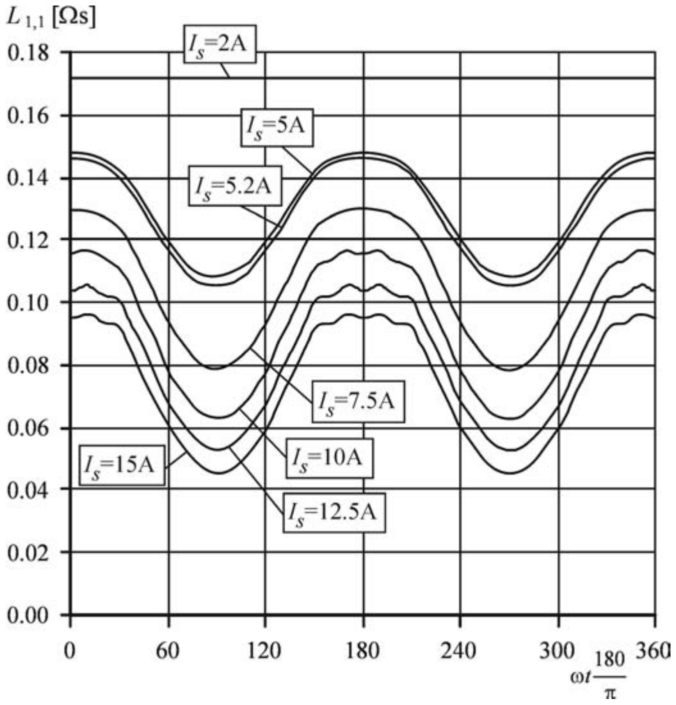

Figure 1.
Self inductance $L_{1,1}$ as a function of ωt

It is interesting to notice that the presented functions are similar to functions which describe the inductances of armature winding in synchronous machine with salient poles (Jones, 1967).

4. Electromotive force

The inductances described earlier can be used in the calculation of flux linkage with the uth phase winding,

$$\psi_u = \sum_{v=1}^{3} L_{u,v} i_v. \tag{10}$$

From this relation, using equations (8) and (9), we obtain

$$\begin{aligned}\psi_u = \Bigg\{ &\sum_{k=0,1,2\ldots} \left[\frac{1}{2}L_{2k} + M_{2k}\cos\left(\frac{2}{3}\pi(2k-1)\right)\right]\sin(2k+1)\left(\omega t - \frac{2}{3}\pi(u-1)\right) \\ &- \sum_{k=0,1,2\ldots} \left[\frac{1}{2}L_{2k} + M_{2k}\cos\left(\frac{2}{3}\pi(2k+1)\right)\right] \\ &\times \sin(2k-1)\left(\omega t - \frac{2}{3}\pi(u-1)\right)\Bigg\}\sqrt{2}I_s\end{aligned} \tag{11}$$

Let us consider the first harmonic of $\psi_u(\omega t)$. The amplitude of this harmonic is

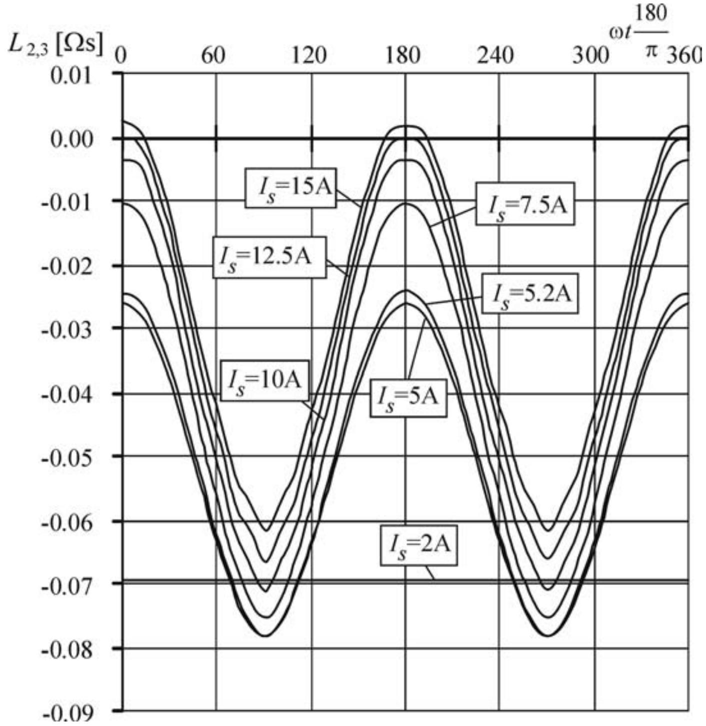

Figure 2.
Mutual inductance $L_{2,3}$ as a function of ωt

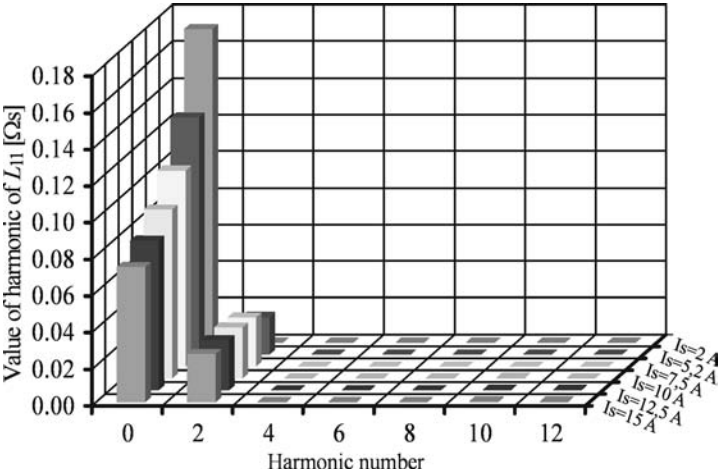

Figure 3.
Amplitudes of harmonics of $L_{11}(\omega t)$

$$\psi_{um} = \sqrt{2} I_s L_q, \tag{12a}$$

where

$$L_q = L_0 - M_0 - \frac{1}{2} L_2 - M_2. \tag{12b}$$

The equivalent inductance in equation (12) is defined similar to the quadrature-axis inductance of an armature winding in reluctance machine. Therefore, we have applied the theory of reluctance machine to explain the model of no-loaded induction machine. The no-loaded induction machine with the core affected by saturation may be represented by reluctance machine which operates with torque angle equal to $\pi/2$ (Figure 4). The difference between the direct-axis and quadrature-axis inductance depends on the rms value of phase current. If this value is small, the rotor of equivalent reluctance machine is cylindrical (case "a" in Figure 4).

The rms value of electromotive force in the stator winding of equivalent machine is defined as follows

$$E_s = I_s \omega L_q = I_s X_q. \tag{13}$$

Thus, if we determine the inductance L_q we can calculate the electromotive force. The inductance L_q is expressed in terms of two components of functions $L_{u,v}(\omega t)$.

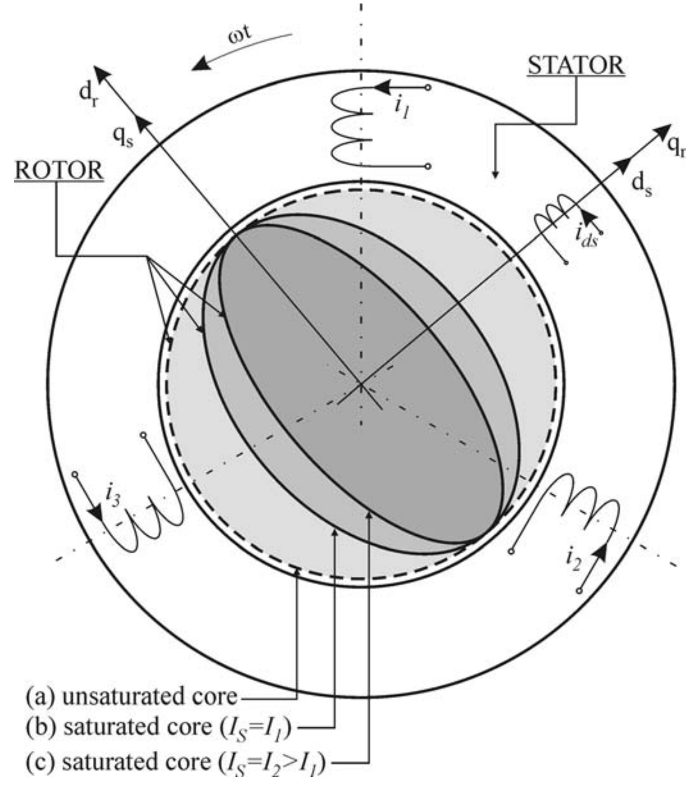

Figure 4.
Equivalent reluctance motor

The trigonometric approximation of $L_{u,v}(\omega t)$ on the three data points ($\omega t_1 = 0$, $\omega t_2 = \pi/4$, $\omega t_3 = \pi/2$) gives us these components. As a result, we obtain the following formula

$$L_q = \frac{1}{12}\left(L_{1,1}^{(1)} + 4L_{1,1}^{(2)} + 7L_{1,1}^{(3)}\right) - \frac{1}{6}\left(5L_{2,3}^{(1)} + 2L_{2,3}^{(2)} - L_{2,3}^{(3)}\right), \tag{14}$$

where $L_{u,v}^{(i)}$ are the values of inductance $L_{u,v}$ for $i_u = i_u(I_s, \omega t_i) = I_s\sqrt{2}\sin\left(\omega t_i - \frac{2}{3}(u-1)\pi\right)$, $(u = 1, 2, 3)$ ($\omega t_1 = 0$, $\omega t_2 = \pi/4$, $\omega t_3 = \pi/2$).

5. Results

The presented method has been successfully applied for the calculation of the magnetization characteristic of a squirrel cage motor. The three-phase, four-pole, 3 kW machine of Sg 100L-4B type has been considered. The rated data of the motor are: $U_N = 220/380\,\mathrm{V}\ (\Delta/\mathrm{Y})$; $f_N = 50\,\mathrm{Hz}$; $I_N = 12.0/6.9\,\mathrm{A}$; $n_N = 1{,}415\,\mathrm{rpm}$. The winding data are as follows: 36 stator slots, 28 rotor slots, single-layer stator winding. The cross-section of the machine may be found in Demenko and Nowak (1996). Table I shows the results of reactance X_q calculation. The results for approximation on the 504 and three data points have been compared.

The rms value of electromotive force can be obtained from equation (13), using the data in Table I. For example, if $I_s = 5.2\,\mathrm{A}$ then $E_s = 229.42\,\mathrm{V}$ (for three data points) $E_s = 229.48\,\mathrm{V}$ (using 504 data points). The resistance of stator winding is $2.27\,\Omega$. Thus, the calculated value of line voltage is $U = \sqrt{3}\,229.72\,\mathrm{V}$ (for three data points) at $I_s = 5.2\,\mathrm{A}$.

We have also considered the field-circuit formulation presented in Demenko (1999). This formulation can be successfully used in the calculations of current waveforms for no-load test, i.e. when three-phase balanced voltage is applied to the stator and the machine is allowed to run with synchronous speed. However, a disadvantage in using the field-circuit formulation is that it takes more computer time. In order to obtain the results for steady state we must analyse the transients.

The calculations have been performed for the stator winding connected in star and for the rms value of line voltages U equal to $\sqrt{3}\,230\,\mathrm{V}$ at rated frequency. We obtained $I_s = 5.21\,\mathrm{A}$ and $E_s = 229.69\,\mathrm{V}$. The measured rms value of magnetizing current at $U = \sqrt{3}\,230\,\mathrm{V}$ is equal to 5.18 A. Thus, for the considered point of magnetization characteristic we obtained:

1. $U = \sqrt{3}\,230\,\mathrm{V}$ and $I_s = 5.18\,\mathrm{A}$ from measurement;
2. $U = \sqrt{3}\,230\,\mathrm{V}$ and $I_s = 5.21\,\mathrm{A}$ from the calculation using the field-circuit formulation; and
3. $U = \sqrt{3}\,229.72\,\mathrm{V}$, $I_s = 5.2\,\mathrm{A}$ from the calculation using the proposed method.

The results presented earlier are related to the first harmonic of calculated waveforms. However, if the stator winding currents are sinusoidal then the electromotive force

Table I.
Calculated values of reactance X_q

I_s (A)	2.0	5.2	7.5	10.0	12.5	15.0
X_q (Ω) – 504 data	71.51	44.13	32.56	25.59	21.23	18.25
X_q (Ω) – three data	71.52	44.12	32.51	25.54	21.19	18.21

waveform contains high harmonics, due to the saturation. Figure 5 shows the calculated waveform of electromotive force with all harmonics given by series (11). It can be seen that the waveform is deformed by harmonics. However, the calculations show that the rms value of the presented poliharmonic waveform is very close to the rms value of its first harmonic.

The relative differences between the rms values have been defined by factor k_h; $k_h = E_{\mathrm{shar}}/E_s$, where E_{shar} is the rms value of electromotive force waveform with the high harmonics. The calculated values of k_h are as follows: $k_h = 1.0035$ for $I_s = 5.2\,\mathrm{A}$; $k_h = 1.0042$ for $I_s = 10.0\,A$, $k_h = 1.0038$ for $I_s = 12.5\,\mathrm{A}$, $k_h = 1.0033$ for $I_s = 15.0\,\mathrm{A}$.

Thus, the rms value of the electromotive force waveform may be determined by the rms value of its first harmonic.

6. Conclusions

This paper shows that the magnetizing characteristic of an induction machine can be successfully calculated using the standard package for edge element method. In order to obtain one point of this characteristic, we should solve the edge element equations for three instantaneous values of phase currents, i.e. for $i_u = I_s\sqrt{2}\sin(2(1-u)\pi/3)$, $i_u = I_s\sqrt{2}\sin(\pi/4 + 2(1-u)\pi/3)$ $i_u = I_s\sqrt{2}\sin\ (\pi/2 + 2(1-u)\pi/3)$ $(u = 1, 2, 3)$.

It is interesting to notice that the no-loaded induction machine with the core affected by saturation may be represented by reluctance machine which operates with torque angle equal to $\pi/2$. The magnetizing inductance of the saturated induction machine may be defined similar to the quadrature-axis inductance of an armature winding of reluctance machine. The presented model with quadrature-axis inductance X_q can be

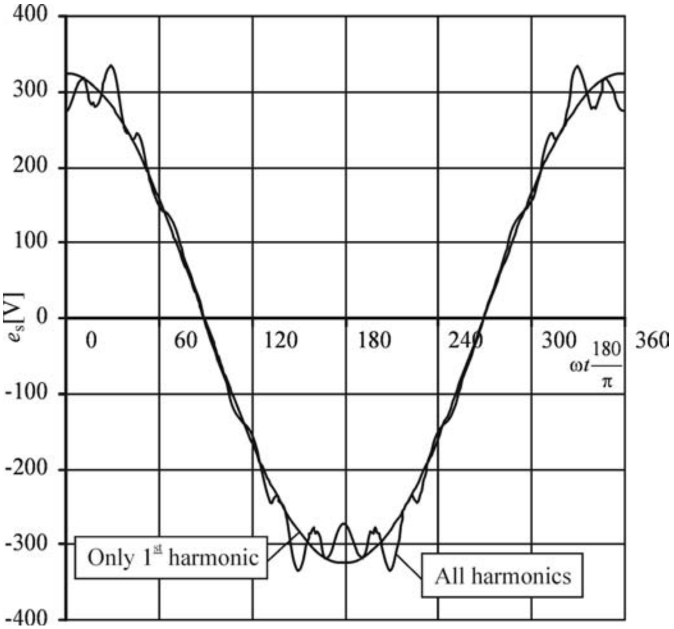

Figure 5.
Calculated waveforms of electromotive force, I_s=5.2 A

used in the analysis of all type of asynchronous and synchronous machines with non-salient rotor.

References

Bossavit, A. (1988), "A rational for edge elements in 3D fields computations", *IEEE Trans. Magn.*, Vol. 24 No. 1, pp. 74-9.

Bouissou, S. and Piriou, F. (1994), "Study of 3D formulations of model electromagnetic devices", *IEEE Trans. Magn.*, Vol. 30 No. 5, pp. 3228-31.

Demenko, A. (1999), "Finite element analysis of electromagnetic torque saturation harmonics in a squirrel cage machine", *COMPEL*, Vol. 18 No. 4, pp. 619-28.

Demenko, A. and Nowak, L. (1996), "Finite element analysis of saturation effects in a squirrel cage electrical machine", *COMPEL*, Vol. 15 No. 5, pp. 89-96.

Demenko, A., Nowak, L. and Pietrowski, W. (2001), "Calculation of end-turn leakage inductances of electrical machines using the edge element method", *COMPEL*, Vol. 20, pp. 132-9.

Jones, Ch. (1967), *The Unified Theory of Electrical Machines*, Butterworth and Co. (Publishers) LTD, London.

Matsubara, T., Ishihara, Y., Kitamura, S. and Inoue, Y. (1995), "Magnetic field analysis in shaded pole motor taking skewed slots effects into account", *IEEE Trans. Magn.*, Vol. 31 No. 3, pp. 1916-9.

Piriou, F. and Razek, A. (1990), "A model for coupled magnetic-electric circuits in electric machines with skewed slots", *IEEE Trans. Magn.*, Vol. 26 No. 2, pp. 1096-100.

Ren, Z. (1996), "Influence of R.H.S. on the convergence behaviour of the curl-curl equation", *IEEE Trans. Magn.*, Vol. 32 No. 3, pp. 655-8.

Williamson, S. (1994), "Induction motor modelling using finite elements", *Proceedings of ICEM*, Vol. 1, pp. 1-8.

The Emerald Research Register for this journal is available at
www.emeraldinsight.com/researchregister

The current issue and full text archive of this journal is available at
www.emeraldinsight.com/0332-1649.htm

Edge element analysis of brushless motors with inhomogeneously magnetized permanent magnets

Dorota Stachowiak
Institute of Industrial Electrical Engineering, Poznań University of Technology, Poznań, Poland

Received September 2002
Revised March 2003
Accepted March 2003

Keywords *Edge element method, Brushless motors, Electromagnetic torque, Electromagnetics*

Abstract *This paper demonstrates how the 3D edge element method can be applied to the analysis of permanent magnet motors. The edge element method using the vector magnetic potential has been used. Special attention has been paid to the analysis of systems with inhomogeneously magnetized permanent magnets. The magnets are not skewed and are mounted on a cylindrical laminated rotor. Calculations have been performed for different magnet widths and different distribution of the magnetization vector. Brushless motors with radially and inhomogeneously magnetized magnets have been compared.*

1. Introduction

Among various configurations of PM brushless machines, two main groups are most commonly distinguished: motors with a trapezoidal back-emf, known as brushless DC (BLDC) motors, and motors in which the back-emf is approximately sinusoidal. The latter, known as brushless AC synchronous motors (PMSM) and usually applied in drives where smooth torque is highly desirable, are the subject of this study (Ishikawa and Slemon, 1993; Jahns and Soong, 1996). Any discrepancy from ideal conditions in either motor structure or associated power converter, typically gives rise to undesired torque pulsations. Sources of torque ripple are threefold: connected with the air-gap flux distortion from the target shape, cogging torque caused by the slotted structure of the armature, and commutation torque from the inductive effect of phase windings (Cai *et al.*, 2000). Optimal motor design requires a detailed analysis of torque.

The applications of the 3D edge element method for the analysis of permanent magnet motors are presented by Demenko (1998) and Kawase *et al.* (1995), where systems with homogeneously magnetized permanent magnets are analysed. The author of this paper has extended the application possibilities of the 3D edge element method by developing an algorithm for the analysis of machines with inhomogeneously magnetized permanent magnets. Systems with inhomogeneously magnetized permanent magnets are well known and have been widely studied (Cai *et al.*, 2000; Marinescu and Marinescu, 1992; Nogarede and Lojoie-Mazenc, 1991). However, these magnets have only been examined by means of a 2D method. The novelty of this

---

This is a revised and enhanced version of a paper which was originally presented as a conference contribution at the *XVII Symposium on Electromagnetic Phenomena in Nonlinear Circuits (EPNC)*, held in Leuven, Belgium, on 1-3 July 2002. This is one of a small selection of papers from the Symposium to appear in the current and future issues of *COMPEL*.

COMPEL: The International Journal for Computation and Mathematics in Electrical and Electronic Engineering
Vol. 23 No. 4, 2004
pp. 1119-1128
© Emerald Group Publishing Limited
0332-1649
DOI 10.1108/03321640410510839

paper lies in the algorithm for the analysis of electric machines with inhomogeneously magnetized permanent magnets by using a 3D method.

2. Edge element equations

In order to describe the distribution of the magnetic field, the edge element method using the vector magnetic potential $\boldsymbol{A}$ has been applied. The considered region is subdivided into edge elements and the field equations are approximated by algebraic equations with an unknown vector $\boldsymbol{\varphi}$ of the edge values of $\boldsymbol{A}$. These equations may be written in the following matrix form:

$$\boldsymbol{S}\boldsymbol{\varphi} = \boldsymbol{N}\boldsymbol{i} + \boldsymbol{F}, \tag{1}$$

where $\boldsymbol{S}$ is the stiffness matrix of the edge element model, $\boldsymbol{N}$ is the matrix that transforms the winding currents $\boldsymbol{i}$ into the ampere-turns associated with the edges, and $\boldsymbol{F}$ is the vector of magnetomotive forces in the permanent magnet region (Demenko, 2000).

The matrix $\boldsymbol{N}$ can be used in the calculations of flux linkage with a phase winding. The flux linkage with a three-phase system may be found from the expression:

$$\begin{bmatrix} \Psi_1 \\ \Psi_2 \\ \Psi_3 \end{bmatrix} = \begin{bmatrix} \boldsymbol{N}_1^{\mathrm{T}} \\ \boldsymbol{N}_2^{\mathrm{T}} \\ \boldsymbol{N}_3^{\mathrm{T}} \end{bmatrix} \begin{bmatrix} \boldsymbol{\varphi}_1 \\ \vdots \\ \boldsymbol{\varphi}_i \\ \vdots \\ \boldsymbol{\varphi}_n \end{bmatrix}, \tag{2}$$

where $\boldsymbol{N}_q^{\mathrm{T}} = [N_{q1} \ \ldots \ N_{qj} \ \ldots \ N_{qn}]$ $(q = 1,\ 2,\ 3)$. The entry N_{qj} of the vector $\boldsymbol{N}_q^{\mathrm{T}}$ is the number of conductors of the qth winding associated with the ith edge. Here, the vector $\boldsymbol{\varphi}$ is the solution to equation (1) and therefore, the vector Ψ can be written as follows:

$$\Psi = \Psi_{\mathrm{m}} + \Psi_{\mathrm{u}} = \boldsymbol{N}^{\mathrm{T}}\boldsymbol{\varphi}_{\mathrm{m}} + \boldsymbol{N}^{\mathrm{T}}\boldsymbol{\varphi}_{\mathrm{u}}. \tag{3}$$

The first component of this equation represents flux Ψ_{m} generated by permanent magnets. The second element represents flux Ψ_{u} created by the phase winding. The vector $\boldsymbol{\varphi}_{\mathrm{m}}$ is the solution to equation $\boldsymbol{S}\boldsymbol{\varphi}_{\mathrm{m}} = \boldsymbol{F}$, whereas $\boldsymbol{\varphi}_{\mathrm{u}}$ is the solution to equation $\boldsymbol{S}\boldsymbol{\varphi}_{\mathrm{u}} = \boldsymbol{N}\boldsymbol{i}$.

3. Calculation of electromagnetic torque

Electromagnetic torque has been calculated using the finite element model with a moving mesh. In the model, the entire volume is divided into two sub-volumes, one moving and the other stationary. In rotational machines, the stationary region is assigned to the stator, whilst the moving region rotates with the rotor. A transition band (a mutual connection band) is produced between these parts. All energy (co-energy) changes result from the modifications of band reluctances. The energy stored in the band can be presented as follows:

$$W_{\mathrm{mb}} = \int_0^{\varphi} (\boldsymbol{S}_{\mathrm{b}}\boldsymbol{\varphi}_{\mathrm{b}})^{\mathrm{T}}\, \mathrm{d}\boldsymbol{\varphi}_{\mathrm{b}}. \tag{4}$$

For the air-gap the integral gives

$$W_{\mathrm{mb}} = \frac{1}{2}\boldsymbol{\varphi}_{\mathrm{b}}^{\mathrm{T}}\boldsymbol{S}_{\mathrm{b}}\boldsymbol{\varphi}_{\mathrm{b}}, \tag{5}$$

where $\boldsymbol{S}_{\mathrm{b}}$ is the stiffness submatrix related to the band, and $\boldsymbol{\varphi}_{\mathrm{b}}$ is the vector of the edge potentials of the band.

The stator core has been divided into 9-edge and 12-edge elements. The nine-edge prisms have been used to represent the rounded corners of slots. The rotor core, permanent magnets and air-gap have been divided into 12-edge curved rectangular parallelepipeds. The author has applied the model proposed by Demenko (2000). The element edges are parallel to the axis of a cylindrical co-ordinate system r, z, θ. A circular band of regular 12-edge elements is placed inside the air-gap (Figure 1). The trace of the elements in the plane perpendicular to the z-axis is the grid with quadrangles of identical angular length of the base β. The band is subdivided into layers of thickness Δl_i (Figure 1). It is assumed that the boundary of the moving area is the surface $r = r_{is}$ (Figure 1).

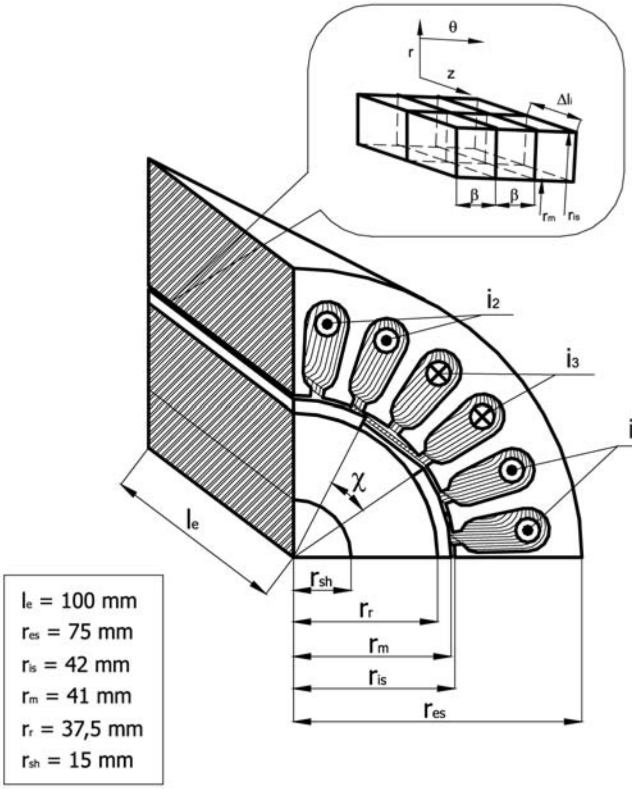

Figure 1.
Permanent magnet motor and part of the band with regular elements

In the presented method, the stiffness submatrix $\boldsymbol{S}_\mathrm{b}$ related to the band is a function of the rotor position α. A trigonometric polynomial is applied to form this function. The polynomial is based on the data for the discrete rotor position $\alpha_i = 2i\pi/m = i\beta$, $i = 0, 1, 2, \ldots, m-1$ (Demenko, 2000).

Electromagnetic torque is calculated on the basis of the virtual work principle. According to this principle, electromagnetic torque is equal to the magnetic energy derivative versus the virtual moving, i.e.:

$$T(\alpha) = -\frac{\partial W_\mathrm{mb}(\alpha)}{\partial \alpha}. \tag{6}$$

Substituting equation (5), equation (6) becomes:

$$T = -\frac{1}{2}\frac{\partial}{\partial \alpha}\left[\boldsymbol{\varphi}_\mathrm{b}^\mathrm{T} \boldsymbol{S}_\mathrm{b}(\alpha)\boldsymbol{\varphi}_\mathrm{b}\right]. \tag{7}$$

The matrix $\boldsymbol{S}_\mathrm{b}(\alpha)$ includes the following components:

$$\boldsymbol{S}_\mathrm{b}(\alpha) = \begin{bmatrix} \boldsymbol{S}_\mathrm{bs} & \boldsymbol{S}_\mathrm{sr}(\alpha) \\ \boldsymbol{S}_\mathrm{sr}^\mathrm{T}(\alpha) & \boldsymbol{S}_\mathrm{br} \end{bmatrix}, \tag{8}$$

where $\boldsymbol{S}_\mathrm{sr}$ is the submatrix of $\boldsymbol{S}_\mathrm{b}(\alpha)$ which describes the interconnections between the rotary and stationary edges of the band. The submatrices $\boldsymbol{S}_\mathrm{bs}$ and $\boldsymbol{S}_\mathrm{br}$ are independent of the discrete rotor position.

In the case of movement simulation of the band interpolation technique, equation (7) becomes:

$$T = -\boldsymbol{\varphi}_\mathrm{bs}^\mathrm{T} \boldsymbol{S}_\mathrm{sr0} \frac{\mathrm{d}\boldsymbol{k}(\alpha)}{\mathrm{d}\alpha} \boldsymbol{\varphi}_\mathrm{br}, \tag{9}$$

where $\boldsymbol{\varphi}_\mathrm{bs}$ is the vector of the edge values of $\boldsymbol{A}$ on the boundary between the band and the stator region, $\boldsymbol{\varphi}_\mathrm{br}$ relates to the other edges of the band. $\boldsymbol{S}_\mathrm{sr0}$ is the matrix of the initial rotor position: $\boldsymbol{S}_\mathrm{sr0} = \boldsymbol{S}_\mathrm{sr}(\alpha = 0)$, and $\boldsymbol{k}(\alpha)$ is the rotation matrix obtained on the basis of the interpolating trigonometric polynomial.

In the model with a band of regular elements, electromagnetic torque can also be expressed as follows:

$$T = -\frac{1}{2\beta}[W(\alpha_i \pm \beta)] = -\frac{1}{2\beta}\left[\frac{1}{2}\boldsymbol{\varphi}_\mathrm{bs}^\mathrm{T} \boldsymbol{S}_\mathrm{sr}(\alpha_i \pm \beta)\boldsymbol{\varphi}_\mathrm{br}\right]. \tag{10}$$

This is the difference representation of formula (6) for $\alpha = \alpha_i$. Here $\boldsymbol{S}_\mathrm{sr}(\alpha_i \pm \beta)$ represents the matrix $\boldsymbol{S}_\mathrm{sr}$ for $\alpha = \alpha_i + \beta$ and $\alpha = \alpha_i - \beta$. Thus:

$$\boldsymbol{S}(\alpha_i + \beta) = \boldsymbol{S}(\alpha_i)\boldsymbol{k}_\beta, \tag{11a}$$

$$\boldsymbol{S}(\alpha_i - \beta) = \boldsymbol{S}(\alpha_i)\boldsymbol{k}_\beta^\mathrm{T}. \tag{11b}$$

As a result we obtain:

$$T = -\frac{1}{2\beta}\boldsymbol{\varphi}_\mathrm{bs}^\mathrm{T} \boldsymbol{S}_\mathrm{sr}(\alpha_i)\left(\boldsymbol{k}_\beta - \boldsymbol{k}_\beta^\mathrm{T}\right)\boldsymbol{\varphi}_\mathrm{br}. \tag{12}$$

This method of electromagnetic torque calculation guarantees good accuracy. If the rotor region is empty, i.e. the density of magnetising and conducting currents is equal to zero, and is subdivided into bands of regular elements similar to the band placed inside the air-gap, the torque calculated from equations (9) and (12) is exactly equal to zero.

Electromagnetic torque can be also calculated from the formula:

$$T = -\frac{\Delta W}{\Delta \alpha} = -\frac{1}{2\alpha} \boldsymbol{i}^{\mathrm{T}} [\Psi(\alpha_i = \alpha) - \Psi(\alpha_i = -\alpha)]. \tag{13}$$

For $\alpha = \beta$, equation (13) is the circuit equivalent of equation (12).

If equation (13) is applied, the field calculations are performed only once. From the calculations we obtain the vector Ψ depending on the rotor position. The method can be considered as a circuit-field approach. The method can be successfully applied in the case of a non-saturated system.

4. Results

A four pole motor with six slots per pole has been designed. Permanent magnets are not skewed and are mounted on a cylindrical laminated rotor (Demenko, 1998). A single-layer winding is composed of four multi-turn coils per phase. The coils are connected in series. The dimensions of the motor are shown in Figure 1. Three-phase stator windings are star connection. The motor is equipped with rare-earth NdFeB-type permanent magnets (material VACODYM 370, Catalogue Vacuumschmelze GMBH, 1996). The demagnetisation curve of permanent magnets is approximated by a linear function with slope μ_0, where μ_0 is the permeability of the free space. Thus, the model of the motor has non-salient poles. It has been assumed that the motor is fed from a balanced three-phase current source, i.e. winding currents are $i_q = I_m \sin(\omega t + 2(q-1)\pi/3)$ $(q = 1, 2, 3)$ (Demenko *et al.*, 2002). The calculations have been performed for synchronous speed at the supply of 50 Hz.

Permanent magnets have been divided into sectors (Figure 2(a)-(c)).

Motors with magnets of varying magnetization direction have been analysed. The vector of magnetization $\boldsymbol{J}$ has two components (Figure 3). The components of the vector $\boldsymbol{J}$ in the ith sector are defined as follows:

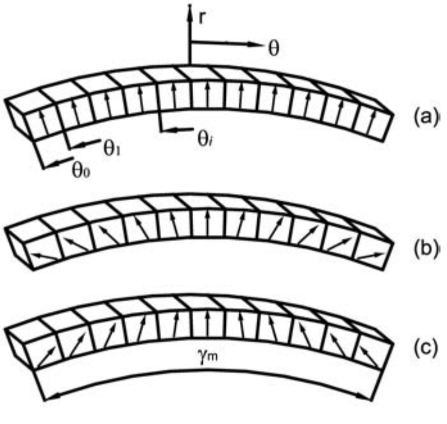

Figure 2.
Permanent magnets divided into sectors with (a) radial magnetization, (b) and (c) inhomogeneous magnetization

$$\boldsymbol{J}_{ri} = \boldsymbol{J}_{r\mathrm{m}} \cos\left(\frac{\theta_{i-1} + \theta_i}{\gamma_\mathrm{m}} \cdot \lambda\right), \tag{14}$$

$$\boldsymbol{J}_{\theta i} = \boldsymbol{J}_{\theta\mathrm{m}} \sin\left(\frac{\theta_{i-1} + \theta_i}{\gamma_\mathrm{m}} \cdot \lambda\right). \tag{15}$$

Here θ_i, γ_m are the angles shown in Figure 2, and λ defines the direction of $\boldsymbol{J}$ in the first segment.

Motors with different angles γ_m and λ have been analysed. First, motors with permanent magnets of the angle of $\gamma_\mathrm{m} = 61.5°$ ($\chi = 28.5°$) have been investigated. The calculations have been performed for the following values of the angle λ:

(1) $\lambda = 60°$,
(2) $\lambda = 45°$,
(3) $\lambda = 30°$ and
(4) $\lambda = 0°$.

If $\lambda = 0°$, then we obtain a magnet with radial magnetization (Figure 2(a)). Figure 4 shows the results of electromagnetic torque as a function of the rotor position. The motor with inhomogeneously magnetized permanent magnets shown in Figure 2(b) gives the same result as the motor with magnetization presented in Figure 2(c). The calculations show that the torque waveform can be assumed to be independent of components $\boldsymbol{J}_\theta$.

The calculated functions $T(\alpha)$ have been interpolated by trigonometric polynomials (Figure 5). Figure 5 shows relative amplitudes of the harmonics in relation to 20 per cent of the constant component.

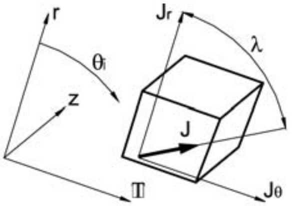

Figure 3.
Sector of the magnet with the vector of magnetization components

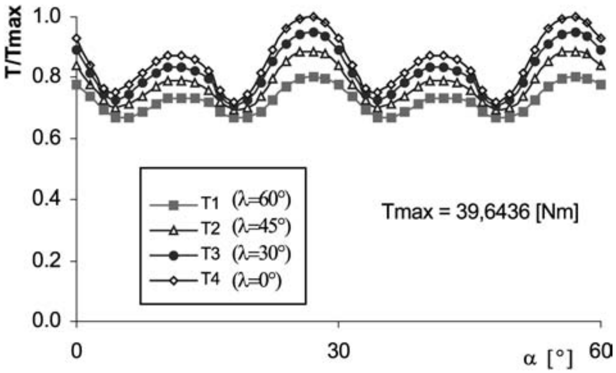

Figure 4.
Electromagnetic torque as a function of the rotor position

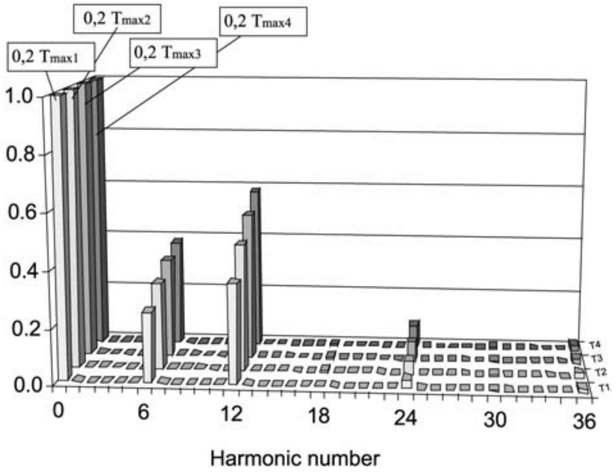

Figure 5.
Relative amplitudes of the harmonics in relation to 20 per cent of the constant component

An inherent drawback of PM motors is the torque ripple caused by stator and rotor anisotropy and non-sinusoidal distributions of the stator magnetomotive force and permanent magnet flux density. This torque fluctuation causes vibrations and acoustic noise deteriorates the control performance of the drive. Generally, a PMSM produces three types of torque: reluctance, cogging and mutual torque. Reluctance torque is produced from the interaction between the current magnetomotive forces with the angular variation in the rotor magnetic reluctance. Surface-magnet PM machines generate almost no reluctance torque. Cogging torque comes from the interaction between the PM field and armature slots. Mutual torque includes main torque and harmonic torque. They are produced by the interaction between the PM field and the armature field due to the phase currents (Cai *et al.*, 2000).

A useful quantity utilised in the analysis of torque in PM machines is the torque pulsation factor. It can be defined in different ways (Cai *et al.*, 2000). Here, the following formula is used:

$$\varepsilon = \frac{T_{\mathrm{max}} - T_{\mathrm{min}}}{T_{\mathrm{av}}} 100\,\%, \tag{16}$$

where T_{max}, T_{min}, T_{av} is maximum, minimum, and average torque, respectively.

Another useful factor may be introduced if there is need to define the percentage amount of cogging torque in electromagnetic torque:

$$\tau = \frac{(T_{\mathrm{cog\,max}} - T_{\mathrm{cog\,min}})}{2T_{\mathrm{av}}} 100\,\%. \tag{17}$$

The above defined quantities as well as the maximum, minimum, and average torque values produced by the motor for the cases considered are summarized in Table I.

Mutual torque comes from non-sinusoidal distributions of flux density in the air-gap. Equation (3) has been solved and the functions $\Psi_{\mathrm{m}}(\alpha)$ (for $i_1 = i_2 = i_3 = 0$) have been calculated. The functions $\Psi_{\mathrm{m}}(\alpha)$ have been interpolated by trigonometric polynomials and the harmonics of $\Psi_{\mathrm{m}}(\alpha)$ have been obtained. Figure 6 shows relative amplitudes of the harmonics in relation to 5 per cent of the first harmonic.

Next, magnets with $\gamma_{\mathrm{m}} = 90°$ $(\chi = 0)$ have been applied. This means that the magnets are joined (Figure 7).

The calculations have been performed for the following values of λ:

(1) $\lambda = 90°$,

(2) $\lambda = 67°$,

(3) $\lambda = 45°$.

Figure 8 and Table II present the results of electromagnetic torque. For $\lambda = 90°$ we have obtained the function $T(\alpha)$ without ripples.

Table I. Calculated values of torque and torque ripples

	$T_{\max}$ (N m)	$T_{\min}$ (N m)	T_{av} (N m)	ε (%)	τ (%)
T1	31.89	26.45	28.67	18.99	0.30
T2	35.17	27.42	30.83	25.14	1.69
T3	37.62	28.09	32.43	29.36	2.87
T4	39.64	28.63	33.76	32.60	3.73

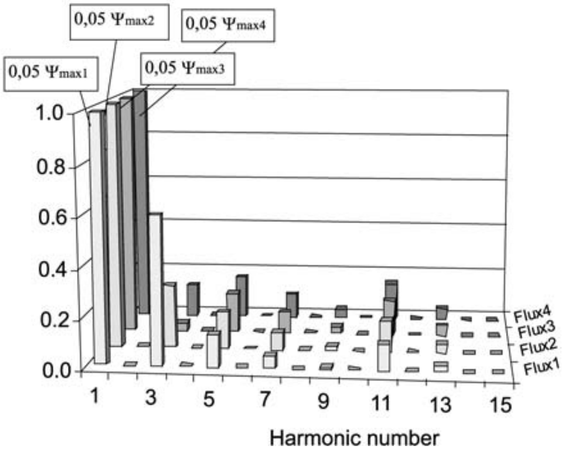

Figure 6. Relative amplitudes of the harmonics in relation to 5 per cent of the basic harmonic

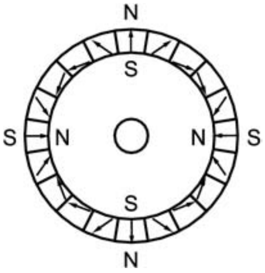

Figure 7. System composed of joined magnets

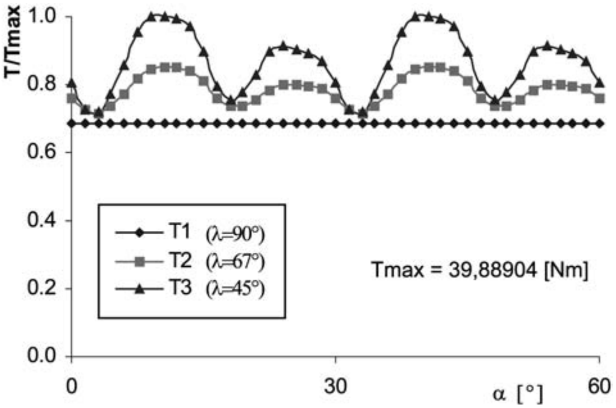

Figure 8.
Electromagnetic torque as a function of rotor position in the motor with joined magnets

	T_{max} (N m)	T_{min} (N m)	T_{av} (N m)	ε (%)	τ (%)
T1	27.36	27.36	27.36	0.00	0.00
T2	34.01	28.59	31.25	17.35	4.06
T3	39.89	28.73	34.51	32.33	10.20

Table II.
Calculated values of torque and torque ripples

5. Conclusions

In this paper, the results of torque calculations in a synchronous permanent magnet machine with inhomogeneously magnetized magnets have been presented. General formulae for the 3D modelling of permanent magnets with a variable magnetization angle have been worked out. Main components of torque pulsations have been categorised and analysed by means of an algorithm written to be applied to the analysis of PM machines. The calculation results show that if the magnetization angle of permanent magnets is selected properly, torque pulsations can be significantly reduced.

References

Cai, W., Fulton, D. and Reichert, K. (2000), "Design of permanent magnet motors with low torque ripples: a review", *Proceedings of ICEM*, Vol. 3, pp. 1384-8.

Catalogue Vacuumschmelze GMBH (1996), *Rare-Earth Permanent Magnets Catalogue*, Hanau.

Demenko, A. (1998), "3D edge element analysis of permanent magnet motor dynamic", *IEEE Trans. Magn.*, Vol. 34 No. 5, pp. 3620-3.

Demenko, A. (2000), "Calculations of permanent magnet motor torque using edge element method", *Proceedings of ICEM*, Vol. 3, pp. 1389-93.

Demenko, A., Nowak, L., Pietrowski, W. and Stachowiak, D. (2002), "3D edge element analysis of saturation effects in a permanent magnet machine", *COMPEL*, Vol. 21 No. 1, pp. 126-37.

Ishikawa, T. and Slemon, G.R. (1993), "A method of reducing ripple torque in permanent magnet motors without skewing", *IEEE Trans. Magn.*, Vol. 29 No. 3, pp. 2028-33.

Jahns, T.M. and Soong, W.L. (1996), "Pulsating torque minimization techniques for permanent magnet AC motor drives – a review", *IEEE Transactions on Industrial Electronics*, Vol. 43 No. 2, pp. 321-30.

Kawase, Y., Yamaguchi, T. and Hayashi, Y. (1995), "Analysis of cogging torque of permanent magnet motor by 3D finite element method", *IEEE Trans. Magn.*, Vol. 31 No. 3, pp. 2044-6.

Marinescu, M. and Marinescu, N. (1992), "New concept of permanent magnet excitation for electrical machines. Analytical and numerical computation", *IEEE Trans. Magn.*, Vol. 28 No. 2, pp. 1390-3.

Nogarede, B. and Lajoie-Mazenc, M. (1991), "Torque ripple minimization methods in sinusoidal fed synchronous permanent magnet machines", *Proc. IEE Conf. Elec. Machines and Drives*, pp. 41-5.

The Emerald Research Register for this journal is available at
www.emeraldinsight.com/researchregister

The current issue and full text archive of this journal is available at
www.emeraldinsight.com/0332-1649.htm

Adaptive observer of rotor speed and position for PMSM sensorless control system

Konrad Urbański and Krzysztof Zawirski
Institute of Control and Information Engineering, Poznań University of Technology, Poznań, Poland

Received September 2002
Revised June 2003
Accepted June 2003

Keywords *Sensors, Magnetic fields, Magnetic variables control*

Abstract *This paper deals with the problem of rotor speed and position detection in sensorless permanent magnet synchronous motor (PMSM) drives. A concept based on detecting the back EMF induced in stator windings was developed and modified. A general structure of an adaptive observer with the proportional-integral function of a corrector is introduced. The non-stationary character of the observer presented in this paper requires an adaptive change of observer corrector settings. Such observer structure was implemented on a DSP system and verified experimentally. Both simulation and experimental results show good properties of the proposed observer structure.*

1. Introduction

Permanent magnet synchronous motors (PMSM) are widely used in industrial drives due to their high power factor, high torque density, high efficiency and small size. However, a position sensor such as an encoder or a resolver is required to enable the effective control of a PMSM. Such sensors increase the overall cost of the drive system so eliminating the need for their installation might allow new applications of the PMSM. This scientific problem remains an open question and is the subject for extensive research in many scientific centres. Several approaches to this problem are reported in the literature, which are based on state observers (Dodds *et al.*, 1998; Hamada *et al.*, 1999; Jones and Lang, 1989), extended Kalman filters (Germano *et al.*, 1994; Parasiliti *et al.*, 1999), sliding-mode observers (Parasiliti *et al.*, 1999; Vittek *et al.*, 2000) or novel methods of applying motor saliency (Kulkarni and Ehsani, 1992). State observers and Kalman filters based on a motor model require complex computational operations to obtain proper accuracy, which always causes problems in real time operation. Several new approaches apply motor magnetic saliency and detect the rotor position by measuring phase inductances. These methods provide a real solution at small speeds and during standstill operation, but requirements with respect to hardware and software are high.

A new and more general structure of an observer is proposed in this paper. The new observer structure is based on a modified concept of back EMF detection (Parasiliti *et al.*, 1999) and introduces a more complex corrector function which differs from the traditional one. The structure contains a corrector with a proportional-integral function

---

This is a revised and enhanced version of a paper which was originally presented as a conference contribution at the *XVII Symposium on Electromagnetic Phenomena in Nonlinear Ciruits (EPNC)*, held in Leuven, Belgium, on 1-3 July 2002. This is one of a small selection of papers from the Symposium to appear in the current and future issues of *COMPEL*.

COMPEL: The International Journal for Computation and Mathematics in Electrical and Electronic Engineering
Vol. 23 No. 4, 2004
pp. 1129-1145
© Emerald Group Publishing Limited
0332-1649
DOI 10.1108/03321640410510848

instead of the proportional correction used in the Luenberger observer. The non-stationary character of the observer presented in this paper requires an adaptive change of observer corrector settings. Such observer structure was implemented on a DSP system and verified experimentally.

2. Observer structure

Assuming ordinary simplified assumptions, the mathematical model of a PMSM in α-β orthogonal coordinates can be expressed as follows (Parasiliti *et al.*, 1999; Urbański and Zawirski, 2000):

$$\begin{aligned}\frac{\mathrm{d}i_\alpha}{\mathrm{d}t} &= -\frac{R}{L}i_\alpha - \frac{1}{L}e_\alpha + \frac{1}{L}v_\alpha\\ \frac{\mathrm{d}i_\beta}{\mathrm{d}t} &= -\frac{R}{L}i_\beta - \frac{1}{L}e_\beta + \frac{1}{L}v_\beta\\ \frac{\mathrm{d}\omega}{\mathrm{d}t} &= \frac{1}{J}(\psi_\beta i_\alpha - \psi_\alpha i_\beta - T_\mathrm{L})\\ \frac{\mathrm{d}\theta}{\mathrm{d}t} &= \omega\end{aligned} \tag{1}$$

where i_α, i_β, ψ_α, ψ_β, e_α, e_β are the components of stator current, stator flux linkage and induced back EMF in α-β coordinates, respectively; v_α, v_β are the components of input stator voltage in α-β coordinates, R and L are the stator windings resistance and inductance, ω and Θ are the rotor speed and the position, J is the moment of inertia and T_L is the load torque treated as an external disturbance.

Flux linkages and back EMF are described in equation (2):

$$\begin{aligned}\Psi_\alpha &= Li_\alpha + \Psi_\mathrm{f}\cos\Theta\\ \Psi_\beta &= Li_\beta - \Psi_\mathrm{f}\sin\Theta\\ e_\alpha &= k_\mathrm{e}\Psi_\mathrm{f}\omega\cos\Theta\\ e_\beta &= -k_\mathrm{e}\Psi_\mathrm{f}\omega\sin\Theta\end{aligned} \tag{2}$$

where Ψ_f is the flux magnitude of a permanent magnet and k_e is the constant coefficient.

As it follows from equations (1) and (2), the motor model with state variables i_α, i_β, ω and Θ is non-linear. All state variables are measurable, but in a concept of drive without a mechanical sensor (sensorless drive) ω and Θ should be estimated. A simple Luenberger observer cannot be applied due to the non-linearity of the motor model and the presence of a non-measurable external disturbance (load torque). Germano *et al.* (1994) proposed an interesting solution which applies a linear observer and avoids the problem of a non-measurable disturbance. This concept is based on using a motor model described only by the first two electrical equations in (1) with state variables i_α, i_β, input variables v_α, v_β and back EMF e_α, e_β considered as disturbances. In such a case, one can write the extended state formulas in a matrix form as equation (3):

$$\begin{aligned}&\dot{\mathbf{x}}_\mathrm{E} = \mathbf{A}_\mathrm{E}\mathbf{x}_\mathrm{E} + \mathbf{B}_\mathrm{E}\mathbf{u}, \quad \mathbf{y} = \mathbf{C}_\mathrm{E}\mathbf{x}_\mathrm{E}\\ &\mathbf{x}_\mathrm{E} = [i_\alpha, i_\beta, e_\alpha, e_\beta]^\mathrm{T}, \quad \mathbf{y} = [i_\alpha, i_\beta]^\mathrm{T}, \quad \mathbf{u} = [v_\alpha, v_\beta]^\mathrm{T}\end{aligned} \tag{3}$$

where the matrices $\mathbf{A}_\mathrm{E}$, $\mathbf{B}_\mathrm{E}$ and $\mathbf{C}_\mathrm{E}$ can be written as

$$\mathbf{A}_{\mathrm{E}} = \begin{bmatrix} -\frac{R}{L} & 0 & -\frac{1}{L} & 0 \\ 0 & -\frac{R}{L} & 0 & -\frac{1}{L} \\ 0 & 0 & 0 & 0 \\ 0 & 0 & 0 & 0 \end{bmatrix} \quad \mathbf{B}_{\mathrm{E}} = \begin{bmatrix} \frac{1}{L} & 0 \\ 0 & \frac{1}{L} \\ 0 & 0 \\ 0 & 0 \end{bmatrix} \quad \mathbf{C}_{\mathrm{E}} = \begin{bmatrix} 1 & 0 & 0 & 0 \\ 0 & 1 & 0 & 0 \end{bmatrix} \tag{4}$$

It should be noted that in the matrix $\mathbf{A}_{\mathrm{E}}$ the derivatives of e_α, e_β were assumed to be equal to zero for simplicity (Germano *et al.*, 1994; Parasiliti *et al.*, 1999). Such a simplified formula does not reveal the non-linear character of the observer structure. In this paper, a significant modification of the observer mathematical description is proposed. The EMF e_α, e_β are not assumed to be disturbances but additional state variables, substituting the mechanical variables ω and Θ, described by formulas (2) or (5) and (6)

$$\sin\hat{\Theta} = -\frac{\hat{e}_\alpha}{|\hat{e}|}, \quad \cos\hat{\Theta} = \frac{\hat{e}_\beta}{|\hat{e}|} \tag{5}$$

where

$$|\hat{e}| = \sqrt{\hat{e}_\alpha^2 + \hat{e}_\beta^2}, \quad |\hat{\omega}| = \frac{|\hat{e}|}{k_e}, \tag{6}$$

From equation (2) we obtain equation (7) describing the EMF derivatives:

$$\begin{aligned} \frac{\mathrm{d}e_\alpha}{\mathrm{d}t} &= e_\alpha \frac{1}{\omega}\frac{\mathrm{d}\omega}{\mathrm{d}t} - e_\beta \omega \\ \frac{\mathrm{d}e_\beta}{\mathrm{d}t} &= e_\beta \frac{1}{\omega}\frac{\mathrm{d}\omega}{\mathrm{d}t} + e_\alpha \omega \end{aligned} \tag{7}$$

Substituting the last two equations in (3) by equation (7) the new extended state matrix $\mathbf{A}_{\mathrm{E}}$ is modified to the following form:

$$\mathbf{A}_{\mathrm{Em}} = \begin{bmatrix} -\frac{R}{L} & 0 & -\frac{1}{L} & 0 \\ 0 & -\frac{R}{L} & 0 & -\frac{1}{L} \\ 0 & 0 & \frac{1}{\omega}\frac{\mathrm{d}\omega}{\mathrm{d}t} & -\omega \\ 0 & 0 & \omega & \frac{1}{\omega}\frac{\mathrm{d}\omega}{\mathrm{d}t} \end{bmatrix} \tag{8}$$

Since four elements in equation (8) contain the speed and its time derivative the system is non-linear. To avoid this non-linearity, it is proposed that the speed and its derivative are considered time-varying parameters. For such a system, one can obtain a modified extended state formula for the observer:

$$
\begin{aligned}
\frac{\mathrm{d}\hat{i}_\alpha}{\mathrm{d}t} &= -\frac{R}{L}\hat{i}_\alpha - \frac{1}{L}\hat{e}_\alpha + \frac{1}{L}v_\alpha + K_{i\alpha}(\hat{i}_\alpha - i_\alpha)\\
\frac{\mathrm{d}\hat{i}_\beta}{\mathrm{d}t} &= -\frac{R}{L}\hat{i}_\beta - \frac{1}{L}\hat{e}_\beta + \frac{1}{L}v_\beta + K_{i\beta}(\hat{i}_\beta - i_\beta)\\
\frac{\mathrm{d}\hat{e}_\alpha}{\mathrm{d}t} &= \hat{e}_\alpha\frac{1}{\tilde{\omega}}\left(\frac{\Delta\tilde{\omega}}{T_\mathrm{S}}\right) - \hat{e}_\beta\tilde{\omega} + K_{e\alpha}(\hat{i}_\alpha - i_\alpha)\\
\frac{\mathrm{d}\hat{e}_\beta}{\mathrm{d}t} &= \hat{e}_\beta\frac{1}{\tilde{\omega}}\left(\frac{\Delta\tilde{\omega}}{T_\mathrm{S}}\right) + \hat{e}_\alpha\tilde{\omega} + K_{e\beta}(\hat{i}_\beta - i_\beta)
\end{aligned} \tag{9}
$$

or in a matrix form

$$\dot{\hat{\mathbf{x}}}_\mathrm{E} = \mathbf{A}_\mathrm{E}\hat{\mathbf{x}}_\mathrm{E} + \mathbf{B}_\mathrm{E}\mathbf{u} + \mathbf{K}[\Delta\mathbf{i}] \tag{10}$$

where the symbol "ˆ" denotes the observer variables and symbol "∼" denotes the time-varying parameters.

In equation (9), the speed derivative is substituted with its discreet form ($\Delta\omega/T_\mathrm{S}$) as the ratio between the speed change $\Delta\omega$ and the sampling time T_S. Formulas (9) and (10) present an ordinary Luenberger observer (Jones and Lang, 1989) with correction based on the error between the measured and calculated value of currents. The system is non-stationary due to time-varying parameters. This fact has a significant influence on the stability of the observer and the synthesis procedure of the observer corrector because time-varying parameters require an adaptation of corrector settings. The correction in an ordinary Luenberger observer is based on the multiplication of an observer error by constant coefficients, the matrix **K** in equation (10), and can be called a proportional correction. The authors proved in their earlier papers (Urbański and Zawirski, 2000, 2001) that a significant improvement of the observer operation can be obtained by introducing a corrector with a more complex proportional-integral (PI) type of function rather than a proportional one. This results in a new general concept of the observer, whose formula can be written as:

$$\dot{\hat{\mathbf{x}}}_\mathrm{E} = \mathbf{A}_\mathrm{E}\hat{\mathbf{x}}_\mathrm{E} + \mathbf{B}_\mathrm{E}\mathbf{u} + \mathbf{F}[\Delta\mathbf{i}] \tag{11}$$

where $\mathbf{F}[\Delta\mathbf{i}]$ is the corrector function of the observer. Figure 1 shows the block diagram of a general observer structure. The inner structure of the observer depends on the function $\mathbf{F}[\Delta\mathbf{i}]$. In the case of the PI correction, the observer equations take the following form:

$$\mathbf{F}_1[\Delta\mathbf{i}] = \mathbf{K}_p[\Delta\mathbf{i}] + \mathbf{K}_i\int[\Delta\mathbf{i}]\,\mathrm{d}t \tag{12}$$

where the matrices $\mathbf{K}_p$, $\mathbf{K}_i$ are:

$$\mathbf{K}_p = \begin{bmatrix} K_{p11} & 0\\ 0 & K_{p22}\\ K_{p31} & 0\\ 0 & K_{p42}\end{bmatrix} \quad \mathbf{K}_i = \begin{bmatrix} K_{i11} & 0\\ 0 & K_{i22}\\ K_{i31} & 0\\ 0 & K_{i42}\end{bmatrix} \tag{13}$$

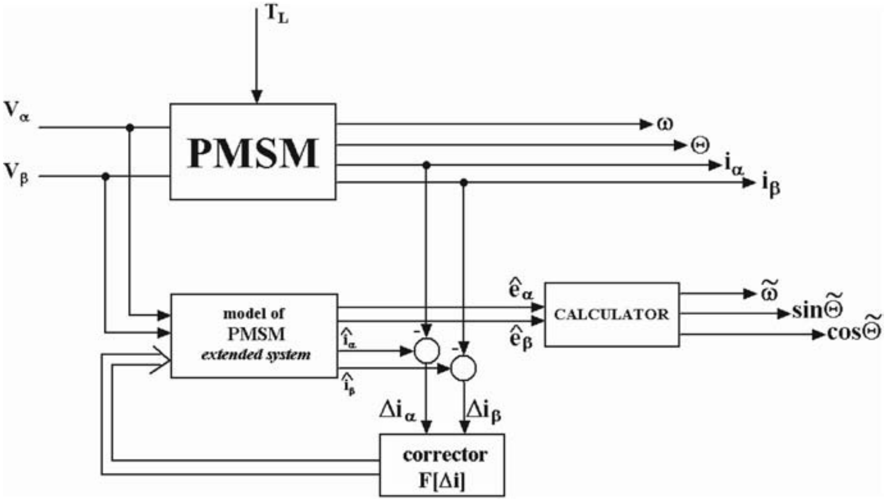

Figure 1.
General structure of observer

On the basis of many simulation tests, a more complex corrector structure with proportional-double integral (PI^2) correction was proposed (Urbański and Zawirski, 2000, 2001):

$$\mathbf{F}_2[\Delta\mathbf{i}] = \mathbf{K}_p[\Delta\mathbf{i}] + \mathbf{K}_i \int [\Delta\mathbf{i}]\,\mathrm{d}t + \mathbf{K}_{ii} \int \left[\int [\Delta\mathbf{i}]\,\mathrm{d}t \right] \mathrm{d}t \tag{14}$$

where $\mathbf{K}_p$ and $\mathbf{K}_i$ are as in equation (13) and $\mathbf{K}_{ii}$ takes the following form

$$\mathbf{K}_{ii} = \begin{bmatrix} K_{ii11} & 0 \\ 0 & K_{ii22} \\ K_{ii31} & 0 \\ 0 & K_{ii42} \end{bmatrix} \tag{15}$$

The advantage of introducing integral and double integral components of the observer corrector is that they ensure the astatic character of observation (estimation) during the transient process, in which fast changes of currents occur. The estimation of back EMF signals by the observer enables the calculation of the new values of the rotor speed and position from equations (5) and (6) at each step of algorithm realization.

3. Adaptive procedure

The synthesis of the observer corrector consists in selecting the coefficients values of the matrices $\mathbf{K}_p$, $\mathbf{K}_i$, $\mathbf{K}_{ii}$ in equation (14). Proper selection is of great importance for the observer stability, static estimation accuracy and good dynamic behaviour. Yet, the synthesis poses some difficulties due to the non-stationary character of the observer. The number of selected coefficients equals 12, but fortunately the mathematical model of the motor assumed in the observer has a symmetrical structure with reference to the axis α-β. Due to this symmetry, the coefficients of the observer corrector have equal values on both the axes, which reduces the number of selected values to six. The process of synthesis was optimized by means of the random weight change (RWC) procedure (Burton *et al.*, 1997). This procedure is fast and insensitive to the local minimum of the optimised criterion. The criterion of observer optimization is formulated as:

$$Q = \int_{t_1}^{t_1+\tau} e_{\Theta}^2(t)\,\mathrm{d}t + \Delta e_{\Theta}(\tau), \tag{16}$$

where e_{Θ} is the position estimation error, Δe_{Θ} is the range of the error value changes of the estimated position during the transient process, t_1 and $t_1 + \tau$ are the time boundaries of the integral calculation.

The optimization procedure was performed "off line" by simulating a transient process. The optimization procedure was repeated for different points of operation, which were determined by the steady state speed value. At each step of optimisation, the transient process of the step response to speed reference changes in the selected point of operation was simulated, and during this process the value of the criterion (16) was calculated in the time range from t_1 to $t_1 + \tau$. According to the RWC procedure, a new set of corrector settings is randomly selected at each step, but only the set which gives estimation improvement (smaller criterion value) is stored. In the procedure, a dimension of search area (a range of randomly change of coefficient values) must be determined at each step. In the presented solution, a wide area was assumed at the beginning of optimisation process and next at the final stage its dimension was reduced to achieve better accuracy. The flow chart of the RWC algorithm is shown in Figure 2. As a result of such "off line" optimisation, a set of optimal values of corrector coefficients is found for each point of operation as shown in Figure 3.

The diagram shows that due to the finite number of points of operation selected during the optimization procedure, the number of optimal corrector sets found is also limited. The optimization was performed for six selected speed values only, and, consequently, the six optimal values for each coefficient were obtained. It follows from the diagram in Figure 3 that the optimal corrector setting values are functions of speed. Therefore, proper values of corrector settings for actual speed value must be found "on line" when the observer procedure is carried out. In this paper, a procedure of "on line" interpolation was proposed to find coefficients values for the actual value of speed. This paper proposes a fuzzy logic base interpolator with six membership input functions determined in the whole range of speed control. These membership functions suit the steady state values of speed for which the optimization process was performed, which means that only six fuzzy rules (input membership functions) for each coefficient must be determined. The input membership functions are shown in Figure 4. At each step of the observer calculations, a set of optimal settings is determined by means of the fuzzy interpolation procedure, which uses the Mamdani implication method and defuzzification by the height method (Drinakov *et al.*, 1993). The input signal for the interpolator is the value of speed estimated at the preceding step of the calculation. For this input signal at each step of observer procedure, only two fuzzy rules are "fired" with degree of membership, which depends on signal value. This process is shown in Figure 4. Determination of the degrees of membership enables to calculate the interpolated value of each coefficient using the height defuzzification method. The height defuzzification is very simple and quick because the crisp value is

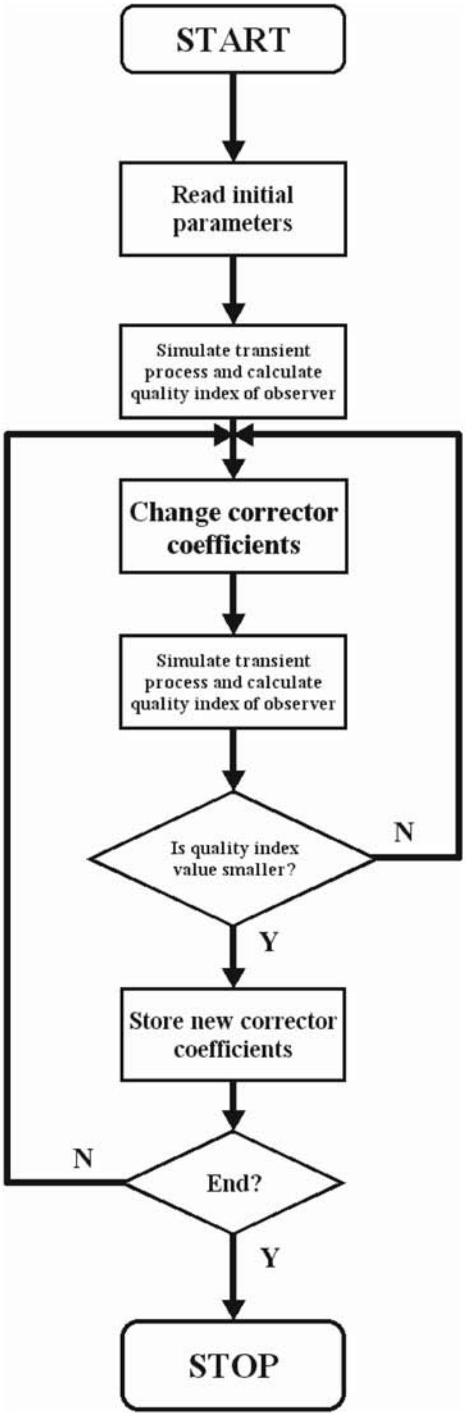
START
Read initial parameters
Simulate transient process and calculate quality index of observer
Change corrector coefficients
Simulate transient process and calculate quality index of observer
Is quality index value smaller?
N
Y
Store new corrector coefficients
End?
N
Y
STOP

Figure 2.
Flow chart of RWC algorithm

calculated as a weighted mean value of neighbouring observer coefficients (Figure 3) by means of formula:

$$k_x^* = \frac{k_{xm}\tau_m + k_{xn}\tau_n}{\tau_m + \tau_n} \tag{17}$$

where k_x^* is the interpolated value of coefficient k_x; k_{xm} and k_{xn} are the optimal values of coefficient k_x found by RWC procedure at the operation point m and n; τ_m and τ_n are the degrees of membership for “fired” rules m and n.

4. Simulation results

The model of the PMSM control system was carried out in MATLAB. The motor was modelled with ordinary simplifying assumptions such as constant resistance and inductance in stator windings, symmetry of windings and isotropic properties of motor (1). The motor model was connected with a model of a control system, which includes a vector control system of stator currents, a speed controller and a model of the analysed observer (Figure 5). The model of the observer was used as an element of feedback sending detected signals of rotor speed and position. The motor model was calculated with a very small step of integration, which simulates its continuous character. The step value was within the range of 0.1 ÷ 20 μs, depending on the simplification level of the inverter model. Contrary to that, the model of the control system with the observer

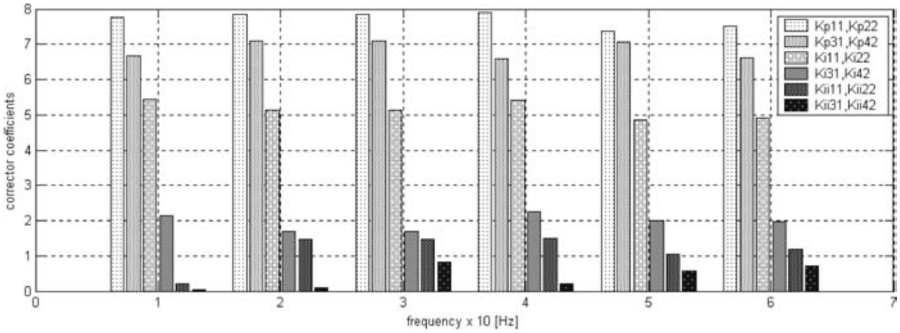

Figure 3.
The optimal values of observer corrector coefficients vs converter frequency

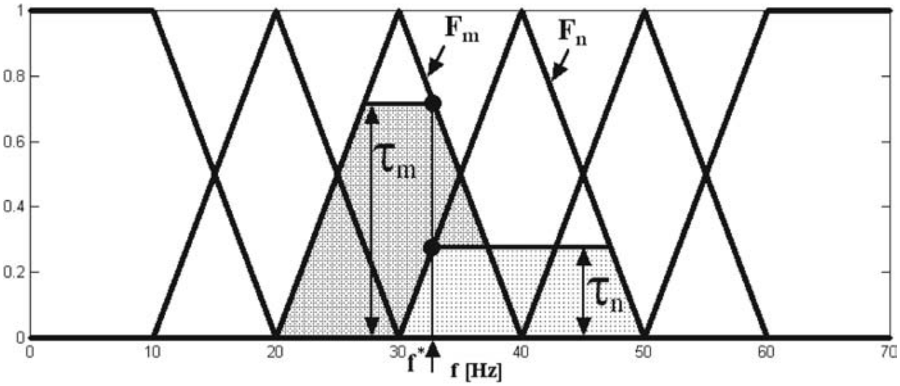

Figure 4.
Input membership functions: F_m, F_n – functions used for illustration of formula (17); τ_m, τ_n – degrees of membership for point f^*

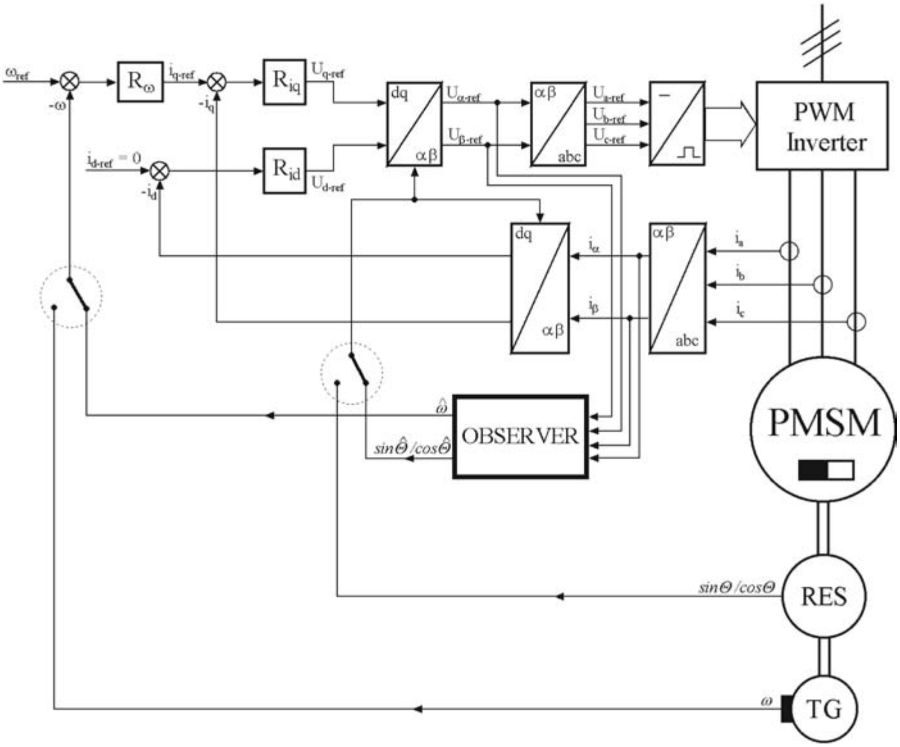
ω_{ref}
$-\omega$
R_ω
$i_{q\text{-}ref}$
$-i_q$
R_{iq}
$U_{q\text{-}ref}$
$i_{d\text{-}ref} = 0$
$-i_d$
R_{id}
$U_{d\text{-}ref}$
dq
αβ
$U_{\alpha\text{-}ref}$
$U_{\beta\text{-}ref}$
αβ
abc
$U_{a\text{-}ref}$
$U_{b\text{-}ref}$
$U_{c\text{-}ref}$
PWM Inverter
dq
αβ
i_α
i_β
αβ
abc
i_a
i_b
i_c
$\hat{\omega}$
OBSERVER
$\sin\hat{\Theta}/\cos\hat{\Theta}$
PMSM
$\sin\Theta/\cos\Theta$
RES
ω
TG

Figure 5.
Structure of drive model

was calculated with much higher step values (60 ÷ 200 μs), simply because it enables a better simulation of how the control system works on a signal processor with a real value of the sampling period.

Motor parameters

- Moment of inertia, $J_m = 0.000135\,\text{kg}\,\text{m}^2$
- Stator inductance, $L = 32\,\text{mH}$
- Stator resistance per phase, $R = 7.9\,\Omega$
- Total moment of inertia (including J_m), $J = 0.000135 \times 3\,\text{kg}\,\text{m}^2$

The waveforms of speed, estimated speed, angle and speed estimation error shown in Figures 6 and 7, illustrate the operation of the observer with and without the adaptive procedure. These waveforms were obtained as responses to the step change of speed reference, generated in the form of a step sequence starting from zero speed and reaching its maximum value. In the presented transients, much higher estimation accuracy of the adaptive observer is displayed.

5. Experiments

The laboratory stand consisted of a PMSM motor supplied from a PWM inverter and controlled by means of a microprocessor system with floating point DSP from the SHARC family. The control system was equipped with current and voltage sensors

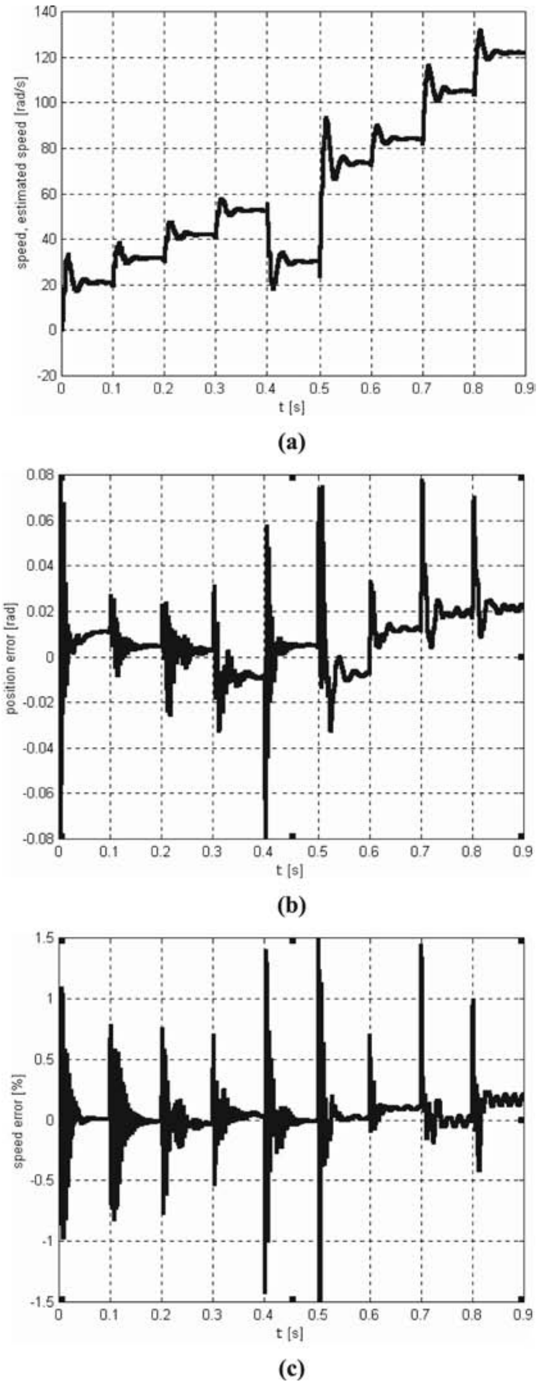

Figure 6.
Waveforms of speed and estimated speed (a), position estimation error (b) and speed estimation error (c) for observer with parameter adaptation

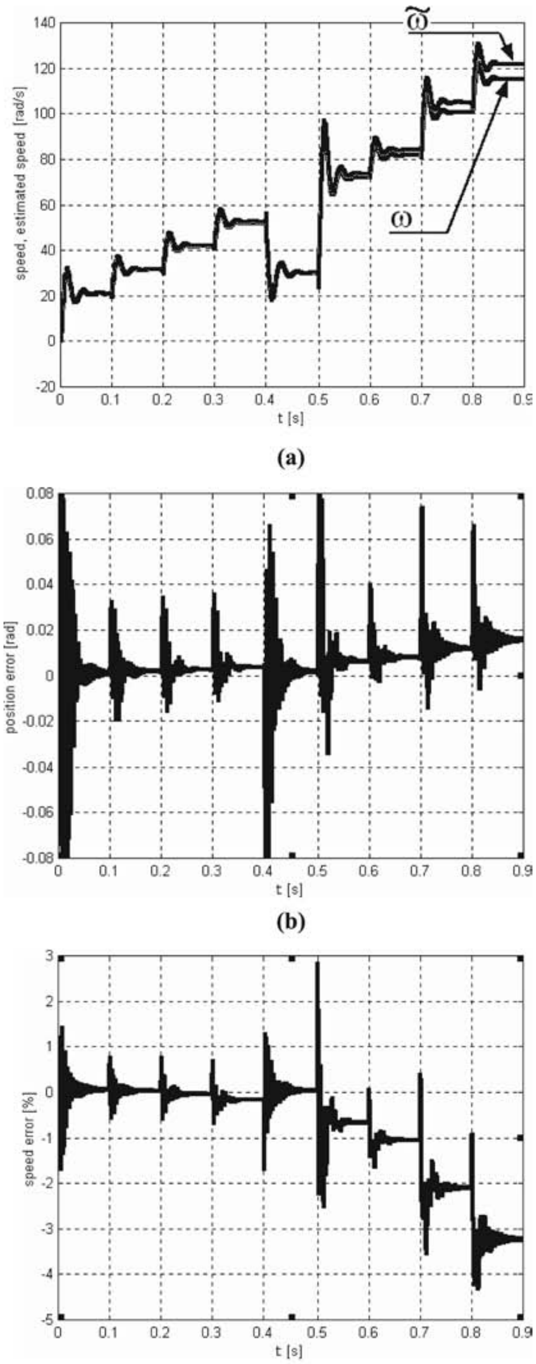

(a)

(b)

(c)

Figure 7.
Waveforms of speed and estimated speed (a), position estimation error (b) and speed estimation error (c) for observer without parameter adaptation

(LEM) and a resolver (Figure 8). As a result of the simulation test, an observer with PI^2 type of correction was selected for the laboratory experiment.

The observer algorithms as well as the control algorithms were implemented on the DSP processor.

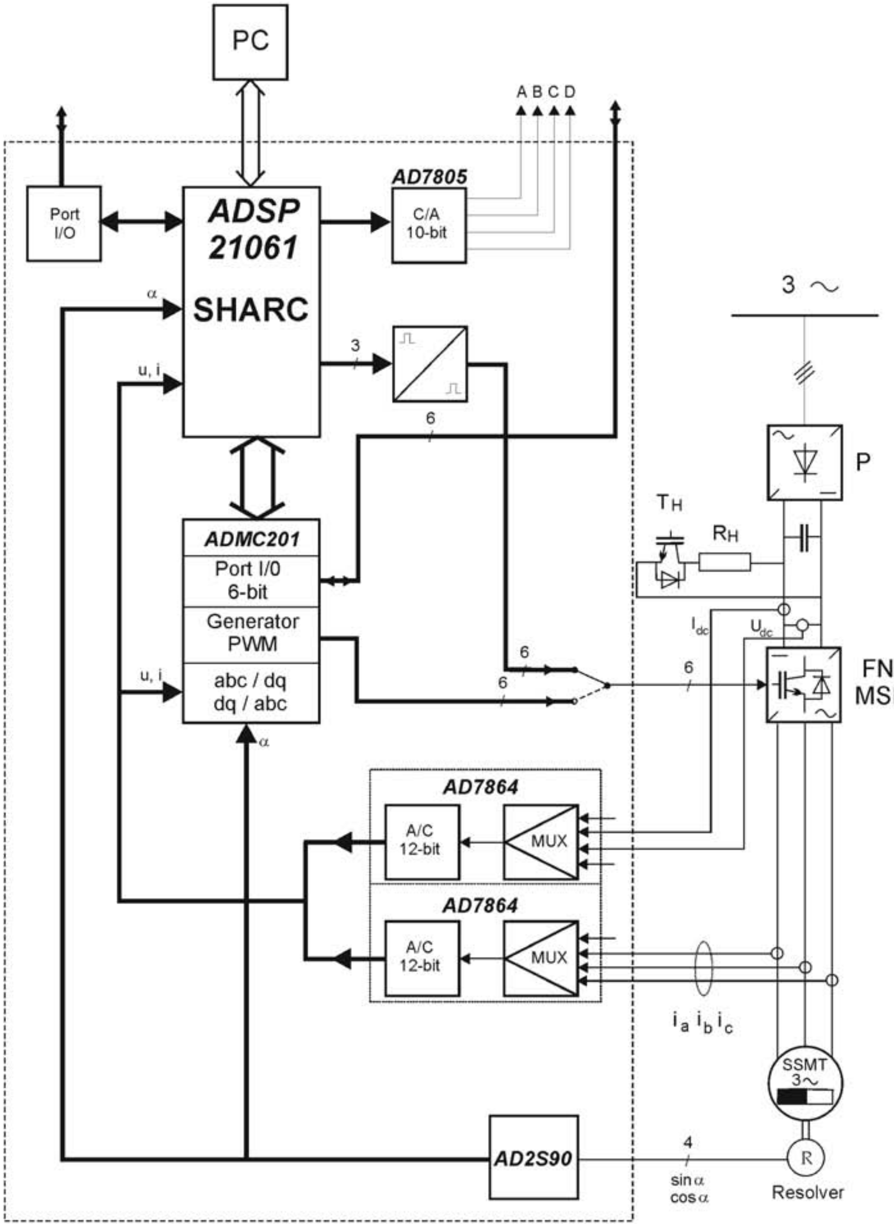
PC
A B C D
Port I/O
ADSP 21061 SHARC
AD7805
C/A 10-bit
α
u, i
3
6
ADMC201
Port I/0 6-bit
Generator PWM
abc / dq
dq / abc
u, i
α
6
6
6
3 ~
P
T_H
R_H
I_dc
U_dc
FN MSI
AD7864
A/C 12-bit
MUX
AD7864
A/C 12-bit
MUX
i_a i_b i_c
SSMT 3~
AD2S90
4
sin α
cos α
R
Resolver

Figure 8.
Structure of laboratory control system based on DSP SHARC

The experiments confirmed good properties of the investigated observer. Figure 9 shows the test of position estimation accuracy obtained for the observer with constant settings, which were selected for the speed equal to 105 rad/s. The maximum estimation error reaches a value of 2.23° for $\omega = 105\,\mathrm{rad/s}$ and a value of 4.6 for $\omega = 37.7\,\mathrm{rad/s}$. This means that higher accuracy is obtained in the operating point $\omega = 105\,\mathrm{rad/s}$ assumed for the optimal synthesis of observer settings. Figure 10 shows the transient process involved by a step change of speed reference ($0 \rightarrow 105 \rightarrow 0\,\mathrm{rad/s}$) for sensor and sensorless control systems. Very similar waveforms of speed,

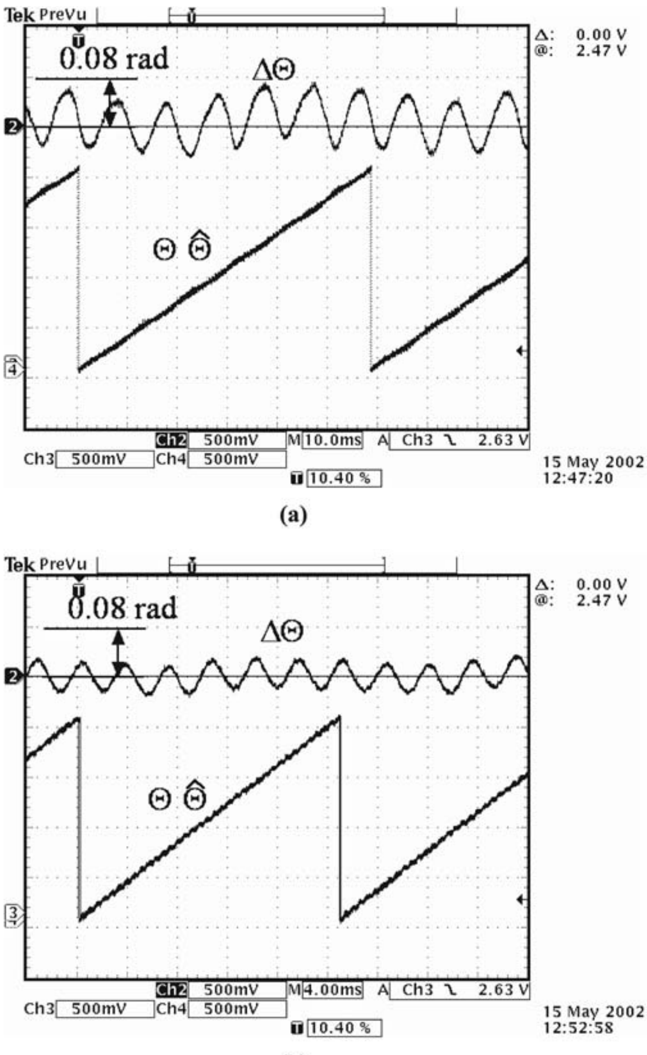

Figure 9.
Test of position estimation accuracy with observer setting selected for $\omega = 105\,\mathrm{rad/s}$. (a) $\omega = 37.7\,\mathrm{rad/s}$, (b) $\omega = 105\,\mathrm{rad/s}$

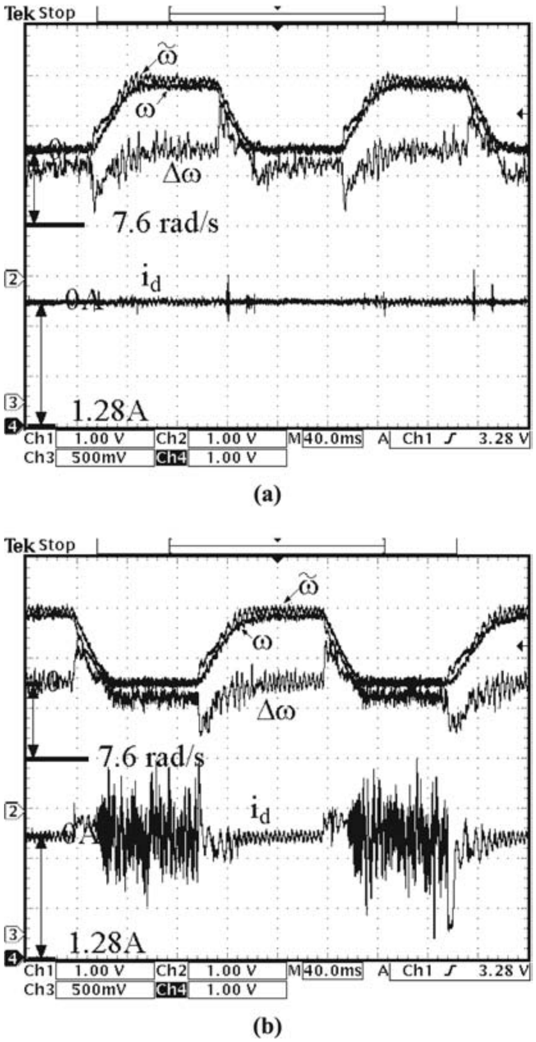

(a)

(b)

Figure 10.
Waveforms of speed (ω), estimated speed ($\tilde{\omega}$), speed observation error and real current in d axis involved by step change of reference: 0 → 105 → 0 rad/s. (a) Sensor control, (b) sensorless control

estimated speed, speed estimation error and current i_{d} confirm the proper functioning of the sensorless systems.

The only difference observed in the waveforms of current i_d for a sensorless system – as a result of the position observation error (Figure 9) – is that the current i_d is not equal to zero but its value reaches 0.7 A, which equals 24 per cent I_{R}. Such a situation occurs only for speed value equal to zero because as a result of it the EMF values also equal to zero and, consequently, very small estimation accuracy is obtained for an immovable motor. The waveforms presented in the figure allow us to make comparisons between the starting process of both systems under consideration. A special starting procedure guarantees a proper start for the sensorless system so both speed waveforms shown are similar. Figure 11 shows the transient process

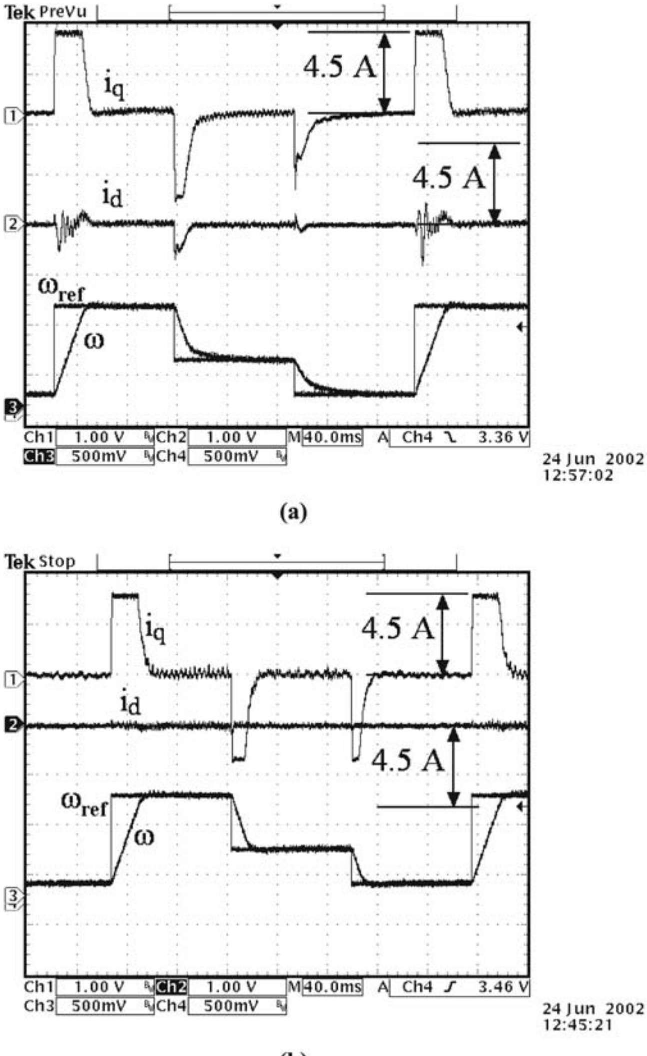

Figure 11.
Waveforms of speed, reference speed and real current in *d*- and *q*-axes involved by step change of reference: 37.7 → 209 → 105 rad/s. (a) Sensorless control, (b) sensor control

involved by a step change of speed reference (37.7 → 209 → 105 rad/s) for sensorless and sensor control systems. The presented waveforms prove the correct operation of the sensorless control and allow us to compare the estimated and real currents on the *d*- and *q*-axes. The difference between the currents on the *q* axis is negligible, while the difference between the currents on the *d* axis is noticeable. Once again, as a result of the errors in the position angle estimation, the real current i_d is not equal to zero in the transient state but reaches the maximum value of 1 A, which is about 34 per cent I_R. The non-zero values of the current on the *d* axis are the cost of sensorless operation in the presented solution. The waveforms shown in Figure 12 allow as to compare the

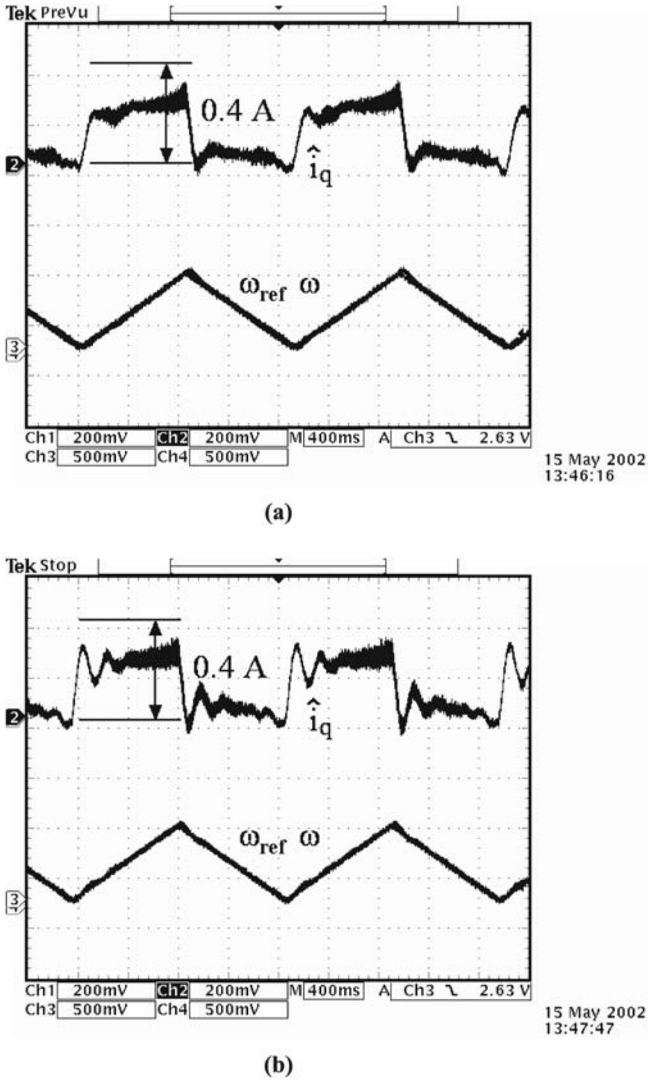

(a)

(b)

Figure 12.
Waveforms of speed, reference speed, real and estimated current in *q* axis involved by speed reference of triangle shape: 12.5 → 52 → 12.5 rad/s. (a) Sensorless control, (b) sensor control

operation of a control system with and without a sensor in a transient process involved by speed reference shaped as a triangle. Both speed and current waveforms are similar, which proves the correct operation of the sensorless control.

6. Conclusions

In this paper, a new structure of an observer for rotor speed and position estimation in PMSMs was proposed. The novelty of this observer structure lies in its complex corrector function of a proportional-double integral type and the adaptive change of corrector settings. This structure implemented on a DSP processor operated properly was confirmed experimentally. The proposed observer was tested on a single machine under well defined conditions. Further investigations are required to determine the robustness of the observer before any industrial applications can be considered.

References

Burton, B., Kamran, F., Harley, R.G., Habetler, T.G., Brooke, M.A. and Poddar, R. (1997), “Identification and control of induction motor stator currents using fast online random training of a neural network”, *IEEE Transactions on Industry Applications*, Vol. 33 No. 3.

Dodds, S.T., Vittek, J. and Jan, S.S. (1998), “Implementation of a sensorless synchronous motor drive control system with prescribed closed-loop speed dynamics”, *Symposium on Power Electronics, Electrical Drives, Advanced Machines, Power Quality SPEEDAM 98*.

Drinakov, D., Heelendoorn, H. and Reinfrank, M. (1993), *An Introduction to Fuzzy Control*, Springer-Verlag, Berlin.

Germano, A., Parasiliti, F. and Tursin, M. (1994), “Sensorless speed control of a PM synchronous motor drive by Kalman filter”, *Proceedings of the 1994 International Conference on Electrical Machines*, Vol. 2, pp. 540-4.

Hamada, D., Uchida, K., Yusivar, F., Haratsu, H., Wakao, S. and Onuki, T. (1999), “Sensorless control of PMSM using linear reduced order observer including disturbance torque estimation”, *Proceedings of 8th European Conference on Power Electronics and Applications*, EPE ’99, CD-ROM.

Jones, L.A. and Lang, J.H. (1989), “A state observer for the permanent magnet synchronous motor”, *IEEE Trans Ind. Electronics*, Vol. 36 No. 3, pp. 374-82.

Kulkarni, A. and Ehsani, M. (1992), “A novel position sensor elimination technique for the interior permanent magnet synchronous motor”, *IEEE Trans. Ind. Applications*, Vol. 28 No. 1, pp. 144-50.

Parasiliti, F., Petrela, R. and Turisini, M. (1999), “Rotor speed and position detection for PM synchronous motor based on sliding mode observer and Kalman filter”, *Proceedings of 8th European Conference on Power Electronics and Applications*, EPE ’99, CD-ROM.

Urbański, K. and Zawirski, K. (2000), “Rotor speed and position detection for PMSM control system”, *Proceedings of 9th International Conference and Exhibition on Power Electronics and Motion Control*, Vol. 6, pp. 239-43.

Urbański, K. and Zawirski, K. (2001), “Rotor speed and position observer for PMSM sensorless control system”, *Proceedings of 9th European Conference on Power Electronics and Applications*, CD-ROM.

Vittek, J., Dodds, S.T., Altus, J. and Perryman, R. (2000), “Sliding mode based outer control loop for sensorless speed control of permanent magnet synchronous motor”, *Proceedings of 8th IEEE Mediterranean Conference on Control and Automation*, MED 2000.

The Emerald Research Register for this journal is available at
www.emeraldinsight.com/researchregister

The current issue and full text archive of this journal is available at
www.emeraldinsight.com/0332-1649.htm

A shunt active power filter: development of properties

Andrzej Szromba
Institute of Electrical Engineering and Electronics,
Cracow University of Technology, Kraków, Poland

Keywords *Circuit elements, Filtration, Current reference diodes, Power measurement, Power transistors, Supply*

Abstract *Numerous types of shunt active power filters have been proposed in many papers. The classification of these filters depends on various points of view. However, every type of a shunt active filter, which compensates non-active component of load current, irrespective of the method used to detect this component and control strategies of the filter, should keep supply source current equal to active current of a load-and-filter circuit. This goal can be achieved in many ways, using various structures of active filters. But different realizations of filters cause differences in their properties. This paper, which is meant to serve as a review and synthesis of earlier work, shows some possibilities of forming of single-phase shunt active filter behaviour. The following active filter properties are discussed: operation with an immediate reaction in the supplying source branch to a load current change, and with the reaction only once in each supplying source cycle; regulation by the filter of the non-active current component of fundamental frequency; active filtering and simultaneous feeding of DC load with stabilizing DC voltage; operation with stabilization of supplying source current amplitude; reducing filter switching frequency; and reducing current distortions in the supplying source branch. All the waveforms presented were produced using a computer simulation method.*

1. Introduction

In order to reduce variable non-active current in the supplying source branch, it is necessary to use a controlled current source as a compensator. This type of compensator is called a shunt active power filter. The behaviour of the compensated load needs to be continuously monitored by the filter so that the source current could be properly regulated. A basic structure and characterization of the main stages of the active filter is shown in Figure 1 (see also Figure 16).

1.1 Measure-and-control stage

As Fryze's split method of load current (Fryze, 1932) indicates, the current may be completely characterized by its two time-dependent components:

$$i_{\text{load}} = i_p + i_q \tag{1}$$

where i_p and i_q are active and non-active load current components, respectively.

This stage is designed to measure currents and voltages and to determine the load current active (or non-active) component reference run. At the same time, this stage has to control the level of energy stored in the active filter energy container. It may be

COMPEL: The International Journal for Computation and Mathematics in Electrical and Electronic Engineering
Vol. 23 No. 4, 2004
pp. 1146-1162
© Emerald Group Publishing Limited
0332-1649
DOI 10.1108/03321640410510857

This is a revised and enhanced version of a paper which was originally presented as a conference contribution at the *XVII Symposium on Electromagnetic Phenomena in Nonlinear Circuits (EPNC)*, held in Leuven, Belgium, on 1-3 July 2002. This is one of a small selection of papers from the Symposium to appear in the current and future issues on *COMPEL.*

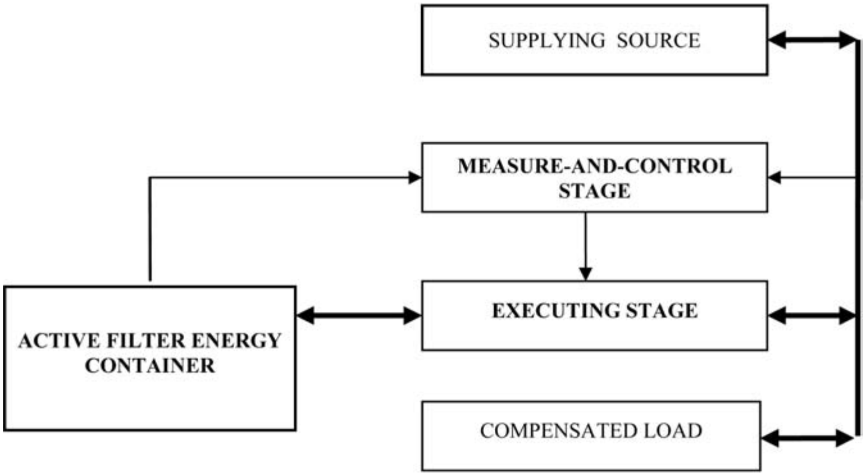

Figure 1.
Block diagram of a shunt active filter (with supplying source and compensated load)

necessary to calculate the additional current components if the performance properties of the filter are to be improved.

1.2 Active filter's energy container

An electrical energy-storing element is necessary to make it possible to generate a non-active current cyclical flow between the filter and the source. This current flow must be of suitable dynamics and magnitude. A capacitor or an inductive coil can be employed as this energy-storing element. Capacitors are preferable because of their greater efficiency in the transfer of energy.

1.3 Executing stage

This stage is a controlled bi-directional channel, transmitting appropriate amounts of energy between the filter energy container and the source.

2. Control circuit structures

Any active filter compensating the non-active load current component, irrespective of its control method, should maintain the source current at a level that is equal to that of the active current component of the compensated load (plus the active filter's). This goal can be achieved using a sample active filter structure, shown in Figure 2.

The active filter (Figure 2) operates as follows: the active current component of the entire circuit (compensated load and the filter) is continuously determined and used as a reference run for source current. While that process continues, the source current is being compared with the reference run. The filter is controlled in such a way as to keep the error (referred to as ε) within a permissible range of ΔI. It should be noticed that the filter forces the reference current not in its own branch, but indirectly – based on Kirchhoff's current law – in the source branch. The filter current, which is a sum of the non-active component of load current and the filter active current, does not need to be monitored by the filter's control circuit. However, this may lead to overcurrent through the filter elements.

This filter structure can be modified to produce some different properties of the filter.

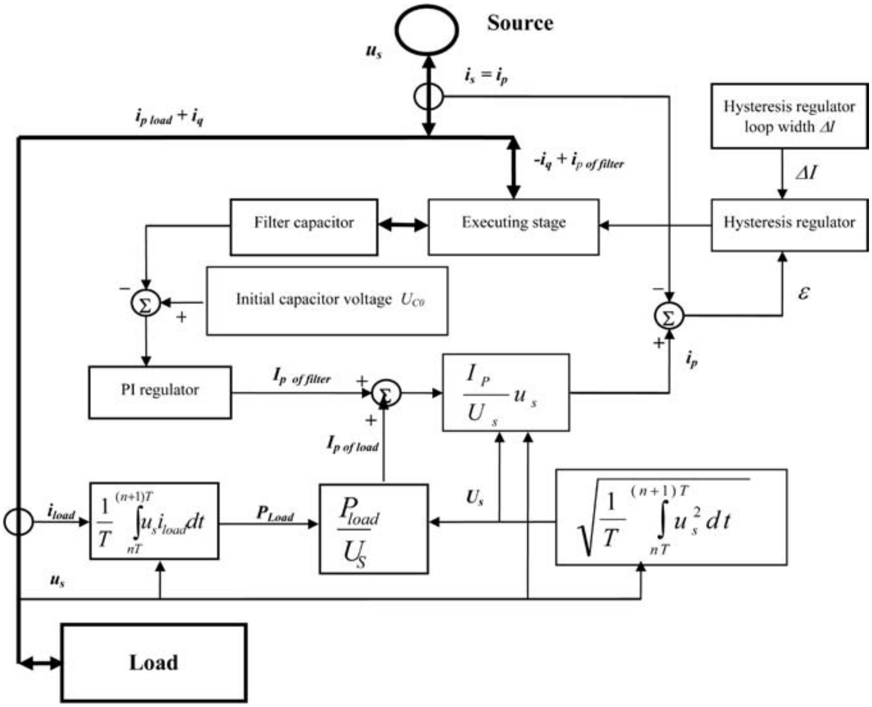
Source
u_s
$i_s = i_p$
$i_{p\,load} + i_q$
$-i_q + i_{p\,of\,filter}$
Hysteresis regulator loop width ΔI
ΔI
Filter capacitor
Executing stage
Hysteresis regulator
−
+
Initial capacitor voltage U_{C0}
−
+
ε
PI regulator
$I_{p\ of\ filter}$
+
+
$\frac{I_P}{U_s} u_s$
i_p
$I_{p\ of\ load}$
i_{load}
$\frac{1}{T}\int_{nT}^{(n+1)T} u_s i_{load} dt$
P_{Load}
$\frac{P_{load}}{U_S}$
U_s
$\sqrt{\frac{1}{T}\int_{nT}^{(n+1)T} u_s^2 dt}$
u_s
Load

Figure 2.
Active filter structure. The load and the active filter active current components constitute the reference run. Only the source current is monitored

(1) In Figure 3, the non-active current component of load (plus the filter active one) is the reference run for the whole filter current. The filter controls the current in its own branch, but keeps the source current equal to active current component of the whole load-and-filter circuit. The filter current is checked in this method and the filter elements may be protected from overload.

(2) It is possible to adjust the filter to a required range of harmonics, using a properly tuned pass-filter. If it is needed, the active filter may compensate only higher harmonics of load current. The fundamental frequency of the non-active load current component may be compensated by passive circuit here. Passive filters are considerably cheaper, but are much less efficient than active ones. An active filter operating in parallel with a passive one may be constructed using cheaper components of lower power rating. Both of the above-mentioned modifications are introduced in the structure shown in Figure 3.

(3) This is not the only scenario for the operation of an active filter. An active filter may also be designed to compensate the non-active current component of the fundamental frequency only, leaving harmonics for tuned LC passive filters. This concept makes it possible to avoid the main drawbacks of "passive technology" which are the large size of passive elements and resonance oscillations.

While in operation, each type of active filter follows the source current, compares it to the reference run, adjusting its shape if compensated load changes. This correction

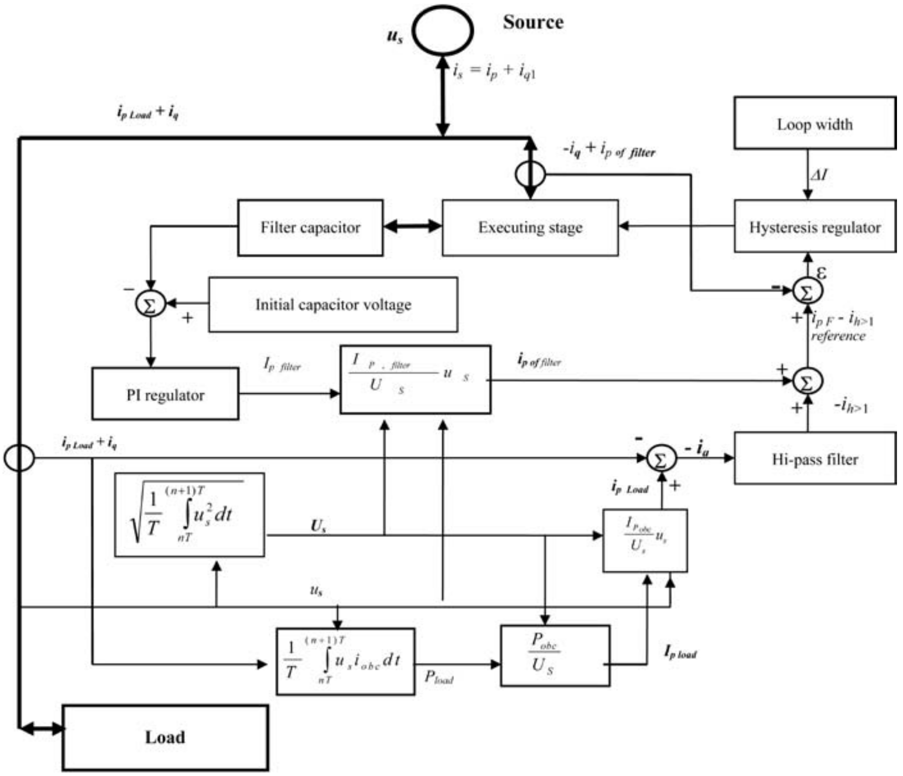
Source
u_s
$i_s = i_p + i_{q1}$
$i_{p\,Load} + i_q$
$-i_q + i_{p\ of\ filter}$
Loop width
ΔI
Filter capacitor
Executing stage
Hysteresis regulator
ε
−
+
Initial capacitor voltage
$i_{p\,F} - i_{h>1}$ reference
PI regulator
$I_{p\ filter}$
$\frac{I_{p.\,filter}}{U_s} u_s$
$i_{p\ of\ filter}$
$-i_{h>1}$
$i_{p\,Load} + i_q$
$-i_q$
Hi-pass filter
$i_{p\,Load}$
$\sqrt{\frac{1}{T}\int_{nT}^{(n+1)T} u_s^2\,dt}$
U_s
$\frac{I_{P_{abc}}}{U_s} u_s$
u_s
$\frac{1}{T}\int_{nT}^{(n+1)T} u_s i_{abc}\,dt$
P_{load}
$\frac{P_{abc}}{U_S}$
$I_{p\ load}$
Load

Figure 3.
Active filter compensating only higher harmonics of load current

may be carried out immediately after the load is changed (Delarue and Bausiere, 1995; Ohnuki *et al.*, 1995), so the source current changes whenever load changes. If the load changes continuously, the source current is always deformed, but in spite of that the source current shape may be considerably improved.

The ideal shunt active filter should maintain the ideal sinusoidal waveform of source current. This is difficult to achieve because of:

(1) load changes – the filter must not influence them, but should adapt to them; and because of the filter's internal imperfection:

(2) the operation of its switches; and

(3) changes in the filter capacitor voltage due to non-active current compensation (see the steady-state areas in Figures 10 and 11).

There are ways to counteract the problems: case (2) requires filtration of current and/or applying a shorter hysteresis loop width; cases (1) and (3) lead to the synchronized manner of operation of the active filter.

The synchronized filter maintains a non-deformed sinusoidal shape of source current in every separately observed source T period. The source voltage run is utilised as a metronome for measuring time intervals, within which the load active power is considered as invariable. The amplitude of source current in every T period is always predicted at the very beginning of each source cycle, on the basis of the load power from foregoing T_{n-1} period (Piróg, 1997; Szromba, 1996, 1999, 2001, 2002). The active filter is synchronized at these moments. It can be seen that energy flowing from the source to the load is shifted (late) for one T period. This does not have any impact on the operation of the load, but is very useful when it comes to improving the quality of the operation of the source: the source current's sinusoidal amplitude cannot change within any T period. The filter balances the flowing energy, operates as the energy buffer and, simultaneously, as a controlled current source which compensates non-active current component in the source branch.

The level of energy stored in the filter (mostly in the filter capacitor) may be used to calculate the active power of compensated load, its equivalent conductance and, finally, the load active current component amplitude (Piróg, 1997). The simplified equation, excluding the energy stored in the input inductance of the filter (see Figure 4 with its caption, and also Figure 16), is expressed in equation (2).

Expression (2) may be implemented as the basic scheme of any circuit, which predicts the active current reference run (Figure 5). The explanation for the markers A and B is given in Section 4.

$$i_{p,T(n)} = G_{T(n-1)}u_{\mathrm{s}} = \frac{C\left(U_0^2 - U_{C,T(n-1)}^2\right)}{2TU_{\mathrm{s}}^2}u_{\mathrm{s}} = K_u\left(U_0^2 - U_{C,T(n-1)}^2\right)u_{\mathrm{s}} \qquad (2)$$

where $G_{T(n-1)}$ is the equivalent load conductance for T_{n-1} period; C is the capacitance of the filter capacitor (the energy container); U_0 is the C capacitor initial voltage $U_{C,T(n-1)}$ is the C capacitor voltage at the end of $(n-1)$th T period; and U_{s} is the RMS of the voltage source.

All remarks relating to the structures shown in Figures 1-3 are valid for the filter arrangement shown in Figure 6. This filter's structure is fundamental for further considerations.

3. Forcing predefined power factor

A sinusoidal non-active current component of fundamental frequency, usually of inductive type, is very often included in the total source current. Its complete compensation is often dispensable, because in many cases this current inductive component is tolerated under permission of electric utility companies. In this situation, the power factor of the compensated load can be controlled or kept constant a little less than the ideal power factor, which should be as near unity as possible. Such action is beneficial, because the active filter current can be lowered, so energy losses across semiconductor switches of the filter can be diminished (Piróg, 1997; Szromba, 1999).

Incomplete compensation of non-active current component of fundamental frequency may be expressed using the tangent function as:

$$\mathrm{tg}(\varphi) = \frac{I_q}{I_p} = \mathrm{const.} \qquad (3)$$

After several transformations, the reference run for the component to be left in the source current within T_n period of source cycle is like in equation (4):

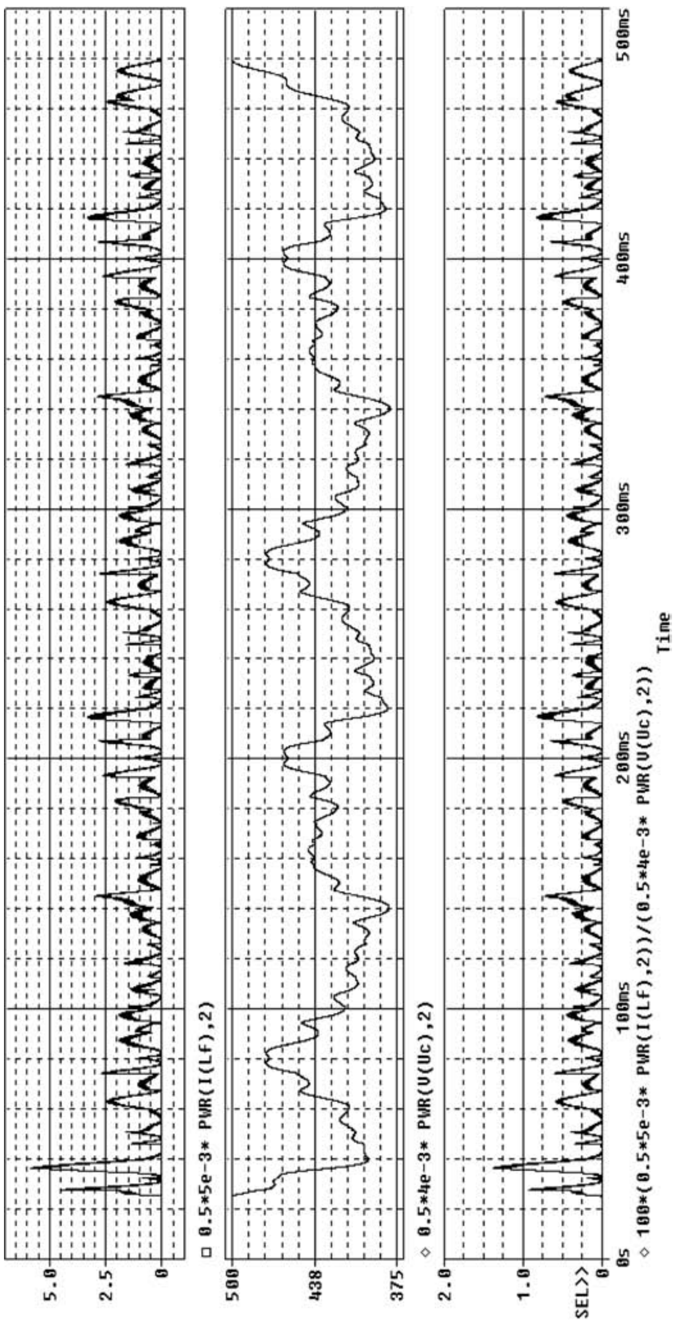

Figure 4.
Active filter in operation – reason for skipping energy stored in the input inductance of the active filter (top to down): energy stored in filter inductance ($L = 5\,\mathrm{mH}$); energy stored in filter capacitor ($C = 4\,\mathrm{mF}$, $U_0 = 500\,\mathrm{V}$); percentage ratio of these energies – it is almost always less than 0.5 per cent

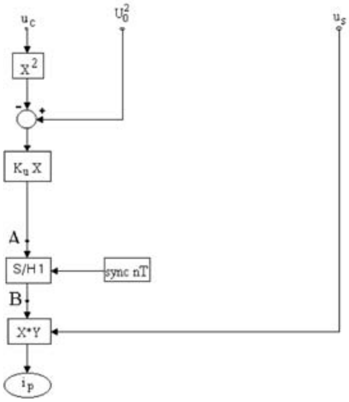
u_C
U_0^2
u_s
X^2
-
+
K_u X
A
S/H 1
sync nT
B
X*Y
i_p

Figure 5.
Block diagram for calculating reference run for load active current, based on equation (2). The S/H 1 block operates as a sample-and-hold device

$$i_{p,T(n)} = G_{T(n-1)} u_s = \frac{C(U_0^2 - U_{C,T(n-1)}^2)}{2TU_s^2} u_s = K_u(U_0^2 - U_{C,T(n-1)}^2) u_s \tag{2}$$

$G_{T(n-1)}$ – equivalent load conductance for T_{n-1} period
C – capacitance of the filter capacitor (the energy container)
U_0 – the C capacitor initial voltage
$U_{C,T(n-1)}$ – the C capacitor voltage at the end of (n-1)-th T period
U_s – the *RMS* of the voltage source

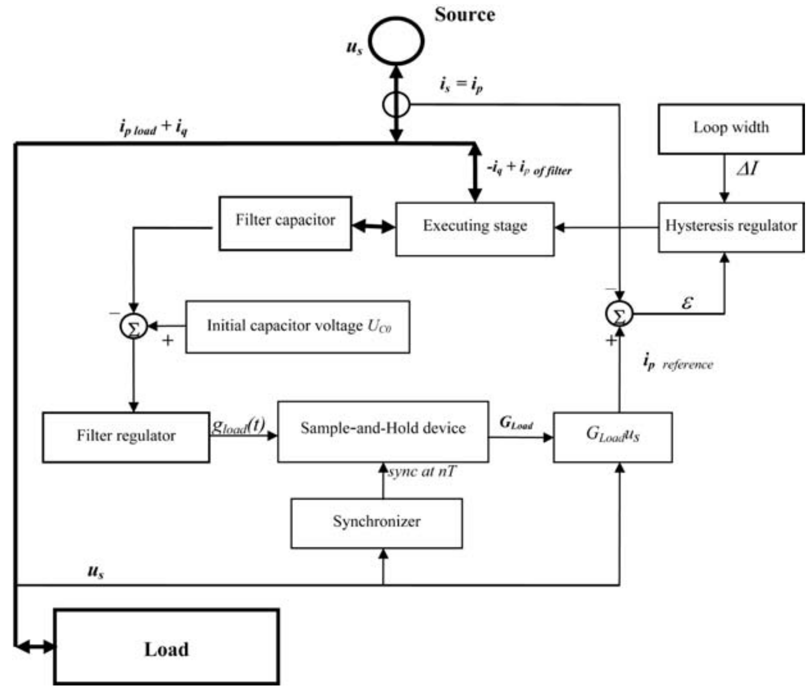
Source
u_s
i_s = i_p
i_p load + i_q
-i_q + i_p of filter
Loop width
ΔI
Filter capacitor
Executing stage
Hysteresis regulator
−
+
Initial capacitor voltage U_C0
ε
i_p reference
Filter regulator
g_load(t)
Sample-and-Hold device
G_Load
G_Load u_S
sync at nT
Synchronizer
u_s
Load

Figure 6.
Synchronized active filter structure

$$i_{\mathrm{qref},T(n)} = 1_{\mathrm{L}}\sqrt{2}G_{T(n-1)}U_{\mathrm{s}}\mathrm{tg}(\varphi) \tag{4}$$

where 1_{L} is the sinusoidal inductive current run with the unitary amplitude.

This non-active current component should be added to the active current reference and then realized by the filter as a new reference run. The example-effect, if expression (4) is implemented, is shown in Figures 7 and 8.

The active filter can also be controlled to generate a non-active current component of capacitive type with constant (as in equation (3)) or variable I_q/I_p ratio.

4. Stabilization of filter capacitor voltage

The filter capacitor must perform two functions simultaneously, during active filter operation.

1. It functions as an energy store. The energy stored in it enables us to force current in the source-filter branch of expected shape and thus the non-active source current can be neutralized.
2. It operates as a "sensor" of load equivalent conductance (see expression (2)).

Changes of capacitor DC voltage are necessary to obtain active current amplitude, but from the other hand, the changes are unfavourable due to the following.

- Value of the load active power is limited, because voltage across the capacitor must be considerably higher than the amplitude of the source voltage at any moment of filter operation.

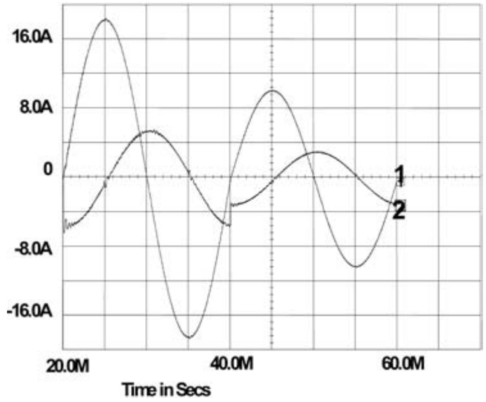

Figure 7. Two current reference waveforms: load active component (1) and the inductive component (2) to be left in source current at $\mathrm{tg}(\varphi) = 0.3$

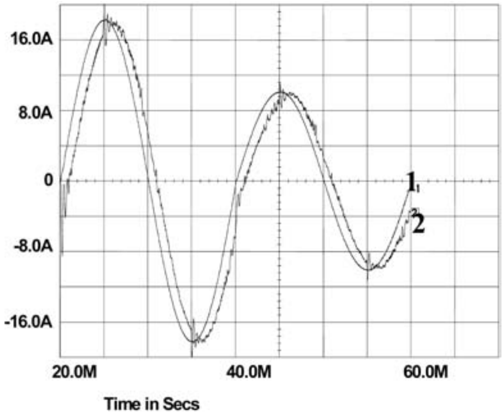

Figure 8. Load active current component (1) and source current (2) with the inductive component (the waveform 2 is realized by the filter as the sum of waveforms shown in Figure 7), $\mathrm{tg}(\varphi) = 0.3$

- Dynamic properties of the filter are worse because the speed of changes of active filter current, which determines the ability to follow rapid load changes, depends on the filter capacitor voltage and the source voltage difference.
- If the active filter operates simultaneously as a rectifier (Figure 16), its rectifying properties deteriorate.

An additional sub-circuit may be provided to the filter to reduce these inconveniences (Figure 9) (Piróg, 1997; Szromba, 1996). The operation principle of the sub-circuit is based on memorizing successive filter capacitor voltage changes. The sub-circuit is built using sample-and-hold (S/H) devices and adders. The position of the sub-circuit in the control algorithm-scheme of the filter is defined by points *A* and *B* (Figure 5).

If the stabilizing sub-circuit is applied, the capacitor of the active filter does not have to perform the task of indicating the existing active load power and its charge can be supplemented from the source. This happens due to the fact that active filter's control circuit allows for the doubling of the source current in the next *T* period after the load change (see the current waveform in Figure 10).

The voltage condition $u_c \gg u_s$ (the capacitor voltage considerably higher than the peak source voltage) should not be referred to the total active power of the load, but to the maximal change of the power during a single *T* period of the source cycle.

The effect of operation of the memorizing circuit on the capacitor voltage is shown in Figure 10 (on comparing, the load current is the same as shown in Figure 11).

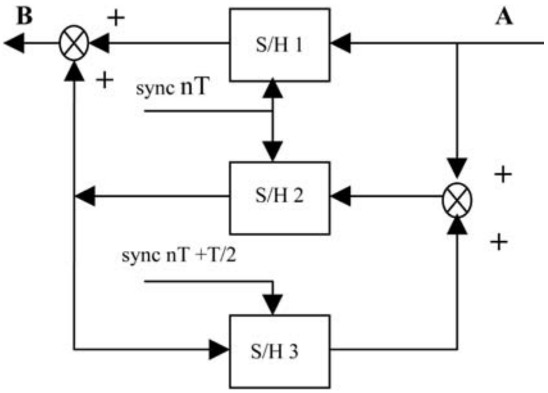

Figure 9.
Sub-circuit for stabilizing voltage across the capacitor of the active filter

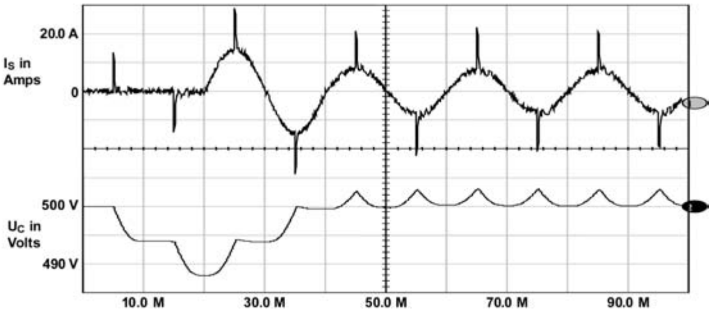

Figure 10.
Source current (upper) and filter capacitor voltage (the stabilizing circuit is used). Start and steady-state operation of the source-filter -compensated load circuit, with load current being the same as in Figure 11

It should be mentioned that – if the stabilizing sub-circuit is in operation – in the next T period after switching the load out of operation, the active filter gives back "the additional" amount of energy (drawn to supplement the capacitor's charge) to the source.

5. Stabilization of source current amplitude

The synchronized active filter presented, maintaining sinusoidal source current in each, separately considered T period, is not concerned with changes in the source current amplitude between the adjacent periods. This is perhaps not optimal. In the case of frequent power changes of compensated load, source current amplitude can be different in every T period. If the filter is regulated in such a manner that the source current amplitude is near its average value in a range of several T periods, the quality of the source operation will be higher. Such a goal can be achieved, in the case of the filter presented, by regulating the filter control coefficient, called: $K_u = C/2TU_s^2$ (see equation (2)).

The value of the K_u coefficient is determined with the assumption of energy balancing in every T period in the circuit: source – compensated load – active filter. Let us assume that this coefficient's value is called nominal. However, if the value of the coefficient is applied lower than the nominal level (keeping C, T and U_s constant), the energy (controlled by the filter) flowing from the source is not balanced exactly in the T period within the load changes. The action of reaching the steady-state will be spread on several subsequent T periods. If within this time period the load power changes in the opposite direction (e.g. first rises and then falls or vice versa) then the load equivalent conductance G will be averaged in some way. The filter capacitor is the energy buffer (between the source and load) in this situation. Consequently, the RMS of source current is lower (there is no change in the active power of compensated load, which is obvious).

There are two waveforms in Figure 12. The first one is the current of an example load to be compensated. The second waveform is the source current while the K_u coefficient is nominal.

The waveforms in Figure 13 show the source current for the coefficient K_u set at 25 per cent of its nominal value, and for two-state K_u regulation (Szromba, 2002).

The manner of the reduction of source current RMS, illustrated by the first waveform (Figure 13), is associated with the longer time of reaching the steady-state,

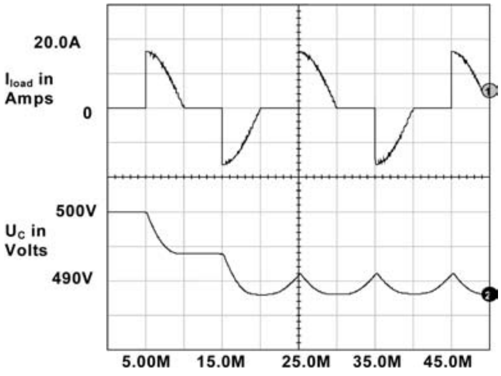

Figure 11.
Current of compensated load and the filter capacitor voltage. Start and the steady-state operation of the source-filter-load circuit

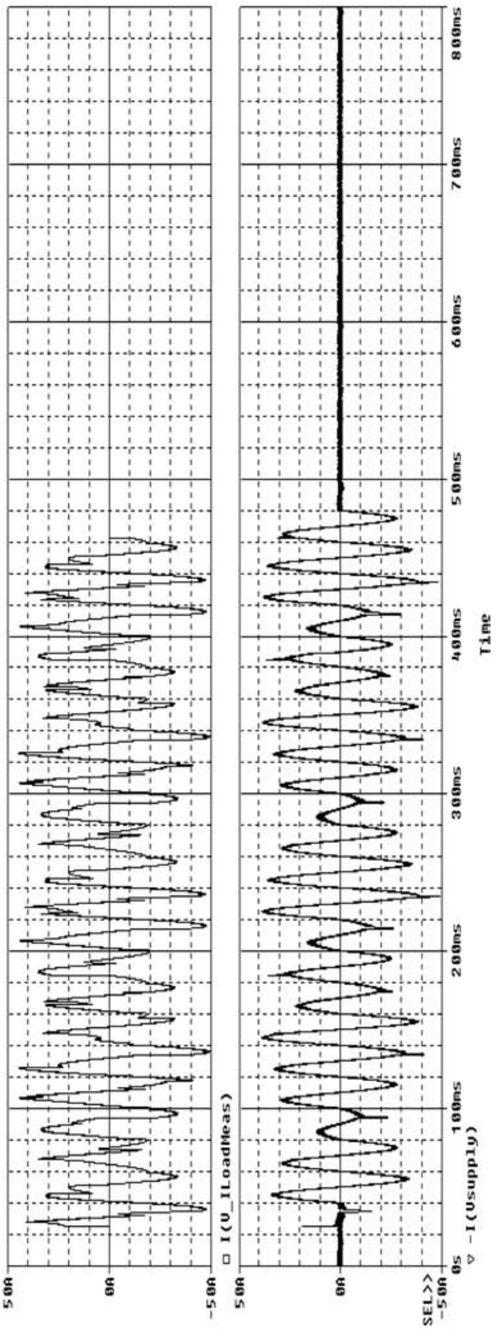

Figure 12.
Compensated load current and the source current before the K_u coefficient regulation

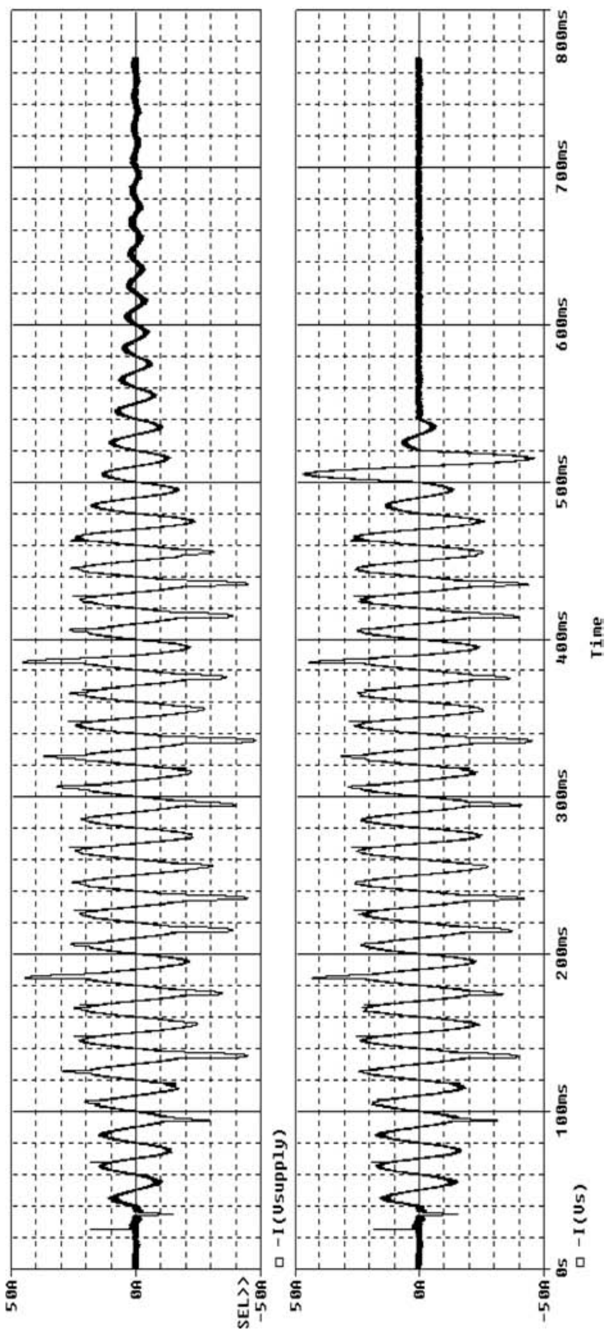

Figure 13.
Source current after the K_u
coefficient regulation
(in two ways)

when the filter (or compensated load) starts or ends its operation. However, if the K_u has its nominal value only during the first and last T period when the filter is loaded, and is diminished between these periods, this inconvenience of filter behaviour may be reduced. The two-state K_u regulation method offers such an opportunity. The filter operates by averaging the source current changes, due to averaging changes of the load equivalent conductance. After the last T period, within which the load draws energy from source, the K_u coefficient returns to its nominal value. This produces the same effect as an increase of equivalent conductance, and the filter forces more energy from source to bring the capacitor voltage to its initial level U_0 (see equation (2) and the second waveform in Figure 13).

Current non-active components, flowing through the source, are significantly reduced within some range around the fundamental frequency. For the example discussed (Figures 12 and 14), the RMS of compensated load current is equal to 23.1 A (its "pure" active component is equal to 16.8 A). The RMS of source current is reduced from 19.2 A (the second waveform in Figure 12) to 17 A (the first waveform in Figures 13, see also Figures 14 and 15) and to 17.5 A (for the second waveform in Figure 13).

The amplitude of the source current is smaller in Figure 15 than in Figure 14, due to the longer time of operation of the source if K_u coefficient is set below its nominal value (see the first waveform in Figure 13). The load current (or work) is naturally the same before and after reduction of the K_u coefficient.

6. Reduction of filter switching frequency

The base diagram of the power circuit of the filter being analysed is shown in Figure 16.

The formulas in equation (5) are a formal mathematical model valid for the currents and voltages shown in Figure 16. The σ coefficient is equal to +1 when the NA-PB pair of switches is in state ON, and -1 when the NB-PA pair is in state ON.

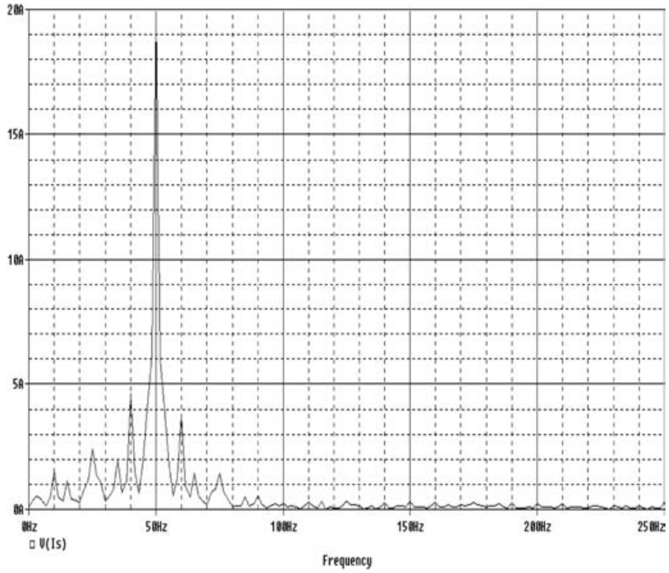

Figure 14.
Frequency characteristic of source current, the filter is present and K_u coefficient has its nominal value

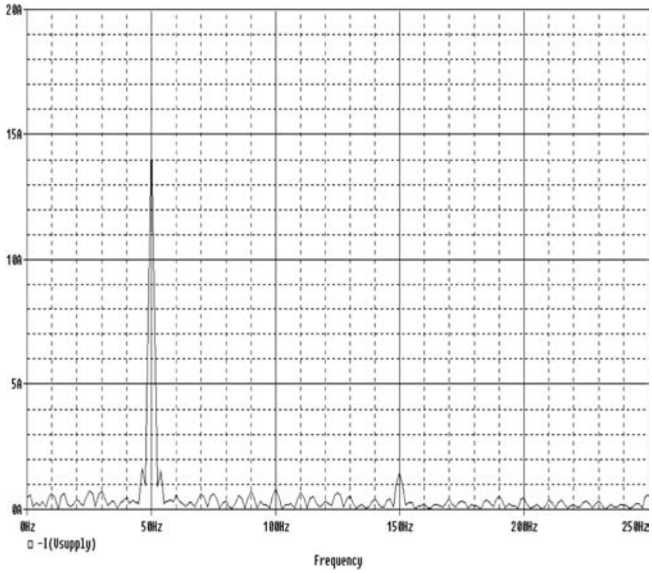

Figure 15.
Frequency characteristic of source current, when K_u coefficient is set at 25 per cent of its nominal value

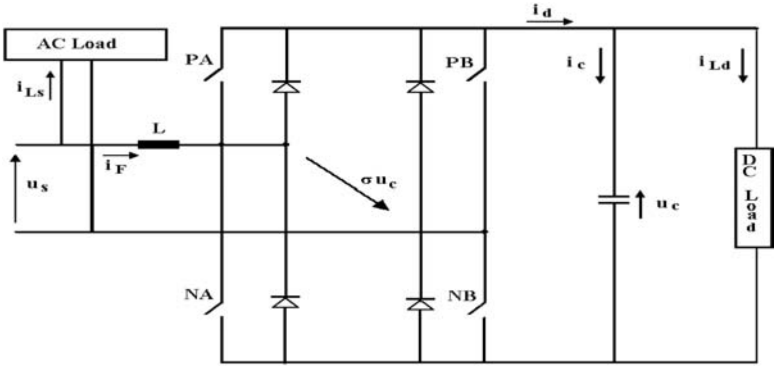

Figure 16.
Base diagram of power circuit of the active filter

$$\frac{\mathrm{d}i_\mathrm{s}}{\mathrm{d}t} = \frac{u_\mathrm{s} + \sigma u_\mathrm{c}}{L} + \frac{\mathrm{d}i_\mathrm{Ls}}{\mathrm{d}t} \quad \frac{\mathrm{d}u_\mathrm{c}}{\mathrm{d}t} = \frac{\sigma(i_\mathrm{Ls} - i_\mathrm{s}) - i_\mathrm{Ld}}{C} \tag{5}$$

If the active filter operates properly, the source current vector I_s and the source voltage vector U_s have the same direction. If the AC load is switched off, and the DC load is switched on, source current is equal to filter current: $i_\mathrm{s} = i_\mathrm{F}$. The active filter functions as a rectifier drawing sinusoidal and in-phase (with voltage) source current. If AC load operates ($i_\mathrm{Ls} \neq 0$), the filter current is not the same as source one ($i_\mathrm{F} \neq i_\mathrm{s}$), and the direction of the source current can be different from the direction of the filter current. In this case, the active filter performs the filtering and, simultaneously, the rectifying function.

The control circuit of the filter contains a hysteresis regulator which controls filter switches PA, PB, NA, NB (Figure 6). The switches are controlled in such a way as to shape the source current i_s to be sinusoidal and in-phase with the source voltage u_s, and the amplitude of the current has to be defined in proportion to the sum of the AC and the DC load active power.

The analysis of the operation of the switches indicates (Szromba, 2001) that it is possible to diminish the switching frequency. It can be done by replacing the sum of the voltages ($u_s + u_c$) by the source voltage u_s. To execute this plan, the pair NA-NB (or the pair PA-PB that produces the same effect) should be turned ON in a required period of time. Formally, this may be done by introducing a new state for the filter switches, namely $\sigma = 0$ (formula (5)).

Results obtained in this way are shown in Figure 17. In the most critical area before, when the source voltage is nearly zero (around the middle vertical line in Figure 17), the filter switches are almost not commuted. So, energy consumed by the active filter's semiconductor switches is lowered.

7. Reduction of current distortions in source branch

The amplitude of high frequency current component, appearing in the source current during the operation of an active filter, can be reduced. This may be effected using two principal methods: filtration of current and/or reducing the active filter regulator's hysteresis loop width. The circuit shown in Figure 18 outlines the idea of the filtration method. It consists of the capacitor CF, the in parallel resistor RR and the damping in series resistor RF. The passive filter, connected in parallel to the active filter, reduces the "from active filter" high frequency current component in the source branch. It may be based on a capacitor instead of the tuned LC circuit because of the frequency range

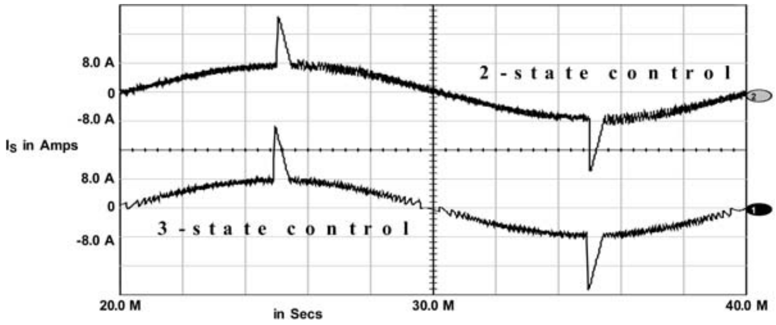

Figure 17.
Source current waveform before and after introducing additional $\sigma = 0$ state for active filter switches. The load current shape is shown in Figure 11

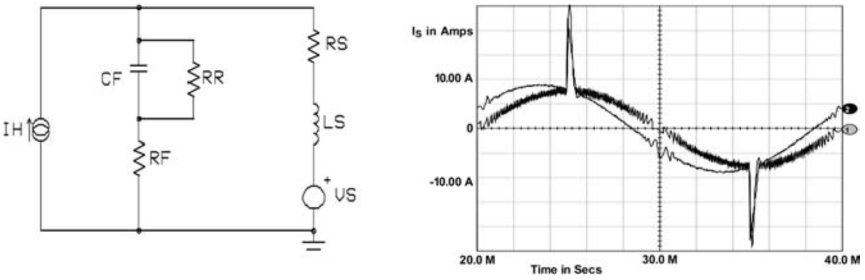

Figure 18.
Schematic of shunt passive filter and its location. Source current waveform: (a) before passive filtration, and (b) with the passive filter. The three-state control method is used

rather than the single frequency of the operation of switches in an active filter (see the first of equation (5)).

The result of the filtration is shown by the second diagram in Figure 18. The "thick" waveform shows the source current without, and the "thin" waveform with, the passive filter as the suppressor. The amplitude of high frequency component has been reduced, but the current run contains the capacitive component (the source current is shifted towards the capacitive type of current).

But the active filter is able to operate with the predefined power factor (see Section 3), and can compensate the passive filter current. This active and passive filter cooperation is shown by the first waveform in Figure 19.

Equation (5) implies that the lower input inductance of the filter is used (or the higher voltage is applied across the active filter capacitor), the more dynamically can the active filter shape the current in its own and in the source branch. Unfortunately, it increases the commutation frequency of the filter switches, and more power is consumed by the filter. However, using the three-state control method (Section 6) one can lower the active filter input inductance (see Figure 16 and equation (5)) without increasing the switching frequency. It gives an opportunity to reduce the amplitude of the kick impulses at the moment when the load rapidly changes. The effect achieved by this way is shown in Figure 19: as the difference of current transients between both the waveforms. This effect may be considerably improved if the compensated load can be connected to the source through a reactor. The active filter has a little more time available to reduce the current transient in this case.

8. Conclusion

A shunt (parallel) active filter is not a "panacea" which can completely eliminate non-active current from an AC supply system, but it often effectively and flexibly improve the power factor and contribute to an improved frequency characteristic of source current. While operating jointly with the source, the filter is able to generate non-active current of almost any shape through the source branch. The possibility of forcing such type of reactive currents may be used to compensate non-linear and varying loads. It can help to obtain the required quality of source operation.

The method of the addition of filter current to the source-load circuit is very important. The synchronized filter can maintain non-deformed source current within

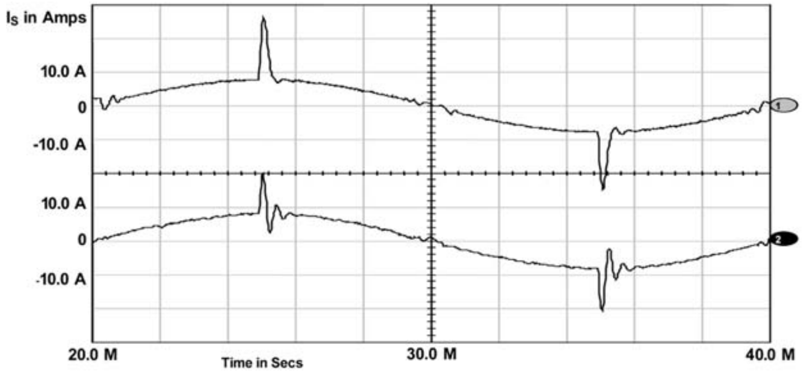

Figure 19. Source current waveform if: the passive filter is present, the capacitive current component is compensated, the three-state control is used; and (the second waveform) the lower inductance of the active filter is applied (from 5 to 2 mH)

each source cycle. It eliminates the impact that continuous load changes and varying voltage across the filter capacitor (resulting from the compensation of non-active current) have on the concurrent sinusoidal shape of the source current.

There are many methods for diminishing distortions of source current that are produced during the operation of an active filter. One can add an additional passive filter and/or improve the active filter parameters, for example, dynamic properties and frequency characteristic of the active filter current.

The functional elements, shown in Figures 5 and 9 for example, are used only as an explanation of how some ideas (of improving the filter properties) may be materialized in the circuit. They may be successfully realized as well as software procedures, using the microprocessor technique.

References

Delarue, P. and Bausiere, R. (1995), "New control method for active power filter needing line current measurement only", *European Conference on Power Electronics and Applications*, Sevilla, Spain, pp. 1.914-19.

Fryze, S. (1932), "Wirk-, Blind-, und Scheinleistung in Elektrischen Stromkreisen mit nichtsinusformigem Verlauf von Strom und Spannung", ETZ, Vol. 53, pp. 596-599, 625-627, 700-702.

Ohnuki, T., Miyashita, O., Lataire, P. and Tomita, H. (1995), "Power conditioning of single-phase AC-DC converters in parallel", *European Conference on Power Electronics and Applications*, Sevilla, Spain, pp. 3.033-8.

Piróg, S. (1997), "PWM rectifier and active filter with sliding-mode control", *European Conference on Power Electronics and Applications*, Trondheim, Norway, pp. 4.831-6.

Szromba, A. (1996), "Some innovations in a shunt active filter", *XIX National Conference on Circuit Theory and Electronic Networks*, Cracow, Poland, pp. 151-5.

Szromba, A. (1999), "Compensation of load non-active current with forcing predefined power factor", *XXII National Conference on Circuit Theory and Electronic Networks*, Warsaw, Poland, pp. 387-92.

Szromba, A. (2001), "Voltage-source shunt active filter", *International Scientific Conference Energy Savings in Electrical Engineering*, Warsaw, Poland, pp. 88-92.

Szromba, A. (2002), "Active filter with stabilization of source current amplitude", *Electromagnetic Phenomena in Nonlinear Circuits*, Leuven, Belgium, pp. 191-4.

Awards for Excellence

Federico Delfino
Department of Electrical Engineering, University of Genova, Genova, Italy

Renato Procopio
Department of Electrical Engineering, University of Genova, Genova, Italy

Mansueto Rossi
Department of Electrical Engineering, University of Genova, Genova, Italy

and

Mario Nervi
Department of Electrical Engineering, University of Genova, Genova, Italy

are the recipients of the journal's Outstanding Paper Award for Excellence for their paper

"A full-Maxwell algorithm for the field-to-multiconductor line-coupling problem"

which appeared in ***COMPEL***, Vol. 22 No. 3, 2003

Federico Delfino was born in Savona, Italy, on 28 February, 1972. He graduated cum laude in Electrical Engineering from the University of Genoa, in 1997 and received the PhD degree from the same University in 2001. He is currently a Researcher at the Department of Electrical Engineering of the University of Genoa. His research interests are mainly focused on electromagnetic field theory, numerical techniques applied to electromagnetic compatibility and transmission line modeling. He is the author or coauthor of more than 40 scientific papers presented at international conferences and published in reviewed journals.

Dr Delfino is a Member of the Institute of Electrical and Electronics Engineers (IEEE) and the Italian Association of Electrical Engineers (AEI).

Renato Procopio was born in Savona, Italy, on 6 March, 1974. He graduated cum laude in Electrical Engineering from the University of Genoa, in 1999 and received the PhD degree from the same University in 2003. He is currently a Researcher at the Department of Electrical Engineering of the University of Genoa. His research interests are mainly focused on electromagnetic field theory, numerical techniques applied to electromagnetic compatibility and transmission line modeling, as well as power quality and custom power devices. He is the author or coauthor of more than 25 scientific papers presented at international conferences and published in reviewed journals.

Dr Procopio is a Student Member of the Institute of Electrical and Electronics Engineers (IEEE).

Mansueto Rossi was born in Savona, Italy, in 1974. He received the Laurea degree cum laude in electrical engineering in 2000 from the University of Genova and the PhD degree at the Department of Electrical Engineering of the same University in 2004.

He is a member of the Italian Association of Electrical Engineers (AEI).

His research interests concern mainly numerical methods for electromagnetic field analysis, lightning modeling and the evaluation of the electromagnetic field to line coupling effects in non-ideal conditions.

Mario Nervi was born in 1964 in Savona, Italy; he graduated with full marks and honours in Electrical Engineering in 1989 at the University of Genova, with a dissertation about the design of resistive toroidal coils for Tokamak fusion machines. During 1990, he worked for the European Commission, as temporary research agent, and was involved in the electromagnetic design of Tokamak fusion machines. During his PhD research (1991-1993) he studied the gauging conditions of 3D nodal finite element potential based formulations. He is now Associate Professor at the Department of Electrical Engineering of the University of Genova, where he teaches Electric Circuits and Electromagnetic Fields. He wrote more than 50 papers about numerical methods for the solution of electromagnetic field problems, project optimisation, finite element formulations for the solution of electromagnetic field problems, and numerical models for electromagnetic compatibility. Currently his research activity is addressed to a project, co-funded by the Italian Ministry of University and Research, about advanced methods for the forecast of the distribution of electromagnetic field for mobile GSM and UMTS telephony systems and channel allocation optimisation in urban environment.